

## **EUSPEN : proceedings of the 3rd international conference, May 26-30, 2002, Eindhoven, The Netherlands**

***Citation for published version (APA):***

Delbressine, F. L. M., Schellekens, P. H. J., Homburg, F. G. A., & Haitjema, H. (Eds.) (2002). *EUSPEN : proceedings of the 3rd international conference, May 26-30, 2002, Eindhoven, The Netherlands*. Technische Universiteit Eindhoven.

***Document status and date:***

Published: 01/01/2002

***Document Version:***

Publisher's PDF, also known as Version of Record (includes final page, issue and volume numbers)

***Please check the document version of this publication:***

- A submitted manuscript is the version of the article upon submission and before peer-review. There can be important differences between the submitted version and the official published version of record. People interested in the research are advised to contact the author for the final version of the publication, or visit the DOI to the publisher's website.
- The final author version and the galley proof are versions of the publication after peer review.
- The final published version features the final layout of the paper including the volume, issue and page numbers.

[Link to publication](#)

***General rights***

Copyright and moral rights for the publications made accessible in the public portal are retained by the authors and/or other copyright owners and it is a condition of accessing publications that users recognise and abide by the legal requirements associated with these rights.

- Users may download and print one copy of any publication from the public portal for the purpose of private study or research.
- You may not further distribute the material or use it for any profit-making activity or commercial gain
- You may freely distribute the URL identifying the publication in the public portal.

If the publication is distributed under the terms of Article 25fa of the Dutch Copyright Act, indicated by the "Taverne" license above, please follow below link for the End User Agreement:

[www.tue.nl/taverne](http://www.tue.nl/taverne)

***Take down policy***

If you believe that this document breaches copyright please contact us at:

[openaccess@tue.nl](mailto:openaccess@tue.nl)

providing details and we will investigate your claim.

proceedings of the

# 3rd International Conference and 4th General Meeting

of the **e**uropean **s**ociety for **p**recision **e**ngineering  
and **n**anotechnology

Volume 2



**euspen**

Editors:  
F.L.M. Delbressine  
P.H.J. Schellekens  
F.G.A. Homburg  
H. Haitjema

Proceedings of the 3<sup>rd</sup> International **euspen** Conference  
volume 1 /volume 2

© **euspen** headquarters, U.K.  
Building 70, Cranfield University, Bedford  
MK430AL, UK  
Phone: +44 (0)1234 754024  
Fax: +44(0)1234 751346  
e-mail: [d.corker@cranfield.ac.uk](mailto:d.corker@cranfield.ac.uk)  
URL: [www.euspen.org](http://www.euspen.org)

ISBN: 90-386-2883-8

*"This work is subject to copyright. All rights reserved, whether the whole or part of the material is concerned, specifically the rights of translation, reprinting, re-use of illustrations, recitation, reproduction and storage in database facilities. Duplication of this publication or parts thereof, is only permitted under the provision of the English Copyright Law. However, this does not restrict the author of a paper from printing and distributing his/her own paper for his/her own non commercial use."*

Printed in the Netherlands, May 2002  
Universiteitsdrukkerij TU Eindhoven  
P.O. Box 513  
5600 MB Eindhoven  
The Netherlands

## Contents

### Volume I

<i>Table of Contents</i>	V
<i>Opening session</i>	1
<i>Precision engineering design principles</i>	7
<i>Precision mechatronic design</i>	53
<i>Micro/nano systems</i>	111
<i>Ultra-precision motion systems</i>	141
<i>Precision engineering manufacturing methods/processes</i>	195

### Volume II

<i>Table of Contents</i>	V
<i>Micro fabrication and manipulation</i>	389
<i>Precision metrology for machines/manufacturing</i>	479
<i>Material properties</i>	661
<i>Sensors</i>	727
<i>Miscellaneous</i>	777





## Table of contents

<b>Opening session</b>	<b>1</b>
W. Menz, R. Förster, C. Müller, A. Schoth <i>Non-conventional Technologies for Fabrication of Microsystems</i>	3
<b>Precision engineering design principles</b>	<b>7</b>
C. Han, C. Lee <i>Development of a 4 DOF micro-positioning stage for error compensation</i>	9
S. Zelenika, S. Flechsig, F. De Bona <i>Analytical and Experimental Evaluation of Kinematic Couplings</i>	13
R.Haberland <i>Ultra-Precision Flexure Hinge Design and Applications</i>	17
M. Termeer <i>Modelling of dynamic behaviour and deformations in high precision instruments</i>	21
P. Fitsos , K. Yamazaki <i>Error budget modelling applied to the conceptual design of a novel 5-axis machine tool.</i>	25
J.K. van Seggelen, P.C.J.N. Rosielle, P.H.J. Schellekens <i>Design of a 3D CMM with elastically guided z-axis and x, y axis with less than 2 mm ABBE offset</i>	29
Y. Gao, Z. Yang, S. Tse, D. Zhang <i>Reduction of the spindle vibration using a compact absorber for surface grinding</i>	33
S. Y. Lim, W. Lin, Y.P. Leow <i>A Precision Decoupled Planar Positioning Stage</i>	37
T. Paardenkooper, P. Rosielle, J. Schouten <i>Design of an orthogonal 3 D scanning touch probe for 25 nm accuracy</i>	41
S. Donders <i>A non-distorting reticle clamp mechanism</i>	45
J.C. Compter, S.A.J. Hol, E. Lomonova <i>Lorentz actuators for nanometer accuracy</i>	49
<b>Precision mechatronic design</b>	<b>53</b>
N. Loix, A. Abu Hanieh, A. Preumont <i>Piezoelectric Stewart Platform for General Purpose Active Damping Interface and Precision Control.</i>	55
S. Dejima, W. Gao, S. Kiyono , Y. Tomita <i>Multi-degree of freedom precision stage system integrated with a surface encoder</i>	59
M. Negishi, K. Matsushita, K. Hosaka, N. Iwakura <i>A Double-Sided Contour Measurement Machine for Aspherical Lenses</i>	63
T. Heeren <i>Mechatronic alignment of color images in a high volume, high speed color printer</i>	67
L.A.M. de Jong, P.C.J.N. Rosielle, R.L. Dumoulin, P.H.J. Schellekens <i>Design of an accurate and fast magnetic head actuator for a back-up tapedrive</i>	71
F. Auer <i>Piezo Actuated Active Damping in a Semiconductor Lithographic Scanner</i>	75

A. Minnaert, P. Spit, W. van Buel, R. Toussaint <i>Off-Line Field Clear-Out Exposure Tool for Process Productivity Improvement</i>	79
Y. Gao, S. Tse, Y. Law <i>A Study of the Signal Switches for Composite Control during Grinding</i>	83
M. F. Byl, J. A. Calzaretta, S. J. Ludwick D. L. Trumper <i>Tuning Controllers with Multiple Adaptive Feed-forward Cancellation Resonators</i>	87
F.G.A. Homburg <i>Dynamic Interface Specification of a Fast Tool Servo onto a High Precision Lathe.</i>	91
S. H. Chang, C. L. Tsai, T. L. Wu <i>Monolithic Design of a Six Degrees-of-freedom Nanometer Resolution Micro-Positioning Stage</i>	95
H.A. van Mierlo, J.R. Nijenhuis <i>Design of the VLTI Cats Eye for optical delay lines</i>	99
P. Hilkens <i>Precision in imageforming for color printing</i>	103
M.M.P.A. Vermeulen, F.G.P. Peeters, H. Soemers, P.J. Feenstra, P.C. Breedveld <i>Development of a Surface Acoustic Wave Planar Motor under Closed Loop Control</i>	107
<b>Micro/nano systems</b>	<b>111</b>
Y. Chen, W. Huang <i>Calculation of diffraction effect of a nano-alignment mask</i>	113
D. Y. X. Zhao, Z. Ping, W. Huang, J. Chu <i>Research on a microtweezers driven by electricity</i>	117
H. Mizumoto, M. Shioe, S. Arij, M. Yabuya <i>Picometer Positioning using Twist-roller Friction Drive Mechanism</i>	121
D. Metz, A. Albers <i>Finite Element Analysis on the Reliability of Components of a Micro Planetary Gear</i>	125
J. Dienelt, K. Zimmer <i>Fabrication of self-aligned silicon field emission arrays using common processing techniques</i>	129
H. K. Tönshoff, T. Friemuth, M. Reichstein, D. Kopp <i>Operating Models of an Aerostatic Guidance for Active Microsystems - Characteristics Investigations</i>	133
F. Bertinetto, M. Bisi, E. Canuto, P. Cordiale, A. Rolino <i>Nanobalance</i>	137

<b>Ultra-precision motion systems</b>	<b>141</b>
J.P. Kappelhof, H. Bokhove, M. Termeer, P. Verhoeff <i>IASI OGSE Spot Scan, Design and realisation of an infrared calibration instrument for in vacuum</i>	143
C. Siebenhaar, V. Guyenot, A. Gebhardt, G. Harnisch, C. Damm, T. Peschel, M. Rohde, M. Thaut <i>Theory and application of an alternative adjustment method based on transfer of momentum</i>	147
S.A.J. Hol, J.C. Compter, A.J.A. Vandenput, R. Munnig-Schmidt <i>Design of a Magnetic Bearing</i>	151
A. Slocum, M. Basaran , R. Cortesi <i>Linear motion carriage with bearings preloaded by inclined Open-face iron core linear Electric motor</i>	155
A. Torii, R. Fukui, A. Ueda <i>A Miniature Robot for A Rotary Stage Driven by On/Off Controlled Piezoelectric Elements</i>	159
T. Shinshi, X. Zhang, L. Li, A. Shimokohbe <i>Precision Radial Magnetic Bearing Using Estimation of the Center of Inertia and Repetitive Control</i>	163
R. H. A. Hensen, M. J. G. v. d. Molengraft, M. Steinbuch <i>Friction in Motion Systems: Performance Deterioration for Regulator Tasks</i>	167
S. Fukada, T. Shibuya <i>Ultra-precise Positioning with Nanometric Resolution over A One-Millimeter Stroke Using Flexure Guide And Electro-magnetic Linear Motor</i>	171
S. Mekid <i>A New Generation of State-of-the-Art Piezoelectric Ultrasonic Micro-Motors.</i>	175
L. Jabben, D. Hobbelen, J. van Eijk <i>Non-linear Control of Reluctance Type of actuators for Ultra High Precision Applications</i>	179
J. Qian, S. Devos, M. Dona, F. Al-Bender, D. Reynaerts, H. Van Brussel <i>A novel set-up combining ELID-grinding with a Piezo-Stepper drive</i>	183
J.S. Chen <i>Low Speed Tracking Control of a Precision Linear-Motor Rolling-Guide Stage</i>	187
N.J. Doelman, T.C. van den Dool <i>An Adaptive Control Strategy for Optical Delay Lines</i>	191
<b>Precision engineering manufacturing methods/processes</b>	<b>195</b>
J. Tarnaki, A. Kubo, J. Xie, J. Yan, T. Iyama <i>Precision Truing of Superabrasive Grinding Wheel by Means of an Envelope Generation Method</i>	197
H. Huang, Y.C. Liu and P.L. Teo <i>High Speed Deep Grinding of Yttria Stabilized Tetragonal Zirconia</i>	201
Q.S. Yan, Z.Q. Zhang, K. Syoji <i>Studies on CBN Quill in Surface Grinding</i>	205
A. Yui, S. Mototani, S. Okuyama and T. Kitajima <i>Prediction of Contact between Grinding Wheel and Workpiece -Detection of Diffused Reflective Laser Intensity from Grinding Fluid</i>	209

## VIII

G. Grathwohl, D. Godlinski, E. Brinksmeier, R. Gläbe <i>Alumina Tools for Precision Machining of Steel</i>	213
K. Katahira, H. Ohmori, J. Nagata, M. Mizutani, J. Komotori, Y. Watanabe <i>Fabrication of High-quality Surfaces on Biomaterials using a New Electrical Grinding Technique</i>	217
K. Cheng, X. Luo, R. Ward, X. Liu <i>Modelling and control of the surface integrity and functionality in precision machining</i>	221
J. Ramírez-Salas, I.D. Marinescu, I.C. Benea <i>Superpolishing of AlTiC Magnetic Heads</i>	225
K. Terada, K. Kawata, K. Nishimura, K. Hirose, R. Tanaka, T. Sato <i>Micro Electro-Discharge Machining of Single-Crystal Diamond</i>	229
S. Kiyohara, H. Takamatsu, K. Mori <i>Effect of fluorocarbon addition to an oxygen gas in electron cyclotron resonance plasma etching of diamond films</i>	233
H. Hidai, H. Tokura <i>Laser processing of silica glass with the aid of condensation</i>	237
X. D. Liu, L. C. Lee, X. Ding, S. T. Ng, S. K. Tung, K. S. Lee <i>An Investigation of Diamond Tool Cutting Edge</i>	241
S. Nakazawa, H. Hidai, H. Tokura <i>Spherical objects molding using liquid-liquid interface</i>	245
C. Zhang, Y. C. Shin <i>Wear and specific energy in precision laser assisted truing of vitrified CBN wheels</i>	249
C. Zhang, H. Ohmori <i>ELID CG-grinding for spherical lens or moulds: principles and application</i>	253
J. E. Bullema, A. H. van Krieken, M. van den Hurk, M. Meuwissen <i>Submicron laser micro machining of metals</i>	257
B. Mullany, G. Byrne <i>Pad-Wafer Interface Temperatures during Chemical Mechanical Polishing (CMP) of oxide Coated Silicon Wafers</i>	261
R. Wüthrich, V. Fascio, D. Viquerat, H. Langen <i>Study of Spark Assisted Chemical Etching Process technology data</i>	265
B. Zhao, X. Zhang, K. Yamazaki, M. Mori, M. Fujishima <i>Autonomous diagnostic system for machining process</i>	269
M. Pruteanu, I. D. Mannescu <i>Mathematical Modeling of the Lapping Process</i>	273
K. Garrard, A. Sohn, R. G. Ohl, R. Mink, V. J. Chambers <i>Off-Axis Biconic Mirror Fabrication</i>	277
S. N. Lavrynenko, A. G. Mamalis, A. I. Grabchenko, N. V. Verezub <i>Kinematic Interaction between Diamond Cutting Wedge and Amorphous Polymer Materials in Dynamics of Precision Machining</i>	281
M. Bobertag <i>Grinding of high-precision surface-structures in tool steels</i>	285
C.H.Lui, D. Louie, L.M.Li. <i>Ultra-Precision Aspherical Surface Generation Using State-of-the-Art Magneto-rheological Finishing Technology</i>	289
D. Spath, K.H. Sternemann <i>Process Control and Monitoring of micro cutting processes in high spindle speed milling machine</i>	293

C.C.A. Chen, L-S. Hsu, C-K. Hsu, and W-C. Liu <i>Study on Pad Dressing Process for CMP of Silicon Waters</i>	297
Y. Uda, T. Ueda, T. Senga, A.Ishikawa, Y. Ushio, E. Yamamoto, S. Hoshino, A. Une <i>Uniformity of residual film thickness obtained by Digital Polishing Method in New CMP System</i>	301
S. Lavrynenko, V. Senchyshyn <i>Manufacturing of precision polymer optical components - problems and solutions</i>	305
S. Devos, F. Al-Bender, D. Reynaerts, H. Van Brussel <i>Active control of a grinding spindle</i>	309
T. Kumon, Y. Takeuchi, M. Yoshinari, T. Kawai, K. Sawada <i>Ultraprecision Compound V-shaped Micro Grooving and Application to Dental Implants</i>	313
W. Michaeli; S. Bölinger; J. Forster <i>High Precision Optical Plastics Parts Through Innovative Manufacturing Technologies</i>	317
W. Michaeli, R. Gärtner, D. Opfermann <i>New Plastification Concepts for Micro Injection Moulding</i>	321
H. H. Gatzen, C. Morsbach, A. Karyazin <i>High Precision Machining of a Longitudinal Bearing for a Linear Microactuator</i>	325
W. T. J. Brugman, A. N. Westland <i>Machining of microchannels using a non-rotating cutting tool</i>	329
H. Ohmori, Y. Dai, T. Suzuki, W. Lin, K. Katahira, N. Ebizuka, A. Makinouchi, H. Tashiro <i>ELID-grinding Characteristics of SiC Mirrors with Weight-reducing Structure</i>	333
V. Piotter, N. Holstein, L. Merz, R. Ruprecht, J. Hausseil <i>Methods for large scale manufacturing of high performance micro parts</i>	337
H.-W. Hoffmeister, B. Menze, J. Gäbler <i>Grinding and honing of micro bores with new abrasive pencils</i>	341
M Day, M. Weck <i>Ultraprecision Milling and Planing Machine for large Workpieces</i>	345
M. Weck, C. Wenzel, M. Winterschladen <i>Process Chains for Replication Technologies of Complex Optic Components</i>	349
P. Morantz, C. Maeda, H. Ueda <i>Ultra-precision machining hard metals: turning versus grinding</i>	353
M. Weck, B. Leithelm, P. Zimmerschitt-Halbig <i>Intelligent Boring Tool – iBo</i>	357
I. Meszaros, M. Huijbers, D. Szepesi <i>Development Results and Industrial Application of Ultra-Precision Finish Hard Turning</i>	361
H. Ohmori, Y. Uehara, Y. Ueno, T. Suzuki, S. Morita <i>Ultraprecision Fabrication Process of Large Double-sided Spherical Fresnel Lens</i>	365
H.A.T.Silva, J. Duduch, C. R. Pagotto, A. J.V.Porto <i>Spectral Analysis of Acoustic Emission (AE) During the Diamond Turning of Brittle Material</i>	369
M. Tricard, D. Golini <i>Improving surface geometry and surface integrity using Magneto-Rheological Finishing (MRF)</i>	373
U. Birnbaum, H. Bernitzki, U. Jungstand <i>Correction Cycles in the Machining of Precision Aspheres</i>	377

J. Carr, A. Chang , P. S. Fiske <i>High Speed Generation of Complex Surfaces Using Non-Contact RAP Technology</i>	381
Y. Uehara, H. Ohmori, Y. Yamagata, S. Moriyasu , K. Yoshikawa, M. Asami, Y. Pan, T. Sasaki, T. Miura <i>Grinding characteristics of glass convex mirror by desk-top type 4-axis machine "TRIDER-X" with ELID system</i>	385
<b>Micro fabrication and manipulation</b>	<b>389</b>
E. Mounier <i>MEMS, the Alternative Semiconductor Business</i>	391
T. Masuzawa, J. Meijer, T. Bourouina, A. Schoonderbeek, J. Eindhoven <i>Laser Beam Machining of Microlenses by Hole Area Modulation (HAM) Method</i>	395
N. Moronuki, E. Brinksmeier <i>Micromachining of brittle materials by ultrasonic lapping with tool wear compensation</i>	399
D. Spath, J. Elsner <i>Quality assurance of micro-mechanical components</i>	403
L. Kudla <i>Fabrication of Miniature Cutters for Eye Surgical Operations</i>	407
K. Zimmer, R. Böhm, A. Braun <i>Microstructuring of dielectrics by laser-induced back side etching</i>	411
T. Pfeifer, S. Driessen, G. Dussler <i>A Fiber-based Fringe Projection System</i>	415
H. Weule, G. Stengel, C. Buchholz <i>Variation of Geometry and Size for Optimized Demoulding, Separation and Handling of Moulded Micro Parts within an Automated PIM-Process</i>	419
E. Brinksmeier, W. Preuss, L. Autschbach <i>Diamond Contour Boring and Ball-end Milling of Microstructures</i>	423
S. Kiyohara, H. Takamatsu, K. Mori <i>Micropatterning of diamond films with composite oxide mask of metal octylates in electron beam lithography</i>	427
J.B. Kim, S.I. Han, S.K. Lee, J.H. Lee, S.H. Jeong <i>Laser-Induced Chemical Vapor Deposition for The Fabrication of Micro Carbon Rods by Pyrolytic Decomposition of Ethylene</i>	431
H. Langen, V. Fascio, R. Wüthrich, D. Viquerat <i>Three-dimensional micro structuring of Pyrex glass devices – trajectory control</i>	435
G. Reinhart, M. Schilp, D. Jacob <i>Economic and sensitive assembly of microsystems in small quantities</i>	439
J. Clijnen, D. Reynaerts, H. Van Brussel <i>Calibration of orientation measurement systems based on tilt sensors and compasses</i>	443
W. Meeusen, D. Reynaerts, H. Van Brussel <i>A CAD-tool for the design and manufacturing of microstructures based on micro- EDM</i>	447
J. Schmidt, H. Tritschler <i>Improvement of Micro End Milling Tools through Variation of Tool Manufacturing Method and Geometry</i>	451

T. Glinsner, N. Roos, L. Bendfeldt, H. Pusch, M. Fink, H.-C. Scheer <i>Nanoimprinting of 4 Inch Substrates and a Strategy for a Controlled Separation Method</i>	455
J.W. Kim, Y. Yamagata, M. Takasaki, H. Ohmori, T. Higuchi <i>Analysis on Deposition Conditions of Surface Acoustic Wave Atomizer with Electrostatic Deposition for Fabricating Protein Chips</i>	459
Y. W. Park, D. Y. Kim <i>Prototype Microactuator for Nanomanipulation Using a Magnetostrictive Material</i>	463
T. Kuriyagawa, K. Syoji <i>Selective Removal Machining of Resinoid Insulator Film for Multilayer Semiconductors with Micro-Ice Jet Technology</i>	467
S. Kato, M. Ono, N. Kato, T. Hamano <i>Design and Fabrication of a Position Surveying Microrobot in the Underground Pipe</i>	471
F. Morrissey <i>Micro and Nano Structuring using Focused Ion Beam and DualBeam Technologies</i>	475
<b>Precision metrology for machines/manufacturing</b>	<b>479</b>
T. Yandayan, S.A. Akgöz, H. Haitjema <i>A new calibration method for polygons with a pitch angle which does not match with the subdivision of the used indexing table.</i>	481
R. Nakajima, T. Miyoshi, Y. Takaya, S. Takahashi, M. Fujita <i>Novel Measurement Method for Nano-Defects of Si Wafer Surface Using Evanescent Wave</i>	485
S.Ueno, Y.Kobayashi, T.Omino, S.Takase, Y.Awano, K.Miyamoto <i>Development of the automatic calibration machine for depth measurement standards for surface texture measurement</i>	489
Y. Kamimura, Y. Tani, K. Watanabe, H. Sato <i>Thickness Measurement of Silicon Wafers Using a Double-Focus Lens</i>	493
R. D. Geckeler, I. Weingärtner <i>Sub-nm Topography Measurement by Deflectometry: Flatness Standard and Wafer Nanotopography</i>	497
S. Patzelt, J. Peters, G. Goch <i>Microtopography characterization of optically smooth and structured surfaces</i>	501
T. Pfeifer, G. Dussler, S. Driessen <i>Confocal Inspection of microscopic parts and structures</i>	505
U. Hübner, W. Morgenroth, H.G. Meyer, Th. Sulzbach, B. Brendel, W. Mirandé <i>Determination of the AFM tip-shape with well-known sharp-edged calibration structures: actual state and measuring results</i>	509
M. Morel, H Haitjema <i>Task Specific Uncertainty Estimation for Roundness Measurement</i>	513
I. Misumi, S. Gonda, T. Kurosowa, Y. Tanimura, N.Ochiai, J. Kitta, F. Kubota, M. Yamada, Y. Fujiwara, Y. Nakayama, K. Takamasu <i>Comparing measurements of 1D-grating samples using optical diffraction technique, CD-SEM and nanometrological AFM</i>	517
T. Doi, T.Kurosawa <i>Accurate surface profilometry using interferometric microscope with high magnification</i>	521



K.R. Koops, K. Dirscherl <i>Nanometrology standards in the Netherlands: the traceable Scanning Probe Microscope</i>	525
S. Jones <i>Developments in homodyne interferometry and real time quadrature compensation provide precision feedback capability</i>	529
F. Meli <i>Roughness measurements according to existing standards with a metrology AFM profiler</i>	533
G. Jäger, E. Manske, H. Wurzbacher, R. Grünwald, H.-J. Büchner, W. Schott, W. Pöschel. <i>Novel Microoptical Fibre Coupled Laser Interferometers for Various Applications in Precision Engineering and Nanotechnology</i>	537
F. Härtig, C. Keck, K. Kniel, H. Schwenke, F. Wäldele, K. Wendt <i>Accuracy enhancement of a co-ordinate measurement machine by flexible integration of a precision tracking interferometer</i>	541
R. A. Nicolaus, G. Bönsch <i>Accurate Measurement of Silicon Spheres by Interferometry</i>	545
K. Hasche, G. Ulm, K. Herrmann, M. Krumrey, G. Ade, J. Stümpel, I. Busch, P. Thomsen-Schmidt, S. Schädlich, A. Schindler, W. Frank, M. Procop, U. Beck <i>About calibration of thickness standards on the nanometre scale</i>	549
A.J. Abackerli, R.M. Martinez Orrego <i>A round-robin process for co-ordinate metrology</i>	553
R.H. Bergmans <i>Metrology for Nanotechnology</i>	557
U. Brand, L. Yu, C. Chang; H. Lüllmann; H. Schwenke <i>Beginning of Operation and Optimisation of a 3D Micro Measuring Device</i>	561
K. Schneefuß, T. Pfeifer <i>Precision formtesting measurement technologies for microstructures</i>	565
G. Kotte, K. Dirscherl <i>New developments on ball diameter measurement</i>	569
O. Sato, M. Hiraki, K. Takamasu <i>The Calibration of Parallel-CMM: Parallel-Coordinate Measuring Machine</i>	573
K. Umeda, H. Sato, T. Sone, W. M. He, M. Sagara, H. Matsuzaki <i>An Evaluation of Error Space in Three Dimensional Coordinate Measuring Machine(3DCMM) by Sequential Two Points Method</i>	577
A. Grant, H.U. Danzebrink <i>Development of a scanning force microscope employing a quartz tuning fork as the force sensor</i>	581
P. de Groot <i>Optical form and geometry measurement of precision machined parts</i>	585
J. Flügge, R. Köning <i>Recent developments at the PTB Nanometer Comparator</i>	589
S.J.A.G. Cosijns, H. Haitjema, P.H.J. Schellekens <i>The influence of polarization states on non-linearities in laser interferometry</i>	593
K. Meiners-Hagen, A. Abou-Zeid <i>Optical roughness measurements with a multiwavelength diode laser interferometer</i>	597
D. van den Heuvel, R.H. Bergmans <i>Probe calibration using a digital piezo translator</i>	601

R. Furutani, K. Shimojima, K. Takamasu <i>Parameter Calibration of Articulated CMM</i>	605
V. Burgarth, A. Abou-Zeid <i>Development of a calibration device for simple measuring instruments</i>	609
H. Haitjema, B. van Dorp, M. Morel, P.H.J. Schellekens <i>Task Specific Uncertainty Estimation in Dimensional Metrology</i>	613
W. Häßler-Grohne, C.G. Frase, H. Bosse <i>Investigations of pitch standards for nanometrology in an metrological SEM</i>	617
M. Schulz, I. Weingärtner <i>Free-form measurement with high lateral resolution</i>	621
J. Garnaes, A. Kühle, L. Blunt, N. B. Larsen <i>Comparison of atomic force and interference microscopy</i>	625
E. Trapet, J. Aguilar, H. Spaan, J.A. Yague, V. Zelený <i>Self-Centring Probe with Parallel Kinematics</i>	629
B. van Dorp, H. Haitjema, P. Schellekens <i>The virtual CMM method for three-dimensional coordinate machines</i>	633
M. Abbe, K. Takamasu <i>Modelling of Spatial Constraint in CMM Error for Uncertainty Estimation</i>	637
S. Moriyasu, K. Katahira, W. Lin, Y. Yamagata, H. Ohmori <i>On-machine Surface Roughness Measurement with AFM</i>	641
K. Nemoto, H. Fukatsu, K. Yanagi <i>A novel scanning instrument for surface geometry measurement with a flat surface as its reference plane -Practical data processing techniques by the use of optical probe</i>	645
E. Savio, L. De Chiffre <i>Advances in uncertainty assessment using uncalibrated objects with freeform geometry on coordinate measuring machines</i>	649
K. Yanagi, M. Hasegawa, S. Hara <i>A computational method for stitching a series of 3-D surface topography data measured by microscope-type surface profiling instruments</i>	653
N.A.J. van der Beek, W.D. van Amstel, D. van Kaathoven, W. Potze, O.T.J. Vermeulen, M. Breukers <i>'Deflectometry on aspheric surfaces': A new approach and generic solution for measuring 'free form' aspheres.</i>	657
<b>Material properties</b>	<b>661</b>
M. Istomin, M. V. Kireitseu, S. Yerakhavets <i>Acoustic Emission Monitoring of Fatigue in Alumina - Chrome Carbide Composite</i>	663
M. V. Kireitseu, M. Istomin, S. Yerakhavets, V. L. Basenuk, <i>Alumina Coating Modified by Ultra Dispersed Diamonds</i>	667
R. G. Jasinevicius, P. S. Pizani, F. Lanciotti Jr, J. G. Duduch <i>Diamond Turning Induced Surface Damage in Silicon Investigated by means of Raman Spectroscopy and Microscopy Technique.</i>	671
R. G. Jasinevicius, F. Lanciotti Jr, P. S. Pizani, J. G. Duduch <i>Raman Scattering used to Probe Residual Strains in Ductile Regime Diamond Turned GaAs.</i>	675
R. Haberland <i>Material evaluation for ultra-precision flexure hinges</i>	679
K. Herrmann, F. Pohlenz, F. Menelao <i>Ways to higher accuracy of the nanoindentation test</i>	683

T. Hosono, H. Hidai, H. Tokura <i>Is cBN really inert with metals?</i>	687
R. Schödel, G. Bönsch <i>Interferometric measurements of thermal expansion, length stability and compressibility of glass ceramics</i>	691
A. Noreyan, I. Marinescu, J. Amar <i>Molecular Dynamic Simulation of Nanoindentation of Silicon Carbide by Diamond Tip</i>	695
M.K. Bakhadirkhanov , K.C. Ayupov., N.F. Zikrillaev, F.A. Kadirova, D. Bobonov <i>Strongly Compensated Silicon as a new Class of Materials for Electronics</i>	699
Y. Watanabe, K. Katahira, H. Ohmori, T. Kato, A. Kawana <i>ELID Grinding and Tribological Characteristics of TiAlN Film</i>	703
Y. Gao, Z. Tao <i>Analysis of Measurement Errors for Light Passing Through Parallel Layers</i>	707
G. P. Howell, D. G. Chetwynd <i>Investigation of Surface Tension at Rough Interfaces</i>	711
D. Antonelli <i>Micro-factors affecting macro-parameters: the foil rolling case</i>	715
X. Liu, T. Bell, F. Gao, D. G. Chetwynd <i>Characterisation of engineered surfaces by a multi-function tribological probe microscope</i>	719
Q. Fang, F. Gao, X. Liu, D.G. Chetwynd, J.W. Gardner <i>Investigation of indentation properties of poly(pyrrole) thin films</i>	723
<b>Sensors</b>	<b>727</b>
H. Hashizume, H. Yoshioka, H. Shinno <i>An in-process micro-sensor for ultraprecision machining</i>	729
H. Matsuoka, S. Kasei <i>Resonance-Based High Sensibility Touch Probe System for CMM</i>	733
P. Pornnoppadol, S. Cao, V. Nesterov, U. Brand , M. Schmidt, R. Wilke , S. Bütefisch <i>Three-dimensional microprobe with reduced probing forces</i>	737
J.J. Aguilar, J.A. Yagüe, J.A. Albajez, J. Santolaria <i>Application of Lateral Effect Position Sensitive Detectors (PSD) to Angles Measuring in a Self-centring Probe</i>	741
T. Ha, T. Miyoshi, Y. Takaya, S. Takakashi <i>Evaluation of Microdefects on SiO<sub>2</sub> Filmed Wafer Surface from the Scattering Light</i>	745
H.E. van den Brom, C.J. van Mullem <i>Nanotechnology and Microsystem Technology in Electrical Metrology</i>	749
M.K. Bakhadirkhanov , H.M. Iliev. A. Khamidov, N.F. Zikrillaev, M.R. Arzikulova <i>Possibilities of Elaboration of Multi-functional Sensors of Physical Magnitudes</i>	753
H. A. M. Dowidar, D. G. Chetwynd <i>Distribution of Surface Contacts on a Simulated Probe Tip</i>	757
G. Kotte, M. Heemskerk , G. Teunisse <i>Characterisation of angle-sensitivity of magnetic field sensors.</i>	761
S.A. Spiewak, D.A. Turcic <i>Accurate Displacement Measurement with Inertial Sensors</i>	765
D. G. Chetwynd, R. K. Leach <i>Dynamic Performance of a Cantilever-Based Topography Probe</i>	769

M. Senoner, L. Koenders, W. Unger, and G. Wilkening <i>Accuracy of step height determination by Atomic Force Microscopy - results of an inter-laboratory comparison</i>	773
<b>Miscellaneous</b>	<b>777</b>
P. Stanev, F. P. Wardle, J. Corbett <i>Investigation of Grooved Hybrid Air Bearing</i>	779
X. Zhang, J. Wang, K. Yamazaki <i>Study on an Automatic Geometric Feature Recognition for Sculpture Surface Machining</i>	783
J.F.F. Klinkhamer <i>Interaction between adjustment philosophy and precision engineering</i>	787
X. Liu, Y. Gao <i>Phase reconstruction using spline regression</i>	791
T.Suzuki, H.Ohmori, Y.Uehara, Y.Yamagata, W.Lin, Y.Dai, K.Ebizuka, A.Makinouchi, H.Tashori <i>Ultraprecision Fabrication of Glass Ceramic Aspherical Mirror by ELID-grinding with Nano-level Positioning Hydrostatic Driving Machine</i>	795



## **Micro fabrication and manipulation**



## MEMS, the Alternative Semiconductor Business

E. Mounier

Yole Développement, 45 rue Ste Geneviève 69006 Lyon, France

### Abstract:

The present article is aimed at analyzing the current trends for European MEMS business and foundries structure. Through this paper, Yole will describe:

- A synthesis of MEMS European foundries
- An analysis of the MEMS markets and technologies trends
- An analysis for each MEMS specific applications

The realization of this analysis showed that, in Europe, the MEMS manufacturing activity employs more than 4000 people for a total annual sales figure of \$1 billion in 2000; the total of processed wafers per year exceeds 500 000.

### European foundries

Europe has more than 250 foundries in the field of MEMS, integrated optics and semiconductors (Figure 1). Europe has more than 150 industrial plants in the field of MEMS, power devices, integrated optics and wafer manufacturing/reclaiming and about 100 semiconductor foundries.

Activity	Number of plants (total 272)
Semiconductors	98
MEMS	78
Power devices	17
Integrated optics (for optical telecommunication)	20
Wafers producers and reclaiming	27
R&D institutes with manufacturing capabilities	32

Figure 1 : Repartition of European plants

In MEMS, it is Germany, then Scandinavia followed by France and Switzerland which has the largest number of foundries (more than 15). In integrated optics, it is UK/Scotland (6 foundries), followed by France. Germany and UK/Scotland have the largest number of power devices foundries (5 foundries each).

In wafer manufacturing and reclaim services, it is Germany (Germany has 7 foundries), France and UK/Scotland. Germany has the highest number of large R&D institutes in MEMS (more than 10 with IMM, FZK and numerous Fraunhofer institutes). In Europe, the MEMS manufacturing activity employs more than 5000 people for a total annual sales figure of Euro 1 billion in 2000 (Figure 2).

Total number of persons in Europe in industrial companies	5 000
Total number of persons in Europe in R&D organizations	2 500
Total wafer processing capacity in 2001 (eq. 4" wafers)	800 000
Expected wafer processing capacity in 2003 (eq. 4" wafers)	+ 30%
Total number of wafers processed in 2000 (eq. 4" wafers)	500 000
Estimated total European MEMS sales (2000)	Euro 1 billion
Estimated MEMS market growth rate	+ 25 %

Figure 2 : European MEMS infrastructure description



Half of the MEMS European companies are processing 100 mm wafers but there is a trend for upgrading to 150 mm (25 % of them are processing 150 mm wafers) and there are 3 MEMS foundries projects for 200 mm wafers. The total number of processed wafers per year exceeds 500 000 for a producing infrastructure of more than 800 000 eq. 4" wafers.

### **The MEMS industrial chain**

There is a increasing offer in equipment manufacturing for MEMS: double side mask aligner (Electronic Visions), deep RIE (Alcatel, STS), X and UV lithography (Karl Süss), hot embossing (Electronic Visions, Jenoptik), micro-injection molding (Kraussmaffeil), wafer bonders (Electronic Visions), test and assembly (Opus, Sysmelec).

For MEMS manufacturers, silicon is still the most used micromachined material but companies process also quartz (Thalès Avionics, Colybris), glass (mgt mikroglass), ceramic (Gesim) and polymer (Gyros Microlab, microTEC, Mildendo). Other semiconductor materials are also used: SOI wafers (manufactured by Analog Devices Belfast, SOITEC, Okmetic) for high performances sensors and actuators and also low power portable systems; GaAs wafers (mainly for wireless and data communication industry); SiC wafers (for high-temperature components such as sensors) and InP (for high-speed fiberoptics components and high frequency wireless applications or for an easier integration of active and passive components).

The use of polymer for the realization of micro systems or micro actuators is recent in Europe (it began only a few years ago). Some countries are very active in polymer activities, and therefore bring this subject to the foreground like Germany, Scandinavia, and UK. The major European player is Microparts in Germany.

### **The MEMS foundries business model**

There is a need for independent design houses for a better access to manufacturing. In the CAD tools activity, Ansys (USA) is still a leader but 3 companies are competing, including a French one: Memscap (F), moving from a CAD tools company to a components manufacturing company for telecommunications, Coventor (USA) and Intellisense (USA), which produces CAD tools as a MEMS foundry activity support. Moreover, there is a strong push from the European Commission to create independent design houses collaborating with foundries (AML in the UK, Acreo in Sweden, Sintef in Norway ...), as the access to the production of MEMS components for small business is still a problem today.

A MEMS manufacturing plant can be of 4 different types:

- Manufacturer of standard products for large volume applications (Bosch, STMicroelectronics, SensoNor).
- System manufacturer with integrated foundries (Thalès Avionics). Such companies work as foundries for customers of their own group.
- Open foundries (Colybris, Tronic's Microsystems, PHS MEMS). These companies develop and produce MEMS according to specifications given by external customers.
- Fabless companies and design houses (AML) using outside manufacturing facilities.

For the last five years, different MEMS business models have been developed in Europe:

- Re-focus on the main business: some companies (such as Sagem) have sold their MEMS activity in order to refocus on their main activity (system makers).
- Development of large-volume market standard products (ink-jet printheads, airbag accelerometers): mainly stemming from micro-electronics (STMicroelectronics).
- Acquisition of strategic technologies by manufacturers of modules or systems, specially in the fields of fiberoptics telecommunications and DNA analysis (mainly an US phenomenon: Corning with Intellisense, JDS Uniphase with Cronos): system manufacturers have thus locked access to key technology and to patent portfolios.
- Emerging of open foundries (Tronic's Microsystems): they take over from development programs by starting specific production according to costs and service quality that satisfies the users.
- Development of a design and simulation offer: next to the manufacture of components, different companies (Memscap) have appeared to facilitate the design and simulation of MEMS or to insure the MEMS design independently (but in contact) with a foundry.

### The future of MEMS

MEMS is already a multi-billion Euro market (Figure 3).

	2000 (billion of Euro)	2004 (billion of Euro)	Growth (% per year)
World MEMS market	30	50	+ 25%

**Figure 3 : MEMS market figures**

According to Yole Développement and Nexus Market survey, the total world MEMS market will certainly reached more than 50 billions of \$ in 2004 (a 25 % growth per year). The next Nexus market survey will give all the details on the world MEMS markets.

This large figure is linked to a very broad range of applications. It has been identified that MEMS cover more than 70 different applications.

Today, the driving markets are mainly the automotive industry, the telecommunication areas (MEMS are a solution to the needs of future all-optical networks and the wireless telecommunication market is an opportunity for RF MEMS) and also the biomedical applications (DNA chips, biochips and microfluidics components such as lab-on-chips). In 2000, 13 MEMS companies have been created with a focus on telecommunication/biomedical markets.



## Laser Beam Machining of Microlenses by Hole Area Modulation (HAM) Method

T.Masuzawa<sup>1</sup>, J. Meijer<sup>2</sup>, T. Bourouina<sup>3</sup>, A. Schoonderbeek<sup>4</sup>, J. Eindhoven<sup>2</sup>

<sup>1</sup>University of Tokyo, Japan; <sup>2</sup>University of Twente, The Netherlands; <sup>3</sup>Ecole Supérieure d'Ingenieurs en Electrotechnique et Electronique, France, <sup>4</sup>NCLR, The Netherlands

### Abstract:

This paper presents a new technology for fabricating micro-3D curved products using an excimer laser. The method is based on the use of a mask which contains holes with different open areas designed to control the material removal at the corresponding position of the workpiece surface. Microlens shapes were machined to prove the feasibility of the method.

### Background and aim of study

There are various methods for realizing micro-3D shapes. EDM[1], USM[2] and LBM[3] are typical examples of such methods. However, these methods basically employ NC technology and generate 3D shapes by removing small portions of the workpiece material, controlling the position and amount of removal[4]. Such a process requires a complex control system and a long machining time. This study aims at a simpler and more efficient system for generating arbitrary micro-3D shapes including microlenses.

### Method

The basic concept of the presented method is shown in Fig. 1. A laser beam passing through the mask which contains holes with different diameters removes the surface layer of the workpiece, while the workpiece is moved to-and-fro with small amplitude. Since the accumulated exposure time at the workpiece surface differs from place to place, different machining depths are realized after some time of machining, as the cross-sectional view of the workpiece shows. This process can be extended to 3D machining when holes with different diameters are distributed two-dimensionally on the mask and the simple movement of the workpiece is two-dimensional (parallel to the mask surface). Since the machining depth at any point on the workpiece mainly depends on the amount of laser radiation ( $J/cm^2$ ), thus on the area of the hole at the corresponding position on the mask, we call this method 'hole area modulation' or 'HAM'[5].

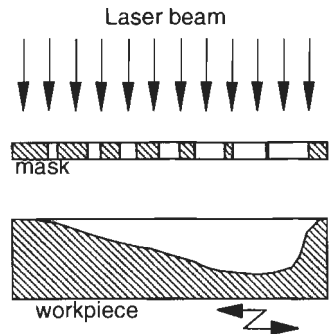


Fig.1. Concept of the

## Experiment

### Mask design

A mask was designed to produce microlenses. As the simplest approximation, it is assumed that the machining depth at a point on the workpiece is proportional to the area of the corresponding hole on the mask. The relationship among the parameters shown in Figure 2 is described as

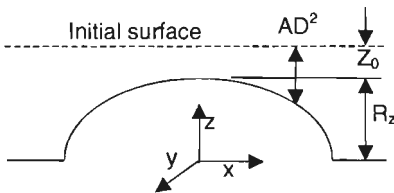


Fig. 2. Relationship among variables.

$$z=R_z+Z_0-AD^2, (x^2/R_x^2+y^2/R_y^2+z^2/R_z^2=1) \tag{1}$$

for an ellipsoidal lens, where  $D(x,y)$  is the diameter of the corresponding hole in the mask.  $A$  is the parameter adjustable by changing the total material removal amount. The diameter of each hole in the mask is then derived as

$$D(x,y)=D_{max}(1-(D_{max}^2-D_{min}^2)D_{max}^{-2}(1-(x^2/R_x^2+y^2/R_y^2))^{1/2})^{1/2}, \tag{2}$$

where  $D_{max}$  is  $D$  at the edge of the lens and  $D_{min}$  is  $D$  at the center of the lens. In practice,  $D_{min}$  is limited by the technology of mask fabrication and  $D_{max}$  is limited by the pitch of the holes. A small pitch and a large ratio of  $D_{max}$  to  $D_{min}$  can achieve smooth curves. In this experiment we chose the set of parameters as follows, considering the practical environment.

$$D_{max}=44\mu\text{m} \text{ (pitch} = 55\mu\text{m)}$$

$$D_{min} = 5.5\mu\text{m}$$

The holes for four ellipsoidal lenses ( $R_x=750\mu\text{m}$ ,  $R_y=150\mu\text{m}$ ) and four spherical lenses ( $R_x=R_y = 375 \mu\text{m}$ ) are located on one mask. An image of part of the mask is shown in Figure 3. Since the image of the mask is projected with the reduction ratio of 1/10 onto the workpiece, the sizes of the product lenses are 1/10 of the dimensions above and the necessary amplitude of the table movement is also 1/10 of the pitch of the holes.

### Machining

Below are the conditions selected after preliminary experiments with varying the beam energy and step size of the table movement.

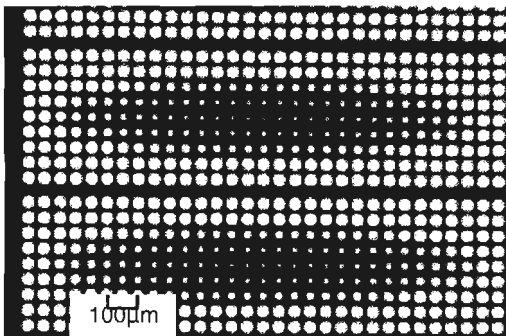


Fig. 3. Part of the mask.

Mask: chromium on glass substrate.

Laser: KrF ( $\lambda = 248\text{nm}$ ),  $100\text{mJ/pulse}$ ,  $2\text{Hz}$ .

Intensity:  $5\text{J/cm}^2$  on the workpiece surface).

Optics: Reduction factor = 10.

Workpiece: Polyimide sheet.

Table movement:  $0.3\mu\text{m/step}$ .

Number of pulses: = 1000.

An example of machined product is shown in Figure 4. Four ellipsoidal lenses and four spherical lenses were successfully formed on the polyimide sheet. Another example obtained under the same machining conditions is shown in Figure 5. In this case, many black spots are observed on the microlenses' surfaces. A close-up view of the spots is shown in Figure 6. These microcones are considered to be formed due to the existence of microparticles of various kinds such as dust on the surface, impurities in the material and debris from the ablation process. Since the sample in Figure 4 is the result obtained with a better cleaned material than that shown in figure 5, the dust on the surface may be one of the major causes of the formation of microcones.

The surface profile of the microlenses contained a waviness of about  $100\text{nm}$ . From the periodicity of the profile curves, the origin of the waviness seems to be the pitch of the holes in the mask, although the height of the waviness is smaller than the original surface roughness of the workpiece,  $150\text{nm}$ .

## Advantages and problems

### Advantages

This method has the following advantages compared with scanning-type 3D machining by lasers.

1. Since the machining depth information is entirely contained in the mask design, the NC for the table (or the beam) movement can be very simple and small.

For example, a simple zigzag movement with the amplitude of several micrometers produces products with 3D curved profiles such as that shown in Figure 4.

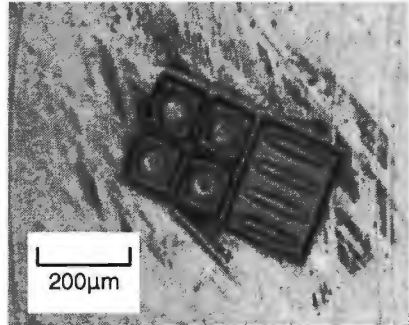


Fig. 4. Microlenses produced by HAM method.

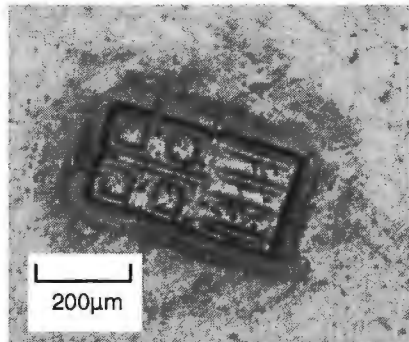


Fig. 5. Microlenses with black spots.

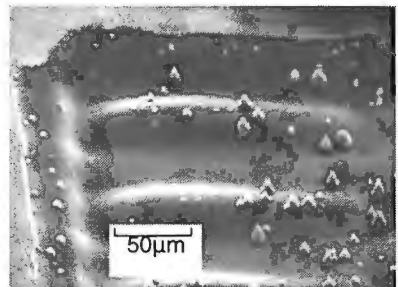


Fig. 6. Close up view of microlenses.

This characteristic makes the mask design more important. However, the designing process is simple, as has been shown in this paper. Not only analytical curves such as lenses, but also any curve expressed as digital data can be converted to obtain the hole diameters in the mask using the modified formula of equation (1),

$$D^2 \propto z_0 + R_z - z = h(x, y), \quad (3)$$

where  $h$  is the depth of the product's profile from the workpiece surface at  $(x, y)$ .

2. The laser beam is not focused to a point. This is effective in avoiding unnecessary melting of the workpiece, leading to better physical/chemical properties of the product's surface layer.

### Problems

1. Since the projected images of the holes have different sizes, the efficiency of ablation changes at different positions on the workpiece. This must be taken into account when the mask is designed.
2. Dust and impurities associated with the workpiece material produce microcones. The selection of pure and homogeneous material and good cleaning will be necessary.
3. The smoothing effect that appears in the LBM processes based on heating such as with CO<sub>2</sub> and YAG lasers is not evident with excimer lasers. This enhances the growth of sharp projections such as microcones. An ultrafast heat ablation process such as that with femtosecond lasers [6] may be a solution to this problem.

### Conclusion and acknowledgement

The possibility of utilizing the hole area modulation method to produce micro-3D profiles is experimentally confirmed. A possible problem in practical application, the generation of microcones, is considered.

This work has been carried out through a collaboration network organized by the Center for International Research on MicroMechatronics (CIRMM) of IIS, The University of Tokyo, in collaboration with the University of Twente and the French National Center for Scientific Research (CNRS).

### References

- [1] Rajurkar, K.P., Yu, Z.Y.: "3D Micro-EDM using CAD/CAM", *Annals of the CIRP*, 49, 1 (2000) 127-130
- [2] Egashira, K., Masuzawa, T.: "Microultrasonic Machining by the Application of Workpiece Vibration", *Annals of the CIRP*, 48, 1 (1999) 131-134
- [3] Tönshoff, H. K., Hesse, D., Kappel, H., Mommsen, J.: "Excimer Laser Systems", *Manufacturing Systems*, 24, 5 (1995) 395-409
- [4] Masuzawa, T.: "State of the Art of Micromachining", *Annals of the CIRP*, 49, 2 (2000) 473-488
- [5] Masuzawa, T., Olde-Benneker, J., Eindhoven, J. J. C.: "A New Method for Three Dimensional Excimer Laser Micromachining, Hole Area Modulation (HAM)", *Annals of the CIRP*, 49, 1 (2000) 39-142
- [6] Meijer, J.: *Micromachining of Engineering Materials*, Edited by J. A. McGeough, Marcel Dekker NY (2002)

## Micromachining of brittle materials by ultrasonic lapping with tool wear compensation

N. Moronuki<sup>1</sup>, E. Brinksmeier<sup>2</sup>

<sup>1</sup> Tokyo Metropolitan University, Japan, moronuki-nobuyuki@c.metro-u.ac.jp

<sup>2</sup> Laboratory for Precision Machining (LFM), University of Bremen, Germany

### Abstract

This paper proposes a compensation method of tool wear that becomes severe in micromachining by ultrasonic lapping. The acoustic emission sensor attached to the workpiece holder detects the tool engagement and enables the compensation of tool wear in real time. The effectiveness of the compensation is demonstrated through the machining of three-dimensional shapes that is required in the field of micro-chemistry.

### Introduction

Ultrasonic lapping has been applied to the micromachining of brittle materials because of its high productivity and applicability to various form generation [1, 2]. With the reduction of the tool size, some problems become obvious. The size of abrasives should be smaller. The touch sensing between tool and workpiece is difficult because the tool breaks easily with slight collision with the workpiece. Finally, tool wear causes crucial problem because the wear rate cannot be neglected and it is difficult to expect. Thus, some compensation becomes necessary. This paper proposes a real-time tool wear compensation method that utilizes an acoustic emission (AE) sensor.

### Experimental set-up and preliminary results

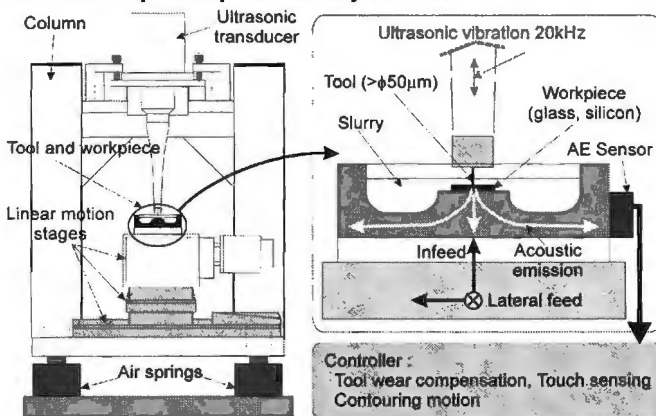


figure 1: Experimental setup

Figure 1 shows the experimental set-up. The tool is fixed at the tip of ultrasonic vibrator (20kHz) that is held with four columns. Beneath the tool, a workpiece is set on a XYZ stage. On the sidewall of the workpiece fixture, there attached an AE



sensor that detects the fracture of workpiece. This sensor detects the elastic waves over the frequency range 100-400kHz, and a AC/DC converter outputs analog voltage that correspond to RMS of the signal, finally a PC acquire the signal through a A/D converter. The PC also controls the motion of XYZ stage including the interpolation. The AE sensor is also used for the detection of the engagement or the touch between the tool and workpiece, that is necessary to determine the zero point in the depth of cut without tool breakage. The repeatability of touch sensing was less than  $0.2\mu\text{m}$ . Table 1 shows the typical machining conditions. The tool material is high-speed steel (HSS) or carbide and the diameter was  $50\mu\text{m}$ .

**table 1:** Typical machining conditions

Workpiece	Glass (BK7 or glass plate), Single crystal silicon (100)
Tool	$\phi 50\mu\text{m}$ (High speed steel or carbide)
Applied vibration	20kHz, $7\mu\text{m}_{p-p}$ (case of Fig. 2) or $12\mu\text{m}_{p-p}$ (others)
Maximum feed rate	$200\mu\text{m/s}$
Slurry (Abrasives)	Diamond, diameter $3\mu\text{m}$

Figure 2 shows examples of the machined results. The tool was contoured along the spiral path applying the step depth of cut  $2\mu\text{m}$ . The nominal width of the groove was  $50\mu\text{m}$  and final nominal depth was  $12\mu\text{m}$ . These kinds of grooves are often used in the field of micro-chemistry. During the process, the lateral feed rate was modified so as to keep the AE sensor level at constant, while the depth of cut was kept at constant. Such control can inhibit the generation of the internal cracks that deteriorate the strength of the structure. In this case, tool wear did not cause any problem because the removal volume was small.

Figure 2 also shows the effect of workpiece material. The figure on the left shows the result of glass of which structure is amorphous with isotropic property. The figure on the right shows the results of silicon of which structure is single crystal with anisotropic property. The effect of the workpiece material is not remarkable. The machined surface of the silicon looks smoother than that of glass, but it seems still rough for the various applications.

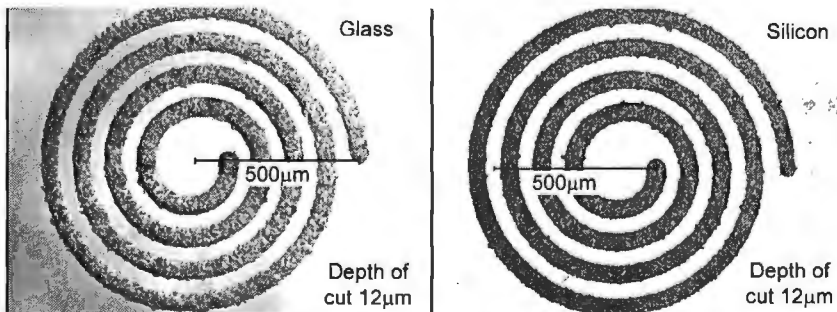


**figure 2:** Spiral groove (left glass, right silicon)

Figure 3 shows another example of three-dimensional shape. Assuming the micro-reactor, two reservoirs are connected to a central chamber for reaction. Designed diameter of the chambers was  $450\mu\text{m}$  and the maximum depth was  $20\mu\text{m}$  of which cross-section was elliptical. Contouring motion is necessary because the tool diameter was  $50\mu\text{m}$ . The width and depth of the channels between reservoirs and

reactor are not constant along its length but they have parabolic curvature.

It was found from the figure that residual stock remained and shape was not completed because concentric patterns are observed in the reservoirs on both sides. This error is caused by the tool wear. Simple tool wear compensation was attempted during the process. Before the machining of each geometrical segment, that is, the chamber or the channel, touch sensing was carried out. However, it was not effective.

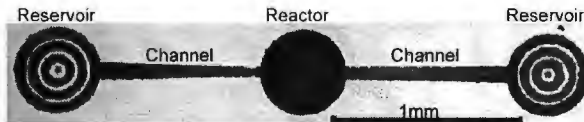


figure 3: Micro-reactor model lapped without tool wear compensation

Figure 4 shows the relationship between removed volume and tool wear volume. The machined pattern is a micro-reactor with five reservoirs as shown on the left. The tool wear is almost proportional to the removed volume, but the rate changes with the machining patterns. It is difficult to estimate the tool wear assuming various pattern of machining. The wear rate of carbide tool was almost same with that of HSS.

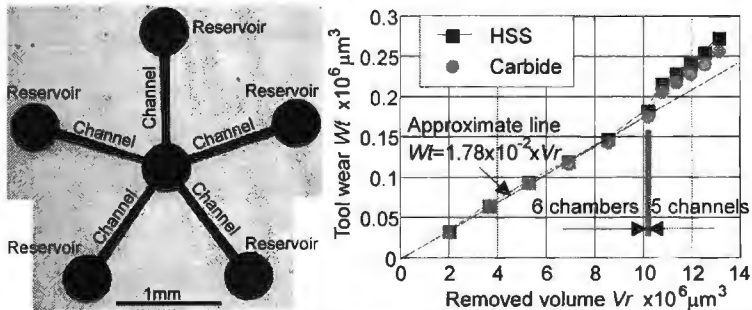


figure 4: Removed volume and tool wear (Left: machined pattern, right: G-ratio)

### Tool wear compensation and results

Figure 5 shows the new tool wear compensation method. The lateral feed rate is kept constant. Assuming that the surface before machining is completely flat and parallel to the tool motion, the AE signal decreases along with the tool wear because the actual depth of cut decreases.

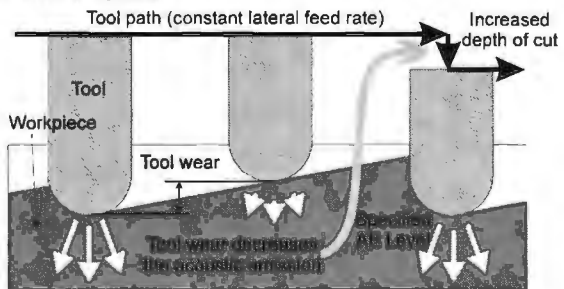


figure 5: Concept of tool wear compensation

When the AE level becomes lower than some threshold value, the depth of cut is increased to keep the AE output at constant. The threshold value and the increase of the depth were determined empirically.

Figure 6 shows the result with the tool wear compensation. The desired shape was obtained, where the design is same with that in Fig.3. In Fig.3, the channels on both sides of the reactor are not perfectly symmetric, but the result in Fig.6 has become symmetric. During the machining of this pattern, the tool wore a few hundred  $\mu\text{m}$  in length. Thus, the compensation was found to be effective.

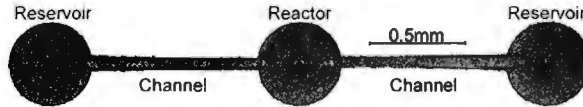


figure 6: Micro-reactor model lapped without tool wear compensation

Figure 7 shows an example of thrust bearing components. In order to obtain bearings with high stiffness and low friction, hydrodynamic groove bearings are adopted in which shallow grooves are machined on the bearing surface. As the size decreases, the groove should be smaller and the machining becomes difficult. In this example, 15 grooves (every 24deg.) were machined on the glass plate between the diameter range between 2.5mm and 5mm. The nominal width of the groove was  $50\mu\text{m}$  and its depth was 5-6 $\mu\text{m}$ .

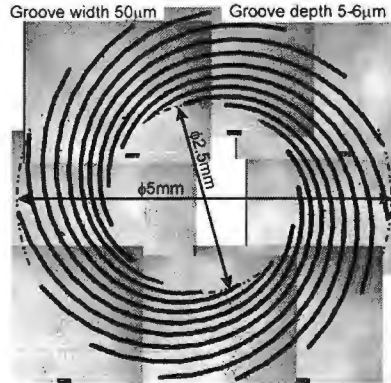


figure 7: Miniature groove bearing

## Conclusion

Problems in the application of ultrasonic lapping to micromachining were made clear as follows:

- Engagement of tiny tool is difficult to detect
- Tool wear compensation during the process is indispensable

Then, the real-time tool wear compensation that utilizing the acoustic emission sensor was developed and its effectiveness was verified through experiments, in which three-dimensional profiles were produced.

The improvement of the surface roughness is one of the future problems.

## References

- [1] McGeough J.: "Micromachining of Engineering ". Marcel Dekker, 2002.
- [2] Brinksmeier, E., Preuß, W., Schmütz, J.: "Manufacture of microstructures by ultrasonic lapping". Proc. 13th Annual Meeting of the ASPE, 1998: pp. 169-172.

## Quality assurance of micro-mechanical components

D. Spath, J. Elsner

Institute of Machine Tools and Production Science (WBK), Karlsruhe, Germany

### Abstract

The development of micro-mechanical parts manufactured in resistant materials demands on the one hand the further development of the manufacturing techniques as well as on the other hand closed information loops between design, manufacturing and quality assurance. The paper presents an approach of the so called Microfeature Catalogue as an information database which is structured by features and which operates as the basis for all kind of preventive and non preventive quality assurance in its specific environment of the fabrication of micro-mechanical components.

### Introduction

The evidence of the market potential of MEMS products is sufficiently proven [1]. Several fabrication methods are in competition to install themselves as the most appropriated method in order to fabricate micro parts in a reasonable time, quality and cost frame. A lot of development has already been done, still enough rest to do. Especially the surroundings of the fabrication processes, aspects of handling and automation devices, as well as quality assurance for micro parts are not yet established.

In the context of the special research project "design, production and quality assurance of primary shaped micro components manufactured in ceramic and metallic materials" (SFB 499) founded by the German Research Society, classical fabrication processes like powder injection moulding (PIM) and precision casting (PC) are further developed to micro component needs. The research work of one project of the Institute of Machine Tools and Production Science of the University of Karlsruhe is focused on the development of the relied quality assurance aspects.

### Special requirements on quality assurance in micro PIM

In conventional powder injection molding it is sufficient to do some kind of basic quality assurance in order to control production. Following the fabrication process usually some samples of the powder components are taken and are analyzed in terms of capability of flow and specific gravity in the stock receipt. In general the confidence to the supplier is high and little tolerances in the composition of the powders are acceptable. Beyond this the geometry of the mold might be inspected by the use of a CMM because form, position and dimensions have been verified by the respective supplier as well. Tolerances are small but reachable by conventional machining methods like milling and refractory dressing. The machine tool in which the mold is located is characterized as well in terms of fitting and a good surface quality is advantageous for the closing procedure of the injection machine.

After the injection procedure the so called "green part" is in general inspected by weight and an optical control either via light microscopy or human eye. In the statistical process control (SPC) quality control charts are used to recognize quality problems early in the serial production in order to avoid dissipation of material and energy. Finally the sintered part is inspected optically by taking samples. The necessary metrology (after feedstock characterization) is limited to light microscopes with or without CCD Cameras, profile-projectors, balances, slide gauges and as the

highest sophisticated metrology tool coordinate measurement machines. Until now even for macro parts a numerical or analytical model of the complete PIM process has not been established. Trail and error is the way of process development [2].

Entering into the micro component world some changes arise. First of all every part which is handled easily and which is carried without any problem to a measurement place or which can be quickly inspected by the human eye is a challenge in the micro part world. It seems to be trivial, but the consequences are non trivial to solve. The measurement process is complicated by necessary optical alignment und tension device handling. The metrology equipment, if it is already available for these micro dimensions in terms of resolution on the one hand and measurement range on the other, is very expensive and high sophisticated in use. Users have to be trained very carefully in order to teach them how to measure within a sufficient accuracy. Evidently accuracy must be very high if structures of few microns are measured. Moreover the measurement strategy attained a new importance which cannot be ignored.

Consequently the micro parts have to be characterized and measured as less as possible, only at the functional important regions. The fabrication process has to be made stable and robust in a statistically meaning and the design of the parts has to be appropriated to the feasibilities of the production and the metrology environment. This can be reached only if design, manufacturing and quality assurance work very tight together from the first drawing on.

The results and analysis of the semi finished und finished products have to be stored and have to be made available with a lot of context information especially regarding metrology information in order to allow a comparison of analysis.

Several conclusions can be outdrawn:

1. The interdisciplinary work of designers, schedulers, manufactures and quality assurance is an essential condition in the production process of micro parts.
2. Common platform for this interdisciplinary work is a brought database of important process and product parameters. These information has to be well-defined structured, stored and consequently used.
3. The structuring method has to be compatible to the needs of the different process steps in regard to content as well as to organisational work structure (e.g. the designer works with the CAD, the work scheduler with CAPP tools.)
4. Aspects of spatio-temporal distribution has to be considered. (Example: The analysis of a sintered part takes place hours or even days after the injection or even the feedstock fabrication, due to the debinding process, the sintering process, the acclimatisation of the parts in order to make them "measurable")
5. The information should be available independently of any specific hard- and software platform and the system has to be expandable.

## Approach

The presented approach consists of a so called Microfeature Catalogue and is accessible for all distributed process steps by a common information platform.

The database is structured by Microfeatures based on the state of art in the feature technology. There is a long history of the definition of a "Feature". First defined by Grayer, 1976, Feature was a geometric region which is machinable with one

machining operation. In the further development, feature were mainly integrated in the design process. Several commercial CAD systems offers a kind of feature catalogue to accelerate the design process. The state of the art knows feature as manufacturing, quality or design features [3]. Depending on each semantic of feature, specific information is attached.

Microfeature =

Geometric functional element

- + micro fabrication specific process and product information  
(process parameters and capabilities, specified sizes)
- + micro fabrication specific Constraints (feedstock data, machine/ machine tool data, metrology data) material information
- + functional requirements of the design (surface quality, form tolerances,...)
- + measurement strategies

**Figure 1:** Definition of Microfeature

The definition of "Microfeatures", shown in figure 1, for micro-mechanical parts overcomes the strict separation of the semantic aspects and offers a holistic approach. Thus the possibility is given to structure the database in the most appropriated way for all concerned users. Information can be supplied accordingly to the specific needs of each process. The adaptation of the manufacturing processes depending on the measured results can take place easier and the change of the micro system in design aspects depending on the actual possibilities of the micro-manufacturing processes can be realized on a brought database.

The Microfeature is defined as a geometric functional element plus its specific process information in terms of process parameters of the injection machine the debinding and the sintering process, further adjoined information concerns the used material and its characteristics, tolerances of surface, form etc. and a appropriated measurement method and strategy which has to be defined for this feature.

The metrology of micro structured components as mentioned before has to be characterized in its demands and integrated with its demands in an early stage of product development. Concepts has to be made of how to engender information out of the measured data. The Microfeature Catalogue permits to handle all these kind of information. Suffering of little experimental knowledge in fabrication and design for micro mechanical components the information supply is an essential need.

Hence inputs of the Microfeature Catalogue are on the one hand empirical results of measurements and analysis and on the other hand as well the defined demands in terms of functionality and quality coupled with special regions of interest in the considered micro parts.

As shown in figure 2 the Microfeature Catalogue is realised on a MS SQL2000 server database which meets all requirements which has been specified above in terms of flexibility, independency and extensibility. Additional information of external suppliers or research institutes can be integrated as well easily and permit a compact database for the specific additional information needs of micro parts.

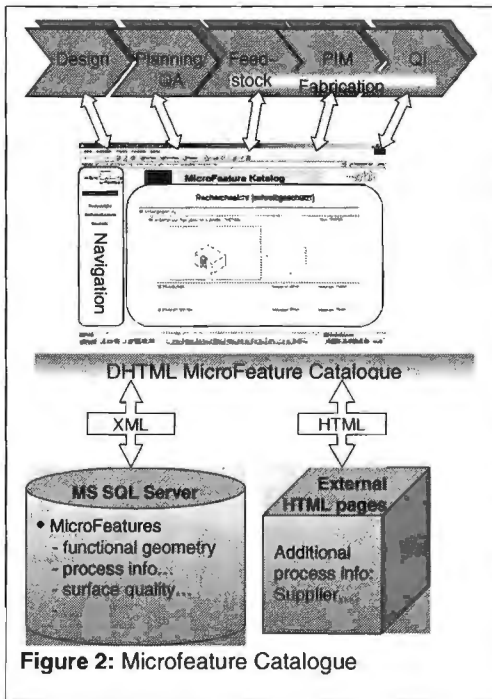


Figure 2: Microfeature Catalogue

processes because especially in the MEMS context it is much more than only quality inspection at the end of the line.

### Acknowledgement

This research is financially supported by German Research Foundation (DFG) via project SFB 499 "Design, Production and Quality Assurance of primary shaped micro components manufactured in ceramic and metallic materials".

### References

- [1] NEXUS! Task Force, Market analysis for Microsystems 1996-2002, Report of October 1998; in: MSTnews 05/01, VDI/ VDE –IT, November 2001, S.26
- [2] K. K. Wang, J. Zhou: "A concurrent-engineering approach toward the online adaptive control of injection molding process", in: Annals of CIRP Vol. 49/1/2000, S. 379-382.
- [3] VDI Richtlinie 2218: "Feature-Technologie", 1998, Springer Verlag

### Conclusions

Micro powder injection moulding is an especially suitable fabrication method for micro-mechanical components but it is suffering from small experimental knowledge although strong efforts are made. In order to develop the process for micro parts it is not longer possible to do this in a "closed" laboratory. The integration of design and metrology is essential for the success. The common platform is embodied by the Microfeature Catalogue which is available at any time and place in order to give quality circles the necessary empirical data background.

The transfer of micro structuring technologies into the world of medium sized companies is only reachable if all surrounding processes are appropriated evolved. It is essential for the economical success to involve in time the quality assurance

# Fabrication of Miniature Cutters for Eye Surgical Operations

L. KUDLA

Warsaw University of Technology, Institute of Precision and Biomedical Engineering

## Abstract

The typical vitrectomy procedure (surgical operation of the vitreous body in the eye) needs three miniature instruments: cutter, infusion and light pipes. The instruments are used many times, what creates the danger of spreading the infections. Therefore the new concept of design of the cutter, and in consequence also its fabrication was investigated. The main idea was to join cutting and infusion functions in one instrument, provided only for single use. In the paper the design of such a microscopic cutter, its fabrication process with a description of the main shaping steps and experimental results of pilot manufacturing in laboratory conditions are presented.

**Keywords:** *biomedical technology, vitrectomy, miniature cutters, fabrication*

## Introduction

In eye surgery various sophisticated methods and tools are used. An example could be the oscillating microscopic cutter, used for operations of the vitreous body or the retina. The diseases treated with the so-called vitrectomy procedure are remains of haemorrhage, some forms of degeneration of vitreous body and some degeneration growth on the retina [1]. The vitrectomy usually begins with preparation of three tiny incisions in the eye-ball, near the iris, for separate instruments, including a cutter (vitrector), an infusion port and a light pipe [2] - Fig.1.

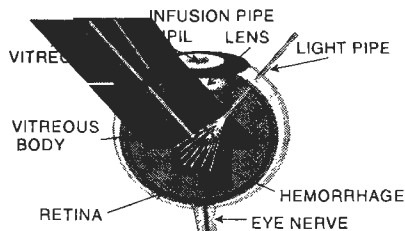


**Fig. 1:** Vitrectomy procedure

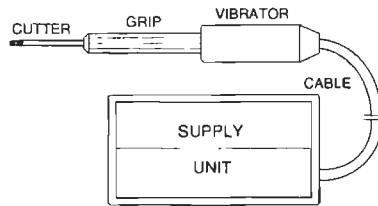


**Fig. 2:** Components of vitrectomy device.

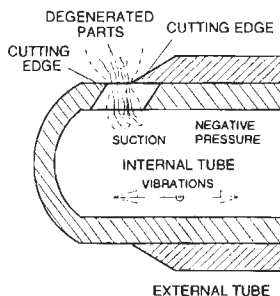
The penetration of the instruments into the vitreous body is observed with a medical microscope through the pupil. The cutter works like a miniature guillotine with two cutting edges. They cut the damaged vitreous gel or fibres grown on the retina, which are next evacuated out of the vitreous body. The removed gel volume is filled up with medical fluid using an infusion pipe. Another pipe is a lighter of the operation field. One of the potential complications with this surgical procedure is infection with the hepatitis virus. It is difficult to sterile clean very small and closed spaces of vitrector. To avoid the danger of such an infection, the concept of the new cutter was investigated (the inventor is Mr. Andrzej Kowalski, M. Eng.). The cutter joins two functions - cutting with infusion in one instrument, and is provided for single use. The other requirements were - simply design form, easiness in connecting and disconnecting



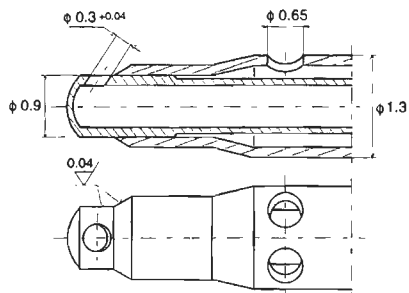
with the grip and possible small manufacturing cost. The complete vitrectomy device consists of the supply unit, vibrator, grip and at least of cutter - Fig. 2. Fabrication of the miniature cutter is most difficult and therefore many various techniques, e.g. plastic forming, mechanical, abrasive and electrochemical machining were taken into account [3,4,5].

### Design of the cutter

Two tubes formed the cutter. The internal tube is closed and a cutting orifice is placed at its tip. The external tube is opened and has a very sharp edge suitable for cutting. In the cutting part both tubes are precisely fit. The internal tube oscillates during the operation. Removing objects are sucked with negative pressure into the orifice and then cut off with the edge of the external tube - Fig. 3. Next they are evacuated out of the cutting tool through the central hole of the inner tube. Circumferential space is created between the outside wall of the inner tube and inside wall of the external tube - Fig. 4. It is intended for the flow of infusion fluid, which runs out through two refill holes in the external tube. Standard overall diameters of the cutters are 1.0, 1.3 or 1.5 mm.



**Fig. 3:** Operation principle with the special cutter – vitrector.

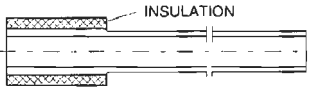
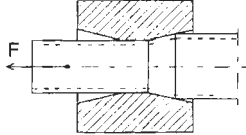
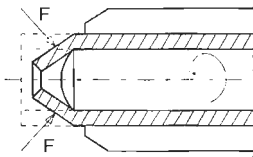
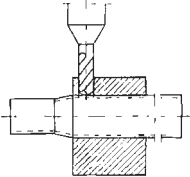
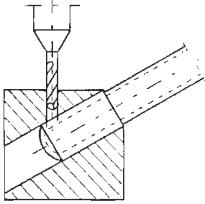
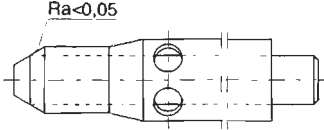


**Fig. 4:** General design of the working part of the vitrector with the diameter 1.3 mm.

### The fabrication procedure

Thin tubes made of stainless steel H18 (~18%Cr) were taken into account as self-evident raw material. Such tubes are usually manufactured for the injection needs. This material is very suitable for plastic forming as well as for mechanical or abrasive machining. Firstly the raw material with required diameters was cut into sections and tube faces were exactly ground. Then so prepared sections of tubes were cleaned and measured (diameter, straightness, roughness). In further operations the tubes were shaped using various machining methods. The schedule of main steps of the fabrication is presented in Table 1, for both the tubes: internal and external. The internal tube firstly was electrochemically etched to make a slit undercut on the outside diameter. The semi-spherical closing of the tip was done using plastic rolling with a shaped core placed inside the tube. Then grinding and polishing of the tip surfaces: semi-sphere and outer diameter was done. Next the cutting orifice was drilled using a special workholder and inner bar. There are possible various forms of the cutting orifice. One of the simplest is a round hole with the inclined axis, which could be produced with mechanical drilling. This solution was verified in many experiments done for the evaluation of the best process parameters. The external tube was

firstly tapered at one of the ends in a drawing die, what caused fragmentary reduction of the inside tube diameter. Next exact grinding and polishing of its surface was carried on.

1. INTERNAL TUBE (L=58 mm)	2. EXTERNAL TUBE (L=40 mm)
 <p>1.1</p>	 <p>2.1</p>
<p>Etching to form the undercut on outside diameter of the tube</p>	<p>Tapering one end in drawing die for partial reduction of the tube inside diameter</p>
 <p>1.2</p>	 <p>2.2</p>
<p>Plastic closing one end of the tube with forming semi-spherical tip</p>	<p>Drilling of two infusion holes for physiological fluid</p>
 <p>1.3</p>	 <p>2.3</p>
<p>Drilling of the hole with cutting edge using a special workholder</p>	<p>Grinding and polishing of the cutting edge of the tube</p>

**Table 1:** The main shaping steps during the fabrication of the cutter.

Further steps were - drilling of two holes for infusion of the physiological fluid and abrasive sharpening of the cutting edge with a core placed inside. The working parts of both tubes must be precisely fit. So in the final machining general problems created tight tolerances of co-operated diameters and high smoothness of their surfaces. In the process many deburring and cleaning operations are also necessary. After the fabrication process both parts were sterilised with standard procedure applied for medical instruments.

## Results

The presented manufacturing option is the result of many experimental trials and their selection step by step to find the optimal solution. Finally the design concept and elaborated fabrication process were verified in the laboratory conditions and a small series of the prototype cutters were produced. The view of the principal part of the vitrector and magnifying view of the cutting hole are shown in Figure 5. The

most difficult operations in the fabrication process were fitting of tubes and machining of cutting edges.

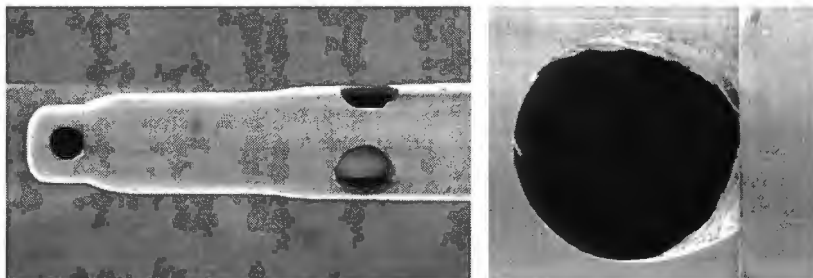


**Fig. 5:** SEM image of the working part of fabricated sample cutter.

Practical cutting tests were firstly done on artificial fibres and at last on animal eye-balls. For good cutting action the most important is sharpness of the edges and the play between the outside diameter of the inner tube and inside diameter of the external tube near the cutting edge. It was found that radial clearance should be much smaller than the thickness of tissue microfibers. If not, they are only crushed without disconnection, because their stiffness and hardness are minimal.

The invested vitrector - its design and its fabrication process ensured both: technological and medical requirements. Structure and machining of cutters is simple so future production seems to be effective and inexpensive.

### **Acknowledgements**

The author gratefully acknowledge Mr. Andrzej Kowalski for the inspiration and for the collaboration in practical preparation of cutters.

### **References**

- [1] Niżankowska M. H.: Fundamentals of Ophthalmology (in Polish). Volumes, Wrocław 1992.
- [2] [www.eyemlink.com](http://www.eyemlink.com) - vitrectomy.
- [3] Groover M.P.: Fundamentals of Modern Manufacturing. Materials, Processes and Systems. Prentice-Hall Inc., New Jersey, USA, 1996.
- [4] Krause W.: Fertigung in der Feinwerk- und Mikrotechnik. Carl Hanser Verlag, München Wien, 1996.
- [5] Kudła L.: Producing of Microholes (in Polish). PAR (Measurements, Automatics, Robotics), No.11/2000, 11-13 and No.12/2000, 11-14.

## Microstructuring of dielectrics by laser-induced back side etching

K. Zimmer, R. Böhm, A. Braun

Institut für Oberflächenmodifizierung, Permoser Str. 15, D-04318 Leipzig, Germany, zimmer@rz.uni-leipzig.de

### Abstract

The direct microstructuring of polymers (PMMA, polyimide, etc.) and ceramics by laser ablation has proved to be a flexible method for the fabrication of micro-mechanical, micro-fluid or micro-optical components. Besides polymers, transparent dielectric materials are suitable for a wide field of applications due to their chemical, optical, and mechanical properties, but they are difficult to machine at conventional excimer laser wavelengths (e.g. 248 nm) due to the low absorption of these materials. KrF-excimer laser etching at the interface to liquids has been studied for the fabrication of well defined microstructures in UV-transparent materials. The etch rates and the surface morphologies of fused silica and quartz depend on the laser parameters, the used solution, and the material itself. Typical etch rates for fused silica and quartz are in the range of some nm to 200 nm per pulse. The etch threshold fluence for fused silica of 350 mJ/cm<sup>2</sup> is one magnitude lower than the ablation threshold in air of more than 15 J/cm<sup>2</sup>. Mask projection and scanning techniques in conjunction with back-side etching were applied to fused silica to fabricate micron as well as sub-micron sized structures with a very low surface roughness.

### Introduction

Besides polymers, dielectric materials and fused silica have high application potential due to their chemical, optical, and mechanical properties, but they are difficult to machine at conventional excimer laser wavelengths (e.g. 248 nm) [1]. The low absorption of these dielectric materials results normally in a very low quality of the excimer laser machined structures, which do not allow any application in micro system technology. Only two particular lasers enable the patterning of transparent dielectrics: (i) the use of short wavelengths (F<sub>2</sub>-laser,  $\lambda = 157$  nm), whose photon energies exceed the band gap of these materials [2], or (ii) the application of ultra-short laser pulses (Ti:sapphire laser,  $t_p \sim 100$  fs) where multi-photon processes play an major role [3, 4].

A new pulsed laser based technique, called laser-induced backside etching, allows now the fabrication of well-defined patterns in UV-transparent materials at low laser fluences and with usual excimer laser wavelengths [5].

### Experimental results

#### Experimental set-up

The experimental set-up used in this investigation for laser-induced backside etching is shown schematically in figure 1. The laser workstation is equipped with a KrF-excimer laser, beam shaping and homogenizing optics, a x-y-z positioning stage and a dielectric attenuator and provides 30 ns pulses at 248 nm with an overall energy deviation in the mask plane of below 5 % rms.

The laser etch chamber capable of fitting 2 inch - samples was fixed on top of the positioning stages. Either a reflective objective ( $\times 15$  demagnification) or a refractive

objective ( $\times 5$  demagnification) was used for projecting mask pattern onto the sample back side. The sub-micron pattern were achieved by projecting a phase mask grating with a period of  $22\ \mu\text{m}$  onto the sample surface. The absorbing liquid was a solution of pyrene either in acetone, tetrachloroethylene or cyclo-hexane with different concentrations up to  $0.4\ \text{M}$  ( $\text{M} = \text{mol/l}$ ). The solutions which have been used at room temperature were completely replaced after every series of etching experiments. The etch depth and the roughness on the bottom of the etched pits were measured with a

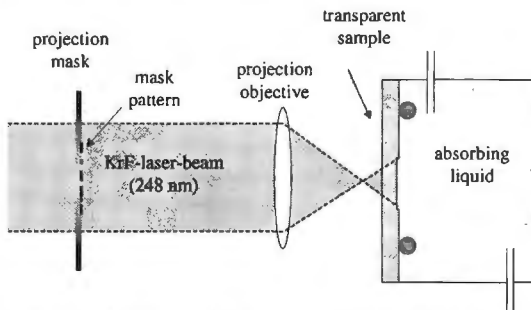


**figure 1:** Experimental set-up for laser-induced etching at the back side interface to liquids

white light interference microscope Micro-map 512. A JEOL JSM 6600 scanning electron microscope (SEM) was employed for taking top-view SEM pictures of the topography as well as monitoring cross-sections of etched samples. The sub-micron surface structures were also characterized by AFM (Nanoscop) measurements using the tapping mode.

### Etch rates

All samples were processed with a fixed set of laser fluences and pulse quantities. The etch rates were calculated from the final depths of etch pits with an area of  $100 \times 100\ \mu\text{m}^2$ . The etch rates of all investigated materials depend on laser parameters, the composition of the used liquid, and the material itself. The laser fluence has the most important effect on the etch rate and the etched surface quality. Figure 2 shows the etch rate of fused silica versus laser fluence for a  $0.4\ \text{M}$  solution of pyrene in acetone. The threshold fluence was determined to be at  $460\ \text{mJ/cm}^2$  which is more than one magnitude less than for laser ablation of fused silica in air being at more than  $15\ \text{J/cm}^2$ .

The etch rate of fused silica can be separated in two fluence ranges. In the low fluence range, up to  $1.5\ \text{J/cm}^2$ , the etch rate per laser pulse increases almost linear with a slope of  $13.4\ \text{nm}/(\text{J cm}^2)$  up to  $25\ \text{nm/pulse}$ . At high fluences, ranging from  $1.5$  to  $3.5\ \text{J/cm}^2$ , the rate increases to  $200\ \text{nm/pulse}$  with an average slope of  $71\ \text{nm}/(\text{J cm}^2)$  [6]. A similar separation into two ranges was observed for sapphire. This change in slope of the etch rate points to different mechanisms dominating the etching process. The soft etch behavior in the low fluence range proposed in [5] seems to be replaced in the higher fluence range by a more ablation dominated mechanism similar to the ablation at the solid-gaseous interface [6].

The surface roughness of the etched surface depends on the processing parameters and may be low as  $10\ \text{nm rms}$  in the low fluence range.

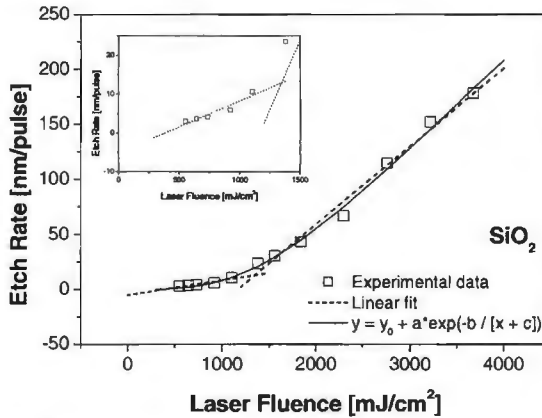


**figure 2:** Etch rate of fused silica using a 0.4 M pyrene/ acetone solution. The experimental data were fitted either by two lines or by an exponential function. The inset shows only the low energy range of etching.

### Laser etching for microstructuring

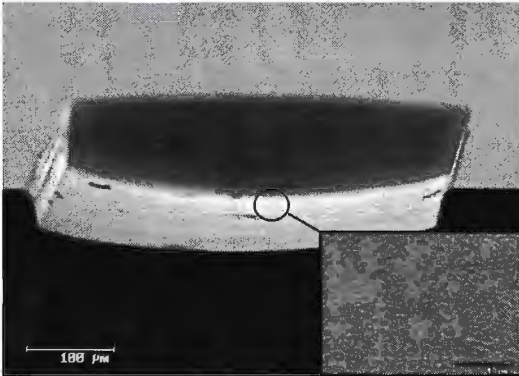


**figure 3:** SEM picture of a cylindrical structure etched into fused silica employing the scanning contour mask technique. The bottom of the structure is very smooth as shown in the inset.

The laser-induced back-side etching process was used for microstructuring of fused silica. For demonstrating the capabilities of the laser etch process the contour mask technique [7] as well as projecting of phase mask gratings has been applied. Figure 3 represents a SEM picture of an etched fused silica sample with a concave cylindrical structure. The micro roughness of the surface is below 10 nm rms at an etch depth of more than 50 μm. This roughness, which may result from the inhomogeneous energy distribution of the laser beam, the machining method or the etching process itself might be improved by more sophisticated processing techniques [8].

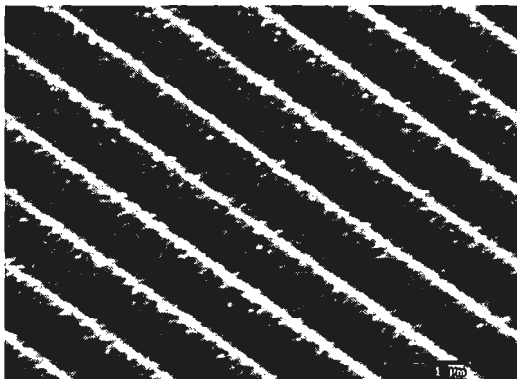


**figure 4:** SEM image of gratings in fused silica etched at  $960 \text{ mJ/cm}^2$  laser fluence with 10 pulses

Sub-micron gratings were laser ablated into surfaces by using interfering laser beams produced by mask projecting [9]. This method, which was improved by using phase mask gratings, was utilized to back side etching for the fabrication of sub-micron gratings in fused silica. In dependence of the applied laser fluence either sinusoidal or deep trenched surface gratings has been achieved. Figure 4 shows an AFM image of a grating etched at high laser fluence. The roughness of the gratings, which has been calculated from AFM-line scans

after numerically removing the sinusoidal grating relief, was as low as 3 nm. Both, the very precise surface gratings and the very low roughness confirm the capabilities of this laser etch technique.

### Acknowledgements

The delicate AFM characterization of the gratings is acknowledged Mr. D. Hirsch. This work was financially supported in parts by the Deutsche Forschungsgemeinschaft (DFG).

### References

- [1] D. Bäuerle, Laser Processing and Chemistry, Springer Berlin (2000)
- [2] J. Zang, K. Sugioka, T. Takahashi, K. Toyoda, K. Midorikawa, Appl. Phys. A 71 (2000) 23-26
- [3] S. Ameer-Beg, W. Perrie, S. Rathbone, J. Wright, W. Weaver, H. Champoux, Appl. Surf. Sci. 129 (1998) 875-880
- [4] R. Bähnisch, W. Groß, J. Staud, A. Menschig, Sens. Act. 74 (1999) 31-34
- [5] J. Wang, H. Niino, A. Yabe, Appl. Phys. A 68 (1999) 111-113
- [6] R. Böhme, A. Braun, K. Zimmer, Appl. Surf. Sci. (2002) in press
- [7] K. Zimmer, D. Hirsch, F. Bigl, Appl. Surf. Sci. 96-98 (1996) 425
- [8] A Braun, K. Zimmer, F. Bigl, Appl. Surf. Sci. 168 (2000) 178-81
- [9] P. Simon, J. Ihlemann, Appl. Phys. A 63 (1996) 505

## A Fiber-based Fringe Projection System

T. Pfeifer, S. Driessen, G. Dussler

Aachen University of Technology,  
Laboratory for Machine Tools and Production Engineering,  
Chair of Metrology and Quality Management, Aachen, Germany

### Abstract

In this article a new approach in order to adapt the well known measuring method of fringe projection to a fiber-based system is shown. By doing that it will be possible to use the fringe-projection on micro-parts to detect their shape and position. This is a need for the automation of handling and the assembly of micro-systems.

### State of the Art

Nowadays, the assembly of micro-systems in a small batch process is mostly done manually [1]. To solve the problems that entail with this fact relating to quality and cost, it is very important to automate this process. A flexible concept of handling along with a secure process control are essential conditions to fulfil the manifold requirements of assembly in the field of micro-technology.

To reach that goal in a first step a flexible fiber-scope has been integrated in the center of the tweezers of a precision handling system [2]. By this way, a direct view onto a micropart is obtained that can be used for identification and classification (figure 1).

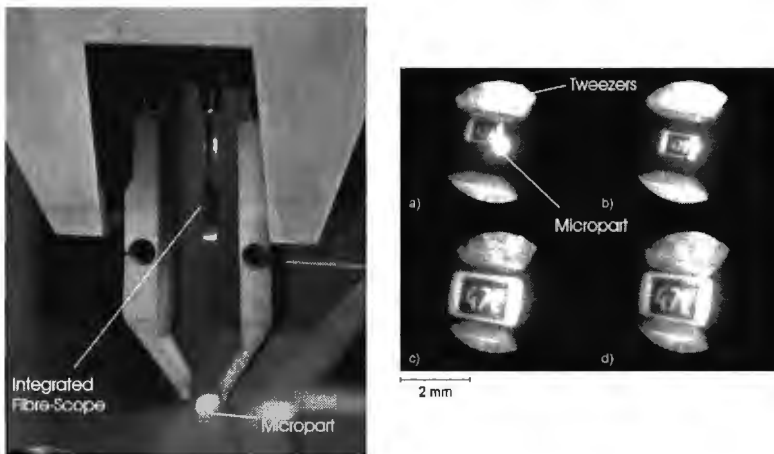


figure 1: Fiber-Scope integrated in tweezers, Positioning Sequence

### Problem

With this identification method it's still only possible to handle the part manually by following the movements on a monitor screen. To get to an automated handling process it's necessary to obtain 3D-data from the object which isn't possible on the basis of a 2D camera image. Furthermore, it's necessary to stick to a flexible concept for the visualization and detection of the micro-parts in order to be as free as possible



in using the sensor on different systems [3].

## New solution

In macroscopic production processes several measuring methods are used to assure the quality of 3D parts. Definitely, one of the most widespread techniques is the fringe projection.

### Fringe Projection

In figure 2 the principle of that technique is shown. A number of fringe patterns are projected in certain timed intervals onto a sample. Under a specific angle those patterns are detected by a camera with the same time intervals. Depending on the shape of the sample and the camera-angle the projected patterns appear to be deformed in a certain way. From the deformed camera images the original shape of the sample can be concluded. An example of a sphere next to a flat surface both illuminated by the same pattern of fringes is given in figure 2.

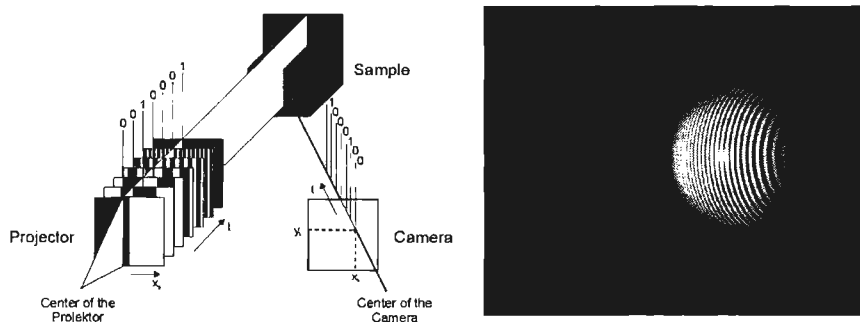


**figure 2:** Principle of the Fringe-Projection

Thus, the fringe projection is a fast and accurate method to receive the topography of a part as a computer file which can be processed in further steps, e.g. to compare the measured part to a given CAD file.

### Fiber Scope

In most cases the assembly of micro-systems distinguishes itself through a very little amount of space. Therefore, flexible fiber-scopes are a suitable means to visualize those processes.

Today, fiber-scopes that consist of more than 50,000 single fibers at a diameter of less than one millimeter are available. That means that on one hand an image taken by such an instrument consists of 50,000 pixels. On the other hand such a fiber scope can be integrated into small handling systems because of the small diameter.

### Concept for the new System

The new system mainly consists of two parts. In the first part the fringe patterns are generated as well as sent. In the second part the signal is received and processed (figure 3).

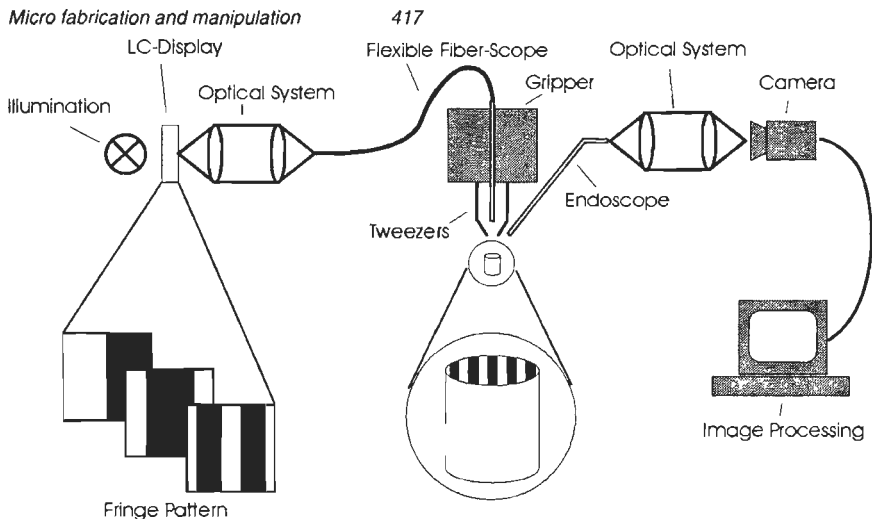


**figure 3:** Fiber-based Fringe Projection System

### **Sending Unit**

The fringes generated by a transparent LC-display are first projected onto the front-end of a fiber-scope using special optics. This image guide serves as a transmitter for the fringe patterns. A microlens is attached to the outlet of the fiber scope in order to focus the fringe pattern onto the surface of the micropart.

### **Receiving Unit**

An endoscope is used to observe the micro part. It's mounted under an angle relating to the illuminating image guide so that the triangulation condition is fulfilled. With a CCD camera connected to the endoscope the projected fringes are recorded and those data is analysed by an image processing system.

The result is a three dimensional cloud of points describing the surface of the micro part.

### **Conclusion**

The sensor concept presented, shows how the use of miniaturized optical components can substantially increase the efficiency of known measuring techniques. The developments open up a considerably more extensive area of application for fringe projection methods.

### **Outlook**

In further steps it will be necessary to examine the prototype-system in detail. Thus, the limits of the system concerning measuring accuracy as well as repeatability have to be tested. It has to be analyzed in which way those system specifications depend on the number of single fibers the fiber-scope consists of. Following, the endoscope integrated into the receiving part will be replaced by another flexible fiber scope in order to gain more flexibility in handling the system.

## **Acknowledgement**

The authors gratefully acknowledge the financial support of the Deutsche Forschungsgemeinschaft (DFG) within the Collaborative Research Center (SFB) 440 "Assembly of Microsystems".

## **References**

- [1] Jansen, B.: Material und Prozeßentwicklung entscheiden über den Markterfolg. VDI-Nachrichten, Nr. 16. 1996.
- [2] Bröcher, B.: Faseroptische Sensoren zur Prozeßüberwachung in der Mikrosystemtechnik. Dissertation RWTH-Aachen, 2000.
- [3] Pfeifer, T., Driessen, S.: Sensorentwicklung und –integration. Tagungsbeitrag zum Statuskolloquium des SFB 440, Montage hybrider Mikrosysteme. 6. September 2001, Aachen, Seiten 119-126.

## Variation of Geometry and Size for Optimized Demoulding, Separation and Handling of Moulded Micro Parts within an Automated PIM-Process

H. Weule, G. Stengel, C. Buchholz

Institute of Machine Tools and Production Science (wbk)  
Karlsruhe, Germany

### Abstract

Powder-Injection-Moulding (PIM) offers a high potential for fabrication of micro-mechanical parts manufactured in wearout resistant materials like metal or ceramic. To ensure an economical Micro-PIM-production in large lot sizes and high quality automation of the process beginning with demoulding, handling, debinding and sintering is a necessity. Within the field of automation research focus is to set up correlations between producible sizes and geometry of microstructures and the ability of demoulding as well as the separation of microstructures from sprues. Another critical success factor within the automation is the handling process where this paper presents an approach of a force-controlled gripper for micro-PIM-parts.

### Introduction

The further economical development of micro-system-technology (MST) depends on the competency to produce parts in mid or large series with a repeatable high quality. Different fabrication methods are developed in both industry and university to produce micro hybrid systems [1]. Beside the process itself surrounding processes like automation and quality assurance are key factors in order to ensure a profitable and high-quality production of micro-mechanical parts manufactured in wearout-material. A production process for micro parts meeting the requirements is powder-injection-moulding. The paper presents automation approaches regarding separation and demoulding within the powder-injection-moulding process as well as developments of a force-controlled handling system for fragile micro-PIM-parts.

Powder-injection-moulding enables the production of three-dimensional, wearout and precise micro-parts in medium to large series (100.000 ->1 Mio. parts/year). In order to process metal powder or ceramic powder ( $d_{50} < 4 \mu\text{m}$ ), it is first necessary to homogenize and granulate the material with a binder in a mixing unit. This compound which is capable of being injection moulded is then injected into the mould. The mould is being formed e.g. via micro-milling with tool diameters of 100  $\mu\text{m}$  in hardened steel. After the injection the parts have to be separated from sprues, demoulded and handled to a furnace. Within the debinding process the binder is first removed from the shaped part (green compact) and the resulting "brown compact" is then sintered. Within these process steps the material specific shrinkage rate of the part is 18-30% [2].

To ensure an economical production as well as a high quality products manual handling has to be substituted by an automated process. Critical success factors within the automation are demoulding, separation from sprues as well as the handling of the parts. Dissenting from the macro-area the maximum tensile stress onto micro-structures during the handling have to be within the range of milli-Newton and the precision of positioning within the range of 1-5  $\mu\text{m}$ .

**Approach**

The approach within the automation of the PIM-process is divided into the field of separation and demoulding of the micro parts as well as gripping concepts for fragile green-compact parts.

**Separation**

Due to the requirements regarding surface quality and precision of structure elements the separation of the micro parts, which are produced in a batch of 4 to 8 parts, from the sprues is very critical. Different possible ways of separation are existing in the macro-world but most themes become challenging when entering the micro-world. Separation of larger parts can either be done with the assistance of the gripper in the tool or by an external separation module. The external separation becomes complicated due to the fragility of the connecting points of parts and sprues as well as the effort for positioning the parts in an external module within the range of 1  $\mu\text{m}$  and below. The alternative of the separation within the gripping and handling module is difficult to implement because space is a problem and tool damage caused by the separation within the sub- $\mu\text{m}$ -range can lead to an uncontrollable process [3]. Therefore a third method of the three-part-tool, well known in the field of macro-parts, has to be realized in micro-structures. The three-part-tool works with an two-staged movement of the tool whereas in the first movement both sides of the cavities move from the fix-plate and thereby separate the parts from the sprues at the injection point. In the second movement both plates with cavities open and the demoulding and handling process can take place. Resulting in the small injection point a problem within this method in form of disruption of the feedstock into binder and powder could arise. The realized injection areas with surface qualities meeting the specs and non-disruptive feedstock-characteristics are about 0,04  $\text{mm}^2$  (core diameter: 525  $\mu\text{m}$ , injection diameter: 572  $\mu\text{m}$ ).

The principal set-up of the three part-tool with a cavity of a toothed-wheel within the millimeter-range is shown in Figure 1 (for better illustration only a one-cavity-tool is shown).

Further developments will determine the minimal injection area without any disruption. Even additional systems for separation within the tooling, e.g. ultrasonic, will be tested within the future.

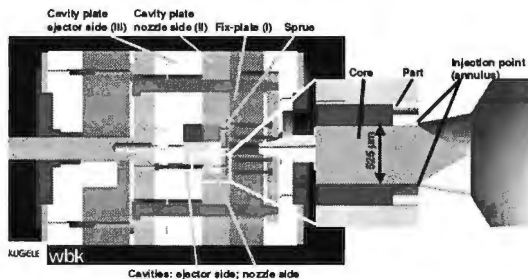


**Figure 1:** Schematic view on the three-part tool for micro toothed wheels

## Demoulding

The demoulding process is very critical when miniaturizing parts and structures. Adhesive forces between feedstock and cavity can overcome the internal material forces. Especially due to the shrinkage rate (about 2% of nominal value) of the part in the cooling time the part sticks on e.g. tool-cores.

The aim of the work is to give designers and tool-makers boundary conditions about necessary surface qualities, tribological characteristics, demoulding slants of the mould and the position and size of ejector pins in the tool. To achieve the correlations we work on geometrical sets with variable structures, sizes and alternatives to ejector pins (e.g. pneumatically) for demoulding parts and structures below 300  $\mu\text{m}$ . The geometrical sets will include structures like circles, triangles and hollow cylinders (to model real parts like toothed wheels), part length from 50-1000  $\mu\text{m}$  and depth from 50-400  $\mu\text{m}$ . Subsequent to this process every part has to be measured to avoid damages.

Even the handling system can demould parts by putting load onto the part. Therefore force sensors in the tool as well as force-controlled handling systems will be used to set up even correlations between optimal gripper system, part geometry, structure size and material.

## Handling

Synchronized with the demoulding process the handling system has to handle the part. Unlike macro parts the tensile strength within micro-PIM is below 4 N/mm<sup>2</sup> resulting in gripping forces on a structure of e.g. 0,1x0,1 mm below 40 mN. Inhomogeneous structure sizes cause a variation of contact surfaces and maximally allowed forces.

Different gripping principals are existing, a reliable force control is only feasible with the use of a mechanical gripper. Due to three-dimensional green compact structures made of stainless steel principals like e.g. electrostatic or vacuum-based grippers had been withdrawn.

Following the prototype set-up of the gripper meeting the requirements of high-precision-positioning and forces control in the milli-Newton-range is described. The actuator of the gripper is a 5 mm Smoovy synchronous motor with a 1:125 gearbox. Via a spindle part A is moved backwards forcing traverse B to bend and due to the fixed joining to the gripper fingers closing the gripper. Strain gauges are placed on both fingers to measure the stress.

The system is controlled with an Infineon C167 micro controller with direct connection (RS232) to a PC. The strain gauge signals are digitalized within the A/D-converter of the C167 and transferred to the PC. Based on algorithm the handling system as well as the Smoovy motor are being controlled.

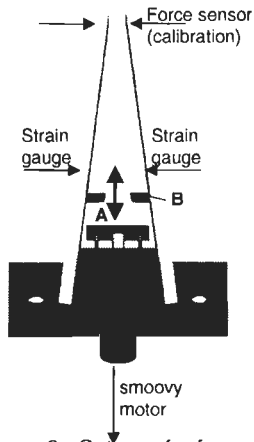


**Figure 2:** Set-up of a force-controlled mechanical gripper

Additional to the measuring system of the strain gauge a calibration of the Smoovy motor can be realized via a high-precision force sensor with a repeatability of 1 mN. The gripping process can be done in two ways: either with strain gauge in "measurement method" or with a calibration characteristics. The characteristics is based on specific part and structure sizes as well as the elastic force of the gripper fingers to develop a correlation between movement of part A and the gripping force at a predefined position.

Further developments within this topic will include both the miniaturization of the described gripping principle as well as the transfer of the measuring and calibration system to other grippers.

## Conclusions

The demand for complex three-dimensional micro-mechanical parts in wearout material in different branches like medical, biological or even telecommunication areas can be covered by the powder-injection-moulding process. To obtain a breakthrough of this technology an economical and high-quality production of middle to high series has to be set up. This could only be achieved with the integration of automation within the process and with special focus on critical sub-processes, e.g. debinding and handling. To counter problems arising from producing smaller parts dependences between structure sizes, material and specific technology criteria, e.g. gripping principles or force control-systems have to be developed and returned to specific sub-processes.

## Acknowledgement

This research is financially supported by German Research Foundation (DFG) within the Collaborative Research Centre (SFB) 499 "Design, Production and Quality Assurance of primary shaped micro components manufactured in ceramic and metallic materials".

## References

- [1] Van Brussel, H. et al: "Assembly of Microsystems". In: Annals of the CIRP Vol. 49/2/2000, p. 451-471
- [2] Plotter, V.; Ruprecht, R.; Haußelt, J.: „Spritzgießen von Mikroteilen aus Metall und Keramik“. In: Werkstattstechnik online, Ausgabe 11/1999
- [3] Weule, H.; Spath, D.; Schmidt, J.; Elsner, J.; Buchholz, C.; Tritschler, H.: „Prozesskette der Fertigung mikromechanischer Bauteile“. In: Werkstattstechnik online 91 (2001), Heft 12, S. 726 - 732

## Diamond Contour Boring and Ball-end Milling of Microstructures

E. Brinksmeier, W. Preuss, L. Autschbach

Laboratory for Precision Machining LFM, University of Bremen, Germany  
 autschbach@lfm.uni-bremen.de

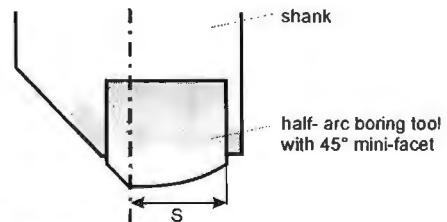
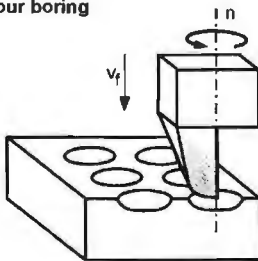
### Abstract

For the ultraprecision manufacturing of complex surfaces and microstructures diamond turning and fly-cutting are commonly employed. However, for certain tasks these processes have geometric and kinematic limitations. Diamond contour boring [1] and ball-end milling [2] extend the types of surfaces which can be generated to almost arbitrarily shaped mirror arrays and profiles with high aspect ratio. The paper will focus on problems of tool alignment, process control, the effect of varying cutting speed along the cutting edge, the process forces, control of chatter and tool wear. It will be shown, that the new implemented diamond contour boring and ball-end milling techniques are suitable machining methods for the fabricating of microstructures.

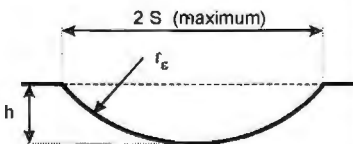
### Experimental setup

The main topic of this research project is the development of contour boring and ball-end milling processes for the manufacture of molds for micro-optic elements. Contour boring is performed by infeeding a rotating half-arc monocrystalline diamond tool, as shown in fig. 1.

#### contour boring



#### mold geometry



monocrystalline  
diamond tool

**figure 1:** Contour boring with half-arc monocrystalline diamond tool.

The contour of the created cavity results from the geometry of the cutting edge. Ball-end milling of microstructures with cylindrical and aspherical shapes is realized by superimposing the rotational motion with a feed parallel to the surface.

Contour boring was performed with commercially available half-arc radius tools with nose radii  $r_c$  between 2mm and 100mm. The cutting edge was provided with a 45°



mini-facet in order to facilitate tool setting.

The achievable figure accuracy of the spherical cavity strongly depends on tool alignment. The lowest point of the cutting edge must be aligned to coincide with the spindle axes. This is achieved with a precision cross-slide mounted on the tool spindle. Moreover, the angular position of the diamond tool has to be aligned in order to avoid a discontinuous slope at the center. Centering of the tool was performed with the help of an optical microscope; tilt alignment was done by drilling of test spheres and measuring the created contour with a white-light interferometer.

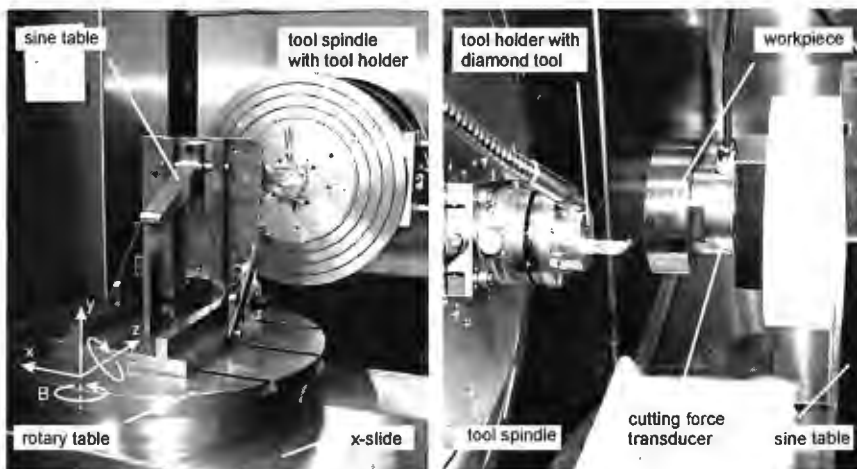


**figure 2:** Experimental setup for contour boring.

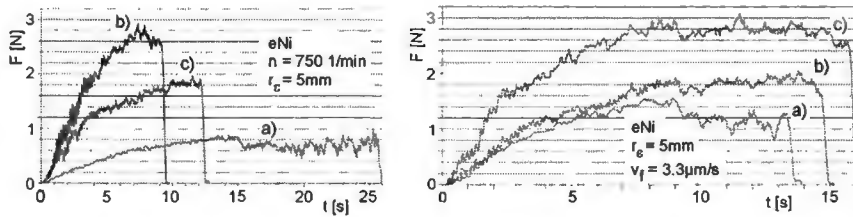
A Nanotech 500 Freeform Generator was used for the experimental setup, as shown in fig. 2. The adjustable tool holder with the boring tool was clamped on the vacuum chuck of the air bearing spindle. The workpiece was mounted on a 3-axis cutting force transducer.

The boring experiments were performed with light mineral oil as coolant. Three workpiece materials were used: electroless nickel, OFHC-copper and aluminum AlMg3. Infeed velocities and rotational speeds were varied between  $v_f = 1\mu\text{m/s} - 40\mu\text{m/s}$  and  $n = 300\text{min}^{-1} - 1250\text{min}^{-1}$ , resp.

## Results

In general, the measured thrust forces were found to be less than 5N for all infeeds and rotational speeds within the a.m. parameter field. In case of electroless nickel, thrust forces were significantly higher than 5N, especially when large tool radii were used. Chatter was observed at low cutting speeds and with large tool radii. The risk of chatter could be reduced by increasing the rotational speed.

As shown in fig. 3, thrust forces increase with increasing infeed and decrease with increasing rotational speed. At constant rotational speed and infeed the forces increase approx. with the square-root of the depth of the created cavity. This is to be expected, if the cross-section of the uncut chip is proportional to the length of the cutting arc.



a)  $v_f = 1.7 \mu\text{m/s}$ ; b)  $v_f = 5.8 \mu\text{m/s}$ ; c)  $v_f = 4.2 \mu\text{m/s}$       a)  $n = 800 \text{ 1/min}$ ; b)  $n = 500 \text{ 1/min}$ ; c)  $n = 300 \text{ 1/min}$   
**figure 3:** Measured thrust forces in contour boring experiments at different infeeds (left) and rotational speeds (right).

Contour boring of aluminum AlMg3 always yielded build-up edges, whatever machining parameters were chosen (cf. fig. 4 a). Tool wear tests were carried out in electroless nickel with  $v_f = 2.7 \mu\text{m/s}$  at  $n = 400 \text{ min}^{-1}$  with a diamond tool with a nose radius  $r_e = 45 \text{ mm}$ . Approximately 3500 spherical cavities were cut with a total cutting time of 25 hours. As shown in fig 4 b), tool wear essentially occurred at the turning center, where the cutting speed approaches zero. At this point, as in a conventional drilling process, material is only burnished but not cut.

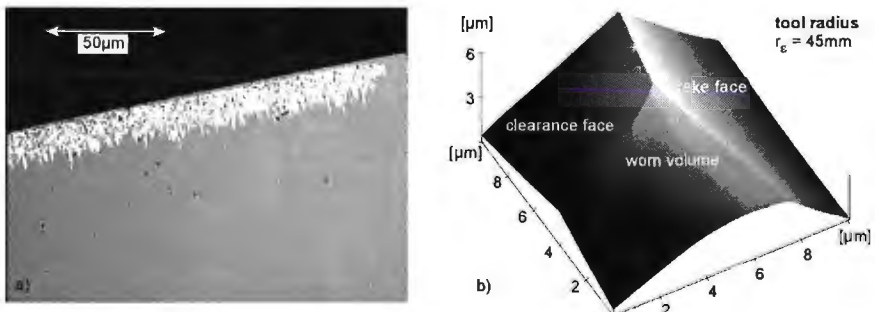


**figure 4:** a) Build-up edge obtained in contour boring of aluminum; b) Tool wear at the turning center after 25 hours of boring operation in electroless nickel.

A mold for a microlens-array generated by contour boring is shown in fig. 5. The contour accuracy is mainly determined by the waviness of the cutting edge. Usually, a peak-to-valley contour deviation less than 100nm could be achieved. The typical Ra roughness was about 20nm.

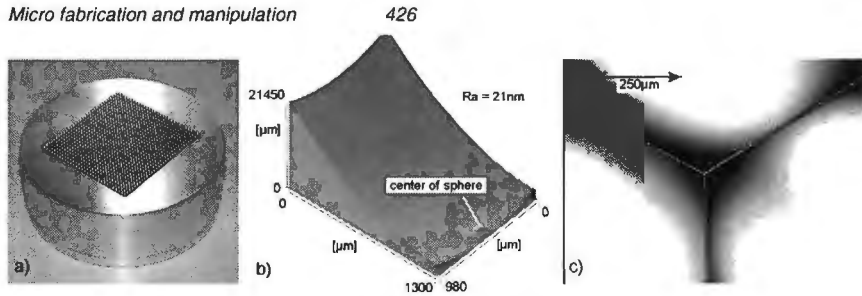


**figure 5:** a) Mold for a microlens-array in aluminum AIMg3 (900 spheres, radius: 2.1mm, depth: 60µm).  
b) White-light interferometric image of a single sphere ( $R_a = 21\text{nm}$ ).  
c) Microscope image of a corner formed by three adjacent spheres.

## Conclusion

We have developed a contour boring process with half-arc monocrystalline diamond tools for the generation of molds for microlens-arrays. It could be demonstrated that spherical cavities can be created in optical quality in different materials relevant to diamond machining. Cutting forces can be reduced by higher rotational speeds which is important for avoiding chatter and reducing tool wear. Future investigations will focus on ball-end milling processes with small tool nose radii and high rotational speeds.

## Acknowledgement

The authors acknowledge the funding of this project by the DFG German Science Foundation.

## References

- [1] Cerniway, M., "Three-dimensional Machining of Optical Quality Surfaces", ASPE Proc., Scottsdale, USA, Oct. 2000, pp. 42-45.
- [2] Taniguchi, N., "The state of the art of nanotechnology for processing of ultraprecision and ultrafine products", ASPE, annual meeting, Seattle, USA, 1993.

## Micropatterning of diamond films with composite oxide mask of metal octylates in electron beam lithography

S. Kiyohara, H. Takamatsu, K. Mori

Department of Electronics and Computer Science, Tokyo University of Science in Yamaguchi, 1-1-1 Daigaku-Dori, Onoda, Yamaguchi 756-0884, Japan

### Abstract:

The fabrication of diamond micropatterns by ECR oxygen plasma with a composite metal octylate mask was investigated using electron beam lithography technology. Most high etching selectivity of 14 was obtained with  $\text{Bi}_4\text{Tl}_3\text{O}_{12}$  octylate film under the plasma etching conditions of a microwave power of 300 W and oxygen gas flow rate of 3 sccm. The metal naphthenates and metal octylates exhibited negative exposure characteristics. The sensitivity and the gamma values of metal naphthenates and metal octylates were  $1.2 \times 10^{-3}$  and  $8.0 \times 10^{-5}$  C/cm<sup>2</sup>, 1.5 and 2.6, respectively. The resulting CVD diamond micropattern of 0.1  $\mu\text{m}$  line-width was fabricated with  $\text{Bi}_4\text{Tl}_3\text{O}_{12}$  octylate mask.

### Introduction

The micropatterning of chemical vapor deposited (CVD) diamond films using electron beam lithography technology was investigated. In this case, the most important point in the formation of micropatterns is the mask materials. In general, resist materials [polymethyl methacrylate (PMMA)] used in the fabrication of semiconductor devices are decomposed to CO and HO on exposure to oxygen plasma, indicating that they are composed of carbon, hydrogen and oxygen. The micropatterning of CVD diamond films using metal naphthenates as mask materials have been investigated [1]. However, it has certain disadvantages, including a low etching selectivity and a low sensitivity (one hundred times lower than PMMA). To overcome these problems, the use of metal octylates as mask materials with resistance to oxygen plasma in order to form an oxide film on the surface was proposed. Here we report the exposure characteristics of metal naphthenates and metal octylates, the etching characteristics of CVD diamond, metal naphthenate and metal octylate films processed with electron cyclotron resonance (ECR) oxygen plasma.

### Experimental apparatus and procedure

Polished polycrystalline diamond films 12  $\mu\text{m}$  thick (arithmetical mean deviation of profile  $R_a$ : 10 nm) and metal naphthenate and metal octylate films approximately 1  $\mu\text{m}$  thick on silicon wafers ( $10 \times 10 \times 0.5$  mm<sup>3</sup>) were used as samples. Metal naphthenates consist of cyclopentanes or cyclohexanes, methylene chains  $-(\text{CH}_2)_n-$ ,  $-\text{COO}-$  and metals, which have mainly following structure:  $[(\text{cyclopentane})-(\text{CH}_2)_n-\text{COO}]_m - \text{M}^{n+}$ , where M is metal atom. Y, Bi, Ba, Cu and Ti naphthenates were used as mask materials. Metal octylates consist of ethylhexane methylene chains,  $-\text{COO}-$  and metals, which have mainly following structure:  $[(\text{CH}_3)-(\text{CH}_2)_6-\text{COO}]_m - \text{M}^{n+}$ , where M is metal atom. Bi, Ti, and Ba octylates were used as mask materials. They were sticky liquids at room temperature and stable in air. The silicon wafers were spin-coated with the metal naphthenates and metal octylates at 2500 rpm for 10 s and then dried in air at 110 °C for 15 min to form metal naphthenate films and metal octylate films. The resulting films thickness of the metal naphthenates and metal octylates were approximately 1  $\mu\text{m}$ . These samples were processed using a plasma (AFTEX PS-501) etching apparatus with an ECR-type oxygen source. The

molybdenum holder was equipped with a thermocouple and a bias voltage electrode. Etching steps were made in CVD diamond, metal naphthenate and metal octylate film surfaces by striping a silver paste mask and an aluminum plate, respectively. Then, step heights were measured using a diamond stylus surface profilometer (ALPHA STEP 200).

### Fabrication of diamond micropatterns

Figure 1 shows the micropatterning process of CVD diamond films. The diamond/Si substrates were first spin-coated with the metal naphthenates or metal octylates at 2500 rpm for 10 s and then dried in air at 110 °C for 15 min. An electron beam drawing system was manufactured in-house by modifying a conventional scanning electron microscope (SEM) (TOPCON DS-130S). An electron beam was scanned on the metal naphthenate and metal octylate films according to patterns entered in the computer. Metal naphthenate and metal octylate micropatterns were developed by the removing the unirradiated area with toluene. The samples were processed with ECR oxygen plasma under etching conditions of high etching selectivity. Finally, the mask micropatterns of the metal naphthenates and metal octylates remaining on the diamond films were removed with phosphoric acid at 80 °C.

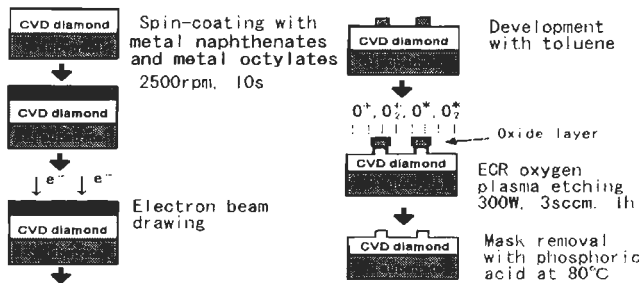
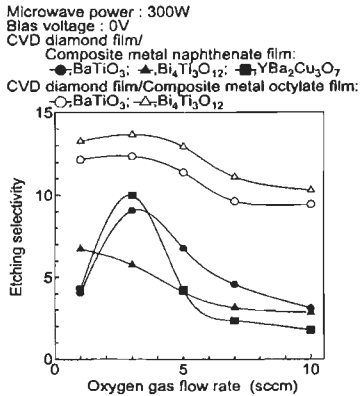


figure 1: Micropatterning process of CVD diamond films.

## Experimental results and discussion

### ECR oxygen plasma etching characteristics

In order to fabricate diamond micropatterns under etching conditions that give high etching selectivity, the dependence of the plasma etching rates of CVD diamond, metal naphthenate and metal octylate films on the oxygen gas flow rate was investigated. It was found that the etching resistance of elemental metal naphthenates and octylates were low to oxygen plasma. Therefore, the resistant mask material which forms a compound oxide was prepared by mixing the metal naphthenate or metal octylate. The dependence of the etching selectivity on the oxygen gas flow rate is shown in figure 2. Most high etching selectivity of 14 was obtained with  $\text{Bi}_4\text{Ti}_3\text{O}_{12}$  octylate film under the plasma etching conditions of 300 W and 3 sccm.



**figure 2:** Dependence of the etching selectivities of composite metal naphthenate films and metal octylate films on the oxygen gas flow rate.

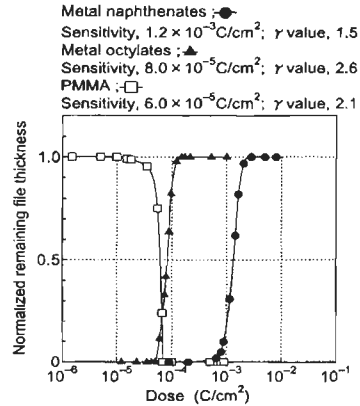


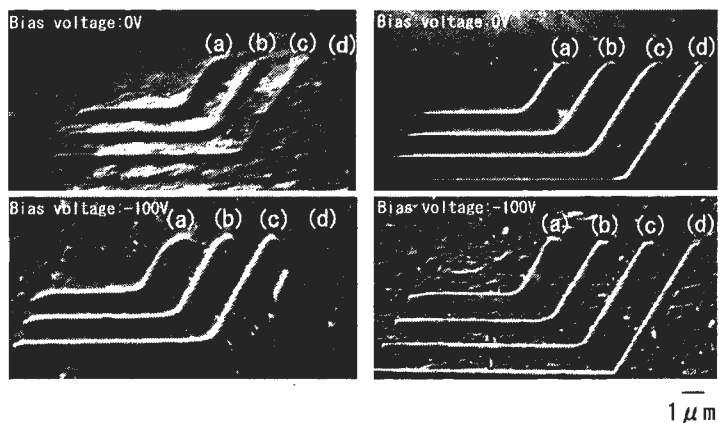
**figure 3:** Dependence of the remaining film thickness of metal naphthenates and metal octylates on the electron dose after development.

### Exposure characteristics of metal naphthenates and metal octylates

In order to obtain the optimum electron beam drawing conditions, the dependence of the remaining film thickness of metal naphthenates and metal octylates on the electron dose after development, as shown in figure 3, was investigated. The metal naphthenates and metal octylates exhibited negative exposure characteristics. The sensitivity and the gamma values of metal naphthenates and metal octylates were  $1.2 \times 10^{-3}$  and  $8.0 \times 10^{-5} \text{ C/cm}^2$ , 1.5 and 2.6, respectively. The sensitivity of metal naphthenates was one hundred times lower than that of PMMA resist, while that of octylates was in good agreement with that of PMMA resist. The electron doses of metal naphthenates and metal octylates were typically set to be  $6.6 \times 10^{-3}$  and  $5.4 \times 10^{-4} \text{ C/cm}^2$ , respectively.

### Fabrication of diamond micropatterns

The micropatterns of CVD diamond films were fabricated under the optimum electron dose and etching conditions of high etching selectivity. The SEM micrographs of the resulting CVD diamond micropatterns fabricated with YBa<sub>2</sub>Cu<sub>3</sub>O<sub>7</sub> naphthenate and Bi<sub>4</sub>Ti<sub>3</sub>O<sub>12</sub> octylate masks which have a height of 0.8  $\mu\text{m}$  (bias voltage: 0V) and 1.2  $\mu\text{m}$  (bias voltage: -100V) for the etching time of 1 hour, are shown in figure 4. The resulting CVD diamond micropattern of 0.1  $\mu\text{m}$  line-width was fabricated with Bi<sub>4</sub>Ti<sub>3</sub>O<sub>12</sub> octylate mask.



(i)  $\text{YBa}_2\text{Cu}_3\text{O}_7$  naphthenate (ii)  $\text{Bi}_4\text{Ti}_3\text{O}_{12}$  octylate  
**figure 4:** SEM micrographs of the resulting CVD diamond micropatterns (microwave power, 300W; oxygen gas flow rate, 3sccm; background pressure, 0.4 pa; etching time, 1 h)

## References

- [1] S. Kiyohara and K. Mori: Jpn. J. Appl. Phys., **39** (2000) 4532.

# Laser-Induced Chemical Vapor Deposition for The Fabrication of Micro Carbon Rods by Pyrolytic Decomposition of Ethylene

J.B. Kim, S.I. Han, S.K. Lee, J.H. Lee, S.H. Jeong

Department of Mechatronics, Kwangju Institute of Science and Technology,  
1 Oryong-dong Puk-gu, Kwangju, Republic of Korea, 500-712

## Abstract

Characteristics of laser-induced chemical vapor deposition for the fabrication of micro carbon rods were investigated with respect to laser power and the pressure of precursor gas. An argon ion laser operated at 514.5nm was used as the light source while ethylene was selected as the precursor gas. When the focused laser beam irradiates on a graphite substrate, the carbon atoms from a decomposition of the ethylene gas deposit on the substrate surface, leading to a growth of a micro carbon rod. The incident laser power varies from 0.3 to 3.8W while pressure of the precursor gas ranges from 200 to 600Torr. For these conditions, the diameter of the rod increases linearly with respect to the laser power but almost independent of the gas pressure. Micro carbon rods with an aspect ratio of about 100 and diameter ranging from 25 to 300 $\mu$ m can easily be fabricated with this method.

## Introduction

Conventional semiconductor processing technologies are widely applied for fabrication of microelements or microsystems due to their advantage in low-cost mass production. However, these processes are mostly optimised for fabrication of planar structures and thus have difficulties in producing three dimensional ones. Microelectromechanical systems(MEMS) for sensors and actuators' applications often require moving or suspended structures, which are in principle three dimensional.

Laser-induced chemical vapor deposition (LCVD) has been investigated to directly fabricate three dimensional structures such as fiber, spring, coil, etc. [1,2]. In LCVD, a focused continuous-wave laser beam irradiates on a substrate and when the surface temperature reaches to a level at which decomposition of the precursor gas can take place a deposition of solid material at the laser spot occurs.

In this study, we investigated the growth characteristics of micro carbon rods produced during laser-induced pyrolytic chemical vapor deposition of ethylene. Specifically, variation of the average growth rate, diameter, and surface quality of micro carbon rods are examined with respect to incident laser power and the pressure of ethylene gas. An optimal condition to obtain good surface quality was determined and fabrication of high aspect ratio structures was demonstrated.

## Experiments

Fig. 1 shows a schematic diagram of the experimental system. An argon ion laser operated at 514.5nm is used as the light source. The diameter of the unfocused laser beam and the maximum output power are 1.8mm and 4W, respectively. The laser beam was expanded to a diameter of 9mm and then focused using a planar convex lens ( $f=200$ mm) onto the graphite substrate to a diameter of 28 $\mu$ m. Ethylene was



selected as the precursor gas because of its reported advantages over other gases for carbon deposition [3] and also safety considerations, i.e. non-toxic material. All substrates were cleaned with ethanol and acetone before deposition. For a laser-induced deposition, the reaction chamber can be either continuously supplied with the precursor gas or filled to an intended pressure and closed during deposition processes. A calculation of the mass of a typical-size carbon rod fabricated in the present study showed that mass of the rod is at least three orders of magnitude smaller than the total mass of carbon contained in the chamber, implying that concentration of the ethylene gas remains almost constant during the deposition reaction. Accordingly, for the present work the chamber was filled and closed during each deposition experiment.

The deposition of carbon can be induced in two ways, namely, either a fixed focus mode or a moving focus mode. In fixed focus mode, the focus of the laser beam is fixed on the substrate surface during reaction. As the deposition progresses, the micro rod grows away from the laser beam focus and subsequently terminates growing due to reduced laser beam intensity at off-focus region. In moving focus mode, the laser beam focus moves along the direction of rod growth. This mode is especially useful to grow rods of high aspect ratio.

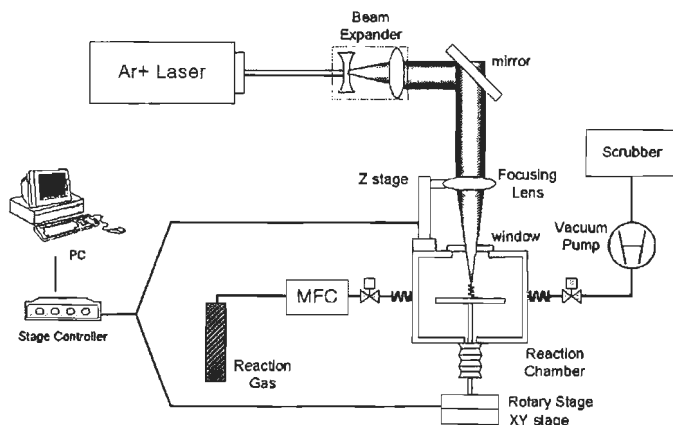


Figure 1: Schematic diagram of the experimental system

## Results and Discussion

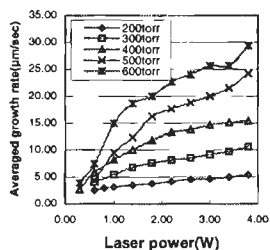
To examine the effect of laser beam power and the pressure of ethylene gas on the growth rate and diameter of the rods, we deposited micro carbon rods at the fixed focus mode. The laser beam power and gas pressure for these experiments ranged from 0.3 to 3.8W and 200 to 600Torr, respectively.

Fig.2 shows the average growth rate of the rods, which is defined as the height of a rod divided by the total growth time. The maximum growth rate was about  $30\mu\text{m}/\text{sec}$  for gas pressure of 600Torr and laser power of 3.8W. For small laser power around 0.5W, the growth rate is almost the same for different gas pressures. As the laser power increases, however, it differs significantly with pressure showing a higher growth rate for a higher gas pressure. Variation of the growth rate at high pressure followed the exponential pattern predicted by the Arrhenius relation. From these results, it is considered that when the laser power is small the rate of chemical vapor

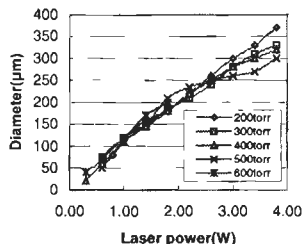
deposition is mostly determined by surface temperature, i.e. the process is kinetically limited, and as the laser power increases the reaction becomes less sensitive to the surface temperature but more influenced by the supply of reactants, i.e. the process is mass transport limited.

Fig. 3 shows the variation of rod diameter. Rod diameter grows almost linearly with the laser power but is independent of gas pressure. A larger diameter at higher laser power is understood due to a wider heated area on the substrate at high power which induces a larger area of initial deposition.

The surface of micro rods varies significantly according to experimental conditions;



**Figure 2:** Averaged growth rate of the micro carbon rods with respect to laser power



**Figure 3:** Diameter of the micro carbon rods with respect to laser power

even the surface of the same rod may change along its height. Typically, bottom of the rod appears rougher and less uniform than near the tip. Laser power rather than the gas pressure is mostly responsible for the surface quality. At high laser power, surface of a rod shows small patterns of irregular shape and size, looking like grain boundaries, covering the entire surface (see Fig. 4(a)). The irregularity of these surface patterns diminishes gradually with decreasing laser power. At a laser power close to the threshold condition, surface of the rod shows none of these irregular patterns but appears very smooth and clean. It is considered that the difference in surface quality with respect to the laser power is attributed to the distribution of nucleation sites during the chemical reaction. For a rod growing normal to the surface, laser energy is first absorbed at the tip of the rod and then transported toward the bottom by conduction. If the laser power is high enough, a finite length of the rod may be heated above the threshold temperature for chemical reaction, inducing localized nucleation of deposits over the side surface as well as the cross-sectional area at the tip. For a laser power near the threshold, on the other hand, only the surface very close to the tip may reach the threshold temperature, leading the deposition only over the top of a rod.

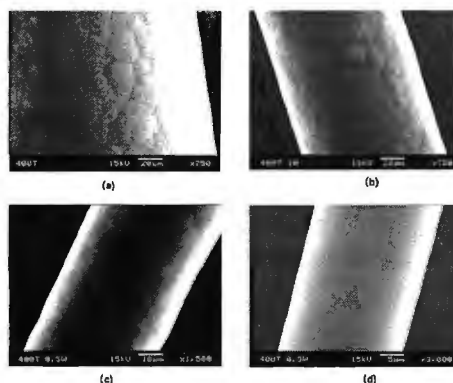


**Figure 4:** Variation of surface quality of the micro carbon rods as a function of decreasing laser power:  $p = 400\text{Torr}$ , (a)  $E = 1.5\text{W}$ , (b)  $E = 1.0\text{W}$ , (c)  $E = 0.5\text{W}$ , (d)  $E = 0.3\text{W}$

It is possible to fabricate micro rods of high aspect ratio with the moving focus mode. In this mode, the laser beam focus is continuously translated along the growth direction using a motorized linear stage. Fig. 5(a) and (b) show the micro carbon rods fabricated with both moving focus and fixed focus modes, respectively. The rod shown in Fig. 5(a) was fabricated by translating the laser beam focus at  $4\mu\text{m}/\text{sec}$  for 10 minutes. The height and diameter of the rod are  $2680\mu\text{m}$ , approximately the same as the translation speed multiplied by the total growth time, and  $28\mu\text{m}$ , respectively, resulting in an aspect ratio of about 100. The rod could be grown to a greater height unless the reaction were intentionally terminated. For the rod grown by fixed focus mode, Fig. 5(b), the growth terminated of itself and the total height after 10-minute laser irradiation was  $1560\mu\text{m}$ . Diameter of this rod varies from 22 to  $28\mu\text{m}$ , showing much poorer uniformity.

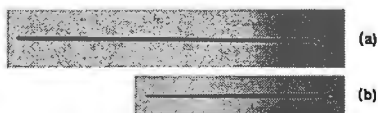


**Figure 5:** Micro carbon rods fabricated with (a) moving and (b) fixed focus modes. ( $E=0.3\text{W}$ ,  $P=400\text{Torr}$ )

## Summary

Laser-induced chemical vapor deposition was investigated as an alternative technique for fabrication of micro structures. The average growth rate of such fabricated micro carbon rods vary widely with respect to laser power and the pressure of precursor gas while the diameter changes almost linearly with laser power. Surface quality of the micro rods is found to be very sensitive to laser power and a cleaner and smoother surface is obtained at near the threshold condition. This technique can be effectively used to fabricate high aspect ratio micro rods.

## References

- [1] F.T. Wallenberger, P.C. Nordine, *Materials Letters* 14, 1992, pp.198-202
- [2] K. Williams, J. Maxwell, MEMS '99, 12th IEEE International Conference in 1999, pp.232-237
- [3] J. Maxwell, Ph.D. Thesis, Rensselaer Polytechnic Institute, U.S.A., 1996

## Three-dimensional micro structuring of Pyrex glass devices – trajectory control

H. Langen, V. Fascio, R. Wüthrich, D. Viquerat

EPFL, Institut de Production et de Robotique, Laboratoire de Systèmes Robotique, Lausanne, Switzerland

### Abstract

A new fabrication technology is introduced for rapid structuring of glass components with microtools. Micro structures are drilled or milled into these materials by spark assisted chemical etching (SACE). The sparks are occurring in the vicinity of the tool tip in a NaOH solution eroding the substrate. High precision micro tools are dressed on the machine itself using wire electrodischarge grinding (WEDG). The whole setup is arranged on a table-top unit in proximity of the clean room. CNC-code and trajectory control were successfully implemented.

### Introduction

With the onset of micro electromechanical device (MEMS) development and micro total analysis system ( $\mu$ TAS) fabrication, the interest for new enabling technologies is increasing. The development and miniaturisation of (machine tool) equipment that could be placed in proximity of clean-room facilities for complementary product processing is an important theme.

This paper presents the development of a prototype machine (figure 1) for three-dimensional micro structuring of glass substrates. The processes that are applied are: wire electrodischarge grinding (WEDG) for micro tool fabrication invented by Masuzawa [1], and spark assisted chemical etching (SACE) for the engraving of three-dimensional structures into Pyrex glass. Figure 2 shows a product example: a part of a micro reactor. Some of the concurrent technologies that are applied in this field are: the exposure and development of photo-sensitive glasses, sand powder blasting, diamond tool drilling, ultrasonic machining, laser machining and the more standard HF etching. The advantages of SACE are its removal rate ( $1.10^{-3}\text{mm}^3/\text{s}$  when applying 30V and using  $\phi 100\mu\text{m}$  tungsten tools), excellent surface quality, its

compact design and the possibility to do rapid micro device prototyping without the necessity of mask design and lithography steps.

Named differently, the process was first applied by Kurafuji [2] in 1968. The combination of WEDG and SACE and the application of SACE on miniaturised machinery (mobile mini-robot with piezo stick-slip motion) were first presented by Langen [3].

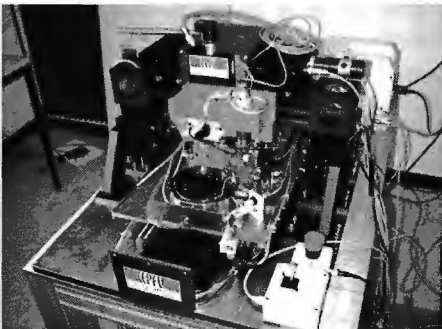


**figure 1:** Prototype machine for micro tool processing and micro structuring on Pyrex glass wafers

## New prototype machine for 4 inch Pyrex wafer processing

Recently we have developed a new prototype machine equipped with xyz-stages and a spindle for micro tool processing. The yz-stages together with the spindle are mounted on a portal structure, while the x-stage is mounted on a base for the positioning of the WEDG unit and an electrolyte container for 4 inch Pyrex wafer processing. The machine's control unit is based on two parallel DSP units (TMS320C40 of Texas Instruments) that address IO-cards on a compactPCI bus. The DSP #1 controls the movement of the axes, while DSP #2 does the signal

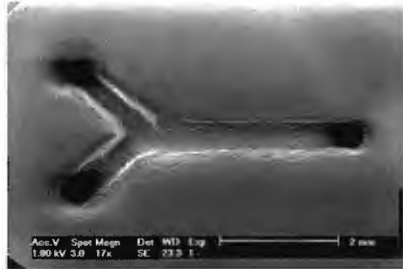


figure 2: Micro reactor

processing of a specially developed voltage/current generator. This generator arranges the voltage/current supply to the anode (Pt) and the micro tool cathode. Both anode and tool are dipped in a NaOH (30% wt) solution close to glass surface. By increasing the voltage, sparks are generated locally at the tool tip. Thermal and chemical erosion occur at the tool tip's extremity. First studies on the process technology were published in collaboration with the Swiss National Science Foundation [4, 5]. Through hole and micro cavity machining for a chemical sensor have been done in collaboration with IMT, University of Neuchâtel [6].

### Motor and trajectory control

The preliminary control that has been applied is digital PID. CNC code has been developed for linear and circular trajectory control. To improve trajectory control for low speeds the algorithm will be enhanced in the future with friction feed-forward and cross-coupling control code. For non-compensated friction and normal PID control the trajectory error during circular interpolation is already satisfactory (encoder resolution:  $0.1 \mu\text{m}$ ) as is shown in figure 3. Due to the limited data space, only the four most important segments with velocity reversals were measured.

For the moment the limitation in machining accuracy is not due to the position accuracy but depends more on the tool bending and the process control itself. Research is done on how the SACE process can be controlled in closed-loop.

### Friction compensation

To improve response time and reduce the trajectory error, the non-linear behaviour of friction for low trajectory speeds should be considered. It can be modelled with a kinetic friction model (KFM), where friction is taken as a function of the velocity only. After application of the static break-away force ( $F_s$ ), stick-slip is initiated and friction reduces normally due to a mixture of boundary lubrication and elasto-hydrodynamic

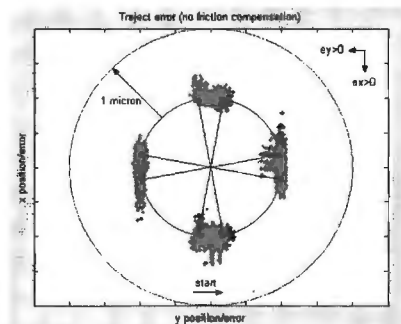


figure 3: Trajectory error for normal PID control ( $R=1\text{mm}$ ;  $v=0.1\text{mm/s}$ )

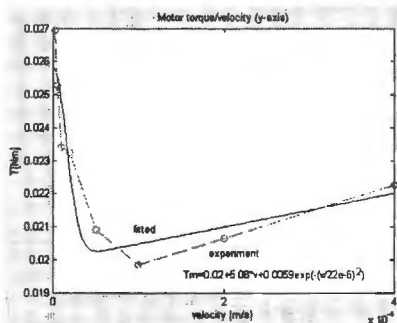


figure 4: Motor torque measurements (y-axis, positive velocity)

	X-	X+	Y-	Y+
Tc[Nm]	-0.0243	0.0231	-0.0256	0.02
Ts-Tc	-0.0064	0.0043	0.0048	0.0059
$\sigma$ [Ns]	31.04	33.91	5.31	5.08
$v_s$ [m/s]	10e-6	4e-6	14e-6	22e-6

Table 1: Motor torque measurements

lubrication. This part of the KFM is called the Stribeck's curve, and is characterized by its negative gradient modelled with the Stribeck velocity ( $v_s$ ).

The KFM model could be written as:

$$F_{KFM} = F_c + \sigma v + (F_s - F_c) \exp(-(v/v_s)^2) * \text{sign}(v),$$

with  $F_c$  the Coulomb friction and  $\sigma$  the viscous friction coefficient. Considerable research has been done on friction modelling and on its application for machine control [7,8,9], and different kinds of functions for describing the non-linear dependency on the velocity are described. Figure 4 and table 1 show some results on motor couple measurements on the x- and y-stages at low trajectory speeds.

Only some preliminary tests on friction compensation (feed forward) were done, but no improvement of trajectory control has been obtained so far. We plan to continue doing research on this subject, and would like to study the possibility of applying cross-coupling control.

### Acknowledgements

The authors would like to thank the people of the mechanical workshop at the LSR and the CIME (EPFL) for the fabrication of some mechanical parts and the taking of SEM photographs, Johan Hemssems for his work on this subject. A part of the research work could be conducted under the sponsorship of the Swiss National Science Foundation (FNS 061533.00).

## References

- [1] Masuzawa, T., Fujino, M, Kobayashi, K. and Suzuki, T., "Wire Electrodischarge Grinding for Micromachining", *Annals of the CIRP*, Vol. 34, 431, 1985
- [2] Kurafuji, H. and Suda, K., "Electrical Discharge Drilling of Glass-I", *Annals of the CIRP*, Vol. 16, 415, 1968
- [3] Langen, H., Breguet, J.-M., Bleuler, H., Renaud, Ph. and Masuzawa, T., "Micro Electrochemical Discharge Machining of Glass", *Int. J. of Electrical Machining*, Vol. 3, 65-69, 1998
- [4] Fascio, V., Wüthrich, R., Viquerat, D., Langen, H. and Comninellis Ch., "A Study of Spark Assisted Electrochemical Etching", *Proc. of the 51th Int. Symp. of Electrochemistry*, 568, 2000
- [5] Wüthrich, R., Fascio, V., Viquerat, D. and Langen, H., "Study of Spark Assisted Chemical Etching – Process Technology Data", *Proc. of the 3rd Int. Conf. on Precision engineering and Nanotechnology*, 2002
- [6] Daridon, A., Fascio, V., Lichtenberg, J., Wüthrich, R., Langen, H., Verpoorte, E. and de Rooij, N., "Multi-layer microfluidic glass chips for microanalytical applications", *Fresenius J. of Analytical Chemistry*, Vol. 371, 261, 2001
- [7] Armstrong-Hélouvy, B., "Control of Machines with Friction", Kluwer Academic Publishers, Massachusetts, 1991
- [8] Canudas de Wit, C., Olsson, H., Åström, K.J., and Lischinsky, P., "A New Model for Control of Systems with Friction", *IEEE Trans. Autom. Control*, 40(3), 419-425, 1995
- [9] Altpeter, F., "Friction modelling, identification and compensation", PhD. thesis, EPF Lausanne, 1999

## Economic and sensitive assembly of microsystems in small quantities

G. Reinhart, M. Schilp, D. Jacob

Garching (Munich), Germany

### Abstract:

Precision alignment and bonding operations are the most costly process steps in manufacturing hybrid microsystems. Particularly specialized microsystems, which are manufactured in small and middle numbers of items, require automated cost efficient assembly solutions. This paper describes a basic approach to a modular structured assembly tool, which can be easily adapted to different jobs due to its structure. Exchangeable grippers, different joining processes as well as flexibly integrable high precision sensor technology enable an economical assembly of most different products with the same tool. Hybrid systems with smallest components are possible by innovative joining processes e.g. application of adhesives by microcapsules.

### Modular assembly tools for small numbers of items

After the triumphant advance in the automotive industry, microsystems spread into ever more areas of daily life. The manufacturers try to meet the vast variety of applications by modularisation of the functional components. Consequently high-specialized individual components must be assembled to hybrid modules. This leads to a rising demand of assembly capacities. Particularly with optical systems and high frequency applications the components must be aligned to each other with high precision tolerances below 10  $\mu\text{m}$ . At the same time the component size is constantly decreasing. Component sizes under 300  $\mu\text{m}$  edge length are no more rarity.

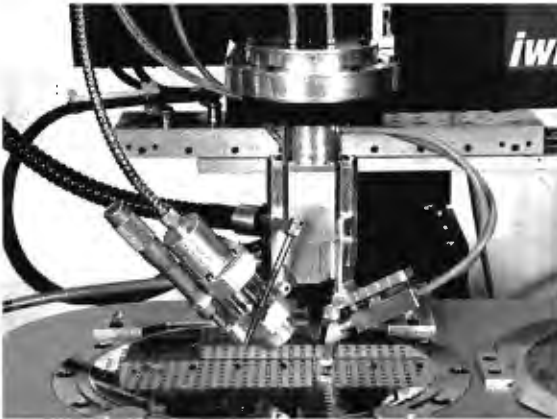


**figure 1:** Flexible, modular assembly tool

By the multiplicity of the hybrid systems version variety is rising and the numbers of items per assembly lot is decreasing. Therefore manual assembly very often is installed as long as the assembly tolerances allow. A partly automated or even automated assembly is very hard to implement, since the capital outlays of conventional high precision diebonders, if they are usable due to their structure at all,

do not permit an application with small numbers of items. At the same time these machines are not optimized for frequent product changes and permit a planar assembly only.

According to studies the costs of the assembly often sum up to 70% of the product costs due to these facts [1]. Particularly for small companies this puts a high entrance



barrier by high capital expenditure and nevertheless high allocation of highly-qualified personnel.

Therefore an assembly tool for the application at standard robots [2], [3] was developed at the *iwb* (figure 1). It is suitable for most different positioning strategies: Both absolute positioning with the help of a suitable handling equipment, relative positioning using sensors and a combination of coarse and fine manipulation by piezoelectric micro positioners are possible.

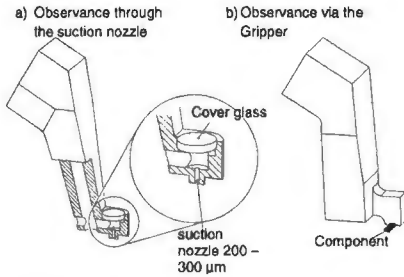


**figure 2:** different shapes of grippers adapted to part geometry

changing modules are corrected by online image processing. The possibility of each module to move into the field of view of the vision system enables real relative positioning, as both positions of part/gripper and target can be compared. The individual gripper modules are designed to be exchangeable and can be adapted to different component sizes and special shapes at few effort (figure 2).

**Modular integrable packaging technologies for tiny components**

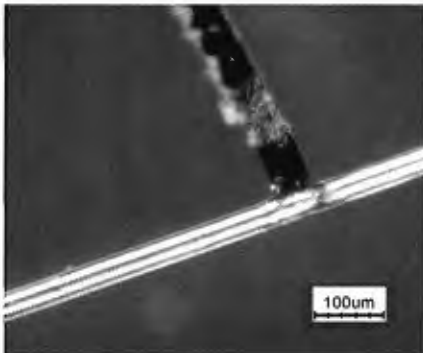


**figure 3:** Microwelding joint of two wires

Basically the tool is characterised by its modular structure. The cost-intensive, frequently used modules like positioning sensors (a telecentric high-resolution optics), the mounting force sensor as well as the fine positioning manipulator are situated in the tool base. [2], [4]

Specific modules are affixed to this basic module, which has to be manually adapted in the current tool design, but which will enable an automated tool change in the future. Changes in tolerances occurring as a result of

Further function modules already implemented are a dispensing tool and a laser optics of a fiber-coupled diode laser, which can be used for heating the splice. Thus microweldings, solder joints or also thermal hardening of adhesives are possible. Beyond that, new liquid apply processes for smallest adhesive joints are developed.

**Laser welding technology**

By the integration of a fiber-coupled diode laser [5] selective soldering as well as microwelding became possible. Using a wavelength of 980 Nm and a laser output of 25 W with a focus diameter of 200 µm even thin sheet metals can be

welded through. Also precise welding of tiny components is possible: The connection of a PtNi wire (diameter of 40 µm) with a wire of the rectangular profile of 8x40 µm could be reproduced and is meets process quality standards (figure 3).

### New liquid applying technology in adhesive bonding by microcapsules

Ever smaller component sizes require ever smaller joints. The feasibility borders of adhesive joints are almost reached. With conventional dosing processes it is very difficult to dispense reproducibly adhesive quantities below one nano-litre using a capillary. The results can be increased within certain limits only by sensing the needle clearance. A further restriction is the limitation of this process to viscosities up to approximately 5000 mPas. [8]



**figure 4:** Adhesive bonding process using microcapsules

adjustable by the process between few micrometers up to millimeter size, dependent on the viscosity of the contents material and the capsule's wall material.

These capsules are transported – like the component itself – by the gripper to the joint position. After destroying this container the adhesive is released and the component can be bonded as usual.

Test series for classifying the capsules diameter, transportation of the capsules to the joint and different pulping processes have already been successfully executed.

This new approach offers many advantages:

- The amount of adhesive dispensed to the joint is exactly predictable by classifying the size of the capsules.
- Liquids of very high viscosities can be encapsulated.
- Due to the capsules' wall pot time of adhesive is no longer important. Hardening of the joint before mounting the component can be avoided.

There are still research activities concerning some unanswered questions:

- Influences of the capsule wall remaining in the splice (less than 5% of the total capsule volume) are not completely cleared.
- Encapsulation processes of one component adhesives broadly used in microsystem technology have to be developed. To this technique especially adapted adhesives are not available on the market. Probably even new adhesive systems have to be found.

In spite of further needs of development efforts this new process is promising a large field of bonding applications of tiny parts due to its advantages.

## References

- [1] Koelemeijer Chollet, S.; Jacot, J.: "Cost Efficient Assembly of Microsystems", MST-News (1990) 1, pp. 30-32.
- [2] Reinhart, G.; Jacob, D.: Positioning Strategies and Sensor Integration in Tools for Assembly MOEMS. In: Motamedi, M.; Göring, R.: MOEMS and Miniaturized Systems, Santa Clara. Washington: Proceedings of SPIE Vol. 4178 (2000), pp. 395 - 402
- [3] Reinhart, G.; Jacob, D.; Zimmermann, J.; Soetebier, S.: Mikromontage als Schlüsseltechnologie. wt Werkstattstechnik (2000) 90, vol. 9, pp. 340 - 345
- [4] Reinhart, G.; Schilp, M.; Jacob, D.: Economic Strategies and Tools for Microassembly. Proc. The Commercialization of Microsystems 2000, 5.-9.9.00, Santa Fe, New Mexico, USA
- [5] Reinhart, G.; Jacob, D.: Automated Assembly of Holder Chips to AFM Probes. In: Nelson, B.J.; Breguet, J.-M.: Microrobotics and Microassembly III, Boston. Washington: Proceedings of SPIE Vol. 4568 (2001), pp. 310 – 317
- [6] Döring, M.: "Flüssigkeiten mikrofein dosieren". Feinwerktechnik u. Messtechnik, 1991/11
- [7] Seitz, H.: "Auftragen von Farben und Lacken mittels piezoelektrischer Mikropumpen", FhG Seminarbericht Mikrofluidkomponenten und -systeme, FhG-IFT, München 1998
- [8] Schilp, M.: Dosier- und Dispenstechnik - das Problem des kleinen Tropfens. In: Reinhart, G. (Hrsg.), Automatisierte Mikromontage, Seminarberichte iwv (2001) 59, Herbert Utz Verlag, München 2001

## Calibration of orientation measurement systems based on tilt sensors and compasses

J. Clijnen, D. Reynaerts, H. Van Brussel

Department of Mechanical Engineering, Katholieke Universiteit Leuven, Belgium  
Joeri.Clijnen@mech.kuleuven.ac.be

### Abstract:

A calibration technique for orientation measurement systems based on tilt sensors and compasses is developed. With this calibration technique, the orientation measurement system is placed in different known reference orientations. These reference orientations are mapped on the measurements of the orientation measurement system using non-linear parameter identification, resulting in a parameter set containing the sensitivities, offsets and misalignments of each sensor. For this calibration technique a new test set-up is constructed, able to put an orientation measurement system in a random reference orientation with an accuracy of 0.1degree. The test set-up is used to calibrate a commercially available 2D accelerometer IC, working as an inclinometer.

### Introduction

The determination of the physical location of systems, people and infrastructure is a hot topic in today's research. Various systems for position and orientation tracking exist, such as GPS, gyroscopes, compasses, tilt-sensors, etc. In the continuous struggle to reduce the price and size, these systems consist of a combination of cheap micro-sensor ICs. The problem with these micro-sensor ICs is the alignment of the ICs during assembly. To obtain accurate measurements, calibration after assembly is necessary. The calibration procedure described in this paper focusses on the calibration of orientation measurement systems with one or more micro-sensor ICs, but it can also be used more widely to calibrate other types of sensors, like accelerometers.

In measurement systems with tilt sensors and compasses, orientation determination is based on the projection of the gravity and magnetic field on the sensor axes. If these sensor axes are not well aligned, these projections will be different and the calculation of the orientation will be incorrect. If the misalignment errors are known, they can be compensated.

Figure 1 shows the compensation diagram for one sensor. First, the sensor output signal is converted to the physical value of the measured field. This value is the projection of the field on the sensor axes. Due to a misalignment, these sensor axes differ from the desired frame axes. A rotation matrix  $R$  transforms the physical value back to the frame axes. This transformation is only possible if the three field components  $x, y, z$  are measured. For 2D sensors, an estimation of the third dimension with the well known formula  $F_z = \sqrt{(F_{tot}^2 - F_x^2 - F_y^2)}$  is possible if the total value of the field is known. In the last step, the angle is calculated starting from the physical value of the field in the frame axes.

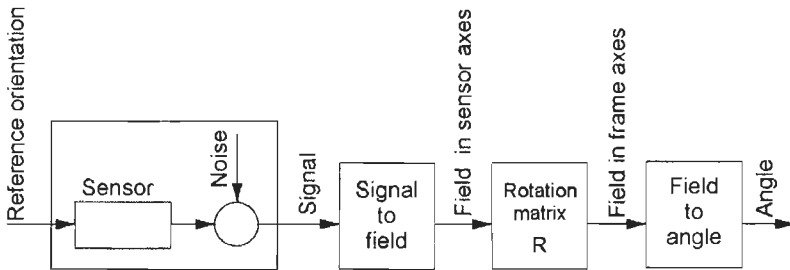


**figure 1:** Compensation diagram for orientation measurement systems.

This compensation diagram contains a lot of unknown parameters, like the sensitivity, the offsets and the misalignment errors. The purpose of the calibration procedure is to identify all these parameters.

### Calibration procedure

The calibration can be split into two parts: collection of the calibration data and parameter identification. The collection of the calibration data is done by putting the sensor in different known reference orientations. These reference orientations are equally distributed over the entire range of interest. The signals of the sensor and these reference orientations form the calibration data.

After collecting the calibration data, the parameter identification determines the optimal parameters by minimising an error criterion.

One possible error criterion is the quadratic difference between the calculated orientation and the reference orientation. In other words, the reference input in figure 1 is subtracted from the calculated angle and squared. However, this error criterion has one weakness. The noise, added in the sensor, is deformed and coloured by the calculations after the sensor. Therefore, the noise contribution in the error will be higher in some orientations than in other. Because the optimisation criterion minimises the overall error, the parameters will be less optimal.

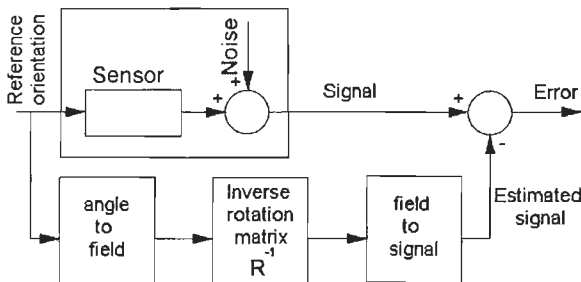


**figure 2:** The second error criterion.

Another possible error criterion is shown in figure 2. The reference orientation is used to calculate the estimated sensor signals. The error criterion is the square of the difference between the measured sensor signals and the estimated ones. With this criterion, the noise added in the sensor is a direct part of the error criterion.

Therefore, a deformation of the optimisation process is not possible.

The error criterion is iteratively minimised by the non-linear least-square algorithm [1,2]. A faster, non-iterative linear algorithm is not possible because the calculations of the estimated sensor signals are non-linear.

### 3D-orientation calibration set-up

The aim of the 3D-orientation calibration set-up is to put the sensor in different known reference orientations. Because the orientation of a body is determined by three angles, the set-up needs three independent axes. These axes are defined according to the ZYZ Euler axes [3]. Each axis is measured with an absolute encoder. In addition the accuracy of the set-up has to be high because the set-up is used as a reference. This means that not only the measurement of the rotation around the different axes has to be accurate, but also the axes have to be perpendicular and have to intersect in the same point. An accuracy of 0.1 degree is reached, which is sufficient for the envisaged calibration. Last but not least, the materials for the set-up are specially chosen to avoid any disturbance of the earth magnetic field, which is necessary to calibrate compasses. All these design aspects result in the set-up shown in figure 3.

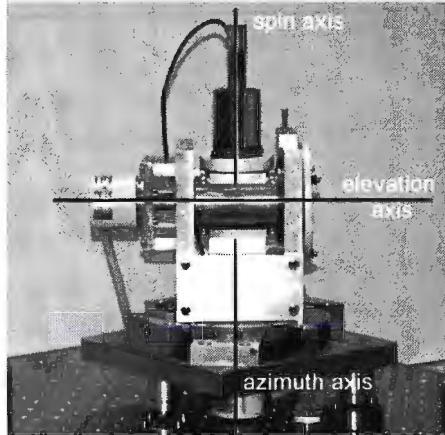


figure 3: The 3D-orientation set-up.

### Calibration of 2D tilt-sensor

The calibration procedure is tested by calibrating a commercially available 2D accelerometer IC, working as an inclinometer. The accelerometer measures the projection of gravity field on the sensor axes, which is a measure for the orientation of the accelerometer.

The accelerometer IC is manually mounted on a PCB with a misalignment of 5.3 degrees. After mounting the PCB board in the calibration test set-up, the sensor is put in 576 reference orientations (12 azimuth angles x 12 spin angles x 4 elevation angles). In every orientation the sensor readings are recorded as soon as the sensor stands perfectly still. These sensor readings are used to calculate the sensor orientation. The difference between the reference orientation and the calculated orientation is shown in figure 4 and 5.

Figure 4 and 5 also show the improvement of the accuracy after calibration. The error on the spin axis decreased with 91% and the error on the elevation axis decreased with 88%.

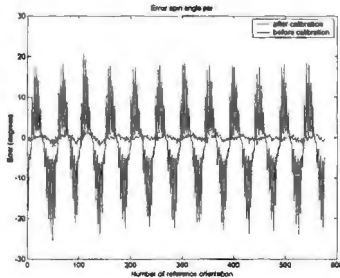


figure 4: Error on spin angle.

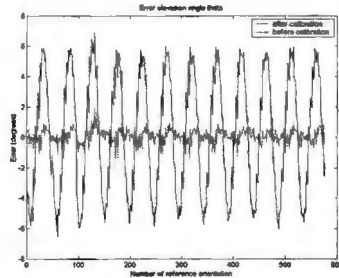


figure 5: Error on elevation angle.

## Conclusions

With IC sensors, a calibration technique for calibration after assembly becomes more important. For this calibration, the orientation measurement system is set in different reference orientations and the sensor readings are compared with the estimated sensor readings. The non-linear least square optimisation determines the sensor parameters and the misalignment errors. For test purposes, an orientation set-up has been built with an accuracy of 0.1 degree. This set-up is used to calibrate a commercial IC-accelerometer, working as an inclinometer. The accuracy could be improved by a factor 10.

## Acknowledgement

This research is sponsored by the Fund for Scientific Research - Flanders (Belgium) (FWO), project G0296.95N, and by the Belgian programme on Inter-university Poles of Attraction initiated by the Belgian State, Prime Minister's Office, Science Policy Programming.

## References

- [1] Ljung, L.: "System Identification: theory for the user", Prentice-Hall Inc., 1987.
- [2] Norton, J.P.: "An introduction to Identification", Academic Press, 1986.
- [3] Sciavicco L., Siciliano B.: "Modeling and control of robot manipulators", McGRAW-HILL, 1996

## A CAD-tool for the design and manufacturing of microstructures based on micro-EDM

W. Meeusen, D. Reynaerts, H. Van Brussel

Department of Mechanical Engineering, Katholieke Universiteit Leuven, Belgium  
 Dominiek.Reynaerts@mech.kuleuven.ac.be

### Abstract

It is known that micro-EDM is a proper and flexible technology to machine freeform three-dimensional microstructures. Unfortunately, its capabilities are underestimated by the ruling microsystem designers due to the lack of widespread modelling and simulation tools. This paper gives a global overview of a implemented CAD-tool for micromechanical systems based the micro-EDM technology. All designs are parametric and feature based. On top of standard features, user defined features can be created, which are automatically assessed on their producibility and added to the feature library. Additionally, tolerance simulations can be performed to gauge the effects of dimensional inaccuracies. Eventually, tool paths are generated for each feature and process parameters are optimised. To compensate electrode wear the multiple electrode strategy is applied and the necessary number of tool electrodes is estimated.

### Introduction

The application of technological processes to fabricate microsystems is increasingly supported by modelling and simulation tools. In mainly all of the approaches the design of microsystems is solely based on the use of standard processes, which are, unfortunately, restricted to the technological basis provided by today's semiconductor industry. With the view to the development of new and more flexible fabrication processes, that offer three-dimensional machining, it is necessary to develop new modelling and simulation tools to spread the application of these innovative technologies. One of these emerging technologies is micro-EDM (micro-Electro Discharge Machining)[1][2]. EDM is an electro-thermal machining process, by which material is removed by the erosive action of electric discharges, that are created between a tool electrode and a workpiece electrode, both electrodes immersed in a dielectric fluid.

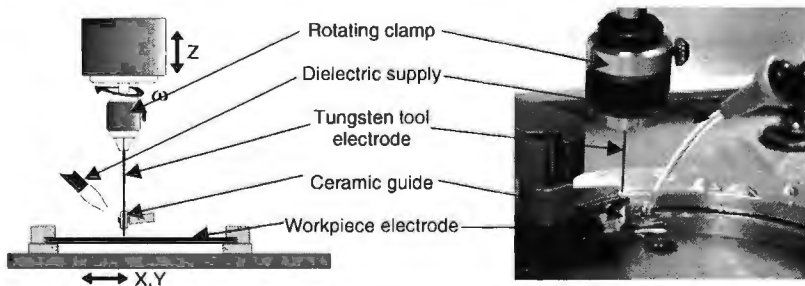


figure 1: Schematic and real view on the micro-EDM workspace

In the micro-EDM case, the tool electrode is a stiff tungsten wire clamped in a rotating chuck and guided by a ceramic guide (figure 1). The tool electrode has a



standard cylindrical shape with a diameter of 150  $\mu\text{m}$ . To dress and shape the tool electrode a WEDG (Wire Electro Discharge Grinding) unit is developed, depicted in figure 2. The WEDG tool electrode is an accurately positioned and slowly moving metal wire. The continuously unwinding of the wire makes this EDM process free from tool wear. The WEDG-technology allows the production, in a repeatable way, of miniaturised and complex shaped tool electrodes on the erosion machine itself, which avoids misalignment errors during reclamping of the tungsten tool electrode.

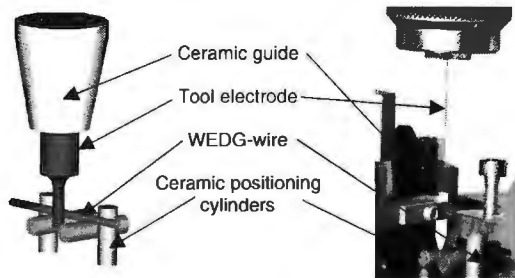


figure 2: Schematic and real view on the WEDG-unit

### Micro-EDM based design environment

The proposed and implemented CAD-tool offers a library of standard parametric manufacturing features, which are all manufacturable by definition. Furthermore, this CAD tool offers a rapid means to create, asses and apply micro-EDM-specific user defined manufacturing features. Eventually, for each feature tool paths are generated and technology parameters are optimised. Additional tolerance simulations will offer more insight on the effects on the microsystem's behaviour due to variations of feature dimensions.

### Manufacturing features

The developed design environment is based on manufacturing features, which contain, except for geometrical data, information associated with desired machining quality and required machining operations. Figure 3 shows, for example, a mechanical design of an inertial sensor, of which the mass is suspended by two parallel beams.

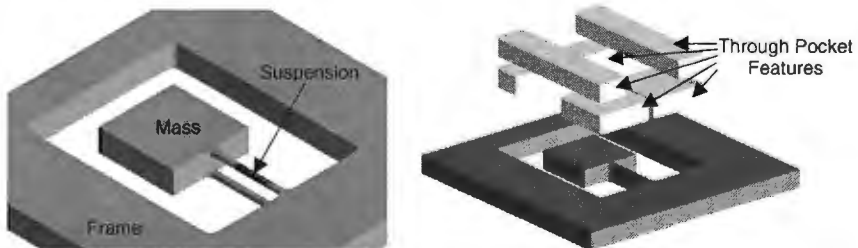


figure 3: Inertial sensor design

Applying the micro-EDM technology, this structure can be machined in a single clamping set-up and in any electrically conductive material such as hardened steel or doped silicon. The design of this inertial sensor starts with the creation of a substrate volume. Next, the major part of the material removal is realised using Through Pocket Features, which are illustrated in exploded view. Only the material between the two suspension beams remains, which is not removable with the basic features

offered by the design environment. To deal with particular details or freeform surfaces the designer is able to create user defined features (UDFs). Each UDF is based on the geometry of a shaped tool electrode. By defining appropriate tool paths for this newly designed tool electrode, desired material removal can be achieved. Figure 4 illustrates a tool electrode moving along the suspension beams, removing the remaining material. Figure 4 also shows a machined tool electrode and the silicon double beam suspension machined by this shaped electrode. All features, predefined and UDFs, are parametric and can be altered any time in the design sequence. Each time a parameter changes, the environment rechecks the producibility of each feature so that the microstructure design sustains producible. The final design can be analysed using FEM to verify the mechanical characteristics of the microsystem.

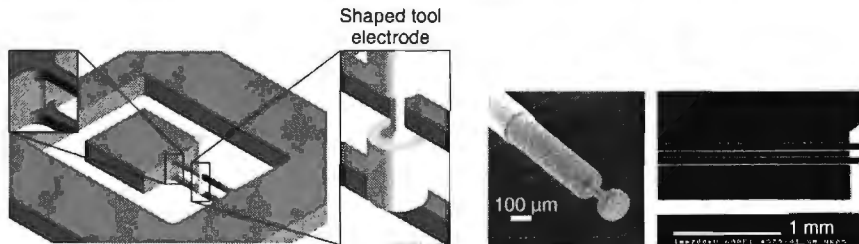


figure 4: Example of user defined feature

### Tool path generation and technology settings

Both standard and user defined features in the design environment are manufacturing features. Consequently, a predefined and optimised tool path strategy can be applied to machine each feature. To minimise the effect of tool electrode wear on the dimensions of the microstructures, wear compensation techniques were developed [3][4]. The multiple electrode method [3] is implemented and the necessary number of electrodes is estimated based on a simplified wear model. To optimise process parameters the micro-EDM process of silicon machining on a AGIE Compact I die-sinking EDM-machine is modelled using a central composite design. The model predicts the material removal rate, the relative electrode wear and the obtainable surface roughness for a given set of machining parameters. The parameter set with the shortest machining time and offering at least the desired surface roughness is chosen. Figure 5 shows the tool path strategy of a pocket feature and the related optimised machining parameters.

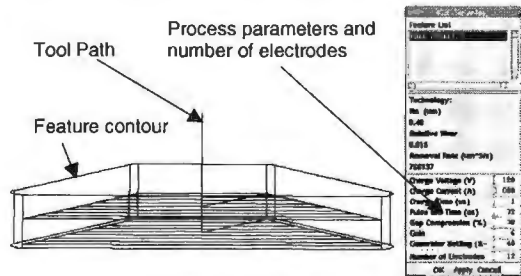


figure 5: Tool path creation and process parameter optimisation

### Tolerance simulation

During fabrication a number of uncontrollable machining uncertainties lead to dimensional variations of the microstructure. Typical uncertainties are for instance local dielectric resistance variation or badly flushed erosion gap leading to an

unpredictable gap dimension, thermal deformation of the erosion machine, eccentric rotation of the tool electrode. The undesired dimensional variations may even result in improper behaviour of the microsystem. To simulate the effect of dimensional variations a Monte Carlo simulation is implemented. Variations in micromould volume or shifts in

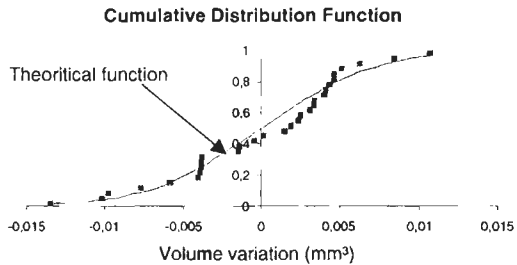


figure 6: Tolerance simulation

resonance frequencies for sensors and actuators can be simulated. Figure 6 shows the cumulative distribution function of the volume variation of a single pocket consisting out of 30 calculation points plotted on the theoretical distribution function.

## Conclusions

The introduced CAD-tool offers a means to design microstructures, which are producible using the micro-EDM technology. The implemented design environment is parametric and feature based. Besides the standard available manufacturing features, the design environment offers the possibility to create complex user defined manufacturing features. Microstructures can be assessed using FEM-analysis and using a build in tolerance simulator. For all microstructures, designed in the CAD-tool, the necessary machine-dependent machining files are automatically created, taking wear compensation techniques into account. Although micro-EDM has already proved to be a versatile micromachining technique, technology-oriented CAD-tools will spread the application of the micro-EDM technology more rapidly.

## Acknowledgements

The research on electro-discharge machining is sponsored by the Fund for Scientific Research - Flanders (Belgium)(F.W.O.), project G0296.95N, and by the Belgian programme on Inter-University Poles of Attraction (IUAP4-24) initiated by the Belgian State, Prime Minister's Office, Science Policy Programming. W. Meeusen has a doctoral scholarship of the Flemish Institute for the Promotion of Scientific-Technological Research in Industry (I.W.T.).

## References

1. D. Reynaerts, X. Song, W. Meeusen, H. Van Brussel; "Silicon bulk micromachining by micro-EDM milling with electrode compensation", Proc. of Int. Congress for Sensors, Transducers & Systems, pp. 249-254, 1999.
2. T. Masuzawa, "Micro-EDM", Proc. of the 13th Int. Symp. For Electromachining, pp. 3-19, 2001.
3. D. Reynaerts, H. Van Brussel, W. Meeusen, X. Song; "A review on micro-electro discharge machining of metal and silicon", Proc. euspen 1st Int. Conf., pp. 24-29, 1999.
4. Z.Y. Yu, T. Masuzawa, M. Fujino, "Micro-EDM for Three-Dimensional Cavities - Development of Uniform Wear Method-", Annals of CIRP, Vol.47 pp. 169-172, 1998

# Improvement of Micro End Milling Tools through Variation of Tool Manufacturing Method and Geometry

J. Schmidt<sup>1</sup>, H. Tritschler<sup>1</sup>

1 Institute of Machine Tools and Production Science, University of Karlsruhe (TH), Karlsruhe, Germany, Tel.: +49-721-608-4288, Fax.: +49-721-699153  
E-Mail: hanno.tritschler@mach.uni-karlsruhe.de

## Abstract

Micro-cutting offers good potentialities for manufacturing small and medium lot sizes of micro-parts with unrestricted geometry at an economically reasonable expense, either by direct machining or as a means to make moulds for micro injection molding. It yields large removal rates, good compliance with allowances, good surface quality and a wide choice of workpiece materials. Particularly when highly wear resistant materials are to be sculptured, as in mould making for powder injection molding, micro cutting of tool steel is quite an eligible option. With the present ultra-precision drive train, guideways and spindle technology being rather advanced, restrictions to the cutting process efficiency results most of all from the cutting tool itself. Overcoming these shortcomings requires variation of tool material, tool manufacturing method and tool geometry.

## Outset

### Motivation

Since machining steel using single point diamond tools brings about substantial difficulties in terms of tool wear, the utilization of ultra-fine grain hard metal tools represents a promising alternative for micro-cutting of steel [1]. In the first step, we chose tungsten carbide end mills in order to manufacture steel microstructures. Micro injection molding as the main scope of application for micro-cutting imposes high demands on the surface quality – 0.5  $\mu\text{m}$  Rz is desirable - and does not tolerate burr formation. Since commercially available micro cutting tools are mostly down-scaled from macroscopic cutting tools, we varied the tool geometry in order to identify suitable geometries for micro cutting.

### Experimental Equipment

In order to obtain a tailored experimental equipment, a three axes micro-milling-machine has been designed, built, run-in and evaluated complementarily to the cutting experiments. The table of the machine is driven by AC servo motors connected to planetary thread screws with a machining envelope of 400 mm by 150 mm by 220 mm. As milling spindle, mainly an ultra-high speed spindle by The Precise Corporation, rotated with 160,000 rpm is used. This kind of extremely high spindle rotation is essential in end-milling with small tool diameters, because otherwise the cutting speed is insufficient. The high-speed spindle is equipped with hybrid ball bearings, i.e. steel bearings with ceramic balls, which provides for higher stiffness compared to air bearings and therefore makes the spindle very suitable for the machining of hard materials like steel. The evaluation of the machine proved that the positioning error as well as the minimum step width is better than 1  $\mu\text{m}$  [2].

### Material

Aside from hot-work tool steels like AISI H11 (X 38 CrMoV 5 1) and AISI H13 (X 40 CrMoV 5 1) [4, 5], which were examined in earlier experiments, recently also AISI O2

(90 MnCrV 8) was machined in different heat treatment states. It represents an oil-hardening cold-work tool steel with particularly high wear resistance against abrasive wear and a comparatively good machinability at the same time. The main application is mold and die making for injection molding and even forming. Like in the earlier experiments, special attention was given to the heat treatment, so that the grain size and – particularly important with a higher content of carbon – the distribution of carbide grains is below  $10\ \mu\text{m}$  and as homogenous as possible. Material hardness after heat treatment was varied mostly between 57 HRC and 64 HRC.

### Capability of Commercial Tools

With commercially available end milling tools, micro structures in hardened tool steel can be manufactured with an accuracy of better than  $0.01\ \text{mm}$  and a surface quality better than  $0.3\ \mu\text{m}\ R_z$  in less than an hour's machining time. Suitable process parameters, strategy and tool geometry provided, little or no burr formation occurs. One of the major drawbacks is that concave structures cannot be machined smaller than  $0.1\ \text{mm}$  due to the available tool diameters.

### Approach and Current Results

#### Manufacturing Methods

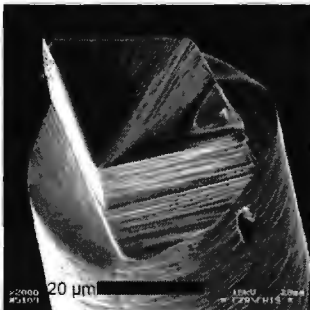


figure 2: tungsten carbide end mill manufactured using FIB

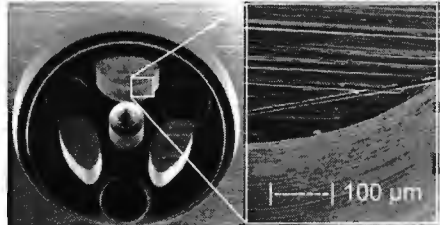


figure 1: Mold cavity for a model car rim (l.) and detail of milled edge (r.)

The common manufacturing method for tungsten carbide cutting tools is grinding using diamond. With grinding wheels of micrometer-size diamond grain quality available, minute structuring of the tool geometry down to diameter  $0.1\ \text{mm}$  has become possible and is being marketed comparatively successfully. Due to the grinding forces and vibrations, though, the yield is dissatisfying. In order to obtain tools of even smaller diameter and also tailor-made geometry, tool manufacturing methods other than grinding were employed, namely laser machining and focused ion beam (FIB) milling.

### Variation of Geometry

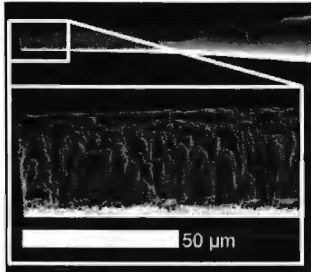


figure 3: laser machined tool

As was established earlier [5], single flute end milling tools appear more reasonable for very small tool diameters due to the disproportionateness of added up roundness errors of the tool, spindle, clamping etc. Therefore, both by FIB and laser machining, single flute end mills were manufactured. While for the laser-machined tool a simple engraving tool geometry was chosen, the FIB-machined tool was furnished with a rather intricate geometry providing for a better stability. The former was machined with a laser source of 1 W at 256 nm, while the latter was machined with Au-ions at 35 keV, a current density of 1.2 A / cm<sup>2</sup> and a spot size of ~0.3 µm. As can be seen from the images in figure 3, the surface quality of the laser machined tool still requires massive process optimisation, whereas the FIB-machined tools are suitable for cutting experiments. The elaborate pre-machining preparations necessary with the currently used FIB-equipment, however, do not allow for statistically based experiments but rather for a mere investigation of feasibility.

Since the FIB equipment currently used in this research is designed to control material removal in a slitting manner rather than in an excavating manner, the manufacturing of a geometry as presented in figure 4 is far more challenging than the one presented in figure 2 and 3. By initial cutting experiments the fundamental ability of such type of cutting tool was established. Burr formation, though, was exceedingly strong with an average burr height of more than 10 µm. Future optimisation is focused on burr reduction, which will be pursued through application of a higher rake angle and eventually through application of a sharper cutting edge using a different tool material.

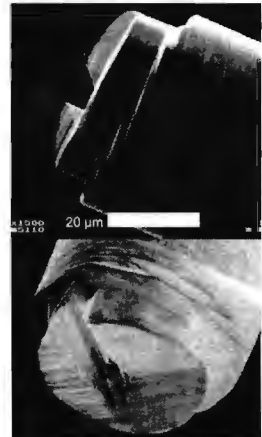


figure 4: FIB-machined end mill

### Variation of Tool Material and Improvement of Cutting Edge

Since both surface quality and – through influence on the cutting forces – the wear life of the tool strongly depend on the micro geometry of the cutting edge, care should be taken to its formation. An extremely sharp and at the same time durable edge is desirable. Depending on the grain size, tungsten carbide tools are in this respect limited to a minimum cutting edge roundness of 2 ~ 5 µm. Exceeding this limitation is only feasible by variation of the tool material. While single crystal cubic boron nitride is hardly available in grain sizes suitable for single point cutting

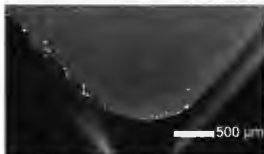


figure 5: artificial sapphire tool

tools, in this research artificial sapphire was used to obtain a sharper cutting edge. Judging from SEM images, the edge appears comparable to single crystal diamond tools. Preliminary cutting experiments on face-turning of O2 tool steel (90 MnCrV 8)

of 58 HRC have been successful. The persistence of the tool material in discontinuous cutting is yet to be assured.

## Outlook

With the preliminary cutting experiments with end mills of abt. 50  $\mu\text{m}$  diameter and complex geometry having been successful, the next step will be the optimization of the tool geometry in order to obtain less burr formation. Further, PVD-coating for an economically reasonable tool wear life appears essential. Long ranged research has to focus on the evaluation of the feasibility of transferring the initial results in facing of tool steel using artificial sapphire towards micro end milling.

Since three years now the 3-axis machine tool has been a useful experimental equipment comparing to other conventional machine tools, although in terms of machining accuracy and particularly in the dynamic behavior of the x/y-table it lies by a factor 10 below the performance of commercially available ultra-precision machine tools. Future work, especially with tools of diameters below 0.1 mm or extremely brittle tool materials will be carried out on a Kugler ultra-precision milling center.

## Acknowledgements

The work presented here are part of a cooperation of various institutes at the University of Karlsruhe and the Research Center of Karlsruhe (FZK) and are financially funded by the Deutsche Forschungsgemeinschaft DFG ("german society for research"). The close cooperation with the Institute of Material Science and Engineering (iwk1) of the University of Karlsruhe (TH) has been particularly beneficial for this research. The experiments with modifications of the tool were carried out in cooperation with Forschungszentrum Rossendorf, Laserpluss AG and HAM GmbH, Germany.

## References

- [1] Masuzawa, T., State of the Art of Micromachining, Keynote Paper in: Annals of the CIRP Vol. 49/2/2000
- [2] Weule, H., Schmidt, J., Hüntrup, V., Tritschler, H., Micromilling of Ferrous Materials, in: Production Engineering Vol. VI/2, 1999, p. 17-20
- [3] Spath, D., Hüntrup, V., Micro-Milling of Steel for Mould Manufacturing – Influences of Material, Tools and Process Parameters, Proceedings of the 1st international conference of the euspen, Bremen (Germany), McKeown P. et al. (editors), Shaker, Aachen, 1999
- [4] Peichl, A., Schulze, V., Löhe, D., Tritschler, H., Spath, D., Microcutting of Steels – Interaction of Material Properties and Process Parameters, Micro.tec 2000, Hannover, 27 September 2000
- [5] Schmidt, J., Tritschler, H., Haberer, H., Cutting Tools and Material Conditioning for Micro End Milling of Tool Steel, Proceedings of the 2st International conference of the euspen, Turin (Italy), 30 May 2001
- [6] Weule, H., Hüntrup, V., Tritschler, H. Microcutting of Steel to Meet New Requirements in Miniaturization, Annals of the CIRP Vol. 50/1/2001

## Nanoimprinting of 4 Inch Substrates and a Strategy for a Controlled Separation Method

T. Glinsner<sup>1</sup>, N. Roos<sup>2</sup>, L. Bendfeldt<sup>2</sup>, H. Pusch<sup>2</sup>, M. Fink<sup>3</sup>, H.-C. Scheer<sup>2</sup>

<sup>1</sup> EVGroup, P.O. Box 160, A-4780 Schärding, St. Florian, Austria; <sup>2</sup> University of Wuppertal, Fuhlrottstr. 10, D-42119 Wuppertal, Germany; <sup>3</sup> microresist technology, Köpenicker Str. 325, D-12555 Berlin, Germany

### Abstract:

Separation of stamp and sample at a defined temperature after a hot embossing process increases reliability of pattern transfer and minimises stress in and damage to the replicated structures. In this extended abstract strategies of controlled separation of substrate and stamp after the imprinting process will be shown as well as experimental results on evaluating the required separation force and the effects of vacuum grooves on the imprint quality.

### Introduction

In recent years nanoimprinting of polymers has evolved as one of the promising new methods for generating pattern sizes in the nanometer scale range [1,2]. This technique has demonstrated a high potential for large area definition of nanometer scaled patterns at low cost [3]. It allows for patterning of polymer coated wafers with structured silicon stamps having feature sizes from <10 nm [4] to up to 100 µm over the whole wafer area.

The controlled parallel separation of a stamp and a substrate is one of the keys to maintain the embossed structures. A new strategy concerning de-embossing of a substrate and a stamp by a vacuum fixture will be demonstrated. It was established that vacuum grooves, which are smaller than 1 mm, have no negative influence on the imprinting result [5]. This fact was taken into account for designing the de-embossing tool.

### Motivation

Automated separation of stamp and sample at the end of a hot embossing process is desirable for a number of reasons. Manual separation by way of inserting a wedge between the two wafers as it is often done introduces shearing forces parallel to the sample surface and may lead to damage to the replicated structures. This can be avoided by fixing stamp and sample to their respective substrate holders and pull them apart while maintaining parallelism, as it is possible with the equipment presented here.

Separation at a well-defined temperature just below the glass transition of the imprinted polymer is advantageous as it minimises mechanical stress in the sample which

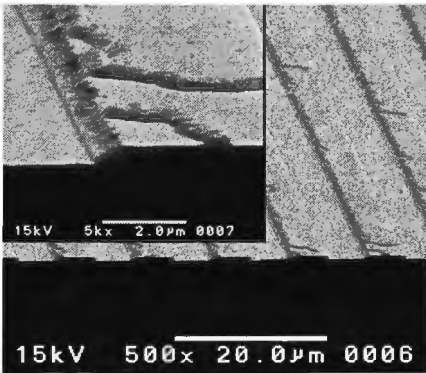


figure 1: damage to imprinted structures



can build up during the cooling due to the strongly differing thermal expansion of silicon and polymer materials. When cross-linking materials are imprinted it becomes essential since it was observed that damage to replicated structures occurs during the cool down cycle (see fig. 1).

## Equipment

The experiments have been conducted with the EV520HE, the hot embossing equipment from EVGroup, Austria. A close-up of the equipment is shown in figure 2. Independent top and bottom heating of up to 550°C guarantees lower thermal stress between the stamp and the substrate. An integrated compliant layer guarantees best uniformity of pressure and temperature to within  $\pm 1\%$ . This equipment is compatible with substrate sizes of up to 6 inches diameter.

The coated wafer and the stamp are mechanically aligned on an embossing chuck and fixed by a substrate holder for later de-embossing. A picture of the de-embossing tool is shown in figure 3.

The fully automated de-embossing process consists of following steps:

1. The coated wafer and stamp are placed on the embossing chuck and covered by the substrate holder.
2. After the imprinting procedure the coated wafer is fixed on the embossing chuck by vacuum while the piston remains down.
3. The stamp is fixed on the substrate holder by vacuum as well.
4. Activation of three de-embossing pins, which are lifting the substrate holder to separate the wafer stack.
5. Raising the piston to ensure parallel de-embossing of the stamp and the substrate to maintain the embossed structures.
6. Removing of the substrate and the stamp by releasing the vacuum of substrate holder and embossing tool.



figure 2: close-up of the EV520HE

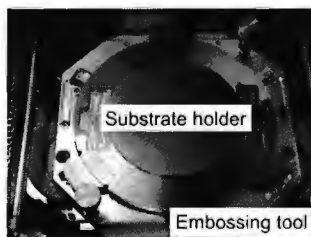


figure 3: picture of the de-embossing setup

### Results

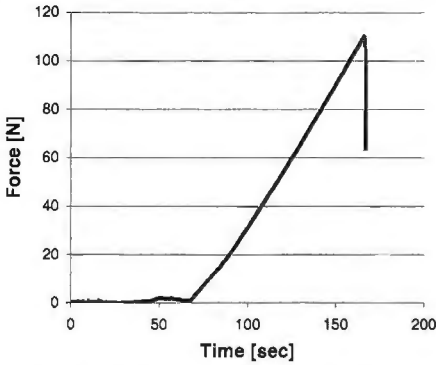


figure 4: measured curve of separation force

For large area samples, the force necessary for separation has been measured with a materials testing setup. For different 4 inch stamps with different anti-sticking layers, separation forces between 100 N and 150 N have been determined. A typical experiment is shown in fig. 4, resulting in a separation force of 110 N. In order to exert a holding force sufficient to separate an imprinted stack of stamp and polymer-coated wafer, a vacuum fixture therefore needs to have a groove area of at least 15 cm<sup>2</sup> when working in atmospheric pressure. Since this is a substantial fraction of the overall wafer area care has to be

taken in the vacuum groove design not to adversely affect the imprint result.

A preliminary design features concentric circular grooves of 0.8 mm width spaced at 3 mm intervals. Imprints of unstructured stamps with thus designed fixtures under conventional hot embossing conditions (T = 200 °C, p = 50 bar) resulted in surface profiles like the one shown in fig. 5. It has a periodic thickness variation of about 70 nm that reflects the 3 mm spacing of the underlying grooves. Although this macroscopic structure can be recognized very plainly by the naked eye it constitutes no severe degradation of the imprint quality.

First de-embossing tests were performed to prove the mechanical functionality of the de-embossing tool. The conducted experiments with a coated wafer and a double-sided polished substrate seem to be encouraging. De-embossing of these wafers were possible with process conditions similar to standard hot embossing parameters. To further improve the holding force of the substrate holder against the adverse effects of leakages between its surface and the wafer it seems desirable to redesign the vacuum supply to deliver more pumping capacity to the vacuum grooves. Further experiments with stamps and coated substrates are being conducted and will

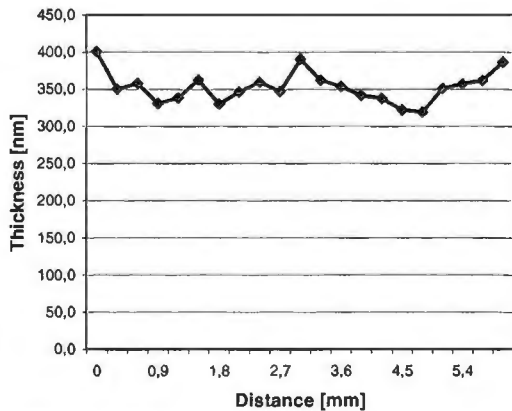


figure 5: surface profile of an imprint with an unstructured stamp using a vacuum fixture

demonstrate the feasibility of the de-embossing procedure in a conventional process.

## Summary

The de-embossing of an imprinted substrate from its stamp may result in damaging of the imprinted structures when it is performed manually. A strategy for a controlled, parallel separation strategy of stamp and imprinted resist coated wafer was introduced in this extended abstract. The experimental set-up for collecting information concerning the design of vacuum grooves and the mechanical tooling for this de-embossing mechanism were presented. Vacuum grooves < 1 mm with separation gap of 3 mm did not adversely influence the imprinting result. These facts as well as the required separation force of 110 N conducted with above experiments were taken into account for the design of the de-embossing tooling. The stamp is fixed by vacuum on the substrate holder and the substrate is fixed by vacuum on the chuck as well after the imprinting process. The separation is actuated with three de-embossing pins, which are lifting the substrate holder. First tests showed that this separation method might be a solution for maintaining the imprinted structures.

## References

- [1] S.Y. Chou, P.R. Krauss, P.J. Renstrom, "Imprint of Sub-25 nm Vias and Trenches in Polymers", *Applied Physics Letters* **67** (1995), 3114
- [2] R.W. Jaszewski, H. Schift, J. Gobrecht, P. Smith, "Hot Embossing in Polymers as a Direct Way to Pattern Resist", *Microelectronic Engineering* **41/42** (1998), 575
- [3] T. Luxbacher, T. Glinsner, K. Pfeiffer, N. Roos, H. Schulz, H.-C. Scheer, "Nanoimprint Lithography with a Commercial 4"-Bond System for Hot Embossing", *Proceedings of the SPIE* **4343** (2001), 427
- [4] S.Y. Chou, P.R. Krauss, W. Zhang, L. Guo, L. Zhuang, "Sub-10 nm Imprint Lithography and Applications", *Journal of Vacuum Science and Technology B* **15** (1997), 2897
- [5] L. Bendfeld, H. Schulz, N. Roos, H.-C. Scheer, "Groove Design of Vacuum Chucks for Hot Embossing Lithography", to be published in *Microelectronic Engineering* (2002)

# Analysis on Deposition Conditions of Surface Acoustic Wave Atomizer with Electrostatic Deposition for Fabricating Protein Chips

J.W. Kim<sup>1,2</sup>, Y. Yamagata<sup>2</sup>, M. Takasaki<sup>3</sup>, H. Ohmori<sup>2</sup>, T. Higuchi<sup>1</sup>

<sup>1</sup> The University of Tokyo, Japan; <sup>2</sup> The Institute of Physical and Chemical Research (RIKEN), Japan; <sup>3</sup> Saitama University, Japan

## Abstract

To fabricate protein chips from solution, we propose a new advanced system by utilizing the surface acoustic wave atomizer and electrostatic deposition, which is named as SAW-ED. SAW atomizer is utilized in order to spray extremely small droplets and the electrostatic force is used for collecting the charged particles onto the sample holder. We can make any shapes of protein chips by using the non-conductive mask of fused silica glass fabricated by abrasive jet machining. The protein chips of complex shapes are successfully formed using bovine serum albumin. For biological activity, the chip of firefly luciferase was performed by SAW-ED and was dissolved in reaction mixture to show strong luminescence. Although SAW-ED needs improvements, it proved to be effective in forming biochemical active protein chips.

## Introduction

Since protein deposition technology is expected to be useful for diagnostics, biochemical sensors and post genome research, numerous technologies with regard to deposition of proteins have been developed, such as screen-printing, spotting, ink-jet printing, and electro-spray deposition (hereafter ESD). Proteins are usually stable in completely dry condition like lyophilised powder or in completely wet condition like buffer solution. Intermediated semi-dry condition is considered to be the worse state for them. Most of methods are not suitable to fabricate biologically active protein chips, since it takes relatively longer to perfectly dry because of large droplet size. Among those methods, ESD is reported to be a very effective means for fabricating protein chips with very small amount of protein sample [1]. ESD is a method of generating very fine liquid droplets and collecting the charged particles through non-conductive glass mask onto the sample holder by electrostatic force. The fine liquid droplets are less than 10  $\mu\text{m}$  in diameter, so that protein particles perfectly dry before they reach the sample holder. This merit makes the functional activity of protein higher. However highly conductive solution like buffer solution for protein sample is difficult to spray with ESD method. As a result, it is necessary to desalt the solution in order to reduce the conductivity. In the process of desalting, many kinds of proteins tend to lose their activity. In order to overcome those limitations, we propose a new advanced technology to fabricate functionally active protein chips, by combining surface acoustic wave (SAW) atomizer and electrostatic deposition (ED).

The atomizing phenomenon by SAW was discovered and reported by Dr. Kurosawa et al. in 1995 [2]. According to the paper, the particle velocity is large enough to make fine droplets (5 to 50  $\mu\text{m}$  diameter) directly from the vibrating surface. Those fine droplets produced by SAW are considered to be useful for fabricating protein chips. Since SAW atomizer can generate very fine droplets, the drying speed of protein solution can be very high. This characteristic is advantageous to the preservation of protein activity.

This research aims at developing a new technology that fabricates biologically active protein chips and analysing the performance and practicality by the experiments.

### Experimental System

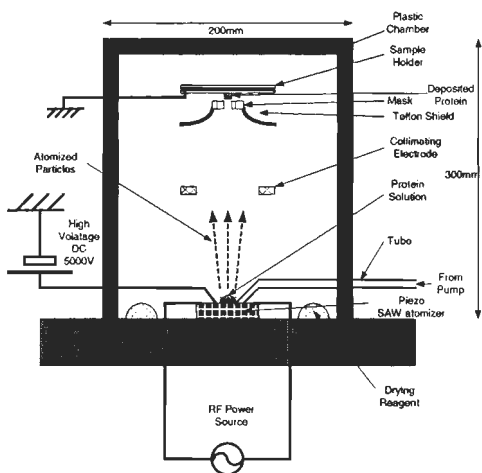


**figure 1:** The schematic diagram of SAW-ED device

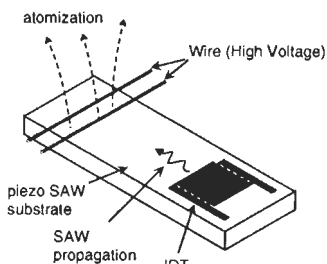


**figure 2:** SAW device (200  $\mu$ m electrode pitch, 100  $\mu$ m electrode strip width, 52 mm x 22 mm substrate)

The system shown in figure 1 mainly consists of three components: the protein solution supply system, SAW atomizer, and the electrostatic particle collector. The protein solution supply system has a computer-controlled cylinder pump. It supplies protein solution at the slow flow rate (0.13  $\mu$ l / sec) to the SAW atomizer. Small amount of the solution located on the SAW substrate is charged by two wires connected to DC 5000 V and then it is atomized by Rayleigh wave of the SAW device, whose driving frequency is 9.6MHz and driving voltage is 60  $V_{0-p}$ . SAW device used in this system is represented in the figure 2.

Since protein is very easy to be denatured at high temperature, we conceived the idea of intermittent excitation at the frequency of 1Hz and 2% of duty ratio for preventing temperature from rising. Two wires that are connected to DC 5000 V charge the solution, so that atomized particles are still charged and can be collected on a sample holder, whose surface is ITO-coated with electrical conductivity of about 100  $\Omega$  / and is connected to the ground. Before protein landing on the sample holder, what should be remembered is there is a patterned insulator mask on the

sample holder. This insulator mask of fused silica glass and electrostatic force determines the freedom of shape fabricated by SAW-ED. We can make any shape of protein chips by using the non-conductive mask of fused silica glass. We explain the collecting process in detail. The charge atomized particles search for and land on the sample holder in order to release their electric charges. The open part of sample holder can directly accept the particles and discharge, while protein particles cannot be deposited on the mask-covered area of sample holder. After one-layer of particles is deposited on the fused silica glass of mask, no more particles are supposed to

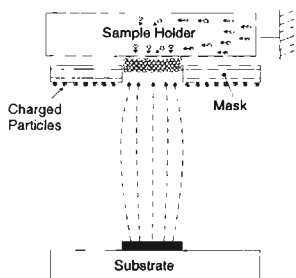


figure 3: The collecting process

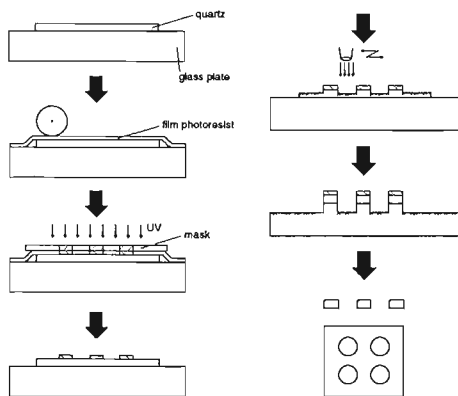


figure 4: The process of fabrication mask

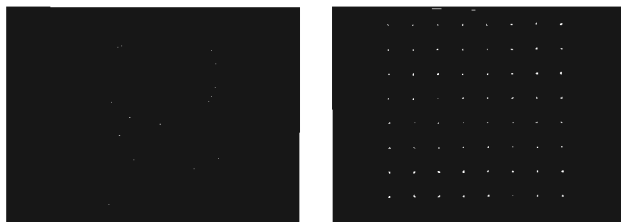


figure 5: Protein Chips (RIKEN and microarray)

land on the mask, since charged particles cannot release their electric charges on the insulated surface and the charges generate repulsive force for next coming particles. This mechanism is drawn with expected electric field in figure 3.

## Experiments and Results

### The Shapes of Protein in SAW-ED

Micro-fabrication of fused silica glass mask is of great consequence to the shape of protein chips. Abrasive jet technology is utilized as the fabrication method of fused silica glass masks. The following are the processes of mask-fabrication by abrasive jet machining graphically indicated in Figure 4. (a) to attach a piece of fused silica glass on the substrate with paraffin, (b) to coat the surface with elastic photoresist film, (c) to expose and develop the photoresist, (d) to do abrasive jet machining with #600 of white aluminium oxide powder, (e) to remove the film mask with the remover provided by Tokyo OHKA CO.,LTD, (g) to detach the

fabricated fused silica glass from the substrate with acetone. The protein chip of RIKEN mark was deposited by using BSA (0.4 mg/ml, Sigma) in figure 5. The width of character in the mark is about 200

µm. The figure shows that SAW-ED can make very complicated shape of a protein chip. In addition, protein microarray chips are fabricated on the substrate shown in figure 5. The pitch of chips is 1.5 mm and the diameter of chips is about 150 µm.

## Activity of Protein in SAW-ED



**figure 6:** the luminescence of firefly luciferase

Proteins can have their functions due to their own specific structures, especially their complex binding sites in the conformation of protein. If the conformation of proteins could not preserve their binding sites proteins would lose their activity. To verify the bio-chemical activity of protein chips, firefly luciferase was used. Luciferase solution (0.25  $\mu\text{g} / \mu\text{l}$ ) with protecting reagents was atomized and deposited by SAW-ED onto an ITO-coated glass by the amount of 40  $\mu\text{l}$ . Deposited film was immediately dissolved in reaction buffer (100 mM tricine buffer pH 8.0, 3 mM  $\text{MgSO}_4$ , 280  $\mu\text{M}$  luciferin, 55  $\mu\text{M}$  coenzyme A, 55  $\mu\text{M}$  ATP) to check the luminescence. Strong luminescence was observed as shown in figure 6, which represents that the activity of luciferase was preserved during the SAW-ED process. Luminescence image was taken by CCD with image intensifier. Luciferase lost its activity during desalting in ESD, while it kept alive during SAW-ED. It is notable that luciferase was able to undergo SAW-ED process without losing its activity, since luciferase is a protein that is quite easy to be denatured.

## Heat Influence in SAW-ED

Since protein is very easy to be denatured at high temperature, we conceived the idea of intermittent excitation at the frequency of 1Hz and 2% of driving period for preventing temperature from rising. As listed in table 1, it is reasonable to say that

intermittent frequency	9.6MHz SAW	20MHz SAW
1 Hz (2% Driving)	21.0 °C	23.4 °C
50 Hz (2% Driving)	20.8 °C	22.8 °C
100 Hz (2% Driving)	20.8 °C	22.8 °C
200 Hz (2% Driving)	20.8 °C	22.6 °C
300 Hz (2% Driving)	20.8 °C	22.6 °C
1 kHz (2% Driving)	20.8 °C	22.4 °C

**table 1:** Temperature of SAW device

there is no heat problem at low percent of intermittent frequency.

## Conclusion

We developed a new advanced method for the fabrication of protein chips by using SAW atomizer and electrostatic deposition. The fabricated microarray and RIKEN symbol of protein show us

that SAW-ED can make any shapes of protein chips. It is notable that luciferase was able to undergo SAW-ED process without losing its activity. As future work, it is necessary to inspect the optimal condition for activity and to perform the quantitative analysis.

## References

- [1] V.N. Morozov, T.Y. Morozova, "Electrospray deposition as a method to fabricate functionally active protein films", *Analytical Chemistry* 71 (1999), pp.1415-1420
- [2] M. Kurosawa, T. Watanabe, A. Futami, T. Higuchi, "Surface acoustic wave atomizer", *Sensors and Actuators A: Physical* 50 (1995), pp.69-74

# Prototype Microactuator for Nanomanipulation Using a Magnetostrictive Material

Y. W. Park, D. Y. Kim

Chungnam National University, Taejeon, Korea

## Abstract:

This paper presents the development of a magnetostrictive microactuator for nanomanipulation. The structural and functional requirements for the microactuator are as follows: It must be a millimeter structure and must achieve controllable displacement with nanometer resolution. For the millimeter structure, a drive rod with 5-mm in diameter and 10-mm in length is selected. Finite element analysis is used to determine the structure with the most uniform and highest magnetic flux density along the drive rod. Based on the analysis, the prototype microactuator is designed and fabricated. The microactuator is composed of the drive rod (Terfenol-D), bobbin and copper wire, a prestress spring, a force sensor, and a stainless steel housing. From the experiments, it is observed that the microactuator shows some level of hysteresis, i.e., about 7  $\mu\text{m}$  and that the generated force and displacement increase as the level of the current increases.

## Introduction

There has been a steady trend toward miniaturization. A typical example is the progression from vacuum tubes and discrete transistors to the very dense integrated circuits (ICs). The semiconductor industry continues to reduce the dimensions of ICs. As the trend toward miniaturization continues, assembling the components into a functional nanosystem is needed. Nanomanipulation can be defined as a positional control at the nanometer scale or as a manipulation of a nanoscale object. Nanomanipulation is one of the fundamental tasks in building nanostructures. Cellular manipulation, molecular docking, nanowriting and nanomachining are some of the prime examples that reflect the need for nanomanipulation and highlight the tremendous economical impact for developing this technology [1].

Microactuator can be defined as a miniaturized actuator for a miniaturized system. The choice of actuation mechanisms includes piezoelectric, electrostatic, electromagnetic, and magnetostriction [2]. Particular attention is given to magnetostrictive actuators because of their ability to generate larger strains and forces. Most microactuators are Si-based and use thin films as the actuator material. In this study, a solid type microactuator is considered.

Magnetostriction is a transduction process in which an electrical energy is converted into a mechanical energy [3]. It is related to the change in the geometrical dimensions of a body subjected to a magnetic field. The magnetostriction effect was first discovered in nickels by James Joule in 1842, and has been well-known for cobalt, iron and alloys of these materials. However, their magnitudes still limited to 50 ppm. Recent development of alloys of rare earth elements with iron has given us the new horizon of the new application of the magnetostriction effect. This rare earth magnetostrictive material, Terfenol-D, exhibits giant magnetostriction of about 2000 ppm [3]. This paper presents the development of the microactuator using a Terfenol-D rod and the experimental results with the developed microactuator.





### Experimental Procedure

Figure 3 shows a schematic diagram for the experimental setup. LabVIEW is used to develop a data acquisition system, i.e., acquisition of input data, and analysis and display of the acquired data. The experiments are performed on an optical table for eliminating possible disturbances such as vibration, shock, etc. Microactuator and displacement sensor are mounted on a test rig. A minivise for a milling machine is utilised as the test rig. The centerline of the microactuator and displacement sensor must be colinear. To this end, its mount is designed and made to sit on the test rig. The displacement sensor is an AEC-5706PS with a sensitivity of 10 mV/ $\mu\text{m}$  on a steel target. As the current flows through the coil, the Terfenol-D expands along the axis. This expansion causes the decrease in the gap between the displacement sensor and the microactuator.

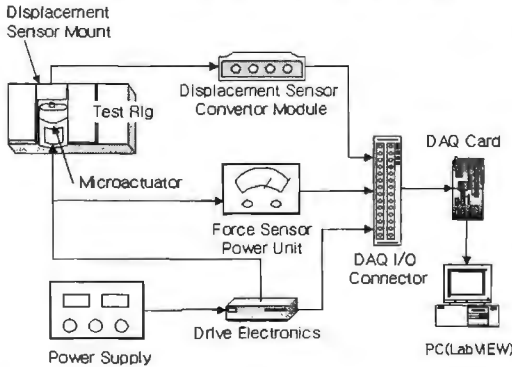


figure 3: Schematic diagram for experiments.

### Results and Discussions

Figure 4 shows the relationship between the generated force and displacement with abrupt change of the current. In figure 4, the top, middle, and bottom graphs are for the current, for the generated force, and for the generated displacement. In this case, the microactuator produces 25 N in force and 3  $\mu\text{m}$  in displacement with 1.5 A of current. Figure 5 shows the variation of the generated displacement due to the continuous change of the current level. It is observed that the displacement level

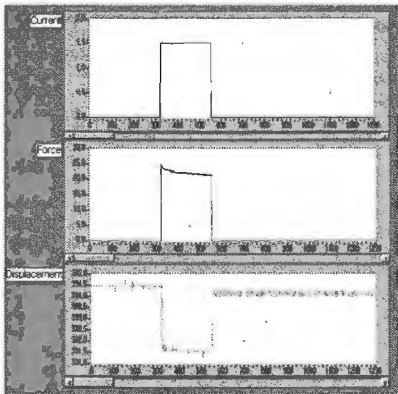


figure 4: Generated force and displacement

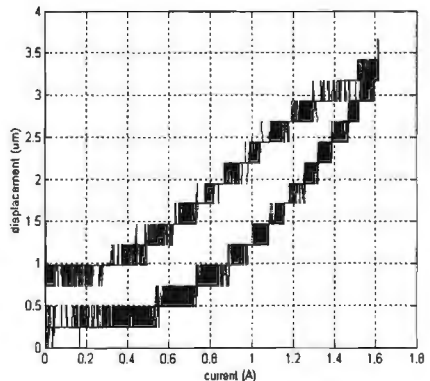


figure 5: Hysteresis curve.

with abrupt change of current. is not likely to return to zero when the level of current is reached from two opposite directions, i.e., 0 to 1.6 A and 1.6 to 0 A. It can be said as the hysteresis of the Terfenol-D, which is caused by a lag in the alignment of magnetic domains in response to the applied magnetic field [2]. The maximum hysteresis is about 7  $\mu\text{m}$ , and must be considered for the precise control. The sensitivity of the microactuator is calculated by using the ratio of the displacement to an incremental change in the current, and is about 3.6 nm/mV. It is also observed that the generated force and displacement are a function of the supplied current. That is, the increase in the level of the current causes the increase in the generated force and displacement. It agrees well with the data found in the literature [4, 5].

## Summary and Conclusions

This paper details the development of the microactuator using Terfenol-D, and the static characterization of the developed microactuator. The followings can be concluded:

1. The prototype microactuator with Terfenol-D is developed, based on the expertise and finite element analysis.
2. The developed microactuator shows some level of hysteresis, i.e., about 7  $\mu\text{m}$ .
3. The sensitivity of the developed microactuator is calculated by using the ratio of the displacement to an incremental change in the current, and is about 3.6 nm/mV.
4. The generated force and displacement by the developed microactuator increase as the level of the current increases.

## Future Work

Future work includes the dynamic characterization of the microactuator for the closed loop control, the reduction in the size of the microactuator, etc. The current microactuator has a built-in force sensor, which gives the limitation in reducing the total size. The next version of the microactuator will include permanent magnets for the better performance.

## References

1. National Research Council: "Visionary Manufacturing Challenges for 2020", National Academy Press, Washington D. C., 1998.
2. Tabib-Azar, M.: "Microactuators", Kluwer Academic Publishers, 1997.
3. Butler, J.-E.: "Application Manual for the Design of ETREMA Terfenol-D Magnetostrictive Transducers", Edge Technologies, Inc., 1988.
4. Park, Y.-W., Won, M.-C.: "Magnetostriction-Based Micropositioning System for the Macnining Processes", Manufacturing Systems, Vol. 29, No.4, 1999.
5. Moffet, M., Clark, A., Wun-Fogle, M., Linberg, J., Teter, J., McLaughlin, E.: "Characterization of Terfenol-D for Magnetostrictive Transducers", Journal of Acoustic Society of America, 89(3), 1991.

# Selective Removal Machining of Resinoid Insulator Film for Multilayer Semiconductors with Micro-Ice Jet Technology

T. Kuriyagawa<sup>1</sup>, K. Syoji<sup>1</sup>

<sup>1</sup> Department of Mechatronics and Precision Engineering, Tohoku University, Japan

## Abstract:

This paper deals with the development of the micro-ice jet machining (IJM) device for the via fabrication on the resinoid isolation film of semiconductors. The IJM device is capable of intermittent blasting of micro-ice of pure water. The IJM process is similar to an abrasive jet machining (AJM), and selectively removes softer materials than the micro-ice. IJM uses fine ice powders, which are produced under the low temperature condition of  $-150^{\circ}\text{C}$  or below. The blasted micro-ice is melted and has no influence upon the environment of production processes. We made a resinoid isolation film on the silicon wafer and a metal mask was overlapped. The silicon, which is harder than micro-ice, was not machined and has no influence on the surface. On the other hand, the resinoid film, which is softer than the micro-ice, was selectively removed.

## Introduction

Sand blasting is traditionally employed for deburring and polishing/cleaning, and essentially has nothing to do with precision machining. However, as the machining mechanism of sand blasting is reinvestigated, it has been suggested as an efficient means of removal of hard and brittle materials, and if more minute areas can be machined, abrasive grains can be improved, and adverse effects on the work environment can be eliminated or reduced, sand blasting can be used in a wider range of applications. Smaller machining area has been achieved through the development of intermittent abrasive jet machining (AJM) [1]. However, the problems of contamination of the target surface and adverse effects on the environment remain, and the machining devices proposed to date in various patents are impractical for these reasons. If these problems can be solved, AJM is expected to have broader applicability, particularly in the semiconductor fabrication. In this context, the micro-ice jet machining method (IJM) has been recently proposed, involving the use of fine ice particles rather than abrasive grains. This paper describes our prototype IJM device, which is capable of producing fine ice particles of ultrapure water as a medium for intermittent blasting, and discusses an example in which the device was used for selective machining of a semiconductor interlayer insulation film.

## Selective machining

Progress in electronic technology is encouraging the development of multilayer connection boards and three-dimensional integrated circuits in which IC chips are stacked, and both technologies allow dense wiring and dense circuit mounting. One of these multilayering techniques is the build-up method, in which insulation layers of resin are formed between boards, micro-holes (i.e., via holes smaller than  $50\ \mu\text{m}$  in diameter) are formed, through which connections are made by metal plating. Currently, the process employs lasers, but dry etching by AJM is being investigated for via hole formation. The IJM proposed in this paper does not employ  $\text{SiC}$  or  $\text{Al}_2\text{O}_3$  abrasive grains as used in conventional AJM, instead using fine ice particles of ultra pure water. This modification gives this IJM the following advantages.

1. A considerable amount of dust may be generated by the conventional method using abrasive grains. This is not a problem in the proposed method because the fine ice particles melt after blasting.
2. An additional process is required for removing the residual abrasive grains from the board surface when conventional abrasive grains are used. The IJM presents no such contamination problems.

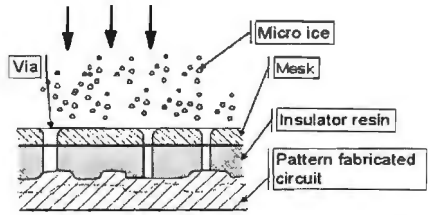


figure 1: Principle of selective removal machining

3. The fine ice particles have a Mohs' hardness of 3 to 4 at  $-60\text{ }^{\circ}\text{C}$  or below, which is slightly harder than the interlayer insulation resin to be machined. Therefore, silicon or alumina board surfaces are not etched at all, allowing selective machining of the interlayer insulation film, as shown in figure 1.
4. Post-machining cleaning is possible using the same device with softer ice particles. This process replaces the current CFC cleaning process, and is thus environmentally sound.

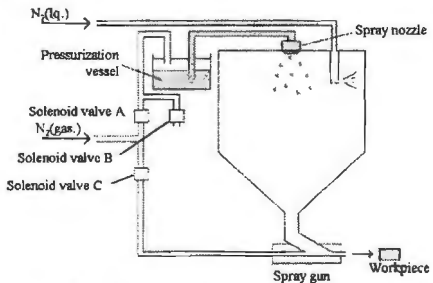


figure 2: Micro-ice jet machining device

**IJM device**

Figure 2 shows a schematic of the IJM device used. Liquid nitrogen was sprayed onto the wall of the ice chamber to cool the inside atmospheric temperature to  $-150$  to  $-120\text{ }^{\circ}\text{C}$ . Ultrapure water is then injected as a fine spray and frozen in the chamber as fine ice particles, or "micro-ice". Liquid nitrogen was repeatedly injected

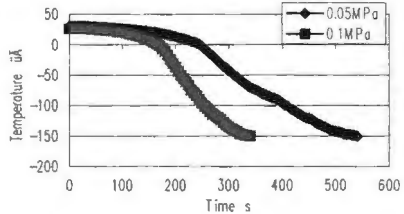


figure 3: Cooling characteristics in ice chamber

for 0.5 s at 1 s intervals until the inside temperature reached  $-50\text{ }^{\circ}\text{C}$ , below which it was injected for 0.5 s at 2 s intervals. Figure 3 shows the temperature change with time measured at the center of the ice chamber. The speed of temperature fall depends on the supply pressure of liquid nitrogen. In this case, the figure shows that the temperature reaches the set temperature after approximately 5 min. This time decreases with increasing supply pressure, but the cooling capacity does not increase at over 0.1 MPa because excessive liquid nitrogen was injected as liquid without being gasified. Based on these results, the injection pressure for liquid nitrogen was set at 0.1 MPa in subsequent experiments.

Figure 4 shows the spraying characteristics of ultrapure water from the nozzle. The figure suggests that the spray volume increases with pressure. At 0.3 MPa or below, the diameter of the sprayed ice particles was too large to be used as micro-ice spray. Based on these results, the pressure of the chamber and acceleration line were both set at 0.8 MPa in this study.

The ice particles formed in the chamber are accelerated due to the pressure from the acceleration line (valve C). This mechanism is identical to that of conventional blasting devices. The micro-ice sprayed under pressure impacts the workpiece and removes material. Various configurations of water pressure and acceleration pressure were examined, yielding various conditions of intermittent micro-ice blasting. The pipeline was assembled using piping with large cross-sectional area to minimize pipeline resistance. The intermittent injection cycle was designed so to be shorter than 1 s.

### Spraying speed and freezing speed

It is important to obtain the spraying speed and freezing speed of water in the chamber in order to determine the intermittent blasting conditions. In this study, spraying speed and the distribution of water were measured using a particle image velocimetry (PIV) system. Water was sprayed at 0.6 MPa from a nozzle with 0.4 mm inner diameter, and a sheet laser was shone down the nozzle centerline. Figure 5 shows the results, with the nozzle at the top in the center. The sprayed water drops were fastest along the spray nozzle centerline, with a maximum speed of approximately 30 m/s. The figure illustrates that the speed decreases with distance from the nozzle, and that the density of water drops decreases with lateral distance from the centerline.

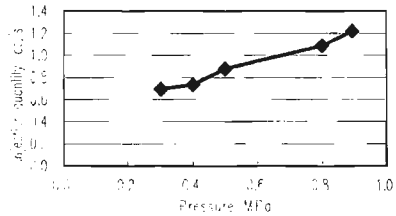


figure 4: Injection characteristics of water spray



figure 5: Injected spray pattern and velocity diagram

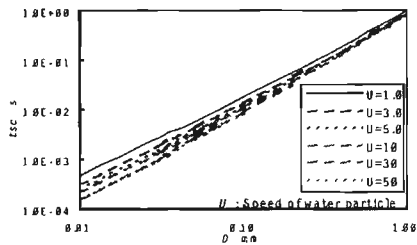


figure 6: Critical freezing time of the water

Next, the freezing time of water was investigated. The mechanism of ice particle growth was analyzed using the following model. The surface of a water sphere with radius  $r_0$ , the temperature of which is uniformly regulated to the initial temperature  $T_i$ , suddenly comes into contact with the gas at temperature  $T_F$  at time  $t = 0$ , and is

uniformly cooled from the surface with constant heat transfer coefficient  $h$ .

Calculations were performed using the Heisler's charts of a sphere. Figure 6 shows the relationship between time  $t_{sc}$  and diameter  $D$  of water drops for several different relative speeds  $U$  of water drops and surrounding gas ranging from 1.0 to 50 m/s, where  $t_{sc}$  is the time to the end of the supercooled state of water droplets, which then begin to freeze (i.e., the critical freezing time). The plots in the figure have practically linear relationships in the log/log plot, with a large positive gradient. The critical freezing time becomes longer with increasing diameter of water droplets and decreasing relative speed of water droplets.

As the average diameter of particles in this experiment was approximately 0.07 mm, the water droplets can be estimated to freeze in approximately 0.01 s. Considering the spraying speed obtained from figure 5, it is concluded that sprayed water freezes completely to ice particles at the point approximately 300 mm from the nozzle.

### Blasting Experiment

The micro-ice was used to blast copper, aluminum, iron, monocrystalline silicon, and polyvinyl chloride plates as workpieces for 45 s at an angle of 30°. The inner diameter of the nozzle was 4.5 mm, and the gap between the nozzle and the workpieces were 38.7 mm.

The Mohs' hardness of the micro-ice is 3 to 4, and only the polyvinyl chloride plate, which is softer than micro-ice, was etched, to a depth of 60  $\mu\text{m}$ . The surface roughness increased from 0.16  $\mu\text{m}Rt$  to 2.87  $\mu\text{m}Rt$  due to impressions caused by impact by micro-ice.

The copper plate, which is almost as hard as micro-ice, was not clearly etched but the surface roughness was increased from 0.36  $\mu\text{m}Rt$  to 1.57  $\mu\text{m}Rt$ . The aluminum plate, which is practically as hard as copper, exhibited no change because the specimen used in this experiment was surface-hardened. The iron and silicon plates, which are harder than micro-ice, exhibited no change.

Figure 7 shows an example of selectively removing the interlayer insulation film. Specifically, polyimide resin was spin-coated as an interlayer insulation film on a 0.5 mm-thick silicon wafer and overlaid by a metallic mask, and the masking process was performed using micro-ice. The figure illustrates that the surface of the monocrystalline silicon was not machined at all, whereas the interlayer insulation film was machined selectively.

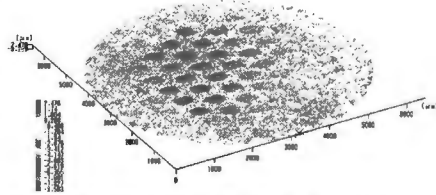


figure 7: Selective removal of resinoid isolation film on Si wafer

### Acknowledgements

This research was supported by a grant-in-aid for scientific research of the Japanese Ministry of Education, Science, Sports and Culture.

### References

- [1] T. Kuriyagawa, T. Sakuyama, K. Syoji and H. Onodera, A New Device of Abrasive Jet Machining and Application to Abrasive Jet Printer, Key Engineering Materials, 196 (2001), pp103-110.

## Design and Fabrication of a Position Surveying Microrobot in the Underground Pipe

S. KATO<sup>1</sup>, M. ONO<sup>1</sup>, N. KATO<sup>1</sup>, T. HAMANO<sup>1</sup>

<sup>1</sup>Nippon Institute of Technology, Miyashiro, Saitama 345-8501, JAPAN

E-mail: kato@nit.ac.jp

### Abstract

A new position surveying microrobot structured by a driving microrobot and a position surveying sensor system is designed and fabricated. The driving microrobot is driven by the pneumatic and vacuum pressure. Position surveying is done by using of two rotary encoder sensors. The position surveying microrobot could measure the position at the accuracy less than 0.9 degrees in the angle and less than 10 mm in the position in a curved pipe of 1000 mm long.

### Introduction

Light-fiber cables for high-speed and large-capacity communication are usually buried under the ground. Once the light-fiber are buried under the ground, it is very difficult to confirm the buried position of the pipe if we use the underground radar, because the light-fiber cables and plastic cover pipes are not the metal. A former way to confirm the buried position of the light-fiber cables is the method, in which a sound source is inserted into the plastic cover pipe and the sound from the source is detected by many in-lined microphones arrayed on the ground. However, the detection is not done at the place where the arrayed microphones can not move along the pipe and the accuracy of the surveying is not good at the place where the position of the plastic cover pipe is so deep in the ground.

We developed a new position surveying microrobot using two rotary encoder sensors. The new position surveying microrobot is structured by a driving microrobot and a position surveying sensor system. The driving microrobot is an inching worm type microrobot using flexible rubber bellows and is driven by the pneumatic and the vacuum pressure [1], [2].

Only two rotary encoders and amplifiers carried on a position surveying microrobot of the position surveying sensor system move in the pipe with the driving microrobot. If the pipe is straight, the two rotary encoders make same pulses. However, the pipe has a curvature, the outside rotary encoder makes larger pulses than pulses made by the inside rotary encoder. The error appears between pulses made by two rotary encoders. The buried position of the pipe is confirmed, because the moving course of the position surveying microrobot is calculated by the error of the pulses.

In this paper, the position surveying sensor system is describes in detail, because the driving microrobot which is an element of the new position surveying microrobot has been reported.



### The position surveying sensor system

The position surveying sensor system is shown in Fig. 1. The inner diameter of the pipe is 80 mm. The system is consisted by a position surveying microrobot which carries both the left and the right rotary encoders and their amplifiers, a signal processor, interfaces, a position surveying software and a computer.

The position surveying robot is shown in Fig. 2. The position surveying microrobot is consisted by two moving mechanisms. The moving mechanism is held to the inside of the pipe by eight small pulleys. The left and the right rotary encoders are held by arms attached through springs to the front moving mechanism. Each rotary encoder has a pulley 30 mm in diameter. Signal amplifiers are carried on the rear moving mechanism. The signal processor is consisted by a detecting circuit of clockwise or counterclockwise rotation of the rotary encoders, counter circuit and a mechanical chattering checking circuit. The signal from the signal processor is introduced into the computer through interfaces.

The computer calculates the length of the moving path and the angle of the moving path of the position surveying microrobot by the average and the difference

pulses of the two rotary encoders. These values are preserved as vector data. The vector data are watched and modified periodically and displayed on the screen.

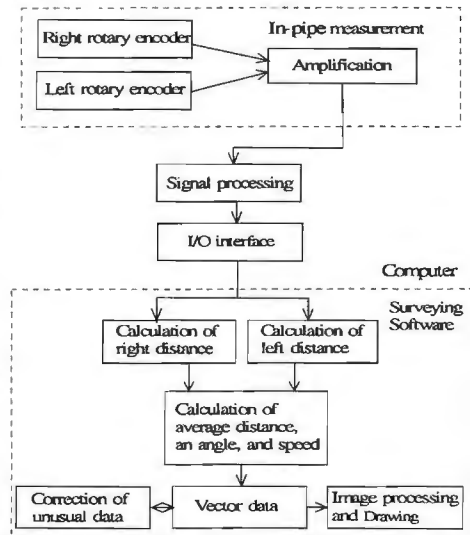


figure 1: A position surveying sensor system

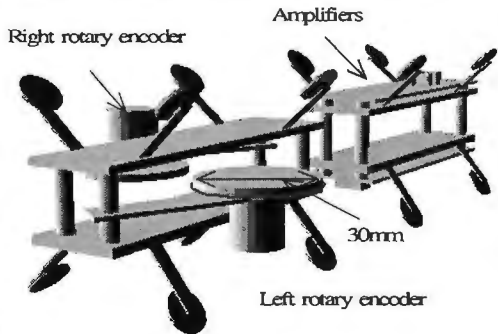


figure 2: A position surveying microrobot

**Principle of position surveying**

The principle of position surveying by the position surveying microrobot is shown in Fig. 3. The original point is  $P_0(x_0, y_0)$ . The angle between the tangential line of the point  $P_n(x_n, y_n)$  which is a point of the centerline of the pipe and the y axis is  $\Theta$ . It is assumed that an error  $\epsilon$  is made by the two rotary encoders when the surveying microrobot moves a small distance  $S$ . This moved point is  $P_{n+1}(x_{n+1}, y_{n+1})$

The radius of the curvature is assumed as  $R$ . The diameter of the pipe is  $D$ . The small angle from the center of the curvature is assumed as  $\theta$ .

Then, next equation is obtained.

$$\left( S + \frac{\epsilon}{2} \right) - \left( s - \frac{\epsilon}{2} \right) = \epsilon = \left( R + \frac{D}{2} \right) \theta - \left( R - \frac{D}{2} \right) \theta = D\theta \quad (1)$$

The small angle  $\theta$  is obtained from the error  $\epsilon$  as

$$\theta = \frac{\epsilon}{D} \quad (2)$$

Then, the co-ordinates of the point is  $P_{n+1}$  calculated from the co-ordinates of  $(x_n, y_n)$  as

$$x_{n+1} = x_n + S \cdot \sin(\Theta + \theta) \quad (3)$$

$$y_{n+1} = y_n + S \cdot \cos(\Theta + \theta) \quad (4)$$

The tangential angle  $\Theta$  is the summation of the small angle  $\theta$  and shown as

$$\Theta = \Sigma \theta \quad (5)$$

The co-ordinates and the tangential angle are preserved by vector data.

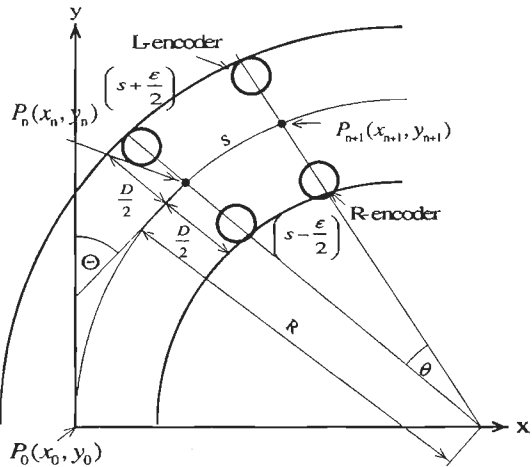


**figure 3:** The principle of the position surveying in the underground pipe by the position surveying microrobot

### Result of position surveying

A curved pipe whose diameter is 80 mm, radius of curvature is 100 mm, angle of curvature is 90 degrees and length of the pipe is 1000 mm is laid horizontally and used for the experiment. The position surveying microrobot is moved at the speed of 30 mm/s. The result of 20 experiments is shown in Fig. 4. The result of errors of angle is less than 0.9 degrees and errors of position is less than 10 mm. The reasons of these errors are supposed to become from the roughness of the inner surface of the pipe, the yawing of the position surveying microrobot and the slip of the rotary encoder.

These errors may be improved by the reform of the position surveying software.

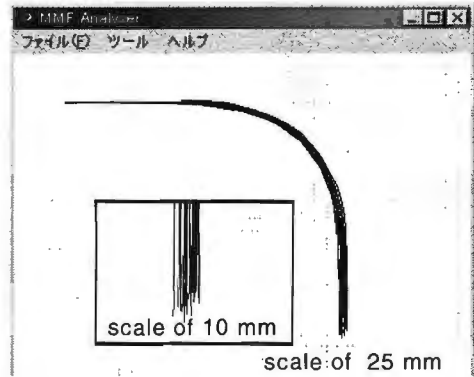


figure 4: Computed loci

### Conclusions

- (1) A new position surveying microrobot which is structured by two rotary encoders and their amplifiers, a signal processor, interfaces, a position surveying software and a computer was developed.
- (2) The position surveying microrobot could measure the position at the accuracy less than 0.9 degrees in the angle and less than 10 mm in the position.

### References

- [1] T. Matsumoto, M. Ono, S. Kato: "Fabrication of an In-pipe Mobile Robot Movable the Long Distance", Proc. of Japan Society of Mechanical Engineers, Meeting at Tagajou of Tohoku Branch (2000), pp. 95-96.
- [2] M. Ono, T. Hamano, M. Takahashi, S. Kato: "Development of an In-pipe Inspection Robot Movable for a Long Distance", Proc. of Japan Society of Mechanical Engineers, Meeting in ROBOMECH'01 (2001), 1A1-B10

## **Micro and Nano Structuring using Focused Ion Beam and DualBeam Technologies**

F. Morrissey

FEI Company, Building AAE, Achtseweg Noord 5, P.O. Box 80066, 5600 KA  
Eindhoven, The Netherlands

Email: fmorriss@nl.feico.com

Micro and nano engineering is becoming far more important with critical dimensions shrinking at a steady rate. At present making micro and nano structures can involve a long process of design, manufacture and modification. As the dimensions demanded by modern applications reduce still further the ability to prototype and make them is becoming more and more difficult. Added to this controlling of these processes is also becoming more difficult. What is required is a fast, reproducible method of machining down to a nanometer level then to be able to verify the dimensions and if necessary, modify them again immediately.

The focussed ion beam (FIB) has the ability to mill features of less than 10nm and when this is combined with the non- destructive, high resolution imaging capability of an electron column in the DualBeam , complex nano- structures can be made and reviewed quickly and accurately.

The FIB uses a liquid metal ion source (generally Gallium) and advanced ion optics to produce an ion probe of ~6nm diameter with a beam current density in the order of 100A/cm<sup>2</sup>. The computer control of this small ion probe coupled with ion- assisted deposition and imaging capability has already made the FIB an important tool for micro- machining and rapid prototyping in the semi- conductor industry. In a DualBeam the FIB is combined with a high resolution FEGSEM both looking at exactly the same point in space giving the ability to directly mill nano- structures and then immediately observe them non- destructively. So nano- structures can be made designed and prototyped extremely quickly. Besides providing non- destructive imaging the electron beam can itself be used for lithography and depositions on a nano- scale. Thus the DualBeam with fully integrated and automated FIB and FEGSEM columns offers a whole range of nano- machining, lithography and sample preparation for various techniques. This technique has already been used to trim and make SQUIBs, Josephson junctions, AFM and atom probe tips and a range of other samples that require site specific nano- machining.

In this presentation FIB and DualBeam will be introduced and their roles in micro- and nano- machining will be explored. Examples will be given from a number of nano- machining projects recently undertaken with DualBeam.



Figure 1: Machining of micro- and nano- test structures in InP for photonic arrays

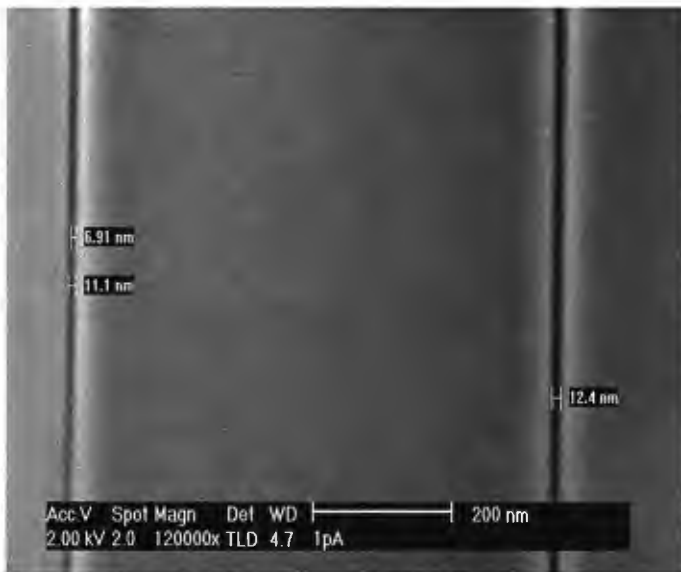


Figure 2. Nano- Machining of test lines in SiN

**References:**

- 1) Young R.J., Carleson P.D., Hunt T., and Walker J.F. (1998) Proceedings of 24<sup>th</sup> ISTFA Conference, 329
- 2) Young R.J. (2000) Microscopy and Microanalysis proc., vol. 6, supplement 2, 512
- 3) H. Ximen, R.K. DeFreez, J.Orloff, R.A. Elliott, G.A. Evans, N.W. Carlson, M. Lurie, and D.P. Bour, "Focused ion beam micromachined three-dimensional features by means of a digital scan", *J. Vac. Sci. Technol.* **B 8 (6)**, pp. 1361-1365, American Vacuum Society, 1990.
- 4) Masanori Komuro, Hiroshi Hiroshima, Hisao Tanoue, and Toshihiko Kanayama, "Maskless etching of nanometer structure by focused ion beams", *J. Vac. Sci. Technol.* **B 1 (4)**, pp. 985-989, American Vacuum Society, 1983.
- 5) J. Poretz and L.W. Swanson, "Focused ion beam deposition of Pt containing films", *J. Vac. Sci. and Technol.* **B 10 (6)**, pp. 2695-2698, American Vacuum Society, 1992.
- 6) J.Brugger, G.Beljakovic, M.Despont, N.F. de Rooij, P.Vettiger, *Microelectronic Engineering* 35 (1997) 401-404



## **Precision metrology for machines/manufacturing**





## **A new calibration method for polygons with a pitch angle which does not match with the subdivision of the used indexing table**

T. Yandayan<sup>1</sup>, S.A. Akgöz<sup>1</sup>, H. Haitjema<sup>2</sup>

<sup>1</sup> Gebze, Turkey, <sup>2</sup> Eindhoven, The Netherlands

### **Abstract**

This work describes a new method for high precision calibration of polygon angles, where more common calibration methods would require a non-integer subdivision of the used indexing table. The method was used for the calibration of a 7-sided polygon by UME, the National Metrology Institute of Turkey, during the intercomparison measurements in the frame work of EUROMET project 371 "Angle calibration on precision polygons" between 12 European countries. 0.24" uncertainty was obtained using the new method based on the circle closure principle. With in this uncertainty the measured polygon angles corresponded very well with the reference values of the intercomparison measurement.

### **Introduction**

It is required to use some kind of angular measuring instrument during the manufacturing of angular parts, e.g. a dividing head, a rotary table or a polygon. The polygons are the most robust and precise angle standards used by laboratories for transferring angular measurands. They are discs made of steel or glass and have equally inclined and optically flat reflecting faces. They may have up to 72 faces but 6, 8, and 12 faces are most common. For precise calibration of such angle standards, two accepted measuring methods are the cross calibration and the two-autocollimator technique [1,2]. In the case of having one autocollimator and one rotary table with an angular indexing or measuring capability, which is the case for most laboratories, an applicable technique is the cross calibration technique. The calibration capability for polygon types in this case depends on the smallest increment of the indexing table. Most common indexing tables [3] have a smallest increment of 15' or 10'. This is not sufficient for polygons such as 7-sided ones as the interval angle cannot be generated by the indexing table accurate enough to remain in the range of common autocollimators. In order to calibrate such polygons, a novel technique has been applied by UME during intercomparison measurements carried out between European countries.

### **EUROMET project 371**

The project covered an international comparison of angle calibrations to be carried out on two precision polygons with 7 and 24 faces respectively. It was completed between 1996-2000. PTB (National Metrology Institute of Germany) was the pilot laboratory. The used 7-sided polygon has the specifications shown in Fig.1. The pitch angle deviations  $\Delta\alpha_i$  and the cumulative angle deviations  $\Delta\beta_i$  measurement results were reported for the normal and inverted position of the polygon (Fig.1). Either one of two well-known methods [1,2], one autocollimator-angle measuring tables or two autocollimators-rotary table were recommended by the Pilot Lab. (PTB) for measurement of these parameters. A mounting device delivered with the polygon has been used for adjustments [4].



the circle is closed to complete 360 degrees in this method, the average of the deviations is the error of indexing table for that certain interval. Mathematically this is derived as following:

The 3-pitch angle intervals  $\gamma_i$  (shown in Fig. 2) are measured by readings  $M_i$  of the autocollimator difference:

$$\gamma_i = M_i + \theta \quad (1)$$

where  $\theta$  is the unknown, but constant, (can vary in repeated operations due to random errors of the indexing table and the manipulation) angle between the two positions of the indexing table of  $154^{\circ}15'$  nominal. Summation over all angles and  $\Sigma\gamma_i = 1080^{\circ}$  (closure condition  $3 \cdot 360^{\circ}$ ) gives from (1):

$$\theta = \frac{1080^{\circ}}{7} - \frac{\sum_{j=1}^7 M_j}{7} \quad (2)$$

This is replaced in (1) and gives:

$$\gamma_i = M_i - \frac{\sum_{j=1}^7 M_j}{7} + \frac{1080^{\circ}}{7} \quad (3)$$

Finally, the deviations of the cumulative pitch angles  $\beta_i$  between the faces were calculated using the  $\gamma_i$  values. Angle  $1/4 (= \beta_4)$  was directly taken as  $\gamma_1$  and the other cumulative angles were calculated as following:

$$\beta_1 = \gamma_1 + \gamma_2 + \gamma_3 + \gamma_4 + \gamma_5 + \gamma_6 + \gamma_7 - 1080^{\circ} = 0^{\circ} \text{ (trivial case)} \quad (4)$$

$$\beta_2 = \gamma_1 + \gamma_2 + \gamma_3 + \gamma_4 + \gamma_5 - 720^{\circ} \quad (5)$$

$$\beta_3 = \gamma_1 + \gamma_2 + \gamma_3 - 360^{\circ} \quad (6)$$

$$\beta_4 = \gamma_1 \quad (7)$$

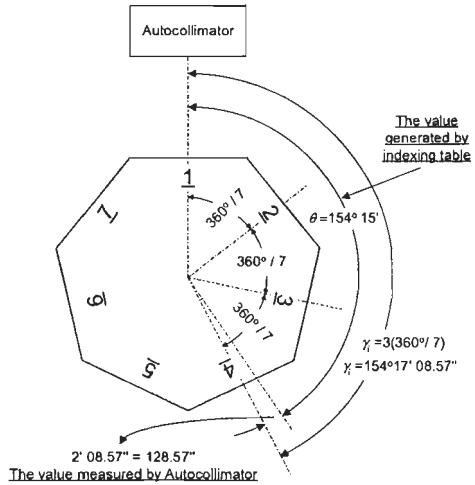
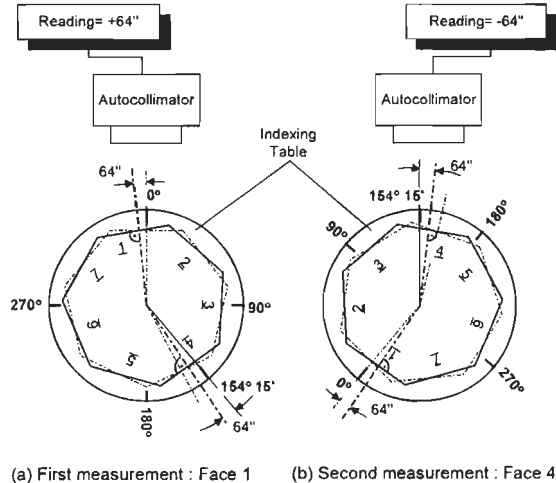


Fig. 2 Explanation of the new technique



(a) First measurement : Face 1 (b) Second measurement : Face 4

Fig. 3 Measurement of the 7-sided polygon

$$\beta_5 = \gamma_1 + \gamma_2 + \gamma_3 + \gamma_4 + \gamma_5 + \gamma_6 - 720^\circ \quad (8)$$

$$\beta_6 = \gamma_1 + \gamma_2 + \gamma_3 + \gamma_4 - 360^\circ \quad (9)$$

$$\beta_7 = \gamma_1 + \gamma_2 \quad (10)$$

The pitch angles  $\alpha_i$  and their deviations can easily be calculated using the cumulative pitch angles  $\beta_i$  and their deviations (**Fig.1**).

## Results and discussions

The 7-sided polygon angle deviations were measured at normal and inverted position of the polygon on the indexing table. The standard deviation of the difference between normal and inverted position among 7 faces is 0.03". **Table 1** illustrates the UME results for 7-sided polygon, the weighted mean as a reference value of the EUROMET intercomparison for each face, and the difference of the UME results from the weighted mean results of the faces [4]. It should be noted that the weighted mean is calculated by the pilot laboratory (PTB) using participant's results and their associated standard uncertainties. It is accepted as the reference value. Participant's results are checked against the reference values with their associated uncertainties. It can be clearly seen that the results agree with the reference values far within the uncertainty limit.

**Table 1** Comparison of UME results with reference values of EUROMET intercomparison for mean of normal and inverted position of polygon

Face No.	Reference values (weighted mean)	UME results	Difference of UME results from the reference values
1	0.22"	0.23"	0.01"
2	-1.09"	-1.09"	0.00"
3	-0.09"	-0.08"	-0.01"
4	0.52"	0.58"	0.06"
5	-0.19"	-0.19"	0.00"
6	0.37"	0.29"	-0.08"
7	0.25"	0.25"	0.00"

(Note: UME uncertainty value  $U=0.24$  arc seconds with  $k=2$ )

## Conclusions

All participants apart from UME have used one of two known standard measuring methods, either the cross calibration or the two-autocollimator technique. The agreement between UME results and reference values apparently states that the new method applied by UME proves to be working well for such kind of applications. It should also be noted that the uncertainty of the applied method is also reasonably small and is the fifth smallest uncertainty among the 12 participants [4].

## References

- [1] Sim PJ. Angle standards and their calibration. In: Hewitt P.L. editor: Modern Techniques in Metrology. World Scientific. Singapore. 1984. pp 102-121.
- [2] Evans JC, Taylerson CO. revised by Palmer EW and Poole SP. Measurement of Angle in Engineering. NPL. 1986.
- [3] ANON, 1440 Precision Index with Mechanical or Hydraulic Lift and 1/10th second Small Angle Divider. Service Manual. Moore Doc. No: 89116. Moore Special Tool Co. Inc. 800 Union, P.O. Box 4088, Bridgeport, USA.
- [4] Probst R, Wittekopf R. EUROMET Project No. 371 Interlaboratory comparison Angle calibration on precision polygons. Final Report (Draft A2). PTB. Braunschweig (Germany). June 2000.

## Novel Measurement Method for Nano-Defects of Si Wafer Surface Using Evanescent Wave

R. Nakajima<sup>1</sup>, T. Miyoshi<sup>2</sup>, Y. Takaya<sup>3</sup>, S. Takahashi<sup>4</sup>, M. Fujita<sup>5</sup>

Osaka University, Osaka, Japan, <sup>1</sup>nakajima@optim.mech.eng.osaka-u.ac.jp,

<sup>2</sup>miyoshi@mech.eng.osaka-u.ac.jp, <sup>3</sup>takaya@mech.eng.osaka-u.ac.jp,

<sup>4</sup>takahashi@mech.eng.osaka-u.ac.jp, <sup>5</sup>fujita@optim.mech.eng.osaka-u.ac.jp

### Abstract

A new optical detection method for evaluating the nano-defect existing in the vicinity of silicon wafer surface is proposed [1], which is applicable to an inspection technique of silicon wafers for next generation semiconductors manufacturing processes. In this method, defects are evaluated by using evanescent light based on near field optics. So it enables to detect the nano-meter scale defects without the diffraction limit to resolution. In this paper, to verify the feasibility of this method, first, computer simulation was performed by means of FDTD method based on Maxwell's equations. Next, we carried out the fundamental experiments. The results suggested that the proposed method is effective for detecting nano-defects existing in the vicinity of the wafer surface with high sensitivity.

### Introduction

In modern semiconductor manufacturing processes, the design rule will be reduced to a scale of 95 nm before long. In order to realize high productivity and reliability of the semiconductor fabrication, silicon wafer inspection technologies [2][3] become more essential. The conventional defects inspection technology will reach physical limits imposed by the wavelength of the incident laser beam. Nevertheless, the killer defect size for next generation processes will be as small as nano-meter scale. Figure 1 presents the concept of our proposed defects inspection method. When the incident laser beam illuminates a Si-air interface from the Si side at over the critical angle, an evanescent light results from the total-internal-reflection at the interface, within near field zone over the Si surface. If the tip of coated fiber probe is placed in the near field zone, the evanescent light localizing on Si surface is converted into the propagating light in the fiber probe. And the fiber can transmit the light with the surface information to a detector. In this instance, the resolution does not depend on the laser wavelength, but the tip size. By detecting the intensity variations of the transmitting light, which means the disturbance of the evanescent light resulting from

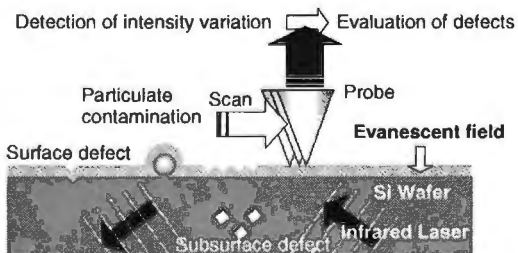


**figure 1:** Concept of nano-defects detection using evanescent light.

the defects existing in the vicinity of the wafer surface, we can evaluate the nano-defects independent of the wavelength. Especially, this method is expected to evaluate the subsurface defects that also influence the yield enhancement of the next generation semiconductors manufacturing processes.

### Computer model for simulation

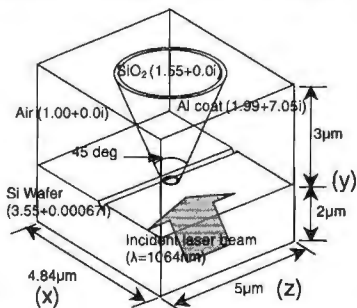


**figure 2:** Diagram of simulation model with Micro scratch (60nm wide, 40nm depth).

In order to verify the feasibility of this proposed method, we have developed a computer simulation tool to solve Maxwell's equations based on the 3-dimensional finite-difference time-domain (FDTD) method [4]. And we analyzed electromagnetic field of near-field in the vicinity of the wafer surface by using this computer simulation. The diagram of simulation model is depicted in figure 2. As shown in this figure, the fiber probe and the Si wafer ( $N=3.55+0.00067i$ ,  $N$ ; complex refractive index) was modeled with the concept mentioned before. The fiber core propagating the light to detector is

made of SiO<sub>2</sub> ( $N=1.55+0.0i$ ). The probe tip is approached towards the surface with a gap of 100nm, and coated with aluminum ( $N=1.99+7.05i$ ) of 160nm thick. To pick up the evanescent signal, the aperture has 420nm in diameter at the tip of this probe. The incident light is set as p-polarized plane wave at 1064nm wavelength and the incident angle is taken at  $45.0^\circ$  exceeding the critical angle of Si  $16.3^\circ$ . The unit grid length is 20nm in the  $242 \times 250 \times 250$  unit space. A micro scratch that is a typical surface defect of Si wafer is located on the Si wafer surface (at  $x=2.4\mu\text{m}$ ) as a model of surface defect. This trigonous sectioned defect size is 60nm wide and 40nm deep.

### Numerical results and discussion

#### Detection of micro scratch

Figure 3 presents the computational result for the case of micro scratch. It is gray-scale representation of time-average field intensity distribution. Here, the field intensity means squared electric field  $|E|^2$ . This result shows the total internal reflection occurs at the Si-air interface and an evanescent field is generated there. This evanescent field is disturbed by the surface defect. And the image of cross section (at  $y=2.5\mu\text{m}$ ) shows the disturbed light is propagating through the fiber as the

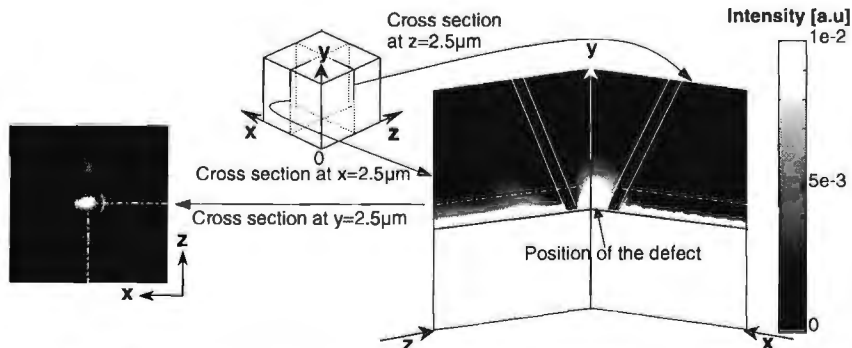
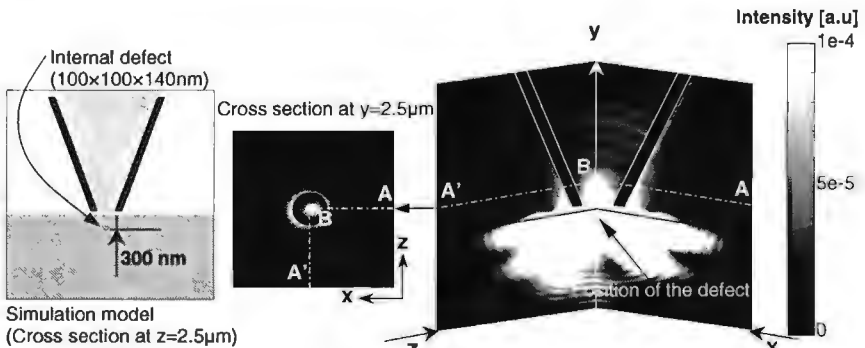


**figure 3:** Gray-scale of field intensity distribution for the case of surface defect.

signal of defect. So the result suggests that the fiber probe can detect the optical information of the micro scratch with sizes of 60nm wide.

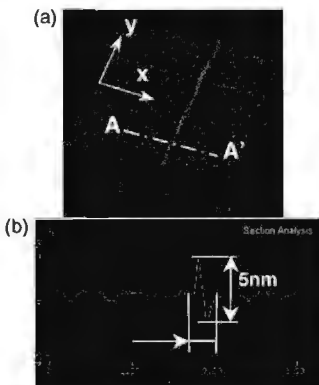
**Detection of void defect**

Figure 4 shows the image of the result for internal defect that is difficult to detect for conventional methods. To enhance the disturbance of the internal defect, this intensity distribution was obtained by subtracting the reference intensity distribution of no defect model. Here, the voids defect is modeled as the subsurface octahedral defect (the size has 100x100x140nm; 300nm in depth). It can be seen that disturbance of the evanescent light resulting from the internal defect is also picked up by the aperture of the fiber probe. This result also suggests that even if the defect exists in the subsurface, this method enables to detect the micro defects with high sensitivity.



**figure 4:** Gray-scale representation of field intensity distribution for the case of internal defect.

**Experiments**



**figure 5:** The AFM image of micro scratch (a: bird view, b: profile of A-A').

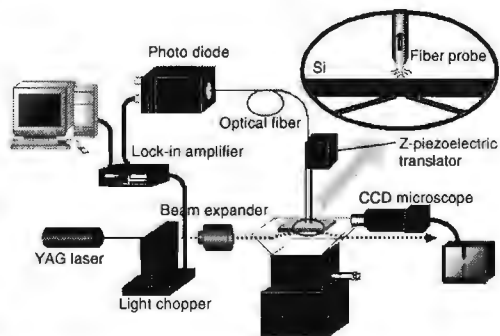


**figure 6:** The diagram of experimental apparatus.



Fundamental experiments are also performed for the micro scratch (figure 5) produced by the traversing the sharp diamond stylus over Si wafer surface. The difference between peak and valley of the scratch is as small as 5nm and the width is about 280nm. Figure 6 shows the experimental schematic diagram. An expanded and p-polarized beam of Nb: YAG laser ( $\lambda=1064\text{nm}$ ; 1W) was used to generate evanescent field on the surface of the sample (Si wafer). The sample is mounted on the trapeziform prism that refracts the incident beam to its upside. And the incident laser beam illuminates the sample on the prism from the back to reach the surface with under total-internal-reflection condition with this prism. To detect the intensity variation of the evanescent field, the fiber probe tip is approached towards the

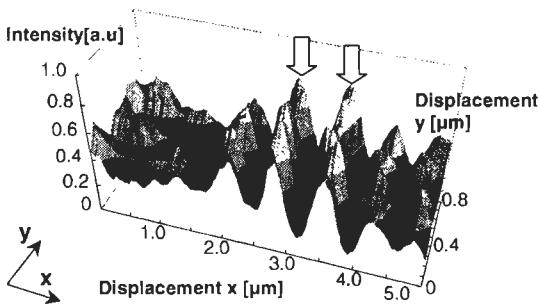


figure 7: Result of the experiment.

sample surface to a gap of 200nm. The tip of fiber probe is coated with metal to effectively convert the detected light. The photo diode is coupled to an optical fiber and detects the transmitted light from the fiber probe. Figure 7 shows the intensity variations detected from the micro scratch by scanning fiber probe. The variations have 2 peak lines in y direction (the arrows in figure 7) corresponding to the direction of the micro scratch having peak and valley shown in figure 5. The fact suggests that our proposed method enables the detection of micro defects with nm scale.

## Conclusions

We proposed a new optical detection method for evaluating the nano-defects existing in the vicinity of Si wafer surface, not by using scattered light but by using evanescent light based on near-field optics. FDTD simulation shows that the proposed inspection method can detect the defects with 10nm scale not only on the surface but also in the internal. And also the fundamental experiments show the validity of this method by demonstrating the detection of micro scratch.

## References

- [1] S. Takahashi, T. Miyoshi, Y. Takaya, R. Nakajima, 2001, Nano-Defects Detection of Si Wafer Surface Using Evanescent Light –Computer Simulation by Means of FDTD Method, Proceedings of the 2<sup>nd</sup> euspen Conference., Vol. 1, pp. 102-105
- [2] Thomas A. Germer, 1997, Angular dependence and polarization of out-of-plane optical scattering from particulate contamination, subsurface defects, and surface microroughness, Applied Optics, Vol. 36, No. 33, pp. 8798-8805
- [3] Howard R. Huff, Randal K. Goodall, Elton Williams, 1997, Measurement of Silicon Particles by Laser Surface Scanning and Angle-Resolved Light Scattering, J. Electrochem. Soc., Vol. 144, No. 1, pp. 243-150
- [4] K. S. Yee, 1966, Numerical Solution of Initial Boundary Value Problems Involving Maxwell's Equations in Isotropic Media, IEEE Trans. Antennas Propagat., Vol. 14, No. 4, pp. 302-307

## Development of the automatic calibration machine for depth measurement standards for surface texture measurement

S.Ueno<sup>1</sup>, Y.Kobayashi<sup>2</sup>, T.Omino<sup>2</sup>, S.Takase<sup>1</sup>, Y.Awano<sup>1</sup> and K.Miyamoto<sup>2</sup>

<sup>1</sup>Technical Research Institute of JSPMI, Tokyo, JAPAN; <sup>2</sup>Kosaka Laboratory Ltd, Saitama, JAPAN.

### Abstract:

Over the last ten years the demand to improve the calibration accuracy of surface texture measuring machines has been increasing. This paper describes the design and performance of an automatic depth measurement machine, which uses a stylus method to reach the calibrate levels required by the new standard.

The machine's accurate detection of stylus displacement, which is paramount in meeting it's requirements, is performed by an LVDT and fibre optic launched Helium Neon laser interferometer. These features, combined with the fact that the total measuring procedure has been programmed to improve measurement repeatability, have resulted in the development of a system with the sensitivity to be applied to calibration work.

### Introduction

New international standards were established in the year 2000, to calibrate roughness measurement instruments against artifacts. These international standards [1][2], specify several types of roughness measurement specimen and their typographical figures to be used as the calibration standard for roughness instrument magnification checking. The standard specimen includes complicated shapes and accurate dimensions. A requirement existed to develop a higher accuracy calibration machine to certify the standards using the new stylus method.

This paper describes a newly developed automatic depth-measuring machine for this purpose; the machine includes a He-Ne laser interferometer to maintain traceability to the international length standard.

### Basic machine design

A bridge type configuration has been adopted to improve vibration stability and to minimize thermal deformation. Moreover, Granite is adopted for the structural material of the base, the column, and the beam for improvement of its thermal stability. Figure 1 shows a basic internal construction.

Both the coarse movement mechanism for the test piece positioning and the fine movement mechanism for the measurement have been installed in the Y-axis structure. The linear motion bearing for a coarse movement is directly put on the base and the mechanical slide guide is prepared for the fine movement. It is placed on the rough movement mechanism.

The guide is a combination of lapped steel and PTFE for both X and Y-axis and both use a dry lubrication system. The reason for this being that the thickness change of an oil film cannot be disregarded when nm level [3] repetition accuracies are required. A digital scale is installed on X and Y-axis for positional detection and to

control the servo drive.

It provides with the LVDT, which has a long range of motion and a parallel spring structure, that there are past results in the stylus position detection of Z-axis. In addition a Renishaw RLE10, a fibre optic guided He-Ne laser interferometer, is installed for positional detection of the X, Y, and Z-axes. By fixing a thin, lightweight plane mirror on the Z-axis of the LVDT it is possible for the interferometer to read the displacement of the stylus directly.

The whole system is mounted on a servod, air vibration isolation platform. In addition, to escape from the influence of air and acoustic disturbance, the system is covered with a stainless steel cover.

The specification of the prototype is as follows;

X-axis travel -100mm: Straightness accuracy -  $0.1\mu\text{m}$  or less

Measurement speed -  $0.005\sim 2\text{ mm/s}$ : Y-axis travel - 10mm

Feeding pitch -  $0.05\mu\text{m}$  or more: Range of Z axis detection -  $100\mu\text{m}$

Z-axis resolution -  $0.1\text{nm}$ (LVDT): Measuring force -  $1\mu\text{N}\sim 0.5\text{mN}$

Parallelism adjustment mechanism: X and Y-axis built-in automatic fine parallel adjustment device

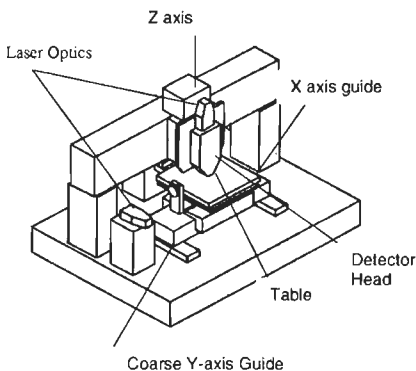
Digital scale: 10nm resolution: Laser interferometer: 10nm resolution with plane mirror

Controller: PC based controller

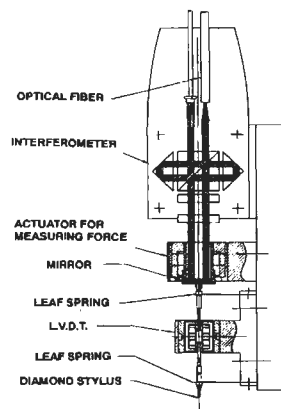
Software: Various parameter calculation programs and control program (sequence control and parallel correction, etc.)

Figure 2 shows a basic construction of the stylus part. There is an LVDT on the interchangeable stylus and in addition an electro-magnetic system that generates dumping and measurement force. The stylus part is supported with a parallel spring, and the mirror is being put by the above part. The interferometer optics are placed on the end of stylus shaft and the laser beam delivered by the fiber. The total mass in the movable part, including the plane mirror, is 1.41gr.

Figure 3 shows a measurement sequence flow diagram for an automatic measurement procedure. The process starts by correcting any



**Figure 1:** Basic construction of the machine



**Figure 2:** Main configuration of the detector system

specimen inclination and then a measurement frequency is prescribed and scanning carried out. This automatic measurement sequence results in a three-dimensional measurement map.

**Test results**

Figures 4(a, b) are the results of measuring the surface of Optical flats for accuracy inspection. The standard Optical flat used is 150mm in diameter and its shape accuracy is less than  $1/30\lambda$ . The straightness result obtained in the X direction is 50nm or less and 15nm or less in the Y direction. The measurement difference obtained when the straightness of the x-axis was measured ten times, consecutively, was 1nm or below. When measurements were made days apart the difference in straightness was about 5nm. As a result, it can be concluded that the prototype's guide mechanism has enough reproducibility for higher calibration tasks.

Table 1 shows the results of measuring various depth standard samples. The standard deviation is approximately 0.3nm of the difference of the measurement result in the table. This result is about 1/5 of past measuring instruments.

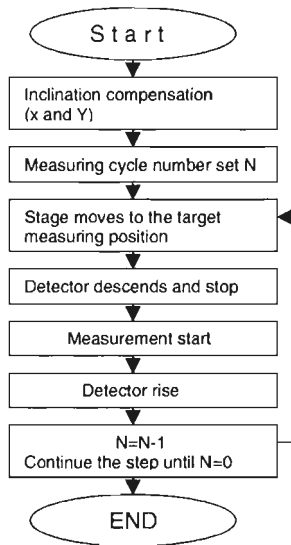
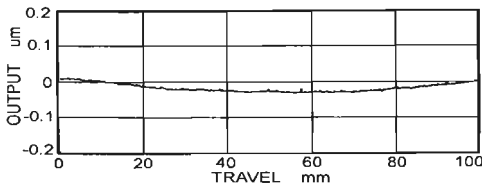
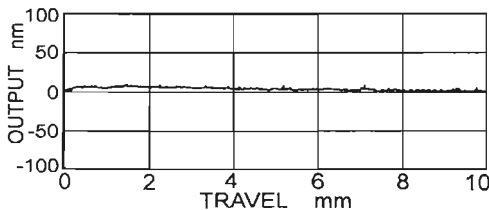


**Figure 3:** The flow diagram of the automatic measurement sequence



a) X axis straightness (47.79nm/100mm)



b) Y axis straightness (12.88nm/10mm)

**Figure 4 (a, b):** Results of the straight motion accuracy check (Optical flat)

Figure 5 shows an example result of transient phenomena that the stylus touched on to the measurement surface first. The output is increased rapidly after it comes in

contact, and decreases thereafter. This phenomenon continues for about three minutes. It is programmed in an actual measurement sequence to avoid the influence of this transitional phenomenon. The change by the transmission of heat to the stylus is thought by one of causes of this phenomenon.

The influence of external air turbulence is extremely large in highly accurate measurements. When measurements were taken with the cover open changes of 20nm or less were recorded and about the detailed 5nm change was admitted.

## Discussion and Conclusion

The LVDT and laser interferometer show a good agreement for large displacements i.e >10nm. The laser interferometer can be used only to prove displacements in excess of 10nm, due to its current resolution, so displacements of less than 10nm are buried in the digital error margin. To enable fine displacements to be tracked the laser resolution will be increased to 1nm.

An automatic calibration machine for artifacts on surface roughness measuring instruments was developed, and the basic performance examined. Results show that the development machine has excellent reproducibility and stability, hence it is possible to use it for the proofreading business. This development machine was marketed in fiscal year 2002.

This development has been supported by the KEIRIN fund.

## References

- 1) ISO5436-1: 2000; Geometrical Product Specifications (GPS), Surface texture: Profile method; Measurement standards Part 1: Material measure
- 2) ISO12179:2000; Geometrical Product Specifications (GPS), Surface texture: Profile method; Calibration of contact (stylus) instruments.
- 3) S.Ueno et al.: Design of a Tiny CMM with Ultra Low Thermal Expansion Glass, Proc. of the 8<sup>th</sup> ASPE, Seattle (Nov.7.1993)404

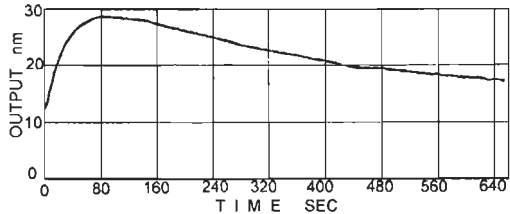


**Figure 5:** Transient phenomena observed when the stylus touched on the work surface

**Table 1:** Results on the calibration example

Specimen	Gage block	SS-T	VLSI
Nominal step height	5.1	0.317	0.449
Average	5.1279	0.31634	0.45050
Maximum	5.1280	0.31663	0.45087
Minimum	5.1270	0.31619	0.45023
R	0.0010	0.00044	0.00064
Standard Deviation	0.0003	0.00012	0.00023
Speed mm/s	0.1	0.02	0.2

10 times measurements result

( $\mu\text{m}$ )

# Thickness Measurement of Silicon Wafers Using a Double-Focus Lens

Y. KAMIMURA<sup>1</sup>, Y. TANI<sup>1</sup>, K. WATANABE<sup>2</sup>, H. SATO<sup>3</sup>

<sup>1</sup>Institute of Industrial Science, University of Tokyo, Tokyo, Japan

<sup>2</sup>Design and Engineering Division, Hitachi Via Mechanics, Ltd., Kanagawa, Japan

<sup>3</sup>Faculty of Science and Engineering, Chuo University, Tokyo, Japan

## ABSTRACT

The realization of on-machine measurement with an accuracy of better than 0.1 $\mu$ m (0.1% of 100 $\mu$ m measuring range) of the total thickness variation (TTV) of large-diameter silicon wafers after grinding on a vacuum chuck is strongly required. In this paper, a thickness measuring method using a double-focus lens and infrared rays that can transmit through the silicon wafers is proposed for high-precision on-machine measurement of TTV without being affected by the flatness or structure of the vacuum chuck surface. In this method the objective lens is moved from the focusing position on the back surface to the focusing position on the front surface, and the thickness is calculated from the distance moved. In this method the refractive index of the wafer is necessary in the calculation; thus the value can be identified using a double-focus lens. The use of a double-focus lens enables shortening of the distance moved which results in shortened measuring time and high measuring accuracy.

## Introduction

The diameter of next-generation wafers has been yet as 450mm and the production of 300mm wafers begun [1]. The production process was investigated for large-diameter wafers and some new process has been proposed. The adoption of a single-sided grinding machine to rough machining to obtain flat workpieces was one of the alternations [2]. In general, concave forms are produced during the grinding process due to elastic deformation of grinding wheels and thermal expansion of workpieces. Thus the wheel spindle is tilted to compensate the form accuracies. However, the machinability of grinding wheels continually changes so that the form of workpieces varies. Then in-situ thickness measurement with an accuracy of better than 0.1 $\mu$ m is necessary to perform precise compensation.

Thickness measurement of small-diameter wafers is carried out using capacitance sensors from both sides of the wafer. This method cannot be applied as an on-machine measurement method of wafers on a vacuum chuck. New measurement method by which thickness can be measured from one side must be devised. The method of using a capacitance sensor can be used to measure the distance from the sensor to a wafer, but it is affected by the flatness and the structure of the vacuum chuck surface. Infrared rays which can transmit through a silicon wafer were selected and the thickness was measured by an optical method.

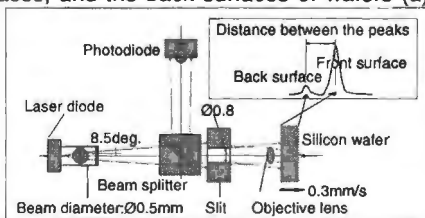
## MEASURING principle of thickness of silicon wafers

### Optical system for thickness measurement

In order to optically measure the thickness of the silicon wafer from one side, it is necessary for the light to transmit through the wafer. The range of wavelengths which can transmit through a silicon wafer is the infrared region from 1.2 $\mu$ m to 8 $\mu$ m.

Therefore, a laser diode of wavelength 1.3μm was used for this optical system (Figure 1). The light from the laser diode enters the beam splitter (transmittance is 50%) un-polarized. The light is emitted straight from the beam splitter and is focused by the objective lens. The reflected light from the front surface and the back surface of the wafer is bent 90° by the beam splitter and the light is detected at the photodiode. In this condition, the focusing point was set far from the objective lens than the back surface of the wafer. Then, the wafer was moved in the direction away from the objective lens at a constant speed of 0.3mm/s under the condition that the wafer was kept vertical. Then, the focusing point agrees on the back surface of the wafer, and optical reflection power becomes maximum at this time. Although optical reflection power declines when the wafer is further away, the maximum value of optical reflection power appears when that focusing point corresponds to the front surface. Therefore, two peaks are obtained, as shown in Figure 1, on the back and front surfaces of the wafer. The distance between the peaks changes corresponding to the thickness of the wafer.

The measured objects were single-crystal silicon wafers, and three wafers of (a) 0.664mm, (b) 0.623mm and (c) 0.502mm thick were used in thickness measurement. The front surfaces of all wafers and the back surface of wafer (c) were mirror surfaces, and the back surfaces of wafers (a) and (b) were rough. The thicknesses

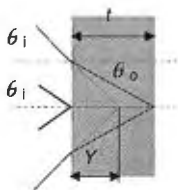


were also measured using a micrometer. Moreover, the refractive indices of wafers (a) and (b) were measured using an infrared-ray-spectrometer, and value of 3.4981 was obtained. On the other hand, the refractive index of wafer (c) was not measured.

**Figure 1:** Optical system for thickness measurement

**Theoretical equation for thickness measurement**

The schematic of the thickness measurement by detecting the focal point is shown in Figure 2. When the light having focusing angle  $\theta_i$  appears at the wafer, incident light is refracted, and it changes in focusing condition to  $\theta_o$ . Therefore, the focal point moves to the back surface (B) when the wafer moved only Y from the focusing condition (A) in the front surface. The relationship between the thickness t and the distance moved Y can be shown by Equation (1). Snell's refractive equation is shown by Equation (2).  $n_1$  in Equation (2) is the refractive index of air, and is about 1.  $n_2$  is the refractive index of the silicon wafer.  $\theta_i$  is the focusing angle and  $\theta_o$  is the focusing angle which changes due to the refraction. If  $\theta_o$  in Equation (1) is eliminated using Equation (2), the theoretical equation (3) for the thickness t can be derived. Like this, the thickness t becomes a function of the distance Y moved to change the focusing point from the front surface to the back surface, the focusing angle  $\theta_i$ , and the refractive index  $n_2$  of the wafer.



$$Y = t \tan \theta_o / \tan \theta_i \quad (1) \quad n_1 \sin \theta_i = n_2 \sin \theta_o \quad (2) \quad t = Y \sqrt{\frac{n_2^2 - \sin^2 \theta_i}{1 - \sin^2 \theta_i}} \quad (3)$$

**Figure 2:** Principle of refraction

## Refractive index of a silicon wafer and thickness measurement using a double-focus lens

### Calculation method of the refractive index of wafer

The refractive index of the wafer may be affected by the presence of oxygen and other elemental impurities. The refractive index of every wafer can be calculated if the thickness can be calculated using the system based on the focusing angle difference. We propose the method of using the double-focus lens to calculate the refractive index. If a double-focus lens is substituted for the objective lens shown in Figure 1, two equations similar to Equation (3) can be derived using  $\theta_1$  and  $\theta_2$  of the double-focus lens. Then, if the ratio of these equations is taken as shown by Equation (4), the unknown thickness  $t$  is eliminated, and the refractive index  $n_2$  can be deduced as shown by Equation (5).

The values of the refractive index calculated using Equation (5) and measured using the infrared-ray-spectrometer are shown in Table 1 for the three wafers. The focusing angles ( $\theta_1=23.357^\circ$  and  $\theta_2=19.201^\circ$ ) of the double-focus lens and distance between the peaks ( $Y_1$  and  $Y_2$ ) measured by the double-focus lens were substituted into Equation (5), and refractive index  $n_2$  was calculated. The calculated refractive index  $n_2$  was close to the value obtained using the infrared-ray-spectrometer, as shown in Table 1. An accurate value of  $n_2$  could be obtained by eliminating the  $t$  value with low measurement precision. Furthermore, even if a refractive index is unknown like the wafer of (c), it can be calculated from equation (5).

**Table 1:** Calculated values of refractive index and the values measured using an infrared-ray-spectrometer

	Incident angle		Refractive index $n_2$	
	$\theta_1=23.357^\circ$	$\theta_2=19.201^\circ$	Measured using an infrared-ray-spectrometer	Calculated
	Distance between the peaks			
	$Y_1$ mm	$Y_2$ mm		
a	0.1754	0.1801	3.4981	3.4976
b	0.1645	0.1689	3.4981	3.4976
c	0.1323	0.1359	-	3.4963

$$\frac{Y_2}{Y_1} = \frac{\sqrt{\frac{1 - \sin^2 \theta_2}{n_2^2 - \sin^2 \theta_2}}}{\sqrt{\frac{1 - \sin^2 \theta_1}{n_2^2 - \sin^2 \theta_1}}} \quad (4)$$

$$n_2 = \sqrt{\frac{(1 - \sin^2 \theta_2) \sin^2 \theta_1 - (1 - \sin^2 \theta_1) \sin^2 \theta_2 \left(\frac{Y_2}{Y_1}\right)^2}{1 - \sin^2 \theta_2 - (1 - \sin^2 \theta_1) \left(\frac{Y_2}{Y_1}\right)^2}} \quad (5)$$

### Thickness measurement using distance between the foci of double-focus lens

In thickness measurement using a single lens, the measured object or the objective lens must be moved the large amount equivalent to the thickness (about  $t/n_2$ ) of the wafer. However, if a double-focus lens is used, the actual distance moved of the wafer can be reduced by an amount equivalent to the distance between the foci ( $f_2-f_1$ ) of the double-focus lens. The measurement time can be shortened if the actual distance moved of the wafer can be reduced. Furthermore, the reduction of actual distance moved enables use of high-resolution actuator which results in high measuring accuracy of the thickness measurement.

Thickness measurement using a double-focus lens of  $f_1=0.358\text{mm}$  and  $f_2=0.753\text{mm}$  (Figure 3) was tried. The measured distance between the peaks  $Y_{2-1}$  is shown in Figure 3. In the measurement, the silicon wafer of  $t=0.664\text{mm}$  (micrometer value)



was used. The thick line and thin line in Figure 3 show correspond to the optical reflection power measured with the lens of  $f_1$  and  $f_2$ . The detected position of optical reflection power obtainable from  $f_1$  and  $f_2$  of the double-focus lens was identified based on the position signal of the capacitance sensor shown in Figure 3. Then, the distance between the peaks  $Y_{2-1}$  was measured. The distance between the front surfaces of the  $f_1$  lens and the  $f_2$  lens shows the distance between the foci ( $f_2-f_1$ ) of the double-focus lens in Figure 3. The distance between the peaks  $Y_{2-1}$  of the light reflected from the front surface by the  $f_1$  lens and the light reflected from the back surface by the  $f_2$  lens shows the actual distance moved of the wafer. Therefore, the theoretical equation of thickness measurement using the

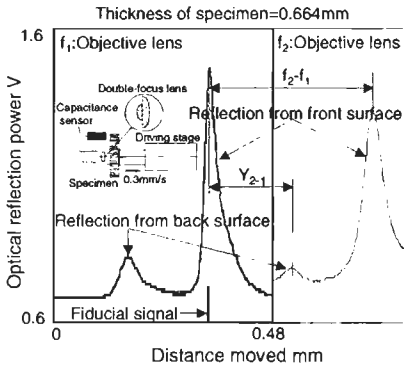


**Figure 3:** Measurement of distance moved using a double-focus lens

The value calculated from the Figure 3 was adopted as the distance between the two foci ( $f_2-f_1=0.3604\text{mm}$ ). The distance between the peaks was calculated using  $Y_{2-1}=0.1802\text{mm}$  taken from Figure 3. Each focusing angle ( $\theta_1=23.357^\circ$ ,  $\theta_2=19.201^\circ$ ) and the refractive index ( $n_2=3.4976$ ) of the double-focus lens are the same as the values presented in the foregoing paragraph. Substituting these values into Equation (6), the thickness  $t$  was calculated to be  $0.6644\text{mm}$ , which agreed to the micrometer scale. It was demonstrated that the thickness of the wafer could be calculated from the distance between the two foci, by this result.

the double-focus lens can be expressed as Equation (6). When  $f_1 < f_2$ , the sign of the distance between the peaks  $Y_{2-1}$  varies as follows. It becomes a minus when the peak of the back surface (detected by the  $f_2$  lens) is detected later than the peak of the front surface (detected by the  $f_1$  lens) as shown in Figure 3, and vice versa. These relations change according to the movement direction of the double-focus lens.

$$t = (f_2 - f_1 \pm Y_{2-1}) \sqrt{\frac{n_2^2 - \sin^2 \theta_2}{1 - \sin^2 \theta_2}} \quad (6)$$

**conclusions**

The on-machine thickness measurement is indispensable for compensating the form accuracy in single-sided grinding of a silicon wafer. The thickness measurement can be performed by detecting the focusing position of both the front surface and the back surface if transmittable light is used. However the refractive index of the specimen becomes necessary in calculation of the thickness. When a double-focus lens is used, the refractive index as well as the thickness can be measured. Moreover the use of a double-focus lens enables shortening of the distance moved for focusing, which results in short measuring time and high measuring accuracy.

**References**

- [1] Takasu, S., 1996, Where does silicon wafer become big to?, Journal of the Japan Society of Applied Physics, 165/8:832-840.
- [2] Abe, T., 1996, The next generation machining technology for large diameter wafer, ELECTRONIC PARTS AND MATERIALS, 35/7:22-28.

# Sub-nm Topography Measurement by Deflectometry: Flatness Standard and Wafer Nanotopography

R. D. Geckeler, I. Weingärtner

Physikalisch-Technische Bundesanstalt Braunschweig und Berlin (PTB)  
Bundesallee 100, D-381 16 Braunschweig, Germany, e-mail: [Ralf.Geckeler@ptb.de](mailto:Ralf.Geckeler@ptb.de)

## Abstract

For the ultra-precise and traceable measurement of slope and topography of large near-flat and slightly curved optical surfaces, a novel scanning facility based on ESAD (*Extended Shear Angle Difference*) deflectometry has been developed. An uncertainty of the topography in the sub-nanometer range can be attained, as the ESAD principle minimizes error influences and allows a highly precise calibration of the angle measuring device. ESAD scanning does not rely on external reference surfaces of matched topography. The measurands are directly traceable to the SI units of angle and length. A primary application of the facility is to establish the improved standard for flatness and straightness of PTB. Another goal is to enable the ultra-precise measurement of the nanotopography of large wafers.

## Introduction

A method for the ultra-precise measurement of slope and topography has been described (ESAD - *Extended Shear Angle Difference*, [1,2]). It is based on the analysis of differences of reflection angles measured at points on the surface of the specimen separated by large (mm to cm) lateral shears. Newly developed algorithms allow the reconstruction of the surface slope from two sets of angle differences obtained with different shear values [3,4]. The reconstruction is mathematically exact, can be obtained over the whole surface area, and allows a high lateral resolution independent of the shears applied. In contrast to interferometric techniques, ESAD scanning does not rely on an external reference surface of matched topography. It allows the measurands to be traced back exclusively to the SI units of length and angle.

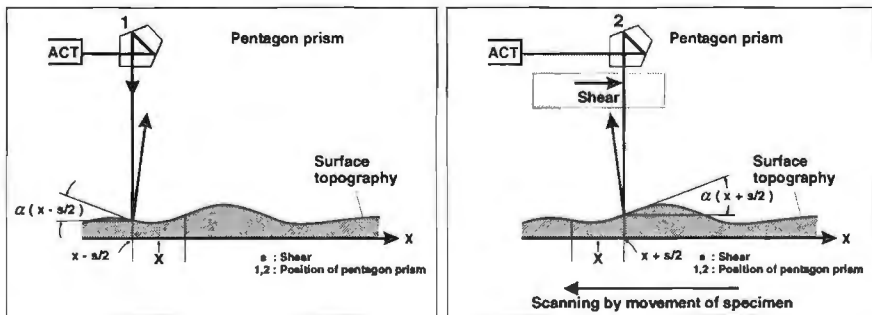


**Figure 1.** Sequential angle difference measurement implemented in our device.

Figure 1 demonstrates the principle of ESAD scanning deflectometry as implemented in our device. The local angle of the surface (slope) at different points is measured with an electronic autocollimator (ACT). A pentagon prism with an active three-axis stabilization reflects the beam of the autocollimator onto the specimen. The shearing

*Proc. of the 3<sup>rd</sup> euspen International Conference, Eindhoven, The Netherlands, May 26<sup>th</sup> –30<sup>th</sup>, 2002*

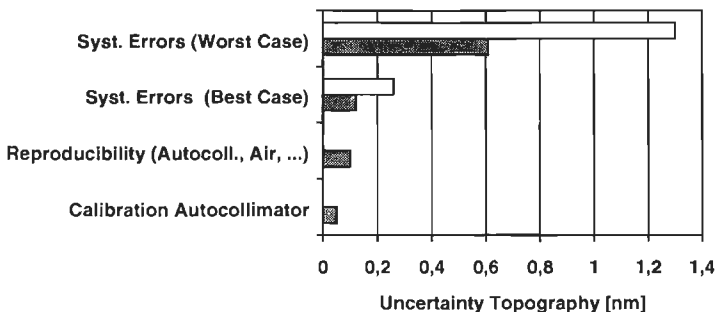
measurements (to obtain slope differences between points separated by the shear lengths) are performed sequentially by shifting the stabilized pentagon prism. This technique avoids the influences of first- and second-order errors of the optical components. In combination with the principle of difference measurement, influences of positional and angular errors of the scanning stages, long-time whole-body movements of the specimen and slow deformations of the measurement device are also reduced / eliminated. The scanning is performed by mechanical shifting of the specimen by a precision 2D scanning stage; shearing (angle differences) and scanning (of the surface) are thus decoupled and performed sequentially.

## Error Influences

Using Monte Carlo simulations we have analyzed the propagation of a given random error of the angle differences through the ESAD algorithms for a single scan (1D surface section). The random errors of the reconstructed slope values (resulting from angle differences with normal distribution) are not normally distributed (due to the mathematical algorithms involved), therefore estimates for the associated uncertainty of the topography after integration of the slope data are preferentially obtained by simulation. The distribution of the random errors of the reconstructed slope (and of the topography) is a function of the values  $s_1$ ,  $s_2$  chosen for shears 1 and 2, with  $n=s_1 \times s_2$  data points per scan. Shears are expressed in units of the lateral distance between measured surface points in this paper, assuming an equidistant sampling of the topography. The physical shear values are thus obtained by multiplication with the lateral distance of the sampling points (scan length divided by  $s_1 \times s_2$ ). For a given number of data points per scan, an optimum shear combination exists with a minimum standard deviation of the resulting topography. For approx. 100, 140, and 500 data points per scan optimum shear combinations  $s_1 / s_2$  ( $n$ ) of 4 / 25 (100) data points, 4 / 35 (140), and 5 / 99 (495) are obtained. Measurements of various optical surfaces have been performed with the new ESAD facility, including series with a duration of up to two weeks. A reproducibility of the reconstructed topography of 0.1 nm after tilt correction is now routinely achieved for the optimized shear combination of 4 / 35 data points and a lateral sampling of approx. 1 data point / mm (actual scan lengths 130–140 mm). The experimentally determined standard deviation of the topography measurements at a given surface point (calculated from a set of topographies obtained over an extended period under reproducible measurement conditions) is dependent on its location in the scan, nevertheless, we use a single (median) value for simplicity. We define reproducibility thus as the typical (median) standard deviation of the topography values in the scan (uncertainties cited also refer to median values). The reproducibility of the topography measurement includes the effects of those components of error influences that are not constant during the measurement series. Error sources include the reproducibility of the angle measurements (autocollimator), residual angle deflections by the minimized air path, mechanical vibrations, etc. We will use the reproducibility of the topography measurements as a conservative upper limit estimate of the uncertainty associated with the cited error influences. The reproducibility does *not* estimate systematic effects of error sources that are constant from topography measurement to topography measurement, e.g., sampling effects due to the finite spot size of the autocollimator, its calibration, and reproducible systematic offsets in the angle differences due to the sequential difference measurements implemented in our device.

The calibration process for the angle-measuring device (autocollimator Elcomat HR,

Möller-Wedel Optical) has been described in detail elsewhere [6]. Using Monte Carlo simulations (equivalent to Type B evaluation, GUM [5]), a standard uncertainty of the reconstructed topography of 0.05 nm results after tilt correction (median uncertainty of surface points in the topography scan) for a shear combination of 4 / 35 data points and a lateral sampling of 1 data point / mm (scan length 140 mm). In addition to random errors inherent in the measured angle differences, systematic errors may be introduced, e.g., by a residual non-linear mechanical drift of the scanning stage during the sequential measurement of the difference data implemented in our device. Because we measure angles at each surface point twice in a symmetrical forward / backward sequence, linear angle drifts are eliminated. Still, small residual non-linear effects remain. Each angle difference is obtained by repeating the same mechanical measurement procedure, the errors introduced into the difference data set can therefore be separated into random errors plus a near-constant offset of the whole set of angle difference data for each shear. Work on the characterization / elimination of systematic offsets is still in progress, but we are confident to provide best / worst case estimates for the residual offsets of 1–2 milli-arcsec and 10 milli-arcsec (5–10 nrad and 50 nrad), respectively. For a shear combination of 4 / 35 data points and a lateral sampling of 1 data point / mm, a safety limit for the rms value (maximum rms for given offset boundaries) of the reconstructed topography of 0.26 nm / 1.30 nm results for the best / worst case estimate ( $\pm 2$  milli-arcsec and  $\pm 10$  milli-arcsec, respectively). According to GUM, the standard uncertainty associated with non-correction of systematic effects has to be assessed differently [5]. For the shear combination of 4 / 35 data points, a standard uncertainty of the topography (median uncertainty of surface points in the scan) of 0.12 nm / 0.61 nm results for the best / worst case offset estimate (using Monte Carlo simulations).



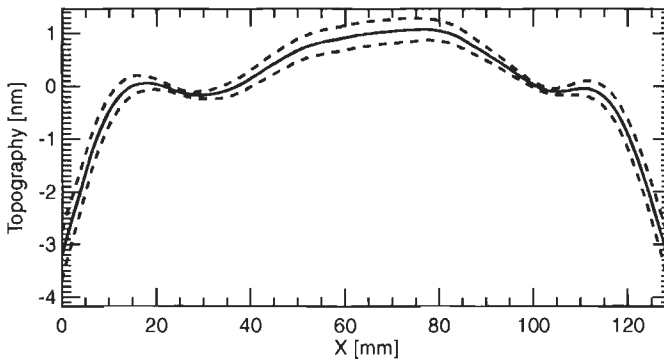
**Figure 2.** Preliminary uncertainty budget for ESAD scanning with optimized shears of 4 / 35 data points (assuming 1 data point / mm, scan length 4x35 mm = 140 mm).

Figure 2 presents a graphical summary of the standard uncertainties for a topography scan associated with the error influences described in this section (optimized shear combination 4 / 35 data points, sampling 1 data point / mm, 140 mm scan length, median uncertainties of surface points in the scan, uncertainties referring to single scans). For the residual systematic errors, both standard uncertainties according to GUM [5] associated with best / worst case estimates for systematic offsets are given (shaded bars) plus safety limits to the maximum rms values (open bars). The quadratic sum of the uncertainty components yields a

preliminary combined standard uncertainty  $u_c = 0.16 \text{ nm} / 0.62 \text{ nm}$  for a best / worst case estimate for residual systematic errors. This preliminary budget excludes the uncertainty associated with sampling effects due to the finite spot size of the autocollimator.

## Results

Figure 3 presents typical measurement results obtained with a plane Zerodur substrate with 170 mm diameter and 50 mm thickness, which has been suspended on three steel balls located in the Bessel points. The mean topography is plotted as a solid line, dashed lines denote the standard deviation of the measured values as derived from the data set (34 topography measurements obtained over 12 days, 130 mm scan length, shears 11 / 13 data points, physical shears 10 / 11.82 mm,  $11 \times 13 = 143$  data points per scan). We have chosen this data set with non-optimized shears and a reproducibility of approx. 0.2 nm for presentation, because the substrate proved to be the flattest yet measured with the new ESAD facility.



**Figure 3.** Topography measurements obtained with our ESAD facility. Mean topography (thick line) and standard deviation of topography (dashed lines) are shown.

The measurements have been performed with a relatively large spot size of 20 mm of the test autocollimator currently in use. It will be upgraded to a spot size of approx. 5 mm within the next months, spot sizes may approach 2 mm within a year.

## Acknowledgements

This work has been supported by the BMBF and the VDI (No. 13 N 7730). We thank Dipl.-Ing. A. Just and Dr. R. Probst, Section 5.202 of PTB, for the scientific collaboration. Also, we wish to thank M. Baier and A. Fitzenreiter for their contributions to the realization of the new ESAD device, and Dr. M. Schulz for GUM related discussions.

## References

- 1) I. Weingärtner, M. Schulz, Proceedings Europto Series, **3739**, 274–282, 1999
- 2) I. Weingärtner, M. Schulz, C. Elster, Proc. SPIE **3782**, 306–317, 1999
- 3) C. Elster, I. Weingärtner, J. Opt. Soc. Am., **16**, 2281–2285, 1999
- 4) C. Elster, I. Weingärtner, Appl. Optics, **38**, pp. 5024–5031, 1999
- 5) *Guide to the Expression of Uncertainty in Meas.*, ISO, Geneva, Switzerland, 1993
- 6) R. Geckeler, I. Weingärtner, A. Just, R. Probst, Proc. SPIE **4401**, 184–195, 2001

# Microtopography characterization of optically smooth and structured surfaces

S. Patzelt, J. Peters, G. Goch

University of Bremen, Germany

## Abstract:

A new approach to characterize the functional properties of optical parts (e.g. lenses, mirrors, replication tools and molds) combines two laser optical measuring principles to measure local and integral features of optically smooth or structured surfaces, which typically show roughness values ( $R_a$ ,  $R_q$ ) in the nanometric range. The method of double scattering by speckle pattern illumination characterizes the integral measure surface roughness in the range of  $R_a < 100$  nm. A modified measuring arrangement based on the principle of angle resolved scattering (ARS) analyses local defects (e.g. scratches, cracks, chips) and structure deviations.

This paper introduces to the optical measuring principles and presents typical measuring effects and their interpretations. Finally, first results of both experimental set-ups will be shown.

## Introduction

The functional properties of optical parts (e.g. lenses, mirrors, replication tools and molds) depend on several microtopographic features, for example the surface roughness and local defects (e.g. scratches, cracks, chips), which affect the surface functionality. Furthermore, in the case of structured surfaces pattern deviations (e.g. insufficient periodicity) affect the structure function. Microtopography measurements enable the characterization of the functional properties. Usually these measurements are performed with well known measuring devices, e.g. tactile profilometer, white light interferometer, confocal microscopy, scanning force microscopy, or near field acoustic microscopy. In recent years, laser optical measuring principles based on scattered light and speckle correlation processes were successfully used for surface roughness characterization. In contrast to conventional measuring devices, scattered light techniques are generally parametric, i.e. integral roughness parameters like  $R_a$  and  $R_q$  can be extracted directly from one measurement without reproducing the 3D-topography. Therefore, scattered light techniques are fast and show in-process capabilities.

A new approach within the Transregional Cooperative Research Center SFB/TR4 funded by the DFG (Deutsche Forschungsgemeinschaft) combines two optical measuring principles to measure local and integral features of optically smooth or structured surfaces, which typically show roughness values ( $R_a$ ,  $R_q$ ) in the nanometric range. A modified measuring device based on the principle of angle resolved scattering (ARS) analyses local defects and pattern deviations. The use of modern CMOS-based CCD-cameras offering a large dynamic intensity range overcomes the blooming effect, which is a problem in connection with conventional CCD-devices. The method of double scattering by speckle pattern illumination quantifies the integral measure surface roughness in the range of  $R_a < 100$  nm. The aim is to characterize the functional properties of optical parts with respect to their future application.

## Angle resolved scattering using CMOS technology

The angular distribution of scattered light intensities is proportional to the power spectrum of the illuminated rough surface area [5]. Fourier transformation of the scattered light intensity distribution gives the surface autocorrelation function, the maximum of which is identical with the roughness value  $R_q$ . Due to the fact that

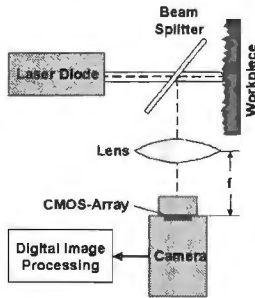


**Figure 1:** Experimental arrangement for the investigation of diffraction patterns.

diffuseness measurements show in-process capabilities, the method of angle resolved scattering was proposed for roughness characterization [6,7,8]. However, the measuring results represent the angular width of the scattered light cone that is strongly dependent on the surface slope distribution instead of the surface height distribution. This restricts the application range of the measuring principle to specific, optically smooth microtopographies ( $R_q \ll \lambda$ ) that fulfill a strong correlation between slope and height distribution (e.g. ground surfaces). A promising application of the ARS

principle is the detection and characterization of smooth surface defects. It requires the simultaneous detection of specular reflected and scattered light, which causes problems in connection with the use of conventional CCD-devices because of the blooming effect. CMOS-based camera technology with a large dynamic intensity range overcomes this effect. A corresponding measuring set-up is shown in Figure 1. The parallel monochromatic Gaussian beam of a laser diode illuminates perpendicularly an engineered surface. A camera with a CMOS-array (512 x 512 pixel) detects the reflected and scattered light intensities in the back focal plane of a double convex lens, i.e. in the Fraunhofer region. The resulting scattered and/or diffracted light distributions will be evaluated with image processing and correlation algorithms in order to characterize surface or pattern defects.

## Doubly scattered light

The method of double scattering is based on the statistical properties of speckle patterns emerging from rough surfaces, which are illuminated with a fully developed

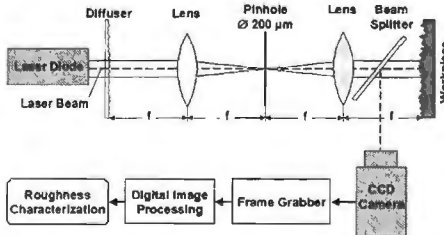


**Figure 2:** Experimental arrangement for rough surface characterization by doubly scattered light.

static speckle pattern. The measuring effect results in a roughness-dependent intensity modulation of the scattered speckle field. Yoshimura et al. [1] introduced the theoretical background of the measuring principle and performed experiments with transmitting isotropic surfaces. Basano et al. [2] described the detection of the resulting speckle patterns by use of an

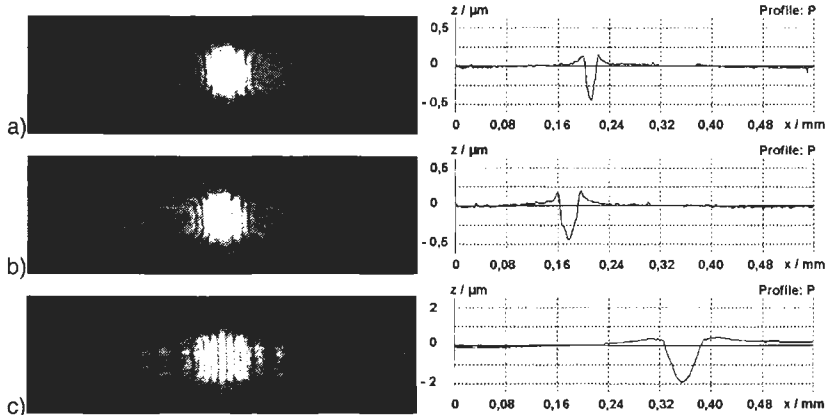


**Figure 3:** Diffraction patterns emerging from scratches of different width (a) 0.03 mm, b) 0.04 mm, c) 0.07 mm) in a polished steel surface (HSS S 6-5-2, material number 1.3343).

intensified CCD camera. Lehmann [3] gives a theoretical extension of the method for reflecting and possibly anisotropic surfaces. The method is suitable for roughness characterization in the range between  $R_a = 1$  nm and  $R_a = 100$  nm [4]. Figure 2 shows the measuring set-up used within the context of this paper. A laser diode with an anamorphic optical system emits a Gaussian shaped 150 mW beam at 812 nm of about 5 mm diameter. A rough diffuser plate scatters the beam. By optical low-pass filtering using a 4-f-arrangement including a pinhole of 200  $\mu\text{m}$  diameter, which is adjusted in the back focal plane of a Fourier transforming lens, a grainy structure, i.e. a speckle pattern, of well defined extension and speckle diameter is generated on the investigated surface. The scattered speckle pattern is recorded in the Fresnel region by a conventional monochrome CCD-array with 768 x 576 pixel and stored for digital evaluation as a gray scale data set with 8 bit resolution.

## Measuring results

First investigations to proof the suitability of CMOS-based ARS measurements for local defects at smooth surfaces were carried out using the experimental set-up according to Fig. 1 at linear scratches in a polished steel plate. Fig. 3 shows cross section profiles of three scratches, which result from scratch tests with a Rockwell-C-diamond (tip angle  $120^\circ$ , tip radius 0.2 mm) at different constant

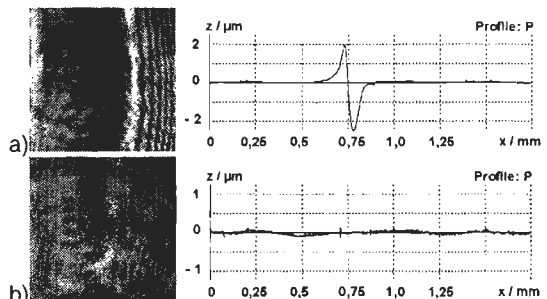


**Figure 4:** Diffraction patterns and the corresponding primary profiles from scratches of depth a) 2  $\mu\text{m}$  and b) 0,25  $\mu\text{m}$  on ball-bearing balls ( $d = 43$  mm).



loads. The corresponding CMOS images show diffusely scattered and diffracted light intensity distributions as well as reflected light without blooming. According to the scratch width the diffraction patterns are significantly different. As surfaces of optical parts are often curved, preliminary measurements at different deep and wide scratches on a ball-bearing ball with a diameter  $d = 43$  mm were performed (Fig. 4).

The double scattering method (Fig. 2) for roughness characterization was applied to curved surfaces, too. Fig. 5 shows speckle intensity distributions emerging from surfaces of two balls under the same speckle pattern illumination. Although a tactile profilometer measures the same roughness ( $R_a = 0.01$   $\mu\text{m}$ ) for both ball surfaces, the

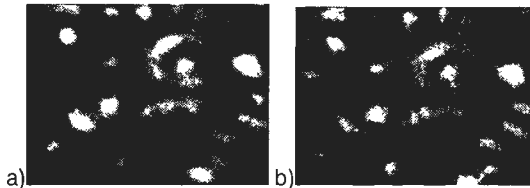


**Figure 5:** Speckle patterns obtained from ball-bearing balls ( $d = 43$  mm) with different roughness under the same speckle pattern illumination.

pattern in Fig. 5.b shows significant speckle intensity modulation, i.e. the roughness should be larger. Further investigations with more sensitive measuring devices like a white light interferometer (WLI) or an atomic force microscope (AFM) are planned to proof the results of the double scattering method.

## Conclusions and prospects

First measurements with CMOS-based ARS technique and doubly scattered laser light at structured and curved optically smooth surfaces ( $R_a \ll 100$  nm) are very promising. Further investigations and the development of suitable image processing algorithms are necessary to characterize and quantify the measured surfaces with respect to the detected light intensity distributions.

## References

- [1] Yoshimura, T., Kazuo, K., Nakagawa, K.: "Surface roughness dependence of the intensity correlation function under speckle pattern illumination", *J. Opt. Soc. Am. A* 7, 2254 – 2259, 1990.]
- [2] Basano, L., Loporatti, S., Ottonello, P., Palestini, V., Rolandi, R.: "Measurements of surface roughness: use of CCD camera to correlate doubly scattered speckle patterns", *Appl. Opt.* 34, 7286 – 7290, 1995.
- [3] Lehmann, P.: "Surface roughness measurement based on the intensity correlation function of scattered light under speckle-pattern illumination", *Appl. Opt.* 38, 1144 – 1152, 1999.
- [4] Lehmann, P., Goch, G.: "Comparison of conventional light scattering and speckle techniques concerning an in-process characterization of engineered surfaces", *Annals of the CIRP* 49/1, 419 – 422, 2000.
- [5] Thwaite, E.G.: "Power spectra of rough surfaces obtained by optical Fourier transformation", *Annals of the CIRP* 29, 419 – 422, 1980.
- [6] Peters, J.: "Messung des Mittenrauhwertes zylindrischer Teile", *VDI-Berichte* 90, 27 – 31, 1965.
- [7] Brodmann, R., Gast, Th., Thurn, G.: "An optical instrument for measuring the surface roughness in production control", *Annals of the CIRP* 33/1, 403 – 406, 1984.
- [8] Lee, C.S., Kim, S.W., Yim, D.Y.: "An in-process measurement technique using laser for non-contact monitoring of surface roughness and form accuracy of ground surfaces", *Annals of the CIRP* 36/1, 425 – 428, 1987.

## **Confocal Inspection of microscopic parts and structures**

T. Pfeifer, G. Dussler, S. Driessen

Aachen University of Technology,  
Laboratory for Machine Tools and Production Engineering,  
Chair of Metrology and Quality Management, Aachen, Germany

### **Abstract**

This article will present a new idea for the confocal inspection of microscopic parts and structures. A new method for the visualisation of complex three-dimensional objects based on confocal microscopy will be introduced. The method, called multiple-view-acquisition, will be shown in detail with its different subtasks and the first results will be presented.

### **State of the art**

For the geometrical inspection of micro parts many different measuring systems exist which are mostly tailored to one specific task. Additionally, the demands for an inspection system in micro technology are various [1]. Above all, a high flexibility concerning measurement field and resolution in vertical and lateral direction is an important criteria. Also, the ability to obtain components completely three-dimensional is essential. Due to its flexibility the confocal microscope is an inspection system which is often used in quality assurance. It permits not only the three-dimensional shape acquisition but also the characterisation of micro structures [2].

### **Problem**

Conventional confocal microscopes are well suited for visualising and analysing surfaces. However, edges, steps and stages within micro parts cause substantial problems. Additionally, the visualisation of undercuts is not possible. Due to the optical path of a standard confocal microscope, surfaces who are nearly parallel to the optical axis do not reflect any light to the photodetector. Thus, there is no information about this surfaces. This means that only 2½D-geometries can be recorded by such a confocal microscope.

### **Multiple-View-Acquisition**

In order to inspect more complex micro-parts the method of the multiple-view-acquisition method is implemented in an existing confocal Laser-Scanning-Microscope. The idea of the multiple-view-acquisition is to inspect the probe from different views. Depending on the probe, different acquisitions might be needed in order to cover it completely. Afterwards, the rotated and tilted images are assembled with the help of an appropriate software to one complete model of the probe. Each of the individual tasks, from the image acquisition to the complete assembly, will be explained in detail in the following sections. Figure 1 illustrates the proceeding of the multiple-view-acquisition for one image stack.

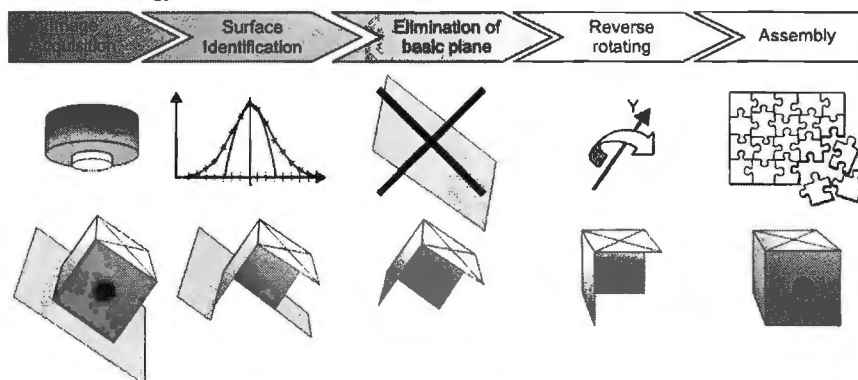


**figure 1:** Proceeding of the multiple-view-acquisition

### Image Acquisition

In order to generate the complete three-dimensional topography of an investigated object, the number of necessary image stacks has to be specified trying to cover all essential characteristics of the probe. In a first step the different image stacks of the rotated and tilted probe is recorded by the confocal Laser-Scanning-Microscope.

### Surface Identification

Thereafter, the three-dimensional surface topography is built by the use of specific surface detection algorithms. For this task different methods already exist: Maximum procedure, parabolic fit, center of gravity method and the adaption on the Gauss distribution. The most common method is the parabolic fit. The proper selection of a surface detection method depends on the geometry and material of the investigated object. Each method has its advantages and disadvantages. But the parabolic fit is the most capable and robust method against different disturbances [3].

### Elimination of the basic plane

The next step within the multiple-view-acquisition is the elimination of the basic plane. In order to record the object by the confocal microscope, the probe has to be installed on a basic plane. This basic plane is also an integral part of the obtained image stack and is therefore also identified by the surface detection algorithm. The geometrical data about the basic plane is firstly unessential information and secondly has disturbing influence on the final assembly of all surface topographies. The elimination of the basic plane is currently realised manually by picking the certain plane in the used software. In the future this task will be done by an image processing algorithm which will identify the basic plane automatically.

### Reverse rotating

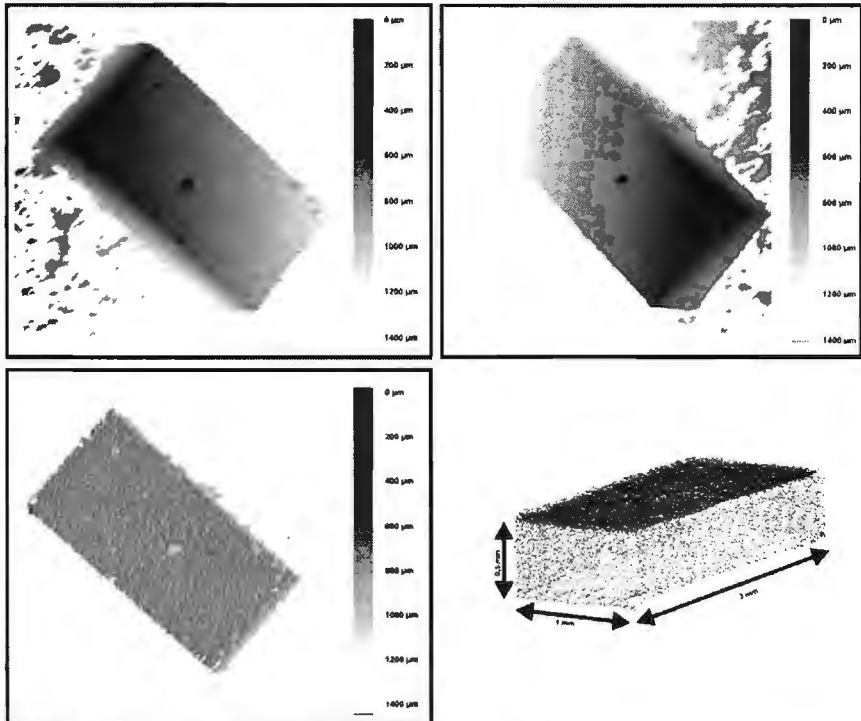
At the start of the multiple-view-acquisition the object has been rotated and tilted for the image acquisition. In order to have one common coordinate system for all obtained image stacks the three-dimensional surface topographies have to be reverse rotated and tilted to their origin location. The angles of twist concerning the image stack acquisition are used for the reverse rotation. The reverse rotation is realised by algorithms based on the Euler rotary matrix.

### Assembly

The last step within the multiple-view-acquisition is the assembly of the specific surface topographies to one complete three-dimensional topography of the investigated object. This is realised manually by stitching each topography manually to the other. Due to the overlap between the different image stacks, the right position of the topographies to each other can be evaluated by common characteristics. Also an advantage in accuracy is achieved because certain measurement points are obtained several times by the different recordings. This overdetermined data is used for an averaging.

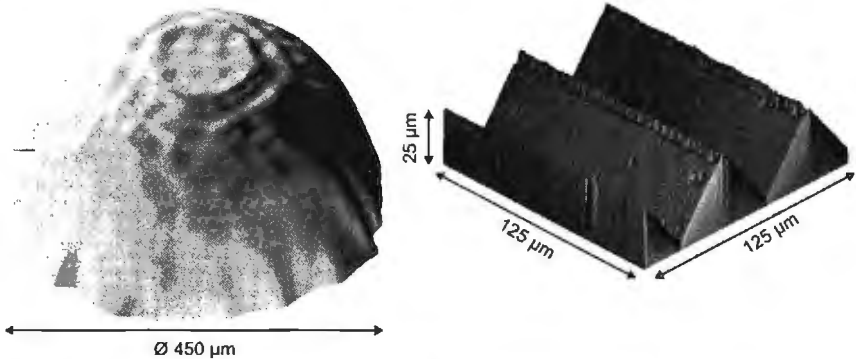
### Examples

Figure 2 shows an example of the multiple-view-acquisition. The topography of a silicon cuboid is obtained by two directions.



**figure 2:** Multiple-view-acquisition using the example of a cuboid – topographies of the cuboid from two different views (top left, top right) – assembled topography (bottom left, bottom right)

Also other geometries and materials can be obtained by the Multiple-view-acquisition (see figure 3).



**figure 3:** One half of a zircon ball (left) – milled steps of a brass probe (right)

### Conclusion and Outlook

A new tool for the visualisation of complex three-dimensional microscopic parts and structures was presented. The method, called multiple-view-acquisition, is based on confocal microscopy and was implemented in a confocal Laser-Scanning-Microscope. The multiple-view-acquisition uses image stacks from different directions of view and put these data sets to one complete 3D-topography of the investigated probe.

So far the multiple-view-acquisition runs mainly manually. The future work will be engaged in the automatic elimination of the basic plane and the automatic assembly process of the different topographies. This will be realised both by image processing algorithm and correlation methods.

### Acknowledgement

The authors gratefully acknowledge the financial support of the Deutsche Forschungsgemeinschaft (DFG) within the Collaborative Research Centre (SFB) 440 „Assembly of hybrid Microsystems“.

### References

- [1] Pfeifer, T.; Bitte, F.; Dussler, G.: Optical Metrology for Microsystem Inspection. In: Proceedings of the international seminar on precision engineering and micro technology. July 19<sup>th</sup> – 20<sup>th</sup> 2000, Aachen
- [2] Wilson, T.: Confocal Microscopy. Academic Press Inc., London, 1996
- [3] Sheppard, C.J.R.; Shotton, D.M.: Confocal Laser Scanning Microscopy. Information Press, Eynsham, 1997

# Determination of the AFM tip-shape with well-known sharp-edged calibration structures: actual state and measuring results

U. Hübner, W. Morgenroth, H.G. Meyer<sup>1</sup>, Th. Sulzbach<sup>2</sup>, B. Brendel<sup>3</sup>, W. Mirandé<sup>4</sup>

<sup>1</sup> Institute for Physical High Technology Jena, PO. Box 100239, D-07702 Jena, Germany, Tel.: (+49) 3641 206126, e-mail: huebner@ipht-jena.de

<sup>2</sup> Nanoworld Services GmbH, Im Amtmann 3, D-35578 Wetzlar, Germany,

<sup>3</sup> Leica Microsystems Lithography GmbH, Göschwitzer Straße 25, D-07745 Jena, Germany,

<sup>4</sup> Physikalisch-Technische Bundesanstalt Braunschweig, Bundesallee 100, PF3345, D-38023 Braunschweig, Germany

## Abstract

In this paper the method of an in-situ determination of the tip shape based on novel tip characterization standards with well-examined and extremely sharp-edged calibration structures is presented. Each calibration chip also contains a selected structure serving as a calibrated width-standard. Also the pitch will be certified. The obtained measurement results demonstrate the potential of the described method.

## Introduction

Typically, AFMs and AFM-profilers are used for the measurement of surfaces and surface details. A good agreement between the measuring results and the real shape of the surface details will be obtained if the surface details have small heights, low aspect ratios and smaller sidewall angles than the AFM-tip. In such cases the shape and the radius of the AFM-tip have only a small influence on the measuring results. However, another situation occurs when an AFM or an AFM-profiler is used to determine the shape of fabricated micro- and nanostructures accurately [1]. Often such microstructures have high sidewall angles and high aspect ratios. In this case the measuring results are strongly dependent upon the AFM tip geometry. The obtained AFM plots show a convolution between the tip geometry and the structure's real shape (figure 1, [2]).

## Principle and realisation

The method is based on the AFM-measurement of a well-known line-space structure and the calculation of the tip shape from the measurement result (figure 1). The sidewalls of the calibration structures are, obviously, steeper than the half-cone angle of the tip. Therefore, the measured sidewalls reflect the shape of the tip. If, in addition to that,

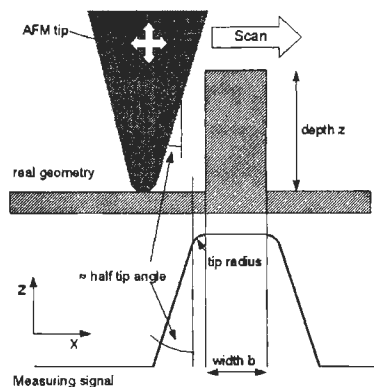


**Figure 1:** Principle of detection of the AFM-tip shape and tip radius

the edge radius of the calibration structures can be neglected, compared to the tip radius, then the measured radii also represent the tip radius. In contrast to other arrangements [3] each calibration chip contains a selected structure as a calibrated width-standard structure. By means of these standards the shape and the radius of the tip can be quickly quantified before and after the AFM measuring process.

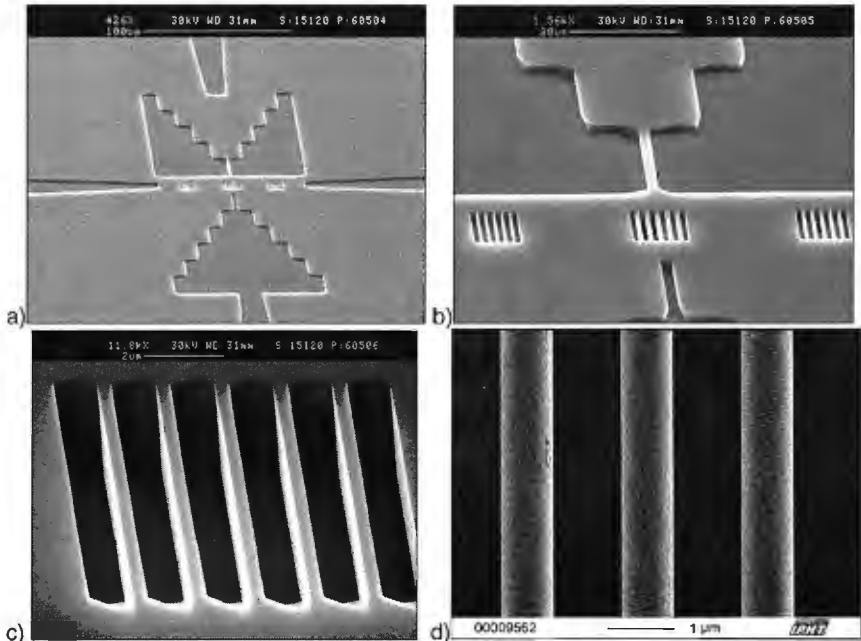


**Figure 2:** SEM-pictures showing the centre of the calibration chip with a) the inner finding structure, b) groups of 300 nm, 800 nm and 500 nm calibration structures (from left to right respectively); length: 10  $\mu\text{m}$ , depth: 1.25  $\mu\text{m}$ , and c+d) details of the final calibration structure.

The calibration standards are etched in [110] silicon wafers by using anisotropic wet etching. The wet-etch technique results in high-grade, highly-parallel line-space structures with little edge roughness and with 90° sidewall angles, established by the intrinsic crystal planes (figure. 2c). More details about this fabrication were published in [4][5].

Each calibration chip has a size of 8 x 8mm<sup>2</sup>. In the centre of the calibration chip, where the two-stage finding structure ends (figure 2a), three groups of line-space structures with different nominal widths (300 nm, 800 nm and 500 nm) are arranged (figure 2b). Each centre structure of these line-space patterns are quantified in width to an accuracy of 10 nm. The space between the lines is 1  $\mu\text{m}$ . The structures are highly parallel and sharp-edged, with edge radii of < 10nm. The edge roughness is very small (figure 2d), in the range of  $\pm 4$  nm ( $3\sigma$ ). The typical calibration pattern is 20 $\mu\text{m}$  long, 800 nm wide and 1.25  $\mu\text{m}$  deep. Additionally, there are flat versions with a depth smaller 1  $\mu\text{m}$ , and also versions with a depth of 6  $\mu\text{m}$  for AFM-profilers using high-aspect-ratio tips.

## Evaluation tests

### Determination of tip-shape

To test the calibration pattern in-situ measurements with different AFM-tips were made. Firstly, averaged line-scans were made. The obtained curve of one structure were split at the maximums and the outer parts of the curve were then linked together. The measured shapes of different commercial AFM-tips (silicon nitride tips, silicon tips and high aspect ratio tips) were in good agreement with SEM examination of the same tips (figure 3).

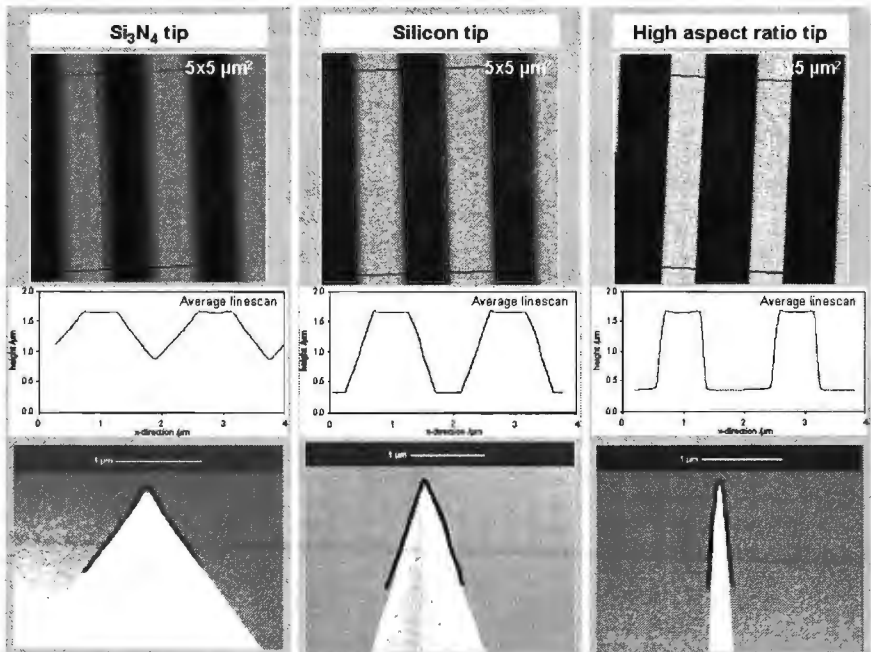


**Figure 3:** AFM-measurements of the calibration structures with three different tip shapes. The extracted tip shapes are layed upon the SEM-images of the tips.

### Determination of tip-radii

The determination of tip radii has been examined by using tips with different radii ranging from 10 to 100 nm. In figure 4 is shown the determination of the tip-radius. The obtained averaged line-scan curve was also split at the maximums and the parts of the curve were then linked together. After this, a circle was fitted to the linked curve, the radius of which gives the tip radius. Using this method, a minimum tip radius of 30 nm is measurable. The averaging of line-scans is not suitable for the determination of smaller tip radii. In this case, the evaluation of single line-scans is more successful.



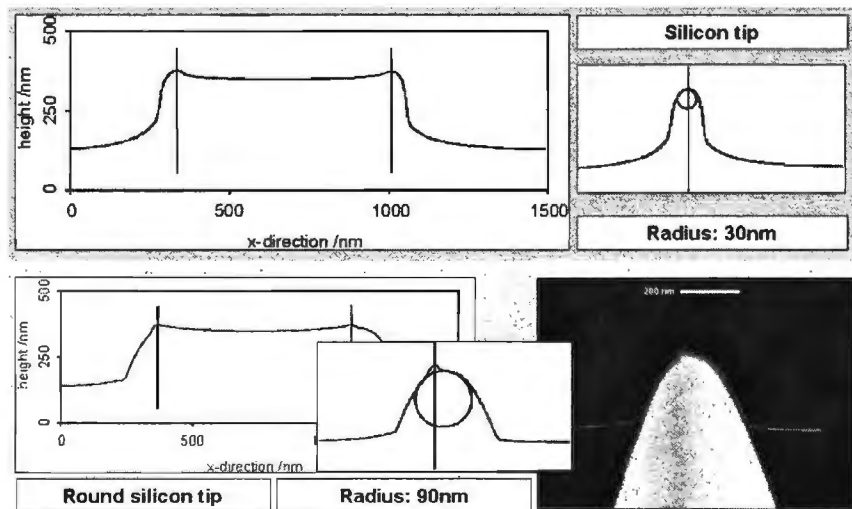


**Figure 4:** Determination of the shape and the radius of an AFM-tip by means of an AFM-measurement (tapping-mode, scan-area:  $2 \times 2 \mu\text{m}^2$ ). The in-situ measurement, clearly, shows details (here: defects) of the tip.

## Summary

Highly sharp-edged silicon structures were realised for use as an in-situ tip characterizer. The measurement results have shown that the shape can be obtained in-situ with an accuracy of 10 nm. Our measurements indicate also that tip radii down to 20 nm can be measured in-situ.

## References

- [1] K. Wilder, C. F. Quate, B. Singh, R. Alvis, and W. H. Arnold, Atomic force microscopy for cross section inspection and metrology, in: *J. Vac. Sci. Technol. B* 14(6), pp. 4004-4008, Nov./Dec 1996.
- [2] G. Torzo, D. Cerolini, SFM Image Reconstruction Reducing Tip Artifacts, in: *European Microscopy and Analysis*, pp. 15, May 2000.
- [3] K. F. Jarausch, T. J. Stark, and P. E. Russel, Silicon structures for in situ characterization of atomic force microscope probe geometry, in: *J. Vac. Sci. Technol. B* 14(6), pp. 3425-2430, Nov./Dec 1996.
- [4] U. Hübner, W. Morgenroth, S. Bornmann, H.G. Meyer, Th. Sulzbach, B. Brendel, W. Mirandé, Calibration standard for in-situ-determination of AFM tip-shapes, *EUSPEN 2001, Proceedings S. 530-533*, Mai 2001, Turin, Italy.
- [5] U. Hübner, W. Morgenroth, S. Bornmann, H.G. Meyer, Th. Sulzbach, B. Brendel, W. Mirandé, Fabrication of calibration standards for the in-situ-determination of AFM tip-shapes, *NanoScale* 2001, 15.-16.11. 2001, Bergisch-Gladbach, Germany (will published in the PTB-Proceedings).

## Task Specific Uncertainty Estimation for Roundness Measurement

M. Morel<sup>1</sup>, H Haitjema<sup>1</sup>

<sup>1</sup> Eindhoven University of Technology, section Precision Engineering, the Netherlands.

### Abstract

As it is necessary to supply uncertainty with measurement [1], fast, task-specific estimation of uncertainty is needed. A concept, already successfully implemented in roughness measurement [4,5], is now adapted to be used for roundness measurements. The concept is implemented in software. As a result, uncertainty budgets for four different specimens, three ring gauges and a spherical standard, are given as examples of the presented concept. The results of these measurements show that noise and spindle errors are specimen dependent.

### Calculation of uncertainty

#### Hybrid method

A classical on-line uncertainty budget is set up, but elements of this budget, such as spindle errors and noise effects, are estimated using Monte-Carlo techniques [3]. The uncertainty budget is given for a single measurement; for calibration of a roundness standard, averaging reversal techniques are used for which the uncertainty is much smaller. The method means that for each influencing factor virtual measurements are calculated with respect to the standard deviation of the influencing factor, related to its nominal value. For each influencing factor, the difference in parameters between the original and the virtual measurements gives the standard uncertainty per parameter per influence. If a recalculated measurement with 'zero' influence is used to calculate the standard uncertainty, the calculated virtual profile with nominal value for that influence is used as the nominal parameter. This way, algorithm errors are kept to a minimum. If both sides cannot be calculated, e.g. the profile recalculated with smaller radius has no additional information, only one side is used to calculate the uncertainty.

#### Total uncertainty

As stated by the GUM [2], the total standard uncertainty  $u_m$  of measurement result  $M$  can be calculated as the squared sum of the independent individual uncertainties multiplied by their sensitivity. This can be rewritten, as shown in formula 1, to express the calculation of the standard uncertainty for a selected influence  $m_i$  by variation of that influence and keeping other influences nominal.

$$u_M^2 = \sum_i \left( \frac{\partial M}{\partial m_i} \right)_{M_n}^2 \cdot u_{m_i}^2 = \sum_i (M(m_1, \dots, m_i + u_{m_i}, \dots, m_n) - M(m_i))^2 \quad [1]$$

The method is a different approach to uncertainty calculation as a full Monte-Carlo calculation [3]. Here, a complete overview of influences and their uncertainty is given. The on-line calculation is carried out fully automatically and takes no extra time or effort.

## Implementation

Software has been written to calculate the on-line uncertainty budget after processing a measurement. The following influences have been incorporated:

### Calibration and linearity deviations of the probe

Linearity can be calibrated with a step standard, with the roundness tester on horizontal straightness mode, or a flick standard can be used. The linearity directly influences the roundness profile. The effect is simply estimated by multiplying the profile with a factor, e.g. 1.01 for a 1% uncertainty, and recalculate the parameters.

### Radius probe

The radius can be measured with a measuring microscope, with a razorblade or micrometer. If the sample contains large peaks or valleys, which significantly affect the amplitude parameters, the influence of the radius is noticeable. The influence is taken as the calculated difference to a 1 mm probe radius, or any other radius the user specifies

### Contact angle probe

The relative angle between the probe and sample is almost zero at calibration. If a complex form is measured, the angle can vary from 1° up to 15°. This causes a second order non-linear effect on the measured roundness profile.

### Low pass filter

Apart from the software implementation, dynamic probe characteristics may cause the real filter characteristics to deviate from the Gaussian filter. The filter characteristics can be obtained by filtering a known multi-wave specimen [6], or by dynamic probe calibration [7].

### High Pass Filter

Although only used in very special cases, the implementation of the high pass filter is realized to complete the budget. The characteristics can be obtained in the same manner as the low pass filter. If used, the influence is specimen dependent.

### Measurement force

Calibrated with a balance, the force can vary between 30 mN to 90 mN. The effect is estimated by correcting the profile to zero measurement force using the Hertzian deformation theory. The contribution to the total uncertainty is in the order of nanometres.

### Spindle errors

The repeatable spindle error diagram is obtained with the reversal technique or multistep method of a roundness standard where the average of many measurements is taken. Once calculated, its effect on the uncertainty is estimated by adding or subtracting the spindle error to the profile, where the spindle profile is rotated in 10° steps, and calculating the standard deviation of the calculated parameter relative to the nominal.

### Noise errors

As the spindle deviations are known from the reversal technique or multistep method, a typical noise profile is estimated by subtracting the average of many measurements from a single measurement of the same used specimen. The influence on the uncertainty budget is estimated in the same Monte-Carlo like way as the spindle error.

## Results

Measurements have been performed on a Mitutoyo Ra 2000 Roundness tester.

Three ring gauges with different diameters are measured with a magnification of 50 000. The Mitutoyo standard is measured with a magnification of 100 000. The rotational speed is 2 revolutions per minute. All measurements are processed using L.S. reference circle and filtered at 150 UPR with the Gaussian filter. The spindle (figure 1) and noise (figure 2) diagram were obtained with reversal technique of a Mitutoyo standard. In the spindle diagram, the step of 10 nm at 0° is due to drift in the probe. In the noise diagram, the non-reproducible periodic deviation of 7 Hz is due to building vibrations. The known systematic spindle error should be corrected as advised by GUM [2], but is taken into account to illustrate the possibility to separate the error contributors.

The results are shown in table 1.

			Mitutoyo Standard	Tesa Ring Gauge	Tesa Ring Gauge	Ring Gauge
Diameter			50 mm	110 mm	50 mm	17 mm
	Nominal	Unc.	Uncertainty RONt = 39 nm	Uncertainty RONt = 393 nm	Uncertainty RONt = 109 nm	Uncertainty RONt= 253 nm
Linearity	1	1%	0	4 nm	1 nm	3 nm
Radius	0.85 mm	10%	0	0	0	7 nm
Angle	0 °	1°	0	0	0	0 nm
LP	150 UPR	1%	0	0	0	2 nm
Pitch	0.05 °	100%	0	0	0	0
Force	10 mN	10%	2 nm	0	1 nm	3 nm
Spindle	1	100%	9 nm	9 nm	9 nm	6 nm
Noise	1	100%	18 nm	9 nm	8 nm	10 nm
Total	(1s)		20 nm	13 nm	12 nm	14 nm

**table 1:** Example of uncertainty budget for RONt of four specimens.

The results for these samples can be expressed in two standard deviations:

Mitutoyo Standard,	RONt = 39 ± 40 nm
Tesa Ring Gauge 110 mm,	RONt = 393 ± 26 nm
Tesa Ring Gauge 50 mm,	RONt = 109 ± 24 nm
Ring Gauge 17 mm,	RONt = 253 ± 28 nm

The results show that the spindle and noise contributions can be quite different for different specimens. For small roundness deviations the spindle and noise influences are dominant, for larger deviations the probe calibration contributes relatively more to the uncertainty.

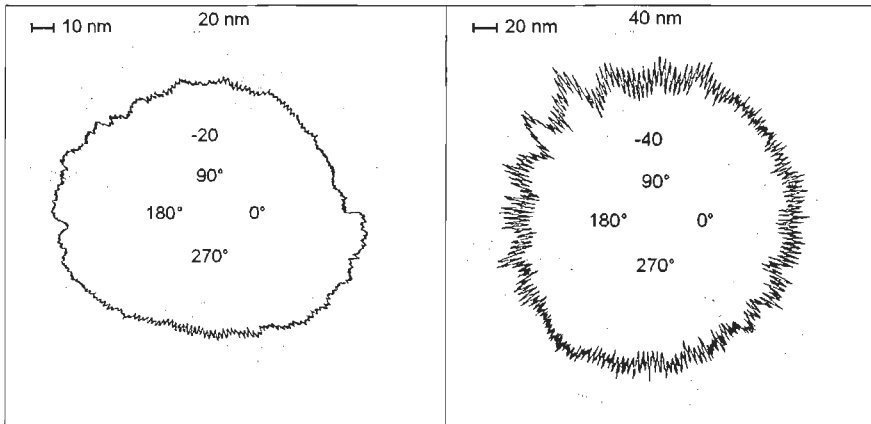


**figure 1:** Spindle of roundness tester.

**figure 2:** Typical noise of roundness tester.

## Conclusion

A new approach to calculate the roundness measurement uncertainty is presented. With this method it is not only possible to calculate a task specific uncertainty budget (specific specimen and specific roundness tester), but the method can also be used to improve measurement results as the budget enables quantification of the major contributor to the measurement uncertainty.

## Acknowledgement

This research is supported by Mitutoyo Nederland B.V.

## References

- [1] ISO 14253-1:1998: 'Decision Rules for proving conformance or non-conformance with specifications', ISO, Geneva, 1998.
- [2] Guide to the Expression of Uncertainty in Measurement (GUM), ISO, Geneva, 1995.
- [3] H. Schwenke et al: 'Assessment of Uncertainties in Dimensional Metrology by Monte Carlo Simulation: Proposal of a Modular and Visual Software', Annals of the CIRP, pp 396-398, 49/1/2000.
- [4] H. Haitjema, M. Morel: 'The concept of a virtual roughness tester'. Proc. X. International Colloquium on Surfaces, Shaker Verlag, Aachen, pp 239-244, 2000.
- [5] H. Haitjema, M. Morel: 'Calculation of 2-D roughness measurement uncertainty with virtual surfaces', Proc. IMEKO Symposium on metrology for quality control, with the special topic 'Surface Metrology for quality assurance', NIS Egypt, pp 1-5, 2001.
- [6] O. Jusko, F. Lüdicke, Novel multi-wave standards for the calibration of form measuring instruments. Proc. 1st EUSPEN, Bremen, Vol. 2, p. 299-302, 1999.
- [7] H. Haitjema, G.J. Kotte: 'Dynamic probe calibration up to 10 kHz using laser interferometry', Measurement vol. 21, No 3, pp 107-111, Elsevier Science Ltd. 1997.

## Comparing measurements of 1D-grating samples using optical diffraction technique, CD-SEM and nanometrological AFM

I. Misumi<sup>1,5</sup>, S. Gonda<sup>1</sup>, T. Kurosowa<sup>1</sup>, Y. Tanimura<sup>1</sup>, N. Ochiai<sup>2</sup>, J. Kitta<sup>2</sup>, F. Kubota<sup>2</sup>, M. Yamada<sup>3</sup>, Y. Fujiwara<sup>3</sup>, Y. Nakayama<sup>4</sup>, K. Takamasu<sup>5</sup>

<sup>1</sup> National Metrology Institute of Japan, National Institute of Advanced Industrial Science and Technology (NMIJ/AIST), Japan; <sup>2</sup> Japan Quality Assurance Organization (JQA), Japan; <sup>3</sup> Hitachi Science Systems, Ltd., Japan; <sup>4</sup> Hitachi Central Laboratory, Hitachi Ltd., Japan; <sup>5</sup> Department of Precision Engineering, The University of Tokyo, Japan

### Abstract:

A round-robin measurement was performed by three institutes for the pitch of 1D-gratings with a nominal value of 240 nm. Three different methods for the measurements, an optical diffractometer (OD), a critical dimension scanning microscope (CD-SEM) and a nanometrological atomic force microscope (nanometrological AFM) were used. Measurements uncertainty for each method was estimated and ranged from 0.14 nm to 1.0 nm for expanded uncertainty ( $k=2$ ). Average values obtained for these methods matched closely with differences less than the expanded uncertainty.

### Introduction

ITRS 2001 estimates that the next technology node will be achieved more than two years earlier than that estimated in 1999. As technology node in semiconductor industry has shrunk, importance of dimensional measurements in nanometer order (nanometrology) is now obvious. In addition, equivalency in certificated dimensions between countries has become a key in international trades or joint R&Ds. Since some products with nanometer-scale precision should be certificated on the basis of traceability to a national standard, a national traceability system in nanometer-scale standards is required.

Japan Quality Assurance Organization (JQA), Hitachi Science Systems, Ltd.(HSS) and NMIJ/AIST performed round-robin measurements of 240 nm-pitch 1D-gratings. Not only an optical diffraction technique (OD) and a nanometrological atomic force microscope (nanometrological AFM) but also a critical dimension scanning electron microscope (CD-SEM) was used for the comparison. We have two aims of round-robin. One is to improve the technological ability in precision measurements for nano-scale standard samples. The other is to prepare for the establishment of a traceability system in Japan. We report the results of this round-robin measurements performed with OD, CD-SEM and nanometrological AFM.

### Measurement methods

#### Samples

The 1D-gratings (HJ-1000, Hitachi co. Ltd) were made of silicon wafer with a size of 4 mm×4 mm×t 0.3 mm<sup>[1]</sup>. The line and space with a nominal pitch of 240 nm was fabricated on Si (110) by optical interference lithography and an anisotropic etching. The gratings were mounted on aluminum disks, with a diameter and a thickness were

12 mm and 1.5 mm respectively, for the easy mounting in AFM. When OD or CD-SEM was used, the grating on the disk was mounted on a solid cylinder with a diameter and a height of 15 mm and 10 mm, respectively. Locations to be measured were defined as center spots of each nine regions of 1 mm  $\times$  1 mm in the center square of 3 mm  $\times$  3 mm of three samples (T002, T005 and T006).

### Measurement instruments

An optical diffraction (OD), a CD-SEM and a nanometrological AFM were used for the round-robin by JQA, HSS, and NMIJ/AIST, respectively.

The OD system consists of a He-Cd laser ( $\lambda = 325$  nm), a rotary table with an encoder, a laser power monitor and mirrors. Pitch values were obtained from angle difference between the positions of a specular beam alignment and a 1st diffraction beam alignment (both side of rotation).

The magnification scale of the CD-SEM was calibrated using another 1D-grating scale (HJ-1000) certificated by JQA. Single pitch between two adjacent lines of each 1 mm $\times$ 1 mm area was obtained by analyzing a secondary electron profile and averaging over 10 times measurements.

XYZ scale of the nanometrological AFM was calibrated with a built-in three-axis interferometer in real-time<sup>[2][3]</sup>. The wavelengths of frequency-stabilized He-Ne lasers ( $\lambda = 633$  nm) as laser sources of the interferometer were calibrated with an  $I_2$ -stabilized He-Ne laser.

### Results and discussions

**table 1:** pitch values  $p$  [nm], combined standard uncertainty  $u_c(x_i)$  [nm], expanded uncertainty ( $k=2$ )  $U_{95}(x_i)$  [nm] and degree of freedom  $\nu_{eff}$  (T002)

participant (method)	pitch value $p$ [nm]	expanded uncertainty ( $k=2$ ) $U_{95}(x_i)$ [nm]	degree of freedom $\nu_{eff}$
NMIJ/AIST 1st (AFM)	239.97	0.262	12.6
JQA (OD)	239.90	0.140	20.1
HSS (CD-SEM)	240.3	1.0	16.2
NMIJ/AIST 2nd (AFM)	240.03	0.310	53.0

Obtained pitch value  $p$  [nm], combined standard uncertainty  $u_c(x_i)$  [nm], expanded uncertainty ( $k=2$ )  $U_{95}(x_i)$  [nm] and degree of freedom  $\nu_{eff}$  for T002 sample are shown in table 2. These values are estimated based on GUM<sup>[4]</sup>.

**table 2:** The reference value and expanded uncertainty of reference value ( $k=2$ ) (T002).

reference value $x_{ref}$ [nm]	expanded uncertainty ( $k=2$ ) $U_{95}(x_{ref})$ [nm]
240.03	0.310

Pitch values obtained by NMIJ/AIST were defined as the reference values since the scale of the instrument is traceable to the international unit of length through He-Ne laser wavelength. Also, NMIJ/AIST (former NRLM)'s calibration ability of the pitch values was verified at supplementary keycomparison of 1D-gratings (CCL-S1, WGDM-7 DG Nano4)<sup>[5][6]</sup>. NMIJ/AIST measured a set of 3 gratings (T002, T005 and T006) twice at the first (NMIJ/AIST 1st) and at the last (NMIJ/AIST 2nd) of this round-robin. The difference between 2 measurement results has to be tested if it is statistically significant or not. As the results of tests for variance ratio and the difference of population mean value.

It became clear that population variance was equivalent and the difference of population mean value between two measurement results was not statistically significant. This means NMIJ/AIST 1st measurement results and NMIJ/AIST 2nd measurement ones were equivalent. Pitch values and expanded uncertainty obtained by NMIJ/AIST 2nd measurement were defined as the reference values and expanded uncertainty in this round-robin.

En number is one of guidelines of the consistency between obtained pitch values and the reference values. Table 3 shows calculated En numbers for OD (JQA) and CD-SEM (HSS) measurement. According to ISO/IEC GUIDE 43-1, an obtained value has a consistency if En number is less than 1. All En numbers are less than 1. We obtained consistency of all measured results.

**table 3:** En number (T002).

participant	En number
JQA	0.38
HSS	0.26

Major uncertainty components and their standard uncertainty for T002 grating are shown in table 4. Major uncertainty components in each measuring method are mostly derived from the measurement instruments. Further efforts should be paid to reduce these uncertainty components.

**table 4 :** Major uncertainty components and their standard uncertainty (T002)

participant (method)	major uncertainty component	standard uncertainty $u_c(x_i)$ [nm]
JQA (OD)	repeatability of rotary table	0.0470
	vertical angle correction at Bragg condition	0.0240
HSS (CD-SEM)	magnification calibration	0.5
	standard sample for magnificationcalibration	0.3
NMIJ/AIST (nanometrological AFM)	interferometer nonlinearity (cyclic error)	0.115
	uniformity of pitch patterns	0.041



## Conclusions

JQA, Hitachi Science Systems and NMIJ/AIST conducted a round-robin measurement for the 240 nm-pitch of 1D-gratings using different measurement instruments, optical diffraction technique (OD), critical dimension scanning electron microscope (CD-SEM) and nanometrological atomic force microscope (nanometrological AFM). Obtained pitch values with three different methods matched within the expanded uncertainty. En values less than 1 for all results indicates the reasonable estimation of uncertainty. Therefore, the consistency of this round-robin was confirmed. These activities are parts of efforts toward an establishment of a traceability system in Japan.

## References

- [1] Y. Nakayama and K. Toyoda: "New submicron dimension reference for electron-beam metrology system", Proc. SPIE 2196 (1994) 74.
- [2] S. Gonda, T. Doi, T. Kurosawa, and Y. Tanimura, N. Hisata, T. Yamagishi, H. Fujimoto, and H. Yukawa: "Real-time, interferometrically measuring atomic force microscope for direct calibration of standards", Rev. Sci. Instrum., 70, (1999) 3362.
- [3] I. Misumi, S. Gonda and T. Kurosawa: "Precision measurements of 1D grating using metrological atomic force microscope", Proc. of 2nd **euspen** International Conference -Turin, Italy - May 27th - 31st, 2001, p474.
- [4] BIPM, IEC, IFCC, ISO, IUPAC, IUPAP, OIML: "Guide to the expression of uncertainty in measurement"
- [5] BIPM homepage <http://www.bipm.org/>
- [6] F. Meli : "International comparison in the field of nanometrology: Pitch of 1D gratings (Nano4)", Proc. of 2nd **euspen** International Conference - Turin, Italy - May 27th - 31st, 2001, p358.

## Accurate surface profilometry using interferometric microscope with high magnification

T. Doi, T.Kurosawa

National Metrology Institute of Japan (NMIJ)

National Institute of Advanced Industrial Science and Technology (AIST)

Tsukuba, Japan

### Abstract

Optical surface profilometer based on Mirau-type interferometric microscope, whose interference fringe spacing is directly and absolutely calibrated, has been designed and constructed. If the objective with high magnification (50x) is used, it is difficult to calibrate the fringe spacing. Because the coherence envelop of the interferogram becomes steep and a slight change of fringe spacing exists at different focus positions. The method to determine the fringe spacing is improved and the uncertainty of determining the fringe spacing can be halved. Using the improved method, a slight change of fringe spacing for 50x objective can be measured. Three kinds of the step height samples are measured by 20x and 50x objectives in order to investigate the performance of our instrument.

### Introduction

Due to the development of various types of SPMs and ultra integrated circuit devices, the step height calibration for line pattern with narrow width will be required. An interferometric microscope is a powerful tool because it provides a noncontact and nondestructive method and 3D profile in a short time. We developed optical surface profilometer based on Mirau-type interferometric microscope, whose interference fringe spacing is directly and absolutely calibrated [1]. To calibrate step height of line pattern with narrow width, Mirau-type objective with high magnification must be used. If an objective with higher magnification is used, the fringe spacing become greater than the half-wavelength of illumination light of the microscope and the coherence envelop of interferogram used to determine fringe spacing becomes steeper. If the step height is calibrated by objective with high magnification (50x), the method of determining the fringe spacing must be improved because of steep coherence envelop of the interferogram. In addition, a slight change of fringe spacings at different focus positions exists unlike with the measurement by 20x objective. This paper focuses on uncertainty of calibration of fringe spacing (basic scale of z-direction). Because the calibration of the fringe spacing is the most serious uncertainty factor to calibrate step height. The improved method to determine the fringe spacing is described. By using this method, a slight change of the fringe spacing at the different focus positions can be measured. On the basis of the results, the three kinds of the step height samples are measured by 20x and 50x objectives. The measurement results by 20x and 50x objectives are compared.

## Scheme of measurement (in the case of 20x objective)

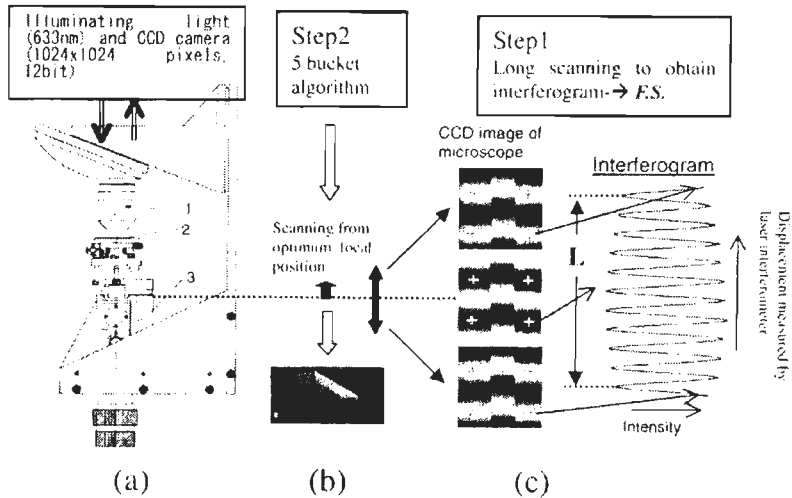


**Figure 1:** Apparatus used to measure fringe spacing and 3D surface profile by phase-shifting technique

As shown in Fig.1, a sample (2 in Fig.1(a)) is measured using the interferometric microscope with a Mirau-type interferometric objective (20x; 1 in Fig.1(a)) [1]. Figure 1(a) shows the design of our instrument and the mechanism. The measurements are carried out through two steps as shown in Figs.1(c) and (b). In step 1 of Fig.1(c), the sample is scanned along the optical axis of the microscope by a PZT device (3 in Fig.1(a)) from -5.25 fringe to +5.25 fringe in the case of 20x Mirau-type objective. The position of the sample at each point is expressed as the number of fringe shifts with respect to the optimum focal position. A negative number indicates *underfocus* (i.e., the distance between the sample and objective is larger than that of the optimum focal position), and a positive number indicates *overfocus*. During the scanning, intensities at four points of CCD images (indicated by + in Fig.1(c)) and the sample positions measured using a laser interferometer are stored. For each measurement point of the CCD image, an interferogram (Intensity vs. Sample displacement) can be plotted as shown in Fig.1(c). From the data shown in Fig.1(c), accurate positions of bottoms in the interferogram are determined.

The fringe spacing ( $F.S.$ ) for each point is calculated by

$$F.S. = (\text{Displacement corresponding to 10 bottoms of the interferogram}) / 10 \\ = L/10. \quad (1)$$

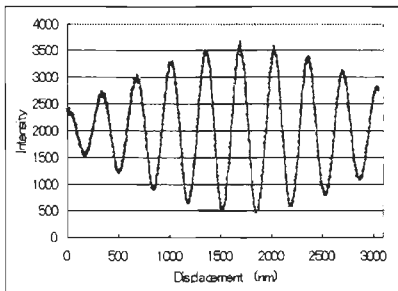
### Improved method to determine fringe spacing

Fig.2 shows the interferogram measured by using 50x Mirau-type objective. In this case, the sample is scanned from -4.125 fringe to +4.125 fringe because of the steep

coherence envelope. In order to determine the fringe spacing in high accuracy, the method and software to determine the fringe spacings (bottom positions) are improved in the following three points.

1. The image capture is carried out by 4x4 binning mode.
2. The data gathering (images and sample positions) is restricted in  $\pm 0.125$  fringe range from bottom points.
3. The second-order fitting is applied to the gathered data for each bottom and the bottom position is determined from the second-order fitted curve.

By the improvement mentioned above, the measurement time is shortened from 240 sec to 23 sec. The standard deviation of fringe space determination is reduced from 0.31% to 0.16%. A slight change of the fringe spacing at different focus positions can be measured by using this method.



**Figure 2:** Interferogram measured by 50x objective

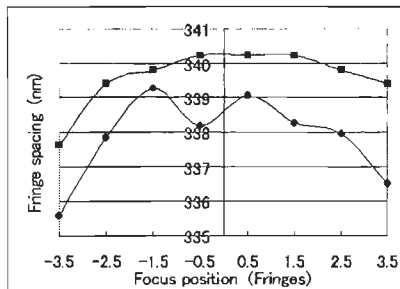


**Figure 3:** Dispersion of fringe spacing

### Dispersion of fringe spacing and determination of fringe spacing

Fig.3 shows measured fringe spacings (denoted by ●) by 50x objective and theoretically calculated fringe spacings (denoted by ■) at different focus positions. Measurement procedures mentioned above are repeated six times and the average of six measurements is shown. Because uncertainty of measuring one fringe spacing at different focus point is around 1.5nm. The dispersion of the fringe spacing is calculated by Eq. (5) in Ref. [2]. In this calculation, 633nm and 0.55 is used as the wavelength of illuminating light and Numerical aperture, respectively. Zero of the horizontal axis means optimum focus position and negative fringe number and positive fringe number mean underfocus and overfocus, respectively. The fringe spacing at  $-0.5$  fringe means the fringe spacing between the optimal focus position and  $-1$  fringe focus position. The discrepancy between measured and calculated fringe spacing at different focus position exists, because the way of illumination to the sample is different. However, the tendency of dispersion of fringe spacing is similar. Assuming that the fringe spacings from  $-2.5$  to  $+2.5$  fringe is uniform, the average of fringe spacings from  $-2.5$  to  $+2.5$  fringe are used for the fringe spacing of 50x objective.

## Comparison of step height measurements by 20x and 50x objectives

The three kinds of standard samples with different step heights (certified values= 45.9, 91.1 and 173.9nm) [3] are measured by 20x and 50x objectives. Each sample has line (step part) and space (base part) patterns whose pitches are from 4 $\mu$ m to 100 $\mu$ m. One of the 60 $\mu$ m pitch patterns, in other words, one line pattern whose width

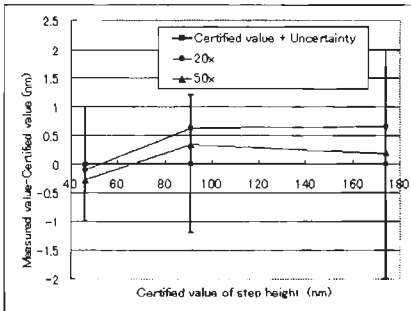


**Figure 4:** Comparison of step height measurements by 20x and 50x objectives

is 30 $\mu$ m can be used for step height measurements. The step height of identical area of the line pattern is measured by 20x and 50x objectives using the mask processing of our instrument. Fig.4 summarizes the results. The discrepancy between the measured step heights by 20x and 50x objectives is from 0.16 to 0.47nm. If the discrepancy is calculated in proportion to the step height, the greatest discrepancy of 0.47nm corresponds to 0.27%. The discrepancy is reasonable because the standard deviation of determining the fringe spacing (basic scale of the measurement) is 0.16%. Therefore,

the step heights measured by 20x and 50x objectives and certified value for each sample are considered to agree well.

## Conclusions

By improving the method of determining the fringe spacing, the uncertainty of determining the fringe spacing for 50x objective can be halved. By this improvement, a slight change of fringe spacing at different focus positions can be measured. Using the improved method, the three kinds of the step height patterns with 30 $\mu$ m width are measured by 20x and 50x objective. The results of comparison are considered to be consistent. The step height of line pattern with narrow width (<30 $\mu$ m) will be calibrated by using the 50x objective.

## References

- [1] T. Doi and T. Kurosawa, "Accurate optical surface profilometer based on Mirau-type interferometric microscope," Proc. of the euspen 2001, Turin, Italy, PP. 462-465 (2001).
- [2] A. Dubois, J. Selb, L. Vabre and A-C Boccara, "Phase measurements with wide-aperture interferometers," Appl. Opt. **39**, 2326-2331 (2000).
- [3] VLSI Standards, Inc. (San Jose, CA)

## Nanometrology standards in the Netherlands: the traceable Scanning Probe Microscope

K.R. Koops<sup>\*</sup>, K. Dirscherl

NMi Van Swinden Laboratorium, Postbus 654, 2600 AR Delft; <sup>\*</sup>rkoops@nmi.nl

### Abstract:

In order to fulfill the industrial needs in the field of nanotechnology for the coming years, the Dutch metrology institute (NMI Van Swinden Laboratorium) has initiated a process to expand their calibration facilities with a number of high performance calibration instruments. One project is aimed at the realization of a traceable Scanning Probe Microscope in the form of an Atomic Force Microscope (AFM) with a desired uncertainty of 1 nm in the entire scanning volume of 100  $\mu\text{m}$  x 100  $\mu\text{m}$  x 10  $\mu\text{m}$ . Main applications for the traceable AFM are calibration of transfer standards. Calibrated transfer standards can serve as calibration artefacts for other Scanning Probe Microscopes and electron microscopes. Additional applications for the AFM are in the field of form and roughness measurements.

### Introduction

Since the introduction of the Scanning Tunnelling Microscope in 1982 [1], an entire class of scanning probe instrumentation has evolved. These instruments have become very versatile tools to study surfaces and interfaces with unprecedented spatial resolution. Although their main use is still mostly limited to imaging, the demand to obtain more quantitative information from the images has increased in recent years. Especially in the field of nanotechnology accurate determination of critical dimensions has gained importance. Although the resolution of Scanning Probe Microscopes is usually more than sufficient for industrial applications, the accuracy can be poor. A European comparison on nanoscale calibration standards performed by the partners of the former European network "The calibration of SPMs" [2] has shown that considerable deviations from the true values can be generated by these instruments if they are not (properly) calibrated [3]. Since SPMs are more and more used in industry the need for accurate measurement results and therefore traceability increases.

### SPM basics

A Scanning Probe Microscope basically consists of a spatially localized probe that interacts with the surface under study and a translation mechanism to control the position of the probe. The translation mechanism is also used to scan the probe across the surface in order to study an area larger than the interaction area. By convention the scanning plane is usually referred to as the X-Y plane and the perpendicular (height) direction is the Z co-ordinate. The translation of the probe or, equivalently, the sample is mostly realized using piezo electric actuators. The position can therefore be conveniently controlled by a voltage signal. However, piezos suffer from non-linear and hysteretic behaviour that can result in large position errors when only the actuating voltage is used to indicate the position. In order to reduce piezo induced image distortions the positioning can be linearized either by calibrating the piezo or by using a position sensor to measure the actual displacement. A calibration involves the determination of the linear and possibly higher order coefficients that couple the actuation signal, usually a voltage, to the actual translation of the scanning mechanism. Additionally the orthogonality between

the individual axis has to be determined.

In terms of cost and effort the approach to calibrate the piezos is the most effective one but requires frequent recalibration because of the nature of these materials. Using calibrated position sensors is a more elaborate and costly approach but results in the most stable and reliable operating mode with the lowest measurement uncertainty.

### SPM calibration

A possible implementation of a calibration procedure is using calibrated transfer standards with specific features to calibrate specific characteristics of the instrument. In order to calibrate the Z-axis several step height standards can be used. The X and Y-axis can be calibrated using 1D or 2D gratings. The 2D grating offers the additional advantage for calibrating the orthogonality between the X and Y-axis.

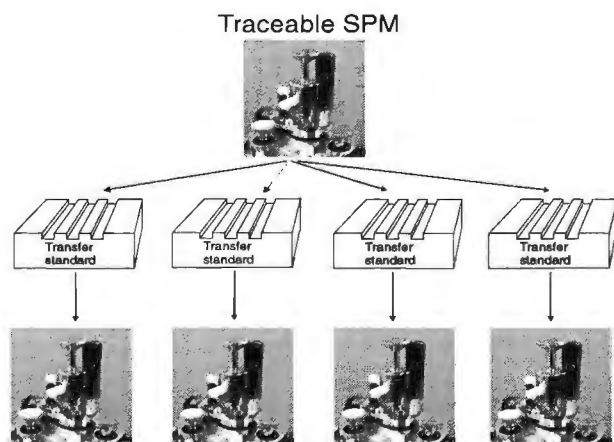


figure 1: The use of transfer standards.

A scanning probe microscope usually combines very high, up to atomic, resolution with a relatively small scanning volume of typically  $100\ \mu\text{m} \times 100\ \mu\text{m} \times 10\ \mu\text{m}$  respectively in the X, Y and Z direction. A useful calibration artefact therefore needs to have comparable dimensions with a feature size in the nanometer range. Although there are some alternative techniques to calibrate nanoscale transfer standards most calibration artefacts can only be calibrated by a Scanning Probe Microscope themselves. Ultimately we therefore require a Scanning Probe Microscope that can be calibrated by an independent method with a small associated measurement uncertainty. The independent method may either be the use of electrical sensors such as resistive, capacitive or inductive displacement sensors or optical sensors e.g. lasers and interferometric techniques. In turn, the calibration of these sensors implies traceability to the national and international standard of length.

### The traceable Scanning Probe Microscope

As the national standards laboratory of the Netherlands, NMI offers calibration services at the highest level of accuracy to third parties. In order to attain this level

we make use of instrumentation that provides the lowest possible measurement uncertainty. In practice this means that the traceability chain between the national standard of length and the calibration instrument is kept as short as possible since each additional step in the chain increases the measurement uncertainty. In order to realize a traceable AFM we have therefore chosen to use a laser interferometer as a position sensor since it offers traceability by direct comparison to the national standard.

The entire set-up, as it is currently being realized, is shown schematically in fig 2. An

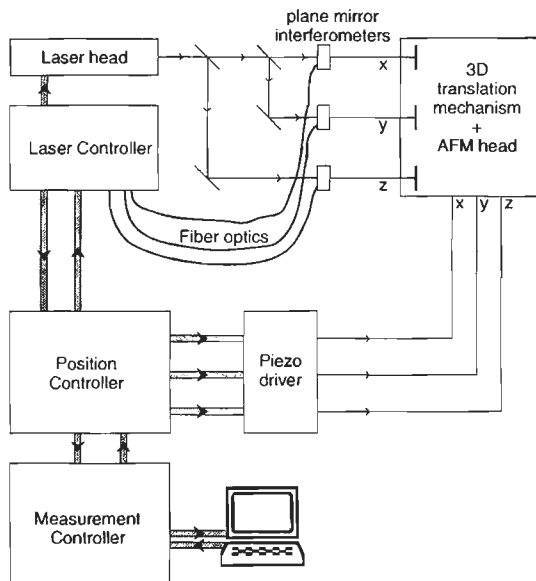


**figure 2:** Schematic overview of the traceable AFM set-up.

existing AFM head, the Topometrix Explorer, is used to obtain SPM functionality. Since this AFM head does not allow direct access to accurately measure the actual probe position and probe translations the head will be placed on an external 3D translation mechanism. The scanning mechanism of the AFM head will remain fixed while the external mechanism will be used for scanning and positioning of the sample with respect to the probe. Although the 3D translation stage offers the possibility to use capacitive feedback in order to linearize the piezos we will only use the interferometers for position control.

Since the AFM head is not optimized for metrological use, the thermal and mechanical behaviour may turn out to be insufficient for nanometer accuracy. Since only the probe and interaction detection mechanism of the AFM head is used, further optimization is possible if the existing head is replaced by an appropriate optimized design. In order to be prepared for future expansion of the scanning range the acquired laser measuring system is able to measure up to several centimeters while maintaining a measurement uncertainty at the nanometer level.



## References

- [1] Binnig G., Rohrer H., Gerber Ch., Weibel E.: Physica 109 & 110B, 1982.
- [2] [www.dfm.dtu.dk/spm-cal/descript\\_SPM-NET.html](http://www.dfm.dtu.dk/spm-cal/descript_SPM-NET.html)
- [3] Breil R. et al: proceedings euSPEN 2<sup>nd</sup> Conference 2001, Vol. 1, pp 510-513

## **Developments in homodyne interferometry and real time quadrature compensation provide precision feedback capability.**

S. Jones

Renishaw plc, Laser and calibration products division, Wotton-Under-Edge, England.

### **Abstract**

Manufacturing industries are continually striving to improve motion system performance. System builders are therefore constantly seeking to eliminate a variety of error sources, enabling them to offer cost-effective systems.

Depending upon the architecture of the motion system and its application, there are many error sources that need to be considered. Amongst the most significant of these are Abbé error and thermal material expansion which effect the position feedback system, the machine structure and the work piece.

This paper discusses a precision motion feedback system consisting of a combination of a multi-axis homodyne laser interferometer and real time quadrature compensation system.

### **Introduction**

As with many areas of technology, position feedback encoders are developing quickly with higher resolutions, velocities and accuracy being key. Motion systems are also becoming more compact; hence the drive to improve performance is accompanied by a need to decrease system footprint, complexity and cost.

Recent developments in homodyne interferometry coupled with real time quadrature compensation provide a solution to many of these requirements for precision applications.

### **Fibre optic launch homodyne laser interferometry**

In conventional laser systems, the size and heat dissipation of the laser head is a major obstacle in reducing the footprint of the motion platform. This is because the laser head contains the laser tube, thermal stabilisation, power supplies and both stabilisation and signal processing electronics.

To overcome this obstacle, a dual axis homodyne interferometer system has been developed. This uses fibre optics to deliver each of the two laser modes directly to interferometers mounted on the axis of measurement.

This system, shown in figure 1, consists of three main elements:

- Laser unit (1)
- 3m fibre optic link (2)
- Detector head (3)

The laser unit (1) contains a class II HeNe laser tube, laser stabilisation system, power supplies, signal processing electronics and a dual axis fibre optic launch. The beam emerging from the laser is split in two and focussed into the 3 $\mu$ m cores of two optical fibres (2). A general overview of the arrangement is shown in figure 2.

Because the operating principal of the interferometers is based upon two light beams combining to produce constructive and destructive interference fringes the light must be coherent. To maintain laser coherence the fibre optic link must consist of single mode optical fibre. This is illustrated in figure 3 where (a) shows the effect on coherence of using multi mode fibre. In this type of fibre the light follows many different length paths hence the coherence is lost. In contrast (b) depicts transmission through a single mode fibre within which coherence is maintained.

At the output of the fibre optic, a beam collimator expands the laser beam to 3mm-diameter. The beam collimator is located into the detector head (3) (internal detail shown in figure 4) which contains all of the interferometer optics (except the target optic which is mounted on the moving element of the axis) and a rotary laser beam steerer to ease alignment.

This dual axis homodyne laser interferometer system can supply industry standard RS422 digital quadrature (figure 5) and 1Vpp sin /cos encoder feedback signals. The system can be used on axis lengths to 4m at 2m/s and provide resolutions to 10nm (<1nm via external interpolation of the analogue sin/cos signals).

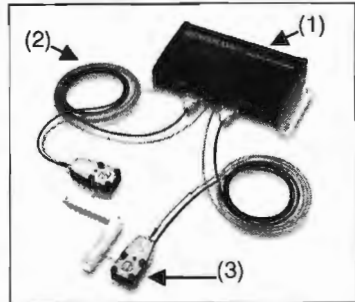


**Figure 1:** Dual axis fibre optic launch laser encoder system.

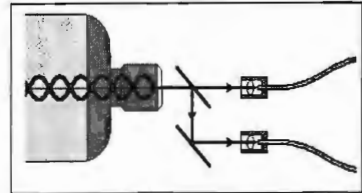


**Figure 2:** Fibre optic launch.

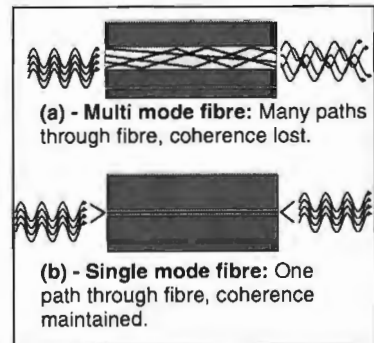


**Figure 3:** Optical fibre properties.

## Requirements for refractive index compensation.

To achieve accurate performance from any laser interferometer operating in air, refractive index compensation is required. This is because the fundamental fringe spacing (unit of count) is a function of the wavelength of the laser light. The wavelength of the laser light varies very slightly depending on the refractive index of the air it travels through, which depends primarily on its temperature, pressure and humidity.

Any of the following changes in the air will increase the laser wavelength by 0.25 ppm (part per million).

~ 0.26 °C increase in air temperature  
(=+0.96 ppm/°C)<sup>1</sup>

~ 0.93 millibar decrease in air pressure (= -  
0.27 ppm/millibar)<sup>1</sup>

~ 29% increase in %RH (= +0.0085  
ppm/%RH)<sup>1</sup>

**Note 1)** These sensitivities are based on changes from a nominal atmospheric environment of 20°C, 1013.25 millibars, 50% RH

One method of achieving refractive index compensation is through a real time implementation of the Edlen equation. This equation calculates the refractive index of air based upon the current environmental conditions.

## Thermal expansion compensation

Thermal expansion is also a significant error source; the dimensions of any material is a function of its coefficient of expansion and the ambient temperature. It is however possible to compensate the effects of thermal expansion within the position feedback loop if knowledge of the expansion origin, part temperature and coefficient of expansion exists.

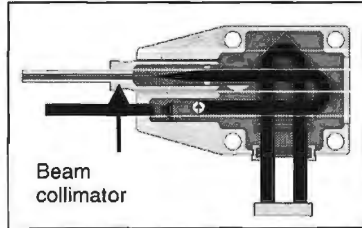


Figure 4: Double pass plane mirror Interferometer detector head.

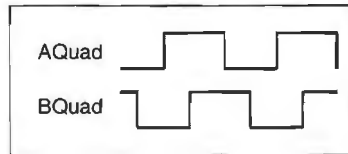
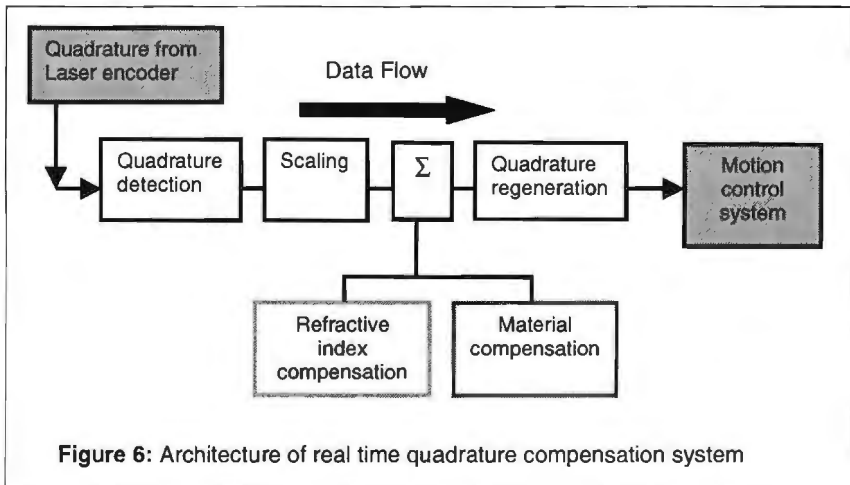


Figure 5: Industry standard digital quadrature (unit of resolution is edge to edge)

### Real time quadrature compensation

The architecture of a real time quadrature compensation system is shown in figure 6. Sensors provide air temperature, pressure and material temperature data to the compensator, which then operates as follows:

- Digital quadrature signals produced by the laser encoder are scaled to a standard resolution (e.g. 79nm signals can be converted to 100nm).
- At the "summing" junction, pulses are added in (or taken out) of the quadrature pulse train, as determined by the calculations of refractive index and material expansion.
- Following the summing operation, differential RS422 quadrature is regenerated and transmitted to the motion control system.



### Conclusion

This real time position feedback system provides a solution to many of today's precision motion problems in that:

- Only a compact, low power detector head needs to be mounted close to the motion hence minimising installed footprint and thermal dissipation.
- Fundamental positioning accuracies of within  $\pm 1$ ppm can be obtained over a wide range of ambient conditions.
- Material expansion effects can be made negligible.

All of the above is performed within the feedback loop adding no additional processing overhead to the motion controller. In fact the complete operation appears transparent to the motion control system which receives feedback signals as with any other encoder system.

Additionally, as the laser system can provide feedback directly from the ultimate work platform, Abbé errors can also be eliminated.

## Roughness measurements according to existing standards with a metrology AFM profiler

F. Meli

Swiss Federal Office of Metrology and Accreditation (METAS)  
Lindenweg 50, 3003 Bern-Wabern, Switzerland

### Abstract:

Conventional surface profilers used for roughness measurements can scratch soft surfaces. By means of an atomic force microscope (AFM) we found scratches on smooth surfaces of gold, aluminium, copper, bronze and steel. To obtain comparable roughness measurements it is important, that, besides the roughness parameters, also the transfer function for the measurement process is normalised. For this purpose roughness standards define the shape of the probe and the transition bandwidth given by two gaussian filters. To apply the filters correctly a minimum scan length of about 160  $\mu\text{m}$  is required. With our metrology AFM profiler it is possible to measure profiles with length of up to 380  $\mu\text{m}$ . The profiles reveal all the fine details of the surface and allow then step by step to study the influence of the profiler tip shape and the filtering process.

### Introduction

Roughness is in many cases related to friction and wear. These surfaces are then made of hard materials and therefore roughness measurements with traditional diamond stylus profilers are adequate. However, roughness can also be interesting in relation with gas absorption, corrosion or optical surface quality. Here the smooth surfaces consist often of soft materials such as pure metals (aluminium, gold, copper, etc.) or polymers and lacquers. For roughness measurements on such surfaces diamond stylus profilers can not be used because they will scratch the surface and the measured value will be meaningless. Optical non-contact methods have a limited lateral resolution and no standardised procedures are available for them. With AFMs the interaction force between the probing tip and the sample is very small and the spatial resolution is high. Unfortunately, typical instruments have measurement ranges which are too short to apply the existing standards for roughness.

In this paper we report on surface damages caused by diamond surface profiling on various metals and introduce roughness measurements made by a long range AFM profiler according to existing standards. The effect of tip shapes and filtering is analysed.

### Experimental setup

The AFM profiler system used consists of a commercial metrology AFM head and a linear sample displacement stage. The AFM head has a parallelogram type scanner with capacitive position sensors. Below this metrology AFM head there is a sample displacement stage with monolithic flexures forming a double parallelogram. This piezo actuated stage provides a highly linear motion over 380  $\mu\text{m}$ . Its displacement is simultaneously measured by a capacitive position sensor and a differential plane mirror interferometer of the Jamin type.

Details about this system and about accurate pitch, step height, CD and particle diameter measurements were published earlier [1-4]. In contrast to classical diamond profiling with probing forces in the mN range the AFM technique works with forces in

the nN range. For all measurements presented here the dynamic force mode was used which minimises the lateral forces on the tip.

### Diamond profiler measurements

A conventional surface profiler for roughness measurements [5] was tested on various polished metal surfaces. A diamond tip with 90° cone angle and 2 µm tip radius was used with a load of (0.5 ± 0.1) mN. Such values are given in EN ISO 3274, a standard about instrument characteristics for roughness measurements.

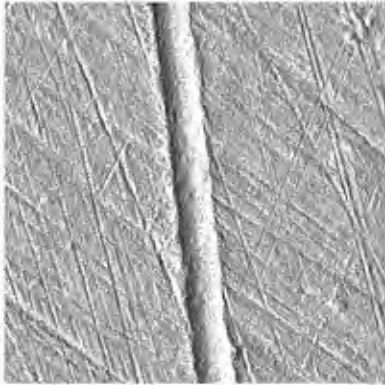


**figure 1:** AFM image of gold surface after profiling.  
Image 10 µm x 10 µm.

Using the AFM we found scratches from profiler measurements on gold, which is of course very soft (Fig. 1). But also on aluminium, copper, bronze and even on steel we found scratches. Only for hardened steel, a gauge block, no scratch was found. The fine features of the surface were destroyed by the diamond tip and a new surface was created at the bottom of the scratch whose roughness was independent of the original surface. Only for surfaces with a roughness much larger than the scratch depth a correlation is found again.

The AFM was used to quantify the scratch depths. Figure 2 shows depths of 5 nm to 60 nm measured on various materials. The harder the material the smaller the depths.

Vliet and Schellekens [7] damages would already be expected at much lower forces. On steel the maximum allowed force on a 2 µm tip would be 2.5 µN and on aluminium only 0.4 µN. In our case the load for steel was 200 times higher. The standard EN ISO 3274 requires even a higher nominal force on the profiler tip of 0.75 mN.

According to Hertz theory as described by

The situation is even worse with respect to dynamic forces that act between tip and surface when the tip is stopped on the surface after the initial approach. The higher the approach speed and the inertia of the stylus, the higher the dynamic forces. With the used approach speed of approximately 0.5 mm/s we found even pits on hardened steel, i.e. a gauge block with a hardness of approx. 64 HRC. These pits had a depth of 50 nm, whereas on steel (St37) the depth was 120 nm.

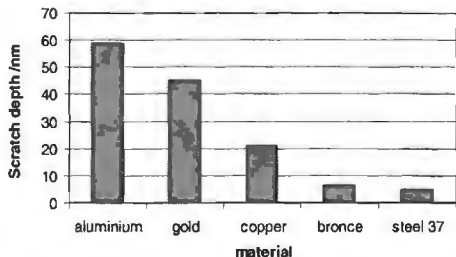


**figure 2:** Scratch depths measured with the AFM on various materials.

### AFM roughness measurements

AFMs use very small probing forces in the nN range. This allows measurements on soft surfaces without any damage.

To obtain comparable roughness measurements it is important, that, besides the definition of the roughness parameter (EN ISO 4287), also the transfer function for the measurement process is normalised. For this purpose the standards define the shape of the probe (EN ISO 3274) and the transition bandwidth (EN ISO 4288) given by two gaussian filters  $\lambda_s$  and  $\lambda_c$  (EN ISO 11562). Unfortunately, conventional AFMs have lateral measurement ranges that are too small to apply the existing standards for roughness. The smallest evaluation length proposed by the EN ISO 4288 standard is 80  $\mu\text{m}$  and therefore a minimum scan length of about 160  $\mu\text{m}$  is required to apply correct filtering. With our metrology AFM profiler it is possible to measure profiles with length of up to 380  $\mu\text{m}$ . The profiles reveal all the fine details of the surface and allow then step by step to study the influence of the profiler tip shape and the filtering process. The profiles were typically acquired over 200  $\mu\text{m}$  with a data spacing of 0.05  $\mu\text{m}$  (4'000 data points).

The roughness value determination out of a raw profile involves several process steps. First, the profile is transformed in a way that corresponds to the effect of probing the surface with a normalised conical tip with a radius of 2  $\mu\text{m}$  and a cone angle of 90° (tip deconvolution), followed by a shape fit which is usually a LS line fit. Second, the profile is low pass filtered to remove the high frequency features by applying a gaussian filter with  $\lambda_s = 2.5 \mu\text{m}$ . This filter should reduce the effect of tip shape variations. Third, the profile is high pass filtered to remove the low frequency features, called waviness, by applying a gaussian filter with  $\lambda_c = 80 \mu\text{m}$ . The gaussian weight function needs data on both sides of a point where it is applied. Therefore a raw profile range is needed which is at least by one  $\lambda_c$  larger than the final evaluation length.

Each step has a considerable influence on the final roughness value (Fig. 3). The influence depends also largely on the surface character. Two different types of surfaces were taken as examples, a smooth and a rough surface. In general the roughness value is reduced by the filtering. The tip deconvolution, however, can have an effect in both directions.

The tip shape, mainly the radius, has a strong effect on the roughness values. After low pass filtering with  $\lambda_s = 2.5 \mu\text{m}$  one would not expect a large influence for radii below 2  $\mu\text{m}$ . This was tested on the two profiles which have different surface characters. The first

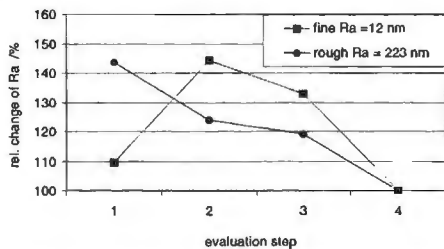


**figure 3:** Effect of profile process steps on the finally calculated Ra value.  
1. Raw data, 2. Tip deconvolution, 3.  $\lambda_s$ -filter and 4.  $\lambda_c$ -filter.

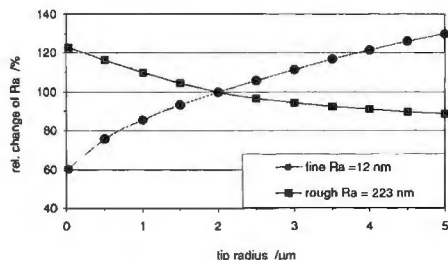


**figure 4:** Effect of tip radius on the final Ra value for two different roughness profiles.



profile was from a ground steel surface with an Ra value of 223 nm. Ra decreased with increasing tip radius, as expected. A variation of the radius from 1  $\mu\text{m}$  to 3  $\mu\text{m}$  resulted in a change from +10% to -5% with respect to the Ra value at the nominal radius of 2  $\mu\text{m}$ . The second profile was from a polished steel surface with an Ra value of 12 nm. Unexpectedly, here, the value increased with increasing tip radius. A variation of the radius from 1  $\mu\text{m}$  to 3  $\mu\text{m}$  resulted in a Ra value change from -15% to +10% with respect to the Ra value at the nominal radius of 2  $\mu\text{m}$  (Fig. 4).

By looking at this profile in detail the reason for this effect can be seen. The surface is mainly flat but there are small sharp bumps on it probably due to polishing grains which got stuck in the soft surface (Fig. 5). These bumps probe rather the tip than vice versa. Therefore the bumps seem to be broader when probed with a larger tip. As the rest of the surface is mainly flat this leads, even after further filtering, to higher Ra values.

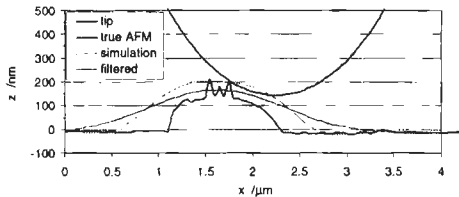


**figure 5:** Detail of the smooth surface. A small sharp bump is probed larger with a larger tip. This leads after further filtering to higher Ra values.

## Conclusion

Conventional surface profilers used for roughness measurements can scratch soft surfaces and lead then to incorrect measurements. The tip load required by the standard EN ISO 3274 is much too high for many technically interesting materials.

With our AFM profiler measurements on soft surfaces can be done without any damage. The profiles with length of up to 380  $\mu\text{m}$  can be processed in accordance with existing standards for roughness. As almost "true" surface profiles are measured by the AFM, the influence of the profiler tip shape can be studied. For reasonable tip variations the influence on the Ra value is in the order of  $\pm 10\%$ . For other roughness parameters like Rp, Rv or Rz this influence can be even larger.

## References

- [1] F. Meli and R. Thalmann, Meas. Sci. Technol., Vol. 9, No. 7, 1998, pp. 1087-1092.
- [2] F. Meli, PTB-Bericht, Vol. F-34, 1998, pp. 61-67.
- [3] F. Meli, PTB-Bericht, Vol. F-39, 2000, pp. 58-65.
- [4] F. Meli, 1st euspen Topical Conference on Fabrication and Metrology in Nanotechnology, Proc. Vol. 2, 2000, pp. 45-51.
- [5] Rank Taylor Hobson, Form Talysurf Series, 120-L.
- [6] W.P. van Vliet and P.H. Schellekens., Annals of CIRP, Vol. 45/1, 1996, pp.483-487.

# Novel Microoptical Fibre Coupled Laser Interferometers for Various Applications in Precision Engineering and Nanotechnology

Jäger, G., Manske, E., Wurzbacher, H., Grünwald, R., Büchner, H.-J., Schott, W., Pöschel, W.

<sup>1-5</sup> Technische Universität Ilmenau; <sup>6-7</sup> SIOS Meßtechnik GmbH; Germany

## Abstract

We have developed a novel highly efficient microinterferometric sensor system with discrete optical components and complete fibre coupling. Improved metrological parameters such as subnanometer resolution, long-term stability, temperature independence and warm-up time makes it suitable for many applications in precision engineering and nanotechnology, e.g. in the positioning control of high-precision linear stages, tactile probes and measuring machines.

## Introduction

Laser interferometers have turned into powerful measuring systems in mechanical engineering and microelectronics technology. Here, the large geometrical dimensions of these devices play a minor role. For applications in precision engineering and nanotechnologies more and more high-precision length measuring systems with smallest dimensions and mass are required. Therefore, a laser microinterferometer was designed for precision displacement measurement with a measuring range of 5 m, a resolution of 0.1 nm and the dimensions of 28 x 25 x 15.5 mm. The increased resolution is an important step for ultraprecision technologies. But also the short warm-up time, no disturbances due to electromagnetic fields and long-term stability are considerable advantages.

Due to its modular structure, the system can easily be adapted to different measuring tasks. In addition, by means of suitable primary transducers the quantities force, mass, acceleration and pressure can be measured with high precision and dynamics.

## Interferometer concept

For precision measurements fulfilling the highest accuracy requirements, laser interferometers which are equipped with classical optical components and HeNe laser with its high frequency stability are used. Nevertheless, the large laser head constitutes a big heat source, exerting a harmful thermal influence on the measuring device as well as on the target. So far, the laser diode has not been a real alternative. The stability of the wavelength of the radiation emitted is considerably lower despite sophisticated thermal and electronic stabilization. The absolute value of the wavelength of a laser diode changes as a result of irreversible processes taking place inside the laser diode.

Therefore, to achieve interferometric accuracy a stabilization on external reference standards like ultrastable cavities or gas cells is necessary. There are a number of known stabilization measures of laser diodes to atomic absorption lines (e.g. ruby, iodine) [1]. However, the result is a laser source with a large volume and higher costs than HeNe laser.

Our concept to counteract the disadvantage of a big laser source is a fibre-optical link between sensor head and the laser provided by a single-mode optical fibre. This

arrangement permits the laser to be positioned at a certain distance, and furthermore, the end of the optical fibre in the interferometer constitutes an extremely small light source which does not exert any thermal influence at all on the sensor and the measuring environment (cold light source).

By applying this optical fiber coupling, any kind of laser light source (HeNe lasers as well as stabilised laser diodes) can be connected to the sensor rather regardless of the emitted wavelength. Here, it is not necessary to modify the sensor layout.

Integrated optical interferometers with smallest dimensions based on silicon or glass technology [2,3] have been developed. In both cases, the light source is a laser diode which is either located in the sensor head or which is fibre-coupled. Both interferometers do not allow the more stable HeNe laser to be employed. The optical design is fixed. Any technical modifications to other wavelength or different measuring tasks require a complete new optical layout and are very expensive. Accuracy and also applicability are limited.

Therefore, a sensor concept has to be designed which takes the particular features of miniaturization into account and which can be adapted to a wide variety of measuring tasks. In doing so, commercially available microoptical or classical optical components presenting smallest dimensions should be used. The requirements to be fulfilled can be summarized as follows:

- miniaturization without loss of interferometric accuracy
- modular structure of the interferometer
- complete optical fibre coupling
- use of commercially available optical components
- simple manufacture of the precision-mechanical components
- easy adaptation to different laser sources.

### Beam propagation in the fibre coupled interferometer

The laser light is coupled into a monomode fibre via a lens of short focal length, and then transmitted to the interferometer. The fibre emits a Gaussian beam. The beam waist is in the order of 3-4  $\mu\text{m}$ , depending on the fibre parameters, and is located in the output plane of the fibre.

Therefore, the light must be collimated as measurements can be performed only by means of a parallel beam. The beam propagation can be described by means of the formulas of Kogelnik [4].

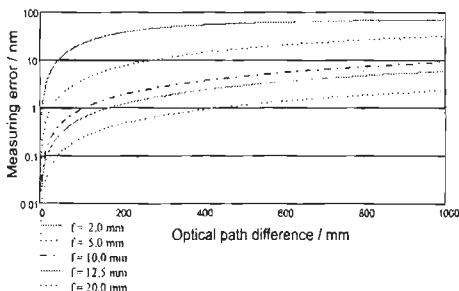


**Fig. 1:** Measuring error as a function of optical path difference and focal length

To achieve a high interferometric accuracy the influence of the focal length of the output lens and of the accuracy of adjustment were calculated. Figure 1 shows the measuring error as a function of optical path difference and focal length of the collimating lens.

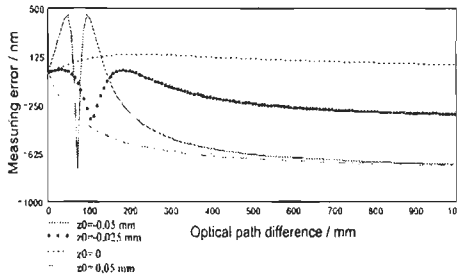


**Fig. 2:** Measuring error due to deadadjustment of lens and detector as a function of optical path difference

( $<10^{-8}$ ). Nevertheless, these measuring errors limit the miniaturization of the interferometer. Furthermore, the dimensioning of the collimating lens is decisive for the geometrical dimensions of all other optical components.

### Interferometer arrangement

Figure 3 shows the complete fibre-coupled Michelson homodyne interferometer arrangement. The relatively simple arrangement guarantees advantageous properties and parameters. Due to the polarization-independent signal generation expensive polarization-maintaining fibres are not necessary. An efficient suppression

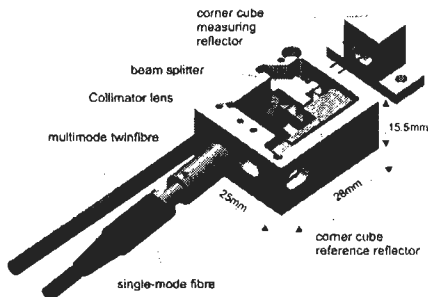


**Fig. 3:** Structure of a fibre-coupled microinterferometer

of back reflection to the laser is achieved by parallel displacement of the laser beam by corner cube reflectors. The weight of the miniature corner cube prism is only 4 g.

The interference signal is received by two multimode fibres and then transformed into two  $90^\circ$  phase-shifted photoelectric signals by the electronic evaluation unit. Thus, the interferometer head does not have to be provided with any photoelectric components, which always constitute potential heat sources.

### Properties of the microinterferometer

Figure 4 shows the fibre-coupled sensor head and the measuring reflector of the microinterferometer. The whole sensor head has the dimensions of  $25 \times 28 \times 15.5$  mm. The measuring reflector is located in a protective casing having the dimensions  $20 \times 8 \times 14.5$  mm. The mass of the sensor head amounts to 35 g. The entire

interferometer consists of five precision-mechanical and six optical components. The electronic evaluation unit was developed by the SIOS Messtechnik company. It houses the HeNe laser as well as the whole electronic system including the

evaluation and correction of the measuring data. The new signal processing unit allows a measuring resolution of 0.1 nm in a verified range of 5 m. The optical fibres connection is realized by means of commercially available optical fibre connectors.

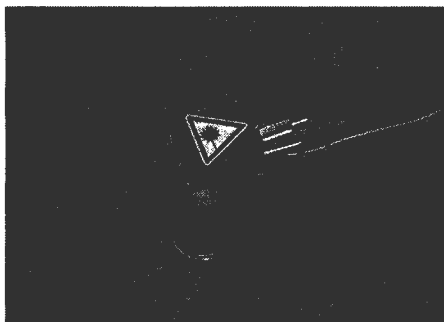


**Fig. 4:** Sensor head with retroreflector

The maximum speed of displacement of the measuring reflector amounts to 600 mm/s. The accuracy of the measuring system can be compared with conventional interferometers and stated to be  $<10^{-6}$  for measurements performed in the air. The evaluation unit also carries out the correction of the environmental parameters such as air pressure and temperature. Afterwards, the measuring data are transmitted to the PC analysis software either via a serial RS 232 or a parallel GPIB interface. In addition, there are a number of analogue outputs and encoder signals

provided for connecting further customer-specific evaluation procedures. The interferometer operates in the temperature range from 15°C up to 30°C.

## Conclusion

The concept presented here makes it possible to set up fibre-coupled microinterferometers presenting smallest dimensions by incorporating discrete optical components. As these components can easily be adapted to a broad variety of measuring tasks, they offer a number of advantages when being applied in nanomeasuring and positioning techniques. Some potential applications of this measuring system are precision linear stages, tactile probes, measuring machines, material testing machines or calibration systems for other length measuring systems.

## Acknowledgement

The project "Microoptical sensors with opto-electronic signal processing" was supported by the BMBF and supervised by the VDI/VDE-IT GmbH Teltow [5].

## Bibliographical references

- [1] Bodermann, B; Burgarth, V.; Abou-Zeid: Modulation-free stabilised diode laser for interferometry using Doppler-reduced Rb transitions: Proc. of 2nd **euspen** International Conference – Turin 2001, pp. 294-297
- [2] CSO Mesure: Laser microinterferometer HC 250; 1998
- [3] Voges, E.: Integrierte Optik auf Glas und Silizium für Sensoranwendungen: tm 58 (1991) 4, pp. 140-145
- [4] Kogelnik, H. and Li, T.: Laser Beams and Resonators: Applied optics, 5 (1966) pp.1550-1567
- [5] Jäger, G., Grünwald, R.: Mikrooptische Systeme für die Präzisionstechnik (MOSEP), Infobörse VDI/VDE-Technologiezentrum Informationstechnik GmbH Teltow, 2002

# Accuracy enhancement of a co-ordinate measurement machine by flexible integration of a precision tracking interferometer

F. Härtig, C. Keck, K. Kniel, H. Schwenke, F. Wäldele, K. Wendt

Physikalisch-Technische Bundesanstalt (PTB), Braunschweig, Germany

## Abstract

This paper presents a novel approach to improve the accuracy of co-ordinate measuring machines (CMM) by integrating a single high precision tracking interferometer (TI) as an additional measurement axis. Improved positions are obtained by a combination of the CMM positions as read from the scales and of the interferometric distances. Monte-Carlo simulations of length and flatness measurements show that the uncertainties can be reduced considerably with an appropriate configuration.

## Introduction

Some measurement tasks require exceptionally high measurement accuracies, which could not be achieved even on high precision CMMs yet. Many approaches have been taken in the past to reduce measurement uncertainty by integrating a metrology frame based on laser interferometers in the CMM. These approaches either employ an orthogonal set of flat mirrors and laser axes [1,2], or they are based on trilateration or multilateration, where the position in space is determined by length measurement of at least four tracking interferometers [3,4], which swivel around fixed points. All these approaches have the drawback, that they need elaborate and expensive measurement set-ups, which are difficult to operate.

A new approach to make high-precision co-ordinate measurements is proposed here, which only employs one single TI integrated in the CMM to acquire additional distance information during the measurement. Together with the information of the CMM scales, this information is used to reduce the task-specific measurement uncertainty. This patent pending approach takes advantage of the fact, that for many measurement tasks the uncertainty in one special direction dominates the overall uncertainty.

## Set-up

Key element of the proposed method is a single high precision TI, which is placed on the CMM's machine table. The TI is integrated into the CMM measurement procedure and records the distance between a fixed point on the machine table and the probing system as shown in Figure 1. It automatically follows a reflector mounted to the probing system of the CMM. However, the position of the interferometer has to be carefully chosen according to the requirements of the measurement task. To obtain a useful improvement of accuracy, the direction of the laser beam should be aligned approximately with the axis dominating the overall uncertainty of the measurement task. Figure 1 illustrates the set-up for the calibration of a step gauge standard. The TI is currently under development. Similar to the tracking system proposed in [2], the interferometer in the current design will rotate around a precision sphere, which serves as a reference mirror. With such a system, distance measurements between two points in space will be possible with sub-micrometer uncertainty. In the following, we will focus on the general approach, how a high-

precision distance measurement can be used to improve the overall accuracy of a CMM measurement.

### Measurement Procedure and Evaluation

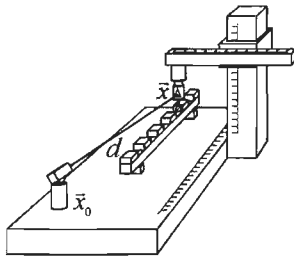


Figure 1: CMM measurement

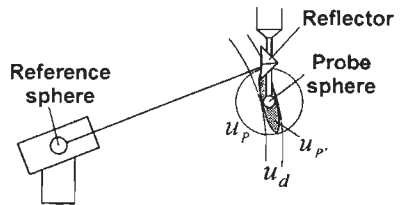


Figure 3: Uncertainty ellipsoid

The improved positions are calculated from the positions obtained from the CMM scales and the distances measured by the interferometer on a point-by-point basis. This requires that the position  $\bar{x}_0$  of the reference point and the dead path  $d_0$  of the interferometer are known. To determine them, the CMM has to be moved into at least four different positions  $\bar{x}_1, \dots, \bar{x}_4$ . The positions must not lie on a common line, plane or sphere. In each CMM position  $\bar{x}_i$ , a measurement of the distance  $d_i$  is made, which results in a discrepancy between the co-ordinate and the distance measurements. The unknown position  $\bar{x}_0$  and the unknown dead path  $d_0$  can be found by numerical minimisation of the total square error covering all positions:

$$\sum_{i=1}^4 (\bar{x}_i - \bar{x}_0 - (d_i + d_0))^2 \rightarrow \text{Min}$$

After the calibration of the TI is completed, the actual measurement is performed. During a measurement, the signal of the probing system, the machine scales and the interferometer signal are recorded simultaneously. The evaluation of the improved CMM position  $\bar{x}'$  is performed as follows: The improved position  $\bar{x}'$  and the position  $\bar{x}$  read from the machine scales are assumed to have a difference of  $\Delta\bar{x}$ . Their distances  $d$  and  $d'$  from the reference position differ by an offset  $\Delta d$ . The improved position is also related to the position  $\bar{x}_0$  and the dead path  $d_0$  of the interferometer:

$$\bar{x}' = \bar{x} + \Delta\bar{x}, \quad d' = d + \Delta d, \quad d' = |\bar{x}' - \bar{x}_0| + d_0$$

The co-ordinate and distance improvements can be found by mathematical optimisation. A target function has to be chosen, that puts a large weight on the distance measurements  $d'$  and a low weight on the position  $\bar{x}'$ . The reciprocal values of the uncertainties of the CMM scale positions  $u_p$  and of the interferometric distance  $u_d$  are appropriate choices:

$$\frac{\Delta x^2}{u_p^2} + \frac{\Delta y^2}{u_p^2} + \frac{\Delta z^2}{u_p^2} + \frac{\Delta d^2}{u_d^2} \rightarrow \text{Min}$$

In principle, the optimisation can be performed with any numerical method. As no directional information is drawn from the TI measurement, an uncertainty reduction of the position measurement can be achieved only in the direction of the straight line connecting the probing system and the interferometer position. If the uncertainty of the original position  $\bar{x}$  is assumed to have the form of a sphere, the uncertainty of the improved position  $\bar{x}'$  will take the form of an ellipsoid, as shown in Figure 2.

## Evaluation by Monte-Carlo Simulations

Since our TI is still under development, a preliminary evaluation of the new approach was done using Monte-Carlo simulations [4]. The simulations are based on a detailed kinematic model of a precision CMM with a length measurement uncertainty  $U(L) = 1.5 \mu\text{m} + 4 \cdot 10^{-6} \cdot L$ . The TI is assumed to have an uncertainty  $U(L) = 0.1 \mu\text{m} + 3 \cdot 10^{-7} \cdot L$ .

Figure 4 shows the results of a simulation of length measurements on a step gauge, if the CMM co-ordinate measurements are corrected by interferometric distance measurements, in comparison to lengths obtained without correction. If the interferometer is placed exactly in line with the gauge (no lateral offset), the measurement uncertainty reaches the uncertainty of the interferometric distance measurement, if probing effects are not considered. In case of lateral disalignment between the TI and the gauge, the TI measurement cannot fully compensate the CMM errors. The uncertainty of the length measurement increases, but remains below the uncertainty obtained without the TI.

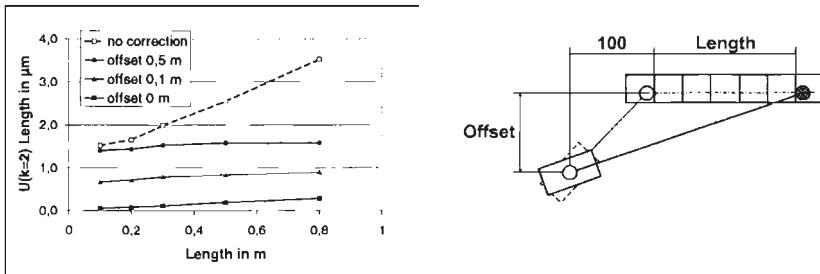


**Figure 4:** Simulation of step gauge length measurements

In Figure 4 the simulation results of a flatness measurement of a 100 mm  $\times$  100 mm flat with 5  $\times$  5 probing points are shown. If the TI is placed very close to the flat, no uncertainty reduction is achieved, as most parts of the flat are not orthogonal to the interferometer's laser beam. If the TI is moved away from the flat, all parts of the flat lie almost orthogonal to the laser beam, and the additional length measurement reduces the uncertainty of the form measurement considerably. Simulations of cylinder sector measurements show similar results. However, if the interferometer is moved too far away from the plane, the length-dependent part of the interferometer uncertainty will increase the uncertainty again.



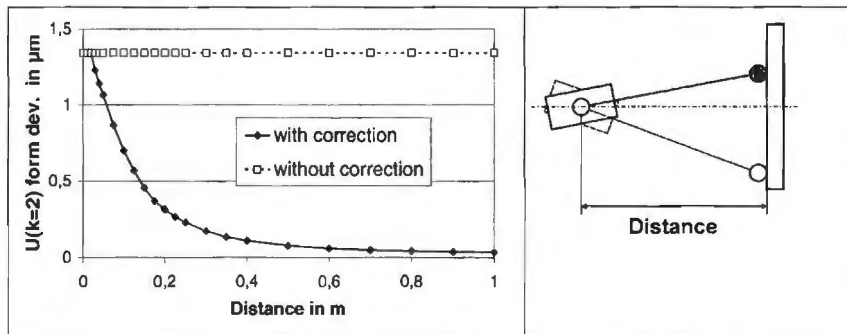


Figure 5: Simulation of flatness measurement

## Conclusions and Outlook

This paper presents a new approach to improve the measurement accuracy of a coordinate measuring machine (CMM) for particular measurement tasks. The method proposed requires just a single additional tracking interferometer (TI). The TI is placed on the machine table of the CMM to improve the measurement accuracy along a task-specific direction. Improved positions in space are calculated from the CMM scale readings and the distances measured by the interferometer on a point-by-point basis. Monte-Carlo simulations have been performed for a first preliminary evaluation of the new approach. The results of the simulations show considerable uncertainty reductions for length measurements of a step gauge and form measurements of a flat. The main advantages of the proposed method are the low amount of additional equipment needed, and its easy operation. In future, it may serve as a flexible option for the accuracy enhancement of a CMM, whenever the build-in accuracy of the CMM does not satisfy the demands. First application of the method will be the calibration of gear standards in PTB with sub-micrometer uncertainty. For this purpose, the TI will be integrated into the control system of a high-accuracy CMM equipped with an ultraprecision rotary table.

## References

1. Design for a compact high-accuracy CMM; G.N. Peggs, A.J. Lewis, S. Oldfield; Annals of the CIRP 48 (1999), p. 417
2. Brandt, U., Kleine-Besten, T., Schwenke, H.: Development of a special CMM for dimensional metrology on microsystem components, Proceedings of the 2000 Annual Meeting of ASPE, P. 361-364, 25 Oct 2000, Scottsdale, USA
3. Hughes, E. B.; Wilson, A.; Peggs, G. N.: Design of high accuracy CMM based on multilateration techniques. Annals of the CIRP 49 (2000) 391-394
4. Takasuji, T.; Goto, M.; Kurosawa, T.; Tanimura, Y.; Koseki, Y.: First measurement of a three-dimensional co-ordinate by use of a laser tracking interferometer system based on trilateration. Measurement Science and Technology 9 (1998) 38-41
5. Schwenke, H.; Siebert, B. R. L.; Wäldele, F.; Kunzmann, H.: Assessment of Uncertainties in Dimensional Metrology by Monte Carlo Simulation: Proposal of a Modular and Visual Software. Annals of the CIRP 49 (2000) 395-398

# Accurate Measurement of Silicon Spheres by Interferometry

R. A. Nicolaus, G. Bönsch

Physikalisch-Technische Bundesanstalt PTB, 38116 Braunschweig, Germany

## Abstract

A re-determination of the Avogadro-constant requires the measurement of the volume of a 90 mm diameter sphere made of single-crystalline silicon. To obtain high accuracy volume measurements, a new type of interferometer with spherical symmetry has been developed, which allows the surface topography and the diameter of spheres to be measured simultaneously. The interferences are evaluated by phase-stepping interferometry with a tuneable laser system of wide frequency tuning range. First measurements have been performed covering the whole surface of Si-spheres. The results demonstrate the measurement performance of the interferometer and the reproducibility in the nanometre range.

## Introduction

Within the scope of a new determination of Avogadro's constant,  $N_A$ , the volume of a silicon sphere has to be determined with highest accuracy possible. The Avogadro constant is determined by measurements of the macroscopic density  $\rho = m/V$  and by measurements of the so-called microscopic density: molar mass over volume of the unit cell ( $M(\text{Si}) / \sqrt{8} \cdot d_{220}^3$ ) [1].

The artefacts for the Avogadro project are designed to be nearly perfect spheres of single crystal silicon. The advantage of this shape is the lack of any edges or corners, which might be damaged. The silicon sphere has a mass of 1 kg to minimize the uncertainties at the weighing and so has a diameter of about 93 mm. As an overall uncertainty of  $N_A$  of  $10^{-7}$  is to be achieved, and one of the main uncertainty contributions is expected for the volume measurements, a special interferometer has been designed for measuring the silicon sphere.

## The sphere's interferometer

The concept is to measure the sphere with matched wavefronts, i.e. spherical waves focused to the centre of the sphere [2]. Fig. 1 shows a sketch of the optical set-up. Main item of the interferometer is the spherical etalon formed by two spherical reference faces. These are the back surfaces of two Fizeau lenses. The light of a diode laser is distributed to two arms, expanded and each collimated to a beam of 150 mm diameter and with excellent wavefront quality. The Fizeau lenses convert the plane wave into spherical waves, which have accurately to be adjusted concentric to the centre of the sphere. The objectives cover an angle of  $60^\circ$ . This approach has the advantage of measuring not only one diameter, but some 10000 diameters simultaneously, depending on the number of pixels of the camera. So  $60^\circ$  topographies can be evaluated.

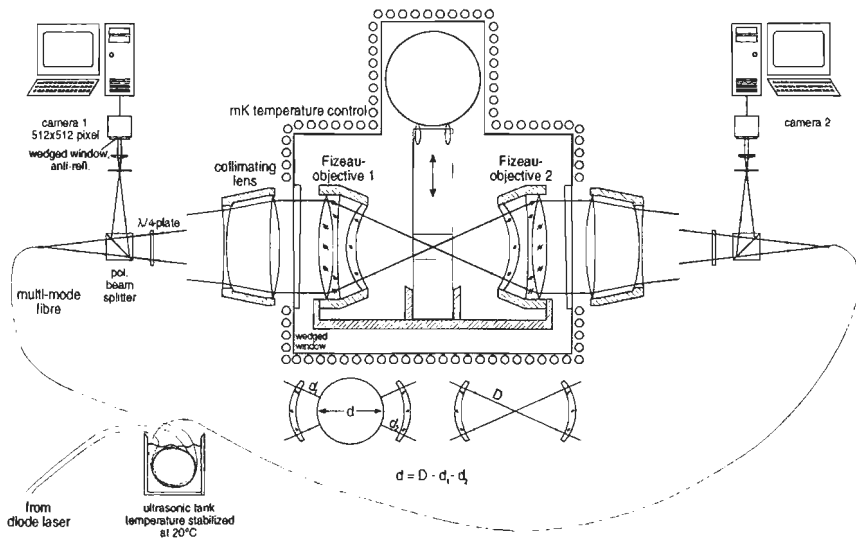


Fig. 1: sketch of the optical interferometer

In the measurement position, the sphere rests on a rigid three-point-support, firmly fixed in a frame, which also contains the two Fizeau objectives and a lifting mechanism for the sphere. This guarantees a stable separation of the etalon faces.

A complete diameter measurement is performed in two steps: first the two gaps  $d_1$  and  $d_2$  between the sphere and the corresponding reference faces are measured. Then the sphere is raised up by the lifting system and the diameter  $D$  of the empty etalon is measured. The sphere's diameters are obtained as the difference  $d = D - (d_1 + d_2)$ . The lifting system also allows the sphere to be rotated around two axes, so that any orientation of the sphere can be positioned.

The interferometer is mounted in a vacuum chamber, allowing measurements without the influence of the refractive index of air. The enclosure is temperature stabilized by means of a system of tubes connected to all walls of the housing in which water of the desired temperature is circulating. Because of weak thermal coupling between housing and interferometer the temperature of the sphere's interferometer shows a very long time constant, resulting in small temperature gradients (10 mk/m) and small slope of temperature change (1 mk/h).

### Interference evaluation

The interferences were imaged onto a CCD camera chip with 512x512 pixels. So far we used electronic binning of 4x4 pixel with reduced spatial resolution, so that images of 128x128 elements were evaluated. For the evaluation we use phase-stepping interferometry with a special 4-step Fizeau algorithm [3], [4]. This method requires four measurements of interferograms, each with the path difference changed by a quarter of an interference order. Because of the spherical symmetry and the operation in vacuum, the interference phase can only be changed by varying

the wavelength  $\lambda$  of the laser used. As the distances of the interfering faces vary from 150 mm for the empty etalon to 30 mm for each gap between reference face and surface of the sphere, the wavelength of the laser has to be changed of about  $2 \cdot 10^{-6}$  and  $10^{-5}$ , respectively. To meet the latter condition, a special diode laser system has to be developed.

### Tunable diode laser system

As the Fizeau lenses designed for use at 633 nm have high chromatic aberrations, only light sources at this wavelength can be used. Phase stepping of one interference order requires a tuning range of 1 GHz and 5 GHz, respectively. For the traceability of the wavelength, an iodine stabilized He-Ne laser at 633 nm serves as a reference. A He-Ne auxiliary laser is locked to this to obtain unmodulated light. As light source for the interferometer serves an external cavity diode laser in Littrow configuration, which is stabilized to the auxiliary He-Ne laser by means of a fast frequency offset lock, providing a tuning range of  $\pm 6$  GHz in the actual stage. With  $10^{-11}$  for the Allan-variance at averaging times of 1 sec, the stability of the diode laser system reaches that of the iodine stabilized laser, combined with the possibility to stabilize the laser at any frequency within  $\pm 6$  GHz.

### Measurements

First measurements were performed at two silicon spheres Si1 and Si2 used as density standards of PTB. For the volume measurements the whole surface of the sphere was covered by measurement areas. The lifting mechanism is used for adjusting the sphere. The sphere is rotated in  $30^\circ$  steps around a vertical axis resulting in a measurement cycle of seven measurements. Further cycles are obtained by a  $30^\circ$  rotation around a horizontal axis once in the starting position.

Fig. 2 shows a typical diameter topography of Si1 as an example. Note that each picture element is a diameter value and does not represent a local topography of the surface of the sphere. The quality of the spheres is characterised by diameter variations which amount to more than 85 nm.

Relatively high wavefront aberrations of the present Fizeau lens systems of the interferometer became apparent in the course of the

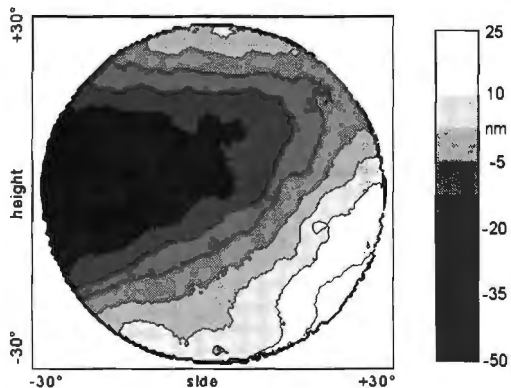


Fig. 2: diameter topography of silicon sphere Si1

investigations. As these distortions are less significant in the central part of the field of view, the evaluation was restricted to a central part of  $10^\circ$  for the time being. To demonstrate the capability of the interferometer, Fig. 3 shows the results of two measurement cycles on the prime meridian (differently marked with "x" and "+") made at intervals of several weeks. In all orientations the mean value for a central cone of diameters could be confirmed within 1 nm.

## Conclusion

A new interferometer for the measurement of spheres was put into operation. Because of the spherical symmetry of the interferometer the evaluation of one set of camera pictures results in a diameter determination in any direction of the  $60^\circ$  divergence angle of the Fizeau lenses. First measurements on single crystal silicon spheres demonstrate the capability for sub nm accuracy. For the present stage of development, a rough estimate of the uncertainty of  $2 \cdot 10^{-7}$  of the volume can be given. For the future, a couple of measures are intended to

reduce several uncertainty contributions. In particular, application of new Fizeau objectives with low wavefront distortions will improve the performance of the whole system so that an overall uncertainty of  $3 \cdot 10^{-8}$  for the determination of the volume is within reach.

## References

- [1] P. De Bièvre, S. Valkiers, R. Kessel, P. D. P. Taylor, P. Becker, H. Bettin, A. Peuto, S. Pettoruso, K. Fujii, A. Waseda, M. Tanaka, R. D. Deslattes, H. S. Peiser, and M. J. Kenny, "A reassessment of the molar volume of silicon and of the Avogadro constant", *IEEE Trans. Instrum. Meas.*, Vol. 50, No. 4, (2001), p. 593-597
- [2] R. A. Nicolaus, G. Bönsch "A Novel Interferometer for Dimensional Measurement of a Silicon Sphere", *IEEE Trans. Instrum. Meas.*, Vol. 46, (1997), p. 563-565
- [3] G. Bönsch, and H. Böhme, "Phase-determination of Fizeau interferences by phase-shifting interferometry", *Optik*, Vol. 82, (1989), p. 161-164
- [4] R. A. Nicolaus "Evaluation of Fizeau interferences by phase-shifting interferometry", *Optik*, Vol. 87, (1991), p. 23-26

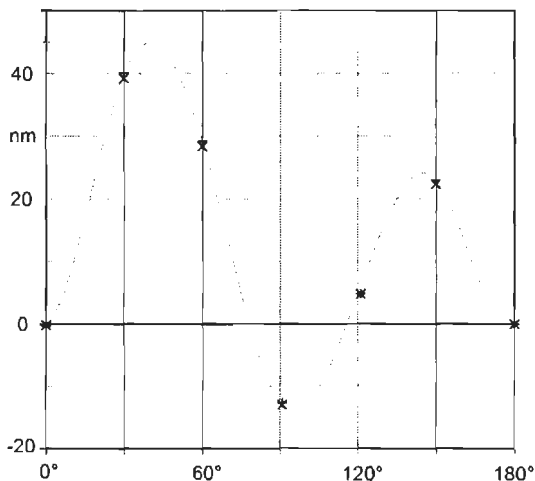


**Fig. 3:** Two measurement cycles on the prime meridian differently marked with "x" and "+" and connected by a spline.

## About calibration of thickness standards on the nanometre scale

K. Hasche, G. Ulm, K. Herrmann, M. Krumrey, G. Ade, J. Stümpel, I. Busch, P. Thomsen-Schmidt, S. Schädlich<sup>1</sup>, A. Schindler<sup>2</sup>, W. Frank<sup>2</sup>, M. Procop<sup>3</sup>, U. Beck<sup>3</sup>

Physikalisch-Technische Bundesanstalt Braunschweig and Berlin, Germany (PTB),  
<sup>1</sup> Fraunhofer Institute for Material and Beam Technology, Dresden, Germany (IWS),  
<sup>2</sup> Institute for Surface Modification, Leipzig, Germany (IOM), <sup>3</sup> Federal Institute for Material Research and Testing, Berlin, Germany (BAM)

### Abstract

Two different kinds of film thickness standards are created. One for typical X-ray methods, like X-ray reflectometry (XRR), X-ray fluorescence analysis (XRF) and electron probe microanalysis (EPMA). The calibration of thickness and evaluation of further parameters characterising the artifact as reference standard base primarily on XRR. The second type of calibration standard is focussed on ellipsometry and has a small structure which allows scanning force microscopic (SFM) determination of the film thickness. A short survey on manufacturing and some results of characterisation for both types of standards are presented here.

### Introduction

The scope of this paper is the development, manufacture and calibration of artifacts being applicable as reference standards for the thickness of films with uncertainties in the sub-nanometre-range.

### Standards for XRR, XRF and EPMA

The artifacts consist of fused silica substrate with a surface smoothed by ion beam polishing to an RMS-value of roughness smaller than 0.3 nm, determined by SFM.



**figure 1:** 10 nm Pt-layer as thickness standard for X-ray facilities on a fused silica

As coating, a platinum layer or a system of carbon-nickel carbon are chosen with a nominal thickness of 10 nm and 50 nm respectively. Films are deposited by physical vapour deposition (PVD) technique being well approved in the field of X-ray mirror production [1]. Fig. 1 shows a thickness standard.

Metrological characterisation of standards for XRR, XRF and

### EPMA

Calibration of film thickness and other parameters characterising the artifact as reference standard base primarily on XRR. Results found on different facilities during independent investigations show satisfying consistence as reported in [1] and [2]. For nanometre layers the quality of the surface and interface between film material and substrate are essential and therefore they were examined by transmission electron microscopy (TEM). As a test a thin platinum layer with a nominal thickness of 10 nm

is deposited on an SiO<sub>2</sub>-wafer and analysed. The wafer has a thickness of 400 μm and is chosen as substrate to minimise the influence of preparation for the TEM cross-section observations. The result of this investigation is documented in fig. 2. The surface of the SiO<sub>2</sub>-wafer is shown on the left; its roughness is estimated at a value of 0.5 nm. On the right the surface is covered by a Pt-film with a thickness of 12.7 nm ± 0.8 nm. The interface between Pt-layer and substrate material is blurred over a width of approx. 0.9 nm. The substrate surface seems to be roughened by the coating process.

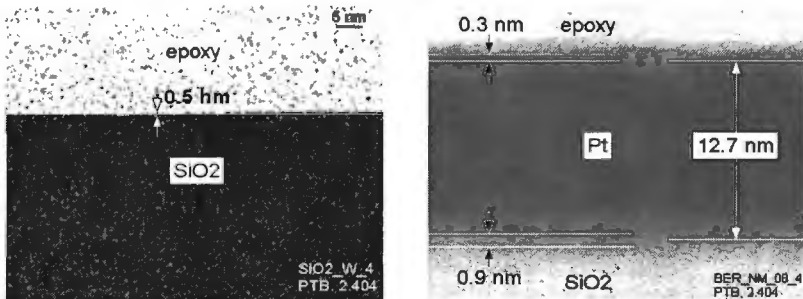


**figure 2:** TEM-investigation of the surface of an SiO<sub>2</sub>-wafer without a top layer (left) and with a Pt-coating (right)

The thickness variations over the whole surface is another important question, which is investigated by XRR and XRF. Fig. 3 shows a map of thickness values over a whole sample measured by XRF.

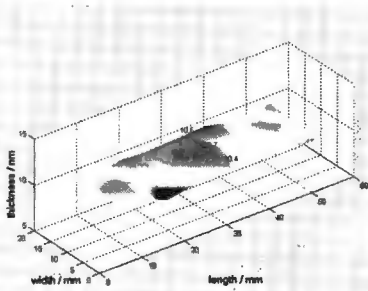


**figure 3:** Mapping of film thickness measured by XRF

The homogeneity of a layer is examined by XRR in a two step procedure. At first, the reflectivity is measured as a function of the angle, and thereafter in a second step the angular value of a minimum in reflectivity is selected and the sample is moved laterally along one axis. Reflectivity changes during such a scan indicate an inhomogeneous thickness and a second XRR measurement can be done at another position on the scanned line to verify this. As a result of such scanning on several samples thickness variations within ± 0.2 nm along the short axis of the sample are

found. This value agrees with the value of uncertainty of a single XRR measurement at the centre of the sample.

### Standards for ellipsometry

On Si-wafers with a diameter of 150 mm and (100) surface orientation a film of thermal oxide is grown and subsequently structured by direct electron beam writing. By dry etching with plasma the thickness of the oxide layer is reduced to a value of

roughly around 100 nm. Wet etching in buffered hydrofluoric acid further reduces the residual oxide. After that the mask is removed and a protecting layer is deposited for sawing. Twenty identical chips are located on a wafer. A number on each chip marks its the location on the wafer. The chip size is 20 mm x 30 mm; the layout is shown in fig. 4. A frame around the main field with four marks serves as finding structure.

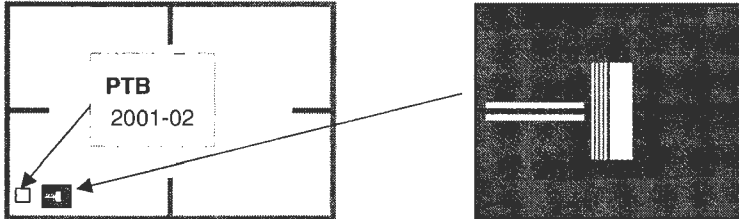


**figure 4:** Design of ellipsometry standards with a structure for SFM calibration

The large field can be used for thickness measurement by methods working with a probe beam like ellipsometry or XRR. The PTB logo is shown in the bottom left hand corner of each chip, and below the year of fabrication and numbers indicating the chip's position on the wafer. Near the logo is a structure within a frame for SFM-measurements and a 200  $\mu\text{m}$  wide field for micro spot investigations. The structure for SFM within the small frame is sketched on the right hand side of fig. 4. It consists of two horizontal search bars on the left, each 50  $\mu\text{m}$  wide with a gap of 50  $\mu\text{m}$  in between. Vertically to these bars are 4 lines, representing topographic structures, each 3  $\mu\text{m}$  wide with a gap of 10  $\mu\text{m}$  to the next one. The micro spot field is positioned parallel to the four lines on the right hand side within the frame. Fig. 5 shows an SFM image of the four lines structure. The four lines can be

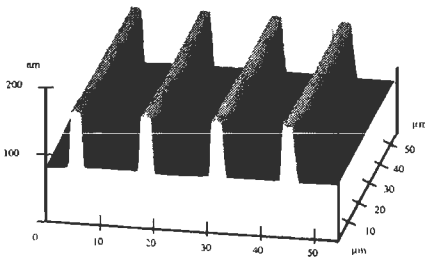


**figure 5:** SFM image of the rectangular structure within the frame for topographical calibration. Height is  $162 \text{ nm} \pm 1.3 \text{ nm}$ .

visualised over a scanning length of 60  $\mu\text{m}$ . The latitude of the lines in relation to the width of the gaps between them is chosen under consideration that the surface on the top of the lines can easily be reached by the cantilever tip of the SFM, because the measurement inside is influenced by the non-vertical slope angle of the side walls, and therefore the gaps are wider. Chips are manufactured with nominal thickness values of 988 nm, 381 nm, 158 nm, 68 nm and 6 nm.

### Metrological characterisation of standards for ellipsometry

As described above each calibration standard can be used for different measurement methods and is not limited to one type of instrument. Par example the scale on the z-axis of an SFM can be referred to XRR measurement results by these standards for the case of the two smallest values of film thickness. Therefore the homogeneity of the thickness over a chip has to be characterised carefully. As a first test a chip from the centre and another from the perimeter of a wafer are both investigated by TEM. The nominal thickness of the  $\text{SiO}_2$  layer is 6 nm. The chip from the centre of a

*Proc. of the 3<sup>rd</sup> euspen International Conference, Eindhoven, The Netherlands, May 26<sup>th</sup> -30<sup>th</sup>, 2002*



wafer has a measured thickness of about  $5.9 \text{ nm} \pm 0.3 \text{ nm}$  at the centre, and about  $5.9 \text{ nm} \pm 0.5 \text{ nm}$  within the frame for SFM measurement. The thickness of the film on a chip from the perimeter of the wafer is about  $5.9 \text{ nm} \pm 0.5 \text{ nm}$ .

An adequate homogeneity in film thickness over one wafer is also verified by XRR measurement. For a nominally 68 nm layer thickness values of 69.2 nm and 68.9 nm are measured on two chips located at the centre of a wafer, and 69.0 nm at the perimeter of the wafer. All these values are measured with an uncertainty of 0.2 nm.

Ellipsometry investigations have been done on a spectroscopic ellipsometer with rotating analyser (RAE-SE) at  $65^\circ$ ,  $70^\circ$  and  $75^\circ$  within the spectral range from 270 nm to 1100 nm, with  $\delta\lambda = 5 \text{ nm}$ . The model consists of a thermal  $\text{SiO}_2$ -layer on an Si-substrate (Jellison). Table 1 gives a survey of the results for all nominal thickness values at two different locations on a wafer.

**table 1:**

Mapping results of spectral ellipsometry measurements at different positions on a wafer.

The uncertainty for all values in the table is  $1 \text{ nm} + 10^{-2} \text{ h}$ . The last

D nominal (nm)	D centre (nm)	D edge (nm)
6	7.0	6.9
68	71.0	71.2
158	164.2	164.4
381	389.9	389.8
988	1005.8	1007.1

column of the table contains the result of a measurement on a VLSI standard using the same modelling. This value gives a feeling for the model; it tends to yield slightly higher thickness values than expected. So far, no advanced modelling has been performed and the derived thickness data are subject to further modelling.

## Conclusions

Two different kinds of film thickness standards are fabricated and characterised by several techniques of film thickness measurement. Results for the X-ray methods standards are consistent on a level below one nanometre.

The standards for film thickness determination by ellipsometry have been fabricated and first results are reported. These results show consistence.

The full characterisation of both types of standards has not yet been finalised.

## Acknowledgement

This work is financially supported by BMBF via project no. 13N 7704 "Calibrated reference standards of coating thickness in the nanometre range". Particular thanks to Mr. D. Hirsch, IOM, for the SFM image.

## References

- [1] K. Hasche, K. Herrmann, M. Krumrey, G. Ulm, S. Schädlich, W. Frank, M. Procop, Proc. euspen International Conference 2001, Turin, Italy, 2001
- [2] K. Hasche, K. Herrmann, M. Krumrey, G. Ulm, G. Ade, P. Thomsen-Schmidt, S. Schädlich, W. Frank, M. Procop, U. Beck, PTB-Report F-44; Proc. 5th Seminar on Quantitative Microscopy, Bergisch-Gladbach, Germany, 2001 (to be published)

## A round-robin process for co-ordinate metrology

Abackerli, A. J., Martinez Orrego, R. M.

Universidade Metodista de Piracicaba - UNIMEP  
Caixa Postal 68 - Piracicaba - SP, Brasil, CEP 13400-911  
Phone +55 (19) 3124-1605 Fax +55 (19) 3124-1723  
abakerli@unimep.br

### Abstract

Companies are increasingly focusing on flexibility to get competitive advantage in world-class manufacturing. In metalworking industries, that means to adopt new technologies for manufacturing and, in most cases, Co-ordinate Measuring Technology - CMM for part inspection. An initial research on the use of CMMs in a Brazilian industrialised area shows the need of conceptual and technical support to help users getting full benefits from such technology. To do so, a round-robin process for co-ordinate metrology has been implemented<sup>1</sup>, based on the comparison of measuring results taken from a reference work piece. This paper outlines the process strategy and its preliminary results, from which details about CMM application in metalworking industries are pointed out.

### The round-robin process

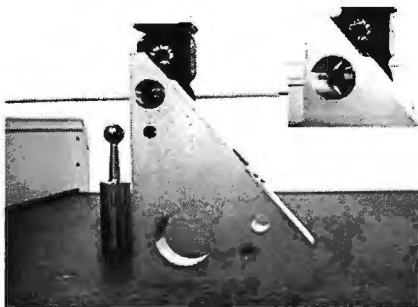


Figure 1: Reference work piece.

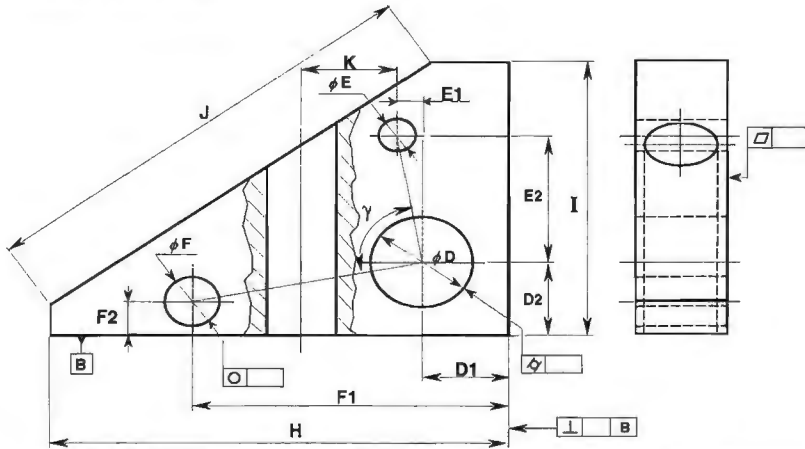
The round-robin is based<sup>2</sup> on the circulation and measurement of a reference work piece, figure 1, from which industrial CMM users get a set of dimensional characteristics. The results of individual measurements are compared to each other and against reference results obtained from the Instituto Nacional de Metrologia, Normalização e Qualidade Industrial - INMETRO<sup>3</sup>. The application of statistical analysis to data provides the basis for characterising the measurements and their correlation with daily co-ordinate

metrology practices in industry. The round-robin is organised to get information from which one can outline a comparative diagnostic regarding equipment, measurement set-up, measurement strategy, environment, and human resources, to establish the user performance against the overall available conditions.

The comparison process is organised to investigate common aspects about CMM measurements on industry, constrained to their regular daily practices. In this sense, the user is oriented to measure the part for comparisons according to the following:

- Measurements are to be done in a regular way, according to the best users' practices;
- Only commercial measuring resources (software, probes, etc.), provided by the machine manufacturer are to be used for measurements;
- At the user discretion, the results are to be the best, considering the available equipment, installation, environment and personnel;

- The measuring strategy is initially decided by the user do measure all but three part characteristics, according to the whole measuring conditions;
- After the initial measurements other three characteristics are to be measured using a predefined strategy, supplied by the process co-ordinator;
- The results and measurement strategies are to be recorded according to the provided instructions.



Measured Geometry	Characteristic	
Hole <i>D</i>	Diameter	$\phi D$
	Position	D1
	Position	D2
	Cilindricity	
Hole <i>E</i>	Diameter	$\phi E$
	Position	E1
	Position	E2
Hole <i>F</i>	Diameter	$\phi F$
	Position	F1
	Position	F2
	Roundness	
Width	Length	H
High	Length	I
Angled surface	Length	J
---	Squareness	
---	Angle	$\gamma$
---	Distance	K
Frontal Plane	Flatness	

**Figure 2:** Measured work piece features.

A small set of characteristics has been selected on the reference work piece to provide the necessary information, resulting in measurements of diameters, lengths,

hole positions and angles, figure 2. Users are also asked to supply the associated form errors such as roundness, cylindricity, squareness and flatness. Redundant measurements are also required to allow checking for the adopted solutions regarding measuring strategies.

To circulate the reference work piece is properly placed in a briefcase, specially designed to accommodate it, together with working instructions to execute the measurements according to the planned process.

The round-robin was set-up into two phases. The test phase organised for checking the adopted strategy and adjusting process parameters such as working instructions, procedures, documentation, etc. The implementation phase is the comparison phase itself, organised according to previous investigations<sup>4</sup> to gather data from industrial users, by circulating the reference work piece among participants, including the INMETRO to perform the reference measurements.

Once the results are collected, the mean and spread of data of each individual measured characteristic (diameter, length, etc.) are calculated to be compared to each other. The Kolmogorov-Smirnov Test<sup>5</sup> is used to identify the data distribution, from which possible outliers are identified by the Chauvenet Criterion<sup>6</sup> at de confidence levels of 95 and 99%.

### **Preliminary results and discussion**

The process has demonstrated to be efficient to gather information to identify the investigated points, besides its additional deliverables, which have shown to be useful to users in many practical situations.

After the test phase, the complete process has been reviewed to optimise its strategy, reducing the total number of required measurements, since the time expended on tests showed to be the greatest process limitation.

The developed management system, including its procedures and working instructions, has provided a sound basis for documentation, to guarantee the process traceability and the reference work piece integrity within comparisons.

To protect the information and the identity of participants, a code system has also provided a "coded front end" to allow data analysis independently from each specific data source, giving additional security regarding proprietary information.

The selected statistical tools provided objective information about data, allowing the identification of discrepancies among users and reference measurements. The Kolmogorov-Smirnov test, with the appropriate correction for sample size, indicates good agreement between data and the Normal distribution, allowing establishing inferences from data using the identified statistical model. The Chauvenet criterion has also been sufficient to provide clear indication of outliers, allowing to identify discrepant results and to correlate them with the adopted measurement procedure.

Based on such statistical analysis only flatness, roundness and cylindricity, in that order, gave indication of systematic discrepancies on data from different industries based on Chauvenet criterion, indicating possible user's difficulties.

Preliminary data analysis shows also that the measured hole diameters have the best agreement among users and the reference values. The hole positions, expressed by centre co-ordinates, show larger spread of results, possibly due to influences of measurement strategy involving the definition of part co-ordinate system. Further investigations are still necessary to state safely about such

correlation.

Regarding measurements relying on geometric constructions, such as the length of the angled surface, results show even larger spread of data, pointing to the influences of different strategies of measurement.

A particular behaviour has been observed on measurements of the distances between the two perpendicular holes, distance  $K$  on figure 2. Initial analysis shows the possibility of influences of either, measuring strategy and probe indexing.

### Final comments

The comparison process is being capable to investigate important aspects about co-ordinate metrology and its related practices. Further analysis is being performed to check whether the adopted measuring strategy is decreasing quality of results beyond the expected limits.

The interaction with industrial partners shows that they are taking great advantage from the process itself, since they have got to exercise further thinking regarding measurement procedures to participate.

Generally speaking, data shows some agreement between measurements results and installed capability, indicating that users are aware about most basic procedures to get reasonable results from their co-ordinate measuring machines. Further investigation is still being done to identify specific relations between measurement results and adopted strategies.

### Acknowledgements

Thanks are due to FAP/UNIMEP, to FAPESP, to INMETRO, and to all industrial partners, for providing the necessary support to carry out this project.

### References

- [1] Abackerli, A. J.; Martinez Orrego, R.M. *Intercomparação em máquinas de medir por coordenadas - II*. Universidade Metodista de Piracicaba. Piracicaba - SP, Brasil. Relatório parcial de pesquisa - FAP no. 205-99. Set. 2001. (in portuguese)
- [2] VAILLEAU, P.G. *Intercomparaison Sur Machine a Mesurer Tridimensionnelle*. In: Congress International de Metrologie, 19, 1993, Lille. Mouvement français pour la qualité, France, Octobre 1993, p.121-143.
- [3] INMETRO - Instituto Nacional de Metrologia, Normalização e Qualidade Industrial. <http://www.inmetro.gov.br/>
- [4] Abackerli, A.J *Análise de desempenho de máquinas de medir a três coordenadas*. Relatório de Projeto FAPESP no. 96/5961-1. Santa Bárbara d'Oeste-SP, Brasil. Maio 1999. (in portuguese)
- [5] ZAR, Jerrold H. *Biostatistical Analysis*. 4<sup>th</sup> Ed. Prentice Hall: New Jersey, 1995.
- [6] HOLMAN, J. P. *Experimental Methods For Engineers*. Sixth Edition. New York: McGRAW-HILL, 1994.

## Metrology for Nanotechnology

R.H. Bergmans

NMi Van Swinden Laboratorium, P.O. Box 654, 2600 AR Delft, The Netherlands, rbergmans@nmi.nl

### Abstract

The emerging of nanotechnology has giving rise to a new kind of metrology, the so-called nanometrology. This paper will start by explaining the role which National Metrology Institutes play in ensuring reliable nano-measurements worldwide, by providing internationally accepted traceability. Examples of nanometrology at NMI VSL, such as the calibration of nanosensors and a high precision 3D-coordinate measuring machine will be presented.

### Introduction

Nanotechnology can be described as: the study, development and processing of materials, devices and systems in which structure on a dimension of less than 100 nm is essential to obtain the required functional performance. Examples are nano-machining and nano-fabrication techniques, nano-structured materials, electronic device fabrication, micro-systems technologies (MST/MEMS) and bio-medical systems. The technologies used in these fields are not only improved versions of existing ones, but can also be quite new and different.

In order to ensure that results in nanotechnology can be compared quantitatively and parts are interchangeable, the measurements must be traceable. This means that standards should be used which are linked through a traceable chain to the corresponding SI-unit, i.e., the Meter, the Kelvin, ... , of the measurand. Due to the quite different nature of nanotechnology the conventional standards, measurement methods and instrumentation are no longer sufficient or cannot reach the desired uncertainty/accuracy. Therefore there is a need for a new branch of metrology, the so-called nanometrology. This is a multidisciplinary kind of metrology since it is not limited to a particular SI-unit.

### International metrological infrastructure

The role of National Metrology Institutes (NMIs) is to provide traceability of measurements to (inter)national standards thereby making measurements

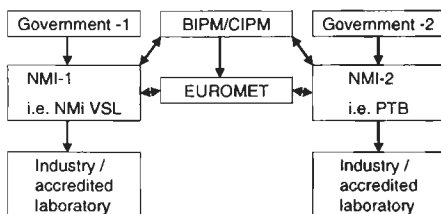


**figure 1:** International metrological infrastructure

quantitatively comparable and trade possible. For these reason NMIs develop and improve standards to fulfil the needs of their national industry and society. Since there is international trade there exist also an international metrological infrastructure. The CIPM (Committee international the Poids et Measure) is the worldwide link between the NMIs. It gets its authority from

“The convention of the Metre”, a diplomatic treaty between fifty-one nations. Further every region in the world has is own linking body. For Europe this is EUROMET. One Proc. of the 3<sup>rd</sup> *euspen* International Conference, Eindhoven, The Netherlands, May 26<sup>th</sup> –30<sup>th</sup>, 2002

of the tasks of the CIPM and its working groups, in cooperation with the regional bodies, is to establish the degree of equivalence between national measurement standards of the NMIs and to provide mutual recognition of the calibration certificates issued by the NMIs. This is done by reviews of the NMIs as well as by carrying out comparisons on artefacts and standards.

Also for nanometrology the equivalence between the NMIs needs to be established. For this reason a first set of nano-comparisons was started by one of the working groups of the CIPM. The subjects are line-width standards, step-height standards, line scales, one-dimensional gratings and two-dimensional gratings. The comparison on 1D-gratings was recently successfully completed. One of the differences between nanometrology and "classical metrology" is the huge investments in money and man-hours by the NMIs that are necessary to keep up with the demands of industry. It is therefore no longer possible for every NMI to develop the necessary standard and measuring instruments individually. Since the time-to-market of the nanotechnology standards/instruments is much shorter than for traditional metrology, a much closer cooperation between the industries and the NMIs is necessary. For this reason in 2001 an "Initiative on nanometrology" has started by the European NMIs (EUROMET). The purpose of this initiative is to co-ordinate the efforts in the field of nanometrology and to satisfy the industrial needs. An inventory of the efforts of the NMIs has been made and the next step is to increase the cooperation with industry.

### **Nanometrology at NMi VSL**

To fulfil the new demands for metrology in nanotechnology, the NMi Van Swinden laboratory has started several nanometrology projects. Some of these projects will be presented below. The emphasis is on length metrology where the needs of industry are most imminent. In the area of electricity there is an increase in use of nanotechnology for metrology purposes. Here one makes use of quantum devices to establish new electrical standards, see the extended abstract "Nanotechnology and Micro System Technology in electrical metrology" in these proceedings. A brand new field for metrology on which NMi VSL is orienting itself is the nano-chemistry/biology. Although this field is in rapid development it is not yet clear what the real metrology demands will be. The length projects described below are carried out in close cooperation with the section Precision Engineering of the Eindhoven University of Technology.

### **Calibration of nanosensors**

Nanosensors are a new class of sensors that has recently appeared. These sensors have nanometer or sub-nanometer resolution over a range of at least several micrometers. The accuracy of these nanosensors is not necessarily of the same level as the resolution. Effects like sensitivity errors, non-linearity, hysteresis and drift may cause deviations of many nanometers. In order to determine these errors in a traceable way, two new measuring instruments were developed. The first one is portable, see its description in these proceedings [1]. The second one is directly traceable to the Meter and has an even higher accuracy and range. The heart of this system is a Fabry-Perot interferometer, which consists of two parallel mirrors separated by a distance  $L$  from each other, see figure 2. Light of a so-called slave laser is directed into this Fabry-Perot cavity and stabilized to the cavity length  $L$ . When one of the mirrors of this cavity is displaced the frequency of the slave-laser will follow its movement. The frequency of this slave-laser is then compared to the frequency of a primary length standard. In this way the displacement of the mirror is

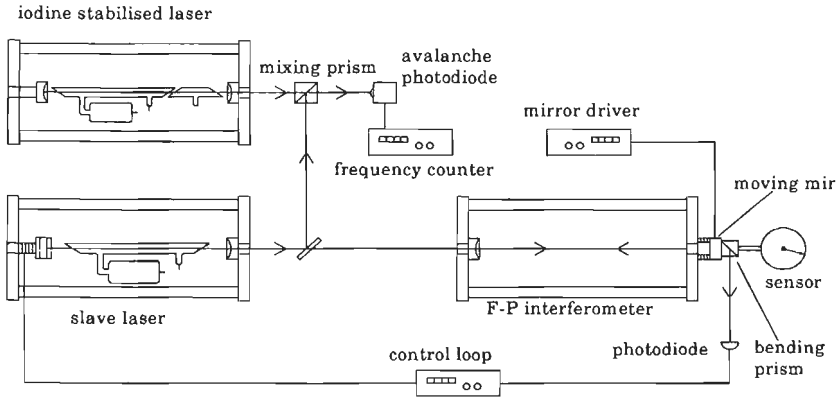


**figure 2:** Schematic view of the calibration set-up for nanosensors

measured. When a nanosensor is placed on top of the mirror it will also follow the movement of the mirror. In this way the nanosensor is calibrated. The resolution of this system is a few picometers, the range is 300  $\mu\text{m}$  and the uncertainty is approximately 1 nm [2,3].

As an example the calibration of a capacitive sensor (Lion Precision type PX 405 HC) is shown in figure 3. The capacitive sensor gives a direct indication of the measured value in nanometers. Therefore the indication of the sensor can be directly compared

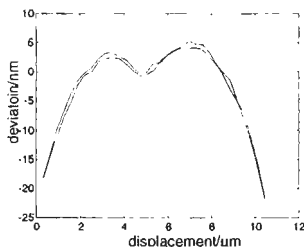


**figure 3:** Residue after a calibration of the capacitive sensor after a first order fit, back and forth

to the true displacement of the Fabry-Perot mirror. A calibration was performed over 10  $\mu\text{m}$ , which is the maximum range of the sensor in its small range setting, the resolution of the sensor is approximately 0.25 nm. From this a first-order sensitivity deviation of -1% was determined. This deviation cannot be explained by a cosine-error due to a misalignment of the sensor since this would yield a positive deviation. The non-linearity of the sensor, after correcting for the first-order sensitivity deviation

can be seen in figure 3. The maximum deviation of the linearity is about 25 nm. This is less than the specification of the manufacturer.

### High-precision 3D-Coordinate Measuring Machine

In Precision Engineering, 3D Co-ordinate Measuring Machines (CMMs) are often used to measure dimensions of rather complex products. As products are getting smaller and their tolerances become tighter the desired measuring accuracy increases. Although downscaling of a conventional CMM reduces the effect of certain systematic errors, the cause of these errors is not averted. Therefore we took a new approach by designing a quite alternative high precision 3D-CMM with an intended



measuring uncertainty of 100 nm in a workspace of 1 dm<sup>3</sup> [4]. This uncertainty is about one order of magnitude smaller than the most accurate commercially available 3D-CMMs.

To attain the intended accuracy, the design philosophy of this CMM is based on eliminating or minimizing the main error sources of conventional CMMs by applying design principles both in the machine concept and at the component level. For instance minimizing the distance between the product and the measuring systems has significantly decreased the Abbe error. This has been achieved by attaching the x and y line-scales to intermediate bodies, see figure 4. These intermediate bodies can move along with the probe. Thereby there are no Abbe errors in the horizontal mid-plane and only small Abbe errors outside the mid-plane. Kinematic design and Symmetry is used to avoid internal stresses and

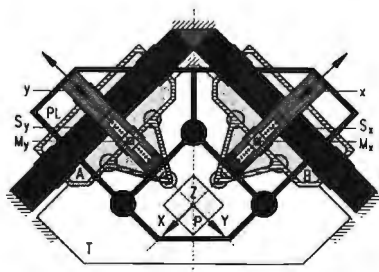


figure 4: Top view of alternative 3D-CMM

asymmetric thermal distortion. Thermal Loop Design is utilized to make the machine less susceptible to temperature changes by extensive use of aluminium and built-in thermal length compensation. Aerostatic bearings are used for all slides to attain a high guiding accuracy and repeatability in positioning.



figure 5: The 3D-CMM in action

A demonstrator, see figure 5, has been developed which shows that the attained goal of a 100 nm 3D-uncertainty can be reached. Currently a prototype based on this demonstrator is under development at ZEISS in cooperation with the Eindhoven University of Technology and NMI VSL.

## References

- [1] van den Heuvel, D and Bergmans, R.H.: *Probe calibration using a digital piezo translator*, these proceedings.
- [2] Bergmans, R.H., et al. : "Recent Developments in Traceable Dimensional Measurements", SPIE Proceedings, Volume 4401, 2001, page 217.
- [3] Haitjema, H., et al. : *Metrologia*, 2000, 37, 25-33
- [4] Vermeulen, M.: "High Precision 3D-Coordinate Measuring Machine", PhD thesis, Eindhoven University of technology, The Netherlands.

## Beginning of Operation and Optimisation of a 3D Micro Measuring Device

Brand, U.; Yu, L.; Chang, C.; Lüllmann, H.; Schwenke, H.

Physikalisch-Technische Bundesanstalt, Braunschweig, Germany

### Abstract

A status report on the development of a 3D Micro Measuring Device in the PTB is given. The instrument is aimed at a 3D coordinate measurement uncertainty of  $< 0.1 \mu\text{m}$  for the measurement of microstructures in a measurement volume of  $25 \times 40 \times 25 \text{ mm}$ . A metrology frame consisting of three plane mirror interferometers for simultaneously measuring position and angle has been integrated into a commercial CMM. Using the interferometers first measurements of the static and dynamic guiding deviations and the vibrations between probing system and workpiece were made. Input of the laser interferometer readings into the  $\mu\text{CMM}$  is still under development. First measurements of the probing sphere diameter repeatability of a 2d fibre probe are reported.

### 3D Micro Measuring Device

A 3D micro measuring device ( $\mu\text{CMM}$ ) for the measurement of the dimensions of microstructures is being developed at PTB [1]. It is the aim of the development work to achieve a 3D coordinate measurement uncertainty of less than  $100 \text{ nm}$  in a measuring volume of  $25 \text{ mm} \times 40 \text{ mm} \times 25 \text{ mm}$ . The  $\mu\text{CMM}$  consists of an optical measurement system and two tactile micro probing systems. The first probing system to be used is the 2d fibre probe with probing sphere diameters available down to  $25 \mu\text{m}$  and probing forces below  $1 \text{ mN}$ , which was developed in the PTB [2]. The second probing system is currently developed [3,4].

Both probing systems will be mounted at different z-columns of the CMM. To improve the measurement uncertainty of the instrument a metrology frame is added to the machine. The translational displacement and all guiding deviations of the CMM are measured by three commercial double axis laser interferometers [5]. Therefore the two tactile sensors are mounted in different Zerodur cuboids which are fixed to the rams. The compact double path laser interferometers for simultaneous measurement of displacement and angle are mounted within an aluminium frame. Inside this frame a second invar frame supports the reference mirrors of the interferometers and the specimen to be measured.

The facility is based on a commercial coordinate measuring machine (CMM) [6] which has been equipped with improved air bearings to meet the high requirements for vibration behaviour. The basic CMM was delivered by the manufacturer in April 2001 and set up at PTB. To minimise disturbing influences from the exterior, the machine was installed on a foundation isolated from the rest of the building. In addition, it was set-up in a separate climatic chamber. The metrology frame manufactured at PTB containing the three double-axis plane mirror interferometers has been integrated into the basic instrument. One Zerodur cuboid has been mounted at the  $\mu\text{CMM}$ , so first measurements of positioning and guiding deviations and of positional stability of the basis-CMM could be made.

### Positioning noise

The vibrations between ram and positioning table of the  $\mu$ CMM were measured with

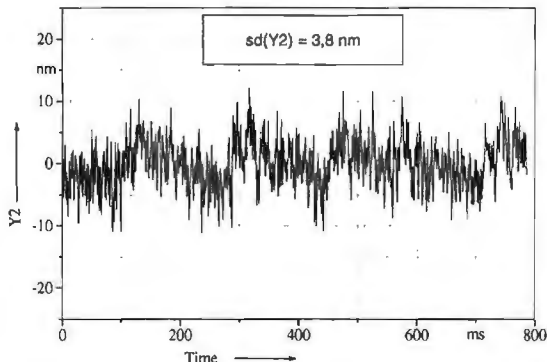


figure 1: Typical vibrations measured between ram and metrology frame on Y2-axis of the  $\mu$ CMM (sampling: 10 kHz, sd: stand. dev.)

a sampling rate of 10 kHz over a period of 0.8 s in all six interferometer axes (fig. 1 shows Y2-signal). As a measure of the positioning noise the standard deviation  $sd$  of the profiles was calculated. The noise levels of all six axes were then averaged. A mean standard deviation of 4.0 nm ( $sd = 0.5$  nm) resulted. In order to find out the main contributions to this noise level several noise sources were switched on and off. The influence of the CMM motion controller, the passive vibration isolation of the CMM, the air

conditioning of the laboratory and the fans used for cooling the laser interferometers

Mot.-Con.		Vib.-Iso.		Air-Cond.		Fans		noise nm	sd nm
On	Off	On	Off	On	Off	On	Off		
✓		✓		✓		✓		4,0	0,5
✓		✓		✓			✓	4,6	1,6
✓		✓			✓		✓	4,2	2,4
✓			✓		✓		✓	3,8	0,9
	✓		✓	✓			✓	1,9	0,3
	✓		✓		✓		✓	2,2	0,4
	✓	✓			✓		✓	2,0	0,4

Table 1: Noise level of the  $\mu$ CMM, measured with different noise sources switched on and off (noise: averaged standard deviation of all 6 interferometer axes)

and the CMM electronic circuits were investigated. Table 1 gives an overview over the results. From row 2,3 and 4 it can be seen that the vibration isolation, the air conditioning and the fans nearly have no influence on the noise level. From row 5 – 7 it can be seen that the CMM motion controller is the biggest noise source. It doubles the noise level from 2 nm to more than 4 nm.

### Zerodur cuboids

The flatness deviations and the orthogonality deviation of the three zerodur cuboid mirror surfaces were measured. These data are planned to be used for online correction of the relative position and orientation of the probing system and the measurement object. The long wavelength flatness deviations are in a range of  $\pm 40$  nm for the x- and y-mirror surfaces. The z-surface contains a 70 mm bore hole for the

optical measuring microscope of the CMM, so polishing was more difficult. The flatness deviations of this surface are  $\pm 70$  nm.

The orthogonality deviations of the three zerodur mirror surfaces were measured to be 1,0"/2,8"/1,4".

### Guiding deviations

Each of the three laser interferometers comprises two measuring beams separated by 50 mm. Assuming an interferometric length measuring resolution of 2.5 nm this

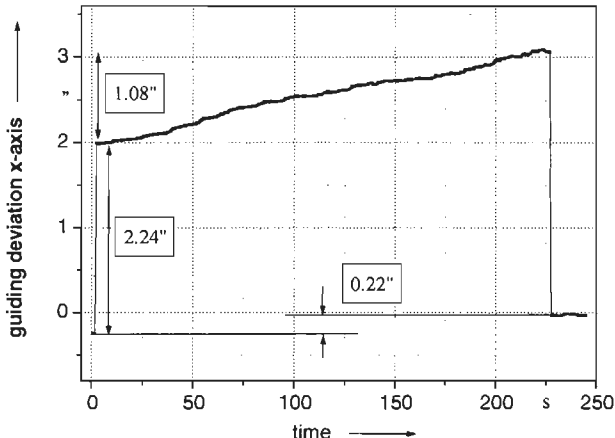


figure 2: Measured  $\mu$ CMM x-axis guiding deviations during x-movement of 45 mm

leads to an angle measurement resolution of 0.01". Figure 2 shows a measurement of the x-axis guiding deviations during x-movement of 45 mm. During acceleration of the  $\mu$ CMM a yaw angle of 2.24" occurs, which disappears during deceleration. During constant velocity movement a yaw angle of 1.08" is added to. These two dynamic guiding deviations are

probably due to a non symmetric point of contact of the driving force. This effect will be investigated in more detail in future. The static guiding deviations which can be observed when the machine has moved 45 mm is only 0.22". Thus it can be concluded that static single point co-ordinate measurements should be possible with very low guiding deviations of approximately 0.005"/mm<sub>x</sub>. The dynamic guiding deviations are a factor of 15 worse. Hysteresis, cross talk and repeatability will be measured in future.

### First 2d Fibre-Probe Measurements without Metrology Frame

Although the interferometer readings could not be used for measurements with the  $\mu$ CMM because the data read-in was no more than prepared during the time of writing, first probing experiments with the 2d opto-tactile micro probe [2] at setting ring standards of 0.5 and 1.0 mm diameter have been carried out. Since the diameter of the setting rings was known with an uncertainty of 0.15  $\mu$ m from a former measurement in the PTB form laboratory the rings can be used to determine the fibre probe sphere diameter. A measurement was made using the 0.5 mm ring. The ring was not cleaned before calibration. The illumination of the fibre probe and the bright field illumination were kept constant during the measurements, since these influence the size of the probing sphere image. 16 probing points equally distributed over the circumference of the setting ring in a well defined height were taken and a circle fit was made. The circle-fit standard deviation is 0.9  $\mu$ m. Thus each point in figure 3 is

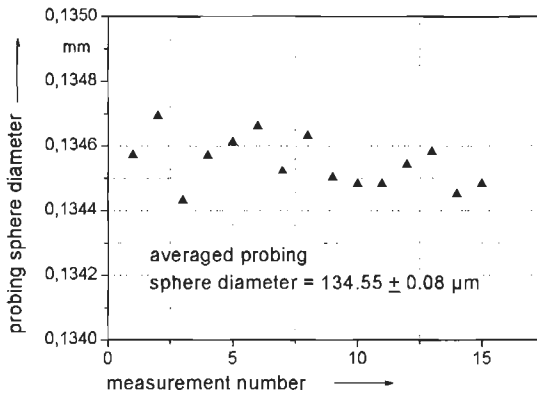


**figure 3:** Fibre probe sphere calibration using a 0.5 mm setting ring standard

one diameter measurement. The spread of all measured probing sphere diameters is  $\pm 0.15 \mu\text{m}$ . The standard deviation of the averaged diameter is  $0.08 \mu\text{m}$ , indicating that the measurement repeatability is good but should be improved in future.

One major uncertainty contribution is the illumination intensity. Two different types of illumination are simultaneously used: bright field illumination

for viewing the workpiece and fibre probe illumination. The measured probing sphere diameter depends on both light levels. Further investigations have to be performed to determine optimum operation conditions of the fibre probe and to determine its 2d measuring uncertainty.

## References

- [1] Brand, U.; Kleine-Besten, T.; Schwenke, H.: *Development of a special CMM for dimensional metrology on microsystem components*, in: Proc. ASPE Conf., Scottsdale, Arizona, 22<sup>th</sup>-27<sup>th</sup> Oct. 2000, 542-546
- [2] Guijun, Ji, Schwenke, H; Trapet, E: *Opto-tactile sensor for measuring small structures on coordinate measuring machines*. Proc. ASPE Conf. (1998)
- [3] Brand, U; Cao, S; Hoffmann, W; Kleine-Besten, T; Pornnoppadol, P; Büttgenbach, S: *A Micro-Probing System for Dimensional Metrology on Microsystem Components*. Proc. of 2nd euspen International Conference, Turin, Italy, May 27th – 31st, 2001, 266 – 269
- [4] Pornnoppadol, P.; Cao, S.; Nesterov, V.; Brand, U.; Bütefisch, S.; Schmidt, M.; Wilke, R.: Three-dimensional microprobe with reduced probing forces, Proc. Euspen 2002, Eindhoven
- [5] Miniature plane mirror interferometer for simultaneous measurement of path and angle, SP 500 D from SIOS Messtechnik GmbH, Am Vogelherd 46, 98693 Ilmenau, Germany
- [6] Coordinate Measuring Machine Video Check IP400 from Werth Messtechnik GmbH, Siemensstr. 19, 35394 Gießen, Germany

## Precision formtesting measurement technologies for microstructures

K. Schneefuß, T. Pfeifer

Fraunhofer Institute of Production Technology IPT, Aachen, Germany

### Abstract

Nowadays large area microstructured surfaces can be cost-effectively produced by innovative production technologies. The task for the measurement technology is to cover the process chain during the production of these 3D-nano- and microstructures. But measurement time and the characterization of steep slopes are the limiting factors for the measurement systems. In the following two possible approaches for solving these problems are presented. Active positioning allows the measurement of steep edges and interferometric formtesting concepts make a fast inspection of certain surface possible. The interferometric formtesting of prisms, spherical lens arrays or gratings are adapted to the microscopic range. Especially for the characterization of gratings, the measurement range has been extended by using multiple wavelength interferometry.

### Large area microstructured surfaces

Surfaces with micro- and nanostructures can be useful for various applications. Self-cleaning street signs with a „lotus leaf“ film for reduction of the surface adhesion of dirt particles can lower cleaning costs. Another example is the antireflecting „moth-eye“ structure that can be used for making computer monitors or other surfaces less reflecting. Further applications are micro retroreflectors or daylight guiding films for windows based on micro prism arrays. The mass production of microstructures on a large area film is the main requirement to make them more attractive for industry.

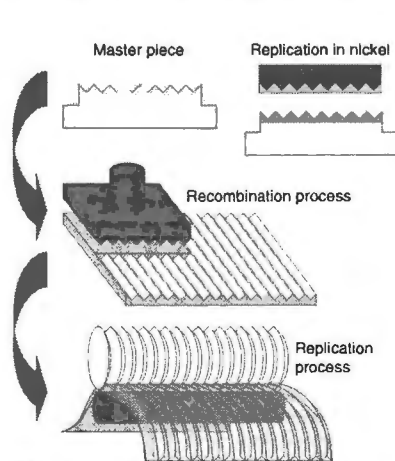


**Fig. 1:** Production process for large area microstructured surfaces

### Production processes for large area microstructures

At the Fraunhofer IPT micropatterns with surface roughness of a few nanometers are produced through micro-machining processes. But due to some limitations of the machine technology, the production of large area printing masters in the range of a square meter is currently impossible. Hence, small area surfaces are recombined through a step-and-repeat process and then replicated by electro-forming in nickel to cover stamping rolls for thin structured films (Fig. 1). In some cases an additional step of electro-forming can be necessary if only the negative masterpiece can be produced due to restrictions of the diamond tool geometry.

### Measurement methods for microstructures

Typical measurement techniques for microstructured surfaces are e.g. confocal microscopy, white-light interferometry,

laser autofocus and optical sensors [1]. The measurement time and the characterization of steep slopes e.g. in right angle prisms are the limiting factors for the use of the mentioned measurement techniques as a quality inspection tool for large area microstructures. In the following two possible solutions for these problems are presented. The active positioning allows the measurement of steep edges and the application of formtesting interferometry reduces measurement time at certain geometries.

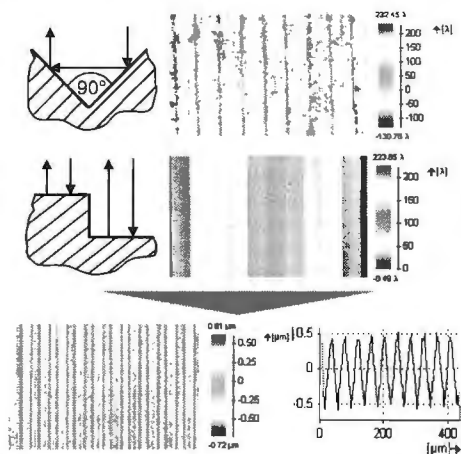


Fig. 2: Use of the active positioning

### Active positioning

During the procedure of active positioning, microstructures with steep slopes are tilted until a part of the surface becomes measurable. The light reflection in a micro prism array leads e.g. to a measuring signal only from the peaks and the valleys of the structure (Fig. 2). The measurement result can be significantly improved by tilting the surface. Two measurements from different directions are performed and linked automatically by means of a stitching algorithm. By this approach a complete characterization becomes possible also if the surfaces are not cooperative.

### Interferometric formtesting of microstructures

Formtesting interferometry has several advantages compared to other measurement techniques. The use of phase information in interferometry provides a very fast form measurement by taking only a few pictures through phase shifting algorithms, but it is very difficult to adapt the formtesting interferometry to the microscopic scale. Highly corrected lens systems have to be used in order to provide a high quality measurement of the microstructured surface. For measuring the angular error e.g. of a right angle prism only five phase shifted pictures have to be taken (Fig. 3). If the right angle is exact without any error, it reflects an incident plane wavefront as a single emerging plane wavefront. Otherwise, the reflected wavefront consists of two plane wavefronts and the tilting error gives information on the angle error of the prism [2]. The same measurement method can be used to determine the geometrical errors in a corner cube.

Another application of interferometric formtesting is the test of spherical lens arrays (Fig. 4) [3]. By using special optical systems it is possible to measure lenses with a radius of about 150  $\mu\text{m}$ . But in these dimensions the detection of the focus point on the lens and the adjustment of the sphere according to the produced radius is time consuming and an automatic adjustment of the specimen is needed.

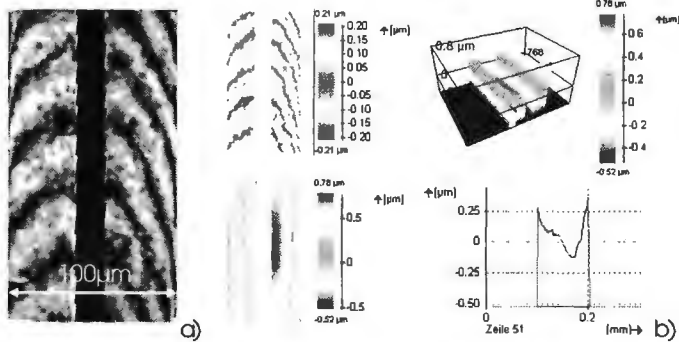


Fig. 3: Interferogram a) and evaluation b) during a prism array test

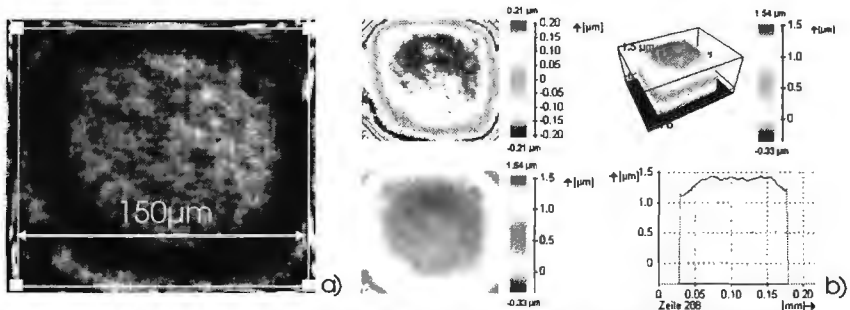


Fig. 4: Interferogram a) and evaluation b) during a spherical lens array test

### Adjustment of the specimen

Not only in the case of micro spheres but also in every other interferometric formtesting method for microstructures the adjustment of the specimen is a very difficult task. To speed up the alignment of the optical system an automatic adjustment mode based on the positioning system WYKO Ultramount with five degrees of freedom is realized. The manual operations are replaced by DC Mike Drives from Physik Instrumente PI. Moreover, a computer control was developed allowing direct communication with the optimization software. The adjustment procedure consist of an automatic alignment mode and a fine adjustment. Different target values and optimization algorithms have been developed and examined to perform the fastest adjustment of the specimen.

### Extension of the measuring range by multiple wavelength interferometry

The limited vertical measuring range of the formtesting interferometry can be extended by sequential multiple wavelength interferometry. By this procedure, measurement results, which were taken using different wavelengths, are linked to simulated measurements with substantially larger effective wavelengths (Fig. 5). Since the vertical measuring range depends on the used wavelength, it can be significantly extended [4].



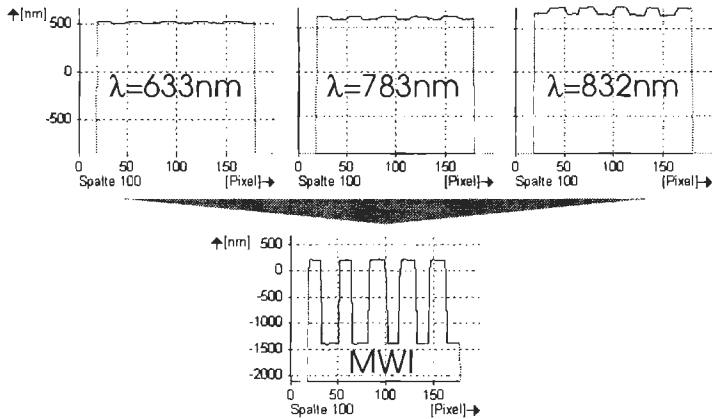


**Fig. 5:** Combination of measurements using different wavelengths to extend the measuring range

## Summary and acknowledgements

Innovative production technologies make low price mass production of microstructures on large area films possible and therefore make the films more attractive for industry and private customers. Two improvements concerning the high measurement time of conventional systems and the measurement of steep slopes have been presented. Thus, steep edges can be measured by using active positioning and certain geometries e.g. right-angle prisms, corner cubes, lens arrays or gratings can be characterized by formtesting interferometry very fast. To increase the vertical measurement range a sequential multiple wavelength approach is adapted to the microscopic range and therefore allows a correct measurement of steps larger than the real measuring wavelength. The adjustment problems using formtesting interferometry for microstructures have been solved by using automatic alignment modes and fine adjustment by optimization algorithms. The presented results have arisen from a national research project financially supported by the German Ministry of Education and Science (BMBF) and the Technology Center Physical Technologies of the Association of Engineers (VDI-TZ) (FKZ: 13N7746).

## References

- [1] Pfeifer, T.; Bitte, F.; Dussler, G.: Optical Metrology for Microstructure Inspection, Proceedings of the International Seminar on Precision Engineering and Micro Technology, Aachen (Germany), 2000, Weck M. (editor), Shaker, Aachen, 2000, pp. 39-52
- [2] Malacara, D.: Optical Shop Testing, John Wiley & Sons, New York, Chichester, Brisbane, Toronto, Singapore (1992)
- [3] Schwider, J.; Falkenstörfer, O.: Twyman-Green interferometer for testing microspheres. In: Optical Engineering 34 (1995) 10, pp. 2972-2975
- [4] Wyant, J.C.; Creath, C.: Two-Wavelength Phase Shifting Interferometer and Method, US Patent 4,832,489 (1986)

## New developments on ball diameter measurement

G. Kotte, K. Dirscherl

NMi Van Swinden Laboratorium, PO Box 654, 2600 AR Delft, The Netherlands

Telephone: ++31 15 2691500; Fax: ++31 15 2692971;

e-mail: gkotte@nmi.nl ; kdirscherl@nmi.nl

### Abstract:

In the recent past a calibration set-up was developed for the calibration of ball diameters in the range of 0,5 up to 12 mm. The ball diameter is measured between two perpendicular planes at several measuring forces. The ball diameter at zero force can be derived by fitting the measurement data (the measured **ball diameter** and the applied **force**), to the Hertz formula for the elastic deformation of a ball on a flat surface.

For a well-founded uncertainty on the ball diameter at zero force both the uncertainty on the diameter measurement and the uncertainty on the applied force should be taken into account. NMI-VSL has developed an application in Mathematica employing an Excel spreadsheet for interface. The software takes the measured ball diameters, the accompanying force and both their **individual uncertainties** as input and returns the ball diameter and the material constant and **both their uncertainties** to the spreadsheet.

### Measurement set-up.

In a gauge block interferometer the perpendicular distance between two reflective, optical flat and parallel surfaces can be measured. Normally this is a gauge block wrung onto an optical flat. This interferometer set-up can also be used to determine the total length from the top of a gauge block to the optical flat with a ball between the gauge block and the optical flat, as long as the top face of the gauge block is parallel to the optical flat (see figure 1). This, however, requires a provision to keep the gauge block on top of the ball and parallel to the optical flat.

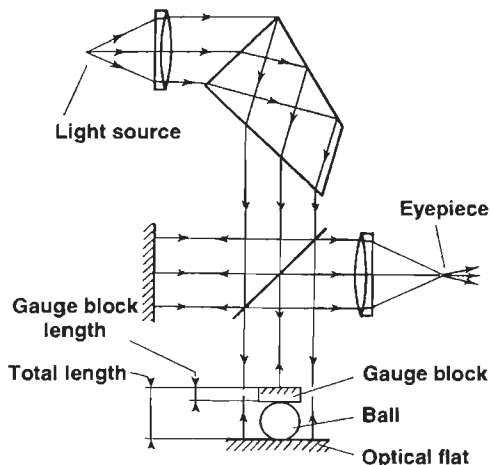
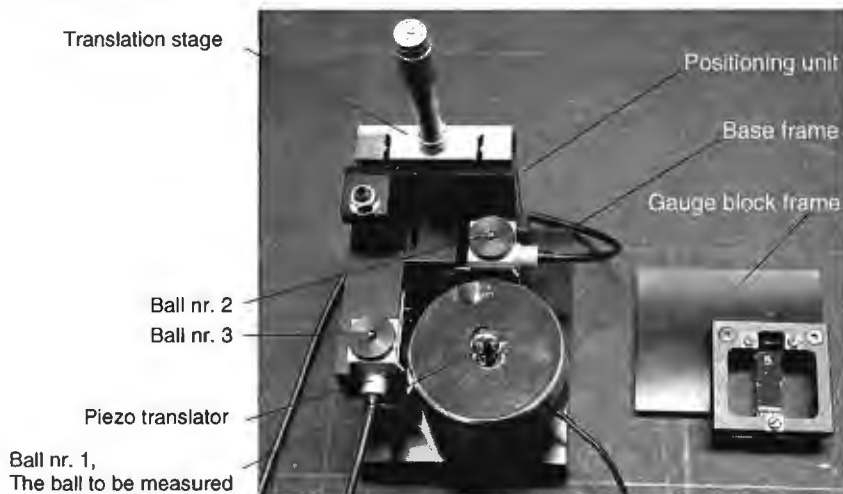


figure 1: The measurement principle applied in a Kösters gauge block interferometer

### The instrument.

The instrument has been developed to meet the requirements as specified in the previous section "measurement set-up". It is a compound of a base frame, a positioning unit and a separate frame containing the gauge block (see figure 2).



**figure 2:** Explanation of the instrument

The gauge block frame is positioned on 3 balls. One of them is the actual ball to be measured located on the optical flat. It supports the gauge block.

The other two balls support the gauge block frame. Their position is adjustable. Each of them is fixed on top of a piezo translator for fine adjustment. Both piezo's are mounted in a frame attached to a translation stage for coarse adjustment.

To ensure a statically determined support of the gauge block, the frame itself is provided with one blind conical hole and a V-shaped groove as contact areas for the balls on top of the piezo's.

To change the contact force of the gauge block on the ball, additional weights can be added on specific positions on the gauge block frame (see figure 3). In total, 7 forces in the range of 0,022 N up to 2,34 N can be generated by weights in pre-defined combinations on pre-defined locations on the gauge block frame.

### Characterisation.

To perform a traceable measurement the instrument is characterized on 3 items:

a) The repeatability of the measurement process in the gauge block interferometer is determined by measuring a ball over the same centre line in 7 different variations. They include rotation of the ball and optical flat, re-positioning of the gauge block frame, re-positioning of the instrument in the interferometer. This resulted in a single standard deviation  $\sigma = 15$  nm.

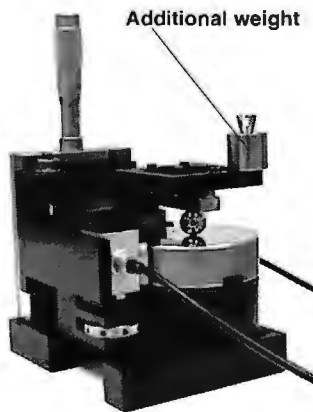


**figure 3:** The gauge block frame on its positioning points.

- b) The gauge block length is calibrated with a standard uncertainty of 15 nm. The deviation in parallelism is determined on 0,03  $\mu\text{m}$ .
- c) The measuring forces are determined on a calibrated weighing machine, 7 measuring forces are defined.

### Calculations.

The true ball diameter at zero force is defined by its nominal diameter and the true deviation at zero force. The deviation at force  $F$  is the measured parameter.

To derive the true deviation at zero force, the formula of Hertz for a one sided indentation is used.

One-sided indentation  $\delta$  according to Hertz:

$C$  : material constant

$$\delta = C_{mat} \sqrt[3]{\frac{F^2}{D}}$$

Deviation  $d_0$  from the nominal ball diameter at zero force:

$df$  : measured deviation from the

$$d_0 = df + \delta$$

From [1] and [2] a function can be derived:

$$df = d_0 - C_{ext} \sqrt[3]{F^2}$$

The measurement result of a ball calibration is a set of data points: values for  $df$  with

$$C \text{ can be calculated } C_{mat} = \frac{\sqrt[3]{D}}{2} \cdot C_{ext} \quad [4]$$

corresponding values for  $F$ . The Mathematica application fits those data points to formula [3]. Together with the set of data points the Mathematica application accepts the individual expanded uncertainties on each value of  $df$  and each value of  $F$ .

The result of the analysis is the value for the constants  $d_0$  and  $C_{ext}$  and both their individual expanded uncertainties.

### Uncertainty evaluation and measurement result.

#### The uncertainty on $df$ .

Using data from the measurement process and the characterisation of the instrument the expanded uncertainty of  $df$  is  $2 \cdot \sqrt{28^2 + (0,44 \cdot D)^2}$  nm, with  $D$  is the nominal ball diameter in mm. For  $D = 4$  mm, the expanded uncertainty is 56 nm.

### The uncertainty on $F$ .

Using data from the measurement process and the characterisation of the instrument, the expanded uncertainty for each measuring force is stated in the table below.

Force number	1	2	3	4	5	6	7
Average force (N)	0,022	0,051	0,168	0,560	1,02	1,75	2,34
Expanded uncertainty (N)	0,007	0,005	0,005	0,015	0,05	0,08	0,12

### The calibration result of a 4 mm steel ball and a 2 mm ruby ball.

Analysis results of the fit

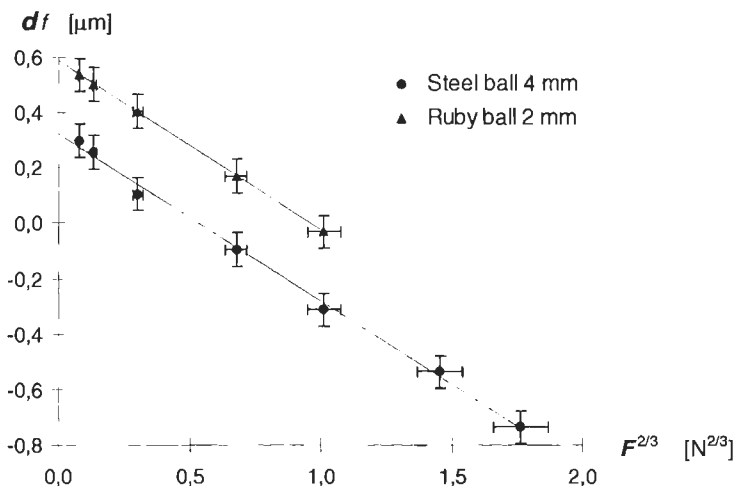


figure 4: Results of the fit of data points to formula [3].

Parameter	Ruby ball	Steel ball
Nominal diameter [mm]	2	4
$d0$ [ $\mu\text{m}$ ]	$+0,587 \pm 0,033$	$+0,320 \pm 0,029$
$C_{\text{mat}}$ [ $\frac{\mu\text{m}^{4/3}}{\text{N}^{2/3}}$ ]	$0,380 \pm 0,040$	$0,480 \pm 0,023$

### Discussion.

Due to the Mathematica application developed by NMI-VSL it is possible to perform the ball measurement fully traceable. A remark should be made regarding the uncertainty in  $df$ . The influence of the gauge block length definition and roughness effects is estimated to have a standard uncertainty of 20 nm. Since this is a dominant value it deserves a closer investigation. The effect of the weight of the ball on measurements appears to be negligible for balls with a diameter  $D \leq 5$  mm.

# The Calibration of Parallel-CMM: Parallel-Coordinate Measuring Machine

O. Sato<sup>1</sup>, M. Hiraki<sup>2</sup>, K. Takamasu<sup>1</sup>

<sup>1</sup> The University of Tokyo, Japan; <sup>2</sup> Tokyo Denki University, Japan

## Abstract:

The Coordinate Measuring Machine (CMM) is widely used for the 3D measurements of objects. Traditional CMM is based on a serial mechanism whose drawbacks are weakness against external forces and the accumulation of errors. We developed a new type of CMM based on a parallel mechanism. The advantages of this mechanism are its robustness against external force and error accumulation. On the other hand, this mechanism has disadvantages. One is its difficulty in its calibration. We make our prototype of parallel CMM to calibrate it easy by using unique joints. This paper deals with the calibration of our prototype of parallel CMM.

## Introduction

The Coordinate Measuring Machine (CMM) is widely used for the 3D measurements of objects. Traditional CMM is based on a serial mechanism: the components from base unit to end-effector i.e. base unit,  $x$ -axis,  $y$ -axis,  $z$ -axis and measuring probe are connected serially. But some drawbacks of this mechanism are its weakness against external force and the accumulation of errors. Therefore CMM tends to become large and heavy in order to avoid the influence of the bending and twisting of its components and to decrease measurement errors. Because of its weight, it has been a very difficult problem to make large CMM capable of fast 3D measurement.

We develop a new type of CMM based on a parallel mechanism where the base unit and end-effector are connected by six links parallel. The advantages of this mechanism are its robustness against external force and error accumulation<sup>[1]</sup>. Therefore we will be able to make larger measuring machine that can measure large objects quickly. On the other hand, there are some disadvantages by using parallel mechanism for CMM. One is the difficulty in the calibration of CMM. Because of its difficulty in solving its forward kinematics and large number of parameters its geometrical model includes, it is hard to calibrate parallel mechanism efficiently.

To make the calibration of parallel CMM easy, we make our prototype by using unique spherical joint consists steel balls and magnets. That allows higher repeatability of positioning and setting-up.

At first, the prototype of parallel CMM that has been developed in our laboratory is introduced. Next we discuss about the parameters we should identify to calibrate parallel CMM and how to calibrate it. Lastly, we give the suggestion of the method to calibrate our prototype efficiently.

## Prototype of parallel CMM

Fig. 1 shows the prototype of parallel CMM. This prototype has 3 DOF and its forward kinematics can be solved analytically.

This mechanism consists three linear actuators, three linear scales, six connecting rods, end-effector and spherical joints. All heavy components, linear actuators and linear scales, are fixed on the base unit, so the upper part of this mechanism is very light and can move quickly. The end-effector can move only  $x$ ,  $y$  and  $z$  axis and does

not rotate. The repeatability of positioning of the end-effector is about  $2\mu\text{m}$ .

The end-effector, connecting rods and carriers are connected by the spherical joints using steel balls and magnets shown by Fig. 2. This spherical joint consists a magnet and triangle hole and holds the steel ball at three points on its spherical surface. The advantage of the joint is high repeatability because of no gap between the housing and the ball.

Using this joint gives the high repeatability of the position of the end-effector when we separate all connecting rods and end-effector from the base plate and reset up them when each position of the carriers are not changed (Fig. 3, 4). This means we can choose each way of calibration for each component.

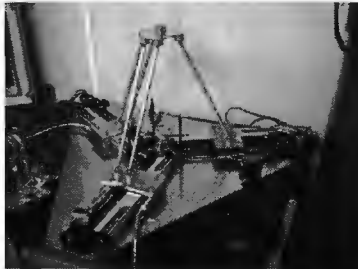


figure 1: Prototype of parallel CMM.

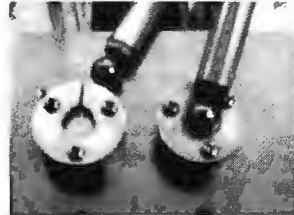


figure 2: Spherical joints using magnet.

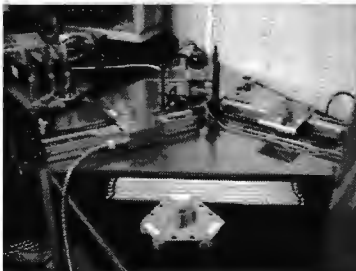


figure 3: Separating all components.

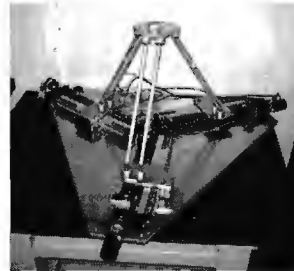


figure 4: Setting up all components.

### Parameter identification

To make high accuracy parallel CMM, it needs to calibrate parallel CMM. The first step of calibration is parameters identification of its geometrical parameters<sup>[2]</sup>. The geometrical model of parallel CMM includes 39 geometrical parameters. When we make a parallel CMM of large size, some parameters can be identified directly with high accuracy. Because of using spherical joints shown in Fig.2, we assures that each geometrical value of parameter measured by other way does not change after setting up. Here we classify into four categories depending on the way of parameter identification.

### End-effector

The geometrical parameters of the end-effector are on the relative position between

the probing sensor and each spherical joint. These parameters are three dimensional data. We can make a small end-effector when we make parallel CMM of large size. Therefore it is good to get the values of the parameters of end-effector by measuring by another CMM.

### Connecting rods

The geometrical parameters of connecting rods are the length between two balls joined at the each end of connecting rods. These parameters are one dimensional data. And they can be measured easily when the connecting rods become longer.

### Carrier

The parameters of the carriers are the height of the joints and the distance between two joints on the carrier. These parameters are three dimensional data. And we can make small carriers when we make parallel CMM of large size. Therefore it is good to get the values of the parameters of carriers by measuring by another CMM.

By measuring each value of above parameters and use their values to solve forward kinematics of parallel CMM, we can reduce number of parameters to calibrate.



figure 5: End-effector.

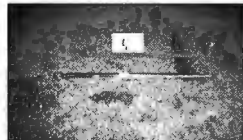


figure 6: Connecting rods.

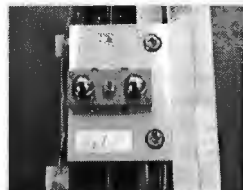


figure 7: Carrier.

### Geometrical model of base plate

Differently from above parameters, the geometrical parameters of linear actuators and linear scales change their values by separating/resetting. And it becomes hard to measure their values directly when the parallel CMM gets larger or regardless of the size of the parallel CMM.

The parameters of linear actuators are the arrangements of them on the base plate. The ones of linear scales are the arrangements of them on it and the initial origin of each scale. We calculate them with the least squares method. Fig. 8 shows the geometrical model of base plate. Geometrical parameters including in this model are the arranged position of each actuator,  $\theta_1$ ,  $\theta_2$ ,  $\phi$ ,  $r$ , and the initial origin of each scale,  $\delta q_1$ ,  $\delta q_2$ ,  $\delta q_3$ .



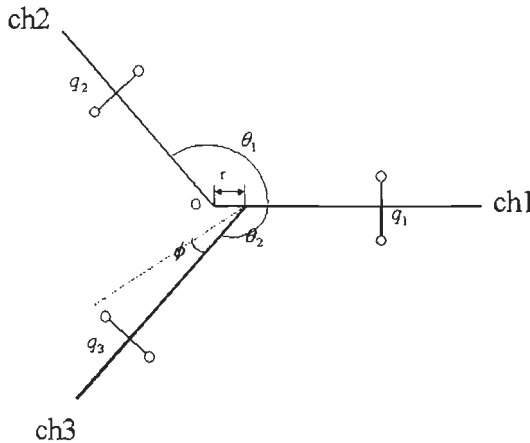


figure 8: Geometrical model of base plate.

## Calibration of parallel CMM

We did the experiment of parameter identification for our prototype. Geometrical parameters of end-effector, connecting rods and carriers are measured by the CMM. And those of base plate are calculated using the result of measuring by the CMM and the signal from each linear scale.

We put a steel ball on the end-effector. Then we move the end-effector at 64 points in the workspace and measured the centre of the ball by CMM.

All geometrical parameters including in Fig.8 and the initial origin of each scales are identified with high accuracy. The result of our experiment, the positioning error after calibration reduced from  $500\mu\text{m}$  to  $7\mu\text{m}$ .

## Conclusion

In this paper, the prototype of parallel CMM is introduced. Using unique spherical joints, this prototype has the high repeatability of the position of the end-effector when we separate all connecting rods and end-effector from the base plate and reset up them. Then we suggested to calibrate each component of parallel CMM by each method.

We classified the geometrical parameters of each component into four categories depending on the way of parameter identification, and decided each method to calibrate each component. We calibrated the parameters of the end-effector, the connecting rods and the carriers by measuring directly with CMM, and the parameters of the base plate by the least squares method.

We calibrated our prototype of parallel CMM. The result of our experiment, the positioning error after calibration reduced to  $7\mu\text{m}$ .

## References

- [1] O. Sato, M. Hiraki, K. Takamasu and S. Ozono: Calibration of 2-DOF parallel mechanism, Initiatives of precision engineering at the beginning of a millennium, Kluwer academic publishers, 2001, pp. 734-7738.
- [2] Merlet, J.-P.: "Parallel Robots", Kluwer academic publishers, 2000.

# An Evaluation of Error Space in Three Dimensional Coordinate Measuring Machine(3DCMM) by Sequential Two Points Method

K. Umeda<sup>1</sup>, H. Sato<sup>1</sup>, T. Sone<sup>2</sup>, W. M. He<sup>1</sup>, M. Sagara<sup>3</sup>, H. Matsuzaki<sup>3</sup>

<sup>1</sup>Chuo University, Tokyo, Japan;

<sup>2</sup>Makino R&D Center, Kanagawa, Japan; <sup>3</sup>Toshiba Machine, Shizuoka, Japan

Abstract:

Sequential two points method which was developed to identify the straightness motion of machine tools and cut surface of machined parts is applied to evaluate the straightness error motion of the probe in 3DCMM. Repeating the measurement on the objective plane, a method to make a planelike error form is proposed by combining the measured straightness error motions. If the procedures are made for the respective coordinates, error space can be evaluated. This could be more easily done by any other conventional methods. A compensation method is proposed, which is possible to improve measurement accuracy without changing hardware configuration of the 3DCMM.

## Introduction

Three Dimensional Coordinate Measuring Machine (3DCMM) is indispensable in manufacturing system as an apparatus of accuracy measurement, and much effort has been made for developing methods of calibration and compensation[1][2] and for evaluating accuracy performance of machines[3][4]. In spite of the effort it seems to have been difficult to obtain definite and reliable results.

Sequential two points method(STPM) was developed to evaluate straight form error of machine tools. By the method it is possible to identify both error forms for the tool post and the machined part by single feed traverse of the tool post in terms of simple algorithm for the data[5][6]. The method has advantages in that any standard of specific straightness is not required, the algorithm is simple, repetitive measurement accuracy is high, and the result is stable even under vibration environment.

In this investigation, application of STPM to 3DCMM is attempted to evaluate straightness error movement of the probe of 3DCMM, and consequently its error space, which makes it possible to compensate the error for the work space and to improve performance in accuracy.

## Experimental facilities

### Principle of STPM

In figure 1 schematic view of STPM is illustrated. When an engine lathe is supposed, two sensors which can measure the relative distance to whatever objective or machined part are located on the tool post with the distance L inbetween. When the tool post is fed and the data are acquired stepwise at positions of L multiplied by integer, two data series

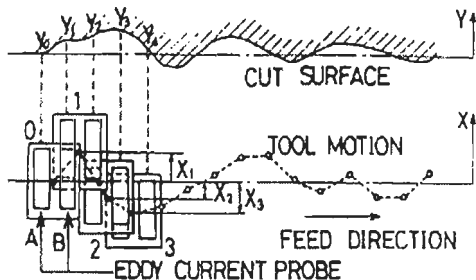


figure 1: Principle of sequential two points method.

for the individual sensors are obtained. The data are processed by the following equations,

$$X_k = X_{k-1} + D_{k,A} - D_{(k-1),B}, Y_k = X_k + D_{k,A} - D_{0,B}; X_0 = 0, X_1 = 0, Y_0 = 0 \quad (1)$$

where  $D_{k,A}$  and  $D_{k,B}$  are the measured data by the sensors A and B,  $X_k$  and  $Y_k$  are the straightness error motion for the tool post and form for the objective respectively. It is shown that error forms could be simultaneously and independently derived.

**Measurement system**

In figure 2 a conceptual schematic view is illustrated. The machine is RVA 600, which is bridge move type and is made by Tokyo Seimitsu Co. Ltd. A plate of Al with the size of 400x650x20 and machined by a conventional milling machine is adopted as the objective. Capacitance type of displacement sensor made by Ono Sokki Co. Ltd., is utilized, whose specification is 0-0.5 mm as measurement range, 0.1µm as resolution, 8 mm as the diameter of the sensor, 20 mm as the distance of the two sensors.

**Example of the measurement**

Basic characteristics of the straightness error forms of the probe parallel to X axis are depicted in figure 3. The first error form was evaluated at Y=0 for range of 380 mm with an interval of 20 mm and same evaluations were repeated at the coordinates of Y axis in the range of 320 mm with interval of 20 mm, which means that 17 error forms of the probe movement are obtained. In figure 3 the error forms of the average and the maximum and the minimum fluctuation are arranged. When the evaluation at the left side of the forms can be made zero, those at the right side are supposed to fluctuate around zero. In the figure these are adjusted zero for the comparison. If the same ones are attempted by system of the laser interferometer, arrangement for the measurement would be much more time consuming, and the data would easily fluctuate due to the environment. In case of STPM the operation to evaluate the bundle of the straightness error forms is easily realized by CNC command of the machine.

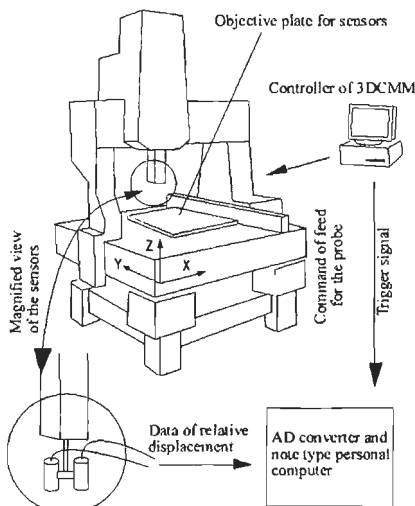


figure 2: Application of the method to 3DCMM.

In figure 3 the error forms of the average and the maximum and the minimum fluctuation are arranged.

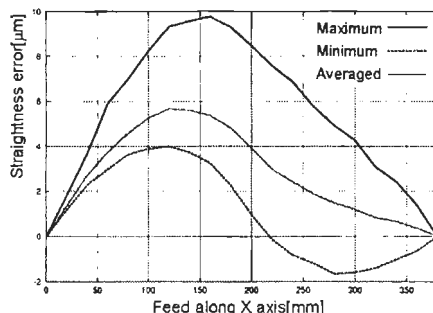


figure 3: Straightness error motion of the probe along X axis.

### Composition of planelike error form

In coordinate system (X, Y, Z) among the work space of 3DCMM, a plane which is prescribed by  $(X_i, Y_j, Z_k)$  is considered, where  $i = 0, 1, \dots, l, j = 0, 1, \dots, m, k = 0, 1, \dots, n$ . A bundle of the straightness error forms parallel to X axis are measured on a plane of  $Z_0$ , that is,  $(X_i, Y_j, Z_0)$ . In practical application of STPM, slight discrepancy  $\Delta$  is inevitably left between the tip of two sensors[6]. It has been demonstrated that  $i\Delta$  is linearly accumulated at  $i$ -th position of the sensors on the measured straightness error form. Then corrected error form can be obtained by subtracting the following accumulation from the raw measured results,

$$z = i\Delta \quad (i = 1, 2, \dots, l) \quad (2)$$

The evaluation at the right-hand edge of the forms in figure 3 shows the results with the subtraction. However, it is presumed that residue  $\delta_z(X_i, Y_j, Z_0)$  would remain for the forms obtained for  $Y_j$  ( $j = 1, 2, \dots, m$ ), even if this correction is conducted. At the starting and the finishing conditions at the both ends of the error forms,  $(X_0, Y_j, Z_0)$  and  $(X_l, Y_j, Z_0)$ , the straightness error forms for the direction of Y axis are measured, which give boundary at the both ends for the bundle of the forms, so that the planelike error form is constructed.

Figure 4 illustrates the flow of composing a planelike error form mentioned above.

In figure 5 a planelike error form for the probe movement is constructed from the straightness error forms in figure 3.

### Error space and its compensation

By the method proposed above, a planelike error form for arbitrary  $Z_k$  can be constructed, and, it is possible to estimate the error space by constructing enough number of planelike error forms. The same procedure can be applied to the directions X and Y which are vertical to Z, and planelike error forms for the  $X_i$  and  $Y_j$  are constructed. Consequently, error space for 3 axes (X, Y, Z) is constructed. Then it is possible to estimate error components for (X, Y, Z) at arbitrary points among the measurement range of a 3DCMM.

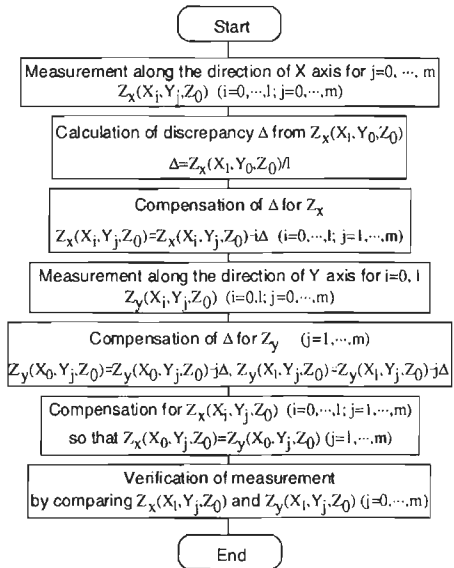


figure 4: Flow of composing planelike error form for  $Z=Z_0$ .

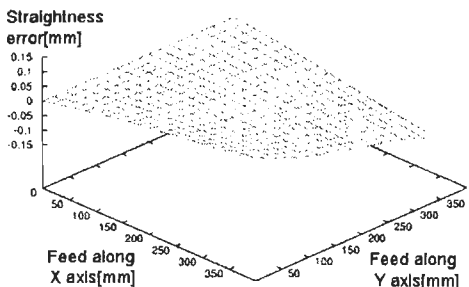


figure 5: Error curved surface of the straightness motion of the probe.

The points on which errors are directly measured are discrete. The error at an arbitrary point can be obtained by applying interpolation or least square method. When the error  $e_z(X, Y, Z)$  is obtained by interpolation or LSM, the compensation of the error is easily performed by subtracting the  $e_z$  from  $Z$ . By applying the method, the measurement accuracy is improved without any change of hardware configuration.

## Conclusion

It was demonstrated that sequential two points method could be well applied to evaluate the straightness error motion of the probe of 3DCMM. The conclusions could be summarized as follows.

1. It was confirmed that the straightness error form can be accurately identified by STPM. The measurement operation can be easily extended to planelike error form.
2. An algorithm which constructs planelike error form from a bundle of the straightness error forms was demonstrated, in which a method that gives conditions at the both ends of the error forms is proposed.
3. A method compensating the error form is proposed and the effectiveness is verified. The accuracy performance could be improved by software alteration.
4. A procedure which derives error space for measurable range of the machine on the basis of planelike error forms is proposed. This makes it possible to compensate error among total measurement range, which certainly improves the accuracy performance of the machine.

## Acknowledgements

The authors express their sincere thanks to the support by Project "Advancement of Measurement of Macro Error Form(97S21-005)" from 1997 to 1999 by New Energy Development Organization(NEDO), and Project "Advancement of Straightness Error Measurement by Sequential Two Points Method" by Foundation, Promotion of Machine Tool Engineering in 1996 and 1997.

## References

- [1] Kunzmann, H., Wäldele, F., 1988, Performance of CMMs, *Annals CIRP*, 37/2:633-640.
- [2] Evans, C., Hocken, R., Estler, W.T., 1996, Self-Calibration: Reversal, Redundancy, Error Separation, and Absolute Testing, *Annals CIRP*, 45/2:617-634.
- [3] Kunzmann, H., Trapet, E., Wäldele, F., 1995, Results of the International Comparison of Ball Plate Measurements in CIRP and WECC, *Annals CIRP*, 44/1:479-482.
- [4] Balsamo, A., Franke, M., Trapet, E., Wäldele, F., Jonge, L.D., Vanherck, P., 1997, Results of the CIRP-Euromet Intercomparison of Ball Plate-Based Techniques for Determining CMM Parametric Errors, *Annals CIRP*, 46/1:463-466.
- [5] Tozawa, K., Sato, H., O-hori, M., 1982, A New Method for the Measurement of the Straightness of Machine Tools and Machined Work, *Trans. ASME, J. Mach. Des.*, 104/3:587-592.
- [6] Tanaka, H., Sato, H., 1986, Extensive Analysis and Development of Straightness Measurement by Sequential Two-Points Method, *Trans. ASME, J. Eng'g Ind.*, 108/3:176-182.

## Development of a scanning force microscope employing a quartz tuning fork as the force sensor

A. Grant<sup>1</sup>, H.U. Danzebrink

Physikalisch-Technische Bundesanstalt (PTB), Bundesallee 100,  
D-38116 Braunschweig, Germany

### Abstract

The high quality factor (Q-factor) of the resonance of a quartz tuning fork has resulted in its wide exploitation as a force sensor in scanning probe microscopy [e.g. 1-3]. We use commercial cantilevers to provide these tuning forks with a sharp tip in order to probe the surface. Furthermore, we demonstrate that amplitude modulation (AM) techniques result in a system response that is too slow for feedback control purposes using these high Q-factors. To this end, we show an adaptation of the system to implement frequency modulation (FM) detection that overcomes this obstacle and facilitates retention of a high system bandwidth.

### Tuning fork probe

In this work, a commercial cantilever was sheared from the main chip body and subsequently glued to the tuning fork [4] in the manner portrayed in figure 1. This figure shows attachment of a probe for use in the shear mode of operation. Alternatively, the probe may be attached parallel to the tuning fork tine, which allows operation in a similar fashion to regular tapping mode (see figure 2).

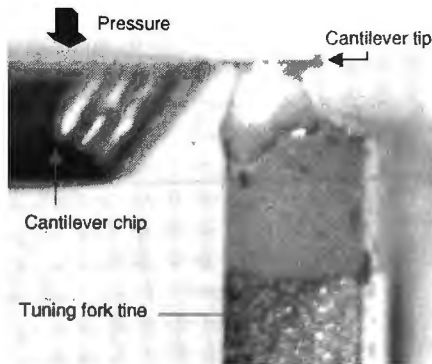


**figure 1:** CCD camera image of probe tip attached to tuning fork tine

Once the glue attaching the cantilever to the tuning fork tine has cured, the cantilever chip is removed by exerting pressure at the point illustrated in figure 1.

Applying a mass to one of the tuning fork tines in this way may disturb the symmetrical mass ratio of the tuning fork tines and lead to a reduction in the Q-factor. However, provided a minuscule mass of glue is added, such as that shown in figure 1, there is a negligible reduction of the tuning fork Q-factor. This helps retain a Q-factor that is much higher than that currently available with commercial cantilevers operated under ambient conditions.

<sup>1</sup> Now at Cork Institute of Technology, Cork, Ireland

## Tip-to-sample distance regulation

### Amplitude modulation technique

Applying amplitude modulation (AM) techniques to regulation of the tip-to-sample distance provides insufficient feedback control due to a delayed amplitude response at these high Q-factors. This is illustrated in figure 2.

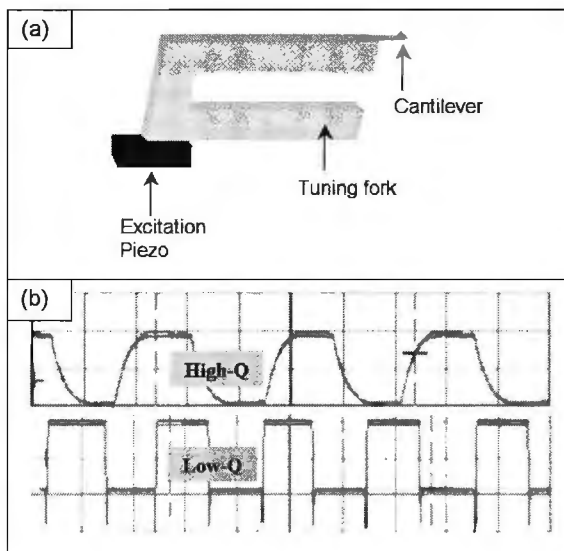


**figure 2:** (a) Tuning fork experimental set-up  
(b) Demodulated amplitude response whilst employing a high and low Q-factor tuning fork.

In this case, the cantilever was glued parallel to the tuning fork line as depicted in figure 2(a). Placing an excitation piezo under the tuning fork body, as shown in figure 2, drives the tuning fork at its resonance frequency. This excitation piezo was driven with a waveform that was amplitude modulated with an external square wave signal. The resultant tuning fork oscillation is demodulated to illustrate the difference between the response of high and low Q-factor tuning forks. Clearly, the integrated square wave signal shown in the upper curve of figure 2(b) for a high Q-factor tuning fork demonstrates a delayed amplitude response to the sharp transitions of the modulating square wave.

The delayed response shown for high Q-factor tuning forks renders AM techniques too slow for adequate tip-to-sample distance regulation. Excessive integration of topography information cannot be eliminated, even at the slowest scan speeds. This has crucial implications for SNOM (scanning near-field optical microscopy) applications, where, ideally, the probe should be maintained at a distance of only a few nanometers above the sample surface with a fast feedback response system.

### Frequency modulation technique

Frequency modulation (FM) techniques are not influenced by this delayed amplitude response and therefore offer a superior method for controlling the tip-to-sample distance in a SPM feedback control system [5].

The FM set-up is shown schematically in figure 3 and consists of a high stability phase locked loop (PLL) offering a high-resolution of  $\pm 5\text{mHz}$  (manufactured by Nanosurf). In addition to the PLL, tuning fork self-drive circuitry and an automatic

gain control (AGC) amplification stage fulfill the requirement to maintain a constant amplitude of oscillation.

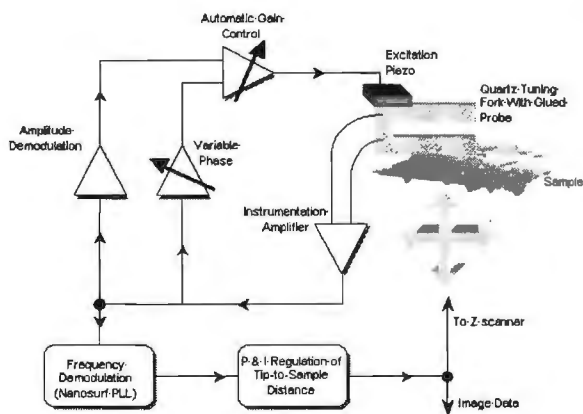


**figure 3:** Schematic of set-up to regulate the tip-to-sample distance whilst employing Frequency Modulation (FM) techniques.

techniques offer the ability to scan at increased scanning speeds due to the increased system bandwidth.

The delayed response associated with AM techniques limits the scanning speed to low values and leads to excessive integration of the feedback control signal. This results in broader image features than those recorded with a similar tip in contact mode. This may lead to false interpretation of images, particularly if the images are subsequently quantified. The use of FM techniques overcomes this constraint and places an increased confidence in quantifying images. Furthermore, FM techniques

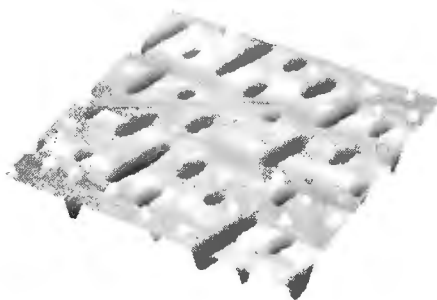


**figure 4:** 3D perspective of a CD sample

**Intercomparison of AM and FM imaging**

A compact disc (CD) sample consisting of pit structures was imaged in non-contact mode utilising both AM and FM techniques. Figure 4 illustrates the structure of this CD sample in a 3D perspective.

A comparison of AM and FM imaging performance can be determined from the two images shown in figure 5.



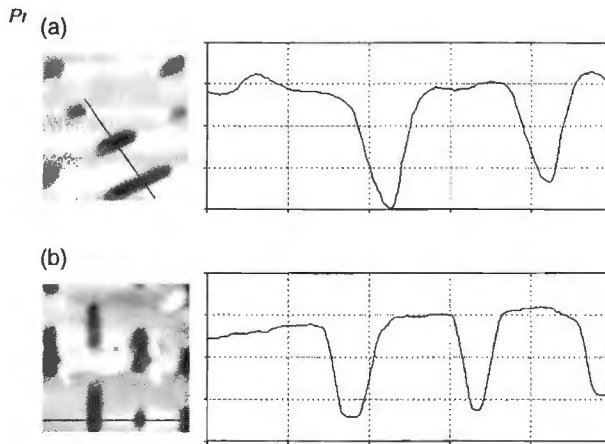


**figure 5:** Images of CD sample with  
 (a) AM and  
 (b) FM control of the tip-to-sample feedback control loop. A section through each image, perpendicular to the pit structure, is shown in the corresponding line profile.

There is a similarity in the imaging performance for both AM and FM control of the feedback control loop. However, the scanning speed during the acquisition of the AM image was significantly slower than that for the FM image. Furthermore, an analysis of the line profile for each image reveals a steeper pit wall in (b). The more gradual structure shown in (a) is due to an insufficient response to fast changes in the surface topography.

## References

- [1] Nonoptical tip-sample distance control for scanning near-field optical microscopy. Y-H Chuang, C-J Wang, J.Y. Huang and C-L Pan, *Appl. Phys. Lett.* **69**, 3312 (1996).
- [2] Piezoelectric tip-sample distance control for near field optic microscopes., K. Karrai, R.D. Grober, *Appl. Phys. Lett.* **66**, 1842 (1995).
- [3] Fast, high-resolution atomic force microscopy using a quartz tuning fork as actuator and sensor, H. Edwards, L. Taylor, W. Duncan and A.J. Melmed, *J. Appl. Phys.*, **83** (3), 980 (1997).
- [4] Non contact scanning force microscopy based on a modified tuning fork sensor. H. Göttlich, R.W. Stark, J.D. Pedarnig and W.M. Heckl, *Rev. Sci. Instrum.* **71**, 3104 (2000).
- [5] Frequency modulation detection using high-Q cantilevers for enhanced force microscope sensitivity, T.R. Albrecht, P. Grütter, D. Horne and D. Rugar, *J. Appl. Phys.*, **69** (2), 668 (1991).

# Optical form and geometry measurement of precision machined parts

P. de Groot

**zygo**, Laurel Brook Road, Middlefield, CT USA 06455, e-mail: peterd@zygo.com

## Introduction

Most measurements of precision-engineered parts are mechanical or tactile, for example using a stylus or contact probe. The often-proposed introduction of interferometric profiling to a machining facility requires many innovations to accommodate unpolished, non-optical surface textures as well as datum-referenced measurements that are unfamiliar in conventional optical testing.

In this short paper I review several candidate optical technologies for simple and complex form measurement and control of geometric dimensions. The list of technologies is not comprehensive, but rather a brief representation with references that may serve as a starting point for a more detailed survey.

## Flatness verification

Many manufactured parts have flat surfaces, often mated to other surfaces to make a seal. Tolerances for engine blocks and heads are typically 0.01 mm; however, extreme pressures in fuel injection systems require a tight metal-to-metal contact and a form tolerance of <0.001 mm to prevent leakage. A similar range of tolerances applies to sliding surface, for example, in precision stages.

Table 1 lists typical characteristics for flatness technologies for machined parts. "Typical" here does not mean "always." Some of the most creative work is the extension of these technologies outside these typical yet highly debatable boundaries.

	Fizeau	Grazing	Desensitized Interferometry	White light	IR scanning
Part size (mm)	5 to 1000	10 to 200	10 to 100	0 to 20	5 to 75
GR&R ( $\mu\text{m}$ )	0.02	0.1	0.3	0.02 to 0.5	0.1
Surface finish	smooth only	smooth & rough	smooth & rough	smooth & rough	smooth & rough
Step height (mm)	0.1	1	3	Unlimited	Unlimited
Relative cost	Med	Med	Low	Med	High
Limitation	Not suitable for many machined surface textures	Image distortion, near contact measurement, shadowing	Sensitive to surface reflectivity	Reduced performance on rough surfaces and large parts	Low lateral resolution, high cost
Benefit	High accuracy	Rough parts appear smooth and highly reflective	Low cost, non contact, near normal incidence	Very flexible 3D measuring microscope	Fast, handles rough and recessed surfaces easily

Table 1: Optical flatness measurement technologies.

If one is fortunate enough to have a nicely polished surface and a flatness error of no more than a few microns, then the ubiquitous laser Fizeau interferometer is an ideal flatness tester<sup>1</sup>, providing surface height resolutions below 1 nm. Most machined and ground surfaces are however too rough for such an extremely sensitive instrument. In such cases, there are several alternatives.

The roughness limitation is closely related to the periodic nature of interference fringes, which also limits the accessible step height between disconnected surface regions. The fringe density and therefore the step height limit vary according to the technology. Grazing incidence<sup>2</sup> and Geometrically desensitized interferometry (GDI)<sup>3</sup> both generate widely separated fringes by means of the measurement geometry and can therefore handle roughness and step height 20 times larger than conventional visible-wavelength laser Fizeau interferometry.

Some interferometric techniques have no fundamental limit on the accessible step height. Scanning white light interferometry (SWLI) distinguishes between interference fringe orders by means of the fringe localization characteristic of a broad spectrum of wavelengths.<sup>4</sup> The scan direction orthogonal to the part surface can be several mm in length, accommodating tall step heights and other discontinuous features without ambiguity. SWLI has the interesting and important property that it has a precision rivalling that of laser Fizeau interferometry on polished surfaces,<sup>5</sup> but is nonetheless capable of handling rough surface textures that generate complex speckle patterns that traditionally was considered fatal to interferometric metrology.<sup>6</sup>

A recent addition to industrial form measurement is IR scanning, which is similar to SWLI but the mean wavelength is near 10 microns, well outside the visible white light regime. IR scanning uses a simple exposed filament and microbolometer in place of the halogen bulb and CCD camera pairing of conventional SWLI. IR scanning has the relative advantage that speckle effects are entirely eliminated and the interference fringes are clear and continuous even for rough surfaces.<sup>7</sup> The benefit is reduced sensitivity to surface texture, easy alignment and improved overall performance, particularly for those parts that are too large for a microscope.

Table 1 also lists the typical gage repeatability and reproducibility or GR&R capability for each of the example technologies. This number represents the 5.15- $\sigma$  range of expected values for repeated measurements of the same part, using different operators and with part removal and replacement. GR&R is the most widely accepted criterion for gage performance in precision parts manufacture and is the starting point for a meaningful assessment of uncertainty.

### **Complex, non-planar shapes**

After flat surfaces, the most common machined shapes are cylinders, bores and cones, followed by more complex 3D shapes. Optical technologies originally designed for flats and spheres must adapt to these more generalized form.

One of the earliest examples of optical metrology adapted to manufactured cylinders and bores is grazing incidence interferometry using axicon optics.<sup>8</sup> Commercial instruments using diffractive axicon optics are now available<sup>9</sup> and an extension to more complex rod forms is feasible.<sup>10</sup> A more general technique ideal for comparison testing is holography, which is highly sensitive to changes in form.<sup>11</sup> Fringe projection is the most affordable and flexible complex form tools,<sup>12</sup> although the gage capability is generally significantly lower than the other technologies listed. Although not listed in Table 2, SWLI is also playing an increasing role in complex form measurement. Adaptations of the technology include endoscopic probes for inspection of internal bores<sup>13</sup> and measurements of steeply curved shapes.<sup>14</sup>

Finally I note optical stylus technology, the idea being to replace a conventional mechanical stylus in a form metrology tool with a much higher speed and higher resolution single-point optical probe.<sup>15</sup>

	Fizeau	Axicon Grazing	Holography	Fringe projection	Optical stylus
Part size (mm)	5 to 1000	10 to 200	>10	>10	All
GR&R ( $\mu\text{m}$ )	0.05	0.3	1 to 10	10 to 100	0.1
Roughness ( $\mu\text{m}$ )	<0.1	<1	>0.1	>0.1	<0.2
Shapes	Spherical	Cylinders, rods	All	All	All
Relative cost	Med	High	Med	Low	High
Limitation	Polished surfaces only	Image distortion, near contact measurement	Limited precision for general shape measurement	Lowest precision	Requires mechanical staging and scanning
Benefit	High accuracy	Rough parts appear smooth and highly reflective	Excellent comparative technique	Very flexible 3D measuring microscope	Fast, handles rough and recessed surfaces easily

**Table 2:** Optical technologies for measurement of complex 3D shapes.

### Geometric dimensions

Unlike lenses and mirrors, precision-machined parts are usually destined for an assembly of tightly fitting, interdependent and sometimes actuated components, often with many sealing areas. The relationships between the surfaces of such parts are just as important as surface form. A new area of optical industrial metrology is therefore geometric dimensions, for which multiple views of a single object using two or more surface profilers are combined to create a volumetric image of the part, including parameters such as size, parallelism and orthogonality. This is not an easy problem, in that the profilers must measure with respect to a fixed datum.

Two solutions come to mind; the first being to perform a direct comparison of the test part to a known artifact such as a gage block of nearly the same size. The comparison may be done with the artifact in the field of view, or by sequential measurement with the artifact as a calibration aid. The second solution is to combine interferometric surface profiling with heterodyne distance-measuring interferometry. This second approach provides the greatest flexibility, and accommodates parts of any size without recalibration or change of artifact.

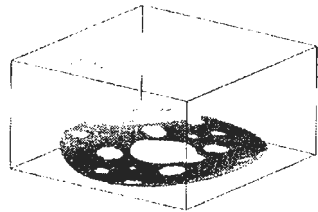


**Figure 1:** 3D volumetric image of a 30-mm diameter, 1-mm thick ground metal disk.

We have developed a dimensional measurement gage following these concepts into for datum-referenced inspection, qualification and sorting of metal parts for fuel injection and similar high-performance systems.<sup>16</sup> The instrument currently performs 100% optical inspection of over 4000 parts per day on a dozen different part types, with a gage capability for flatness, parallelism and thickness of 0.1, 0.15 and 0.3 microns, respectively; using a dual-port profiler and IR Scanning technology.

This last example completes this brief overview of high-precision optical metrology tools for industrial applications.

## References

- [1] D. Malacara, "Optical shop testing" 2<sup>nd</sup> Edition (John Wiley & Sons, Inc., NY, 1992).
- [<sup>†</sup>] N. Abramson, "The Interferoscope: a new type of interferometer with variable fringe separation," *Optik*, 30, 56-71 (1969).
- [3] P. de Groot, X. Colonna de Lega and D. Stephenson, "Geometrically desensitized interferometry for shape measurement of flat surfaces and 3D structures," *Opt. Eng.* 39(1) 86-90 (2000).
- [4] J. C. Wyant, "How to extend interferometry for rough-surface tests," *Laser Focus World* (September), 131-135 (1993).
- [<sup>‡</sup>] P. de Groot and Leslie Deck, "Surface profiling by analysis of white-light interferograms in the spatial frequency domain," *J. Mod. Opt.* 42(2), 389-401 (1995).
- [6] T. Dresel, G. Häusler and H. Venzke, "Three-dimensional sensing of rough surfaces by coherence radar," *Applied Optics* 31(7), 919-925 (1992).
- [7] X. Colonna de Lega, L. Deck and P. de Groot, "Method and apparatus for the metrology of precision engineered components" US 6,195,168 B1 (Feb. 27, 2001)
- [8] A. Archbold, J. M. Burch and A. E. Ennos, "The application of holography to the comparison of cylinder bores," *J. Sci. Instrum.* 44 489-494 (1967).
- [<sup>§</sup>] L. Denes and J. Salsbury, "Flatness, parallelism and other novel uses of grazing-incidence interferometry in precision engineering," *Proceedings ASPE*, 20- 23 (1995).
- [<sup>¶</sup>] T. Dresel, S. Brinkmann, R. Schreiner and J. Schwider, "Testing of rod objects by grazing incidence interferometry: theory," *Appl. Opt.* 15(11) 2921-2928 (1996).
- [11] S. Seebacher, W. Osten, T. Baumbach, W. Jüptner, "The determination of material parameters of microcomponents using digital holography," *Opt. And Lasers in Eng.* 36(2) 103-126 (2001)
- [12] K. Patorski and M. Kujawin'ska, "Handbook of the Moiré fringe technique," (Elsevier, Amsterdam, 1993).
- [13] M. W. Lindner "White-light Interferometry via an Endoscope," *Proc. SPIE Laser Interferometry XI: Techniques and Analysis* (to appear, 2002).
- [14] P. Andretzky, G. Häusler, "Interferometrical measurement of strongly curved polished surfaces," *Annual Report, Chair for Optics, University of Erlangen Nürnberg* (1996).
- [15] P. Drabarek, "Interferometrische Meßeinrichtung zum Erfassen der Form oder des Abstandes insbesondere rauher Oberflächen," German patent application DE19808273A1.
- [16] X. Colonna de Lega, P. de Groot and D. Grigg "Dimensional measurement of engineered parts by combining surface profiling with displacement measuring interferometry" *Proc Fringe 2001*, 333-340 (Elsevier, 2001).

## Recent developments at the PTB Nanometer Comparator

J. Flügge, R. Köning

Physikalisch Technische Bundesanstalt, Bundesallee 100, 38116 Braunschweig, Germany

### Abstract:

This paper describes recent developments and current status of the PTB nanometer length comparator. The comparator now is equipped with a heterodyne interferometer setup. Due to changes in the interferometer electronics, a higher data acquisition rate and subsequently a better repeatability of the detection of line edges was obtained. The paper also addresses the current situation of green light fiber coupling in vacuum.

### Introduction:

The PTB nanometer length comparator [1], was developed in cooperation with the Dr. Johannes Heidenhain GmbH and Werth Messtechnik GmbH. The comparator is designed to calibrate line-graduation scales, probes, photomasks, interferometers and incremental linear encoders in one axis with a maximum length of 610 mm.

The vacuum laser interferometer and its integration according to the comparator principle is a key component of the nanometer comparator. The light source of the interferometer is a frequency-doubled iodine stabilised Nd-Yag laser, which provides frequency-stabilized green light by means of monomode optical fibers. The setup of the optical interferometer consists of two Jamin type interferometers, one for the displacement measurement of the moving carriage, the other for a compensation of angular motion of the microscope bridge as well as phase changes induced by the fibers. These interferometers are interleaved in a way that measurement and reference beam can be guided by two different fibers and remain spatially separated until the interference occurs. This design removes the polarization mixing, the main sources of interferometer nonlinearities [2] in common heterodyne interferometers.

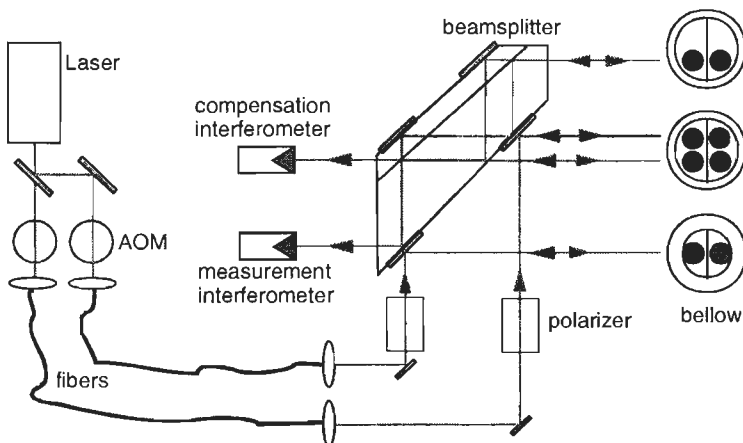


figure 1: Principle of the heterodyne interferometer setup

The interferometer is now operating according to the heterodyne principle, the signal of the second compensation interferometer is directly used as the phase reference for the measurement interferometer. Therefore only one phase meter is required for both interferometers. The principle of the interferometer design is shown in figure 1.

### Measurements:

For the measurements of line scales up to now a slit microscope is used. The magnification and numerical aperture NA of objective lens used is 50 respective 0.5. The reflected light from the scale after the slit is detected by a photomultiplier and measured by a 16 Bit A/D converter simultaneously to the interferometer readings. The line scale on the carriage is moved with a constant velocity of 1 mm/s. The implementation of the heterodyne electronics has led to an increase of the measurement rate under Windows NT up to 40 KSamples/sec. This arrangement results in an improvement of the localization of structure edges with respect to the original homodyn design by a factor of three.

The repeatability of six consecutive measurements of a 200 mm Zerodur line scale with one line per millimeter is shown in figure 2 as the deviation from the arithmetic mean for every single measurement.

The repeatability will be further improved in the future by increased data acquisition rates using hardware buffers and a more accurate time synchronization of the readings by shorter transit times in the electronics to minimize the influence of noise respectively carriage vibrations on the edge detection. In addition to this, implementation of the autofocus mechanism by active z-control control of the carriage will in the future allow to use microscope objectives with higher magnification and numerical aperture.

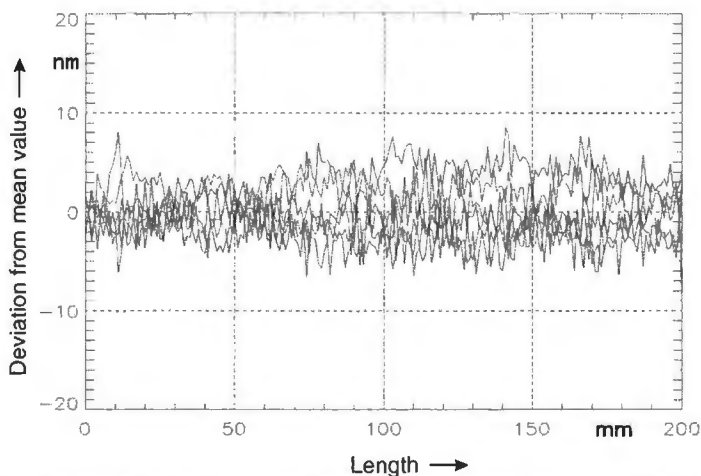


**figure 2:** Repeatability of single line scale measurements. Deviation from mean values.

The optical fiber may influence the phase and - mainly due to polarisation changes - also the amplitude of the interferometer signals. These parameters variations are caused by temperature changes and mechanical motion of the fibers. Due to the

heterodyne principle, which is insensitive to slow variations in the signal amplitude strength, we no longer observe significant influences of strong manual movements of the fiber on the length measurement.

To check for the current length measurement capability of the comparator a comparison with the results of other line scale comparators is shown in figure 3. It can be seen that a length proportional deviation of around 40 nm occurs on the latest measurements with the nanometer comparator. There are two known reasons which could have led to this deviation. Firstly, the Nd-Yag laser has shown a constant degraded steadily during the time of its use for the last measurements and meanwhile had to be replaced. Secondly, the intensity and the beam shape at the optical fiber outputs changes significantly after evacuation of the interferometer housing. Furthermore, after some months they could no longer be used because of strong changes in the beam shape of the transmitted light as described below.

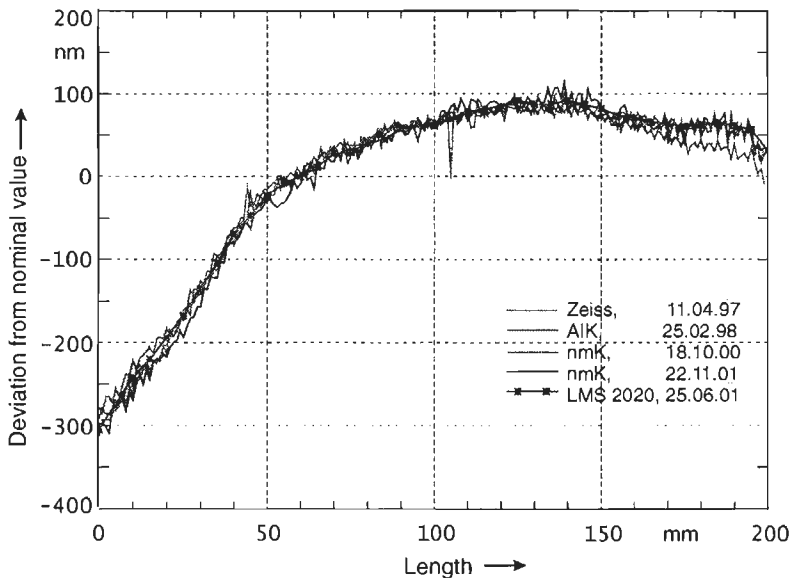
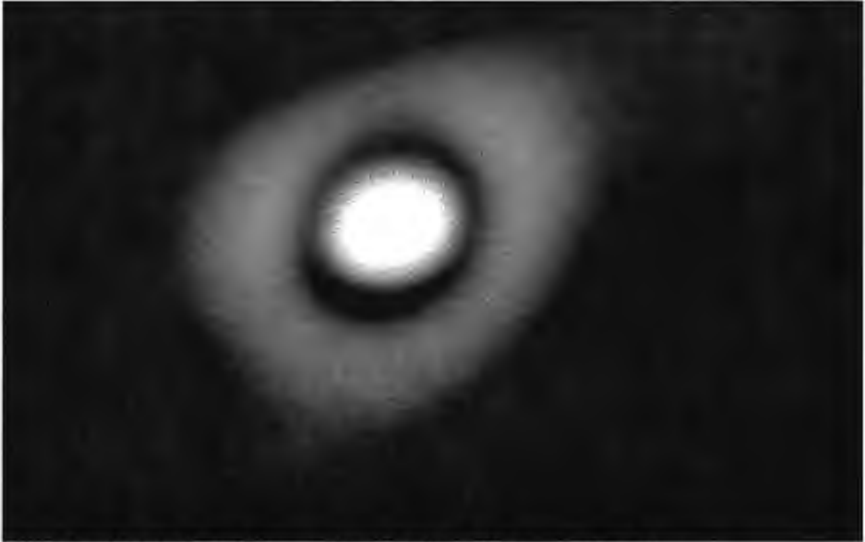


figure 3: Comparison with different length comparators at PTB and Zeiss.

### Optical fibers in vacuum:

Unexpectedly, the main current challenge of the nanometer comparator are the optical fibers which are used to guide the light into the vacuum chamber. After two days in vacuum the beam shape has changed in a way that the light intensity inside of the aperture of the interferometer beam of 22 mm decreases by a factor of about 8. After re-aerating the chamber the intensity reaches nearly the original signal level after about two days. However, after some evacuation/aeration cycles and a resulting longer time period in vacuum the fibers could hardly be used any more. An illustration of a typical beam shape, observed 10 cm away from the fiber end after some days in vacuum is shown in figure 4.





**figure 4:** Beam shape 10 cm behind the fiber after some days in vacuum

This behavior could be reproduced with polarization-preserving single mode fibers of two manufacturers as well as with non-polarization-preserving single mode fibers as long as the fiber end is mechanically attached by clamping or glueing. Also tests with different types of glue and different ferrule diameters provided the same results. Up to now, only on a fiber which was slightly fixed on the jacket 10 cm behind the cuted fiber end did show a stable beam profile in vacuum over a time period of four days. This must be checked again over a longer time period. But in any case this mounting principle is too unstable for the interferometric measurements To achieve stable working conditions with the comparator as soon as possible we now concentrate further on the fiber coupling problem in vacuum but in parallel also prepare the use of optical windows to feed the light into the vacuum chamber .

#### References:

- [1] Flügge, J., Dangschat, H., Spies, A., Tschirnich, J., Piele, H. : Concept of a interferometric length comparator with measurement uncertainties in the nanometer scale, 1<sup>st</sup> euspen Int. Conf., Bremen (Germany), 1999, 227-230
- [2] Tanaka, M., T. Yamagami, and K. Nahayama, Linear interpolation of periodic error in a heterodyn laser interferometer at subnanometer levels. IEEE Trans. Instrum. Meas., 1989. IM 38: p. 552-554.

# The influence of polarization states on non-linearities in laser interferometry

S.J.A.G.Cosijns, H.Haitjema, P.H.J.Schellekens

Section Precision Engineering, Department of Mechanical Engineering, Eindhoven University of Technology, The Netherlands.

## Abstract

With use of an ellipsometric measurement the polarization state of several optical components used in interferometry was measured. A model of a heterodyne laser interferometer was developed, enabling to predict the non-linearities resulting from non-ideal polarization optics.

## Introduction

The principal limitation of laser interferometer systems for achieving (sub-)nm uncertainties in small displacements is in the photonic noise and in the residual non-linearities which are inherent of periodic interferometer signals and which repeat each fraction of a wavelength. These deviations are both present in the phase measurement system of the interferometer itself, but they can also result from the optics: beam splitters, retardation plates, and corner cubes can influence the polarization state in interferometers working with polarizing optics, or influence the contrast in interferometers working with non-polarizing optics. Here we deal with a heterodyne interferometer using polarizing optics.

## Heterodyne laser interferometry

In figure 1 a schematical representation is given of a heterodyne laser interferometer using differential optics. A heterodyne interferometer consists of a laser source with two orthogonal polarized beams with a different frequency ( $f_1$  and  $f_2$ ). The reference signal (RS) consists of an interference signal of the initial frequency difference:

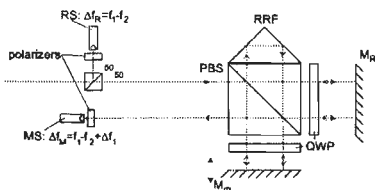


figure 1: Schematical representation of a differential interferometer.

$\Delta f_R = f_1 - f_2$ . The measurement is done by splitting the two frequencies using a polarising beam splitter (PBS). One frequency is reflected by the reference mirror ( $M_R$ ) and the second frequency is reflected from the measuring mirror ( $M_M$ ). Since the measurement mirror is moving an extra frequency shift is gained, resulting in a phase shift in the interference signal (MS).

The principle of splitting frequencies by polarization splitting can result in non-linearities as was already published by [eg. 1, 2, 3, e.a.] when this splitting is not perfect.

## Characterization of components

In the heterodyne setup polarization mixing results in frequency mixing. This mixing can occur in all polarizing and non-polarizing components. Therefore it is essential to characterize the polarization mixing of each component.

This is done by an ellipsometric setup as shown in figure 2. Here we assume no depolarization in the optical component. Further the assumption is made that the Jones representation of the component is a diagonal matrix of the form:

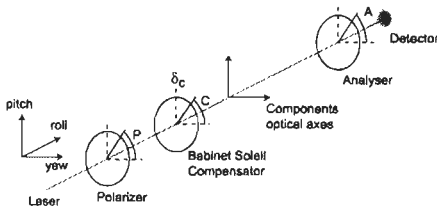


**figure 2:** Schematical representation of the ellipsometer setup.

$$T_{Os} = A_o \begin{bmatrix} 1 & 0 \\ 0 & T_o e^{i\delta_o} \end{bmatrix}$$

With  $A_o$  the amplitude attenuation of the entire optical system,  $T_o$  the amplitude difference between the o

and e polarization and  $\delta_o$  the phase retardation between the two polarization components.

From the laser source circular polarized light emerges through a polarizer with azimuth angle P, a compensator of the Babinet Soleil type enabling a phase difference of  $\delta_c$ , azimuth C, both in front of the optical system and a polarizer with azimuth angle A behind the optical system. By finding a set of azimuth angles for polarizer, compensator and analyser (P,C and A) such that the light flux falling on the detector is extinguished, the Jones matrix of the optical system can be resolved. This results in the following formula [4]:

$$T_o e^{i\delta_o} = \tan \psi e^{i\Delta} = - \tan A \left[ \frac{\tan C + T_c e^{i\delta_c} \tan(P - C)}{1 - T_c e^{i\delta_c} \tan C \tan(P - C)} \right]$$

Where  $T_c$  is the amplitude attenuation of the two polarization directions of the compensator. The process of finding these azimuth angles is called null-ellipsometry. A fourth variable that can be adjusted is the relative phase retardation of the compensator ( $\delta_c$ ). Since the resolution to which this parameter can be measured compared to the azimuth angles is magnitudes poorer this is not done. In stead we use four zone averaging. The compensator is fixed to an azimuth of  $\pm \pi/4$  and the relative phase retardation is fixed to  $\delta_c = \pm \pi/2$ . With  $T_c = 1$ , for each fixed azimuth of C two combinations of P and A result in an intensity minimum. Four zone averaging consists of taking the mean of these angles resulting in the two ellipsometric angles  $\psi$  and  $\Delta$ . The advantage of this method is that any imperfections of the ellipsometer other than entrance and exit window birefringence are cancelled out. Therefore in our setup all ellipsometer imperfections are cancelled out.

### Measurement results

Since the method assumes a compensator azimuth angle of  $\pm 45^\circ$  with the axis of the optical component under testing the optical system was aligned before measurement. The extinction ratio of polarizer and analyser combination was better than 1:100 000. The reproducibility of the measurement was tested using a polarising beam splitter in the setup shown in figure 2.

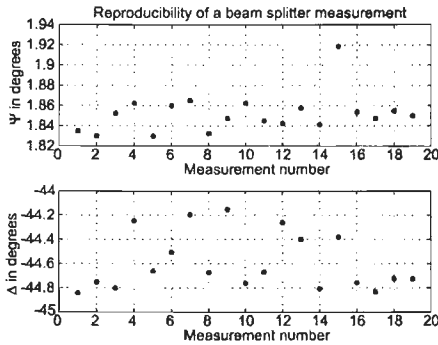


**figure 3:** Reproducibility of the ellipsometric measurements

The results are shown in figure 3, the standard deviation for  $\psi$  was  $0.02^\circ$ , and the standard deviation for  $\Delta$  was  $0.25^\circ$ .

With this knowledge some measurements were done for a polarizer and a quarter wave plate under different angles around the pitch axis in figure 2. The different angles were chosen to investigate the influence of on axis rotational misalignment. For each angle 2 measurements were made, except for  $0^\circ$ , there 4 measurements were made. The results are shown in figure 4.

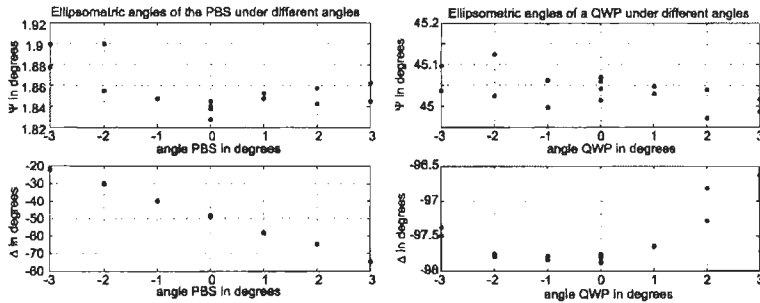


**figure 4:** Angle dependence of a polarising beam splitter and a quarter waveplate.

The left figure shows a minimal angle  $\psi$  of  $1.84^\circ$ , representing an amplitude leakage of 3% in the beam splitter for the transmitted polarization component. The phase shift of the polarising beam splitter depends on the angle of the beam splitter. Therefore also the resulting polarization state after the beam splitter depends on this alignment. In the right figure the ellipsometric angles of a quarter wave plate are shown, the leakage is less than 0.2%, however the phase difference between fast and slow axis is in a normal alignment  $-97.85^\circ$  instead of the expected  $-90^\circ$ . From the figure it can be seen that not only the rotational alignment around the optical axis influence the polarization state of the output, but also the alignment.

### Resulting non-linearities

With use of Jones Matrices a modular model was built up in Matlab<sup>®</sup> in which a simulation can be made of the non-linearities resulting from non-ideal optical components, or misaligned optical components, non-ideal input parameters (like non-orthogonality of the laser beams or elliptical polarized laser beams). The model was tested using an experimental setup. Standard deviations of measurements compared to this model were 0.2 nm [5].

Simulations done with this model on a deviation equal to the standard deviation with which the optics could be measured resulted in a non-linearity of  $4 \cdot 10^{-4}$  nm. Based on the previous measurements the calculated non-linearities of the measured optics are shown in figure 5.

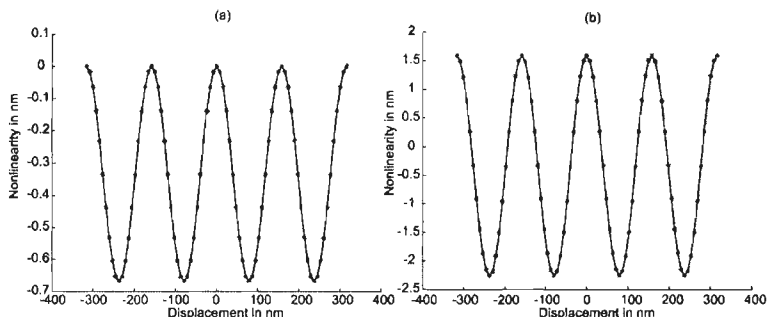


**figure 5:** Non-linearities resulting from deviations in the polarising interferometer optics (5a) and from an additional error in the laser source polarization (5b).

From the figure 5a can be seen that the non-linearities resulting from the deviations in the optics alone have a maximal amplitude of 0.67 nm. Addition of possible laser source ellipticity (1/4000 in intensity) and non-orthogonality ( $0.1^\circ$ ) result in a non-linearity shown in figure 5b.

## Conclusion

With use of null-ellipsometry the deviations from ideal optical components were measured with a standard deviation of  $0.02^\circ$  for  $\psi$  and  $0.25^\circ$  for  $\Delta$ , representing a negligible non-linearity of  $4 \cdot 10^{-4}$  nm. The resulting non-linearities from these measured deviations were calculated using a Jones matrix formalism. The results show a minimal non-linearity in the flat mirror optics of 0.67 nm.

## Acknowledgements

This work was financially supported by the Dutch Ministry of Economic Affairs in the framework of the program "IOP Precisietechnologie"

## References

- [1] Hou, W., Wilkening, G.: "Investigation and compensation of the non-linearity of heterodyne interferometers", *Precision Engineering*, 14, 1992.
- [2] De Freitas, J.M., Player, M.A.: "Importance of rotational beam alignment in the generation of second harmonic errors in laser heterodyne interferometry", *Meas. Sci. Technol.*, 4, 1993.
- [3] Rosenbluth, A. E., Bobroff, N., "Optical sources of nonlinearity in heterodyne interferometers", *Precision Engineering*, 12, 1990.
- [4] Azzam, R.M.A., Bashara, N.M.: "Ellipsometry and polarized light", Elsevier Science B.V., ISBN 0 444 87016 4, 1999.
- [5] Cosijns, S.J.A.G., Haitjema, H., Schellekens, P.H.J.: "Modelling and verifying non-linearities in heterodyne displacement interferometry", submitted for publication to *Precision Engineering*.

## Optical roughness measurements with a multiwavelength diode laser interferometer

K. Meiners-Hagen, A. Abou-Zeid

Physikalisch-Technische Bundesanstalt, Bundesallee 100,  
D-38116 Braunschweig, Germany  
Karl.Meiners-Hagen@ptb.de

### Abstract

Measurements on roughness standards were performed with a multiwavelength diode laser interferometer which was originally designed for surface profile measurement. A comparison of the roughness parameters derived from the interferometer data with the reference values obtained with a stylus instrument exhibit a well agreement within 9% for the averaged parameters like the roughness average  $R_a$ . The peak values like  $R_z$ , however, are up to 17% smaller than their reference values.

### Introduction

Surface roughness is commonly measured using a mechanical stylus instrument. Optical methods like interferometry are hardly utilised for this task since they do not reach the accuracy of the stylus instruments. For objects which can not be accessed by a stylus instrument, e.g. large samples or soft surfaces, an optical measurement technique would be advantageous.

A scanning multiwavelength diode laser interferometer for surface profile measurement was developed. Using three different wavelengths in the near infrared simultaneously a measuring range in the z-direction of 145  $\mu\text{m}$  without ambiguity could be achieved with a resolution of 4 nm. A detailed description of the interferometer can be found in [1,2]. Previous measurements of surface profiles and step heights were performed on specular smooth surfaces like glass or gauge blocks. On rough surfaces the intensity of the reflected light fluctuates during the scan of the surface profile. This leads to a decrease or even a temporary loss of the interference signal. As a result of the multiwavelength technique no counting of the interferometer phase is necessary. A temporary signal loss within a scan results in a lack of data only for this region. Roughness parameters are calculated from scan lines of the surface. For a characterisation of the surface roughness continuous profile data for a certain length are needed which restricts the applicability of the interferometer.

### Experimental procedure

The interferometer consists of three diode lasers with wavelengths  $\lambda$  of 779.5 nm, 822.95 nm and 825.3 nm which are coupled into a Michelson interferometer. The resulting synthetic wavelengths of  $\sim 15 \mu\text{m}$  and  $\sim 290 \mu\text{m}$  allow a measuring range of  $\sim 145 \mu\text{m}$  with the resolution of 4 nm given by the optical wavelengths. By a modulation of the injection currents of the three diodes with different frequencies around 1 MHz the interferometer signals can be measured with one photo detector simultaneously at the second and third harmonic frequencies [1,2]. The surface to be measured acts as one mirror of the interferometer on which the laser beams are focused. Using different lenses or microscope objectives the lateral resolution and the measuring range can be selected by the focus diameter and focal depth. The

measurement of surface profiles is accomplished by moving the sample with a mechanical x-y translation stage while the interferometer itself remains fixed.

The measured rough samples are so called “superfine roughness standards” with  $R_z$  values between 134 nm and 450 nm. These standards are cylindrical disks with approx. 50 mm diameter with a 4 mm wide rough zone around the centre as sketched in figure 1.

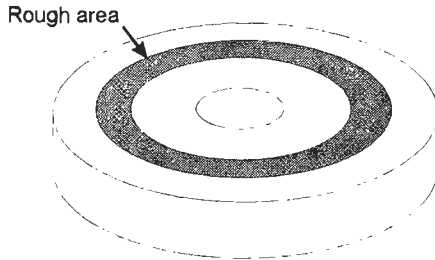


**Figure 1:** Schematically illustration of a superfine roughness standard.

The rough zone on the disks was scanned along four lines rotated by  $90^\circ$  with a distance of 200 nm between the measured points. It should be emphasised that the focus diameter of the microscope objective used for these measurements is approx.  $2 \mu\text{m}$  and far above the point distance. The value of 200 nm was chosen to be the same as used for the calibration of the standards with a contact stylus instrument. Each scan line was separated in three sections according to the calibration procedure. The resulting data were processed in the PTB section 5.12 “Micro- and Nanotopography” with their reference software for roughness analysis [3].

## Results

Figure 2 shows a part of the surface profile of a roughness standard with an average maximum height  $R_z = 134 \text{ nm}$  as measured with the diode laser interferometer in comparison with the contact stylus instrument. It turns out that the profile is well reproduced by the interferometer. However, fine details like the sharp spike at position  $\sim 1.4 \text{ mm}$  and the narrow groove at  $\sim 0.3 \text{ mm}$  are smoothed by the interferometer. It is caused by the focus diameter of  $\sim 2 \mu\text{m}$  of the microscope objective used for these measurements so that the measured height values are averaged over this range. This smoothing leads to an apparent decrease of the roughness but it has a different impact on the particular roughness parameters derived from the surface profiles. The peak values like the average maximum height  $R_z$  or the maximum roughness depth  $R_{max}$  are more reduced than the averaged parameters like roughness average  $R_a$  or root mean square (rms.) roughness.

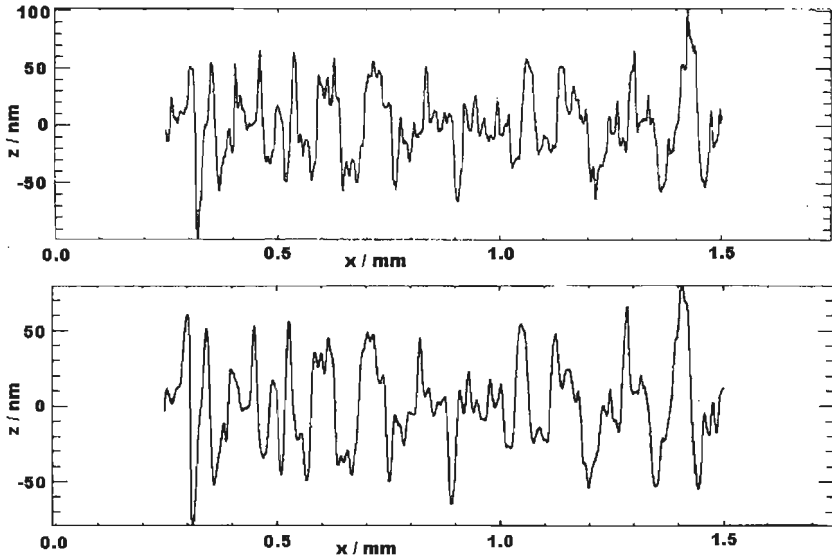


**Figure 2:** Surface profile as measured with a contact stylus instrument (upper curve) and with the interferometer (lower curve)

Three different roughness standards with  $R_z = 134.4$  nm,  $R_z = 315.3$  nm, and  $R_z = 449.8$  nm, were measured with the diode laser interferometer and compared with the reference values from the calibration. Selected roughness parameters are given in table 1.

All roughness parameters measured with the interferometer are smaller than their reference values from the calibration with a contact stylus instrument. The roughness average  $R_a$  is well reproduced by the interferometer data. The maximum difference appears at sample 2 with a deviation of 9% (three times the standard deviation  $\sigma$ ) to the reference values. The other averaged roughness parameters like rms. roughness  $R_q$  which are not shown here have similar deviations. The average maximum height  $R_z$  and the maximum roughness depth  $R_{max}$  as peak values are up to 17% smaller than their reference values.

A correction of these systematically smaller values seems to be impossible since the averaging of the height information over the laser spot size leads to a loss of information about fine details of the surface. A microscope objective with a smaller focal length and smaller spot size would improve the results but the basic problem of the averaging will not be resolved. Another limitation appears at surfaces with higher roughness due to temporary loss of the interference signal. It turned out that the sample 3 with an average maximum height  $R_z$  of 450 nm is almost at the limit.

In conclusion the multiwavelength diode laser interferometer is applicable for roughness measurements. On surfaces which can be accessed by a contact stylus instrument this gives more reliable results. The main advantage of the interferometer



is that it is a non contact technique. Soft surfaces which would be modified by a stylus could be characterised with the interferometer.

	Reference data		Interferometer data	
	value / nm	$\sigma$ / %	value / nm	$\sigma$ / %
<b>Sample 1</b>				
$R_a$	23.8	2.0	22.9	2.3
$R_z$	134.4	2.8	118.4	3.1
$R_{max}$	174.0	9.2	154.9	9.2
<b>Sample 2</b>				
$R_a$	59.9	3.2	55.8	3.3
$R_z$	315.3	2.9	279.2	2.9
$R_{max}$	402.6	6.5	349.7	9.0
<b>Sample 3</b>				
$R_a$	82.5	1.8	80.8	2.1
$R_z$	449.8	2.5	390.5	2.7
$R_{max}$	562.9	5.6	469.3	4.3

**Table 1:** Comparison of selected roughness parameters derived from the interferometer profile data with the reference values from the calibration. The standard deviation  $\sigma$  is taken between the 12 sections of measurement.

## Acknowledgement

The authors are grateful to the Deutsche Forschungsgemeinschaft (DFG) for financial support and to PTB Lab. 5.12 for analysing the data.

## References

- [1] K. Meiners-Hagen, M. Wolf, A. Abou-Zeid, "Measuring Micrometer Steps With Nanometer Resolution", Proc. of the 2<sup>nd</sup> Int. Conf. euspen, Turin, Italy, A. Balsamo et. al. (Eds.), Vol. 1, p. 226, 2001
- [2] A. Abou-Zeid, J. Löbau, M. Wolf, "Profilometry using a Diode Laser Interferometer with Two Wavelengths", Proc. of the 1<sup>st</sup> Int. euspen Conference, Pat McKeown a.o. (Ed.), Bremen, Germany, 2, p. 239, 1999
- [3] L. Jung, R. Krüger-Sehm, B. Spranger, L. Könders, "Reference software for roughness analysis", Proc. of the 2<sup>nd</sup> Int. Conf. euspen, Turin, Italy, A. Balsamo et. al. (Eds.), Vol. 1, p.500, 2001

## Probe calibration using a digital piezo translator

D. van den Heuvel, R.H. Bergmans

NMi Van Swinden Laboratorium, Delft, The Netherlands, dheuvel@NMI.nl

### Abstract:

For high accuracy static and dynamic calibrations of probes a novel calibration set-up was developed, i.e. the Digital Piezo Translator (DPT). The calibration of the DPT is described and a detailed uncertainty budget is shown. Finally two examples of probe calibrations are described.

### Introduction

Probes are commonly used to measure displacement in a variety of measuring instruments, such as gauge-block comparators and roundness measuring machines. Normally the calibration of these probes is done by making use of physical standards, i.e. gauge blocks. For high accuracy measurements, the accuracy of these physical standards (at best 15 nm) is insufficient. A further drawback is that the calibration with physical standards is usually a static one, while the probe is actually often used in a dynamic way. This raises the question of how representative the static calibration is for the dynamic measurements performed with the probe. For this reason a novel probe calibration set-up was developed at our institute [1].

### Digital Piezo Translator

The probe calibration set-up consists of a Digital Piezo Translator (DPT), which imposes a parallel displacement to a mirror over a range of  $\pm 6 \mu\text{m}$ . A feedback circuit equipped with a capacitive sensor is used to keep the mirror at the set value. Using a digital control unit this set value can be changed and thereby the displacement of the mirror is controlled. This also gives the possibility to simulate any surface profile, for instance a sinus profile, with the DPT.

### Calibration

The static displacement of the mirror is calibrated using a laser with a high-resolution plane-mirror interferometer, see figure 1.

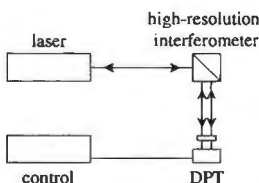


figure 2: Schematic set-up

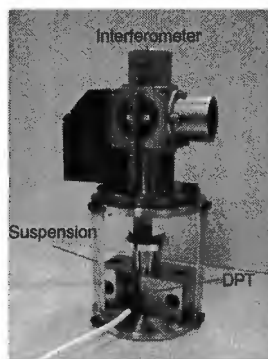


figure 1: DPT with interferometer

The range is calibrated in steps of  $\frac{1}{2}\lambda$  to avoid interpolation errors by the interferometer, resulting in 39 points including the zero point.

The calibration is performed in an insulated box to obtain a very stable temperature of the set-up (variation  $< 1\text{mK}/\text{min}$ ). Also the suspension of the interferometer is made of invar to improve thermo mechanical behaviour.

Next the dynamical behaviour of the DPT is calibrated by determining a Bode diagram for several amplitudes, from which the  $-3\text{dB}$  frequencies are derived. For an amplitude of  $6\ \mu\text{m}$  the  $-3\text{dB}$  frequency is  $85\ \text{Hz}$  and for smaller amplitudes  $>85\ \text{Hz}$ .

The reading of	Value	Variation
Air pressure	Atmospheric	$2.6 \cdot 10^{-3}\ \text{hPa}$
Air temperature	$20.0 \pm 0.5\ ^\circ\text{C}$	$6.6 \cdot 10^{-5}\ ^\circ\text{C}$
Air humidity	$40\text{-}50\ \text{RH}$	$1.3 \cdot 10^{-2}\ \text{RH}$
CO <sub>2</sub> content	$450 \pm 75\ \text{ppm}$	$3.3 \cdot 10^1\ \text{ppm}$

**table 1:** conditions for one measurement point

To determine the uncertainty caused by the tilt of the DPT, the magnitude of the tilt is determined with an autocollimator. The maximum tilt from the zero point to  $\pm 6\ \mu\text{m}$  is  $1.25''$ . When the laser interferometer is aligned in the center of the mirror, the influence of the tilt of the DPT on the measurements is minimized (see figure 1 and figure 2). Logically when calibrating probes with the DPT, the probes should also be aligned in the center.

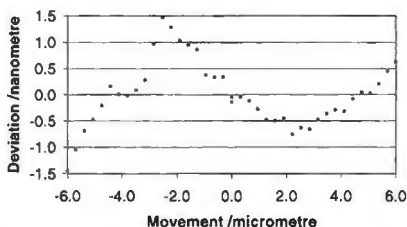


**figure 3:** Deviation from linear fit when positioned in the center of the mirror

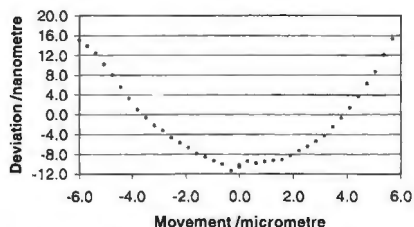


**figure 4:** Deviation from linear fit when positioned 6 mm from the center of the mirror

## Uncertainty

Sources of uncertainty	Uncertainty
Tilt	$2.02\ \text{nm}$
Thermo mechanical behaviour	$0.24\ \text{nm}$
Deadpath error	$0.13\ \text{nm}$
Resolution interferometer	$0.01\ \text{nm}$
Resolution DPT	$0.08\ \text{nm}$
Polynomial fit	$0.31\ \text{nm}$
Repeatability	$0.05\ \text{nm}$
Skew of the mirror	$3.52 \cdot 10^{-6} \cdot L$
Cosine error	$1.39 \cdot 10^{-6} \cdot L$
Refractive index uncertainty	$3.35 \cdot 10^{-8} \cdot L$
Refractive index variation	$3.18 \cdot 10^{-8} \cdot L$
Wavelength of laser	$2.06 \cdot 10^{-9} \cdot L$
Combined standard uncertainty	$2.07\ \text{nm} + 3.79 \cdot 10^{-6} \cdot L$
Expanded uncertainty ( $k=2$ )	$4.13\ \text{nm} + 7.57 \cdot 10^{-6} \cdot L$

**table 2:** Uncertainty budget of the DPT, when used statically

Using the DPT statically, the expanded uncertainty is  $4.13\ \text{nm} + 7.57 \cdot 10^{-6} \cdot L$  (table 2). When used dynamically, the expanded uncertainty is  $5.17\ \text{nm} + 7.57 \cdot 10^{-6} \cdot L$  due to an

increased resolution of the interferometer in time-dependent measuring mode and interpolation errors.

### **DPT as a calibration facility**

After the DPT has been calibrated, it can be used to calibrate different kind of probes. Because of its small size, the DPT can be easily transported, which makes on-site calibrations possible. Below two examples of probe calibrations are described.

#### **Gauge-block comparator**

A gauge-block comparator is used to measure the difference between a reference and a client gauge block. The probes of a gauge-block comparator are statically calibrated with the DPT in a straightforward manner. The DPT is placed under the probe like a gauge block and several displacements are measured. The uncertainty in the standard used for calibration, i.e. the DPT, is as stated above  $4.13 \text{ nm} + 7.57 \cdot 10^{-6} \cdot L$ . By way of comparison, conventionally a gauge-block comparator is calibrated using a special set of gauge blocks. The uncertainty in these standards is  $15 \text{ nm}$  and only a few points are measured.

#### **Roundness measuring machine**

The probe of a roundness measuring machine (RMM) is calibrated statically and dynamically with the DPT. Because often a RMM can't process a sudden step of the probe, the static calibration is in fact a dynamic calibration at a low frequency. For the dynamical calibration of the probe a sine profile is generated with the DPT, which is followed by the probe. This is done for different frequencies and amplitudes. Thereby the filters of the RMM are also tested.

### **Conclusions**

With the development of the DPT a standard for the calibration of probes, with a much smaller uncertainty compared to physical standards, has been realized. Furthermore a probe of, for example a RMM, can now be calibrated dynamically. As a result the characteristics of the probes can be better determined.

The DPT is now part of the calibration services of NMI VSL and offered to clients.

### **References**

- [1] Haitjema, H.: Dynamic Probe Calibration in the  $\mu\text{m}$  Region with Nanometric Accuracy, Precision Engineering 19:98-104, 1996
- [2] Stone, J.S. and Phillips, S.D.: Corrections for Wavelength Variations in Precision Interferometric Displacement Measurements, Journal of Research of the National Institute of Standards and Technology vol. 101 no. 5, 9-10 1996
- [3] Birch, K.P. and Downs, M.J.: Correction to Edlen Equation for the Refractive Index of Air, Metrologia 31pp 315-316, 1994
- [4] Sacconi, A., Picotto, G.B. and Pasin, W.: The IMGCC Calibration Setup for Microdisplacement Actuators, IEEE Transactions on Instrumentations and Measurement vol. 48 no. 2, 1999



## Parameter Calibration of Articulated CMM

R. FURUTANI<sup>1</sup>, K. SHIMOJIMA<sup>1</sup>, K. TAKAMASU<sup>2</sup>

<sup>1</sup>Tokyo Denki University, Japan; <sup>2</sup>The University of Tokyo, Japan

### Abstract:

Articulated CMMs are widely used to measure a large scale work and/or a complicated work, as it is very flexible. On the other hand, to measure the works, the kinematical parameters should be calibrated in advance of measurement. We planed and tested an artifact. The artifact has nine spheres with different heights on the flat plate. The kinematical parameters are calibrated based on the measurement result of all spheres on the artifact. In this paper, we will describe the model of the articulated CMM, the structure of the artifacts and the result of parameter calibration. We will compare the kinematical parameters calibrated by the artifact in different locations and orientations. After parameter calibration, we show that the calibration to use the artifact is useful for wider area and the measurement result by CMM is correct.

### Introduction

Articulated CMMs are widely used to measure a large scale work and/or a complicated work, as it is very flexible. On the other hand, to measure the works, the kinematical parameters should be calibrated in advance of measurement. We calibrated an articulated CMM which has six rotational joints. We used nine spheres fixed on the flat plate as the artifact and used the concave conical shape as a stylus. When this stylus contacts with these spheres, the distance between the center of sphere and the top of the stylus is always same length. Therefore this articulated CMM can directly measure the center of sphere. The kinematical parameters are described in DH notation. These parameters are calibrated by comparing the result of measurement of 3DBP and the calibrated coordinates of center of spheres.

After calibration, we estimated the effectiveness of the calibration and the correctness of the calibration by 3DBP in different locations and orientations.

### Model of articulated CMM

The articulated CMM in our project has six rotational joints. In the DH notation, four kinematical parameters are necessary for each joint. As the base arm could be fixed in any locations and orientations in world coordinate system, three parameters could be reduced. The artifact should be calibrated in advance by any methods and described in the workpiece coordinate system on the artifact itself. The center of spheres are measured by the articulated CMM in world coordinate system and the calibrated coordinates of the center of spheres are described in the workpiece coordinate system. Therefore, six parameters are necessary to convert from the world coordinate system to workpiece coordinate system. Totally, the number of kinematical parameters is  $27(=4*6-3+6)$ . However, six additional parameters are necessary to calibrate the kinematical parameters based on the artifact, but they are not necessary in measurement.

### Artifact with nine spheres

The artifact is shown in figure 1. The artifact has nine spheres on the flat plane and is called 3DBP. These spheres are measured by the ordinary CMM and the center of spheres are calibrated. As the accuracy of the ordinary CMM is higher than that of the articulated CMM, the measured centers by the ordinary CMM are enough

accurate to be used as the calibrated coordinates of center of spheres.

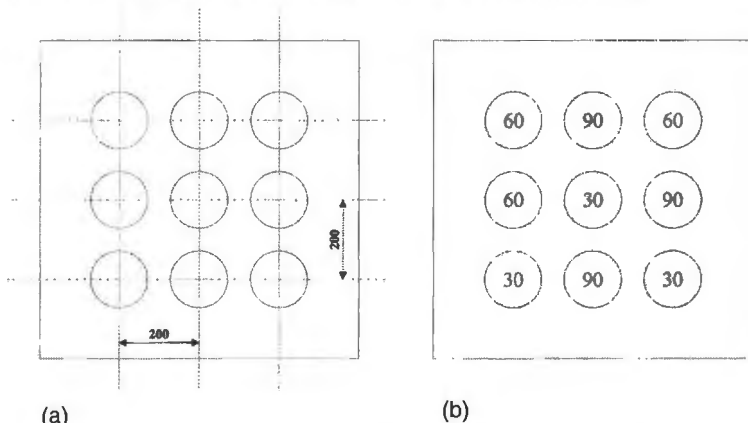


**figure 1:** Configuration of artifact: (a) shows the location of spheres in horizontal plane. (b) shows the height of spheres from the flat plane.

### Procedure of calibration

As the number of kinematical parameters are 27, 27 equations are necessary to determine the parameters. When nine spheres are measured, 27 equations are just derived. In this paper, to get more precise kinematical parameters, nine spheres are measured five times. Finally 27 kinematical parameters are solved by non-linear least square method.

The kinematical parameters have the uncertainty, the amount of the uncertainty is depend on the location and the orientation of the artifact. So, we put the artifact in seven different locations and orientations. Figure 2 shows the examples of different locations and orientations. Totally seven groups of kinematical parameters are solved by non-linear least square method. The kinematical parameters are a little bit different from other groups.

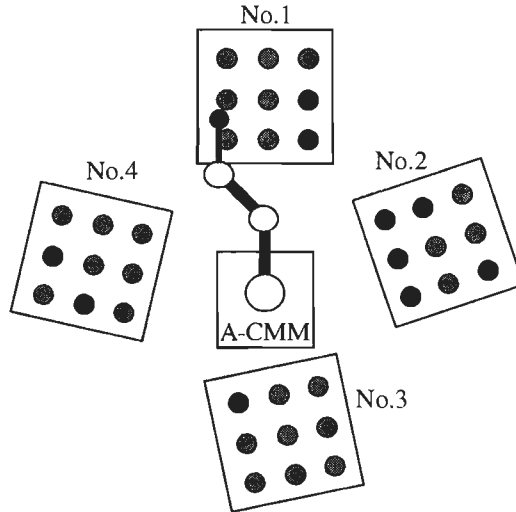


**figure 2:** The artifact is put in some different locations and orientations.

### Result of Calibration

So, the combination of column  $n$  and row  $n$  means the data in the artifact are used for calibration of kinematical parameters and estimation of kinematical parameters. Therefore the value in column  $n$  and row  $n$  is smaller than others.

Location 6 and 7 are worse than others in both kinematical parameters and measured values. As the artifact in location 6 and 7 are put in tilted orientation and it is difficult for the articulated CMM to accurately contact with the spheres, these results could be affected by the mis-contact and the bending of the arm of CMM.

It is proved that the kinematical parameters are useful to measure wider area from location 1-5.

### Estimation of Kinematical Parameters

The Ball-Bar(KOBA) is measured to show that the kinematical parameters are absolutely calibrated. This Ball-Bar has five balls. The distance between two balls is 250mm. The Ball-Bar is put in four different locations and orientations and five balls are measured 5 times. After that, the measured values are converted to the coordinate system of the articulated CMM and the distances between two balls are calculated. The results in location 1 to location 5 fit about 250mm.

Therefore it is proved that the kinematical parameters are calculated well and the articulated CMM is absolutely calibrated.

At this moment, the diameter of sphere of 3DBP is 20mm and that of Ball-Bar is 30mm. The contact point between the conical stylus and Ball-Bar is different from 3DBP. This compensation is necessary to measure the distance between two balls. This result shows that the stylus could be changed after calibration process.



## Summary

1. The articulated CMM with six rotational joints are modeled in DH notation.
2. Nine spheres, which are located in three dimensional space, is used as the artifact.
3. It is shown that the location and orientation of the artifact affects the calibration of kinematical parameters.
4. The calibration of kinematical parameters is confirmed by measuring the reference length(Ball-Bar).

## Development of a calibration device for simple measuring instruments

V. Burgarth, A. Abou-Zeid

Physikalisch-Technische Bundesanstalt, Section 5.21, Braunschweig, Germany,  
volker.burgarth@ptb.de

### Abstract

A transportable device for the traceable calibration of most existing industrial simple measuring instrument (SMI) types with internal and external dimensions is developed and tested under laboratory as well as under workshop and production conditions. The calibration device consists of a linear guidance way with 300 mm travel range, accessories for the calibration of numerous types of SMI and a diode laser interferometer. For inherent compensation of changes of the refractive index of air and the temperature of the object to be tested the diode laser is stabilised to a resonance of an air filled optical resonator with a spacer made of steel.

### Calibration of simple measuring instruments

In relation to measurement and testing for control of production and for quality assurance, regular calibration of SMI is necessary to guarantee the reliability of the measurement results obtained. Within the scope of the inspection of testing length measurement instruments, most such instruments are calibrated today by comparison with material measures, in compliance with the relevant regulations, e.g. ISO, DIN, VDI [1,2]. These calibrations are carried out in special measurement laboratories in which the standards are held in readiness.

Depending on the number and the types of SMI used in production processes, the holding in readiness of standards is a considerable cost factor. Moreover, the nominal values of the standards available often cover the measurement range in which the SMI is used only insufficiently. A reduction of the operating costs and the availability of a universal measurement range is achievable with universal calibration devices.

Most of the calibration devices use an interferometer with a He-Ne laser as the light source. Even though frequency stabilisation of the He-Ne laser with relative uncertainty below  $10^{-8}$  is the state of the art, the uncertainty of the calibration devices exceeds the frequency uncertainty of the laser at least two orders of magnitude because the wavelength uncertainty and the thermal expansion of the object to be measured determines the uncertainty of the length measurement. In practice frequent recalibration of the emission frequency of the laser, the weather station that is used for the determination of the refractive index of air and the temperature sensors that are used to detect the temperature of the object to be measured is necessary.

### The universal calibration device

With the new universal calibration device the effort to achieve traceable measurement results and the environmental conditions demanded for calibration are reduced. By means of various complementary modules, the user can adjust the device for the calibration of the following SMI: external micrometers, internal micrometers with two-point or three-line contact, dial gauges, dial test indicators, precision indicators, lever gauges and callipers. The universal calibration device has

a measurement range of 300 mm. The carriage with three-speed manual driving mechanism can be positioned with a step width of 0.1  $\mu\text{m}$ . The device is extremely rugged and easy to transport. Calibrations can be carried out also in rooms without air-conditioning and even under workshop conditions.

The interferometer is set up with polarisation optics and mounted at the bottom side of the guidance way. Using a sin-cos-receiver the direction of the displacement of the carriage can be detected. A pre-amplifier board is integrated close to the detector to increase the electromagnetic compatibility of the interferometer signal. The signals are analysed using a counter card, which calculate the carriage displacement with 0.4 nm LSB-increment.

A diode laser with wavelength-selective beam feedback from a diffraction grating in Littrow-configuration was chosen to fulfil the requirements on reliability, smallness and inexpensiveness. The laser diode is mounted in a temperature stabilised aluminium block. The laser module base is made out of invar. With a piezoelectric transducer the grating angle and therewith the wavelength can be tuned. The tilt of the direction of the exit beam is corrected with a right angle prism. A mode hop free wavelength tuning range of 0.06 nm is achieved. This tuning range enables the system to compensate changes of the refractive index of air and the thermal expansion of the object to be measured [3].

After investigations about the suitability of different length references [4] a resonator was chosen as length reference. The laser wavelength is stabilised to a flank of a resonance. The resonator spacer is made out of a steel cube using only standard machines like lathe, drilling and milling machines. The resonator mirror mountings applies no force to the mirrors in axial direction and the resonator is attached only on one side to prevent deformation. The mirror spacing is 18 mm which yields a free spectral range of 4 GHz. A nearly confocal resonator geometry is used, which is advantageous for adjustment. Both mirrors are 90% reflection coated on the inner side. The resonator could be fed efficiently with collimated light by means of a meniscus mirror.

## Test procedure

Seven types of SMI (as listed above) are calibrated each at nine calibration values over their respective measurement ranges. This was done at different locations, namely in the laboratory at six temperatures between 18 and 28 degree centigrade, each after 12 hours temperature equalisation, and at three different places in the workshop. These tasks were done by four different users. The measuring instruments tested are listed in table 1. They were selected in such a way that the hole measurement range of the calibration device was covered and the most frequently used measuring instruments are represented.

The significance of the measured data depend, amongst other things, on the reproducibility of the setting point of the measuring instrument. In practice the scale value can be estimated on a quarter of the scale pitch if the readout is analogue. Except of the calliper all tested measuring instruments have an analogue read-out. In contrast to the practical use of the measuring instruments in the case of a calibration the scale value can be set to the intended value with an estimated uncertainty of a tenth of the scale pitch and then the calibration value can be read out from the calibration device. The calibrations of the micrometers with two point contact, the dial gauge, the precision indicator and the dial test indicator were done in this way.

**Table. 1:** Simple measuring instruments tested

Measuring instrument	Measurement range / mm	Scale Pitch / $\mu\text{m}$
Dial gauge	0-5	1
Internal micrometer with two point contact	250-275	10
External micrometer with two point contact	125-150	10
Micrometer with three line contact	35-42.5	5
Calliper	0-150	10
Dial test indicators	-0.1 +0.1	2
Precision indicators	-0.05 +0.05	1
Lever gauges	0-300	50

## Test results

For the statistical analysis all measurement data were arranged according to temperature, operator and location. The temperature dependence of the mean values, the person dependence of the mean values (relatively to an overall mean value) and the person dependence of the variances were calculated. The zero-points on the scales of the measuring instruments tested are variable and can be set by the user. Therefore all calibration curves start with zero deviation at the smallest nominal value.

**Table.2:** Results of the test procedure

Measuring instrument	temperature dependence / ( $10^{-6}$ / K) correlation coefficient $r^2$	person dependence							
		averaged deviation from overall mean value / $\mu\text{m}$				variance / $\mu\text{m}$			
		a	b	c	d	a	b	c	d
Dial gauge, retracted pin	+24.0 $r^2 = 0.42$	-0.5	-0.2	0.2	0.7	0.5	1.0	0.6	1.3
Dial gauge, extended pin	-24.0 $r^2 = 0.02$	1.9	1.6	0.5	-2.7	1.5	2.1	1.6	2.3
External micrometer with two point contact	+18.4 $r^2 = 0.05$	4.1	2.5	4.6	10.1	2.1	6.2	2.0	14.8
Micrometer with three line contact	+136 $r^2 = 0.47$	5.0	0.7	-2.8	-1.7	8.5	1.9	1.0	3.9
Internal micrometer with two point contact	+23.2 $r^2 = 0.30$	-2.6	1.6	2.8	-2.9	2.9	1.6	1.4	3.5

The relevant results are shown in table 2. The measured temperature dependence relates to half the measurement range, e.g. 12.5 mm for the external micrometer, and to temperatures between 18 °C and 28 °C. Also the Pearson coefficient of correlation is listed. The columns that quantify the person dependence are subdivided according to the operators, which are referred to as a, b, c, and d.

## Discussion

The negative sign of the temperature dependence detected with the dial gauge with extended pin (see table 2) is obvious because the nominal value indicated from the calibration device decreases with increasing displacement, which is inverted compared to the other measurements. An explanation for the temperature dependence detected for the micrometer with three line contact, which is six times greater than the others, could not be given. The spread of the data is too big, that one could recognise a temperature dependency by means of the statistical analysis. This is verified by the correlation coefficients  $r^2$ . Without linear correlation of the data the correlation coefficient is zero and with perfect linear dependency it is one.

The person dependence of the mean values is an indicator for different handling of the calibration device including its accessories. The mean values of the dial gauge with retracted pin are in good agreement. The mean values of the dial gauge with extended pin have a wider spread. A possible explanation for this disagreement is the screw that fixes the dial gauge to the measuring anvil. The force of this fixing may cause variable friction to the pin of the dial gauge. The mean values of the external micrometer show a significant deviation for one operator. The variations of the mean values of the internal micrometers are sufficiently small, e.g. for the internal micrometer with two point contact 0.3 times the scale pitch.

The person dependence of the variance can be interpreted as an indicator for the complexity of the handling. An "easy-to-use" device should yield a high reproducibility of the variance, independent from the user. This target is achieved for the dial gauges and the internal micrometers with two point contact. The external micrometer shows a significant greater variance. The variances for the internal micrometer with three line contact vary too much because of difficulties with the alignment.

## Acknowledgement

The work was done within the framework of the Project SMT4-CT98-2213 supported by the European Union. The authors thank the companies Helios, Danfoss and Monocrom for their co-operation as project partners and the European Commission for the financial support.

## References

- [1] ISO: Guide to the Expression of Uncertainty in Measurement, International Organisation for Standardisation, Geneva, 1993
- [2] VDI/VDE/DGQ 2618 Part 1 (draft): Checking Gauges and measuring tools, Instruction for testing measuring tools for geometric quantities, Basic principles, Beuth Verlag, Berlin, 1998
- [3] V. Burgarth, A. Abou-Zeid; Wavelength stabilised diode laser interferometer for calibration of length measuring instruments, Proceeding of the 2nd euspenn Topical Conference, Turin 2001, A. Balsamo et. al. (editors), Augusta Edizioni Mortarino, Vol. 1, pp.338
- [4] A. Abou-Zeid, V. Burgarth; Study of length references for calibration devices, Proceeding of the 1st euspenn Topical Conference, Copenhagen 2000, Leonardo De Chiffre, Kim Carneiro (editors), Technical University of Denmark, pp. 358

## Task Specific Uncertainty Estimation in Dimensional Metrology

H. Haitjema, B. van Dorp, M. Morel and P.H.J. Schellekens

Precision Engineering section, Eindhoven University of Technology, PO Box 513,  
5600 MB Eindhoven, The Netherlands e-mail h.haitjema@tue.nl

### Abstract

With the acceptance of ISO standard 14253-1 [1], the requirement for the traceability and uncertainty in dimensional measurements is extended from the measuring instruments to artefacts or industrial products which are measured with those instruments. For the calibration and uncertainty estimation of length standards and instruments, various methods are available for which usually an uncertainty budget according to the GUM [2] can be set up. However, especially where many measured data are involved, such as in CMM measurements, but also in typical dimensional geometry measurements such as roughness, roundness and flatness measurements, setting up an uncertainty budget according to the GUM for each measurement can be tedious and is a rather impossible demand.

In this paper it is shown that the 'mainstream' GUM-uncertainty budget can be modified in several ways to allow for more complicated measurements. This can lead to a measuring instrument where, next to the measured value, also the uncertainty is displayed. As an example of how measured deviations can be treated and what difficulties this may give the treatment of measured scale deviations is briefly given.

### Mainstream GUM approach

The term 'mainstream GUM' was used in a paper on Monte-Carlo methods [2], to characterise the method which is described in the main text of the GUM in contrast to its alternatives. This approach is repeated here briefly. In general, a measurement result  $Y$  is a function of  $n$  input quantities  $x_i$  ( $i=1,2,..n$ ). This leads to the general functional relationship, known as the 'model function' [1]:

$$Y = f(x_1, x_2, \dots, x_n) \quad (1)$$

The model function incorporates the measurement and the calculation procedure. It can be an analytical function, but also a complicated, iterative, computer algorithm. The measurement data  $x_i$  can be estimated either by a type A (statistic) approach or by a type B approach which accounts for all kind of known and unknown systematic deviations and uncertainties.

However this grouping does not influence the uncertainty evaluation; it is just essential that a standard uncertainty  $u_{x_i}$  is attributed to any influencing quantity  $x_i$ .

The quantity  $Y$  is best approximated by using the best approximations for  $x_i$ , which are usually the measured data, in equation (1). Now, the uncertainty  $u_Y$  can be written as:

$$u_Y^2 = \sum_i \left( \left[ \frac{\partial f}{\partial x_i} \right]_{x_i} \right)^2 \cdot \langle \Delta_i^2 \rangle + 2 \cdot \sum_{i < j} \left[ \frac{\partial^2 f}{\partial x_i \cdot \partial x_j} \right] \cdot \langle \Delta_i \cdot \Delta_j \rangle \quad (2)$$

where  $\Delta_i$  and  $\Delta_j$  are the deviations from the true value of  $x_i$  and  $x_j$  respectively; and  $\langle \rangle$

denotes the average over a large ensemble. The squared expected deviation of  $x_i$ ,  $\langle \Delta_i^2 \rangle$ , is known as the variance, which is the square of the standard uncertainty  $u_i$ . So  $u_i^2 = \langle \Delta_i^2 \rangle$ . The product  $\langle \Delta_i \Delta_j \rangle$  is known as the covariance of the deviations in  $x_i$  and  $x_j$ . In the case of uncorrelated measurement data  $x_i$  and  $x_j$ , equation (2) reduces to:

$$u_Y^2 = \sum_i \left( \left[ \frac{\partial f}{\partial x_i} \right] \right)^2 \cdot u_{x_i}^2 \quad (3)$$

### Direct variational calculation

The calculation of the derivative can be replaced by two evaluations of the model function  $Y$ , which is equivalent in first order. The correspondence with Monte-Carlo methods which are discussed later is illustrated by rewriting equation (3) as:

$$u_Y^2 = \sum_{i=1}^n (f(x_1 \dots x_i + r \cdot u_{x_i} \dots x_n) - Y)^2 \quad (4)$$

where  $r$  is a random number with average 0, a standard deviation of 1 and an absolute value of 1, so  $r = \pm 1$ . This probability distribution is known as the bi-modal distribution which we introduce here to illustrate the consistency between the mainstream GUM approach and the Monte-Carlo technique. An example of its use is given in [4] where it is explained how the effect of the uncertainty in the probe diameter  $R$  in a roughness measurement on the uncertainty in the roughness parameter  $Ra$  is calculated.

### Monte Carlo method

With a Monte-Carlo method, parameters are varied simultaneously in some random manner. As for a specific measurements problem there are many ways of doing this, one can only speak of 'a' Monte Carlo method. If we define a random number  $r$  as having an average of 0 and a standard deviation of 1, so  $\langle r \rangle = 0$ ,  $\langle r_i r_j \rangle = \delta_{ij}$  ( $\delta$  being the Kronecker  $\delta$ -symbol with  $\delta_{ij} = 1$  for  $i=j$ , otherwise 0) and  $\langle r^2 \rangle = 1$ , where  $\langle \rangle$  denotes the average over a large ensemble, then we can simulate a measurement result by varying all input quantities at a time, as following:

$$Y_k = f(x_1 + r_{1k} \cdot u(x_1), x_2 + r_{2k} \cdot u(x_2), \dots, m_{Nk} + r_{Nk} \cdot u(x_N)) \quad (5)$$

the estimate for the standard uncertainty becomes:

$$u(y) = \sqrt{\frac{\sum_{k=1}^K (Y_k - Y)^2}{K}} \quad (6)$$

If one takes  $K=n$  and  $r_{ik} = \delta_{ik}$  then equations (5) and (6) (without dividing by  $K$ ) become identical to (4) which is equivalent to (3). This illustrates the consistency between the methods. The main difference is that, where all parameters are varying simultaneously in equation 5, the factor  $1/\sqrt{K}$  in the calculation of  $u_M$  corrects for that. Next to estimating the standard uncertainty by (6), the Monte-Carlo method also enables the calculation of distributions and percentile points (confidence intervals) for  $Y$ , depending on the distributions of the input parameters  $x_i$  [3]

### Geometrical deviations along an axis

A major source of errors and uncertainties in dimensional metrology are linear, rotary and straightness deviations along one axis. A dimensional measurement usually

consists of a combination of measurements along axes: from a simple length measurement along one axis, fulfilling the Abbe-principle, up to a full 3-D measurement in which 3 orthogonal machine-axes and all associated deviations are involved. We consider a measurement along one axis where at each point the axis deviation is considered. For the general case we can rewrite (2) as:

$$u_y^2 = \sum_i \left( \left[ \frac{\partial f}{\partial x_i} \right]_y \right)^2 \cdot AC(0) + 2 \cdot \sum_{i \neq j} \left[ \frac{\partial^2 f}{\partial x_i \cdot \partial x_j} \right] \cdot AC(x_j - x_i) \quad (7)$$

Here the deviations  $\Delta$  denote the - known or unknown - scale deviations. We have used  $\langle \Delta_i \cdot \Delta_j \rangle = \langle \Delta_i \cdot (\Delta_i + (\Delta_j - \Delta_i)) \rangle = AC(x_j - x_i)$ , where  $AC(x)$  is the autocorrelation function of the deviations of the scale reading  $x$ . This means that, when making Monte-Carlo simulations of measurements along a scale, the autocorrelation of the scale deviations must be maintained. This is equivalent to maintaining the power spectral content, and with this automatically the variance is maintained. This can be achieved by randomising the phases in the Fourier spectrum and transforming back [4]. For uncorrelated noise-like deviations the second term in (7) vanishes and (5) can be used straightforward.

What makes this problem less straightforward is that for a dimensional measurement, e.g. of a length, the second measurement  $x_2$  cannot have any position along the axis once  $x_1$  is fixed: with an axis length of  $L$  and a measurement length  $l$  the domain for  $x_2$  is restricted to  $L-l$ . This restricts the possible summations in both terms of (7). We will illustrate this for a simple length measurement along an axis with coordinates  $x_i$ . For the length of an object  $l = x_2 - x_1$ , the uncertainty is, according to (7):

$$u^2(l) = \frac{1}{N-n} \left( \sum_{i=1}^{N-n} \Delta x_i^2 + \sum_{i=n}^N \Delta x_i^2 - 2 \cdot \sum_{i=1}^{N-n} \Delta x_i \cdot \Delta(x_i + l) \right) \quad (8)$$

Where  $N$  is the number of measurement points  $x_i$  in the domain  $L$  and  $n$  is the number of measurement points in the domain  $L-l$ . An application is illustrated in figure 1, where the length deviations of a CMM-axis are given as they are measured using a step gauge. Figure 2 gives the uncertainty in a length measurement as it is calculated from equation (8). This figure gives much more useful information than when just the standard deviations in both measurements  $x_1$  and  $x_2$  are added quadratically which gives here a standard uncertainty of  $1.6 \mu\text{m}$ . Figure 2 illustrates that for measuring small sizes the uncertainty can be much smaller. When simulating these scale deviations in a Monte-Carlo manner, precautions must be taken as to maintain the autocorrelation as it is written in (8), taking into account the limited scale length and the limited range in which it can be used for a specific length measurement. The simplest way of doing this is inverting and/or flipping the deviations as depicted in figure 1; however this gives only four possible simulations. For the Fourier-analysis and phase-randomisation method [4-7], especially edge-effects must be avoided as illustrated in [4]. Note that these considerations apply to any measurement instrument which is calibrated at a number of points in a certain range. Equations (7) and (8) also hold for straightness and rotational errors of axes. For a full rotation, giving a roundness deviation, the restricted domain is not a problem.



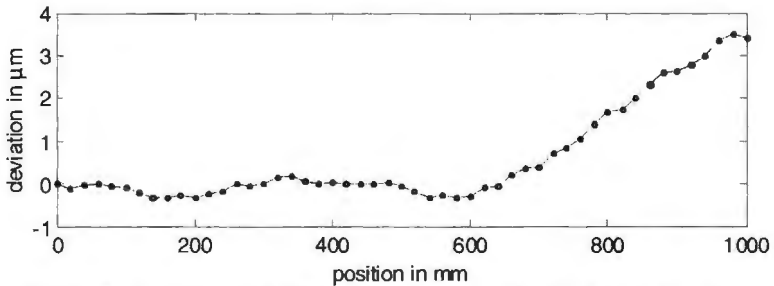


**Figure 1.** Deviations of a CMM-axis as measured using a step gauge

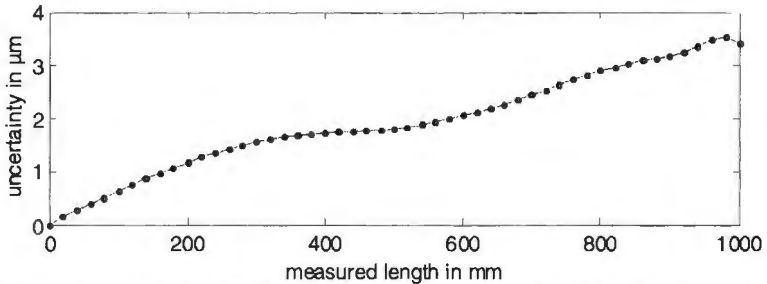


**Figure 2.** Standard uncertainty in a measured length along the CMM-axis

In this case the phase-randomisation method can be used or the roundness deviation can be rotated over a random angle to obtain a randomised deviation which can be added to the measured data to obtain an uncertainty in some parameter.

## References

- [1] ISO 14253-1: GPS - Inspection by measurement of workpieces and measuring equipment, Part 1: Decision rules for proving conformance or non-conformance with specifications. ISO, 1998.
- [2] GUM-Guide to the expression of uncertainty in measurements, ISO, Geneva, 1993.
- [3] Cox, M.G., M.P. Dainton and P.M.Harris, 'Software Specifications for Uncertainty Calculation and Associated Statistical Analysis'. NPL Report CMSC 10/01, 2001.
- [4] H. Haitjema, B.W. van Dorp, M. Morel and P.H.J. Schellekens, 'Uncertainty estimation by the concept of virtual instruments' in: Recent developments in Traceable Dimensional Measurements, Proceedings SPIE 4401 pp 147 - 157, Munchen, 2001
- [5] Schwenke, H., Abschätzung von Messunsicherheiten durch Simulation an Beispielen aus der Fertigungsmesstechnik, Thesis, PTB-F-36, Braunschweig, 1999.
- [6] Schwenke, H., B.R.L. Siebert, F. Wäldele, H. Kunzmann, Assessment of Uncertainties in Dimensional Metrology by Monte Carlo Simulation, Proposal of a Modular and Visual Software, Annals of the CIRP, 49/1/, pp 395-398, 2000
- [7] Trapet, E. et al, Development of Methods and Guidelines to Establish Traceability for Measurements with Coordinate Measuring Machines, EU project MAT1-CT94.0076, 1998

## Investigations of pitch standards for nanometrology in an metrological SEM

W. Häblier-Grohne, C.G. Frase, H. Bosse

Physikalisch-Technische Bundesanstalt, Bundesallee 100,  
D-38116 Braunschweig, Germany

### Abstract:

We report on investigations of the capability of a special metrological scanning electron microscope (SEM) to be applied for high precision pitch calibrations of standards used in nanometrology. The application of this type of instrument for calibration of pitch standards shows the advantage to combine a larger travel range with a high resolution e-beam probe of less than 10 nm. Correlation methods are used to determine global pitch values as well as pitch variations. We will discuss procedures and achieved results on 2D Si-pitch standards with grating periods of 100 nm and 300 nm. Obtained uncertainties for global pitch are less than 60 pm.

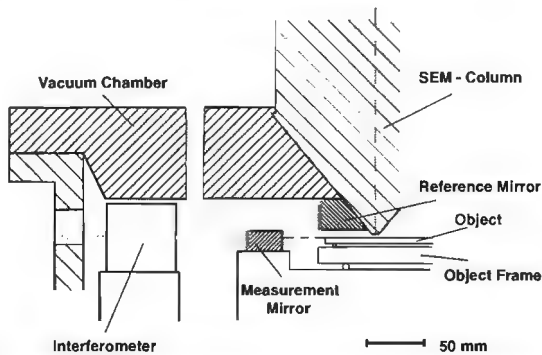
### Introduction

One- and two-dimensional pitch standards with submicrometer nominal pitches are important calibration standards for different types of high resolution microscopes, like e.g. scanning probe or scanning electron microscopes. Different types of high quality standards are available, which are produced by different techniques, like e.g. holographic methods or e-beam lithography [1]. Generally speaking, sequential structuring methods provide the possibility to exactly define the measurement area and to use additional alignment or finder structures for navigation on the sample. In this paper we report on measurements on 2D-pitch silicon standards produced by anisotropic etching after e-beam lithography. The calibration pattern is an array of inverted pyramids with nominal pitch of 100 nm or 300 nm contained within a square measurement area of 100  $\mu\text{m}$  width.

Smallest relative calibration uncertainties reported are about  $10^{-5}$  and could be obtained either by diffractometric or by long-range AFM measurement techniques [2]. We will focus on investigations of the capability of a special metrological scanning electron microscope to be applied for calibrations of 2D pitch standards. The electron optical metrology system (EOMS) basically consists of a low voltage e-beam column which is mounted on top of a large vacuum chamber with an integrated, laser-controlled precision 2D stage with 300 mm travel range [3].

The application of this type of instrument for calibration of pitch standards shows the advantage to combine a larger travel range with a high resolution e-beam probe. Moreover, the displacement of the measurement object on the stage is measured with laser interferometry in vacuum with sub-nm-resolution. The results of these displacement measurements are used to perform on-line calibrations of the magnification and non-linearities of the e-beam scanning system which is applied for imaging the structures of interest. Correlation methods are used to determine the global pitch value as well as pitch deviations. The EOMS can thus be regarded as a promising measuring instrument for pitch calibrations, supporting and complementing other techniques like AFM and laser diffractometry.

## Description of measurements



In figure 1 a view on the metrological frame of the EOMS is shown, the actual stage position is always referred to the position of the SEM objective lens by reference plane mirror interferometry. By means of this arrangement, the magnification and nonlinearities of the SEM scan generator used for imaging the secondary electrons can be precisely determined too.

**figure 1:** Side view on metrological frame of EOMS.

The precise knowledge of scan generator behaviour in principle already allows to determine local pitches from single image scans, see figure 2. From such single scans, a local pitch value can be determined with uncertainties of a few nanometer. A smaller uncertainty for the global mean pitch within the measurement area can be obtained, if one uses the interferometrically measured stage positions to correlate the phases of contrast profiles determined within subsequent image scans.

The phases of line profiles generated by vertical integration of SEM-images were determined by correlation to a synthesized reference profile. This in turn was generated by approximation of a synthesized Fourier series to the integrated profile, see figure 2 for illustration.

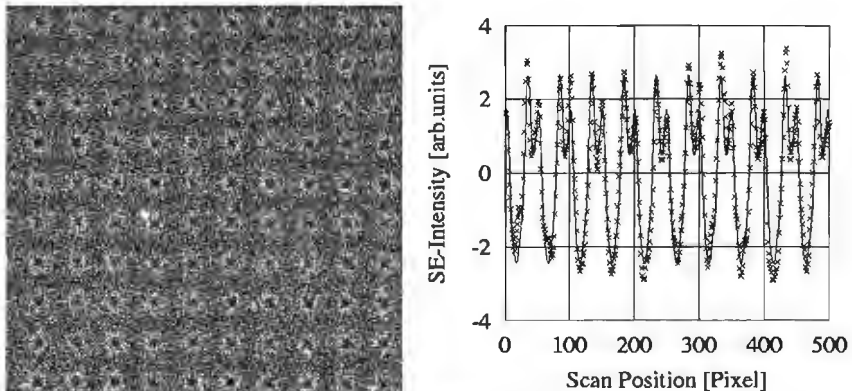


**figure 2:** Left: Typical EOMS image of a 2D Si-pitch standard with 300 nm nominal pitch. Image scan parameter: 3 keV  $E_p$ , 250 kHz pixelclock,  $512^2$  pixel. Right: Phase determination of integrated profile by correlation to a synthesized reference profile

### Measurement results

A series of measurements was performed, which each consisted of image scans taken along selected rows and columns of the 2D samples. By this approach we could measure pitch as well as straightness deviations of the silicon standard. Figure 3a shows the resulting deviations from nominal pitch as determined from 4 repeat measurements in x- and y-direction for the central row and column within the qualification area of the sample with 300 nm nominal pitch. There is an obvious discontinuity at around 50  $\mu\text{m}$  which might be caused by field stitching errors of the lithography tool used.

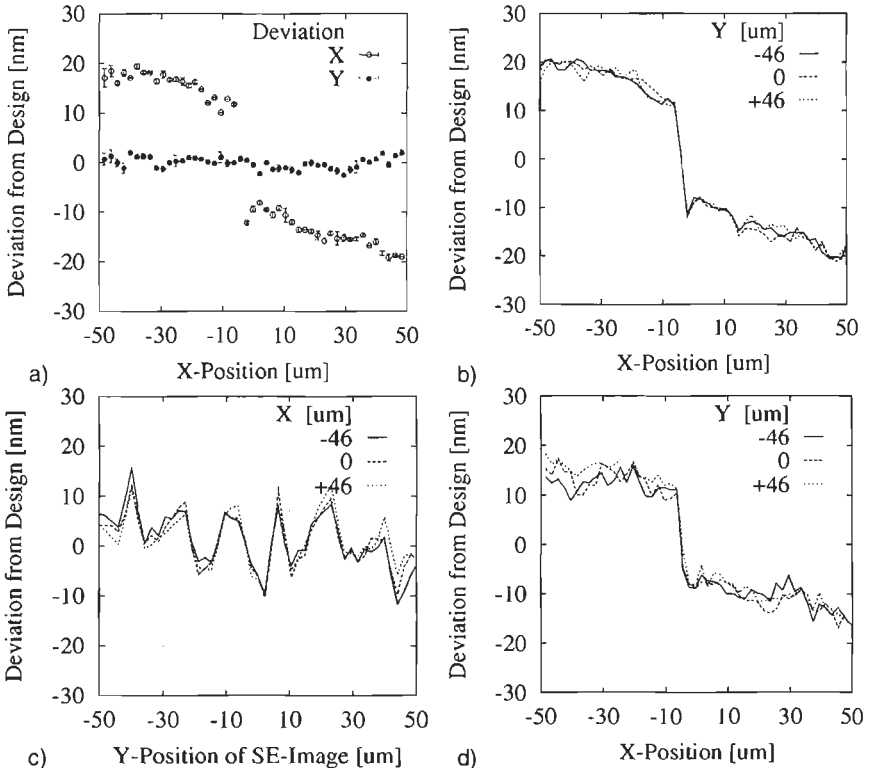


**figure 3:** **a)** Measured position deviations from nominal positions in x- and y-direction for center row on 300 nm sample; **b)** Measured position deviations for 3 rows at different y-positions on 300 nm sample; **c)** Measured position deviations for 3 columns at different x-positions on 300 nm sample, **d)** Measured position deviations for 3 rows at different y-positions on sample with 100 nm nominal pitch.

Figure 3b displays the results for pitch measurements along 3 rows in different y-positions on the sample, whereas in figure 3c the corresponding results for measurements along 3 different columns are illustrated for the 300 nm standard. Only in x-direction there is a clear indication of a single phase jump of about 20 nm, whereas in y-direction we observed a different characteristics of pitch variation. One

should bear in mind, that the single phase jump will normally not be resolved by diffractometric methods. In order to compare global pitch measures with different techniques, this irregularity should thus be excluded from further analysis. In addition to the results for the 300 nm sample, figure 3d shows the measured data for 3 different rows of the Silicon 2D-standard with 100 nm nominal pitch.

The mean pitch values which could be deduced from the measurements shown in figure 3 on the 2 different standards, after omitting apparent single phase jumps, are given below. The values denoted in brackets describe the range of linear regression slopes for the number of repeat pitch measurements performed. These variations are influenced by the reproducibility of our measurements as well as the quality of the particular graduation under investigation.

- for 300 nm standard in x-direction: 299.936 nm ( $\pm 0.012$  nm)
- for 300 nm standard in y-direction: 299.980 nm ( $\pm 0.020$  nm)
- for 100 nm standard in x-direction: 99.990 nm ( $\pm 0.004$  nm)
- for 100 nm standard in y-direction: 99.995 nm ( $\pm 0.006$  nm)

Preliminary estimations of achievable relative measurement uncertainty by means of the EOMS on the type of standards with qualification area of 100  $\mu\text{m}$  yield values smaller than about 60 pm ( $k=2$ ). For the 300 nm sample experience from other measurement methods shows, that the deviations from nominal pitch usually are smaller than 100 pm.

## Conclusion and outlook

We measured the positions of etched features within the qualification area of 2D silicon standards by means of a metrological SEM in order to calibrate the global pitch and to investigate pitch and straightness deviations of 2 standards with nominal pitch of 100 nm and 300 nm. We observed variations of local pitch values which may be attributed to deviations of the writing tool used in lithographic production of the standards. Continuing activities will also include x-y-grid calibrations for determination of orthogonality of the 2D standards and further optimization of the measurement procedure.

## References

- [1] J. Gaernes et al., "Nanometer scale transfer standards", Proc. of 1<sup>st</sup> euspen Intl. Conf., Vol. 2, pp. 134-137, 1999
- [2] F. Meli, "International comparison in the field of nanometrology: Pitch of 1D gratings (Nano4)", Proc. of 2<sup>nd</sup> euspen Intl. Conf., Vol. 1, pp. 358-361, 2001
- [3] W. Häßler-Grohne, H. Bosse, "*Electron optical metrology system for pattern placement measurements*", Meas. Sci. Technol. 9, 1120-1128 (1998)

# Free-form measurement with high lateral resolution

M. Schulz, I. Weingärtner

PTB - Physikalisch-Technische Bundesanstalt Braunschweig,

Bundesallee 100, D-38116 Braunschweig, Germany

## Abstract:

The topography of a surface has contributions of figure (form), mid-spatial frequency range (MSFR) and high-spatial frequency range (HSFR). Figure or form can be accessed using interferometers measuring the whole test specimen with low lateral resolution, such as the Fizeau type, or by pointwise scanning devices which usually have long measuring times and do not provide areal information. In the following, an extension of the LACS (Large Area Curvature Scanning) method is presented, which is capable of combining the advantages of a form scanning method and high resolution, and at the same time measures not only a single scan line of the surface.

## 1. Introduction: Accessing the topography contributions of a surface

The topography of a surface covers a wide range of information. The lateral resolution will usually be classified in terms of figure (form), mid-spatial frequency range (MSFR) or high-spatial frequency range (HSFR). Figure or form describe the macroscopic topography which, in optical applications is responsible for the well-known imaging aberrations introduced by surfaces, while MSFR describes the region characterized by so-called waviness, and HSFR the roughness.

Many measuring methods furnish information only in one of these spatial frequency ranges. In interferometers the lateral resolution is mainly determined by the pixel distance. In the case of scanning deflectometers, e.g. angle measuring systems, the diameter of the light beam and the scan step determine the lateral resolution.

Other scanning devices like mechanical profilers are capable of scanning one section line with high depth resolution and high lateral resolution, but collecting two-dimensional information on the surface takes extremely long measuring times.

As to tasks which involve more than one section line and for which the spatial frequency ranges of figure and MSFR are of interest, there is a gap in the measurement technique, which can be filled by extending the LACS method as described in the following.

## 2. The Large-Area Curvature Scanning method

In the LACS method [1], "curvature scanning" means that a curvature sensor is guided along the surface under test using a mechanical facility [2]. In the most general case this can, for example, be a Hexapod system. If there is no symmetry, a grid of profile lines has to be scanned, and these profiles can be mathematically combined to generate the three-dimensional surface topography. The method can achieve an accuracy in the single nanometer range [3].

"Large area" in the LACS method refers to the monitoring of a large area around the point for which the curvature value is to be determined.

A small interferometer is a suitable curvature sensor ( $\mu$ Phase® compact



**figure 1:** The small interferometer used as curvature sensor is guided along a diamond-turned aspherical profile on a flat substrate.

interferometer with an aperture of 3 mm, but smaller apertures are also available). With the interferometer the surface topography of a small local area is measured. As curvature is an intrinsic property of the local surface, the interferometer may be adjusted perpendicular to the local surface. Due to this and the small aperture, an interferogram with few fringes even for strongly curved surfaces is obtained.

To the small local topography, a suitable mathematical model surface is fitted. From the parameters of this fit, the curvature tensor at the centre is taken, and especially the curvature value in scanning direction is extracted. Subsequently, when the

curvature values of the one-dimensional scan over the complete surface have been determined, the surface form profile is calculated by adequate mathematical means [4], exceeding a simple twofold integration. A two-dimensional (global) surface form can then be generated by performing several scans in both Cartesian and diagonal directions and combining them using conventional mathematical tools. In practice, it is easily possible to reach a lateral resolution below 1 mm for the form with nanometer uncertainty [5], but this principle can be extended to achieve higher spatial frequency information as well.

### 3. Extension to the MSFR

The starting point for the following is that there is a form curve, describing the low frequency contributions of the test specimens topography with high accuracy.

Large-Area Curvature Scanning includes gathering information around the curvature measurement points with high spatial resolution. In the LACS set-up used at PTB, for example, the small interferometer with an aperture of 3 mm and a CCD of about 200 pixels in each direction is used, and the pixel distance corresponds to 15  $\mu\text{m}$  on the surface to be measured. The commercial interferometer used is also offered with an aperture of 1 mm and 1000 pixels in each direction, resulting in a nominal lateral resolution of 1  $\mu\text{m}$ . A LACS scan thus is sufficient also to gather the MSFR information in the vicinity of the points where the curvature values are determined.

Although the LACS method was primarily intended to record the form in a spatial frequency range below 1  $\text{mm}^{-1}$ , the combination of the data from the curvature evaluation with the interferogram information, which also has an accuracy of a few nanometers when tilt and offset are not regarded, can extend the spatial frequency range of the surface topography to several hundred  $\text{mm}^{-1}$  with an accuracy in the nanometer range.

As a method to combine the information, it is most useful to fit the small local topographies into the curve from the LACS form determination. This will include adjusting offset, tilt, lateral magnification and distortion of the interferometers imaging

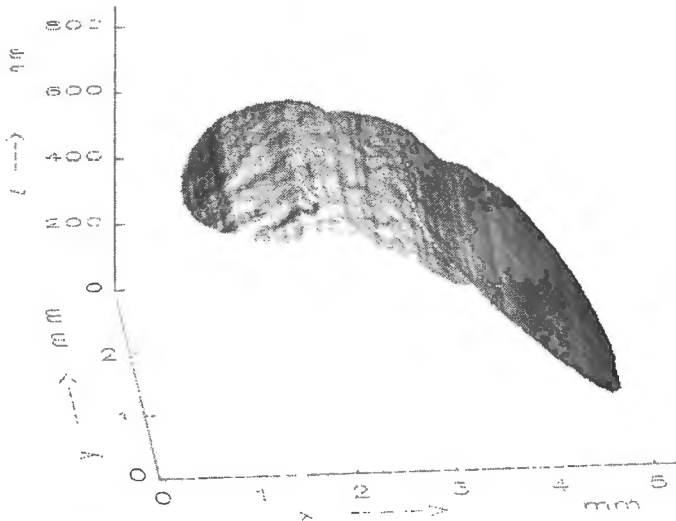


**figure 2:** Example of fitting the single small local topographies, captured with a step width of about 1 mm. The grooves perpendicular to the scanning direction are due to the diamond-turning process. The lateral resolution in this case is 15  $\mu\text{m}$ .

system. To characterize this Extended LACS method, the term ELACS will be used in the following. Fig. 2 shows a part out of a sequence of 150 LACS local topographies from a scan along a diameter of the asphere shown in fig.1. With an interferometer aperture of about 2 mm a lateral step width of about 1 mm was chosen. The single small local topographies have a circular aperture due to the interferometer software settings. The grooves perpendicular to the scanning direction stem from the diamond-turning process and can clearly be resolved. From each LACS scan a band about 2 mm in width and not only a single scan line can be obtained.

#### 4. ELACS versus stitching

Combining the surfaces as shown in fig. 2 is at first glance similar to pictures known from stitching interferometry [6]. Although the definition of stitching interferometry is not exclusively limited to one single method, it is usually achieved by fitting together the single interferograms from the overlap information. For curved surfaces, the centre is usually adjusted perpendicular to the interferometer beam. Then, for the



fitting process the outer parts of the single interferogram are used, where the measurement error increases. Moreover, the single patches often are fitted in a step-by-step process in which the overall topography error increases.

The procedure is quite different in the ELACS method. Here the macroscopic form is determined by mathematical curvature evaluation so that the form uncertainty is in the nanometer range [3]. For the curvature determination the centre of the interferometer is used, with usually the highest accuracy in the field of view. The fitting in of the small local topographies then does not increase the overall form uncertainty. Therefore, ELACS is based on principles differing much from what is usual in conventional stitching interferometry.

## 5. Perspectives

With the ELACS method a powerful tool is available for building topography measuring instruments to simultaneously assess the low spatial frequency range (form) and the MSFR with nanometer accuracy. This can serve, for example, for learning more about production processes and their global and local parameters.

## References

- [1] Schulz, M.: Topography Measurement by a Reliable Large-Area Curvature Sensor, *Optik* 112 (2001) 86-90.
- [2] Thomsen-Schmidt, P., Schulz, M., Weingärtner, I.: A facility for the curvature-based measurement of the nanotopography of complex surfaces, *Proc. SPIE* 4098 (2000) 94 – 101.
- [3] Weingärtner, I., Schulz, M.: Analysis of the uncertainty of the ultraprecise large-area curvature scanning technique for measuring steep aspheres and complex surfaces, *Proc. SPIE* 4451 (2001).
- [4] Elster, C., Gerhardt, J., Thomsen-Schmidt, P., Schulz, M., Weingärtner, I.: Reconstructing surface profiles from curvature measurements, submitted to *Optik*.
- [5] Schulz, M., Weingärtner, I.: Measurement of steep aspheres by curvature scanning: an uncertainty budget, *Proc. EUSPEN 1* (2001) 478 – 481.
- [6] Greivenkamp, J.E., Bruning, J.H.: Aspheric testing, in: "Optical Shop Testing", Malacara, D., (1992), 584- 585.

## Comparison of atomic force and interference microscopy

J. Garnaes<sup>1</sup>, A. Kühle<sup>1</sup>, L. Blunt<sup>2</sup>, N. B. Larsen<sup>3</sup>

<sup>1</sup>Danish Institute of Fundamental Metrology, Building 307, Matematiktorvet, DK-2800 Lyngby, Denmark <sup>2</sup>University of Huddersfield, Queensgate, Huddersfield, HD1 3DH, UK <sup>3</sup>The Danish Polymer Center, RISØ National Laboratory P.O. 49 DK-4000 Roskilde, Denmark

### Abstract

To understand and improve the manufacturing of functional surfaces, made by mechanical or chemical techniques, it is essential to know the physical shape of the surface, preferably as an image. Two methods often used to obtain calibrated image measurements of roughness and height structures below 100 nm in scientific and industrial applications are interference microscopy (IM) and atomic force microscopy (AFM).

### Introduction

It is the task for the surface metrologist to find a relationship between the unique but unknowable "true" surface and the known response from different measurement techniques such as atomic force microscopy and interference microscopy. When manufacturing any surface it is the "true" surface which is manufactured, and an improved knowledge about the this surface can help in the understanding and improvement of the manufacturing processes and the functionality of the surface.

To get consistent measurements of step heights between the two methods is in principle straight forward [1]. However, roughness measurements are much more difficult, and the resolution of the two methods, limited by the wavelength of light and the tip shape respectively, has to be addressed [2, 3].

To asses this, three different applied surfaces was investigated. Similarities in the images, recorded by the two methods, are seen but the visual appearance and the calculated roughness are significantly different. A simple model is set up to simulate the effective filtering inherent in the application of an interference microscope.

### Theory and experimental methods

A surface is a transition area between the bulk material properties of one material and those of another. There is no reason to expect in general that an AFM and an interference microscope will give exactly the same shape for a surface in the measurement range where they overlap.

An AFM image deviates from the "true" surface because the tip has a finite size, the specimen surface is not infinitely hard and because many diverse forces, such as charging and capillary forces influence the interaction between the tip and surface. An interference microscope probes the reflectivity of the bulk material near the surface. Strictly, the image is not a response to the surface, it depends on the optical properties of the specimen material, and resolution is limited by the wavelength of light. Edges and narrow deep holes will give rise to different artefacts inherent in the techniques caused by optical effects and tip shape.

However, for a clean and hard surface of a single phase material with good reflectivity where voids, edges and narrow holes are not significant there must be a close relationship between the measured surface shapes with the two methods. The hypotheses are that (1) the above criteria are fulfilled for most smooth machined metallic surfaces such as the three surfaces investigated in this paper (2) that the dominating difference between the observed surfaces by interference microscopy

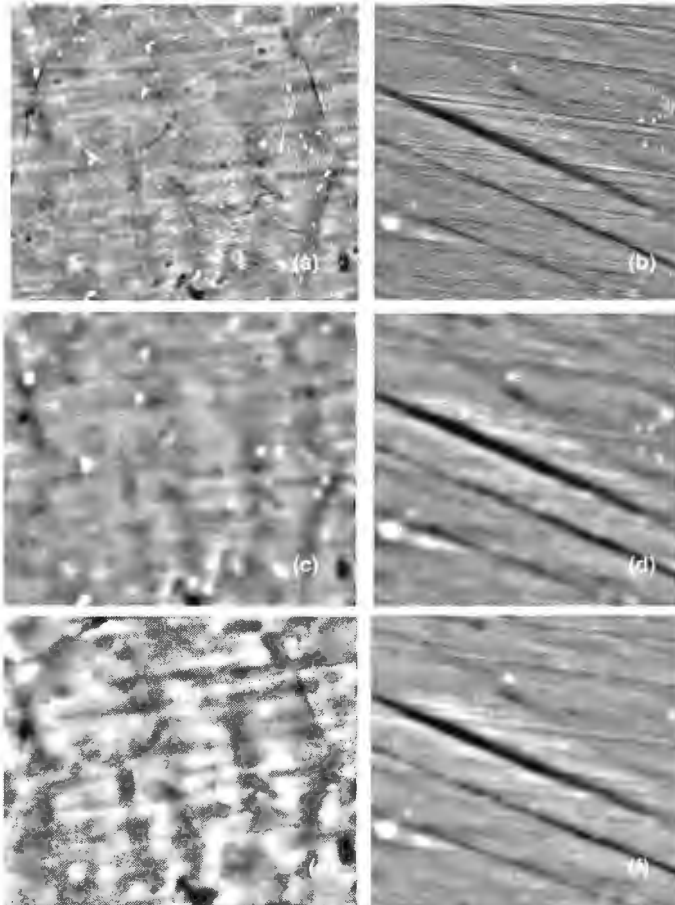


**Figure 1:** (a) is a  $35\ \mu\text{m} \times 41\ \mu\text{m}$  and (b) is a  $46\ \mu\text{m} \times 48\ \mu\text{m}$  atomic force microscopy image of a polished surface and a rolled surface. (c) and (d) are the same image as in (a) and (b) but they have been lowpass filtered with a two-dimensional Gaussian weighting function with a cut-off wavelength of  $\lambda_c = 1.8\ \mu\text{m}$  (polished) and  $\lambda_c = 2.4\ \mu\text{m}$ , to resemble the limited resolution of light. (e) and (f) are interference microscopy images of the same surface segments as in (a) and (b).

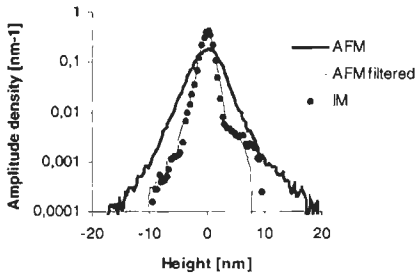


**Figure 2:** Histogram of the hip joint and interference microscopy [4] on exactly the same spot on the surfaces and images were then processed by dedicated image measurements software [5].

A least mean squares fit first order line was subtracted from each recorded line and images were then highpass filtered by subtracting a two-dimensional Gaussian weighting function with cut-off wavelength equal to 1/5 of the scan length. The surface root mean square roughness is defined as

$$s_q = \sqrt{(1/nm) \sum_{j=1}^m \sum_{i=1}^n z(x_i, y_j)^2}.$$

## Results and discussion

Figure 1 shows images of the polished and rolled surface. The polished surface when measured by AFM shows the random nature of the topography, however, there is clear evidence of grain boundaries. The filtered AFM images and the interferometric images show a less distinct surface topography with the grain boundary distinct. This is as expected due to the resolution of the instrumentation. What is evident is that choosing the filter condition to mimic the optical resolution has given an image that is remarkably similar to the interferometric image. The rolled stainless steel sheet shows similar results. The AFM image has a better resolution showing rolling effects more clearly but when the filtering is applied the two instruments give remarkable similar results.

Figure 2 shows an amplitude histogram of the hip joint surface measured using both techniques, Here again the filtered image shows a remarkable similarity to the interferometric image showing the associated reduction in the spread of amplitude levels, for the lower resolution techniques/filtering.

Table 1 compares the  $S_q$  values of the unfiltered measurements and the filtered AFM image. As expected the unfiltered AFM figure are higher for all the surfaces. The table gives the cut-off wavelength  $\lambda_c^F$  for the lowpass Gaussian filter applied to the AFM image for which the surface roughness of the AFM image become equal to the surface roughness of the interference microscopy image, that is,  $S_q^{AFM}(\lambda_c^F) = S_q^{IM}$ . The average value is  $\langle \lambda_c^F \rangle = 1.9(0.4) \mu\text{m}$ . The surface roughness for the AFM image, after application of the average value of the cut-off wavelength  $S_q^{AFM}(\lambda_c = 1.9 \text{ nm})$  is

and AFM is due to the limited resolution of light, and (3) that this limited resolution can be approximated by a lowpass Gaussian filter of the AFM image with a cut-off wavelength a little larger than the wavelength of light. The approximation is not based on a physical model.

Three surfaces were investigated, a polished block of stainless steel, a piece of bright annealed rolled stainless steel, and a hip joint prosthesis of a CoCr alloy [1]. Images of  $\approx 400$  by  $\approx 400$  points were recorded by AFM [4] and

also stated. These roughness values are very similar to the roughness values from the interference microscope and within the expected scatter of such measurements.

	$S_q^{AFM}$ [nm]	$S_q^{IM}$ [nm]	$\lambda_c^F$ [ $\mu\text{m}$ ]	$S_q^{AFM}(\lambda_c=1.9 \text{ nm})$ [nm]
<b>Hip joint CoCr</b>	<b>2.9</b>	<b>1.35</b>	<b>1.6</b>	<b>1.27</b>
<b>Polished stainless steel</b>	<b>10.2</b>	<b>6.3</b>	<b>2.4</b>	<b>6.9</b>
<b>Rolled stainless steel</b>	<b>10.8</b>	<b>6.2</b>	<b>1.8</b>	<b>6.0</b>
<b>Average</b>	<b>NA</b>	<b>NA</b>	<b>1.9</b>	<b>NA</b>

**Table 1:** The surface root mean square roughness  $S_q^{AFM}$  and  $S_q^{IM}$  is calculated from the AFM and interference microscopy images.  $\lambda_c^F$  is the cut-off wavelength of the lowpass Gaussian filter applied to the AFM image to resemble the resolution of an interference microscopy and  $S_q^{AFM}(\lambda_c=1.9 \text{ nm})$  is the roughness when the same filtering of  $\langle \lambda_c \rangle = 1.9 \text{ nm}$  is applied (see the text).

## Conclusion

Applying a lowpass filter with a cut-off wavelength in the order of the wavelength of light  $\lambda_c=1.9(0.4) \mu\text{m}$ , the appearance of the images and the calculated roughness become almost identical. This strongly suggests that the two methods are consistent, at least when measuring surfaces with a consistent strong reflectance where the optical response is from the surface rather than sub-surface layers, and that the observed differences in shape and roughness in the nanometre range can be explained by the limited lateral resolution of the interference microscope.

## References

- [1] Traceable Step height and roughness measurements with atomic force microscopes, J. Garnaes et al., Proc. of 2nd euspen International Conference – Turin, Italy – May 27th –31st, 2001
- [2] Capabilities and limitations of interference microscopy for two- and three-dimensional surface-measuring technology, W. Hillmann, et al., Measurement Vol. 19, No. 2., pp. 95-102 (1996)
- [3] Advances in traceable nanometrology at the National Physical Laboratory, R. Leach, et al., Nanotechnology 12 R1-R6 (2001)
- [4] Dimension 3000 SPM and Dimension 3100 SPM with metrology AFM head, Digital Instruments and WYKO NT2000, Veeco Instruments. The instruments were calibrated using step heights.
- [5] The Scanning Probe Image Processor (SPIP) made by Image Metrology ([www.imagemet.com](http://www.imagemet.com)) Denmark

## Self-Centring Probe with Parallel Kinematics

E.Trapet<sup>1</sup>, J.Aguilar<sup>2</sup>, H.Spaan<sup>3</sup>, J.A.Yague<sup>2</sup>, V.Zelený<sup>4</sup>

<sup>1</sup>Vitoria, Spain; <sup>2</sup>Zaragoza, Spain; <sup>3</sup>Eindhoven, The Netherlands; <sup>4</sup>Prague, Czech Republic

The work was sponsored by the European Commission (Measurement and Testing). Partners were: CMI, Fidia, Lemmen, Mecaner, Spaan, UNIMETRIK, Univ. Zaragoza.

### Abstract

A new type of self-centring probe to verify the performance of machine tools using ball artefacts is presented. When positioned with the machine head against a sphere of the artefact, the probe delivers the position X, Y, Z of this sphere in the coordinate system of the probe. Unlike existing analog probe systems for three-dimensional point measurement, which all use three serially arranged orthogonal stacks of linear motion systems with one linear position sensor each, the here-described probe contains three independently movable probe styli (parallel kinematics).

### Needs for the new Probe and Criteria for its Design



**figure 1:** 4m ball bar of carbon fibres on a CMM

Ball artefacts, like multi-ball bars with the positions of the balls calibrated in three dimensions, have the potential to facilitate the verification of linear axes of machine tools (MTs) as they do for coordinate measuring machines (CMMs): Only one type of reference standard is needed in contrast to 5 types required by present day techniques to measure a full set of error parameters of three linear MT-axes. With 3-dimensionally calibrated ball bars, this can be done with one object, placed in 6 axial positions fully to be measured, and 6 diagonal positions partially to be measured. A probe that can measure the deviations of the 3D-positions of the MT relative to the balls of a ball artefact, would greatly facilitate the use of such objects, as it would neither be required to perform measurement functions with a MT nor to transfer measured data: The probe would serve to compare calibrated ("true") ball positions with the positions of the MT (ideally programmed to go to the calibrated positions). Once having recognised the advantages of such a probe for linear axes verification, the application for rotary axes verification is obvious: the probe serves the same purpose as a ball bar [1], however, the test would be three times faster, as axial, tangential, and radial errors are verified at the same time as with 4-axis tests, as they were designed for CMMs [2]. Here the rotary table with a reference sphere attached to its top is stepped through a large range of angles. The position of the ball is tracked with the probe fixed to the head of the machine, moving the Cartesian axes of the machine to those positions at which the sphere is expected

to be, according to the programmed nominal angular positions of the rotary table. Besides, methods have been proposed and partly realised for CMMs that allow to assess a full set of error parameters with a single sphere measured in a number of positions on a rotary table [3]. These methods would become available for MTs too, opening a wide field of possibilities of error correction e.g. for rotary work tables and rotary milling heads. The problem was, that such a probe was not existent, at least not fulfilling the combination of all requirements: uncertainty  $<2\ \mu\text{m}$ , small size, small probing force, small moving masses to avoid problems of impacts on the object and vibrations, measurement range  $>4\ \text{mm}$  (to cope with imperfections of the alignment, the ball bar, and the machine), and of a maximum market price of 10000 Euro. Thus a new probe concept was needed.

### New Probe Concepts based on Parallel Kinematics

Methods to probe the spheres on the artefact directly optically were excluded from the beginning as the optical properties of the spheres and the cleanliness are not assumed to be sufficiently under control. About a dozen of alternatives to realise a tactile self-centring probe were studied, beginning with classical triple stacks of spring parallelograms. These were as well excluded for reasons of too big masses creating the danger of probe and object damages. Systems, in which the centring is done by a separate centring attachment in form of a cone or a nest of three balls and the orientation and position of this attachment measured with linear sensors was regarded as realistic, however, because of the mass problem, the measurement of this attachment would need to be a contactless one; capacitive sensors were studied, but did not yield the required repeatability over the entire measurement range of about 1:25000. Optical (photometric) sensors seem promising after the first tests, however no such sensors exist from the shelf, and a new development of a high resolution optical sensor could only be considered if the probe would be produced in quantities.

It was then soon realised that the specific task, i.e. to measure only the position of a sphere centre, the sphere diameter being known, could be solved with a probe of much simpler structure than that implemented in a measuring probe of a CMM. Having here to probe a sphere with a well defined and precise surface, this could be done with three styli independently making contact with the object..

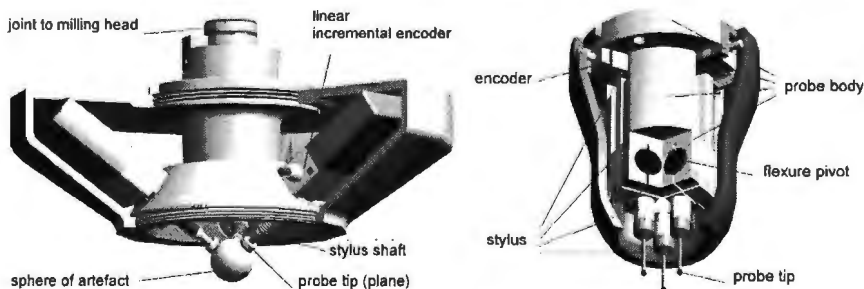


**figure 2:** self centring probe with linear styli (left) and with rotary styli (right)

This idea of "parallel kinematics" was then implemented in two prototypes, one with linearly movable styli and with flat probe tips, the other with rotationally movable styli and with spherical probe tips, both with incremental sensors to measure the displacement of each stylus (fig. 2). Main advantage of the first prototype is that linear incremental probes are commercially available and come already with a very

precisely guided stylus. The probes are here arranged orthogonally to each other (which gives maximum sensitivity in all directions) and touch the spheres of the reference object with their tips on measurement lines passing all three approximately through the sphere centre; this makes Abbe errors negligible. Main advantage of the second prototype is that it is more handy. Here the probe touches the sphere in a similar way as a person that wants to pick up a ball with three fingers, slightly above the equator. The rotations of the three styli are measured each separately with an angular encoder. The axis of rotation and the spring action that pushes the styli against the sphere, are realised by flexure pivot elements.

The transformation of the sensor readings to X, Y, Z coordinates is done by calculating first the probe tips' positions, based on the sensor readings and on the known geometry of the styli and their suspension. Then the centre of the sphere of the artefact is calculated from the three centre points of the tips or from the tangential contact planes of the stylus tips (according to whether the tip is spherical or flat).

Different calibration techniques have been developed to measure the geometrical parameters needed for these calculations: One is the measurement of the relative location and orientation of the probe components directly on a CMM. In case of linear stylus probes with plane probe tips, the only required measurements are that of the cylindrical stylus shaft (orientation) and that of the tip's contact plane (orientation and position). In total 21 parameters are needed for all styli together. In case of rotary stylus probes with spherical probe tips, the axis of rotation, the probe tip centre coordinates and the distances between probe tip centre and the axis, as well as the distance between axis and the grating of the rotary encoder have to be measured for each stylus. If the axis is not directly measurable, for example because it is realised by a flexure pivot, other points on the stylus are measured with the stylus in different angular positions; this allows to calculate the axis direction and location. For all rotary styli together, there are 21 parameters, plus the (same) diameter of the probe tips. All the above model parameters describe ideal components. Only in one case this assumption was not justified: when using a flexure pivot element; its axis position was found to be a function of the angle of rotation. To solve the problem, additionally 2-axial translations in form of 2<sup>nd</sup> order functions of the rotary angles were introduced.

Another way of calibration is to attach the probe to the ram of a CMM and move it to a great number of known positions with the stylus tips in contact with a sphere to be probed. The values indicated by the probe system and the "true" positions are recorded. The required geometry parameters are best-fitted to the so-gathered data. This process can best be applied to an already approximately modelled probe system. A new calibration device has been developed to carry out the same calibration as before described, but without the need of a highly accurately positioning CMM (most

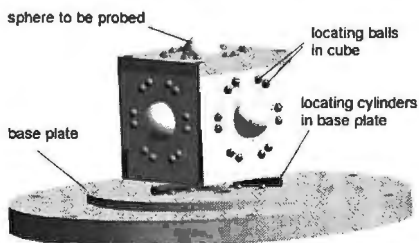


**figure 3:** calibration device for probes

CMMs measure only accurately but do not position accurately). This calibration device is a kind of miniature ball cube (fig. 3) which has a multiple of surfaces with spheres fixed to these surfaces; to each sphere exist several sets of corresponding locating elements, by which the device is precisely positioned on a base plate. The locating elements and the corresponding spheres to be probed, have, from face to face, different



relative positions and orientations, thus, by repetitively placing the calibration device on the base, and engaging different locating elements, a multiple of positions of the spheres relative to the base are obtained. The positions of the spheres to be probed with respect to the base plate are prior calibrated on a CMM.

## Results

The self centring probe was verified, using the technique of the calibration cube. Fig. 4 shows the errors in X,Y,Z for one prototype after being thoroughly calibrated. The linear probe yields about 1  $\mu\text{m}$  range of the errors of position over the full travel of 4 mm in each axis direction and the rotary probe 3  $\mu\text{m}$ . The 36 positions are randomly numbered. The cube itself is calibrated with an uncertainty of 0.5  $\mu\text{m}$ . First measurements were performed on machine tools (fig.5). Results coincide with laser interferometers measurements for position, straightness, and rotations.



figure 5: self centring probe on a machine tool while measuring a ball bar

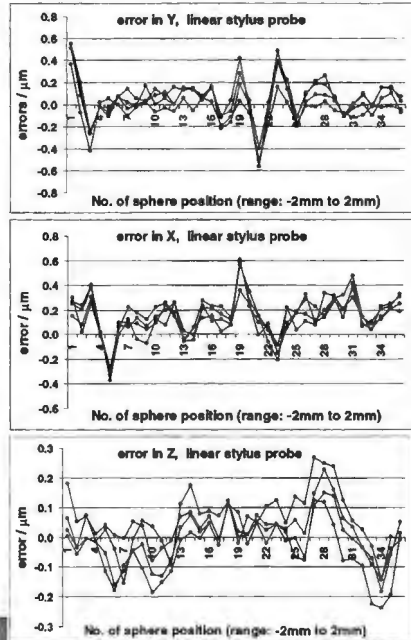


figure 4: Deviations of values indicated by a linear stylus probe from the "true" values of a calibration tool

## Future Developments

While the linear stylus probe is fully developed regarding its reachable uncertainty, the rotary stylus probe has still potential for improvement with respect to its calibration and its model (more measurement data and better simultaneous fitting algorithms). Both probes still have potential for miniaturisation by dedicated sensor designs.

## References

- [1] ASME B5.54: "Methods for Performance Evaluation of Computer Numerically Controlled Machining centers", ASME, 1992
- [2] Trapet, E.: "Rückführung von Koordinatenmeßgeräten durch Abschätzung der zu erwartenden Meßabweichungen durch Simulation", DFG-Report, PTB, 1996
- [3] ISO 10360-3: "Acceptance and Verification tests of CMMs ... with the axis of a rotary table as the fourth axis", ISO, 2000

## The virtual CMM method for three-dimensional coordinate machines

B. van Dorp, H. Haitjema, P. Schellekens

Precision Engineering section, Eindhoven University of Technology, PO Box 513, 5600 MB Eindhoven, The Netherlands

### Abstract

In coordinate measurement metrology, assessment of the measurement uncertainty of a particular measurement is not a straight forward task. We have developed a Monte Carlo method that can be used for CMM's that takes into account the most important error sources, including linearity errors, rotational errors, straightness errors, squareness errors and temperature uncertainty. Special measurement tools have been developed and applied to measure straightness and linearity errors. The short-wave as well as the long-wave behavior of these errors of two machines have been calibrated. A machine model that takes these effects into account is used to calculate the respective measurement uncertainties of several tasks on these machines. These calculations were compared to real measurements.

### Uncertainty calculation

Assessing measurement uncertainty implies assessing the distribution of the possible measurement results. Methods involving Monte Carlo simulation consist of a model of the measurement process, and knowledge of the most important influence quantities. Knowledge of influence quantities can be determined analytically or by calibration, and in both cases it should consist of a probability distribution. Such a model is called a virtual machine. In case of a coordinate measurement machine, it is called a virtual CMM [1]. This virtual CMM is used to numerically estimate the distribution of the possible results, which is a measure of the uncertainty. For every simulation, a sample of every influence quantity is taken using a random generator. These samples are evaluated by the model resulting in a distribution of virtual results.

In general, a measurement result  $M$  is a function of a number of measured values, the input quantities  $m_i$ .  $M$  is calculated using a model function  $f$ :

$$M = f(m_1, m_2, \dots, m_n)$$

This model function  $f$  often is not a function, but an algorithm that is implemented in a computer. The measurement uncertainty of  $M$  is defined as:

$$u_M^2 = \sum_i \left( \frac{\partial M}{\partial m_i} \right)_M^2 \cdot u(m_i)^2 + 2 \cdot \sum_{i \neq j} \left[ \frac{\partial^2 M}{\partial m_i \cdot \partial m_j} \right] \cdot \langle u(m_i) \cdot u(m_j) \rangle$$

Here,  $u(m_i)^2$  is the uncertainty of input quantity  $m_i$  and  $\langle u(m_i) \cdot u(m_j) \rangle$  is the covariance of  $m_i$  and  $m_j$ . Consider a simple one dimensional length measurement, with only two measurement points,  $x_1$  and  $x_2$ , and one result:  $L = x_2 - x_1$ . Using the above equation, we find the following expression for the uncertainty  $u_L$  of the measurement:

$$u_L^2 = \left( \frac{\partial L}{\partial x_1} \right)^2 \cdot u_1^2 + \left( \frac{\partial L}{\partial x_2} \right)^2 \cdot u_2^2 + 2 \cdot \left( \frac{\partial L}{\partial x_1} \right) \left( \frac{\partial L}{\partial x_2} \right) \langle u(x_1) \cdot u(x_2) \rangle$$

In the above expression,  $u_1 = u(x_1)$  and  $u_2 = u(x_2)$  are the random errors on these

positions. The term  $\langle u(x_1) \cdot u(x_2) \rangle$  is the auto correlation of the error signal, with lag  $\Delta x = x_2 - x_1$ . This leads to the conclusion that a satisfactory machine model should take into account the auto correlation of the error signal.

A model that uses this approach using a virtual CMM, would require the errors of all simulated points within one simulation to be correlated with each other in the same way they are correlated in the actual machine. In the above example, this would imply that the points  $x_1$  and  $x_2$  are drawn from a signal that has the same auto correlation as the original error signal of the machine. A signal with this property is called a surrogate signal.

### The machine model

The geometric errors of the machine are separated in linearity errors, straightness errors and squariness errors. Linearity errors are errors that occur in the direction the machine is moving. For example, when the machine moves in  $x$ -direction, there's an error in  $x$  direction. This error is called the  ${}_xT_x$  error. In a three dimensional measurement machine, there are three linearity errors,  ${}_xT_x$ ,  ${}_yT_y$  and  ${}_zT_z$ . The linear terms of the respective straightness errors are ignored at this point. The linear term of these errors can be the result of an actual linearity error, but also of incorrect temperature measurement during calibration. In the model, all linear terms of the linearity errors are accounted for in the temperature uncertainty.

Straightness errors are the errors that occur perpendicular to the moving direction of the machine. For example, when the machine moves in  $x$ -direction and there's an error in  $y$  direction, this error is called the  ${}_xT_y$  error. In the three dimensional case there are six straightness errors. A straightness error does not have a linear term. A linear straightness error can be the result of either misalignment during calibration or of the squareness error.

The axes of the machine are not perfectly perpendicular to each other. The expected value of the deviation of the right angle is defined the squareness error. In the three dimensional machine, there are three squareness errors.

The rotational errors are not calibrated directly, but are incorporated in the machine model by measuring the straightness and linearity errors on different positions, making it possible to calculate the rotational errors from these errors.

### Calibration of errors

In calibrating the errors we take several basic assumptions. First, we want all calibration data to be the result of actual probings of the calibration artefact by the machine. Second, we want to make sure we gather enough data to provide the model with enough information on the autocorrelation spectrum.

The model uses the autocorrelation information of the straightness and linearity errors. To calculate these autocorrelations, the calibration data have to provide both long wave information and short wave information. Therefore, it is necessary that the measurement setup allows us to measure a small step (for example 1 micrometer), and also extends to almost the maximum length of the machine axes, for example 300 mm. It is evident that it is not possible to measure the complete axis with the smallest step, as this would require 300.000 measurement points. For this reason, the measurement of the error was split up in three levels of magnification. For example, the first level consists of 41 points with a stepsize of micrometer, resulting in a total measurement length of 40 micrometer. The second level consists of 41

points with a stepsize of 40 micrometer, total length is 1.6 mm. The top level consists of 188 points of 1.6 mm, total length 299.2 mm. This scheme should provide us with sufficient data, only when we can assume that the short wave behavior of each axis on one position can be assumed roughly the same as the short wave behavior of that axis on another position. Looking at the construction of a coordinate measurement machine with stacked axes, there is no reason to believe that this short wave behavior is much different on different positions. The investigated machines, a Zeiss Prismo and a Zeiss UMM 550, did not show that this assumption was not valid.

Straightness errors of a CMM can be determined by probing a straightness gauge. A calibrated straightness gauge with a length of 320 mm and a straightness error smaller than 0.1 micrometer was used to determine both straightness errors. The straightness gauge is placed on the machine and probed on different positions using the data collection scheme mentioned in the previous section.

Linearity errors are traditionally measured using a stepping gauge. This instrument has a fixed step, and this fixed step is usually not smaller than 10 mm. This makes the stepping gauge not suited for small wavelengths, certainly not if we want to measure the 1 micrometer step. Therefore, an instrument that can measure linearity errors using a variable step has been developed, a laser stepping gauge. A flat plane is mounted on the carriage of a computer controlled linear positioning stage. The position of the carriage can be accurately measured using a laser interferometer setup. The moving mirror is mounted on the carriage, the fixed mirror is mounted on the base of the instrument. The instrument is used as follows: the carriage is moved to the desired position, and stopped. Its position is measured accurately using the laser interferometer. The CMM moves to the flat plane and determines its position by probing it. When this is done, the CMM moves back and waits for the carriage to move to the next position where the process repeats itself. The entire process is automated, which makes it possible to reliably collect large amounts of data. The positions given by the machine can now be compared to the positions given by the laser interferometer, which makes it possible to calculate the machine error.

### **Generation of signals**

An simple and straightforward way of generating a signal with the same auto correlation as the measured signal is to take the original signal and perform a transformation on it that does not affect the auto correlation. There are four simple transformations that have this property: 1. don't change the signal, 2. reverse the sign, 3 flip the signal from left to right, 4. a combination of 2 and 3.

This would allow four simulations to be done with one signal. Because the signal is measured in three levels with different stepsize, there are three signals on every axis. This gives a total of  $4^3=64$  possible simulations for one axis.

### **Temperature and squareness**

An error in temperature measurement of a real measurement would result in a systematic error of this measurement. To express the uncertainty of this error, it is simulated as if it were a random error. The temperature error or length dependent error is simulated as if every simulated measurement were performed with a different random error in the temperature measurement.

The squareness error of a CMM results in a systematic error that is the same in all measurements. Analogous to the length dependent error, to express the uncertainty of the squareness error, it is simulated as if it were a random error.

## Evaluation of results

The machine model is implemented in a computer using Matlab. A calculation of the measurement uncertainty is now performed by generating a number of sets of virtual measurement points. These data sets are evaluated by the software of the

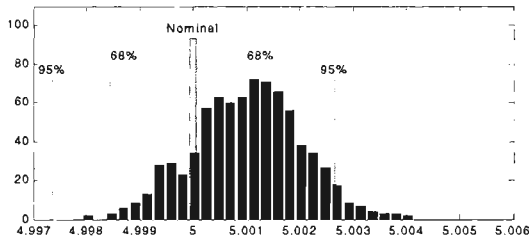


**Figure 1:** evaluation of simulation results

measurement machine, resulting in a set of *virtual results*. The evaluation of these virtual results is demonstrated from an example. Let's say we have a measurement with a nominal result of 5 mm. An example of a histogram of possible measurement results is shown in figure 1. The measurement uncertainty with a 95% confidence level is the half width of the interval that covers 95 % of the area of the histogram. In figure 1, this is 2,6 micrometer. For the 68% confidence level, this width is 1,5 micrometer.

## Conclusions

A fully operational virtual CMM, including a machine model, a calibration procedure, calibration setups, and an implementation of the model in a computer are realized. This entire system is tested on two different machines and preliminary results have shown the approach to be successful.

## Acknowledgement

This project is financially supported by the Dutch Ministry of Economic Affairs in the framework of the BTS-project "Traceable Calibrations using CMM's", project number BTS98032. Other participants in this project are IBS Precision Engineering B.V., Zeiss Nederland B.V., Stork FDO B.V. and the NMI Van Swinden Laboratorium B.V.

## References

- [1] Schwenke, H. e.a. "Assesment of Uncertainties in Dimensional Metrology by Monte Carlo Simulation: Proposal of a Modular visual Software", *Annals of the CIRP*, Vol. 49(1), p. 395 – 398, 2000.
- [2] Dorp van, B. e.a. Virtual CMM using Monte Carlo Methods based on Frequency Content of the Error Signal, *Proceedings of SPIE Vol. 4401*, p. 158 - 167, 200

## Modelling of Spatial Constraint in CMM Error for Uncertainty Estimation

M. Abbe<sup>1</sup>, K. Takamasu<sup>2</sup>

<sup>1</sup>Mitutoyo Corporation, Japan; <sup>2</sup>The University of Tokyo, Japan

### Abstract

Authors propose a noble simulation method applicable for estimating uncertainty in coordinate metrology. Recognizing a key point for uncertainty estimation on task specific measurement on CMM is to determine uncertainty of a single coordinate reading, a simple and effective modelling procedure to derive not only variance but also spatial covariance expressing mutual constraint between plural observation points is presented. Actual spatial constraint observed on 350 CMMs on the production floor shows good agreement with that predicted by the proposed model.

### Introduction

Uncertainty analysis of CMM (Coordinate Measuring Machine) becomes important concern today. Monte Carlo simulation method is a major possibility to derive a trial value from given variance information. However since the method normally adopts a simple random number generator, plural trial values mutually constrained as result of contribution from unknown systematic component, e.g. geometrical error of CMM or probe can not be modeled directly. Typical preceding studies adopt an additional model based on randomized combination of a sort of basis functions [1-4]. The basis function can be described by Fourier spectrum, harmonics function, or sinusoidal function for example. As the result, a combination made by random trials and the other model composed by basis function builds an uncertainty contribution component with constraint. This way can be understood as modelling of variance and related covariance conforming to GUM [5]. The covariance is equivalent to auto-correlation or correlation factor naturally.

Authors proposed a simple way of modelling variance and covariance observed in geometrical deviation of CMM, such as position error, straightness error and so on [6]. Proper quantification scheme for the spatial constraint was not found at that stage unfortunately, and assumed parameters were adopted. Following study [7] proposed an idea of derivation of spatial constraint information from the template expression of the verification standard of CMM such as ISO 10360-2 [8]. It is noted that this way of modelling realizes a possibility of task specific uncertainty estimation on coordinate measurement in the maximum permissible sense.

### ISO10360-2 Template and spatial constraint

According to ISO10360-2 standard for acceptance and reverification of CMM, seven independent size measurements on the material standard of size are performed in any location and/or orientation within the measuring volume of the CMM. Performance of the CMM is verified if all the measured deviation lie with in the specified range. The range may adopt a typical template expression as shown in equation (1). Increasing size to be evaluated, permissible length error enlarges correspondingly.

$$MPE_E = \pm(A + L/K) \text{ and } B$$

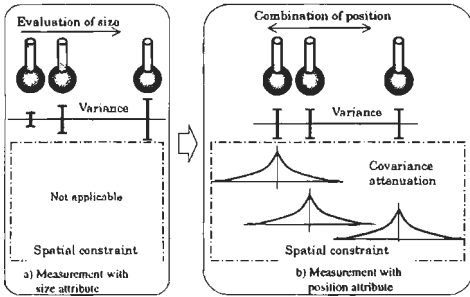


**Fig. 1** Modelling of measurement uncertainty of size with spatial constraint

mutual distance. This way of modelling is shown in Fig. 1–b). Note that both way of modelling leads to very similar algebraic unfolding result.

**Task specific uncertainty based on model with spatial constraint**

Task specific uncertainty estimation by using the proposed model with spatial constraint can be performed as drawn in Fig. 2. The method requires very limited input parameters such as ISO10360-2 specification and specific measurement strategy. Since the ISO10360-2 specification is tolerance to be satisfied always, uncertainty estimation result by the method becomes maximum permissible sense. In the other word, the method derives some over estimation in resulted uncertainty. The method may become economically beneficial estimation method if the over estimated

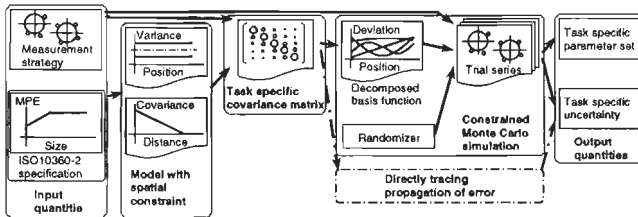


**Fig. 2** Estimating task specific uncertainty based on model with spatial constraint

quantity is acceptable for industry. Further study on this over estimation will be necessary. The given ISO10360-2 specification is transferred to variance and covariance by the proposed model with constraint. Task specific covariance matrix reflecting also the given measurement strategy is then calculated. We need one more step to derive task specific uncertainty according to GUM. That is to calculate uncertainty of a feature which user of the CMM wish to know. We may have two possibilities namely: i) Feature based metrology [9] which directly traces propagation of error from observed value to target feature, and ii) Constrained Monte Carlo simulation which rolls plural dice constrained each other at once.

**Rolling constrained plural dice for trial series**

Typical uncertainty estimation utilizes Monte Carlo simulation that rolls a die several

Recognizing the maximum permissible error range as an indirect expression of uncertainty in size measurement, the way of modelling is drawn in Fig. 1-a) schematically. Since verification measurement may be allocated to any location and orientation in the volume, a simple error model with homogeneous variance in any location and orientation of the volume is believed to be realistic.

Furthermore spatial constraint between plural observation points is understood as attenuating correlation effect depending on the

Further study on this over estimation will be necessary.

The given ISO10360-2 specification is transferred to variance and covariance by the proposed model with constraint. Task

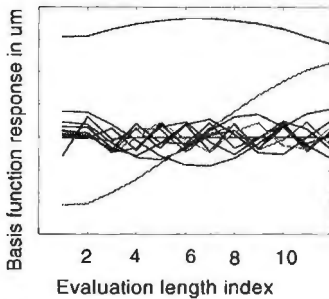
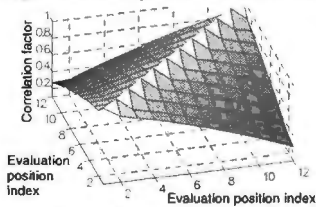
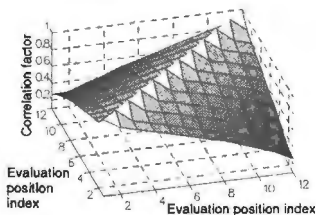


**Fig. 3** Decomposed basis function



b) Correlation factor in Model with constraint



a) Correlation factor resulted by Constrained Monte Carlo simulation

**Fig. 4** A verification result of Constrained Monte Carlo simulation

times to give possible deviation value for all the necessary input parameters. This characteristic requires, on the other hand, the extra basis function to describe uncertainty contribution with constraint. Proposed model in this study fundamentally includes variance and also covariance as spatial constraint too. A new idea to roll plural dice with constraint characteristic is considered. Authors propose an algebraic solution for this problem. The proposed method is drawn in Fig.2 on its right bottom side as the constrained Monte Carlo simulation. It

utilizes the eigenvalue decomposition of the task specific covariance matrix into a linear combination of spatial basis functions. An example of the decomposed basis function is shown in Fig. 3. This example simulates size measurement on a step gauge with 12 different length inline. The horizontal axis indicates observation position by the indexing number, and the vertical axis does geometric deviation derived by respective basis function. Qualitatively speaking, respective basis function represents spatial frequency with order of 0th, 1st, 2nd, and so on.

The recomposition process is performed by setting randomly fluctuated amplitude to respective basis function, and by combining them. A series of trial values satisfying the statistical process defined by the constrained covariance matrix can be generated by simply applying random generator on the basis function. A verification result of the constrained Monte Carlo simulation is presented in Fig. 4.

The top figure a) shows an example of correlation factor distribution derived from ISO10360-2 template by the proposed model with constraint. Both horizontal axes indicate observation position by the indexing number identical to that of Fig.3. The vertical axis corresponds to correlation factor from 1,0 to attenuated value. Simulations were executed 1.000 times, and the task specific correlation factor was calculated from 1.000 population of trial series. The result was shown in the bottom figure b) of Fig. 4. Not only variance, but also correlation factor was well controlled by the constrained Monte Carlo simulation.

### Spatial constraint on real CMM

The proposed model with constraint was applied on the real CMM on the production floor. The verification procedure conforms to that specified by ISO10360-2. Totally 350 CMMs were examined to extract statistical characteristic, especially spatial constraint observed on geometric deviation of real CMMs. The spatial constraint



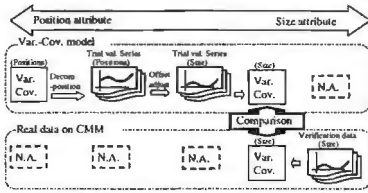


**Fig. 5** Comparison procedure of spatial constraint

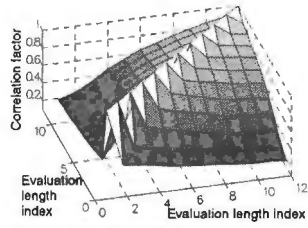
extracted from real CMMs is compared to that predicted by the proposed model with constraint. The comparison procedure is schematically drawn in Fig. 5. Since the model with constraint stands on attribute of position, and experimentally observed verification results on real CMMs do on that of size, comparison is performed by statistical parameters with length attribute. A comparison result is shown in Fig. 6. Correlation factor predicted by the model with constraint con-forms to that observed on real CMM on the production floor.

**Summary**

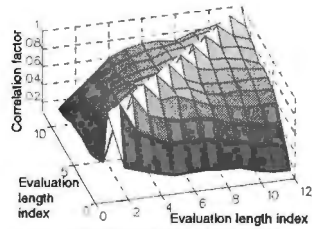
A simple method of modelling task specific uncertainty on CMM is presented. Distribution profile of correlation factor predicted by the proposed model conforms to that observed on real CMM on the production floor. Application of this model on practical feature evaluation and comparison with the other uncertainty estimation procedure will be on consideration.

**References**

- [1] Schwenke, H. et al., Assessment of uncertainties in dimensional metrology by Monte Carlo simulation: Proposal of a modular and visual software, *Ann. CIRP*, Vol. 49/1, p. 395 (2000)
- [2] Haitjema, H. et al., Uncertainty estimation by the concept of virtual instruments, *Proc. SPIE*, Vol. 4401, p. 147 (2001)
- [3] van Dorp, B. et al., Virtual CMM using Monte Carlo methods based on frequency content of the error signal, *Proc. SPIE*, Vol. 4401, p. 158 (2001)
- [4] Phillips, S., A general quantitative method to validate instrument calibration techniques, *Proc. ASPE* (1999)
- [5] Guide to the expression of uncertainty in measurement, 1st edition, ISO (1993)
- [6] Abbe, M., Takamasu, K., and Ozono, S., Reliability of parametric error on calibration of CMM, *Proc. IMEKO2000*, p. 3 (2000)
- [7] Abbe, M., Takamasu, K., and Ozono, S., Proc. A study of uncertainty in CMM calibration (3rd report), JSPE academic lecture meeting, p. 71 (2000), (In Japanese)
- [8] ISO10360-2, GPS-Acceptance and reverification tests for coordinate measuring machines(CMM)- Part 2: CMMs used for measuring size, ISO (2001)
- [9] Takamasu, K., Furutani, R. and Ozono, S., Basic concept of feature based metrology, *Measurement*, 26, p. 151 (1999)



b) Correlation factor in Model with constraint, calculated on attribute of length



a) Correlation factor observed on 350 CMMs, calculated on attribute of length

**Fig. 6** Correlation from model with constraint vs. real CMMs

## On-machine Surface Roughness Measurement with AFM

S. Moriyasu, K. Katahira, W. Lin, Y. Yamagata, H. Ohmori

The Institute of Physical and Chemical Research (RIKEN), Japan

### Abstract:

Ultraprecision optical components, such as X-ray mirrors, require ultrafine smooth surface quality of sub-nanometer or sub-angstrom in Ra. To evaluate the surface quality more accurately, AFM was used on the machine after each polishing procedure. When the surface roughness of an X-ray mirror was measured on the machine with AFM, a fine surface quality of sub-nanometer in Ra, which is almost the same level of the AFM resolution, was evaluated successfully. This measured data has a small vibration error of about 300Hz, but the possibility of the on-machine surface roughness measurement with AFM was confirmed experimentally.

### Introduction

Ultraprecision optical components, such as X-ray mirrors used in the synchrotron radiation facilities, require ultrafine smooth surface quality of sub-nanometer or sub-angstrom in Ra. And some mirrors require the length from several hundred millimeters to more than 1 meter. In the measurement of the surface roughness of these large-scaled and ultrafine components, there were some problems. For example, these mirrors are too large to measure with the conventional surface roughness measuring instruments, and it takes efforts to move them to the measuring instrument. The conventional handy-type surface roughness measuring instruments have not enough measuring resolution for X-ray mirrors. In this paper, the new surface roughness measuring system, in which a compact-type AFM (atomic force microscope) with which the surface fine structures can be measured accurately is mounted on the machine, was developed.

### On-machine surface roughness measuring system with AFM

Figure 1 shows the on-machine surface roughness measuring system with AFM. Since the stages of the ultraprecision machine are positioned in about 10 nanometers with the full closed loop control, the vibration in about 20-50 nanometers caused by the servo control is happened continuously. The measuring resolution of AFM is so fine that this vibration might become the cause of errors. Then the AFM measuring head is mounted directly on the machine stage, and it can move together with the stage and the measured object. Thus the effect of vibration to measurement was removed. By mounting the AFM head on the machine, it is possible to measure the surface roughness in the any size of the measured object accurately without removing it from the machine. Since it is possible to confirm if the surface roughness has been satisfied with the requirement during the polishing procedures, and it is possible to keep polishing when the surface roughness has not been enough yet, there are merits in both precision and efficiency.

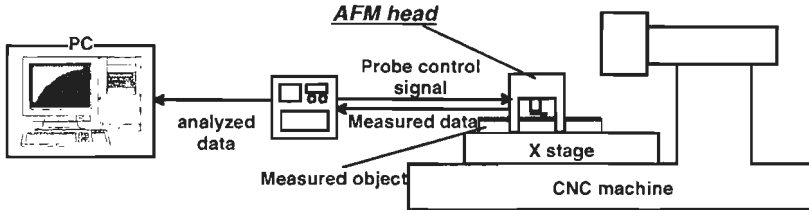


**figure 1:** On-machine surface roughness measuring system with AFM

### On-machine surface roughness measuring experiments with AFM

For the experiments, a Nanopics by SII was used as the AFM head on the machine. Measured object was Ti sample. Figure 2 shows the profile map measured by AFM and the frequency map calculated by FFT. First, the AFM head with the anti-vibration mechanism was mounted on the machine, and the sample was measured on the anti-vibration system. In this case, the surface roughness measurement could be done successfully without almost any influence on the vibration from the machine and surrounding environment. Then, the anti-vibration system was removed, and the AFM head was mounted directly on the stage of the machine. The measured data included the influence of vibration. By processing the measured data to remove high frequency components, the surface roughness with almost the same value as that under the experiment with the anti-vibration system could be achieved. Thus, it can be confirmed that it is possible to measure the surface roughness precisely on the machine with AFM by mounting the AFM head directly on the machine to remove the influence of the vibration.

### On-machine surface roughness measuring experiment of X-ray mirror substrate

In the same way, a sample with more accurate surface was measured. The sample was an X-ray plane mirror substrate with the length of 1 meter made of Zerodur. To adjust the height between the AFM cantilever and the measured object, the special jig was made for the adjustment. Figure 3 shows the surface roughness before and after the data processing. The influence of the vibration could relatively be removed by the data processing, but it was difficult to divide the surface roughness and vibration completely because the measured surface roughness of sub-nanometer level in Ra was so accurate as the measuring resolution of AFM (0.5nm).

### Conclusion

In this paper, the surface roughness measurement with an AFM head mounted on the machine is proposed and it was confirmed that the surface roughness measurement of sub-nanometer level in Ra was possible from the experiments.

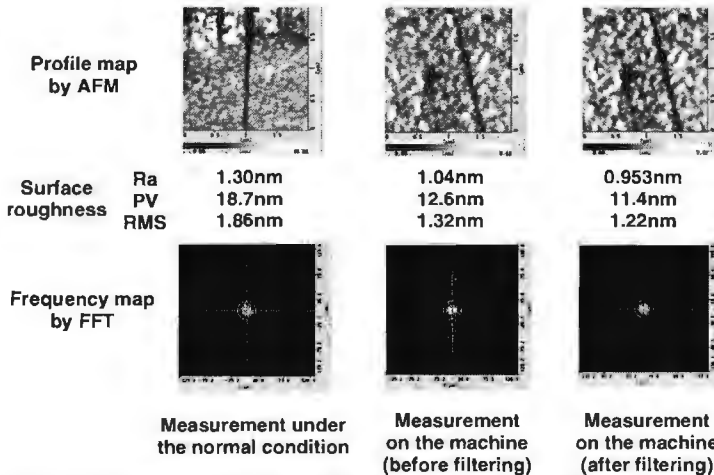


**figure 2:** Profile map measured by AFM on the machine and frequency map calculated by FFT (Ti sample)

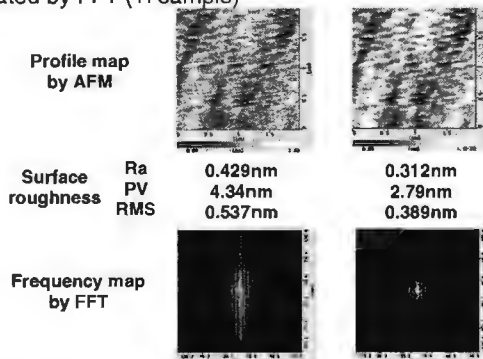


**figure 3:** Profile map measured by AFM on the machine and frequency map calculated by FFT (1m-long Zerodur X-ray plane mirror substrate)



## **A novel scanning instrument for surface geometry measurement with a flat surface as its reference plane - Practical data processing techniques by the use of optical probe**

K. Nemoto<sup>1</sup>, H. Fukatsu<sup>2</sup>, K. Yanagi<sup>3</sup>

<sup>1</sup> Nagaoka University of Technology, Graduate School of Mechanical Engineering, Japan [stomi@stn.nagaokaut.ac.jp](mailto:stomi@stn.nagaokaut.ac.jp)

<sup>2</sup> Tokyo Metropolitan College of Technology, Department of Production Systems Engineering, Japan

<sup>3</sup> Nagaoka University of Technology, Department of Mechanical Engineering, Japan

### **Abstract**

Most optical probes tend to generate different values of surface profile from that with mechanical stylus. This is mainly because of the peculiar characteristics of optical probes. Light reflection is dependent upon both macroscopic and micro-geometry of target surface. We selected several optical probes on the market to investigate their functional performances and to develop a correction method for obtaining the similar result to those by the mechanical stylus. In order to overcome the problem, we developed at first a novel scanning instrument and then a modified over-sampling method such that the height data at a point is derived from the plural sampling points in the vicinity. Their data handling techniques are described.

### **Introduction**

Demanded functional performances of industrial products have been remarkably improved, and the geometrical product specifications (GPS) of component parts such as form geometry and surface texture are regarded as extremely important. Therefore, it is indispensable to control and establish the measurement technology in the production processes. For the form geometry measurement in industry, three-dimensional measuring instruments and contour form measuring instruments with a stylus or mechanical probe are widely used. However, the following problems arise when those measuring instruments are used;

- (a) Influence of the probing force on the target surface i.e. surface deformation and damage.
- (b) Slow tracing speed and the resulting long measuring time.
- (c) Being sensitive to the vibration from surrounding objects, their setting-up conditions are restricted. And so an adequate room is needed.

Therefore, non-contact measurement system using an optical displacement sensor is expected to appear on the market that can evaluate three-dimensional surface geometry precisely and quickly without any influence from surrounding vibration. Then, we proposed and developed a novel measuring method that can utilize all-purposed spot-type optical probes. By preparing the reference plane datum inside the measuring instrument, the insensitive measurement was attained to the vertical motion error of traversing unit. The main optical displacement sensor is for measuring the target surface profile and auxiliary non-contact displacement sensor is for obtaining the reference datum. But the output characteristics of all the optical probes are different from those of a mechanical probe or stylus when measuring high frequency surface irregularities. In this study the necessary and sufficient conditions were considered for both the displacement sensors.

### Novel scanning instrument

The Structure of developed measuring instrument is shown in fig.1. The dimension of the equipment is 420mmx420mmx340mm. Granite of which the thermal expansion is small is used for surface plate and column. The stage is composed of the x-y stage. The linear scale installed it in each stage in order to obtain the position information of moved point. The scanning region of the stage is 35mmx35mm. The reference plate (material: SK-5) attached to the table back for correcting stage

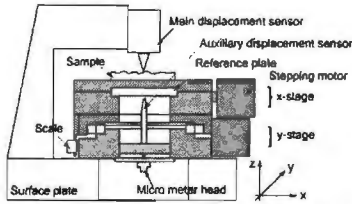


Fig. 1: Schematic of the instrument

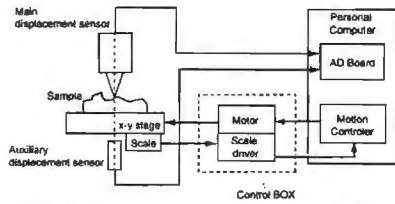


Fig. 2: Measuring system and signal

motion error. The uncertainty is known for the reference plate, and the accuracy is supposed to be guaranteed, and it is made to be a datum level of the measurement. Various types of displacement sensor on the market are installable for the main displacement sensor in order to measure geometrical product specifications of the target surface. So, it is possible to measure the surface that consists of 1µm at the surface wavelength from the ruggedness of several decade nanometers in proportion to the purpose. However, an output from displacement sensor will get contained measurement result in respect of x-y stage motion error. Then, using auxiliary displacement sensor that the displacement measurement of the z direction with the traversing of the stage was fixed in reference plate does it and stage inside installed

**Table 1** Comparison of tracing methods

	Conventional scanning	Novel tracing method
Measurement locus		
Features	<p>advantage Mechanical motion error can be systematic</p> <p>disadvantage Unnecessary return traces are included</p>	<p>advantage Any measurement locus can be set to comply with a request</p> <p>advantage Measurement time is markedly shorter than the conventional scanning</p> <p>disadvantage An auxiliary sensor is needed</p>

in the table back. This displacement becomes the motion error, and it is possible to measure the geometrical product specifications of the measured object which is more high precise the measured value main part motion error component. The measurement system and signal flow are shown in fig.2. Since the motion

error of the stage is sampled in the point equal to the main displacement sensor, from them, it is possible that it is real-time and that the motion error is measured, and that it deducts it from the measured value of main part. Therefore, return motion like the raster scan method is no necessity, it is possible to choose measurement condition for showing in table 1 and scanning route put together by the shape of the measured object. It is possible to obtain advantages such as the shortening in a measuring time by it.

### Measurement characteristics of non-contact displacement sensor

Displacement sensor which can measure the displacement without receiving the effect of roughness component of reference plate shown in fig.3, are necessary for auxiliary displacement sensor of this measuring instrument in order to measure the

motion error with the transfer of the stage. Then, the following should be used: Optical fiber displacement sensor and electric capacitance displacement sensor that the probe is small and that easy to integrate to the equipment. However, shown in fig.4, amplitude transmission of the small wavelength component is the zero on the electric capacitance displacement sensor, and it is proven that the effect of the roughness is not received. Therefore, the electric capacitance displacement sensor shall be used as auxiliary displacement sensor. Next, it is an optical displacement

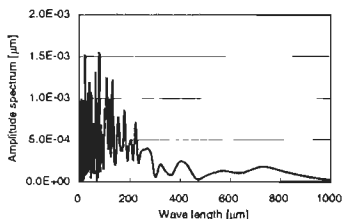


**Fig.3** Amplitude spectrum of reference plate

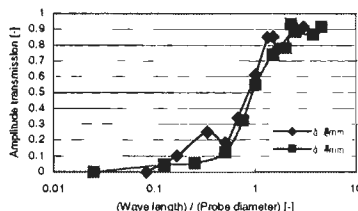


**Fig.4** Amplitude transmission of electric capacitance displacement sensor

sensor used as main displacement sensor. The specification of using displacement sensor is shown in table 2. Then, we investigated of displacement output characteristics of the each optical displacement sensor. Fig. 5 shows the measured profile of roughness standard specimen (Ra2.9 μm). From them, it is proven that the result of being comparatively approximate to measured value of contact process has been obtained the optical displacement sensor. However, high frequency component from 1 μm to 2 μm exists for the measurement result of optical displacement sensor at the amplitude. In Fig. 6, it is proven to differ from the stylus at small wavelength component of 50 μm or less, though the optical amplitude spectrum with stylus at the 100 μm of fundamental wavelength is equal. From these measurement results, it is possible to consider that the measurement error occurs by effect of the microscopic roughness and effect of a macroscopic inclination. Then, the following were investigated using the pin-gage: Effect of a macroscopic inclination and effect of the minute roughness. The result is shown in Fig. 7. The pin-gage diameter is 600 μm. When the critical inclination angle would be obtained from this it became 31.6° in case of the A sensor, and 27.8° in case of the B sensor. But, the reflected light has returned to the lens, after the critical inclination angle is exceeded. This seemed to occur otherwise even in the angle without the reflected light by the microscopic roughness of the surface of a macroscopic inclination. And, it is proven that the reflected light widely spreads by the microscopic roughness, as it is shown in reflected light intensity distribution using the Beckmann theory in fig. 8. Therefore, it is possible to consider that the measurement error becomes productive by the microscopic roughness.

**Table 2** Specifications of sensors under test

Sensor	Resolution [nm]	Measurement range [mm]	Working distance [mm]	Spot diameter [μm]	NA
A	10	1	1	1.5	0.55
B	12	1	2	0.5	0.68
C	100	0.6	5	2	0.37



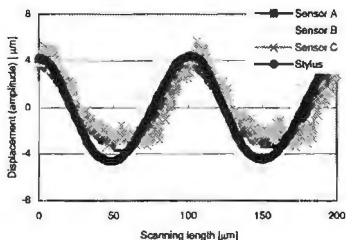


**Fig.5** Measured profiles (Roughness standard specimen)

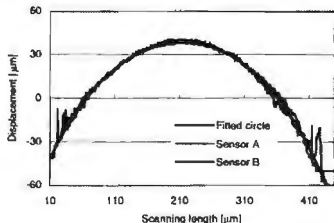


**Fig.7** Measured profile of pin-gage

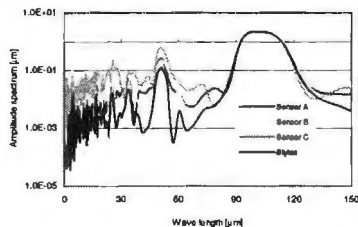


**Fig.6** Amplitude spectrum for Fig.5

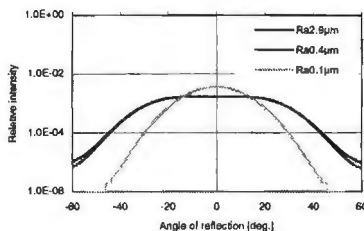


**Fig.8** Simulated angular distribution of reflected light intensity

**Practical correction of measurement error**

Then, we proposed the new technique as decrease of the measurement error except for the filter process. Shown in Fig. 9, the technique is increasing the displacement sensor spot intentionally (over-sampling method). The increased irradiation area gets larger in proportion to the spot diameter of each sensor. In the optical displacement sensor, the spot diameter is small. Then, by increasing suspected, effect and compensation of the sudden outlier of the microscopic roughness are carried out like equalization effect of the electric capacitance displacement sensor.

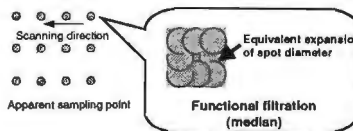


**Fig.9** Over-sampling method

**Conclusive remarks**

By using roughness standard specimens, pin gages, performance tests were carried out and the fundamental output characteristics were made clear for each probe. The experimental analyses showed that the output characteristics of all the optical probes are different from those of a mechanical probe or stylus when measuring high frequency surface irregularities. So, we proposed increasing the displacement sensor spot intentionally. From the technique, it was possible to decrease in the effect of short wavelength and noise components. To obtain the flatness equal to that of the mechanical probe or stylus, the area has nearly to be double in the size of the spot diameter of the optical sensor.

**Reference**

[1] ISO 4288: Geometrical Product Specifications (GPS) - Surface texture: Profile method - Rules and procedures for the assessment of surface texture

# Advances in uncertainty assessment using uncalibrated objects with freeform geometry on coordinate measuring machines

E. Savio<sup>1</sup>, L. De Chiffre<sup>2</sup>

<sup>1</sup>DIMEG, University of Padova, Italy; <sup>2</sup>IPL, Technical University of Denmark, Denmark

## Abstract:

The paper describes some advances regarding establishment of traceability of freeform measurements on coordinate measuring machines using the “Uncalibrated Object” approach, which is currently being considered for development as a new ISO standard. The method deals with calibration of artefacts by: i) repeated measurements of a given object in different orientations, ii) measurement of calibrated length and form standards, and iii) additional investigations with variation of measuring parameters. The feasibility of this approach for the case of complex freeform geometries is documented through calibration of a turbine blade.

## Introduction

Freeform surfaces, sometimes called sculptured or curved surfaces, have complex geometry. Their relevance for industry is well-known in the design and manufacturing of parts with functional surfaces [1]. They have relevance also for aesthetic, since in the modern design of many goods, aesthetic is becoming more and more important for the market impact of a product. Coordinate measuring machines (CMMs) are modern tools for the inspection of complex geometry. Traceability of measurement results may be established by different approaches. The uncertainty assessment method using “Calibrated Workpieces” is a well-known metrologically correct procedure [2], based on the substitution method. The main limitation to the applicability of this method are the similarity requirements between calibrated objects and actual workpieces in terms of dimensions and form, and the need of a calibrated item [3]. Other approaches are “Computer Simulation” [4] and “Expert Judgment”, but uncertainty assessment related to the inspection of complex tolerances create difficulties, especially at industrial level [5].

An alternative approach is the procedure using “Uncalibrated Objects”, currently under the attention of ISO TC213 [6] and being developed within an EU project. The basic idea is to perform the uncertainty assessment by means of experiments where uncertainty contributors are varied. Repeated measurements are carried out on a workpiece representative of those that are typically inspected, introducing variations on CMM geometrical errors (different workpiece positions/ orientations), measuring parameters (probing force, scanning speed, approach speed and distance, etc.) and measuring strategy (point density and distribution). Environmental conditions should vary for the duration of the experiments as accepted during actual measurement. Some uncertainty contributions can not be estimated with the above mentioned experiments. This is the case for contributions due to the metrological characteristics of the CMM, the most evident being the transfer of the unit of length. Other contributions not accounted for during the experiments are some temperature effects, probe calibration procedure, form measuring capability, etc.. For these reasons, additional tests are performed on calibrated length and form standards, and analytical formulas introduced for Type B estimation of those uncertainty contributions.

## Investigations on the calibration of a freeform object

The investigations were concerned with a classical freeform measurement: the verification of profile tolerance on the aerofoil of a turbine blade. For the selected geometry, the feature deviation assessment was performed by CAD-based measurement of 9 sections in scanning mode by contact probing. In order to focus the experiments on the freeform measuring capability of CMMs, an external datum was created by means of 3 precision spheres and no bestfit introduced. All other measuring conditions were identical to industrial practice. Data evaluation was performed using a dedicated external software tool, due to limitations of the evaluation features embedded in the CMM measuring software. The feature deviation assessment of profile tolerance related to datum is based on the calculation of maximum absolute deviation from nominal profile. Therefore, the measurand is the maximum distance from nominal CAD model of all points measured on a section.

According to the procedure, the uncalibrated turbine blade was inspected with different measuring conditions. Variations were introduced in point density (4 times



**figure 1:** The turbine blade being measured in one of the different workpiece orientations, to estimate the uncertainty contribution from the geometrical errors of the CMM.

higher), probing force (double), scanning speed (a tenth), with respect to the actual measurement. To estimate the effect of CMM geometrical errors, the turbine blade was measured in 3 different workpiece positions on the CMM. One of these positions is shown in Figure 1. Every position was obtained by at least one rotation of the part around a CMM axis, focusing attention on feasibility and good measuring conditions. The measuring volume was approximately the same for all measurements, and a total of 45 measuring cycles were performed. Contributions due to CMM metrological

characteristics were estimated from performance verification tests (length measuring capability) and measurements on calibrated spheres (form measuring capability), using measuring and operating conditions as close as possible to the actual measurement. The whole procedure was repeated on two different CMMs: CMM1 (Zeiss UPMC 850,  $u_1 = 0.4 + L/900 \mu\text{m}$ , L in mm) located at IPL, Denmark and CMM2 located at DIMEG, Italy (Zeiss Prismo Vast 7,  $u_1 = 2.2 + L/300 \mu\text{m}$ , L in mm). The uncertainty assessment on CMM2 was carried out 9 months after CMM1 (February-November 2001).

The investigations demonstrated that the “Uncalibrated Objects” approach is practicable for freeform measurements. The procedure demonstrated very nice compatibility of calibration data between two CMMs in different laboratories, as demonstrated in Figure 2. From the practical point of view, the different workpiece positions required by this method may cause difficulties. Attention must be given to the choice of “natural” alternative positions with good measuring conditions. The procedure is time consuming, but has the great benefit of absence of similar calibrated artefact. The full establishment of traceability is accomplished by means of measurements of simple length and form standards.

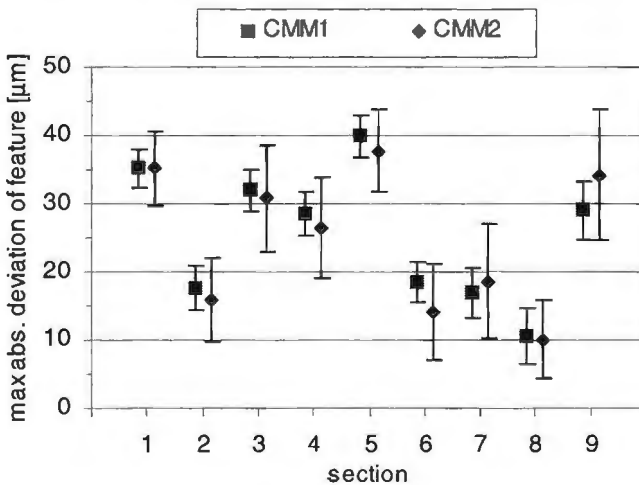


**figure 2:** Comparison of freeform calibration data on two different CMMs. Error bars represent expanded uncertainty ( $k=2$ ) of the max absolute deviation of feature from nominal geometry.

## Conclusions

The “Uncalibrated Objects” procedure for uncertainty assessment, currently being developed within ISO TC213, was applied to the calibration of a turbine blade. The procedure has delivered reasonable uncertainty statements and demonstrated compatibility of calibration data between two CMMs of different accuracy. The estimated uncertainty was in the order of 3-4  $\mu\text{m}$  for a high accuracy CMM and 6-10  $\mu\text{m}$  for a medium accuracy CMM. The investigations were limited to a single geometry and no general evaluation of the “Uncalibrated Objects” approach can be

given. Improvements are needed in terms of uncertainty calculations and compatibility to GUM, but the method is very promising, also because it forces the user to investigate the performance of the CMM. In fact, the procedure is giving information on CMM measuring capabilities that may be used also for the “Expert Judgment” approach to uncertainty estimation.

### **Acknowledgments**

The authors would like to thank the European Commission for funding the EASYTRAC project under the programme Competitive and Sustainable Growth, Contract No: G6RD-CT-2000-00188, coordinated by UNIMETRIK S.A. (Spain). The authors are also grateful to the turbine blade manufacturer Pietro Rosa TBM (Italy) for providing information on their inspection process.

### **References**

- [1] Weckenmann, A. et al.: Testing of sculptured surfaces with coordinate measuring machines, *Technisches Messen* 7/8/1987, pp.277-284, 1987.
- [2] ISO/DTS 15330-3, Geometrical Product Specifications (GPS) - Coordinate measuring machines: Techniques for determining the uncertainty of measurement - Part 3: Uncertainty assessment using calibrated workpieces, 2000.
- [3] Savio, E., De Chiffre, L.: An artefact for traceable freeform measurements on coordinate measuring machines, *Precision Engineering*, 26/1:58-60, 2002.
- [4] Trapet, E. et al.: Traceability of Coordinate Measuring Machines According to the Method of the Virtual Measuring Technique, PTB-F-35, PTB, Braunschweig, ISBN 3-89701-330-4, 1999.
- [5] Hans, N. H., De Chiffre, L.: An industrial comparison of coordinate measuring machines in Scandinavia with focus on uncertainty statements, *Precision Engineering*, 23:185–195, 1999.
- [6] Working Draft ISO/TS 15530-6 - GPS - Coordinate measuring machines (CMM): Techniques for determining the uncertainty of measurements. Part 6: Uncertainty assessment using uncalibrated workpieces, ver. 18 September 2000.

# A computational method for stitching a series of 3-D surface topography data measured by microscope-type surface profiling instruments

K. Yanagi\*, M. Hasegawa\* and S. Hara\*\*\*

\* Nagaoka University of Technology, Department of Mechanical Engineering,

\*\* Tokyo Institute of Technology, Graduate School of Information Science and Engineering,

## Abstract

A new novel stitching method for a series of 3-D surface topography data was proposed. That is based on areal regression filtering technique and cross correlation of the processed height data in an overlap region. The matched position for two sequential data sets is obtained by matching the orthogonal pistons over the related core area. The protruded parts are removed from combined data sets and the grid-type height data in the true overlap region are replaced by linearly weighted mean values. The computational procedures are described in detail and an implemented example is shown. The proposed stitching process is able to produce apparently reasonable topography data over a large field area.

## Introduction

When high resolution measurements are required for the use of microscope-type surface profiling instruments such as laser scanning microscope, scanning electron microscope, atomic force microscope and so on, their measurable areas are inevitably subject to restriction. In order to obtain a wide range of measurement area with high spatial resolution, it is essential to stitch together a series of adjacent measurement areas. Several stitching methods have been proposed <sup>[1], [2]</sup> and some of them are now put to practical use. However, their computational procedures are not open to public. So we here propose a new novel stitching method in this study from a practical point of view.

## Fundamental conditions

3-D surface topography data in this study is in the form of Cartesian coordinates and a so-called data set is a rectangular measurement area. In order to stitch plural number of the data sets, a certain linear motion stage with good positioning accuracy is required. The data sets shall be regularly ordered in one direction ( $x$ -axis), and then shifted by one row in the other orthogonal direction ( $y$ -axis). Overall combined

measurement area is composed of  $m \times n$  data sets.

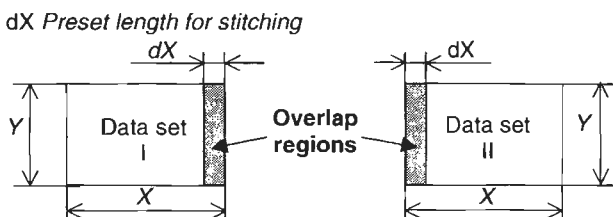


Figure 1: Definition of data set size and overlap region

### Stitching process in one direction

#### Standard data set and overlap region for stitching

A standard data set is rectangular and of the fixed dimensions. Overlap area can be defined as shown in Fig. 1 with artificially preset length  $dX$ .

#### Exclusion of long wavelength components

As a preprocessing of measured data, areal regression filtering technique was applied to eliminate distortion of long wavelength components along data set border. This means that two adjacent data sets are stitched together by short wavelength components on the same reference plane. Figure 2 shows the case when Gaussian regression filter<sup>[3]</sup> was applied to a distorted data set measured by a topography SEM<sup>[4]</sup>.

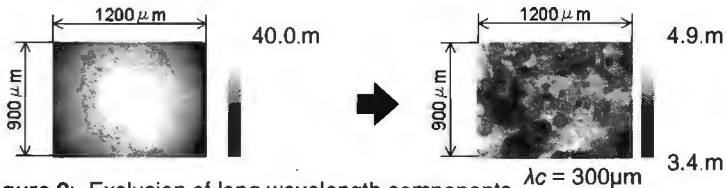


Figure 2: Exclusion of long wavelength components  $\lambda_c = 300\mu m$

#### Calculation of matched position for the two data sets

Cross-correlation between two data sets can give us a matched position in the overlap region. By matching the orthogonal pistons over the related core area ( $dX - 2\alpha, Y - 2\beta$ ) shown in Fig.3, we can obtain the matched position ( $\alpha=A, \beta=B$ ) where the

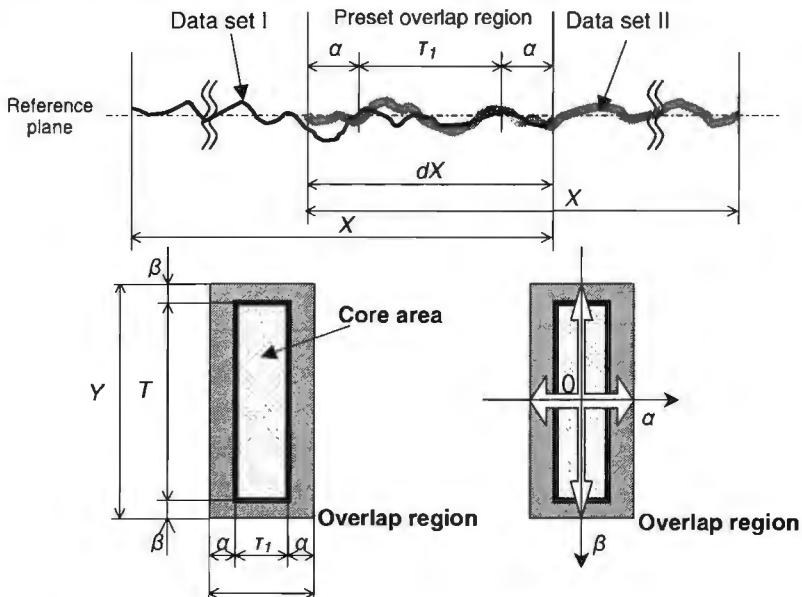


Figure 3: Calculation of matched position for the two data sets

cross correlation value is the maximum.

Cross - correlation function :  $\phi_{12}(\alpha, \beta)$

$$\phi_{12}(\alpha, \beta) = \frac{1}{\tau_1 \tau_2} \int_0^{\tau_2} \int_0^{\tau_1} f_1(x, y) f_2(x - \alpha, y - \beta) dx dy$$

Max  $\phi_{12}(\alpha, \beta)$  :  $\alpha = A, \beta = B$

**Adjustment of each data set size**

For further stitching process it is necessary to remove protruded parts from original data sets as shown in Fig. 4(a). It occurs frequently that the next data set is vertically wider than the previously stitched data set like Fig. 4(b). In such a case the remaining part has to be finally removed after the same stitching process.

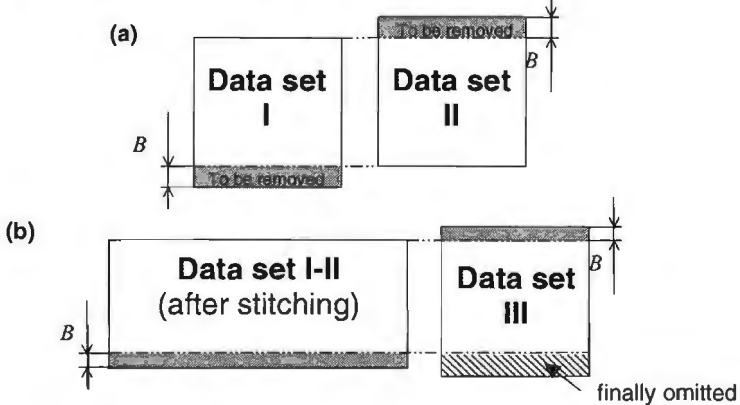


**Figure 4:** Removal of protruded parts

**Data modification in the overlap region**

The grid-type height data in true overlap region are replaced by linearly weighted mean values of the related two data sets in keeping the reference plane constant (Fig. 5).

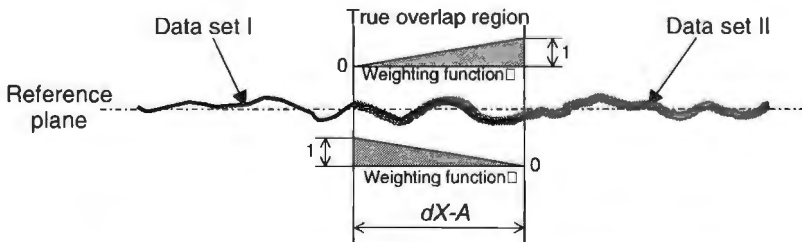


**Figure 5:** Modification of height data in the true overlap region

**In the case of more than 3 sequential data sets**

When stitching more than three sequential data sets, the last overlap region should cover the previous overlap region. If not, or when a location gap between the two



overlap regions occurs like Fig.6 (a), it is necessary to shift the overlap region of the last data set in vertical direction by a certain distance.

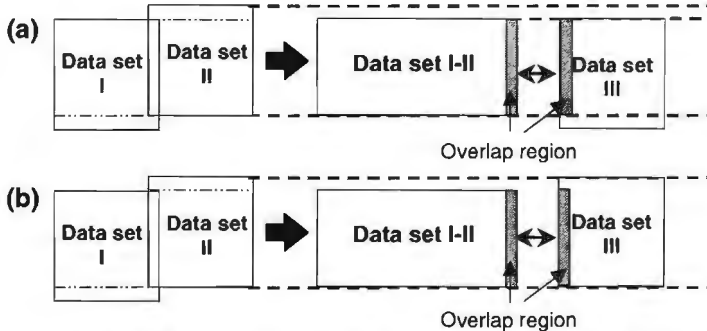


Figure 6: Additional shift of overlap region in the y-direction

### Stitching process in the other orthogonal direction

Once a series of horizontal data sets in the x-direction is stitched, a banded rectangular data set is obtained. The similar stitching process can be applied to connect those banded data sets in the y-direction. Then the size adjustment by removing protruded parts in the x-direction is required.

### Implemented example

The proposed stitching process was applied to 3x3 data sets measured by a topography SEM<sup>[4]</sup>. An obtained overall combined area is apparently reasonable as shown in Fig.7. However, its suitability has not been discussed. A further analytical study is needed.

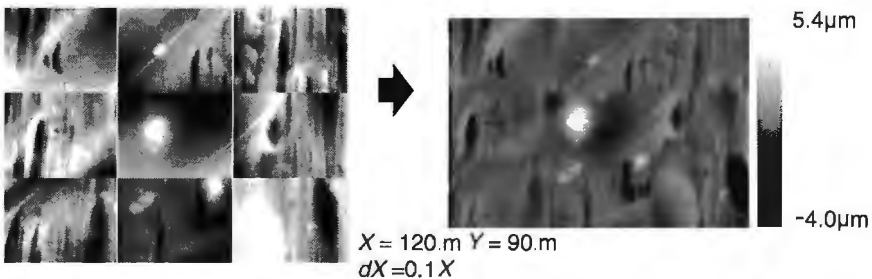


Figure 7: Application of the proposed stitching process

### References

- [1] Michael Bray "Stitching interferometry: how and why it works", SPIE, Vol.3739, 1999.
- [2] Yingjie Yu "Correlative stitching technique for measuring flatness" SPIE, Vol.4221, 2000.
- [3] S. Brinkmann, H. Bodschiwinna and H.-W. Lemke "Accessing roughness in three-dimensions using Gaussian regression filtering" ,Int. J. Machine Tools & Manufacture, Vol.41, 2001, 2153-2161.
- [4] Tadao Suganuma " Measurement of Surface Topography using SEM with Two Secondary Electron Detectors", Journal of Electron Microscopy, Vol.34, No.4 1985.

## **‘Deflectometry on aspheric surfaces’: A new approach and generic solution for measuring ‘free form’ aspheres.**

N.A.J. van der Beek<sup>2</sup>, W.D. van Amstel<sup>1</sup>, D. van Kaathoven<sup>2</sup>, W. Potze<sup>1</sup>, O.T.J. Vermeulen<sup>1</sup>, M. Breukers<sup>3</sup>

<sup>1</sup>Philips CFT, Eindhoven; <sup>2</sup>SAI-TU Eindhoven, <sup>3</sup>Philips ETG-HTE-CTC Eindhoven

### **Abstract:**

A new measurement approach for measuring ‘free form’ aspheres will be presented. Instead of measuring surface shape directly, from height or distance, this new method uses an optical slope sensor that is scanning the surface under test in a polar co-ordinate system. For this surface slope measurement, a two-dimensional Position Sensitive Diode (2D-PSD) is applied. From the measured slope vector data, the original surface topography can be reconstructed by integration. This method can achieve sub-micron accuracy easily and is very fast: it can be used even at a machining station. It’s generic in the sense that convex or concave and large or small ‘free form’ surfaces can be measured with the same set-up. Preliminary results from experiments on a steel sphere show that the method looks very promising.

### **Deflectometry on aspheric surfaces**

In metrology, the science of measuring the topology of surfaces, two different techniques are commonly used. A first technique uses a mechanical probe, which scans the surface much like a blind person reads Braille. The second is interferometry, an optical technique that measures the path difference between a laser beam reflected at a reference surface and one at the surface under investigation. With a known reference surface the investigated surface can be reconstructed.

About 1.5 year ago, a new technique was developed at the Philips CFT in Eindhoven capable of competing with the two methods mentioned above. This technique, called Deflectometry, is an optical method. It uses a laser beam to obtain the local slope vector of the surface on a small spot. This slope is determined by measuring the angle difference between the incident and reflected laser beam. The slope of the surface is scanned point by point along different lines evenly spaced on the surface. If these local slopes are stitched together, a slope map is created and with this map the original surface can be reconstructed by integration. This technique is generic in the sense that it can be used to measure spherical and aspherical surfaces of a wide variety of radii of curvature (both concave and convex) with the same set-up. This flexibility is an important asset of the technique that makes it possible to implement this technique on a lathe in a later stadium.

Compared with the established techniques, deflectometry has two major advantages. It would take an offline measurement to use a mechanical probe to scan a surface with the desired resolution, because these measurements take too long to do online. Non-destructive measuring is the main cause of this long duration. If we compare this to a measurement that uses Deflectometry, the same surface could be scanned in less than a few seconds with the same resolution, resulting in measurements that can be done online in the production process. This speed advantage has two causes, one being the fact that Deflectometry is non-destructive by nature, the other concerns

the usage of 2D-PSD's and associated analogue electronics, which allow for very fast data-acquisition.

A possible application for the deflectometer would be in the ophthalmic industry that produces spectacle-glasses and contact lenses. Here a trend towards complex designs for lenses is seen. For example, one can buy spectacle-glasses that have two different regions. One region is used for close reading and the other for distant looking. The design for such a lens is very complex and has no symmetry. To check a surface with such a design the whole surface has to be measured, due to the lack of symmetry. These free-form designs, as they are called, also need a large lateral range. The development of a machine, which can measure these surfaces, is therefore a hot topic of research within metrology. Deflectometry may prove a valuable technique for such an application.

In order to show the feasibility of this method, a laboratory set-up has been built that will be described and some results will be shown.

### Principle

Deflectometry measures the angle difference between an incident laser beam and a reflected laser beam. The reflection law tells us the angle between the incident laser beam and the normal ( $\underline{n}$ ) of the surface is equal to the angle between the normal  $\underline{n}$  and the reflected beam (see figure 1).

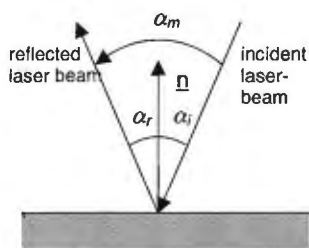


figure 1: The reflection law

### Set up

The Phi-Theta actuator system at which the 'aspherical surface under test' and the slope sensor are placed is shown in figure 2.

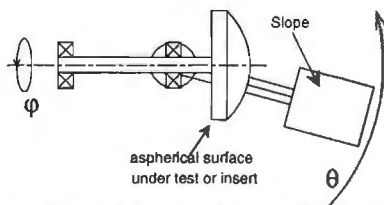


figure 2: The two rotational axes of the set-up

The surface under test is placed at the  $\phi$ -actuator and the slope sensor is mounted on the  $\theta$ -actuator. Both axes can be driven under PC-control and are provided with encoders. All kind of scanning patterns can be programmed to scan the surface under test. In the high-

speed mode, the  $\phi$ -axis is continuously rotating at high speed and the  $\theta$ -axis driven at a lower speed, continuously or stepping, making a single scan.

Since the slope measurement is relative, a reference plane has to be defined normal to which the laser beam is aimed. For this reference plane a spherical surface (phi-theta system) is chosen, because the aspherical corrections are small compared to the base form of the surfaces, which is more or less spherical.

The slope sensor itself consists of three main parts: a laser unit for generating a probing beam, a prism and a PSD unit as a slope detector. At the laser unit (figure 3) a laser beam is generated, which is then modified by an optical system to create a round spot of 100  $\mu\text{m}$  diameter at the surface under test. The laser used is a diode

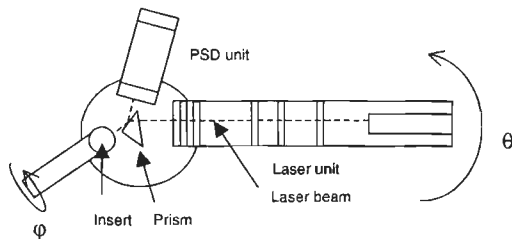


**figure 3:** The slope sensor

laser (670 nm). The prism is used to split the incident and reflected beam and the PSD unit is used to measure the angle of the reflected beam, relative to the optical axis of the system. This PSD unit is a 4x4 mm PSD in combination with a 30 mm lens. The PSD is capable resolving up to 10000 slope

increments in 2 directions and in combination with the lens this results in an optical angular resolution of  $15 \mu\text{rad}$ , which is  $7.5 \mu\text{rad}$  in the object domain since the measured angle is twice the angle of the surface normal. At this moment the accuracy of the slope sensor is only about  $50 \mu\text{rad}$  (in the object domain). The main reason for this are problems with false reflections in our first 'quick and dirty' slope sensor, thus limiting accuracy temporarily.

### Preliminary results of measurements on steel sphere

In order to get insight in the aspects of the deflectometer; several experiments have been done with a polished steel sphere. When using a perfect sphere as a surface under test, a measured zero result is expected if the sphere and detector would be aligned perfectly. Since the reference sphere and the actual measured sphere are then equal.

In figure 4 we show the reconstruction of the surface, created by using a simple line integration. In the figure the height deviation from the reference sphere as a function of phi and theta is shown. Phi is represented by the left flank axis running from zero to 360 degrees in steps of one degree. The right flank axis represents the theta angle and runs from  $-12$  degrees to  $11.25$  degrees taking steps of  $0.75$  degree. The height deviation is shown in  $\mu\text{m}$ . Because measurements were taken at both positive and negative theta angles the concentric circles have been measured twice but with a  $180$  degree phase difference. This can be seen from figure 4, the sinusoidal height deviations in the right part of the plot are phase shifted over  $180$  degrees with respect to the left part.

The expected signal in our set-up when measuring a spherical surface would be zero at all angles. The reason, for *not* measuring a zero signal, is caused by an eccentric placement of the reflecting sphere with the respect to the phi-axis. This misalignment is deducted from the sinusoidal height deviation along the phi-direction. The amplitude of the height deviation can be used to calculate the amount of eccentricity. We've developed a preliminary model that predicts the measurement results when measuring a sphere. In this model we included some misalignments that are possible in the set-up. The eccentricity is than calculated by the model and this results in a misalignment of  $14.0 \pm 0.4 \mu\text{m}$ . Measurements done on the same sphere with mechanical 'Tesa' probes indicated a eccentricity of  $13.8 \pm 0.2 \mu\text{m}$ . Thus yielding the conclusion that the method seems accurate and functioning.

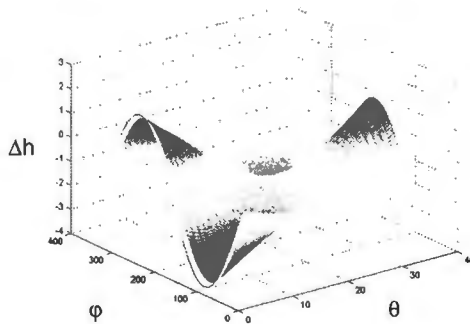


**Figure 4:** Isometric view of the height deviation with respect to a perfect sphere.

improvements (or even a redesign) since it is suffering from false reflections that are reducing its accuracy.

### Acknowledgements:

Among the many persons who stimulated us with support we would like to mention:

Stefan Baumer, Rene Duijve, Yujian Fan, Jelm Franse, Peter van de Goor, Jan van Leest, Jan van Lievenoogen, Theo van der Putten, Marten Sikkens, Andre Verhulst and Jan Windey

### Concluding remarks

In short, a global view of the deflectometry method is shown, including some preliminary results that we established with our laboratory set-up. These preliminary results give an indication that the method is feasible. But in order to measure actual aspheric surfaces a couple of developments still have to take place. It is necessary to improve and expand the mathematical model to include all possible misalignments and to include aspheric surfaces. Also the slope sensor itself needs some

## **Material properties**



## Acoustic Emission Monitoring of Fatigue in Alumina - Chrome Carbide Composite

M. Istomin, M. V. Kireitseu, S. Yerakhavets

NAMATEX System Division, Institute of Machine Reliability (INDMASH), National Academy of Sciences of Belarus

### Abstract:

The fracture and fatigue characteristics of alumina coating strengthened with chrome carbide layer, is presented and discussed. The essential aspects of the methodology include acoustic emission monitoring of crack activity and its propagation under cyclic loads. Structural analysis of the alumina revealed an effect of CrC on fatigue life of the alumina-based coating. It is found to be cracks initiation and propagation in the coating interface that result in the catastrophic failure of the composite. An ultimate load resulted in intensive crack growth in CrC-Al<sub>2</sub>O<sub>3</sub>-Al is found to be about 1.5 GPa that is higher than that in alumina coating.

### Introduction

Alumina-based composite coatings is useful as a structural coating because of its high hardness and load rating, low wear rate, high stiffness-to-weight ratio, and high-temperature stability, but it suffers from low fracture resistance (1).

A ductile substrate like aluminium or its alloys coated with a brittle thin film is one of common coating-substrate structures encountered in engineering applications. Fracture behaviour of the thin film coating and the coating adhesion are among the major considerations in evaluating the integrity and quality of such coating-substrate systems. A reliable and consistent measurement of these properties is also critical in improving the thin film processing technologies.

An important engineering problem in structural design is evaluating structural integrity and reliability. Depending on the structural design, material type, service loading, and environmental condition, the cause and degree of strength degradation due to the different mechanisms differs. One of the common causes of strength degradation is the result of crack development in the structure.

A previous study established that toughness variations result from introducing texture to ceramics, structure of the composite (2-4). Usually, alumina coatings crack through pores, internal voids, and some oriented alumina crystals within the structure. Under applied load the cracks are initiated from surface and prolongs to the underlying layer or to rough base material.

Recently, alumina ceramic coatings were improved with chrome carbide layer. The results in (4) revealed advanced load rating and tribological characteristics of the new composite coatings. It has been found that chrome carbide layer strengths the alumina by filling the pores and by healing the defects in the structure on the top and in depth of the alumina layer. The composite coatings potentially exhibit a significant improvement in toughness, because most of the defects are favorably healed by chrome carbide layer, thereby decreasing the stress concentration and number of pores and voids.

### Objective

In this paper, fatigue and fracture of the Al-Al<sub>2</sub>O<sub>3</sub>-CrC coatings have been



investigated by in situ experiments performed under acoustic emission monitoring and in a scanning electron microscope, so as to exclude the possibility that they are environmentally controlled. This paper reports on the characterization of the fracture mechanisms in the alumina-based ceramic composite hardened by CrC layer.

## Experimental setup

The aluminum alloy with 2-3% of Si particles in the structure was the base substrate in which alumina  $Al_2O_3$  layer was produced by micro arc oxidizing process. Thickness of the alumina layer was 250  $\mu m$ . The pores and defects of alumina layer were filled by the chrome carbide layer produced by the pyrolysis method described previously in (5). Thickness of the CrC layer was 25  $\mu m$ . In fact, particles of CrC penetrate into the pores of the  $Al_2O_3$  layer strengthening the composite in depth of 10-20%.

Starting with alumina layer is fabricated by micro arc oxidizing. A sharp notch can be obtained by controlling the etching time and solution. Figures 2 and 3 show the photographs of the alumina-chrome carbide coating and cracks in the coating respectively.

Fracture resistance often is measured in ceramics using indentation methods (3-5). The samples used in this study were loaded by indentation. The indenter was SiN

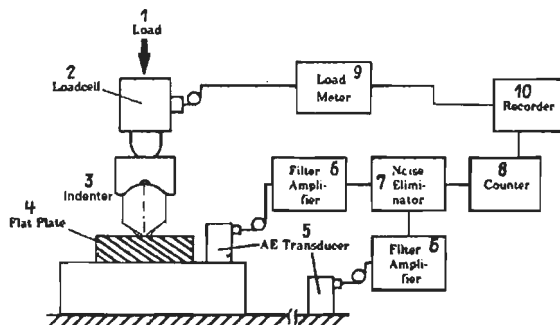


**Figure 1:** Acoustic emission monitoring experimental device

The electrostatically actuated test device shown in Figure 1 was used to evaluate microfracture properties through a microcrack diagnosis of materials forming the systems for improvement of micromechanical reliability. The test device consists of comb drives for loading and a suspending beam for testing. In the figure 1 the device consists of 1 applied load, 2 load cell unit, 3 ceramic or steel indenter, 4 flat plate sample with the coatings, 5 AE transducers, 6 filter amplifier, 7 noise eliminator, 8 counter, 9 load meter, 10 recorder.

Signal levels were monitored with Allen MSY-4 system (Matsuoka, Japan). The sample holder works as a waveguide initiated the signal measured by the sensors. Expected cut on amplitudes was about 15 dB. The threshold level was maintained relatively low because of the attenuation of the signal between the coated sample and the transducers.

## Results and discussion

Figure 2 shows microstructure of CrC-Al<sub>2</sub>O<sub>3</sub>-Al composite. Alumina-based composite with strong morphologic and crystallographic texture was successfully produced by incorporating relatively hard particles of chrome carbide that promote faceting. The micrograph indicate that, in the CrC-Al<sub>2</sub>O<sub>3</sub>-Al composite, most of the pores and defects are filled and healed by CrC particles.

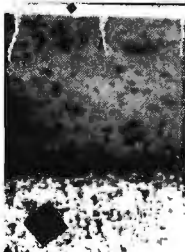


Figure 2: Coating structure

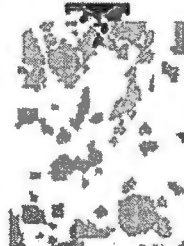


Figure 3: Crack propagation

Figure 3 shows loaded segment of the composite. The alumina coating has light color in the figure. Darker segments show crack propagation in the zones of voids and pores in the alumina coating due to initiated stresses distributing into the layer from the contact track under indenter. In the figure the cracks path goes through pores and internal voids of alumina layer.

Acoustic emission response of CrC-Al<sub>2</sub>O<sub>3</sub>-Al on applies cyclic load is shown in figure 3. The data plot in fig. 4 illustrates an ultimate increase in output acoustic signal at applied load about 130 N. High acoustic signal indicates an intensive crack growth. The increase in the acoustic activity indicates the rapid propagation of the crack in the coatings (see fig. 3).

The analysis of the AE data acquired during fatigue tests revealed that the amplitude analysis of the signal involved in this phase shows output peek levels of acoustic signal were 65 dB and 35 dB for alumina and CrC-Al<sub>2</sub>O<sub>3</sub> coating respectively. It is found to be cracks initiation and propagation in the coating interface that result in the catastrophic failure of the composite.

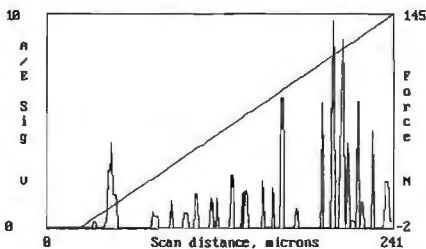


Figure 4: AE response of CrC-Al<sub>2</sub>O<sub>3</sub>-Al on applied load.

Usually, the coatings resist until a critical crack propagates in a catastrophic way. In the alumina, the fracture path is in general intergranular, whereas, in the alumina hardened by chrome carbide, a transition from transgranular fracture at fast crack growth in long time of cyclic loading to intergranular fracture at slow crack growth in short time of cyclic loading occurs. Consistent with previous observations (5, 6), when the crack velocities are slower, intergranular fracture is much more prevalent.

In view of ultimate load initiated intensive crack growth in CrC-Al<sub>2</sub>O<sub>3</sub>-Al composite illustrates that the applied load reaches about 100 N, but the CrC-Al<sub>2</sub>O<sub>3</sub>-Al coating has no significant failure due to crack initiation measured in output acoustic signal.

It is to be expected that the lack of the strengthening results from the plane of weakness introduced by CrC layer that forces internal stresses by filling the pores

and defects resulting in the macroscopic crack path to grow at an angle with respect to the plane of structure (see Fig. 2).

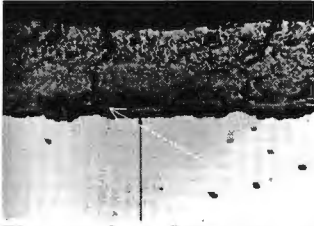


**Figure 5:** Crack Path in the coating.

## Conclusion

Alumina-based composite with strong morphologic and crystallographic texture was successfully produced by incorporating relatively hard particles of chrome carbide that promote faceting.

Structural analysis of the alumina-based composite coating revealed an effect chrome carbide on fatigue resistance.

Output peak levels of acoustic signal

indicate 65 dB and 35 dB for alumina and CrC-Al<sub>2</sub>O<sub>3</sub> coating respectively. High acoustic signal indicates an intensive crack growth. It is found to be cracks initiation and propagation in the coating interface that result in the catastrophic failure of the composite. Composite is found to have improved fatigue with 10-20 μm CrC thickness. Alumina coatings show a low number of cycles to failure (microcracks formation). In the alumina, the fracture path is in general intergranular, whereas, in the alumina hardened by chrome carbide, a transition from transgranular fracture to intergranular fracture occurs. The deflection angles typically are between 60-90° (see fig. 5). The implications of the observed behavior are significant for engineering design using these materials. The degree of toughening associated with crack bridging and overall strengthening are determined by the number of bridging alumina crystals and the effectiveness of the individual strengthening.

## References

- [1] Jerry L. Patel, Nannaji Saka, Ph.D. A new Coating Process for Aluminum. Microplasmic Corp., Peabody, Mass. 2001. [www.microplasmic.com](http://www.microplasmic.com)
- [2] L. M. Braun, S. J. Bennison, and B. R. Lawn. Objective Evaluation of Short Crack Toughness Curves Using Indentation Flaws: Case Study on Alumina-Based Ceramics. *J. Am. Ceram. Soc.*, 75 [11] pp. 3049-57 (1992).
- [3] J. A. Salem, J. L. Shannon, and R. C. Bradt. Crack Growth Resistance of Textured Alumina. *J. Am. Ceram. Soc.* 72 [1] 20-27 (1989).
- [4] Kireitseu M. et al. Study of load rating of composite coating based on hard oxide ceramic layer. Proc. of IUVSTA 15th, AVS 48th, 11th ICSS. October 28 - November 2, 2001 Moscone Center and Marriott Hotel, San Francisco, CA, USA.
- [5] S. Tandon, T. Faber. Influence of Loading Rate on Crack Bridging Processes in Al<sub>2</sub>O<sub>3</sub>. *Ada Mater.*, 46 [10] 3547-55 (1998).
- [6] P. L. Swanson, C. J. Fairbanks, B. R. Lawn, Y. W. Mai, and B. J. Hockey, "Crack Interface Grain Bridging as Fracture Resistance Mechanism in Ceramics: I. Experimental Study on Alumina. *Am. Ceram. Soc.*, 70 [4] pp. 279-89 (1987).

## Alumina Coating Modified by Ultra Dispersed Diamonds

M. V. Kireitseu, M. Istomin, S. Yerakhavets, V. L. Basenuk,

NAMATEX System Division, Institute of Machine Reliability (INDMASH), National Academy of Sciences of Belarus

### Abstract:

Alumina coating formed by electroplating on aluminum base was modified by ultra-dispersed diamonds (UDD). It was revealed that by strengthening the coatings have high microhardness of 19 GPa, fine structure and smooth surface. In view of technological regimes, pulse current regimes improve microhardness, roughness and internal stresses in the coating. Hertzian indentation technique discovered that load rating of alumina coating can be improved in several times by UDD particles. Crack inducing load depends on mechanical properties of the layers such as thickness, structure, hardness, scheme of composition. Potential application of the coating is sliding bearings, insulators, and aerospace units.

### Introduction

In practice, engineers indicate (1, 2) that localized load and stress applied to thin alumina layer induce its peeling and significantly limit area of their application. Engineers concentrate attention on better strength and hardness of the coatings to be used in particular machine.

One approach to be improved structure and mechanical properties of alumina layer is to control technological regimes and environment in electrolyte. Another one is to strength alumina by smart particles that produces composite material. Studies in (3, 4) showed that reinforcement by hard particles improves microstructures and mechanical properties of alumina and alumina-based composites .

Ultra-dispersed diamonds (UDD) are a new type of synthetic diamond powders. UDD are produced by chemical purification of explosion products. In result, particles of UDD have spherical and isometric form without crystalline facets and a fractional structure of clusters. It is a high-dispersed powder with active surface.

Prior to this investigation, it is expected that ultra dispersed diamonds will improve mechanical properties of alumina coating formed on aluminium or its alloy. The paper outlines some results of the work.

### Objective of the work

The objective of the work is to investigate mechanical properties and microstructure of composite alumina-based coatings modified by ultra dispersed diamonds.

### Experimental setup

#### Materials.

Alumina coating was formed by electroplating process on aluminum substrate with Si particles in the structure. The ultra dispersed diamonds of  $60 \cdot 10^{-4} \mu\text{m}$  ( $60 \text{ \AA}$ ) in average size of clusters was used in experiments to strength alumina layer. Diamonds were synthesised in strong non-equilibrium conditions of a detonation surge. The diamonds look like isometric fragments. Table 1 lists characteristics of ultra dispersed diamonds.

**Table 1.** Characteristics of UDD

Characteristics of ultra dispersed diamonds	
Regular chemical composition of UDD	82 – 92 % carbon, 1 – 3 % of nitrogen, 1 – 2% of hydrogen, and up to 1 % of other additives.
Phase composition of UDD	80 – 100 % of cubic diamond, 0 – 10 % of hexagonal diamonds, and up to 20 % of diamond like X-ray amorphous carbon.
UDD particles size	4 to 8 nm
Aggregated clusters	20 -30 nm
Surface area	300±30 m <sup>2</sup> per gr
Density	3.1 -3.2 gr per cm <sup>3</sup>

### Technology.

The coating was formed with special equipment and electrolyte. The electrolyte was based on distilled water with some additives to regulate electrical resistance, pH, temperature of the process etc. The equipment provides either processes electroplating or micro arc oxidizing. Scheme of the equipment consists of the

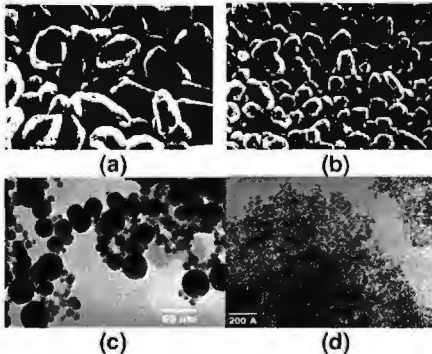


**Figure 1:** Structure of the coatings strengthened by UDD.

intelligent controller that consists of control unit (CU), control desk (CD), filter unit (FU) and one or two power supply unit (PSU). The used power supply worked in the anodic-cathode regime on high frequencies of current that has special form of periodic impulses (8, 9). The main computer (CC) manages and controls the work under program in all devices. Read-only memory (ROM) stores the program of the process. Random-access memory (RAM) records discrete information through the interface module (IM). In result the process regimes can be changed cyclically in accordance with defined program, using direct current (DC),

reverse current (RC), pulse current (PC), programmable regime (PrR) with positive and negative impulses of current at various frequencies bands.

### Experimental Technique and Equipment.

Morphology of the samples was investigated by the scanning electron microscope (SEM). Crystalline structure of the alumina films was analyzed by X-ray diffractometer. Microstresses, grain size and orientation index (texture degree) were calculated by using well known methods highlighted in (6, 7). Electron Spectroscopy for Chemical Analysis (ESCA) identified composition of thin films. Roughness and microrelief of the coatings were measured by the profilograph-profilometer. Microhardness was measured with Vickers indentation at load on the indenter of 0.5 N for 30 seconds.

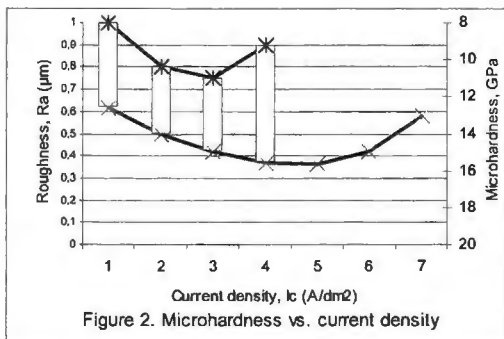


Figure 2. Microhardness vs. current density

Spherical indentations were produced at five points. Indentation has been done by steel balls with radii of 7.978 mm. Five sets of load-unload data were obtained at each point, with the maximum load being increased from  $P_1=100$  N to  $P_2=2000$  N. For each indentation, unloading was continued to 10% of the maximum load. After each indentation, the contact radius ( $a$ ) was measured from the residual contact trace on the top layer.

Then, the plot of indentation stress (mean pressure  $P$ ) versus indentation strain ( $a/r$ ) was obtained and plotted at fig. 3. According to Hertz theory these two parameters should show a linear relationship within the elastic zone. A transition from elastic to fully plastic deformation was observed in the load range investigated. A first order approximate value of  $a$ , the radius of the contact circle at each maximum load, was calculated, with the plastic depth determined by differentiating the first part of the unloading curve. A plot of ( $P$ ) vs. ( $a$ ) was produced for all five indentation sets. The "pile up" correction parameter (actual contact radius) was found to be disproportional changed in contrast to load rate, thus indicating different types of deformation.

## RESULTS AND DISCUSSION

The porosity of alumina layer ranges between 5 and 18 % in depth of the layer. Diameter of the pores was up to 3.5 µm. Thickness of the alumina layer was about 200 µm. The hardness of alumina layer was 12-14 GPa. The alumina structure has in general axial texture. Coating grains orientate mainly in  $\langle 111 \rangle$  direction.

Figures 1 (a-d) show morphology of the coatings. Structure analysis in Fig. 1 (c) revealed that within the coating UDD particles conglomerate in the clusters. Process observations show that size of the clusters and its distribution in the coating depends on UDD concentration in electrolyte and current density at various regimes. Observations discovered that particles suspended in the electrolyte have continuous contact with electrodes because of being natural and artificial mixing, phenomenon of electrophoresis and diffusion. In fact, UDD particles do not effect on electrolyse conditions in view of viscosity, conductivity, pH, and electrode polarization, but it effects on crystallisation mechanism of the coatings. However, it is expected that UDD particles placed on the surface cathode prevent normal growth of coating grains. It results in higher internal stresses observed in the coating.

On surface the coating in fig. 1 (a) can be observed strong pudding rocks of diamond-based fragments. Clusters and separate UDD particles diffuse into the alumina layer that reinforces the last.

Figure 2 illustrates an effect of applied current regime on microhardness in view of alternating current frequency. The coatings are formed with PC or DC regimes in electrolyte with UDD concentration of 15 gr per liter (downside line) or without UDD particles in electrolyte (upper line). The cathode current density effects on the grain size and the internal stresses of the coating. In fact, UDD concentration in electrolyte and the cathode current density improve grain size, porosity and roughness.

UDD particles increase both internal stresses and microhardness. In fact, roughness of the coating surface strengthen by UDD became smother in either DC or PC regimes. In result, the coating has maximal hardness of 19 GPa at PC regime. It is expected that by increasing UDD concentration and at higher current frequencies the coating is to be have better quality.

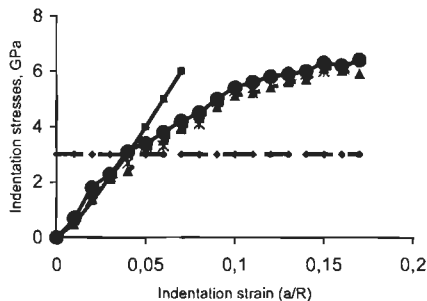


Figure 3. Indentation stress vs. strain

Load rating of the composite coating in fig. 3 was investigated by in suite Hertzian indentation. It was discovered that load rating of alumina coating can be improved in 50-100% by UDD particles. The analysis of contact pressure and stresses in the contact zone revealed that UDD strength the alumina layer by incorporating in the alumina structure. In complex applied load softly distributed among fine granular structure of the composite. In result, the composite deflects cracks distribution under

contact pressure and corresponding tensile and sear stresses. Crack inducing load depends on mechanical properties of the layers such as thickness, structure, hardness, scheme of composition.

The Hertz theory gives reliable explanation of the contact at loads up to 500 N for investigated composite coating. The calculated pressure and diameter of residual track are close to actual values. Contact pressure reaches 3 GPa corresponding with high stresses of 400-800 MPa that might be an ultimate for the composite.

## CONCLUSION

Ultra dispersed diamonds improves alumina coatings formed on aluminium base by electroplating. Considering the data, it was revealed that an effect of strengthening by UDD particles appears in better microhardness of 19 GPa, fine structure and smoother surface of the coating. In some way UDD increase an internal stresses in the coating.

## REFERENCES

- [1] Jerry L. Patel, Nannaji Saka, Ph.D. A new Coating Process for Aluminum. Microplasmic Corp., Peabody, Mass. [www.microplasmic.com](http://www.microplasmic.com), (2000)
- [2] Apitcote Ceramic Coatings. A T Poeton & Son Limited, Gloucester, GL43DN, UK. [www.poeton.co.uk](http://www.poeton.co.uk)
- [3] K. Euh, W. S. Kim, K. Shin, S.-H. Lee. Vacuum Compo-Casting Process of A356 Aluminium Alloy Composites Reinforced with SiC. <http://www.alumtrans.com>
- [4] M. Manoharan, M. Gupta. On Predicting the Fracture Strain of an Age Hardened SiC Reinforced AA6061 Aluminium Metal - Matrix Composite. <http://www.alumtrans.com>

## DIAMOND TURNING INDUCED SURFACE DAMAGE IN SILICON INVESTIGATED BY MEANS OF RAMAN SPECTROSCOPY AND MICROSCOPY TECHNIQUE

R. G. Jasinevicius<sup>1</sup>, P. S. Pizani<sup>2</sup>, F. Lanciotti Jr.<sup>2</sup>, J. G. Duduch<sup>3</sup>

<sup>1</sup>Instituto Superior de Tecnologia, C.P.401, CEP 89201-972 Joinville, S.C., Brazil

<sup>2</sup>Dept. Mech. Engg.- USP – C.P. 359 – CEP 13560-970 - São Carlos - S.P. - Brazil

<sup>3</sup>Dept. of Physics, UFSCar – C.P. 676, CEP 13 565-905 São Carlos - SP - Brazil

### Abstract

This paper presents an investigation on the extent of damage induced by ductile diamond turning on the surface structure by means of Raman scattering and microscopy techniques. Transmission Electron Microscopy (TEM) cross section view of the surface was successfully performed in order to clear whether there is any remnant crystal structure. Raman spectroscopy was applied on ductile/brittle mode machined surfaces in order to correlate the structural disorder observed by TEM. Atomic force microscopy (AFM) was used to probe the surface generated in the ductile mode in the nanometer range.

### Introduction and Experimental

The fabrication of infrared optics as well as electronic devices widely use silicon crystal as raw material. By virtue of this fact, surface and subsurface integrity is of extreme relevance to be investigated when mechanical material removal is applied. Material response to single-point diamond turning (SPDT) has prompted much effort in order to achieve better comprehension of surface formation mechanism. The use of multiple characterization techniques have been tried in order to have a better mapping of the surface as well as subsurface condition. In a recent work [1], Raman spectra results called the attention to the presence of a crystalline phase in an amorphous medium. However, the crystalline peak (at  $521\text{ cm}^{-1}$  [1]), could be attributed to the fact that  $488.0\text{ nm}$  lines of an argon laser, used as an exciting light, can probe the depth profile of disorder effects up to  $270\text{ nm}$  for crystalline silicon and some tenths of nanometers in amorphous silicon. Based on this assumption it is possible that Raman scattering is probing also a crystalline phase from underneath the surface vicinity. TEM planar view was also conducted and diffraction pattern indicated that remnant crystalline silicon is embedded in amorphous Si phase [2]. Anyhow, the doubt of probing remnant crystalline phase from underneath the amorphous layer still remained.

This paper describes experiments which were undertaken to study the effect of diamond turning on the surface structure generated by the ductile regime material removal mechanism. Raman scattering along with Transmission Electron Microscopy (TEM) cross sectional view of the machined surface was successfully performed in order to confirm whether exist any remnant crystal structure in an amorphous medium or the crystalline phase detected is from the bulk. Atomic force microscopy (AFM) was used to probe the surface finish state in the ductile mode in order to characterize the surface integrity in the nanometer range.

Cutting tests using facing operation were performed on  $10\text{ mm} \times 10\text{ mm}$  square,  $0,5\text{ mm}$  thick samples of (100). Silicon. Coolant cutting fluid was used (synthetic water



soluble oil ). A  $-25^\circ$  rake angle diamond tool (Contour Fine Tooling®) with nose radius  $R = 0.762$  mm and a clearance angle of  $12^\circ$  was used in the tests. The cutting conditions were respectively, depth of cut  $a_p = 5$   $\mu\text{m}$ , feedrate range ( $f$ ) =  $2.5$   $\mu\text{m}/\text{rev}$ , spindle speed  $1000$ rpm. were. Digital Nanoscope IIIa. was operated with a standard  $50$ - $60^\circ$  conical silicon nitride stylus of  $15$ - $20$  nm radius tip, with cantilever spring constant of  $\sim 0.06$  N/m. Conventional contact mode was employed where the stylus is scanned raster style over, and in contact with the surface with contact forces of typically  $10$ - $100$  nN. The Raman measurements were performed on a U1000 Jobin-Yvon double monochromator coupled with a cooled GaAs photo-multiplier and conventional photon counting system. All measurements were made at room temperature. The output power of the laser was kept within  $100$ - $200$  mW and a cylindrical lens was used to avoid overheating of the samples. A Transmission Electron Microscope, Phillips CM-200, operated at  $200$  kV was used to conduct the cross section view. Sample preparation procedure is described elsewhere [2].

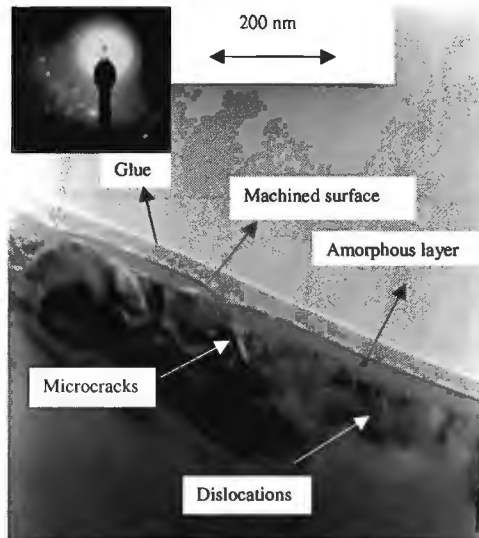
## Results and Discussion

Fig. 1 shows TEM cross sectional image of the machined sample and the diffraction pattern respectively. Fig. 1 displays a bright field cross section TEM micrograph where dislocations and microcracks are seen underneath the dark gray outmost layer which was identified as the amorphous layer formed after machining. This assert is based on the diffraction pattern from this area which contains both halo rings and diffraction spots as shown in the detail in right superior portion of Fig 1. The diffraction spots of the crystalline Si is from the portion of material within the amorphous layer. The amorphous layer is estimated to be in the range of  $50$  nm.

Figures 2a and 2b show the Raman spectra of machined silicon samples excited with  $457.9$  nm and  $487.9$  nm, respectively. Besides the characteristic Raman peak at  $521$   $\text{cm}^{-1}$  from crystalline silicon, the spectra are characterized by the presence of a broad and low intense band at about  $475$   $\text{cm}^{-1}$ . This band can be ascribed to the optical band of the amorphous silicon (a-Si) and is a indicative that the machining was realized in the ductile mode. It is interesting to note that, by changing the exciting wavelength from  $457.9$  nm to  $487.9$  nm, the intensity of the crystalline peak is increased by a factor of approximately  $6$ , followed by a reduction of the linewidth from about  $6$   $\text{cm}^{-1}$  to  $4$   $\text{cm}^{-1}$ , for the same intensity of the amorphous band in both spectra. According to previous results [1] it was proposed that the ductile machining leads to the generation of a crystalline phase immersed in an amorphous medium at the outmost surface. The comparison of the present results with that from Ref. [1] indicates that the  $457.9$  nm line is still probing the amorphous layer whereas the  $487.9$  nm line can reach the crystalline layer. The penetration depth of the  $457.9$  nm and  $487.9$  nm lines in the crystalline silicon are about  $140$  nm and  $270$  nm, respectively, and these depths reduce to about tenths of nanometers in the case of a-Si. By considering both results presented it is possible to assert that there is presence of crystalline phase within the amorphous medium. This result corroborates and confirm previous reported works.

Another interesting result was observed by means of AFM of the surface at the nanometer level. A three dimensional AFM image of the surface diamond turned in the ductile mode are shown in Fig. 3 a) and c). In Fig. 3 a), the cross feed of the cutting tool is advancing at  $2.5$   $\mu\text{m}/\text{rev}$ . The cut grooves can be clearly seen, regularly spaced and running parallel with the cutting direction. Surface roughness of the section analysed shown in Fig.3 b) is in the range of  $2.2$  nm Ra. A closer examination of the machined surface and surface roughness analysis depicted in Fig. 3 c) show that the surface is composed of small "sphere-like" is estimated to be

approximately 80 nm, measured and represented by the spectral period provided by the section analysis. The formation of such interesting morphology do not have plausible explanation in literature.



**Figure 1.** TEM cross sectional image of the machined sample and the diffraction pattern respectively.

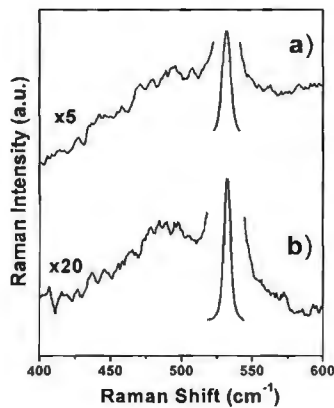


**Figure 2.** Raman spectrum of the machined surface. (a) Raman spectrum of machined sample excited with 457.9 nm; (b) Raman spectrum of the machined silicon sample excited with 487.9 nm.

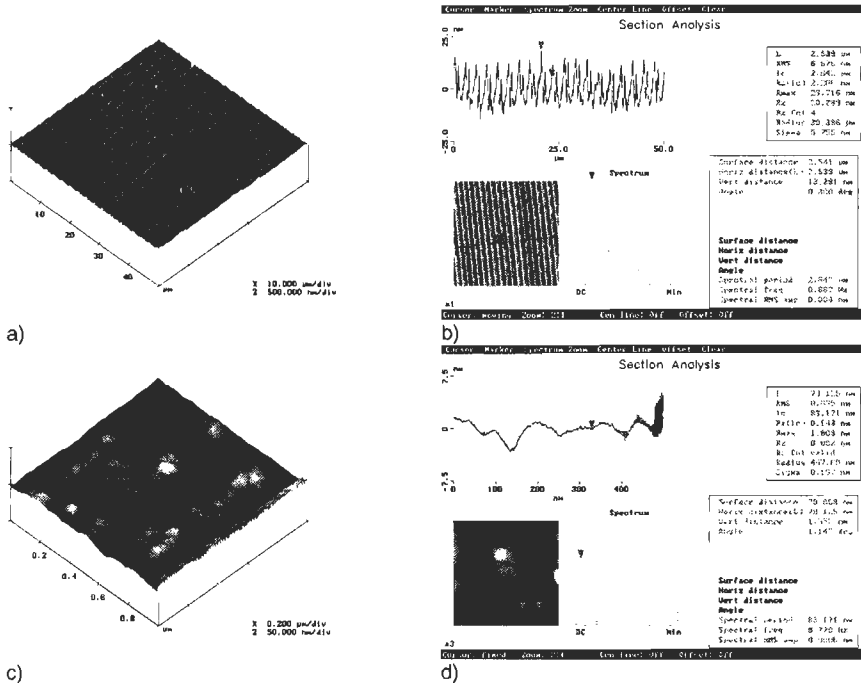


**Figure 3.** Three dimensional surface and surface analysis of the diamond machined sample. a) 3D surface image and b) section analysis of the machined sample. c) 3D surface image and d) section analysis of the machined sample in the submicrometer range. A closer examination of the surface shows a “sphere-like” finish.

In conclusion, a crystalline phase immersed within a amorphous layer generated from ductile regime diamond turning of monocrystalline silicon was detected by means of Raman spectroscopy and TEM cross sectional analysis. The use of two different characterization techniques, Raman spectroscopy along with microscopy, demonstrated a powerful tool to proceed surface and subsurface integrity of diamond turned semiconductor single crystals. The use of atomic force microscope for the evaluation of surface finish in very small section has showed very interesting results.

**Acknowledgments**

The authors also would like to acknowledge the financial support by CNPq and FAPESP (Brazil).

**References**

[1] Pizani, P. S., Jasinevicius, R.G., Duduch, J.G. and Porto, A J.V., J. of Mat. Sci. Lett., **18** 1185 (1999).  
 [2] Jasinevicius, R.G., Santos, F. J., Pizani, P. S., Duduch, J.G. and Porto, A J.V., J. of Non Crystal. Solids, Vol. 272 (2-3), pp.274-278, Aug. 2000

## **RAMAN SCATTERING USED TO PROBE RESIDUAL STRAINS IN DUCTILE REGIME DIAMOND TURNED GaAs**

R. G. Jasinevicius<sup>1</sup>, F. Lanciotti Jr<sup>2</sup>, P. S. Pizani<sup>2</sup>, J. G. Duduch<sup>3</sup>

<sup>1</sup>Inst. Superior de Tecnologia, C.P.401, CEP 89201-972 Joinville, S.C., Brazil

<sup>2</sup>Dept. of Physics, UFSCar C.P. 676 CEP 13560-905 São Carlos – S. P. – Brazil

<sup>3</sup>Dept. Mech. Engg. -USP, C.P.359 CEP13560-970 São Carlos – S. P. - Brazil

### **Abstract.**

Raman scattering was used to probe strain effects and structural disorder in ductile mode diamond turned single crystal GaAs (100) oriented samples. The sample cut in the ductile regime was heat treated by annealing and Raman spectrum showed that the crystalline phase was partially recovered. Surface quality and chip formed were observed by means of microscopy technique. Results showed that machinability of this material is very low if compared to other semiconductors under the same cutting conditions used. The reasons were attributed to the elevated transition pressure value presented by the former single crystal.

### **Introduction**

The research on the machinability of semiconductor crystals has prompted many works in recent years. The study of the effect of tool/material interaction can provide more accurate understanding on the relation between material properties and cutting mode. The main obstacle found in micromachining of GaAs is related to the degree of surface damage generated by the cutting process. In a recent work [1] on single point machining of GaAs it was shown that this material presents a lower level of ductile response along with ribbon-like chip removal. Evidence of highly disordered structure within the near surface vicinity probed by Raman scattering in single point diamond turned GaAs were recently reported [2].

In this paper, GaAs single crystal was diamond turned with the aim to study the effect of material removal mode on the final structural properties. Residual strains generated by tool/material interaction were detected by means of Raman spectroscopy technique. Annealing heat treatment was carried out in order to observe the recover of the crystal phase of the ductile regime machined sample. Results on the machinability of GaAs (100) in terms of chip produced and surface qualitative finish probed by microscopy technique are reported.

Cutting tests using facing operation were performed on 10 mm x 10 mm square, 0,5 cm thick samples of (100). GaAs produced by Princeton Instruments Co (USA). Coolant cutting fluid was used (synthetic water soluble oil). A 0° rake angle diamond tool with nose radius  $R = 1.52$  mm and a clearance angle of 12° was used in the tests. The cutting conditions were respectively, depth of cut  $a_p = 0,1, 1$  and 5  $\mu\text{m}$ , feedrate range ( $f$ ) = 1.25 – 3.75  $\mu\text{m}/\text{rev}$ , spindle speed 1000rpm. Digital Scanning Microscope, Zeiss model DSM 960, operated at 20 kV was used to conduct the observation of chip and surface finish. The Raman measurements were performed using a T64000 Jobin-Yvon triple monochromator and the 488.0 nm line of an Ar ion laser was used as exciting light. An optical microscope Olympus model BX40 was employed to obtain a laser spot of 1  $\mu\text{m}$ . The annealing was performed in a Linkan TS1500 Stage with temperature control mounted on the microscope base. Flow of dry nitrogen gas was employed to avoid oxidation of the sample

## Results and Discussion

Figure 1 show the machined surface cut in the ductile regime. In this case, feed rate was  $1.25 \mu\text{m/rev}$  and  $a_p = 1.0 \mu\text{m}$ . Table 1 shows the results obtained with the cutting conditions used in the tests.

**Table 1.** Critical thickness of cut estimated from the uncut shoulder analysed under the machined conditions compared with the values estimated by theory.

Feed $f$ ( $\mu\text{m/rev}$ )	$t_{\text{max}}$ theory ( $\mu\text{m}$ )	GaAs $t_c$ ( $\mu\text{m}$ )	Cutting mode Uncut shoulder*	Surface quality
1.25	0.101	0.093	D-B	Smooth
1.85	0.150	0,077	D-B	Damaged
2.50	0.203	0,046	B	Damaged
3.75	0.305	—	B	Damaged

\* Obs.: **D** – Ductile; **D-B** – Ductile-Brittle; **B** – Totally Brittle

The ductile mode was only achieved with the smallest feed condition. It is worth mentioning that, under larger cutting conditions used in the tests, it is possible to achieve smooth surface finish in other semiconductors such as silicon and indium antimonide [3]. Although GaAs presents smaller hardness value than silicon, this does not mean that the ductile response could be reached more easily. Instead of that, this can be considered a strong argument to support the fact that, to machine semiconductor crystals, the ductile response of semiconductor single crystals can not be directly related to the hardness of the crystal. Instead of that, the ductility presented by different semiconductor single crystals is inversely related to the transition pressure value of the material [3]. The transition pressure value of GaAs ( $> 17 \text{ GPa}$ ) is about 50% larger than silicon ( $11.3 - 12.5 \text{ GPa}$ ) [idem]. In this case, the appropriate cutting condition to achieve the ductile mode in GaAs might be in a range smaller than that for silicon. Despite the pressure generated by the tool cutting edge interaction, estimated to be around  $10 \text{ GPa}$ , is still *akin* to the transition pressure value of GaAs it is worth mentioning the high shear strain component under the edge contact present in machining favor the lower the phase transformation [3]. Consequently, in order to reach an ideal pressure under the tool tip to trigger the phase transformation, the chip cross section area would have to be smaller. This explanation is related to the fact that the pressure induced by the tool increase with the decrease of the chip thickness. The contact area between the tool cutting edge (length  $\times$  radius) and the GaAs sample has to decrease in order to make the pressure under the tool becomes sufficiently high to drive the phase transformation and the ductile response take place. This assert corroborates well with the type and width of the chips shown in Fig. 2 a) and b). For both conditions, i.e.,  $a_p = 1 \mu\text{m}$  and  $a_p = 0.1 \mu\text{m}$ , it was found very thin ductile chips among brittle debris. The ductile debris might be formed very close to the tool center once they are apparently very thin and the width is very small.

Figure 3 b) and 3 c) shows Raman spectra obtained from two different regions (at 5 and 15 microns from the entrance of the tip – see *detail photomicrograph*) in the machined surface and the spectrum of bulk crystalline GaAs, Figure 3 a). The spectra from the machined surface show two important differences compared with that from the bulk crystalline: the LO mode present a positive frequency shift of  $5 \text{ cm}^{-1}$ , indicating a residual compressive stress of about  $1.3 \text{ GPa}$ , while the broadening of the peak and the activation of the TO mode indicate high structural disorder caused by the machining process. Figure 3 d) shows the spectrum of the machined sample undergone a thermal annealing at  $600 \text{ }^\circ\text{C}$  during 60 min in a microfurnace. The result indicate that, although the strain is completely relaxed, the activation of the TO mode denounces the presence of structural disorder, indicating that the thermal annealing could

not recover the original crystalline phase.

If we follow the rationalization discussed in this paper two important facts are raised. First, the cutting to edge sharpness has to be in a range smaller than 100 nm radius which is very plausible. Second, the chip cross section area has to be smaller than that normally used for silicon for instance. These two facts may sound obvious but it seems that the ductility of semiconductor is in fact governed by the transition pressure value. In addition, this is a way to avoid introducing brittle damage and use very slight etching after machining in order to remove residual stresses.

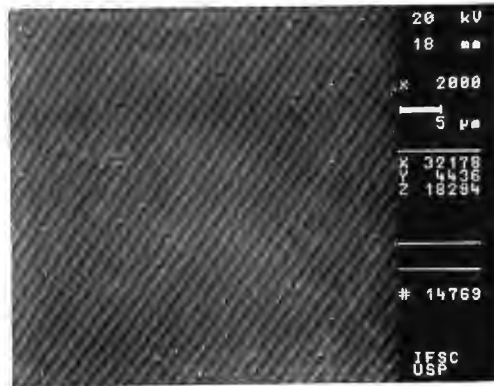


**Figure 1** Photomicrograph of the machined GaAs Sample machined in the ductile mode; surface cut in the ductile mode ( $f = 1.25 \mu\text{m}/\text{rev}$  and  $dc = 5 \mu\text{m}$ ).

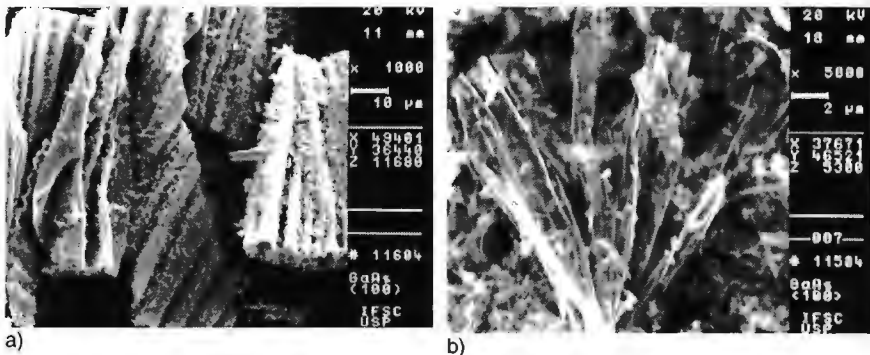


**Figure 2.** Photomicrograph showing typical chips found on the surface after machining tests. a) Small ductile ribbon chips can be observed among brittle debris for depth of cut of 1,0 μm. b)  $ap = 0,1 \mu\text{m}$

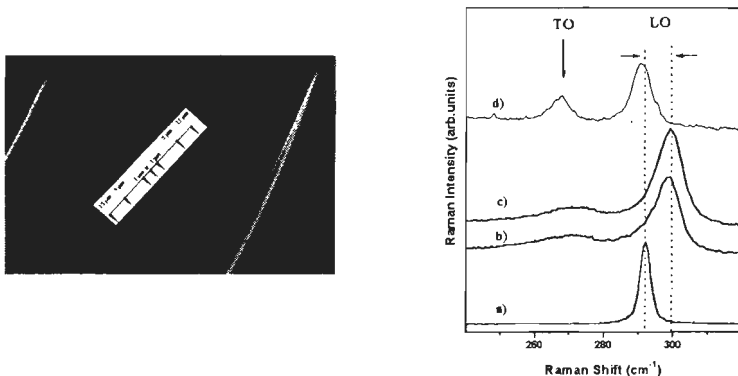


**Figure 3.** Raman spectrum (excited with the 488.0 nm line) of GaAs machined sample in the ductile conditions. The spectra are obtained at different points in the vicinity of the tool entrance showed schematically by the photomicrograph detail on the right. (a) spectrum of bulk crystalline GaAs; (b) and (c) Raman spectra obtained from two different regions (at 5 and 15 microns from the entrance of the tip, respectively); (d) spectrum of the machined sample undergone a thermal annealing at 600 °C during 60 min in a microfurnace.

In conclusion, material removal change from ductile to brittle mode at very shallow cutting conditions. This means that the critical chip thickness along the cutting edge length has to be reduced in order to achieve higher pressure values as possible in the contact region in order to trigger the phase transformation in this material. The microfracture found along the uncut shoulder can be avoided by controlling the dimensions of the cutting conditions. The plasticity observed is much smaller when compared to other semiconductors. This was attributed to the larger transition pressure value of GaAs. Raman Spectroscopy analysis was used to indirect evidence structural alteration and crystalline phase recover after machining and after heat treatment, respectively. The Raman spectra indicated high structural disorder caused by the machining process. It was shown that, although the strain is completely relaxed after annealing, the activation of the TO mode denounces the presence of structural disorder, indicating that the thermal annealing could not recover the original crystalline phase.

**Acknowledgements.** The authors also would like to acknowledge the financial support of FAPESP and CNPq (Brazil).

## References

- [1] Jasinevicius, R. G., Herrmann Jr, P. S. P., Duduch, J. G., Porto, A. J. V., Silva, H. A. T., Pagotto, C. R., 1st EUSPEN Conference, Bremen, Germany, V. 1 p.349, 1999.
- [2] Pizani P.S., Lanciotti Jr., F., Jasinevicius R.G., E Duduch J.G., Porto A. J. V., Journal of Applied Physics, 87 (3): 1280, 2000.
- [3] Gilman, J.J., Journal of Materials Research, 7, 535, 1992.

## Material evaluation for ultra-precision flexure hinges

R. Haberland,

Feinwerktechnik, Universitaet Kaiserslautern, Germany. haberland@mv.uni-kl.de

### Abstract:

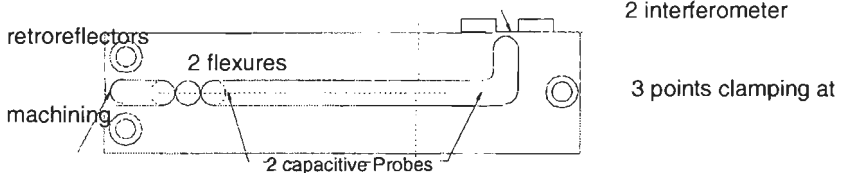
Material testing and evaluation has to be performed for precision structures, for example flexure hinges, to get the best possible quality.

A new simple test machine and test sample is presented. The test machine incorporates interferometer- and capacitive deformation measurement a voicecoil force motor in a temperature stable housing. Measurement is performed down to a residual strain below  $10 \times 10^{-6}$ .

### Realization

The specimen (Fig1) is machined from one block of material and has two thin flexures -one is loaded in tension one in compression. The two bores that form one flexure (mid cross section typically  $0.1 \times 20\text{mm}$ ) are flycut with diamond tools with a ballbearing spindle (good but not perfect). Mounting in the milling machine is done by 3 point stress free clamping. Early deformation is prevented by cutting free the flexures at test start

**Fig.1. Test probe:** dimensions 200 x 20 x 40 mm



From rolled sheet material this specimen is CNC milled and the flexures machined to dimensions by flycutting. Residual stress from this machining is remaining near the surface and is part of the test program. Specimen is finally heat treated after machining, then - immediately before use the securing regions are freed. Before installing the specimen two capacitive specimens are glued in place, also small steel foils to permit magnetic attachment of the retroreflectors.

The specimen is freed, bolted to the test machine, the force applying hook is installed, the interferometers initialized by adjustment of the retros which can be freely moved on the surface, held in place only magnetically.

Before loading the test machine is closed and some time waiting is necessary to reach thermal stability.

### Fig.2 Test machine

The test-machine is designed to permit short (1s) to long (hours) time loading of the specimen. A typical test cycle is started with some minutes of data storing of capacitive and interferometer-data. These data are useful in compensating residual temperature effects. Then cyclic loading and unloading is started with some waiting time after unloading to separate the elastic recovery after unloading from plastic strain. In the next cycle the loading force is raised by a programmable factor typically



1.1 to 1.4.

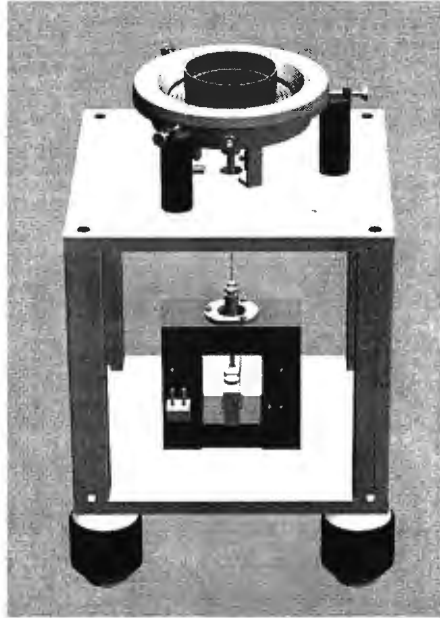
In contrary to early work /Lit 2/ this test is measuring plastic strain incrementally between load  $n$  and load  $n+1$ !

The machine is optimized to test aluminum alloys by using these as frame material.

**Fig.2 Test machine:** 4 vibration isolation feet, aluminum frame (doors and insulation removed), clamping frame with quadratic opening to accept specimen, bearing the two cylindrical finger shaped interferometers, vertical force transmission wire. Above upper plate: voice-coil (magnet-assembly removed) and its clamping and adjustment.

Thermal decoupling of voicecoil is necessary, voicecoil to magnet thermal coupling is augmented by ferrofluid in the airgap.

Special care is necessary to prevent coupling of thermal deformations of voicecoil and magnet-assembly into deformation of specimen or measurement. Not shown: force transducer, capacitive sensors and electronic, temperature sensors and electronic, programmable current source computer for programmed operation, measurement.



Data:

Force 0.2 to 200 N, Interferometer resolution 10 nm, capacitive resolution 0.3 nm, temperature resolution 0.001K, measurement and control of outside temperature 1 K, outside vertical vibration 100nm suppressed by isolators to 10nm and by digital data filtering to below 1 nm.

Data are gathered typically overnight as temperature, seismic and electric disturbances are minimal at night-time.

### Material evaluation for flexure hinges

Any high stability application: optical, laser, space, inertial is demanding very high material stability. Stability is mechanical stability without load: relaxation of internal stress or nonequilibrium, mechanical stability with short time load: impulse, shock and vibrations and mechanical stability with medium to long time load.

Typical stability requirement is  $10^{-6}$  that is translating to 2 nm deformation in a 2 mm flexure. This deformation has to be distributed by an error budget between different error mechanisms so there is the necessity to measure deformations down to 0.1 nm.

### Typical materials for high stability flexures

There are typical materials used for high stability applications: Carbon steels  
*Proc. of the 3<sup>rd</sup> euspen International Conference, Eindhoven, The Netherlands, May 26<sup>th</sup> -30<sup>th</sup>, 2002*

including chromium- and nitrogen containing steels, maraging (non-carbon) steels, bronze (mostly the beryllium containing alloys), titanium and (not so typical) aluminum-alloys.

The carbon steels are hardened and stabilized by raising the temperature to austenitic region, held at this high temperature to get full austenitic structure, quench to room-temperature or slightly above with to be evaluated quenching rate, cooled to cryogenic temperature to complete austenite to martensite transformation, temper at slightly elevated temperature to remove excess quenching stress. This is difficult to achieve but widely used for example in ballbearing manufacture. These steels get hardness and strength after quenching. All other stable materials of the above list are solution treated, quenched and aged. These materials get strength after ageing. All steels have high magnetic permeability and other undesirable magnetic data.

As aluminum alloys are much cheaper than any of the other alloys and this relation is even more pronounced if compared on a per volume basis we made a material evaluation on 4 typical aluminum alloys: A2024 (mostly copper alloyed), A6061 (mostly magnesium and silicon alloyed), A7075 (mostly zinc alloyed) and M101 (oxide particle reinforced).

Aluminum alloys are advantageous also with respect to low elastic modulus resulting in thicker flexures that are easier to fabricate.

**Fig.3 unloading curves**

(high load is down oriented!) unloading is total by disengaging the loading force train, loading started at 67800s and ended at 70050 seconds elastic recovery takes up to 3000s to establish the plastic strain measured strain is at sensor location and has to be scaled to flexure strain by the geometry

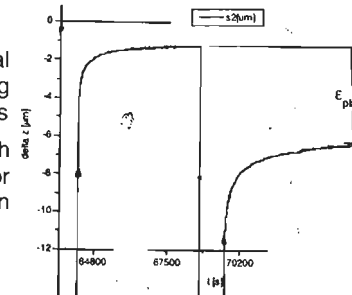
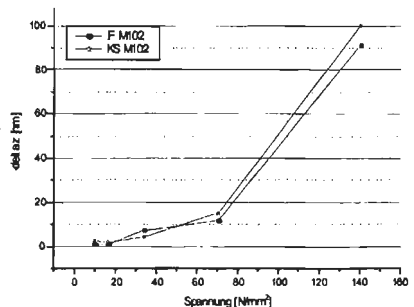


**Fig.4 plastic strain / stress**

! incremental diagram, integrate to convert to total strain !  
 material: Dispal M 102  
 deformation (in µm) of 0.1 mm thick flexure made by flycutting 2 holes 10mm diameter  
 actual equivalent length of flexure is near 2.7mm  
 beginning plastic strain near zero up to 30 ppm  
 specimens are cut in the as rolled direction  
 data for capacitive (dots) and interferometric (stars) measurements agree sufficiently



Not shown here but thought to be important: machining is not stress free, so at removal of the securing regions some residual stress is freed that was not removed by heat treatment. Aluminum alloys will change temper status by attempts to remove residual stress.

To be learned from the diagrams:

Nanometer behaviour is different from micrometer behaviour.

Two independent measurement possibilities are very useful for verification of difficult measurements. Limits of capacitive measurements are not reached here.

Fig.5 (above) A2024 T351

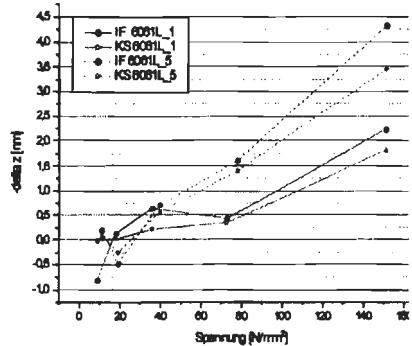
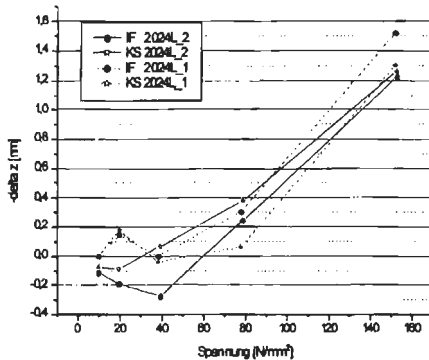


Fig.6 (upper right) A6061 T6

Fig.7 (lower right) A7075 T6

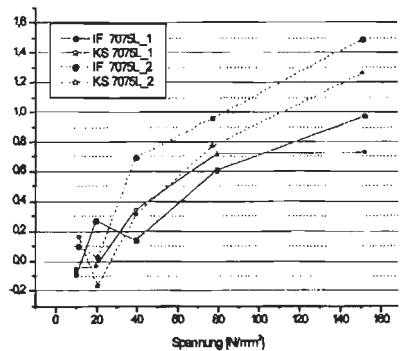
Figs.5 to 7:

beginning of plastic deformation in the region of 0.1 to 1 ppm ( $10^{-7}$  to  $10^{-6}$ ) strain  
interferometric and capacitive measurements agree to within 2nm  
spread of data from specimen to specimen (cut from same plate in same direction) is a factor from 1.2 to 2

vertical: deformation ( $\mu\text{m}$ ) of flexure

horizontal: stress  $\text{N}/\text{mm}^2$

incremental plots as Fig.4



Further resolution is limited by thermal

drifts of the total machine: geometry and measurement devices and clamping induced distortion of the specimen.

It should be possible to improve this situation by dynamic compensation of temperature.

Next step in material evaluation would be a check of data spread of different manufactured batches of nominally the same alloy. Also a survey on different thermal treatments is necessary. Improvement of manufacturing procedure can be very useful too.

## References

1. Bernst; Werkstoffe im wissenschaftlichen Gerätebau; Akad. Verlagsges.; Leipzig 1975
2. Marschall, Maringer; Dimensional Instability; Pergamon; 1977

## Ways to higher accuracy of the nanoindentation test

K. Herrmann, F. Pohlenz, F. Menelao

Physikalisch-Technische Bundesanstalt Braunschweig, Germany

### Abstract:

The accuracy of the nanoindentation test as result of prenormative investigations mainly is raised by two ways:

1. Application of sufficient calibration methods
2. Stipulation of unified test methods and measuring strategies

The state of the art of newly developed calibration methods is outlined. The test cycle recommended for the nanoindentation test in a new ISO draft standard plays an important role for the accuracy raise by unification. Moreover, for the measurement of coating properties strategies are stipulated which consider the material type of the substrate.

### Motivation

The nanoindentation method plays an increasing role in the characterisation of the mechanical properties of thin layers in surface technology, microelectronics, micromechanics, optics etc. Such thin layers are mostly required for functional and protective purposes.

The requirements of the instrumented indentation test for bulk material in the macro-, micro- and nano-range are addressed in the draft standards ISO/DIS 14577-1.2, -2.2, -3.2 [1]. Here, the nano-range is defined for an indentation depth  $h < 0.2 \mu\text{m}$ , or if one assumes a ratio  $h/t_c = 1:10$ , for a layer thickness  $t_c < 2 \mu\text{m}$ .

In order to stipulate the peculiarities of determining elastic and plastic properties of thin layers with the nanoindentation method the elaboration of a corresponding standard is underway which will supplement the above mentioned ISO/DIS 14577 as ISO 14577-4 [2].

Important results of corresponding prenormative investigations were achieved in the EU-project „Determination of Hardness and Modulus of Thin Films and Coatings by Nanoindentation“ (INDICOAT) [3].

In the paper it will be shown that the accuracy of the nanoindentation test as result of prenormative investigations mainly is raised by two ways:

1. Application of sufficient calibration methods
2. Stipulation of unified test methods and measuring strategies

### Application of sufficient calibration methods

An analysis of the influences on the uncertainty of the nanoindentation test has clarified that the following main items at calibrating a nanoindentation instrument have to be considered:

- Indenter tip geometry
- Measurement uncertainty of the depth measuring system
- Uncertainty of the zero point determination
- Measurement uncertainty of the force measuring system
- Compliance of the nanoindentation instrument
- Thermal drift of the nanoindentation instrument

### Indenter tip geometry

In order to measure the indenter tip geometry PTB used the metrological Scanning Force Microscope (SFM) Veritekt-3 with a measuring range  $x = 70 \mu\text{m}$ ,  $y = 15 \mu\text{m}$ ,  $z = 15 \mu\text{m}$ . The geometry of the indenter is measured by a series of scans at the tip surrounding. From the thus received two-dimensional data sets the projected area of the indenter is calculated as the so-called area function  $A_c = f(h_c)$  ( $A_c$  – indenter area,  $h_c$  – contact depth). The calculated area function is then used for the determination of hardness and indentation modulus of the sample. The area function determined by SFM was verified by comparison with the area functions determined by indentation into three different reference materials according to a modified Oliver/Pharr method [4][5].

The relative uncertainty of the area function determined by SFM for pointed indenters like Berkovich and Vickers indenters is 16 % to 6 %, and for ball-shaped diamond indenters 4 % to 0.3 % in the range of  $h_c = 50$  to 1000 nm.

### Measurement uncertainty of the depth measuring system

For calibration of the depth measuring system of a nanoindentation instrument laser interferometers with sub-nanometric capability are recommended. The laser interferometer delivers traceability to the unit of length via the laser wavelength.

Laser interferometers suitable for this purpose are e. g. a multi-pass Jamin laser interferometer developed at NPL [6] and a plane mirror interferometer developed at the Technical University of Ilmenau [7].

Recently, with the help of an x-ray interferometer, it was possible to verify that the measurement errors of the NPL interferometer type are  $E_I < 50 \text{ pm}$  [8].

### Uncertainty of the zero point determination

Generally, for the determination of the zero point uncertainty either the first increase of the test force or of the contact stiffness is used. For different nanoindentation instruments the uncertainty of the zero point determination is in the range between 1 nm and 10 nm. The zero point uncertainty mainly depends on the size of the contact load, the type of test material, its surface roughness, presence of surface layers, initial test force data available, environmental vibrations and type of fit to the function data  $F = f(h)$  at initial load.

### Measurement uncertainty of the force measuring system

In general, electronic balances or calibrated weights are used for the calibration of the force measuring system in a nanoindentation instrument. Due to the small indentation depth electronic balances with depth compensation have been used very successfully. The achievable uncertainty of calibration is estimated as  $U \approx 0.1 \text{ mg}$ , which corresponds with  $1 \mu\text{N}$ . If weights are used for the force calibration, they are usually directly hung from the indenter shaft. The corresponding uncertainty is estimated as  $10 \mu\text{N}$ .

### Compliance of the nanoindentation instrument

In a newly developed method, using two different reference materials, it is possible to determine the frame compliance  $C_f$  of the instrument and the area function of the indenter [9]. An iterative procedure is adopted, assuming the well known elastic properties of two reference materials. The procedure is schematised in Fig. 1, where  $C_t$  – total compliance,  $C_s$  – sample compliance,  $E_r$  – reduced Young's modulus.

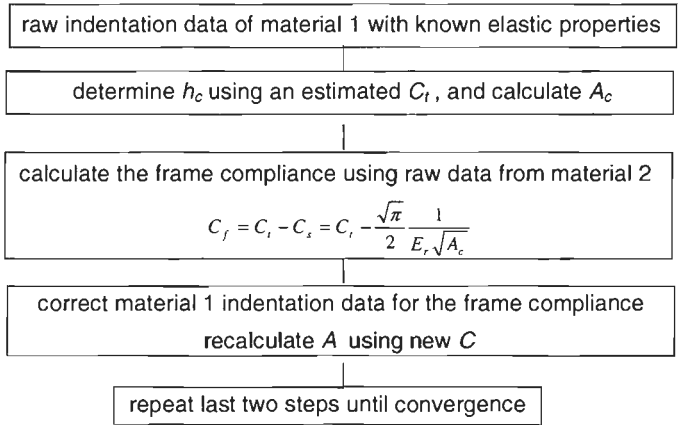


**figure 1:** Iterative procedure for compliance and area function determination

Typically the frame compliance is determined using reference material with high Young’s modulus, like tungsten single crystal W(100), while the indenter area function is derived from a reference material with small modulus, like fused silica.

**Thermal drift of the nanoindentation instrument**

The following decision path to assist in estimating the thermal drift during the experiment is proposed: if an elastic contact can be obtained, a hold period at initial contact is preferred. In this way, material influences can be avoided. If no elastic contact can be obtained, there is no generally recommendable method. Depending on the material under investigation, a hold at initial load (e.g. visco-elastic material) or at 90 % unload (e.g. soft material) may be preferred. Because of the stiffer contact (higher contact area) at 90 % unload, dispersion of the data when using this method is generally lower. For materials with strong creep behaviour, a hold period at both ends of the indentation cycle may be included. It is recommended that the hold period should be at least the loading time, and the data measured at the first 10 to 20 s of the hold period should be discarded from the analysis since these initial data may be significantly influenced by time-dependent effects.

**Stipulation of unified test methods and measuring strategies**

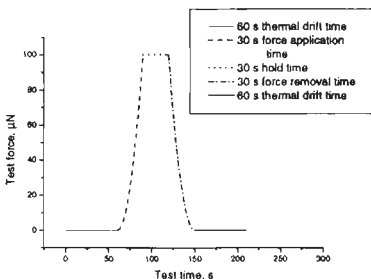


**figure 2:** Recommended test cycle for the nanoindentation test

**Recommended test cycle**

In the above mentioned draft standard [2] a test cycle as depicted in Fig. 2 is recommended.

Besides the test force increase and decrease curves, the test cycle also contains two hold periods in order to take into account the material creep and the thermal drift. The hold period for determining the thermal drift can be chosen either before the force application or after the force removal.

### Strategies for the measurement of coating properties

The investigations in the framework of the EU-project revealed that the influence of the material combination of coating and substrate on the result of the nanoindentation test must be considered. It was shown that it is relatively easy to measure the hardness of ductile coatings or the indentation modulus of brittle coatings. It is more difficult to determine the hardness of brittle or hard coatings or the indentation modulus of ductile coatings.

According to this classification the strategies for the determination of hardness and indentation modulus as given in Tab. 1 were derived.

**Table 1:**

#### Strategies for the determination of hardness and modulus of coated samples

Property to be determined	Strategy
<b>Hardness</b>	<ul style="list-style-type: none"> <li>• Performance of the indentation test in the plastic range</li> <li>• Pointed indenter recommended</li> <li>• Experimental determination of the onset of the plastic deformation of the substrate</li> <li>• Carry out indentation experiments so that the critical displacement is not exceeded</li> </ul>
<b>Indentation modulus</b>	<ul style="list-style-type: none"> <li>• Performance of the indentation test in the elastic range</li> <li>• Ball-shaped indenter recommended</li> <li>• Maximum test force must not exceed the value of plastic deformation</li> </ul>

### Acknowledgement

The support of the EU-SMT contract no. SMT4-CT98-2249 „Determination of Hardness and Modulus of Thin Films and Coatings by Nanoindentation“ (INDICOAT) is gratefully acknowledged.

### References

- [1] ISO/DIS 14577-1.2, -2.2, -3.2: Metallic materials – Instrumented indentation test for hardness and materials parameters – Part 1: Test method, Part 2: Verification and calibration of testing machines, Part 3: Calibration of reference blocks
- [2] CEN TC 184 WG 5, prENV 1071-7: Advanced technical ceramics – Methods of test for ceramic coatings – Part X: Determination of hardness and Young's modulus by instrumented indentation testing (WI 152)
- [3] EU-SMT project: Determination of Hardness and Modulus of Thin Films and Coatings by Nanoindentation (INDICOAT), contract no. SMT4-CT98-2249, final report, NPL Report MATC(A)24, May 2001
- [4] W.C. Oliver, G.M. Pharr: *J. Mater. Res.*, **7** (1992) 1564 – 1583
- [5] T. Chudoba, K. Herrmann: *Härtereitechnische Mitteilungen* (2001) **4**, 258 – 264
- [6] M.J. Downs, J.W. Nunn: *Meas. Sci. Technol.* **9** (1998) 1437 – 1440
- [7] H.-J. Büchner, G. Jäger: *Techn. Messen* **59** (1992) **2**, 43 - 47
- [8] A. Yacoot, M.J. Downs: *Meas. Sci. Technol.* **11** (2000) 1126 - 1130
- [9] K. Herrmann, N.M. Jennett, W. Wegener, J. Meneve, K. Hasche, R. Seemann: *Thin Solid Films* **377 – 378** (2000) 394 – 400

## Is cBN really inert with metals?

T. HOSONO<sup>1</sup>, H. HIDAI<sup>1</sup>, H. TOKURA<sup>1</sup>

<sup>1</sup> Department of Mechanical Science and Engineering, Tokyo Institute of Technology, 2-12-1, O-okayama, Tokyo.

### Abstract

Cubic boron nitride (cBN) has high hardness and little reactivity with steel. This makes cBN be one of the most promising materials as abrasive grains and cutting tools for ferrous alloys. However, cBN may react with workpieces and coolant because cutting tool edge reaches high temperature.

In this work, we studied about the thermal reactivity of cBN with metals. Metal powder and cBN grains were mixed and heated in a thermal gravity analyser. The mass of mixture was decreased while heating. Surface observation of cBN grains by a SEM revealed that many pits and bright grains eat into the surface. From the EDX analysis, these pits turned out to be made by thermal reaction between cBN and metal powder.

### Introduction

Cubic boron nitride (cBN) has high hardness (Hk 4800) next to diamond, and it is believed to have little reactivity with steel. This makes cBN one of the most promising materials as abrasive grains and cutting tools for ferrous alloys.

Although it is known that cBN is very stable material, there may be a possibility of reaction of cBN with some metals by following reasons. Cubic BN reacts with water to form ammonia at high temperature. Single crystalline cBN cutting tools have poor life time<sup>1)</sup>. Therefore, in this work, we studied about the thermal reactivity of cBN with metals.

### Experimental details

To confirm the reactivity of cBN with metals, metal powder tool and cBN grains (approximately 0.7mm in diameter) were mixed (1:1 mass ratio), heated up to 1100°C (heating rate was 20K/min) and held 30 minutes in a thermal gravity analyzer. The heating experiments were done in argon or nitrogen or air at flow rate of 200 sccm and pressure of  $1.0 \times 10^6$  Pa. After cooling, metal powder was removed from cBN grains and the grains were observed by a SEM. Experimental conditions are summarized in table 1.

**table 1:** Experimental conditions

Heating rate	20 K/min
Holding temperature	1000°C (Cu) 1100°C (Others)
Holding time	30 min
Mixture mass	15 mg
Atmosphere gas	Ar or N <sub>2</sub> or Air
Pressure	$1.0 \times 10^5$ Pa
Flow rate	200 sccm



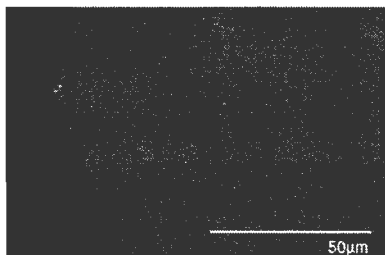


**figure 1:** SEM image of cBN surface after heating without metal powder

**table 2:** Tested materials

Fe	99.9% up, 53 um pass, Electrolytic
Cr	99%, 63 um pass, Pulverized
Ni	99% up, 53 um pass, Reduced
Mo	99.9% up, 63 um pass, Reduced
Mn	99.9%, 75 um pass, Pulverized
Cu	99.9%, 75 um pass, Electrolytic
cBN	0.7mm in diameter

Tested materials were iron, chromium, manganese, nickel, copper and molybdenum. Properties of metal powders and cBN are shown in table 2.

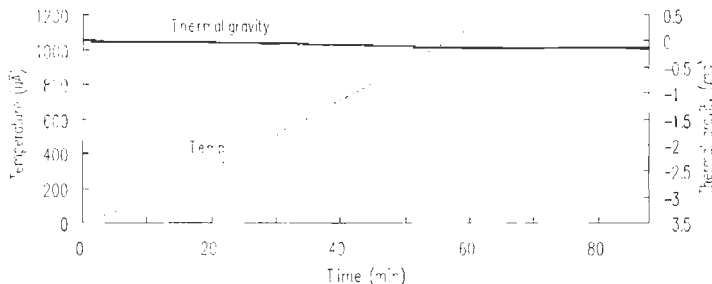
## Result and discussion

### Thermal reaction of cBN

Cubic BN grains (not mixed with metal powder) were heated on the conditions of table 1 in argon atmosphere. Figure 1 is a SEM image of cBN surface after heating. Wear of edge and pit is not observed and they are not different from the unprocessed ones. And figure 2 shows the mass change of cBN grains as a function of heating time. Slight mass reduction is detected. From these results, cBN itself is stable at high temperature.

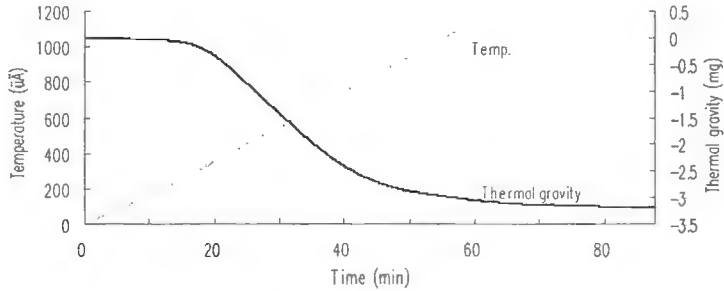
### Thermal analysis

Figure 3 shows the mass change of mixture (cBN greins and iron powder) as a function of heating time. From 250°C mass decrease bocome to remarkable. Mass decrease reaches more than 3mg. This is equivalent to 20% of the whole mass. Such mass decrease may depend on degas on desiccation of the mixture and pyrolysis of cBN.



**figure 2:** Diagrams of temperature and thermal gravity vs heating time (Tested material is cBN)

**Male**



**figure 3:** Diagrams of temperature and thermal gravity vs heating time (Tested material is the mixture of cBN and iron)

### **SEM observation (Mixture with iron powder)**

Figure 4 is a SEM image of cBN surface which was heated with iron powder in argon. There exist some pits and bright grains eating into cBN surface. Because the shape of grains corresponds to pits, these bright grains may take part in the forming of pits.

### **SEM observation (Mixture with other metal powders)**

When chromium, manganese, nickel and copper were tested in argon, similar pits or unevenness on cBN surface were also detected. Varying the atmosphere to nitrogen or air, similar change were observed for iron, chromium and nickel.

Because the reaction does not depend on atmosphere gas, the cause of this reaction should be an interaction of cBN and metals.

### **EDX analysis**

To identify bright grains observed in Figure 4, Fe element analysis was carried out by an EDX and Fe-K $\alpha$  map is shown in Figure 5(b). By comparing with a SEM image (Figure 5(a)) shows bright grains are iron powder. Figure 5(c) is an enlarged image of a pit. Figure 5(d) shows Fe-K $\alpha$  signal remarkably detected at the fringe of the pit. From these facts, it is thought that the main cause of forming of these pits is the reaction between cBN and metals.

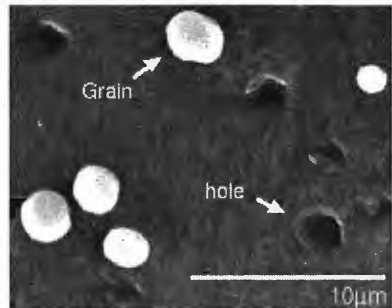


**figure 4:** SEM image of cBN surface after heating without metal powder

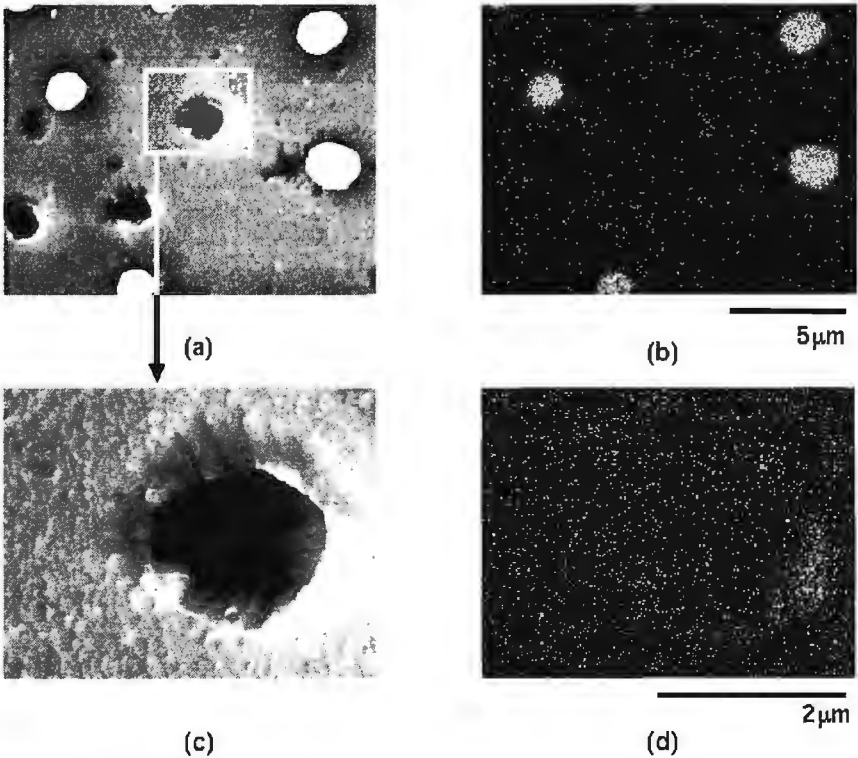


**figure 5:** FE-SEM images of cBN surfaces and x-ray maps obtained by an EDX. (a) FE-SEM image of cBN surface after heating. (b) Fe-K $\alpha$  map. (c) Enlarged image of (a). (d) Enlarged map of (b).

## Conclusions

1. Pits or unevenness are formed on the cBN surface by heating with metal powder.
2. Surface change of cBN mainly depends on the reaction with metals at high temperature.

## References

- [1] Takashi NISHIGUCHI, Masami MASUDA: J. of the Japan Society for Precision Engineering, 54,2(1988).

## Interferometric measurements of thermal expansion, length stability and compressibility of glass ceramics.

R. Schödel, G. Bönsch

Physikalisch-Technische Bundesanstalt, Braunschweig, Germany

### Abstract:

Development of specific techniques for phase-stepping interferometry resulted in progress of high accurate length metrology. The performance of the used Twyman-Green interferometer is demonstrated by measurements of the thermal expansion and compressibility of a rod shaped Zerodur sample. Although the investigations were performed in a small temperature interval near room temperature, small length relaxations continuing over several days were observed. An empirical formula for these relaxation allows the prediction of a "fully relaxed state" on the basis of which the thermal expansion coefficient can be clearly defined and calculated. Beside relaxations, effects caused by inhomogeneities of the thermal expansion are visible.

### Introduction

The value of the thermal expansion coefficient is required for accurate dimensional measurements. Increasing demands on the accuracy call for better knowledge of this coefficient.

When material standards are calibrated under vacuum and used under atmospheric pressure, the knowledge of the compressibility of the material is necessary in addition. For most accurate measurements of masks, the actual air pressure corresponding to weather conditions and height position of the laboratory has to be corrected using the compressibility.

A further interesting aspect is the dimensional stability of materials. It was reported that ultra low expansion materials reveal a length hysteresis upon cycling a large temperature interval [1-3]. High accuracy length measurements are necessary to investigate such effects near room temperature under small temperature changes.

For such investigations, an experimental precision interferometer has been improved. It allows to measure length changes of rod shaped samples with sub-nanometer uncertainty under varied, well defined environmental conditions. For this purpose, new methods of phase-stepping interferometry have been applied so that the evaluation uncertainty could be reduced effectively [4].

A Zerodur sample (15 x 35 x 280 mm<sup>3</sup>) was investigated. The material is more than ten years old so that the slow length shrinking effect usually continuing over years [5] is expected to play a minor role and the described features can be separated clearly.

### Experimental Setup

The interferometer is situated within a vacuum tight environmental chamber which is temperature stabilized by thermostats. The temperature of the sample and the environment is measured with an uncertainty of 0.8 mK [6]. For the measurements under air pressure, a pressure balance is used stabilizing the pressure within 1 Pa. The length measurement of samples up to 400 mm is performed by three wavelength interferometry with stabilized lasers at 543 nm, 633 nm and 780 nm. A vacuum cell of approximately 400 mm in length is situated beside the sample so that the refractive index of air can be accurately determined for the specific environmental conditions.

The interference pattern containing information of the vacuum cell and the sample is evaluated by phase stepping interferometry (PSI) and the equidistant phase steps

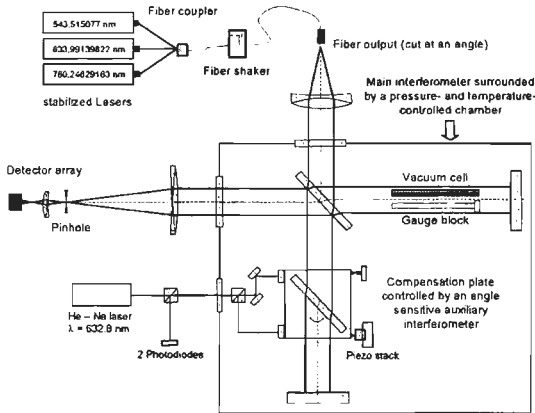


**figure 1** Experimental setup used for the length measurements

needed for the evaluation technique are achieved by tilting the compensation plate. The very small tilt angle is servo-controlled by an angle sensitive auxiliary interferometer. In this way, step width errors are negligible. Together with new methods removing the effect of detector nonlinearity [4], precise phase data with an uncertainty of less than 1/1400 interference order are obtained corresponding to an uncertainty contribution of about 0.2 nm. However, the quality of

the sample itself, especially with respect to parallelism, limits the uncertainty of the measurements. A very effective edge finding method was developed. The application of this tool allows a precise assignment of the measurement area within the measuring face, thereby drastically reducing the corresponding uncertainty contribution. The total uncertainty of length changes of the Zerodur rod in vacuum is below 1 nm.

## Results

### Compressibility of Zerodur

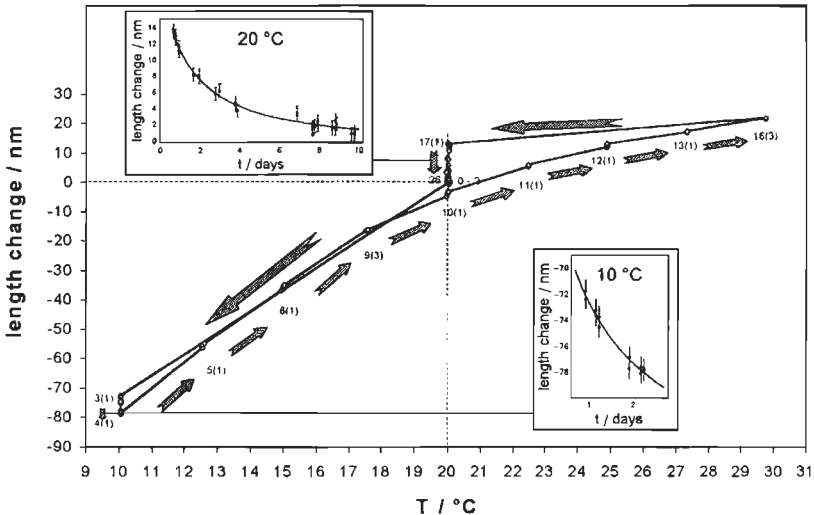
The compressibility is calculated from the length difference of the 280 mm rod between vacuum and atmospheric pressure :  $\Delta L = (161 \pm 2)$  nm. Via the relation  $\Delta V/V = 3 \times \Delta L/L = -K \times \Delta p$ , where  $\Delta V/V$  is the relative volume change and  $\Delta p$  the pressure difference (-1000.212 hPa), the compressibility results to:

$$K = (1.73 \pm 0.03) \times 10^{-11} \text{ Pa}^{-1}.$$

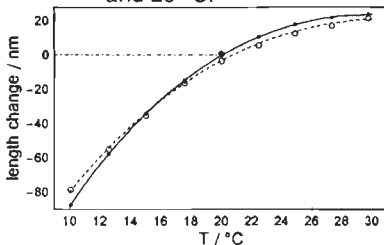
### Temperature induced length changes and length stability of Zerodur

Figure 2 shows the temperature induced length change measured at different temperatures. The arrows illustrate the sequence of the measurements. The temperature equilibration within the sample after temperature changes was completed before length measurements were started. However, figure 2 reveals that there are length relaxations continuing over several days. The length relaxations at 10 °C and 20 °C observed after a temperature change of 10 K are shown in the inserts of figure 2 together with an empirical non-exponential fit function (solid lines). Based on this knowledge, a model was proposed allowing the calculation of "fully relaxed" lengths changes at each temperature. Figure 3 shows these data as closed circles together with selected "raw data" of figure 2 as open circles (data points

measured before the next temperature step). The lines in figure 3 represent third order fit functions based on the calculated full relaxed data (solid line) and the "raw data" (dashed line). From these fit functions the corresponding coefficients of thermal expansion defined as  $\alpha(T) = 1/L \times dL/dT$  are calculated and shown in figure 4.



**figure 2:** Measurements of thermal induced length changes of Zerodur. The numbers at the data points indicate the day of the measurement and the approximate time in days after the previous temperature change (in parentheses). The inserts show the length relaxation observed at 10 °C and 20 °C.



**figure 3:** "Fully relaxed lengths" (closed circles) with fit (solid line) and "raw data" (open circles) with fit (dashed line).

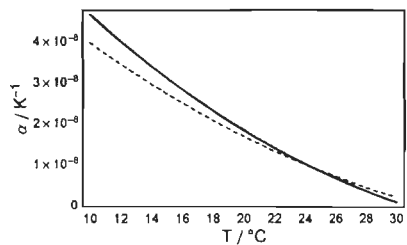


**figure 4:** Temperature dependent coefficient of thermal expansion obtained from the temperature derivation of the solid and the dashed line of figure 3.

The two  $\alpha$ -curves of figure 4 partially differ by more than  $3 \times 10^{-9} \text{ K}^{-1}$ . This is large compared with uncertainties of  $\alpha$  obtained for materials without length relaxation [7].

Bending of the Zerodur rod sample was observed as another temperature dependent

effect which is caused by expansion inhomogeneities. Figure 5 shows the length difference of front face measured at temperatures 30 °C and 10 °C. The length in each point of the front face is the perpendicular distance from the fitted plane of the end plate. The tilt along the 15 mm edge is about  $\pm 10$  nm. It was checked that temperature dependent effects of the interferometer can be excluded.

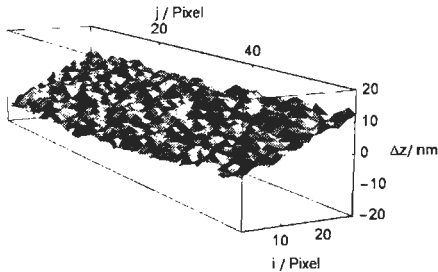


**figure 5:** Temperature induced tilt of the rod's measuring face related to the wrung auxiliary plate.

## Conclusions

Beside the expected temperature and pressure induced length changes a length relaxation in the nm-range was observed at Zerodur. This relaxation takes place under constant temperature and pressure conditions and was observed over several days. It has to be considered when a clear definition for the coefficient of thermal expansion is desired. Furthermore, from the tilting of the front face it can be concluded that the thermal expansion of Zerodur is inhomogeneous. For a single crystal sample of silicon [7] this was not observed, although the thermal expansion of silicon is about 100 times as large compared to Zerodur. Properties like dimensional stability and homogeneity of thermal expansion for only small temperature changes become more important as demands on accuracy, also for technical applications as EUV lithography, are increasing. The described interferometer is a valuable tool for measurement of sub-nanometre length changes to investigate appropriate materials.

## References

- [1] O. Lindig and W. Pannhorst. Thermal expansion and length stability of Zerodur in dependence on temperature and time. *Appl. Opt.* 24, 3330-3334 (1985)
- [2] S. F. Jakobs. Expansion hysteresis upon thermal cycling of Zerodur. *Appl. Opt.* 23, 3014-3016 (1984)
- [3] J.J. Shaffer and H.E. Bennet. Effect of thermal cycling on dimensional stability of Zerodur. *Appl. Opt.* 23, 2852
- [4] Schödel, R., A. Nicolaus, and G. Bönsch 2001. *Phase stepping interferometry: Methods to reduce errors caused by camera nonlinearities.* *Appl. Opt.* 41:55-63.
- [5] F. Bayer-Helms, H. Darnedde und G. Exner. Längenstabilität bei Raumtemperatur von Proben der Glaskeramik Zerodur. *Metrologia* 21, 49-57 (1985)
- [6] Bönsch, G., H. J. Schuster und R. Schödel 2001. *Hochgenaue Temperaturmessung mit Thermoelementen.* *Technisches Messen* 68:550-557.
- [7] Schödel, R. and G. Bönsch 2001. Precise interferometric measurements at single crystal silicon yielding thermal expansion coefficients from 12 °C to 28 °C and compressibility. *Proc. SPIE* 4410:54-62.

# Molecular Dynamic Simulation of Nanoindentation of Silicon Carbide by Diamond Tip

A. Noreyan<sup>1</sup>, I. Marinescu<sup>1</sup>, J. Amar<sup>2</sup>

<sup>1</sup>Mechanical, Industrial and Manufacturing Engineering Department, University of Toledo, USA

<sup>2</sup>Department of Physics and Astronomy, University of Toledo, USA

## Abstract:

The interaction between workpiece and diamond indenter was investigated using ninety-thousand atom molecular dynamic simulation with Leonard-Jones potential. At the special value of applied strain to the surface, a crack forms on the workpiece surface and moves toward perpendicular direction of indentation. The changes of energies (kinetic potential and total), pressure and temperature are observed during the process. The depth of indentation, the speed of indentation and the initial temperature of workpiece were varied to study the phenomena.

## Introduction

Current research efforts in fabrication are focused on achieving machining accuracy of less than 100 nm. To guarantee such accuracy, the surface roughness of the worked material should be an order of magnitude smaller, and to obtain such smooth surfaces the machining tools must have similar dimensions. This has led to the realization that progress in controlling/obtaining brittle-to-ductile transition for grinding of hard materials hinges on understanding the fundamental processes at the atomic level when a tool (such as a diamond grain) with an applied force (load) acts on a workpiece. Depending on the load, these processes include friction, elastic deformation, plastic deformation, and fracture, while the workpiece undergoes indentation, scratching, and eventual detachment of a chip of material. Such ultraprecision machining and microcutting is not trivial to characterize in the laboratory because of increasing in-process measurement problems, inaccessible contact area of tool and workpiece, and the difficulty of surface analysis in this range. On the other hand, atomistic simulations of the workpiece material/machining-tool interface, coupled with an analysis of the surface/interface mechanics provide a powerful approach to understanding factors that govern nanoscale precision production.

## Concept and basic elements of Molecular Dynamics

Molecular dynamics comprises macroscopic, irreversible thermodynamics and reversible micro mechanics. The thermodynamic equations form a link between the micro mechanical state, a set of atoms and molecules, and the macroscopic surroundings, the environment. The thermodynamic equations yield the quantities *system temperature* and *hydrostatic pressure* into the model and allow to determine energy changes involving heat transfer. In mechanics it is usual to consider energy changes caused by displacement and deformation. By the term "mechanical state" of a microscopic system, a list of present coordinates  $\{r\}$  and velocities  $\{v(t)\}$  of the constituents is meant [1]. As the governing equations of motion for a system of constant total energy, the well-known Newton's equations of motion can be chosen. The resulting force on an atom is expressed by an integral over all force contributions. The force contribution is calculated by employing partial derivatives of



so-called potential functions, which describe the energetical relation between atoms with respect to the separating distance, bonding angle and bonding order, possibly. To advance the atoms in space, the equation of motion has to be integrated with respect to time once to obtain the new velocity and twice for the new position of each atom. Numerically, this operation is more efficiently carried-out by approximation schemes, for instance using finite difference operators and the so called Verlet or Stoermer algorithm [1,2]. With the present positions ( $R_i(t)$ ), velocities ( $v_i(t)$ ) and forces ( $F_i(t)$ ), first the new positions and forces at  $t + \Delta t$  can be calculated and then the new velocity as well. Given the equations of motion, forces and boundary conditions, i.e. knowing the current mechanical state, it is possible to simulate future behavior of a system.

### Material Representation: the Potential Function

The key to computational efficiency of atomic-level simulations lies in the description of the interactions between the atoms at the atomistic instead of the electronic level. This reduces the task of calculating the complex many-body problem of interacting electrons and nuclei like in quantum mechanics to the solution of an energetic relation involving, basically, only atomic coordinates [1]. The central element of the MD-code is the force calculation. As it is the most time-consuming part in an MD computer program, it determines the whole structure of the program. First van der Waals described a model of a material, which can form liquid and solid condensed phases at low temperatures and high pressures. Such condensed phases require both attractive and repulsive forces between atoms [1]. Since the simplest possible representation of many-body interactions is a sum of two-body interactions, the so-called pair potentials were the first potential descriptions of such type. One of the best-known pair potential functions is the Lennard-Jones potential (1). The well-depth of the functions is given by the parameter  $\epsilon$  for the minimum potential energy, while  $\sigma$  is a constant that define the position of the energy minimum. These parameters are derived from fitting to experimental data like lattice constant, thermodynamic properties, defect energies and elastic module.

$$\text{Lennard-Jones: } V_{LJ}(r) = 4 \epsilon [(\sigma / r)^{12} - (\sigma / r)^6] \quad (1)$$

The potentials describe chemically active materials as bonds can be established or cut at the long-range part. They represent reasonable descriptions for two-body forces to the extent, that they account for the repulsion due to overlapping electron clouds at close distance and for attraction at large distances due to dispersion effects. Generally in solids, a shielding effect is expected to make interactions beyond the first few neighbors of limited physical interest. Tersoff [3] developed an interatomic potential for multicomponent systems and applied it very successfully to the SiC system. The Tersoff potential is a many-body potential that describes accurately the single elemental structures as well as the multi-component ones.

$$E = \sum_i E_i = 0.5 \sum_{i \neq j} V_{ij},$$

$$V_{ij} = f_c(r_{ij}) [ f_R(r_{ij}) + b_{ij} f_A(r_{ij}) ] \quad (2)$$

In the case of SiC, the potential was first fitted to describe very accurately the elemental systems Si and C independently. This is an essential feature of the potential as the workpiece should mimic realistically crack propagations, fractures and other structural modification occurring during a micro-machining process. A single additional parameter is then added to up-grade the potential into treating

mixtures of the two elements in a variety of structures.

### Simulation Model

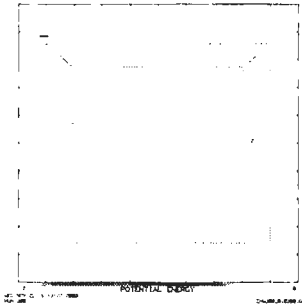
In recent years atomistic studies involving molecular dynamics (MD) simulations of abrasive processes from the perspective of nanofabrication have taken a big leap, particularly with a group of researchers in Japan [4,5]. Initial MD studies on small systems based on simple pair potentials for metallic systems and those including three-body interactions and angular terms like Stillinger-Weber [6] and Tersoff [3] potentials for Si and C have been supplemented recently by large-scale simulations using thousands [7] of atoms. Calculation of macroscopic stress and strain distributions [8], atomic potential energy profiles [8], and radial distribution function [9] have provided preliminary information on surface integrity, crack propagation and brittle-ductile transition. Related MD simulations [9] have also shown that most materials, in spite of their brittleness, can be machined in ductile mode under a sufficiently small scale of machining. The aim of the simulation is to examine the atomistic mechanisms taking place during brittle and ductile nano-machining of SiC. A careful analysis of the structural and energetics changes of the individual parts (at the atomic level) of the system during simulated machining under a variety of initial conditions will allow us to rationalize the brittle to ductile transitions and to provide criteria for the occurrence of this transition from a knowledge of the intrinsic properties of the materials (work piece and indenter) that govern plasticity and fracture. There are several stages in a theoretical study of the structure and energetics of a given system. The choice of atomic structure, i.e. crystallographic orientation, presence of defects, and voids etc., forms the first stage. Next the atomic positions are allowed to relax to their minimum energy configuration. Relaxation patterns are then analyzed in terms of atomic coordination. Finally, the energetics of different regions of the system are calculated. In order to directly study the dynamics of nanoindentation, molecular dynamics simulations of these processes is carried out using large-scale molecular dynamics code - SPaSM (Scalable Parallel Short-range Molecular dynamics), which was developed by T.C. Germann and P. S. Lomdahl. The SPaSM code uses domain-decomposition techniques in order to efficiently carry out parallel molecular dynamics simulations. In all simulations, the indenter is made from a closed packed stacking of carbon atoms in the diamond structure. The indenter is constructed as a pyramid. For this indenter, the minimum energy configuration is calculated by allowing the atomic positions to relax via the conjugated gradient scheme. SiC material is used extensively in several industries including those involved in micro-electronic devices and memory components. The materials used in the industrial fabrication lines are polycrystalline made of hard grains, which make them both hard and brittle at the same time. Because of this brittleness, these materials fracture easily during grinding. Polishing, on the other hand, proceeds by mainly ductile plastic removal of matter with no fracture. The aim of nano-grinding is to operate in the ductile regime of the polishing while maintaining the ultra-high precision of the grinding. Since plastic removal of matter proceeds in confined regions in which the local structure may be that of a perfect crystal, or contain a local defect (a void, a dislocation or a grain boundary) and since fracture essentially occurs in polycrystalline multigrained systems, we are planning to include all these factors in our simulations in three different stages.

The single crystal work piece will be made from a stacking of closed packed layers with a free surface. Periodic boundary condition is applied in the x and y directions (parallel to the planes) while the free surfaces will be allowed to relax.

## Nanoindentation

The external forces are applied to the indenter. Since the system is not isolated (the indenter is kept under external forces) it is necessary to dispose of this extra energy realistically. In a real system, this energy will dissipate in the bulk. One way of simulating this disposal of the energy is by placing some thermostat layers above bottom clamped layer of the workpiece. The atoms in this thermostat region are kept at constant temperature all along the simulation. Energy will dissipate also into the indenter, and hence, we will keep the layer just below the static layers at constant temperature.

Currently SPaSM code is being modified for Tersoff potential, which, as it was stated above, is the best match for diamond and SiC materials.



The figure 1 shows a snapshot of the early stages of indentation using Leonard-Jones potential with fcc crystal structure. As can be seen, the indentation process leads to a localized heating of the substrate and indenter in the interaction region. Light gray substrate atoms undergo unconstrained molecular dynamics while the dark gray atoms at the bottom of the substrate undergo constant temperature (Langevin) dynamics and serve as a heat sink. Bottom layers correspond to fixed atoms.

figure 1: Indentation

## References

1. Hoover, W.G., 1991, Computational Statistical Mechanics, Studies in Modern Thermodynamics 11, Elsevier Science Publisher, Amsterdam-Oxford-New York-Tokyo, 313 pages.
2. Allen, M.P., Tildesley, D.J., 1987, Computer Simulation of Liquids, Clarendon Press, Oxford.
3. Tersoff, J., 1989, Modeling Solid-State Chemistry: Inter atomic Potentials for Multi-component Systems, *Phy.Rev. B*, Vol.39, No.8, 5566-5568, and 1990, Vol.41, No.5, 3248.
4. Shoichi Shimada, Naoya Ikawa, Toyoshiro Inamura, Nobunior Takezawa, Hitoshi Ohmori, Toshio Sata, *Brittle-Ductile Transition Phenomena in Microindentation and Micromachining*, *Annals of the CIRP*, Vol 44, 523 (1995).
5. Inasaki, "Application of Simulation Technologies for Grinding Operations," *VDI Berichte Nr. 1276*, 197 (1996).
6. F.H. Stillinger, A.W. Weber, Computer Simulation of Local Order in Condensed Phases of Silicon, *In Phys. Rev. B* 31 5262-5271(1985).
7. D.B. Boercker, J. Belak, I.F. Stowers, R.R. Donaldson, and W.J. Siekhaus; *Simulation of Diamond Turning of Silicon Surfaces*, *In unpublished*.
8. T. Inamura, S. Shimada, N. Takezawa, and N. Nakahara, *Brittle/Ductile Transition Phenomena Observed in Computer Simulations of Machining Defect-Free Monocrystalline Silicon*, *In Annals of the CIRP*, 46, 31 (1997).
9. Shoichi Shimada, Naoya Ikawa, Hiroaki Tanaka, Junichi Uchikoshi, *Structure of Micromachined Surface Simulated by Molecular Dynamics Analysis*, *In Annals of the CIRP*, Vol. 43, 51(1994).

## STRONGLY COMPENSATED SILICON AS A NEW CLASS OF MATERIALS FOR ELECTRONICS.

M.K. Bakhadir Khanov , K.C. Ayupov., N.F. Zikrillayev, F.A. Kadirova, D. Bobonov

Tashkent State Technical University, Tashkent, Republic of Uzbekistan

Concentration of equilibrium charge carriers in strongly compensated semiconductors becomes hundred thousand times less than that of ionized impurity atoms. Local electric neutral areas are absent in the crystal volume in this case, which causes increase of Debye screening distance. Due to that properties of the material are quite different from those with partial compensation.

Possibilities of application of the material in construction of principally new types of semiconductor devices, and sensors of different physical magnitudes are showed.

Although concentration of charge carriers in semiconductors is sometimes hundreds of thousand or even million times less than that of ionized impurity atoms, the system is considered to be in non-equilibrium state. The type of semiconductors are known as strongly compensated. Absence of local screening of charge impurity potentials as well as random distribution of potential relief in the bulk change transport mechanisms and trigger new physical effects.

Strongly compensated Silicon has been obtained by means of diffusion of Mn into p-type Si. Investigations showed that magnitude and character of temperature dependence of Hall mobility of carriers vary for samples with different specific resistance (Fig.1). The dependence is usual for Si(B) samples and described by  $T^{3/2}$

(curve 1). Decrease of Hall's mobility with temperature increasing is observed in Si(B,Mn) samples. The dependence does not obey  $T^{3/2}$  function (Fig.2). Growth of resistance of p-Si(B,Mn) the  $\mu(T)$  relationship has different character (curves 3-5). Mobility increases with temperature and reaches its maximum at  $T_{max}$ , then rapidly decreases reaching the minimum at  $T_{min}$ . Further increase of temperature causes increasing of mobility. Both  $\mu_{max}$  and  $\mu_{min}$  values are displaced to higher temperatures with growth of the resistance. Temperature dependence of mobility of carriers in strongly compensated samples of Si(B,Mn) with  $\rho \sim 10^5$  Ohm-cm at illumination with white light showed more clear relationship of  $\mu(T)$ .  $T_{max}$  and  $T_{min}$  values are displaced to lower temperature region and second minimum of the mobility at  $T_{min2}$  is observed. Investigations of magnetic resistance  $\rho(H)$  in Si(B,Mn) showed its unusual character. Fig.2a presents  $\rho(H)$  relationship of Si(B,Mn) samples. Positive magnetic resistance takes place in overcompensated n-Si(B,Mn) samples and it is weakly related to the material's resistance. Similar situation is revealed for Si(B). In case of compensated p-Si(B,Mn) samples increase of specific resistance leads to change of both value and sign of magnetic resistance. Negative magnetic resistance is always observed in samples with  $5 \cdot 10^5 < \rho < 2 \cdot 10^5$  Ohm-cm. Its value reaches maximum in samples with  $\rho \approx (3-4) \cdot 10^3$  Ohm-cm. Positive magnetic resistance is observed in samples with  $\rho > 2 \cdot 10^3$  Ohm-cm, which grows with increase of specific resistance. Increase of negative value of magnetic resistance with increase of illumination intensity is observed (Fig. 2.c). Fig.3 presents spectral dependence of photo-conductivity in p-Si(B,Mn) with  $\rho \sim 10^5$  Ohm-cm at different

levels of background illumination (white light). As we see, independently on magnitude of background illumination photo-current decreases under infra-red radiation of  $h\nu = 0.4$  eV and reaches its minimum at  $h\nu = 0.47 - 0.48$  eV. In the range of  $h\nu = 0.4 - 0.48$  eV photo-current decreases by 6-7 orders and infra-red quenching of photo-current is observed.

It is necessary to underline that increase of background illumination spectral region of the quenching narrows and multiple of the quenching slowly decreases. The anomalous deep quenching has not been observed in any of semiconductor materials.

The experimental results are difficult to explain by existing theories kinetic phenomena in semiconductors. So, we consider strongly compensated semiconductors to be a separate, new class of materials and it is important to learn more about the material and develop its physics.

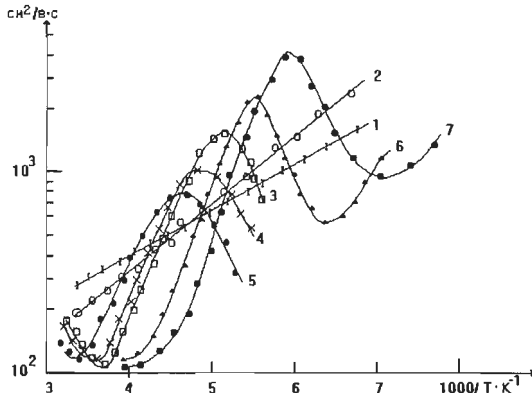


**Figure 1:** Temperature dependence of Hall mobility for different samples 1-p-Si(B) with  $\rho = 10^4$  Ohm-cm, 2-p-Si(B,Mn);  $\rho = 10^2$  Ohm-cm, 3-p-Si(B,Mn) with  $\rho = 10^3$  Ohm-cm, 4-p-Si(B,Mn) with  $\rho = 10^4$  Ohm-cm, 5-p-Si(B,Mn) with  $\rho = 10^5$  Ohm-cm, 6,7-overcompensated Si(B,Mn).

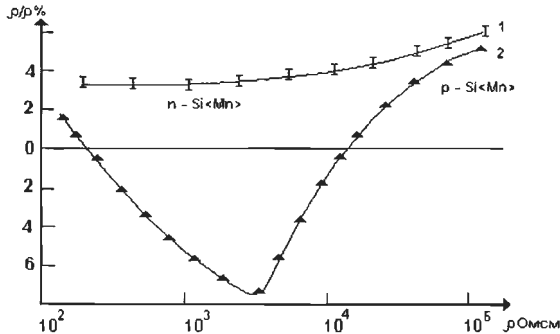


**Figure 2.a:** Dependence of magnetic resistance of Si(B,Mn) samples at  $T=300$ K.  $E=5$ v/cm,  $H=15$ kOe. 1-n- Si(B,Mn), 2-n- Si(B,Mn).

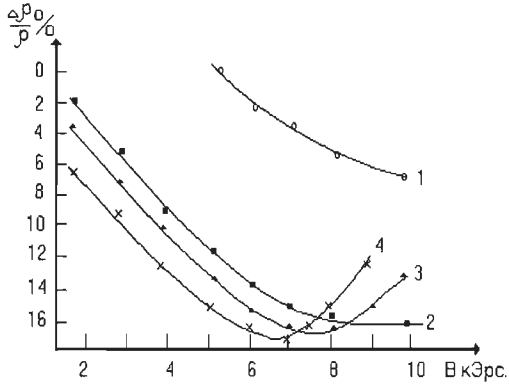


**Figure 2.b:** Relationship of negative magnetic resistance and magnetic field at illumination with white light of different intensities. 1-without illumination. 2,3,4- $I_2, I_3, I_4$  intensities respectively.

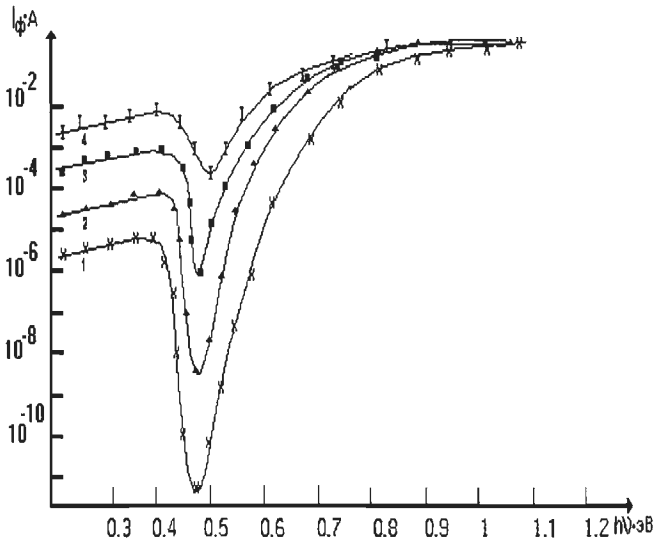


**Figure 3:** Spectral photo-conductivity p-Si(B,Mn) with  $\rho = 10^4$  Ohm-cm at different illumination levels (white light).  $I_4 > I_3 > I_2 > I_1$ .



# ELID GRINDING AND TRIBOLOGICAL CHARACTERISTICS OF TiAlN FILM

Y. Watanabe<sup>1</sup>, K. Katahira<sup>2</sup>, H. Ohmori<sup>2</sup>, T. Kato<sup>2</sup>, A. Kawana<sup>3</sup>

<sup>1</sup> Hirosaki University, Japan; <sup>2</sup> RIKEN, Japan; <sup>3</sup> Japan Coating Center, Japan

## Abstract:

This paper presents the results of electrolytic in-process dressing (ELID) grinding experiments on TiAlN film and the characterization of the tribological characteristics of the films produced. High-quality TiAlN film surfaces were fabricated in this study using the ELID technique, achieving a typical surface roughness of around  $Ra$  0.0024  $\mu\text{m}$  using a SD #30,000 wheel. It can be considered that oxide-layer in the machined surface of TiAlN film was formed with ELID grinding. Therefore, in addition to the highly smooth surface, the formation of oxide-layer with ELID grinding also results in superior tribological properties of ELID-finished TiAlN film.

## Introduction

TiAlN is a potentially useful hard coating that effectively enhances the wear and thermal oxidation resistance of tools and that overcomes the shortcomings of TiN and TiCN coatings. However, the surface roughness of TiAlN films produced by only coating process is not low enough to realize superior tribological characteristics compared with other new films such as CrN and DLC [1][2]. The electrolytic in-process dressing (ELID) of grinding wheels makes it possible to achieve specular finishes on brittle materials, with surface roughness on the nanometer scale (4 to 6 nm) [3]-[5]. This paper presents the results of ELID grinding experiments of TiAlN film and the characterization of tribological properties of the films produced.

## Experimental Procedure

TiAlN films were deposited by arc ion plating, a PVD technique, under the conditions listed in Table 1. Specimens of disk-shaped cemented carbide alloy were prepared as substrates. Droplets of un-melted TiAl intermetallic alloy were observed on the surface of TiAlN film as shown in Figure 1.

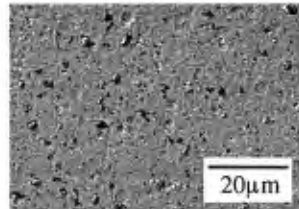


Figure 1: Surface appearance for TiAlN film

Table 1: Coating conditions for TiAlN film

Process	Conditions	
Cleaning	Ultrasonic cleaning using Methylene Chloride	
Exhaust	4 $\times$ 10 <sup>-5</sup> Torr	
Pre-coating	Substrate sputter cleaning using Ti (673K)	
Coating	Film	TiAlN
	Apparatus	Cathodic arc ion plating (Physical vapor deposition)
	Temperature	723 K
	Target	TiAl intermetallic alloy
	Process gas	Nitrogen (N <sub>2</sub> )
	Film thickness	About 10 $\mu\text{m}$

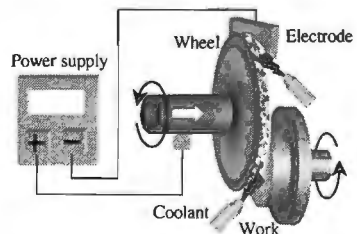


Figure 2: ELID grinding system



The ELID grinding technique is a relatively new process, in which the abrasive characteristics of a metal-bond grinding wheel are maintained by an electrolytic process. Figure 2 shows the principle of the ELID-grinding technique employed in this study. The wheel acts as the positive electrode, and the negative electrode is fitted near the wheel with small clearance. A chemically soluble grinding fluid is supplied in the gap, and electrolysis occurs under an applied electric current. Table 2 lists the experimental conditions for ELID grinding. The tribological characteristics of ELID-finished TiAlN films were determined through ball-on-disk tests [SHINTO Scientific Co., Ltd.].

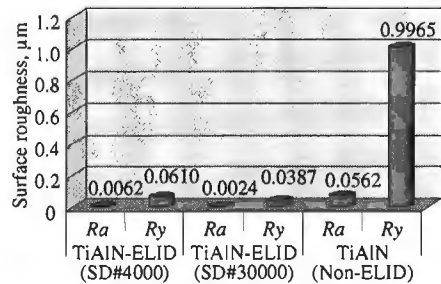
**Table 2:** ELID grinding conditions

Workpiece	TiAlN film
Grinding machine	Precision rotational grinder HSG-10A2 [Nachi-Fujikoshi corp.]
Grinding wheel	Cast iron bonded diamond wheel; SD #4,000 SD #30,000 [FUJI DIE Co.]
ELID power source	ED-910 [FUJI DIE Co.]
Grinding condition	Grinding wheel rotating speed; 2,000rpm Workpiece rotating speed; 300rpm Feed rate; 1µm/min
Machining time	Feed rate 1µm/min; 30min
Surface roughness measurement system	SURFTTEST-701 [Mitutoyo Co.,Ltd.], Nanopics-1000 [Seiko Instruments Inc.], JSM-5600LV [JEOL Ltd.]

**Experimental results and discussion**

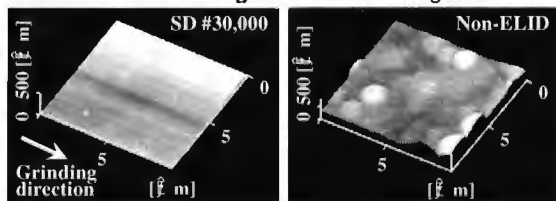
**Surface roughness and Observation of finished surfaces**

Figure 3 shows the surface roughness of films produced by a non-ELID process, and by the ELID processes using a SD #4,000 and SD #30,000 wheels. It can be seen that a better surface finish is achieved by the ELID processes, with surface roughness similar to that obtainable by loose abrasive processes such as polishing or buffing.



**Figure 3:** Surface roughness

Figure 4 show the AFM topographies of ELID finished and non-ELID TiAlN film. This demonstrates that highly smooth surfaces can be produced by ELID process using extremely fine abrasives. High precision and efficiency are also characteristics of this technique, attributable to the metal-bonding of the abrasive.



**Figure 4:** Surface roughness

**Tribological characteristics of ELID-finished TiAlN film**

Typical friction coefficient vs. sliding distance curves for ELID-finished TiAlN film and non-ELID finished TiAlN film against a Al<sub>2</sub>O<sub>3</sub> ball are given in Figure 5. The friction coefficient of the ELID-finished TiAlN film and non-ELID TiAlN film initially increased with sliding distance up to a maximum at about 100 m, thereafter reaching a steady state. After the sliding distance of 100 m, the average friction coefficient of ELID-finished TiAlN film was low at 0.53 compared with non-ELID TiAlN film, 0.73.

Figure 6(a) and (b) show 3 dimensions and cross section profiles of wear tracks using AFM. The non-ELID TiAlN film exhibited the most wear, and the wear tracks were rough with a significant amount of abrasive wear. The abrasive wear is attributable to droplets adhered to the TiAlN film surface. In contrast, the ELID-finished TiAlN film had excellent wear resistance, exhibiting less wear and smoother wear tracks.

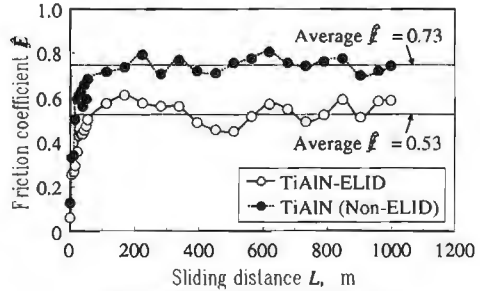


Figure 5: Friction coefficient

Figure 7 shows the wear rate of disk and ball specimen. The wear rate of the ELID-finished TiAlN film is approximately one half of that of non-ELID TiAlN film. Also, the wear rate of Al<sub>2</sub>O<sub>3</sub> ball for ELID-finished TiAlN film is approximately one tenth of that for non-ELID TiAlN film.

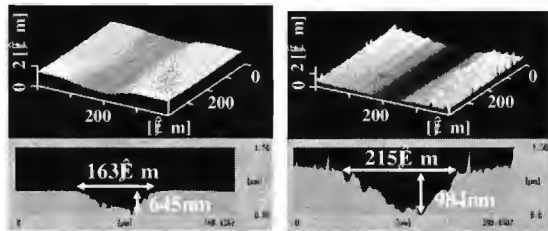


Figure 6: AFM topographies of wear tracks

**Effects of ELID grinding**

It has been clarified in our recent study that the electrical grinding method proposed, in which electric current is applied to the grinding fluid in the machining process, improves oxide formation on the finished surfaces, thereby realizing finished surfaces with very thick and stable oxide layers [6]. Therefore, the oxide layers can be formed on the surface of ELID-finished TiAlN film in this study.

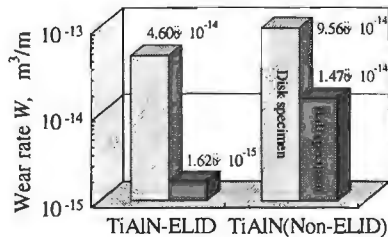


Figure 7: Wear rate

The properties of the machined surface for TiAlN film were examined by chemical element analysis using an energy-dispersed x-ray diffraction system [SHIMADZU

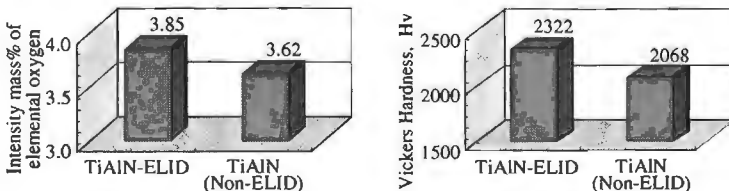


Figure 8: Properties of the machined surface for TiAlN film

Corp.), and by the measurement of Vickers hardness using a nano-hardness tester [CSM Instruments]. A sharp peak corresponding to element oxygen in case of ELID-finished TiAlN film was highly detected compared with non-ELID TiAlN film as shown in Figure 8(a). The elemental oxygen detected in the improved surface is believed to exist on the surface as a stable oxidized layer [7][8], strongly supporting the hypothesis that oxide-layer on the surface of ELID-finished TiAlN film was formed with ELID grinding. The Vickers hardness of ELID-finished TiAlN film had higher than that of non-ELID TiAlN film as shown in Figure 8(b). Therefore, in addition to the highly smooth surface, it can be considered that the formation of oxide-layer with ELID grinding results in superior tribological properties of ELID-finished TiAlN film.

## Conclusion

- (1) High-quality TiAlN film surfaces were fabricated in this study using ELID technique, achieving a typical surface roughness of around  $Ra$  0.0024  $\mu\text{m}$  using a SD #30,000 wheel.
- (2) Compared to coating process, the ELID grinding of TiAlN film produced excellent results in terms of tribological characteristics.
- (3) It can be considered that oxide-layer in the machined surface of TiAlN film was formed with ELID grinding.

## Acknowledgements

The authors would like to express their sincere appreciation to kind support provided by Dr. Komotori J. and Mr. Mitani Y. of Keio University. This study was supported by the Sasagawa Scientific Research Grant from The Japan Science Society.

## References

- [1] Jeon G. Han, Joo S. Yoon and J. Kim: "High Temperature Wear Resistance of (TiAl)N Films Synthesized by Cathodic Arc Plasma Deposition", *Surface and Coatings Technology*, 1996.
- [2] Young-Ze Lee and Ki-Hum Jeong: "Wear Life Diagram of TiN-coated Steels", *Wear*, 1998.
- [3] H. Ohmori and T. Nakagawa: "Mirror Surface Grinding of Silicon Wafers with Electrolytic In-Process Dressing", *Annals of the CIRP*, 1990.
- [4] H. Ohmori and Ioan D. Marinescu: "Super-smooth Surfaces with ELID Grinding Technique", *Abrasives*, 1998.
- [5] K. Katahira, H. Ohmori, M. Anzai, A. Makinouchi, S. Moriyasu, Y. Yamagata and W. Lin: "Grinding Characteristics of Large Ultraprecision Mirror Surface Grinding System with ELID", *Advances in Abrasive Technology*, 2000.
- [6] H. Ohmori, K. Katahira, J. Nagata, M. Mizutani and J. Komotori: "Improvement of Corrosion Resistance in Metallic Biomaterials by a New Electrical Grinding Technique", *Annals of the CIRP*, 2002.
- [7] E. Brinksmeier and A. Walter: "Generation of Reactionlayers on Machined Surface", *Annals of the CIRP*, 2000.
- [8] T. Inamura, G.Y. Feng, N. Takezawa and N. Mohri: "Effect of Surface Oxidation on Micromachinability of Monocrystalline Silicon", *Annals of the CIRP*, 2001.

# Analysis of Measurement Errors for Light Passing Through Parallel Layers

Y. Gao, Z. Tao

Department of Mechanical Engineering, Hong Kong University of Science and Technology, Clear Water Bay, Kowloon, Hong Kong

## Abstract

An analysis of the measurement errors for light passing through parallel layers is presented. The situation involving parallel layers is typical during an in-process measurement. Due to the effects of the parallel layers, measurement errors such as deviation of object image and multiple interface reflections are induced. Mathematical models are presented and methods to reduce such errors proposed. The results of the investigation should be useful to reduce the errors in an actual in-process measurement.

## Introduction

In a measurement system to be used for a machining process, the situation involving light passing through parallel layers is typically experienced [1]. Due to the light transmission characteristics of the parallel layers, significant amount of measurement errors could be induced. This is particularly evident when triangulation sensors are used in the system. If a measurement laser beam passes through the layers, the object image position on the sensor could deviate a significant amount, and errors in the measurement results will be generated. Therefore, it is necessary to analyze such effects on measurement results due to the parallel layers and to characterize the errors. The results of the analysis should be useful to reduce the errors in an actual in-process measurement.

## Reflections at multiple interfaces

Due to the use of multiple layers, the reflection effects of multiple interfaces are significant. In our investigation [1], the upper parallel layer is the optical window of glass, in which there are two interfaces between the glass and the adjacent materials. The upper interface is made of air and glass, where laser beam will reflect back and refract into the glass, respectively. Figure 1 illustrates the operation of a laser triangulation sensor to be utilized for in-process measurement. The position of the reflection laser beam in the detection sensor array indicates the distance that the object has moved in relation to an initial position. At the interface between the next two materials (Fig. 1), the laser beam reflects again. This will repeat until the laser beam reflects from the workpiece surface (Fig. 1).

## Deviation of object signal due to multiple parallel layers

Due to the effect of refraction [2] (Fig. 2), the sensor array will receive two laser beams,  $s_1$  and  $s_2$ . It is clear that  $s_1$  is a false signal and signals generated by the sensor array should be processed correctly to remove the light intensity signal of  $s_1$  to obtain correct measurement results, which are represented by the laser beam  $s_2$  (Fig. 2). An alternative approach is to properly adjust the design parameters of the parallel layers, such that  $s_1$  will be reflected elsewhere and will not be visible on the sensor array (Fig. 1).

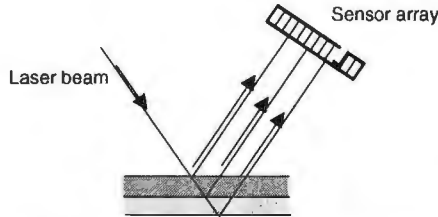


**Figure 1** Multiple reflections to the laser triangulation sensor

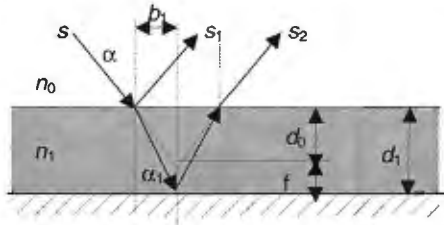


**Figure 2** Refractions due to one layer parallel to the workpiece surface

In addition, the laser beam  $s_2$  will deviate a short distance  $\Delta d$  over the sensor array.  $\Delta d$  is also indicated in Fig. 2. This is due to the refractions in the parallel layer (Fig. 2).  $\Delta d$  can be determined as:

$$\sin \alpha_1 = \frac{n_0}{n_1} \sin \alpha_0 \tag{1}$$

$$b_1 = d_0 \tan \alpha_0 = d_1 \tan \alpha_1 \tag{2}$$

$$d_0 = d_1 \frac{\tan \alpha_1}{\tan \alpha_0} \tag{3}$$

$$\Delta d = d_1 - d_0 = d_1 \left( 1 - \frac{\tan \alpha_1}{\tan \alpha_0} \right) \tag{4}$$

Equations (1-4) shows that  $\Delta d$  will be affected by the layer thickness  $d_1$ , the incidence angle  $\alpha_0$ , and the index of refraction of the layer  $n_1$ .

Figure 3 shows a typical plot of the relative light intensity signals generated in the sensor array. The results of a situation without parallel layers plotted (Fig. 3). In the case of no parallel layers, only  $s_{2n}$  will be involved (Fig. 3).

It can be seen that the object image has moved a short distance  $\Delta d$ . The deviation can be determined using Eq. (4). It is noted that due to the simultaneous development of  $s_1$  and  $s_2$ , it will be quite difficult to remove  $s_1$ , in an attempt to obtain measurement results based on  $s_2$ . However, this problem may be resolved if the layer is designed to be sufficiently thick. This is due to that if  $d_1$  is increased, the distance between  $s_1$  and  $s_2$  will be quite large. If further increased,  $s_1$  will exceed the range of the sensor

array (Fig. 1) and only  $s_2$  will be received. It is noted that, in the experiment (Fig. 3), the layer thickness  $d_1$  was 0.11mm.

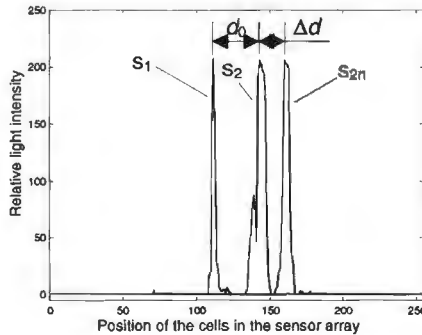


**Figure 3** Relative light intensity signals for an object with and without parallel layers

In the case of two parallel layers (Fig. 4), more interfaces will be involved. It is noted that the configuration of two parallel layers is quite frequently used for in-process optical measurement (Fig. 1).

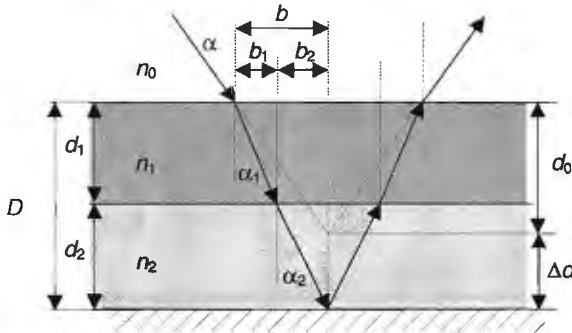


**Figure 4** Refractions due to two layers parallel to the workpiece surface  
For the light passing through two parallel layers (Fig. 4), the deviation of the object signal  $\Delta d$  can be determined as:

$$b = b_1 + b_2 = d_1 \tan \alpha_1 + d_2 \tan \alpha_2 \tag{5}$$

$$\frac{b}{d_0} = \tan \alpha_0$$

$$d_0 = \frac{b}{\tan \alpha_0} = \frac{b_1 + b_2}{\tan \alpha_0} = d_1 \frac{\tan \alpha_1}{\tan \alpha_0} + d_2 \frac{\tan \alpha_2}{\tan \alpha_0} \tag{6}$$

$$\begin{aligned} \Delta d &= D - d_0 = d_1 + d_2 - d_0 \\ &= d_1 + d_2 - \left( d_1 \frac{\tan \alpha_1}{\tan \alpha_0} + d_2 \frac{\tan \alpha_2}{\tan \alpha_0} \right) \end{aligned} \tag{7}$$

$$\begin{aligned} &= d_1 \left( 1 - \frac{\tan \alpha_1}{\tan \alpha_0} \right) + d_2 \left( 1 - \frac{\tan \alpha_2}{\tan \alpha_0} \right) \\ \Delta d &= d_1 \left( 1 - \frac{\cos \alpha_0}{\sqrt{\left( \frac{n_1}{n_0} \right)^2 - \sin^2 \alpha_0}} \right) + d_2 \left( 1 - \frac{\cos \alpha_0}{\sqrt{\left( \frac{n_2}{n_0} \right)^2 - \sin^2 \alpha_0}} \right) \end{aligned} \tag{8}$$

Due to  $n_0=1$ , Eq. (8) can be expressed as:

$$\Delta d = d_1 \left( 1 - \frac{\cos \alpha_0}{\sqrt{(n_1)^2 - \sin^2 \alpha_0}} \right) + d_2 \left( 1 - \frac{\cos \alpha_0}{\sqrt{(n_2)^2 - \sin^2 \alpha_0}} \right) \tag{9}$$

In the experiment,  $d_1=0.97\text{mm}$ ,  $d_2=0.7\text{mm}$ ,  $\alpha_0=35^\circ$ ,  $n_1=1.4470$ ,  $n_2=1.3330$ . Based on Eq. (9), therefore,  $\Delta d=0.595\text{mm}$ . It can be seen that the deviation is quite significant.

It is noted that the device should be mounted parallel to the workpiece surface, so that the layers will be parallel to the workpiece surface. If the parallelism between them is not sufficient, additional errors will be induced (Fig. 5). A typical case of the measurement error against the angle of misalignment between the layers and the workpiece surface is shown in Fig. 5.

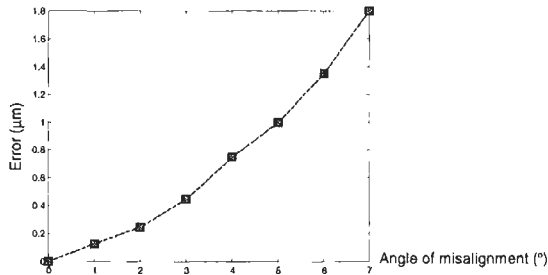


**Figure 5.** Error of measurement versus the angle of misalignment between the parallel layers and the workpiece surface

### Conclusions

In a measurement system involving light passing through multiple parallel layers, significant errors could be induced due to the deviations of the object signal. The errors are caused by the reflection and refraction at the multiple interfaces between the layers and the workpiece surface. The analysis shows that the layers should not be too thin in order to avoid reflection signals at the multiple interfaces. In addition, the parallelism between the layers and the workpiece surface should be sufficient. The analysis can be used to remove the errors in an actual in-process measurement.

### References

- [1] Gao, Y., and Tao, Z., Tests of flow patterns of grinding coolant interfered using an injection of stream, *Proc EUSPEN 2001*, 2, pp. 684-687.
- [2] Klein, M. V., and Furtak, T., *Optics*, 2e, John Wiley and Sons, New York, 1986.

## Investigation of Surface Tension at Rough Interfaces

G. P. Howell, D. G. Chetwynd

School of Engineering, University of Warwick, Coventry

### Abstract

We report on an experimental study into the forces generated at liquid-solid-air interfaces, when the surface has significant roughness. This is intended to give greater understanding of how surface wetting might be influenced by roughness, a question of importance in fields such as microfluidics. Forces were measured while immersing and withdrawing thin flat glass plates into clean water – a test-geometry relatively simple to analyse. Roughness appears to have a small but measurable influence on the attractive force at the meniscus. It also introduces a ‘memory’ of previous immersions that affects the wetting properties.

### Introduction – surface tension and roughness

The continual push towards miniaturisation in precision engineering introduces a new class of systems that may be affected by surface tension, e.g. small mechanical dampers and micro-fluidic delivery systems. The role of static and, for non-stationary systems, dynamic surface tension is of great interest. Since surface roughness becomes proportionately larger as feature sizes reduce, there is a growing need to assess the practical implications of surface heterogeneity.

The three-phase interface between air, a liquid and a smooth solid surface experiences a force of which the most familiar manifestations are the meniscus and capillary lift. The interactions at a classical interface have been studied since the work of Gibbs [1]. When solids, liquids and gases come into contact, the liquid and gases align to produce the lowest free energy state for the system [2]. The contact angle of the interface depends on the kinetics of the system. The models for capillary systems usually assume that the substrate is smooth, flat, rigid and chemically heterogeneous. Proposed modifications to Young’s law to compensate for such inhomogeneities [2, 3] require exact knowledge of surface composition. More sophisticated models [4] provide useful insight, but still are reliant on assumptions of surface conditions. At some reduced scale, the assumption that roughness is negligible must start to break down; present models poorly predict the behaviour of the contact line for real engineering surfaces.

The interface force depends directly on the liquid surface tension, the length of the interface and the contact angle of the liquid to the solid. The latter depends on chemical affinity, including that due to cleanliness. If the interface is not a straight line, the local force at each infinitesimal segment along it will be added vectorially. If a rough surface is approximated as consisting of small facets, we might expect a consistent contact angle on each and so local variations in the component of force parallel to the solid surface. Since the average slope must be zero, the integrated surface tension effect might be closely the same as that for a smooth surface. A similar, perhaps weaker, argument can be applied to the roughness-induced changes to the edge as seen in a plan view of the surface. In practice, established interface edges tend to be quite stable, with significant forces being required to move them along the solid surface. Similar behaviour on the micro-scale might confound the simple arguments used above. Hence, experimental work has been undertaken to investigate how roughness affects wetting behaviour and surface tension, using



smooth and deliberately roughened surfaces in contact with deionised water. Such information will aid the generation of empirical and theoretical models.

## Experimental method

Some earlier feasibility tests suggested that roughness typical of that on machined surfaces has some affect on tension forces. Consequently, a special test-rig has been set up by modifying a small vertical tensile and compressive testing machine. It is based conceptually on the Wilhelmy plate method for measuring surface tension [2] and is shown in Figure 1. A small beaker of de-ionised water (from a Purite water purification system) is moved vertically on the lower jaw of a Hounsfield vertical testing machine. The test specimen, a thin rectangular glass plate of dimension 70 mm wide, 20 mm height and 2 mm thick, hangs from a high-sensitivity load-cell. The load cell is a specially designed, using two acrylic beams (Perspex), loaded centrally and bonded together at both ends with a small gap between them. The displacement of the beams is measured by capacitive micrometry with a Queensgate NanoSensor detector, to give an accuracy to 20  $\mu\text{N}$ . As the beaker is raised the specimen becomes partially immersed. The sample's apparent weight will be modified by a buoyancy effect and by surface tension along the interface. The interface is nominally straight and, compared to other potential error sources, constant in length. The edges contribute very little compared to the faces, so changes to roughness on the faces should directly indicate the strength of roughness-related effects. The net variation of force from that of the free-hanging weight is, to a reasonable approximation,

$$F = 2\sigma_l \cos \alpha_l \pm \Delta\rho Vg \quad (1)$$

where  $\sigma_l$ ,  $\alpha_l$ ,  $\Delta\rho$ ,  $V$  and  $g$  are the liquid surface tension, contact angle, difference in density of the liquid and solid, the immersed volume and gravitational acceleration.

The force exerted on the specimen plate is measured directly, since this parameter governs many applications. Continuously measuring the forces at different depths while the plate is dipped and then withdrawn allows separation of the tension and buoyancy forces. The testing machine controller governs speed and depth of immersion to a precision of 1  $\mu\text{m}$ . The surface roughness was modified on only one side of the plate, so as to maintain a control surface. The roughness was produced by rubbing with various grades of abrasive paper, which produced four bands of roughness which varied between 0.1  $\mu\text{m}$  Ra (mean roughness) and 1.2  $\mu\text{m}$  Ra measured on an interferometric microscope (WYKO) and also on a Form Talysurf (Taylor Hobson).

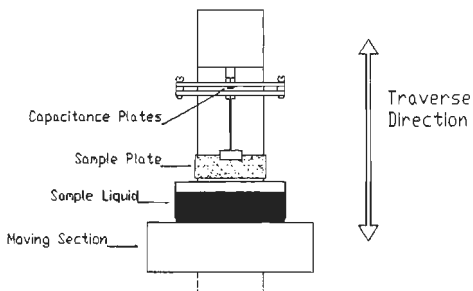


**Fig. 1:** Schematic of test rig, showing the sample position and the load cell.

## Results

Figure 2 shows some typical results of immersion tests. The free hanging weight is set to zero. The water captures the plate and there is an initial jump in the force on the plate, followed by a linear drop off in the load as the buoyancy force increases. Then, on reversal, the load increases at a slightly higher rate as the plate emerges. The load continues to increase as the plate draws liquid above the initial level. After initial contact the load tends to increase slightly before it starts to drop off.

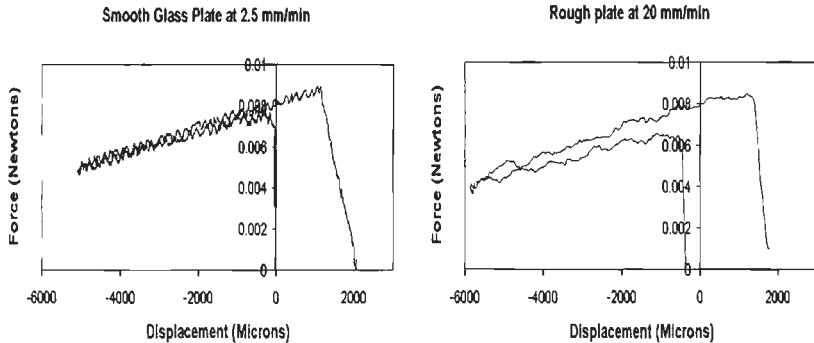


**Fig. 2:** Typical load displacement graphs. Left: a smooth clean plate on the first dip. Right: one of the roughest plates on first dip.

The increase following initial capture is seen most clearly on the dry plates immersed at slower rates. This curvature is much less on plates that have been previously dipped and re-immersed after a delay of approximately 20 s. It may be that a liquid film retention mechanism on the surface encourages a more stable contact line. On rough plates, the force-immersion curves are different, with larger displacements in the data. As illustrated in figure 2, this displacement is larger still at higher speeds. The cause probably lies with changes in the dynamic contact angle as it dips in and pulls out of the liquid.

With smooth clean glass dipped at a rate of 2.5 mm/min the average capture force was 7.81 mN, with a standard deviation of 0.24 mN. The fracture force was 9.1 mN, giving a difference from capture of around 1.31 mN with a standard deviation of 0.15 mN. With the roughest surfaces (around 1  $\mu\text{m}$  Ra) at the same rate, the capture and fracture loads were 7.6 to 8.8 mN, with standard deviations of 0.3 mN and 0.2 mN respectively, a difference of 1.10 mN. A second dipping of the smooth plate, produced capture and fracture forces of 7.9 mN and 9.3 mN. Although only of the order of the standard deviation, the small increase in force appears consistently. At a speed of 20 mm/min, the capture and fracture forces on smooth glass were respectively, 6.7 mN and 8.5 mN on dry glass and 7.2 mN and 8.5 mN on previously dipped. Similarly, the rough glass on a second dipping produced forces of 7.8 mN

and 9.2 mN at 2.5 mm/min and 6.9 mN and 8.2 mN at 20 mm/min. The considerable differences are probably reflecting the increasing inertial distortion at the contact line and also greater entrainment of liquid in the roughness.

The effect of surface roughness can be readily seen when plates are dipped into the liquid. The contact line is uneven and has a tendency to stick and then to release as it moves up the plate. This is reflected in the second graph of figure 2, which has larger force swings. On repeat dipping the contact line tends to be level and closer in shape to that of the smooth plates.

The likely explanation for these effects is that at low levels of surface roughness, i.e. the smooth plate, the shifts in contact angle are slight and do, to a large extent, average out along the perimeter. On rougher surfaces, a larger number of contact angle states exist which average out less completely and reduce the vertical force on the plate. On a second dipping, retained water on the surface acts as a pre-layer, and the contact line then rides along on top of the liquid layer which sits within the valleys on the surface, negating some of the effects of the roughness.

## Conclusions

While there is insufficient measurement data to provide high statistical significance, evidence is building up that surface roughness of below 1 micron Ra, can affect the value of the surface tension force. The effect is greater at increased dipping speed, probably because the dynamics at the contact edge lead to contact angle hysteresis, although viscous drag cannot yet be ruled out. Variations are less marked on repeat measurements of previous dipped plates, possibly due to liquid retention on the surface. The effect of surface roughness on the measured surface tension value is subtle, but appears to be at a level that could be significant in microsystems. Further work, will examine the effect of roughness on partially-wetting and non-wetting systems with different liquids and specimen materials. Incorporation of a power spectral model of surface roughness with contact angle behaviour could also provide valuable insight.

## References

- [1] Gibbs, J. W., 1878, "Equilibrium of Heterogeneous Substances", Amer. Jour. Sci. series 3, Vol. xvi, p. 441-458, taken from "The Collected Works of J. Willard Gibbs", Vol.1 Thermodynamics, Yale University Press, 1948
- [2] Adamson, A. W., "Physical Chemistry of Surfaces", 5<sup>th</sup> ed., Wiley, 1990.
- [3] Wenzel, R. N., 1936, Ind. Eng. Chem, Vol: 28, p. 988, taken from Neumann, A. W., "Applied Surface Thermodynamics", Surface Science Series, New York, 1996
- [4] Cassie, A. B. D., Baxter, S., 1944, Trans. Faraday Soc, Vol: 40, p. 546, taken from Neuman, A. W., "Applied Surface Thermodynamics", Surface Science Series, New York, 1996
- [5] Lin, F. Y. H., Li, D., Neumann, A. W., "Effect of Surface Roughness on the Dependence of Contact Angles on the Drop Size", J. Colloid and Interface Science, Vol: 159, p. 86-95, 1993.

## **Micro-factors affecting macro-parameters: the foil rolling case**

D. Antonelli

Politecnico di Torino, ITALY

### **Abstract:**

The paper addresses a common though underestimated issue of several metalworking processes during the setting of operating parameters. Some factors acting on a microscopic scale influence significantly the results of the overall process although the latter are developing on a quite larger scale.

The author analyses a method for the assessment of process parameters by the Finite Element (FE) simulation in order to deal with multi-scale problems. The method is presented and discussed in the case of the thin foil rolling process.

### **Micro-factors influence on the global process**

Among the numerous examples of micro-factors whose effect is experienced by the overall process, it is worth quoting the development of damages inside the material, the lubrication of the die-workpiece interface, the elastic deformation of the die due to contact pressure or local thermal changes, local changes in material flow speed.

Without claiming to accomplish a classification among factors related to such different fields as tribology or fracture mechanics, it is important to distinguish the factors among those having only a local effect on the process and those influencing the process in a widespread way. One can model the material damage with a continuous approach applied to a meso-domain including a large number of microvoids but small enough for the stress state to be considered homogeneous [1]. Conversely the elastic deformation of a limited die area is able to change the flow of the material with effects on the producibility or, at least, on the dimensional accuracy of the part. Either material damaging or interface friction have been introduced in the equations of continuum mechanics used in solving metalworking problems by means of continuum variables. Nevertheless there are factors that cannot be averaged without losing the capability of describing their effects on the production process. They must be studied in their own scale regardless of the overall dimensions of the problem. A factor is the local deformation of the die, another one is the local heating or cooling of the die or of the workpiece.

When the process is dimensioned using FE simulation, the mechanical problems are solved by replacing the equilibrium equations with the weak formulation of virtual work statement. It is easy to fall into the known inconvenient of having a system globally in equilibrium despite high local errors on single elements. This easily happens when different element sizes are used together, as in the simulation of many metalworking processes.

To describe adequately local phenomena a very fine mesh is required. Elements must have dimensions many orders of magnitude smaller than the problem scale. In a linear domain the solution is in submodeling. Submodeling is a technique by which a local zone of the model is analyzed using a refined mesh with boundary conditions obtained by interpolating the solution from a global model. The detailed modeling of

that region should have negligible effects on the overall solution which does not happen in the examined case study.

Present study proposes a method to execute an effective FE simulation of foil rolling by splitting it in different simulations for each scale/dimensional level. The method consists in extending submodeling to different solution techniques in the nonlinear domain. The solution of small scale problems is found by FE and applied to numerical model of the mill using the influence coefficient matrices [2]. It is therefore possible to deal at the same time with large displacements ( $>1\text{mm}$ ) and small ones ( $<1\mu\text{m}$ ) without numerical conditioning errors. To reduce the mesh dimension, FE model makes use of rigid dies on which a thin skin of deformable elements is glued.

### The foil rolling process

In order to better discuss the implications of the presented issues for multi-scale problems, a case study is analyzed. The process studied here is the flat rolling of thin metal foils. In the standard industrial setup the two work rolls are supported by two large-size backup rolls. Each roll deflects due to the rolling force. Roll surface flattens because of the rolling pressure distribution. The combination of these effects produces a non-uniform strip thickness across strip width [3] (named crown). Many crown control schemes are used: roll camber, roll benders, thermal control devices. Strongly nonlinear roll flattening is apparent along the rolling direction during foil rolling [4, 5] and it is responsible for the great deviation of the experimental force and torque from the theoretic values.

The typical industrial problem is the dimensioning of the roll pass schedule, in terms of separating force, rolling torque and production per hour. Another problem is the setup of the parameters for the run time crown control devices. The two problems usually accept an uncoupled solution. Foil rolling is characterized by large changes of the separating force in the transversal section because the foil naturally opposes to crowning by means of a natural feedback mechanism. Therefore the solution scheme must be coupled.

The process is characterized by large overall dimensions: work rolls are two meters long, 250mm diameter, backup rolls are 900mm diameter, the coil width rang between 800 and 1700mm. Sheet thickness start from 10mm to reach as a foil  $10\mu\text{m}$  thickness or less. The contact length between roll and strip is of the order of a few millimeters with a non-circular profile because of roll flattening ( $10\text{-}40\mu\text{m}$ ).

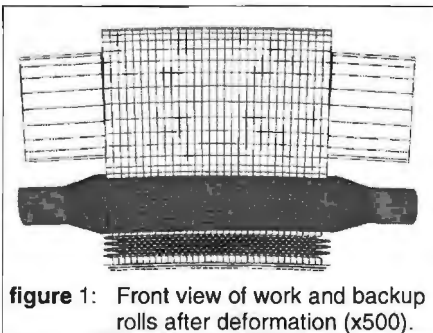


**figure 1:** Front view of work and backup rolls after deformation (x500).

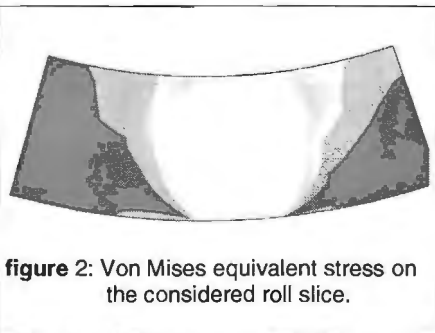


**figure 2:** Von Mises equivalent stress on the considered roll slice.

There are several feedback effects between microscopic behavior of the contact zone and macroscopic roll deflection. Deviations of the foil exit profile from the inward

profile produce locally a large change in the exit tension and in the separating force which conversely change the roll transversal flattening. The feedback has a positive effect in the sense of the reduction of the amount of crown.

A simulation with FE requires a 3D model of the mill (see figure 1). Element size should be small enough to have more than 10 elements along the contact length which under some rolling passes can be only 1mm long [6]. To simulate the entire mill about 50mm elements are advisable. The difference in dimensions among these elements make the simulation model greatly unreliable.

The followed approach consists in a 2D FE simulation of the rolling process in the rolling direction. Because the roll diameter is much larger than the foil thickness the roll is considered rigid and a small deformable skin is applied on the outer surface. The skin thickness is enough to allow a nearly full development of the elastic stress state inside the roll, as can be seen in figure 2. The model of roll-foil interface lubrication is analytical because it involves considerations on a very small scale [7]. The simulation is executed repeatedly for every different gauge and tension encountered along the foil section.

The exit profile and the effect of bending corrections is simulated with 3D FE as far as the sheet thickness is above the millimeter, giving the results reported in figure 3. Reducing the thickness a modified numerical solution scheme has been applied combining the influence coefficient matrix method for the mechanical crown and the heat balance integral method for the thermal crown [8, 9]. The roll flattening is obtained by the former mentioned 2D longitudinal simulation. The combination of FE simulations and numerical solution schemes gives the result plotted in figure 4.

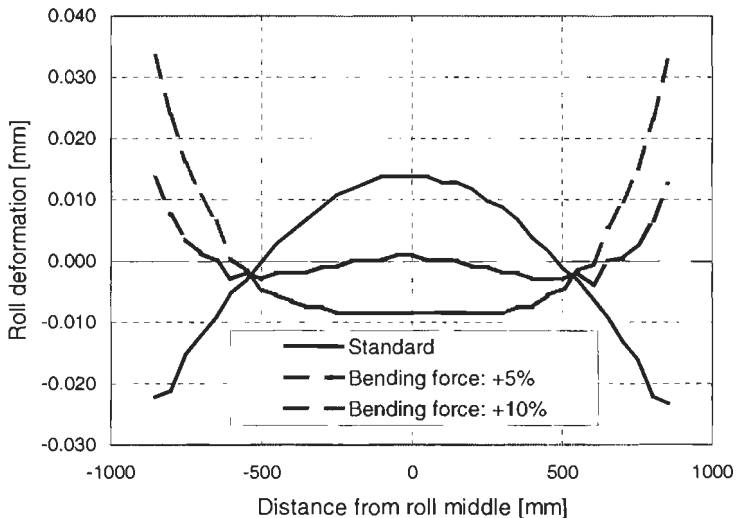


**figure 3:** The deformed longitudinal profile of the coil in a sheet rolling pass (3mm exit gauge). Bending forces are a percentage of the separating force.

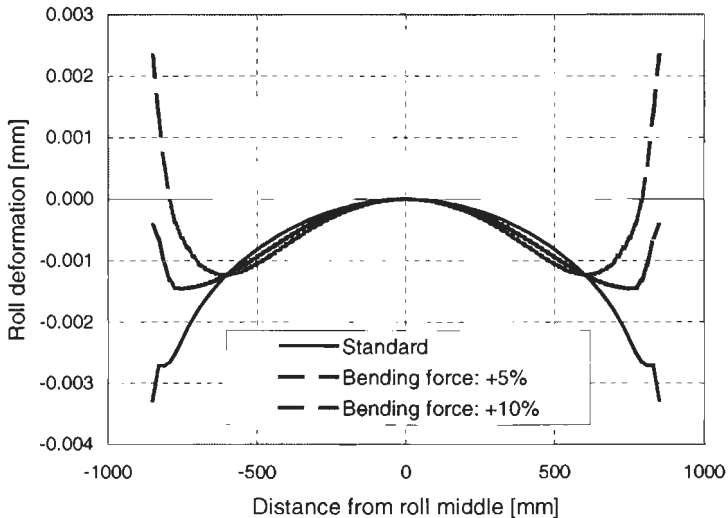


**figure 4:** The deformed longitudinal profile of the coil in a foil rolling pass (20 $\mu$ m exit gauge). Bending forces are a percentage of the separating force.

Therefore a advisable way to deal with phenomena developing on different scales is a combination of 2D, 3D FE simulations with numerical-analytical solution figures. The latter must be used every time different dimensional values must be combined.

## References

1. Skrzypek J., Ganczarski A., "Modeling of Material Damage and Failure of Structures: theory and applications", Foundations of engineering mechanics, Springer-Verlag, Berlin, 1999.
2. R.-M. Guo, Prediction of strip profile in rolling process using influence coefficients and Boussinesq's Equations, Transactions of the ASME, Vol.119, pp.220-226, May 1997.
3. H.W. O'Connor, A.S. Weinstein, Shape and flatness in thin strip rolling, Journal of Engineering for Industry, pp.1113-1123, November 1972.
4. Fleck N. A., Johnson K. L., Mear M.E., Zhang L.C. "Cold rolling of foil", Proc. Instn. Mech. Engrs. , vol. 206, 1992.
5. Grimble M. J., Fuller M.A., Bryant G.F., "A non-circular arc roll force model for cold rolling", Int. J. for Numerical Methods in Engineering, pp. 643-663, vol. 12/1978.
6. Gratcos P., et al., "A plane-strain elastoplastic finite-element model for cold rolling of thin strip", Int. J. Mech. Sci., pp. 195-210, Vol.20/1992.
7. Marsault Nicolas, et al., "A model of mixed lubrication for cold rolling of strip", Simulation of Materials processing: Theory , Methods and Applications, NUMIFORM 1998, Balkema, Rotterdam, pp715-720, 1998.
8. R.-M. Guo, Computer model simulation of strip crown and shape control, Iron and Steel Engineering, pp.35-42, November 1986.
9. R.B. Cresdee, W.J. Edwards, P.J. Thomas, An advanced model for flatness and profile prediction in hot rolling, Iron and Steel Engineering, October 1991.

## Characterisation of engineered surfaces by a multi-function tribological probe microscope

X. Liu, T. Bell\*, F. Gao, and D. G. Chetwynd

Centre for Nanotechnology and Microengineering, School of Engineering,  
University of Warwick, COVENTRY CV4 7AL, UK

\*School of Metallurgy and Materials, University of Birmingham, Edgbaston,  
Birmingham B15 2TT, UK

### Abstract

This paper reports some preliminary results on characterisation of engineered surfaces by a novel multi-function Tribological Probe Microscope (TPM) at the micro and nanometre level. The TPM is capable of measuring four functions, topography, friction, Young's modulus and hardness, of a surface in a single scan. The four measured functions can be linked in space and in time, which enables us to determine whether a surface treatment is effective in influencing its mechanical or tribological properties or how local surface features affect these properties. Evaluations have been carried out on some specially prepared engineered surfaces such as Ti-6Al-4V, UHMWPE and austenitic stainless steel 316.

### Introduction

It has been widely recognised that surface and subsurface properties at the submicrometre scale will critically influence the design of future generations of components used in engineering, bioengineering and nanotechnology. Most materials exhibit different properties from those expected of the bulk materials at light loads. The contact mechanism and the effect of surface finish are reasonably well understood at a macroscopic level by empirical and statistical methods. However, at the sub-micrometre level, it is still not clear what is really taking place on the surface during the contact nor how the local surface geometry affects its mechanical and tribological properties. At the microscopic level where modified surface layers or coated films are fraction of a micrometre, the local properties and their correlation are important in determining the surface function and performance. At present, engineered surfaces or function orientated surfaces are produced by trial and error and there is no quantified approach to link them. At Warwick University we have developed a novel measurement system, the multi-functional Tribological Probe Microscope (TPM) [1], to provide the measurement of surface topography, Young's modulus, hardness and friction at the micro and nanometre scale.

Engineered surfaces such as plasma immersion ion implanted ultra high molecular weight polyethylene (UHMWPE), rutile surface modified titanium-aluminium-vanadium (Ti-6Al-4V) and austenitic stainless steels (AISI 316) are widely used in automotive engineering and bioengineering industries. This paper will present some preliminary results of multi-function evaluation of some engineered surfaces specially prepared by Birmingham University. Such directly correlated measurements will help to identify the critical surface features for a particular function which, in turn, will guide the optimisation of the surface formation processes used.



## The TPM system

Fig. 1 shows a photograph of the mechanical system of the TPM. It consists of a sensor probe attached to a z-positioner, which can be coarsely adjusted by three micrometers, an x-y stage and an electronic drive and control system. The essential part of the TPM is the sensor probe, which has a magnet/coil force actuator and two precision capacitive sensors for measuring surface height/deformation and frictional force between the probe tip and the surface being scanned.

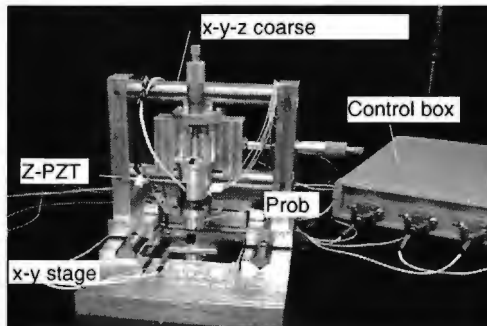


Fig. 1 Photograph of the TPM mechanical system.

The specifications of the TPM are:

Scan area:  $100 \times 100 \mu\text{m}$  with the position feedback to give a linearity of 0.02%.

Force range: 0.01 ~ 30 mN.

Height range:  $15 \mu\text{m}$  with a resolution of 0.1 nm.

Tip size: Berkovich diamond tip with a radius of  $0.1 \mu\text{m}$ .

Other specifications and details of the instrumentation and calibration can be found in reference [2].

The measurement of the four functions of a surface, that is topography, frictional force, Young's modulus, and nano-hardness, is achieved by operating the TPM in two scanning modes; the normal scanning mode and the force ramping mode. At each surface point, the TPM measures the surface height first in the normal scanning mode then switches to the ramping mode to increase the contact force to a preset value and decrease it again, while the deformation/penetration is measured. Then the TPM moves to next surface point and at the same time measures the frictional force. The process then repeats itself. At the end of scanning, four sets of data representing surface topograph, friction, Young's modulus and nanohardness are available for 2-D and 3-D displays. Because these functions are measured point-by-point in one scan, they are dynamically correlated in space and time (to a sub-second interval). The hardness is expressed as the load divided by the contact area. In our case, the load and deformation are continuously monitored, the hardness  $H$  is determined by the maximum load  $P_{max}$  divided by the projected area  $A_c$  that is related to the contact depth  $h_c$  [3]. The Young's modulus is derived from the initial slope of the unloading curve called 'stiffness' because the initial unloading is an elastic nature.

## Measurements

Measurements were carried out on four specially prepared specimens. These are austenitic stainless steel plasma nitrided at a temperature  $425^\circ$  for 12 hours, rutile ( $\text{TiO}_2$ ) treated Ti-6Al-4V, plasma immersion ion implanted UHMWPE and untreated UHMWPE. Here the surface topography, Young's modulus and hardness mappings are of most concern. Before carrying out the multi-function measurements, the preset loading force for each specimen needs to be determined. In general, we run a series of individual indentation tests to see the level of deformation being made and then decide the preset loading force. Fig. 2 shows a typical series of indentation curves

made on treated UHMWPE specimen. Fig 3 shows the comparison of the measured hardness between the treated and untreated UHMWPE specimens. The results show that the hardness values are much lower at a very light loading, which indicates that there may be a contamination layer formed on the specimens as there was no cleaning involved. All specimens were measured as they were delivered. It can be seen from Fig. 3 that the hardness of the treated UHMWPE is higher than the untreated one. For Young's modulus there is a similar trend with an average  $E=0.35$  GPa for the treated and 0.25 GPa for the non-treated UHMWPE.

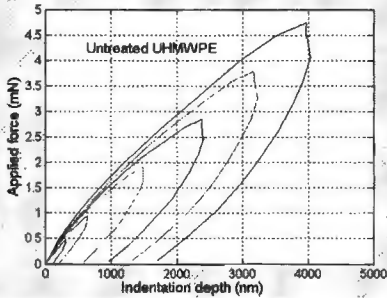


Fig. 2 A series of indentation made on treated UHMWPE.

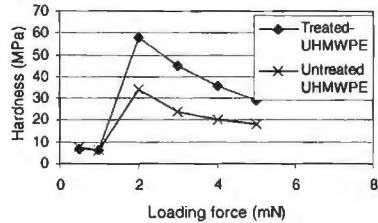


Fig. 3 Comparison between treated and untreated UHMWPE specimens.

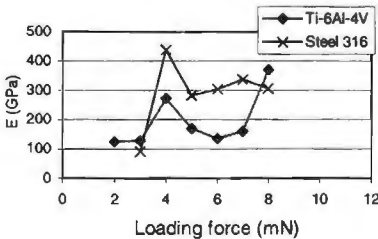


Fig. 4(a) Comparison of Young's modulus.

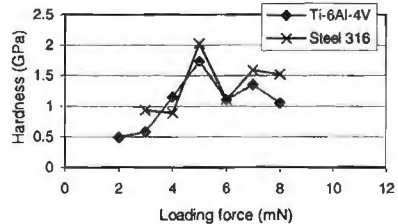
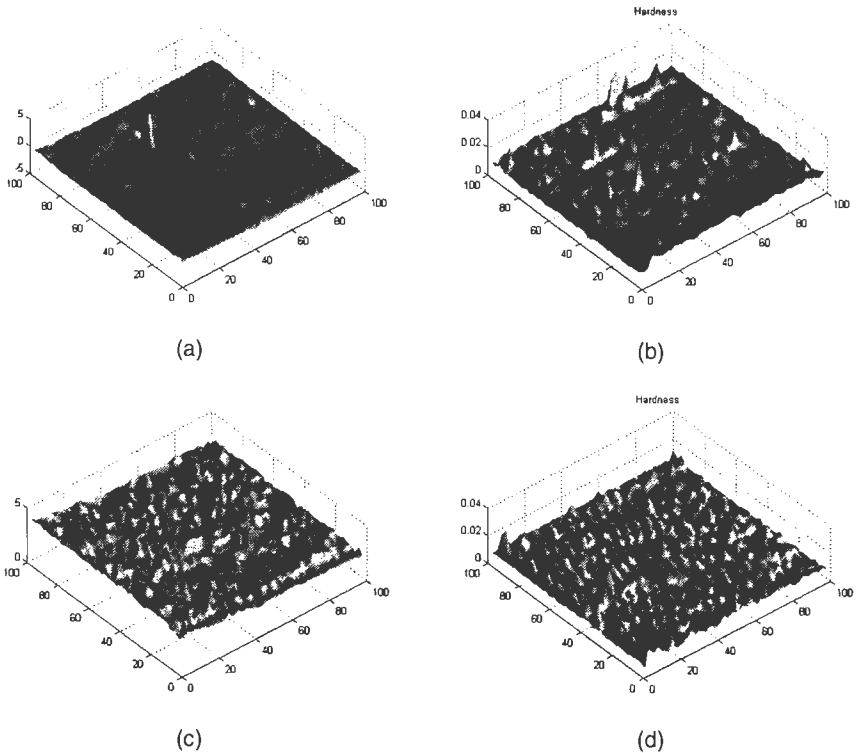


Fig. 4(b) Comparison of hardness.

Indentation results on the other two specimens under different loading force are shown in Fig. 4 (a, b). The hardness values for both materials are very similar but there is a difference in the elastic modulus where the austenitic stainless steel is generally higher than Ti-6Al-4V. Again the lower values at small loading force may be caused by some contamination or other surface effects on the specimens.

In multi-function measurement, the scanning force for topography measurement was kept at about 0.05 mN, the ramping was 4mN for Ti-6Al-4V and austenitic stainless steel, and 3 mN for both UHMWPE specimens. Due to a limited space, only topography and hardness mappings for two specimens are shown in Fig. 5 for comparison. The results show that the treated UHMWPE has a much smoother surface topography than the untreated one. The surface roughness is 124 nm for the untreated and 89.6 nm for the treated surface. The roughness values for other specimens are 265 nm for Ti-6Al-4V and 118 nm for austenitic stainless steel.



**Fig. 5** Mappings of surface topography and surface hardness for treated and untreated UHMWPE specimens: (a) topography for the treated, (b) hardness for the treated, (c) topography for the untreated and (d) hardness for the untreated UHMWPE. The units in x and y axes are  $\mu\text{m}$  and in z axis is GPa.

## Conclusions

We have demonstrated the power of the multi-function tribological probe microscope for characterising certain properties of engineered surfaces at the micro-nanometre scales. Surface or contaminant effects at low loadings are still being investigated.

## References

- [1] Liu X., Nanotribological Probe Microscope, WO99/45361, 19 Sept. 1999.
- [2] Gao F. and Liu X., Development of a new multi-function tribological probe microscope, 1<sup>st</sup> **euspen** Topical Conference on Fabrication and Metrology in Nanotechnology, Copenhagen, Denmark, 30 May 2000. Vol. 1. pp52-62.
- [3] Oliver W. C. and Pharr G. M., An improved technique for determining hardness and elastic modulus using load and displacement sensing indentation experiments, *J. Mater. Res.*, **7** (6) 1564-1583, 1992.

## Investigation of indentation properties of poly(pyrrole) thin films

Q. Fang\*, F. Gao, X. Liu, D.G. Chetwynd and J.W. Gardner

The Centre for Nanotechnology & Microengineering, School of Engineering,  
University of Warwick, Coventry CV4 7AL, UK

### Abstract:

We report here on a new investigation of poly(pyrrole) films prepared by electrochemical deposition and characterised by use of our newly developed multi-function tribological probe microscope (TPM). This TPM is capable of measuring directly surface topography, friction, Young's modulus and nanohardness in a single scan measurement. Poly(pyrrole) with two dopants, methylphosphonic acid (MPA) and 1-butanepulphonic acid (BSA) films were deposited electrochemically with a thickness between 100nm and 2000nm. The mechanical properties of the PPY thin films have been investigated by the TPM and a commercial nano-scratch tester (NST). The measurement results show that the mechanical properties such as tensile stress, Young's modulus and hardness of PPY thin films depend strongly upon the thickness of the film and the dopants in the polymers.

### Introduction

Conductive polymers have attracted a lot of interest in a wide range of applications from electronic displays and solar cells to sensors and actuators in microengineering and nanotechnology due to their extremely small size, ease of fabrication and low cost. This has led to some serious attempts at exploiting their potential for mechanical and tribological applications. Poly(pyrrole) is one of the most promising candidates for use as an active component in many technological applications such as light emitting diodes (LEDs), solar cells, sensors and actuators. The microstructures and mechanical properties of conducting polymers are critically important for many of their applications. We have previously investigated the friction and tensile strength of polypyrrole film, which has been claimed to be one of the most stable conductive polymers. There is strong evidence that the film morphology and film thickness play an important role in their mechanical and tribological properties [1,2].

The hardness is expressed as the load divided by the contact area. In conventional indentation hardness test, the contact area is determined by measuring the indentation size by an optical microscope after the sample is unloaded. More recently, in depth sensitive indentation tests where the load and deformation are continuously monitored, the hardness  $H$  is determined by the maximum load  $P_{max}$  divided by the projected area  $A_c$  that is related to the contact depth  $h_c$ . The Young's modulus is derived from the initial slope of the unloading curve called stiffness because the initial unloading is elastic in nature. The indenter used in our Tribological Probe Microscope (TPM) [3] is a Berkovich diamond tip with a nominal radius of 100nm and 142° included angle. Table 1 shows the formulas used in calculation of

---

\* Q. Fang is now working at Dept. of Electronic and Electrical Engineering, University College London, Torrington Place, London WC1E 7JE. E-mail: q.fang@ee.ucl.ac.uk

the hardness and the reduced Young's modulus  $E_r$ . Due to the fact that  $E_{tip}=1140\text{GPa}$ ,  $\nu_{tip}=0.07$ , the difference between  $E_r$  and  $E_{sample}$  will be very small for most materials. Thus the reduced Young's modulus is presented here.

**Table 1** Details of formulas used in the calculation of hardness and elastic modulus.

Hardness	$H = \frac{P_{max}}{A_c}$	where $A_c = 25.4h_c$
Young's modulus	$E_r = \frac{\sqrt{\pi} S}{2 \sqrt{A_c}}$ and $\frac{1 - \nu_{sample}^2}{E_{sample}} = \frac{1}{E_r} - \frac{1 - \nu_{tip}^2}{E_{tip}}$	$S = \frac{dP}{dh} \Big _{P_{max}}$ $h_c = h_{max} - 0.75 \frac{P_{max}}{S}$

## Experimentation

Poly(pyrrrole) (PPY) thin films were deposited by electrochemical methods under an electrical potential of 0.85V. Two substrates (Si-wafer and glass), which were coated with about 20 nm of gold, were employed as working electrodes in a standard three-electrode electrochemical cell. Poly(pyrrrole) (PPY) coatings were electro-polymerised onto the substrates. Freshly distilled and filtered pyrrole monomer was dissolved in the solvent along with an appropriate counter-ion. Two types of poly(pyrrrole) films were obtained, doped by methylphosphonic acid (MPA) and 1-butanedisulphonic acid (BSA). All polymerisations were carried out in nitrogen atmosphere and at an ambient temperature of  $20 \pm 1^\circ\text{C}$ .

Chemical composition, morphological and micro-structural properties of the deposited conducting polymers were characterised by FTIR, SEM, scanning white light interferometry (WYKO NT2000) and optical microscopy.

Fig.1a shows a typical surface morphology of deposited poly(pyrrrole) film grown on gold-coated Si-wafer(100) with MPA electrolytes with a thickness of  $0.45 \mu\text{m}$ , while Fig.1b is a PPY-BSA film with a thickness of  $0.45 \mu\text{m}$ . Clearly, the surface of PPY-MPA is much smoother than that of PPY-BSA. The averaged surface roughness values of PPY(MPA) and PPY(BSA) films measured by WYKO are listed in Table 2.

**Table 2.** Average surface roughnesses of PPY(MPS) and PPY(BSA) with different deposition time

Sample number	Deposition time (s)	Average roughness (nm)
PPY-MPA-30	30	2.70
PPY-MPA-60	60	18.19
PPY-BSA-30	30	28.12
PPY-BSA-60	60	106.35

Fig.2 shows a relationship between electronic charge  $Q(\text{C})$  and deposition time for both PPY-BSA and PPY-MPA. Clearly, the deposition rate of PPY-MPA is much lower than that of PPY-BSA. However, The deposition rate of PPY-MPA remains constant up to 240 s, while that of PPY-BSA slows down after 100 s. It may give rise to the difference in microstructures between two types of PPY films.



**Fig. 1a** Surface morphology of PPY-MPA film with a thickness of 0.45  $\mu\text{m}$ .

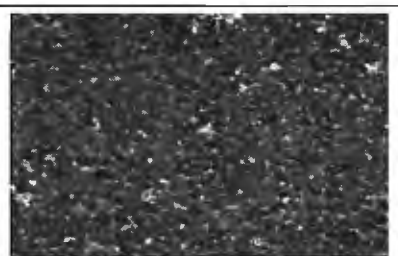


**Fig. 1b** Surface morphology of PPY-BSA film with a thickness of 0.45  $\mu\text{m}$ .

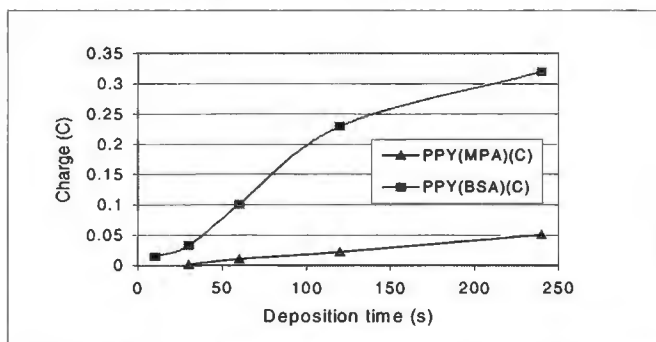


**Fig. 2** The electrochemical deposition of PPY-MPA and PPY-BSA.

## Results and discussion

A commercial nano-scratch tester (NST) [4] from CSEM Instruments was used to test for coating rupture, which is very different for the PPY thin film and pure gold-coatings. The polymer shows a total delamination at a weak critical load of 1.36 mN. The test showed a clear step corresponding to coating rupture for the PPY sample. SEM of a typical coating rupture and delamination for a PPY-MPA film is shown in Fig.3. However, for the pure gold coating, the delamination is progressive and takes place at greater critical loads (26 mN). The first cracking appears inside the scratches, followed by rupture and cracking outside the scratches. The nano-scratch tests reveal that delamination of PPY film and gold-coating co-exists and it is necessary to further improve the adhesion of both PPY films and the gold-coating.

Indentation tests were carried out by TPM. The contact force at the tip of the TPM is controlled by a magnet/coil force actuator, which applies a constant force in a range of 0.01-25 mN. The topography measurement has a height range of 15  $\mu\text{m}$  with a resolution of 0.1 nm. The 100  $\mu\text{m}$  by 100  $\mu\text{m}$  scanning area is closed loop controlled with an accuracy of 1 nm. At each of the surface points, the TPM measures the surface height first and then switches to its force ramping mode to increase force to a preset value and decrease it again while the deformation/penetration is measured. The choice of the preset indentation loading force is critical – if too high the indenter will penetrate through the film into the substrate material. Based on the scratch tests

by NST, a maximum force of 0.3 mN was chosen for PPY films. The measured results, Table 3, show that the mechanical properties of thinner films are better than those of thicker ones. Also, PPY-MPA films perform better than PPY-BSA films. Fig. 4 shows two typical force-deformation curves of both PPY-MPA and PPY-BSA films with the same thickness.

**Table 3.** Measurements of PPY films by TPM under a ramping force of 0.3 mN.

Samples	Deposition time (s)	Young's modulus (GPa)	Hardness (GPa)
PPY-MPA-30	30	37.3	2.1
PPY-MPA-60	60	31.7	1.0
PPY-BSA-30	30	9.1	0.72
PPY-BSA-60	60	8.2	0.60

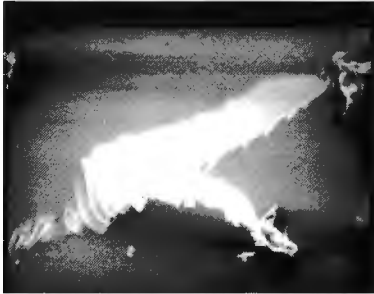


**Fig. 3** SEM micrograph of a typical coating rupture after a scratch test.

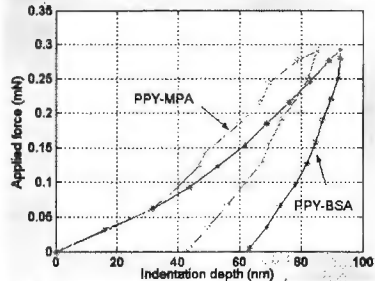


**Fig. 4** Two typical indentation curves on both PPY-MPA and PPY-BSA films. Units are nm in x-axis and mN in y-axis.

## Conclusions

We have demonstrated a new way to evaluate the mechanical properties of conductive polymers using the TPM. Further insights into PPY growth and performance are undertaken to obtain more data to confirm observed trends.

## References

- [1] X.Liu, D.G. Chetwynd, J.W. Gardner P.N. Bartlett, C. Beriet, *Tribology International*, 31(6) (1998)313-323.
- [2] Q. Fang, D.G. Chetwynd, J.W. Gardner, "Tensile Properties of Conducting Polymer Fibres " Proc. of 2<sup>nd</sup> euspen International Conference, Turin, Italy, 2001 May.
- [3] Gao F. and Liu X., Development of a new multi-function tribological probe microscope, presented at 1<sup>st</sup> euspen Topical Conference on Fabrication and Metrology in Nanotechnology, Copenhagen, Demark, 28-30 May 2000. Vol. 1. pp52-62.
- [4] R. Consiglio, N. X. Randall, B. Bellatona and J. von Stebutb, "The nano-scratch tester (NST) as a new tool for assessing the strength of ultrathin hard coatings and the mar resistance of polymer films", *Thin Solid Films*, 332, (1-2)(1998) 151-156.

## Sensors





## An in-process micro-sensor for ultraprecision machining

H. Hashizume<sup>1</sup>, H. Yoshioka<sup>1</sup>, H. Shinno<sup>1</sup>

<sup>1</sup> Tokyo Institute of Technology, Tokyo, Japan

### Abstract

The successful implementation of intelligent and ultraprecision machining systems requires in-process monitoring function of a machining environment. To meet the requirements, the sensor which has properties such as high reliability, sensitiveness and quick response is urgently required. In particular, it is difficult to monitor the machining status during ultraprecision machining, because the emission of energy and cutting force are very small in comparison with conventional machining procedures. In this study, an in-process micro-sensor which can detect thermal behavior near the cutting point has been proposed. Through a series of cutting experiments, it has been verified that the micro-sensor is effective and applicable to the status monitoring in an ultraprecision machining environment.

### Introduction

The demand for higher accuracy and higher productivity in manufacturing is increasing steadily. On the other hand, the supply of skilled workers is gradually dwindling. Consequently, researchers and manufacturers are putting a lot of effort into the materialization of fully automated and intelligent manufacturing systems. In order to successfully implement such a manufacturing environment, it has become important to develop an effective in-process monitoring system to establish the status of the constituents of the machining systems. In particular, the development of an in-process status monitoring system for the unmanned and closed ultraprecision machining environment [1] is of the utmost importance.

In general, an in-process status monitoring system for machining environment is mainly constructed from sensor, data transfer, signal processing, and status recognizing functions. The high performance in-process sensor is especially important to construct such an in-process status monitoring system for ultraprecision machining. However, the effectiveness and usefulness of the currently available sensors [2,3,4] in the industrial machining environment, such as the force, power, and acoustic emission sensors [5,6], are quite limited in the ultraprecision machining environment, because the emission of energy and cutting force are very small in comparison with conventional machining process. In order to precisely grasp the status of the machining space, it is required to monitor thermal behavior near the cutting point using a new sensor device. The authors have already proposed and showed that it is effective to monitor the status of the ultraprecision machining based on thermal behavior near the cutting point using a micro-sensor [7].

Therefore, in order to establish a future ultraprecision machining environment, an in-process status monitoring method using a new integrated thermal micro-sensor has been proposed in this study. The developed micro-sensor is a thin-film platinum resistance thermometry type and mounted directly on the rake face of a single crystal diamond tool tip. Furthermore, by integrating two gauge elements on the tool surface, the temperature distribution of the tool surface can be measured. This paper describes the concept and measuring principle of the integrated micro-sensor and some results of performance evaluations.

## Concept and measuring principle

Various types of sensors have been applied to the in-process monitoring systems of the industrial manufacturing environments. However, the in-process measurement of temperature using a conventional sensor has not been applied for the monitor of an actual manufacturing environment, because of having demerits such as low sensitivity, long response time, low reliability, etc. In order to monitor multifaceted information, i.e., tool, workpiece, coolant, and swarf status, it is most effective and important to monitor the thermal behavior near the cutting point.

Therefore, the authors mounted a platinum resistance thermometry type micro-sensor directly on the rake face of a diamond tool tip having the nose radius of 0.2mm and the rake angle of 0 degree. The platinum has the physical property available for resistance thermometry, because it has quick response to thermal phenomena, linear resistance to temperature behavior, high resistivity, and high temperature coefficient of resistance.

The developed micro-sensor was made of thin platinum film composed of two gauge elements and three electrodes, as shown in fig. 1. The integrated gauge elements were designed as a simple structure, in order to obtain quick response and a large resistance change to a small temperature change. The micro-sized gauge elements of the sensor can detect thermal behavior near the cutting point during ultraprecision machining, because it is mounted directly on the surface of the single crystal diamond tool tip and it has very small heat capacity. The fluctuations of resistance during cutting were detected by the change of voltage in bridge circuits. By using the integrated micro-sensor, the temperature and its distribution on the tool tip surface can be measured without disturbing the objective machining field.

The device structure of the micro-sensor was made by using a micro-fabrication process for semiconductor product, i.e., photolithography, sputtering and lift-off, as shown in fig. 2.

Figure 3 shows the relationship between resistance and temperature for each gauge element of the developed micro-sensor. As clearly shown in this figure, the linear and parallel relationships between them can be confirmed.

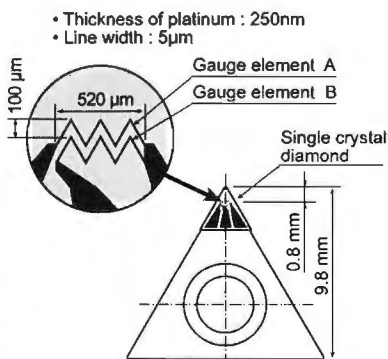


**Figure. 1:** Micro-sensor on the surface of a single crystal diamond tool tip.

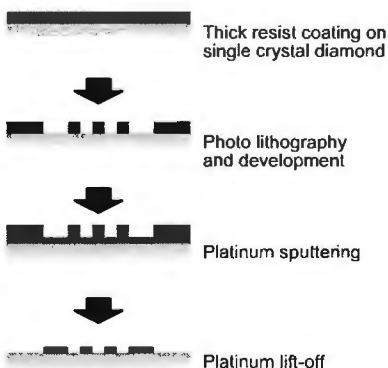


**Figure. 2:** Micro-fabrication process of the micro-sensor.

## Performance evaluations

The actual cutting experiments of the disk substrate made of Al-Mg alloy were carried out by an ultraprecision diamond turning machine [1]. The inner and outer diameters of the disk are 30mm and 90mm, respectively.

Figure 4 shows the typical temperature outputs of each gauge elements in ultraprecision face turning from inside to outside at constant spindle rotational speed. As shown in this figure, the sensor output changes quickly at the start and stop of the cutting, and increases linearly during steady-state cutting in accordance with cutting speed. Thus, the developed micro-sensor outputs clearly contain useful information of thermal behavior during ultraprecision cutting.

Figure 5 shows the difference between the outputs of gauge element A and B ( $T_A - T_B$ ). In the case when the depth of cut is zero,  $T_A$  is lower than  $T_B$ , because the cutting edge is cooled by a mist of white kerosene. At the start and stop of the cutting, the temperature difference changes stepwise, and the step height is depend on both the depth of cut and cutting speed. Hence, the differential output of the integrated micro-sensor denotes the amount of heat passing through the tool tip at the cutting point with quick response.

In order to clarify the sensitivity and response time of the developed micro-sensor, the face turning experiments were carried out with Al-Mg alloy disk substrates having two through holes. The diameter of the holes is 2mm. In the case when a cutting tool passes over the holes, cutting is interrupted for about 0.2msec. As can be seen in fig. 6, the outputs of the micro-sensor decrease by the holes. In particular, the contact conditions between the tool tip and workpiece synchronizing the spindle rotation can be clearly detected by monitoring the differential output.

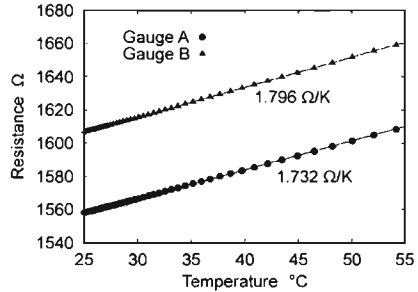


Figure 3: Relationship between resistance and temperature.

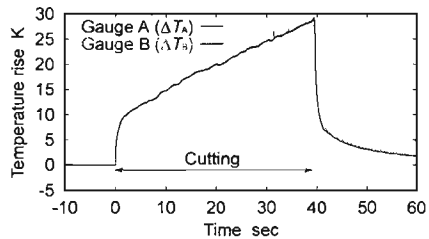


Figure 4: Temperature output pattern of the developed micro-sensor.

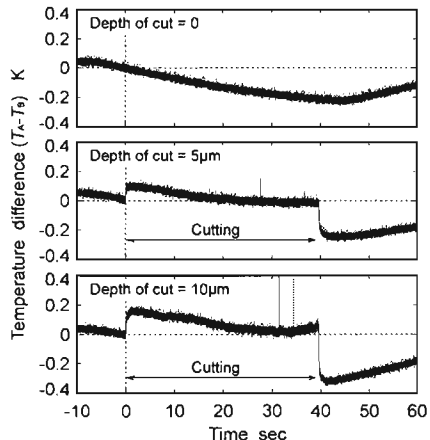
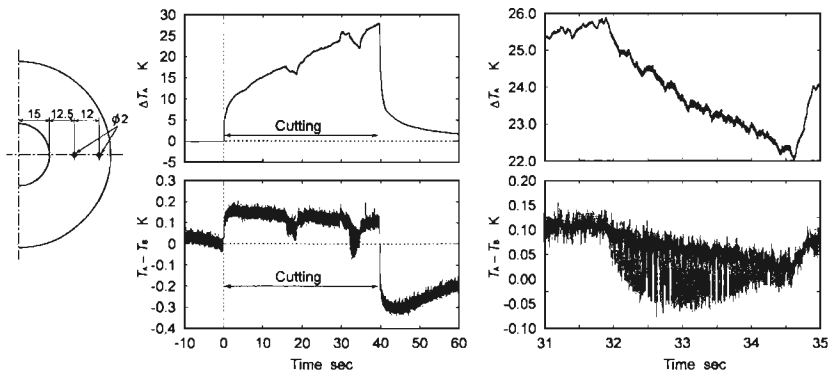


Figure 5: Differential temperature output pattern of the micro-sensor.



**Figure 6:** Response pattern of the micro-sensor during face turning of the disk substrate with holes.

## Conclusions

An in-process micro-sensor for monitoring the status of ultraprecision machining was proposed in this paper. The developed micro-sensor is integrated with two gauge elements, and consequently the temperature and its distribution on the tool tip surface can be monitored with high resolution and quick response. In particular, the differential output, i.e., the amount of heat passing through the tool tip at the cutting point, has quicker response.

## References

- [1] Shinno, H., Hashizume, H., Ito, Y. and Sato, C., 1992, Structural Configuration and Performances of Machining Environment-Controlled Ultraprecision Diamond Turning Machine 'Capsule', *Annals of the CIRP*, 42/1, pp. 425-428.
- [2] Micheletti, G.F., Koenig, W. and Victor, H.R., 1976, In-Process Tool Wear Sensors for Cutting Operations, *Annals of the CIRP*, 25/2, pp. 483-496.
- [3] Tlustý, J. and Andrews, G.C., 1983, A Critical Review of Sensors for Unmanned Machining, *Annals of the CIRP*, 32/2, pp. 563-573.
- [4] Byrne, G., Dornfeld, D.A., Inasaki, I., Ketteler, G., Koenig, W. and Teti, R., 1995, Tool Condition Monitoring (TCM) - the Status of Research and Industrial Application, *Annals of the CIRP*, 44/2, pp. 541-567.
- [5] Iwata, K. and Moriwaki, T., 1977, An Application of Acoustic Emission Measurement to In-Process Sensing of Tool Wear, *Annals of the CIRP*, 26/1, pp. 21-26.
- [6] Dornfeld, D.A., 1990, Neural Network Sensor Fusion for Tool Condition Monitoring, *Annals of the CIRP*, 39/1, pp. 101-105.
- [7] Hashizume, H., Yoshioka, H. and Shinno, H., 2001, In-Process Monitoring of Thermal Behaviour near the Cutting Point during Ultraprecision Machining, *Proceedings of the 2nd International euspen Conference*, Vol. 2, pp. 652-655.

# Resonance-Based High Sensibility Touch Probe System for CMM

H. MATSUOKA, S. KASEI

Faculty of Engineering, Shinshu University, Nagano, Japan,

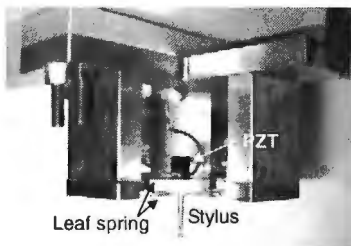
[vendoe@gipwc.shinshu-u.ac.jp](mailto:vendoe@gipwc.shinshu-u.ac.jp)

## Abstract

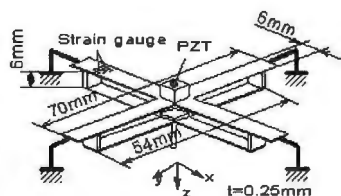
A resonance based touch trigger probe is developed. It is the method of detecting the mode change by contact with the leaf spring structure arranged at two layers. A prototype is constructed and tested. According to the results of experiments, the measuring force is smaller than  $50\mu\text{N}$ , and the repeatability could be smaller than  $300\text{nm}$ . Furthermore, measurements of ring gauges show that differences of characteristics depending on the contact direction are very small. Meanwhile, because the trajectory of the tip of the stylus remains still unknown, further analytic investigation is needed and it will lead to the optimum design.

## Introduction

The use of coordinate measuring machines (CMMs) is an effective way to measure complicated 3D form. The touch trigger probe is important equipment that detects contacts with workpieces. As the accuracy of measurements goes up, some problems inherent in the touch trigger probes have emerged. Measuring force makes deformation of workpieces and reseated position errors brings uncertainty of measurements. This study aims to develop a new touch trigger probe that detects contact in lower measurement force with high accuracy. The probe introduced here is used in the state of resonance, and the mode change by contact is detected. Since



(a) Touch trigger prob



(b)Schematic drawing of the probe

**Figure1:** Resonance based touch probe

the stylus is supported in elasticity, there are no reseated errors. Furthermore, measurement by  $50\mu\text{N}$  or less of measurement force was possible.

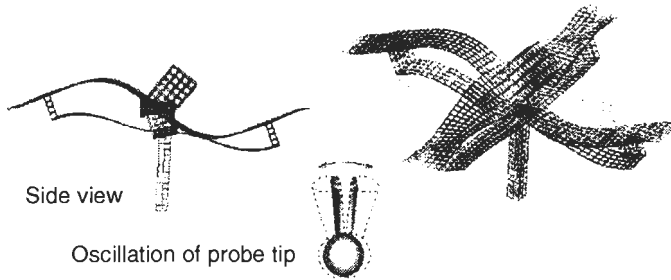


**Figure 2:** Mode analysis of the probe (5th and 6th mode)

## Principle of Probe System

### Structure of Probe

Figure 1 shows the structure of the probe. The probe consists of 2 parallel cross-shaped thin leaf springs and a piezoelectric actuator. The piezoelectric actuator is attached to the center of an upside leaf spring, and on the other hand, the stylus is attached in the center of a lower leaf spring. 2 strain gauges are stuck on one both sides of a lower arm in order to observe the situation of oscillation.

### Analysis of oscillation

Figure 2 shows the 5th and 6th natural mode shape analyzed with FEM. The natural frequency for this mode is 417.35 Hz. In the case of this mode, the stylus oscillates like an inverted pendulum that sets the center of oscillation near the tip of stylus.

### Detection of contact

When a probe is in a steady state by un-contacting, the output of the strain gauge indicates the sine wave of amplitude regularity. But when the stylus contacts to a workpiece, the output waveform would be changed. Therefore detection of the change of waveform leads to detection of contact. In practical use, the output signal is converted into RMS values, and when it crosses the threshold level defined arbitrarily, the interrupt signal to a

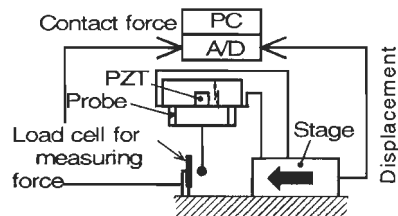


**Figure 3:** Measuring force

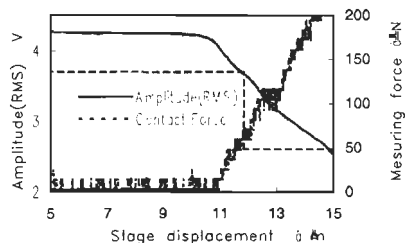


**Figure 4:** Measuring force and amplitude

computer is generated. The threshold level is set to 80% of the steady state in consideration of the experimental results. It is equivalent to  $50\mu\text{N}$  or less in the sense of measuring force as it is shown below.

### Measuring force

Figure 3 shows an apparatus for measurements of measuring force. The object of contact is a load cell that is a thin leaf spring with which the strain gauge is pasted on both sides. The X-Y stage that mounts the probe is moved manually and then the stylus is brought into contact with this load cell. Figure 4 is an example showing change of the contact force over the amount of stage movements and the amplitude RMS value at that time. The dashed line points out the point that corresponds to  $50\mu\text{N}$  of the measurement force, and simultaneously, in the meaning of the RMS of the amplitude, it is equivalent to 80% of the steady state. In addition, since the experimental results from four directions in every 90 degrees show the same tendency, it is understood that the contact detection by  $50\mu\text{N}$  or less is possible.

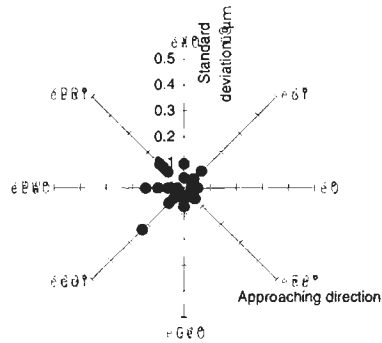


**Figure 5:** Dispersion in contact position

### Dispersion in the position of contact detection

The dispersion in contact detection positions is verified using the repetition contact experiment to a steel block. A steel block fixed on the precision positioning stage of a piezoelectric actuator drive is brought into contact with the probe at the rate of about  $100\mu\text{m/s}$ . The amount of movements from the starting point defined arbitrarily to a contacting point is measured by an electric micrometer. This experiment is carried out by a unit of 20 times from the circumference 8 direction of a probe, respectively. An example of results is shown in Figure 5. In all directions, dispersion is  $300\text{nm}$  or less as this figure shows. Next a ring gauge has been measured. The nominal roundness of the ring gauge is  $0.3\mu\text{m}$ , whereas result of this experimental measurement is  $2.8\mu\text{m}$  in the roundness. Although the experimental value is larger about  $2.5\mu\text{m}$  than the nominal value, this is because the resolutions of the measuring instruments used for the experiment are insufficient, and the experimental value itself should be stopped to the reference grade. However, it can be certified that this measuring method has the low dependability to measuring directions.

### A resonance probe using solenoids

As for the resonance probe that uses a piezoelectric actuator, generation of heat by the actuator brings some problems. It makes deformation in the probe and finally it causes dispersion in contact detection. Then it is reconstructed so that oscillation is given using two solenoids. Although the use of solenoid also generates heat in the



probe, it is expected that optimal design can control the generation of heat. The case of newly designed probe that uses 2 solenoids, the influence by heat was not accepted after 8-hour continuation operation. Figure 7 shows the newly designed probe. The size of each part is the same as piezo-type. These solenoids are controlled by means of on-off control to oppose at the ON time. Also in this case, it drives in the 5th natural mode. As a result of measuring the deformations of lower arms, it turned out that the stylus oscillates like a cone that makes the tip of the stylus a vertex. The experiments about the dispersions above-mentioned are carried out using this probe. An example of results is shown in figure 8. As shown in the result, the dispersions are reduced to 80nm or less.

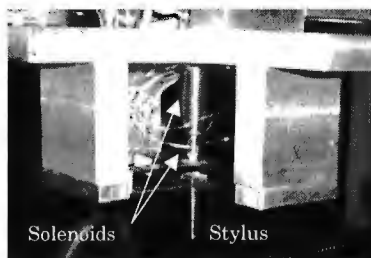


Figure 7: Newly designed probe

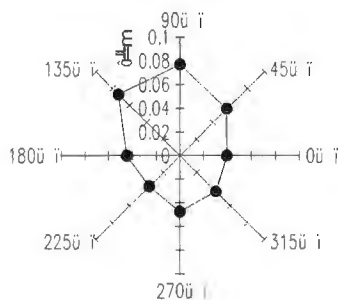


Figure 8: Dispersion in contact position by newly designed probe

## Conclusion

The resonance based touch trigger probes that consist of parallel cross-shaped springs of two sheets are manufactured. Measurement force was less than  $50\mu\text{N}$ , and dispersion in contact detection positions are 300nm or less. Especially, variation 100nm or less was acquired by the type using solenoids.

## References

- [1] OHYA.M: "A Study of the Accuracy of Touch-Trigger Probe", TRANS. Of the JSME, Vol.59, No.563,1993.

## Three-dimensional microprobe with reduced probing forces

P. Pornnoppadol<sup>1</sup>, S. Cao<sup>1</sup>, M. Schmidt<sup>2</sup>, R. Wilke<sup>2</sup>, S. Bütefisch<sup>2</sup>, V. Nesterov<sup>1</sup>, U. Brand<sup>1</sup>

<sup>1</sup>Physikalisch-Technische Bundesanstalt, Braunschweig, Germany

<sup>2</sup>Institute of Microtechnology, Technical University Braunschweig, Germany

### Abstract

A three dimensional microprobe for dimensional measurements of micro structures based on a silicon boss-membrane has been further developed in order to reduce the probing forces and to minimise its size. Reduction of probing forces is achieved by using stripe membranes instead of full membranes. The size of the new probing system could be successfully reduced by integrating the wiring of the piezoresistors on the membrane and using spring contact pins.

### Introduction

The development of micro system technology progressed very fast during the last years. This leads to an increasing demand for mechanical and dimensional measuring methods. For this reason the PTB developed a Micro-Coordinate-Measuring-Machine ( $\mu$ CMM) [1] with a measuring volume of 25 mm x 40 mm x 25 mm [2]. In co-operation with the Institute of Microtechnology of the Technical University of Braunschweig a 3D-microprobe for the  $\mu$ CMM was developed. The aim is to achieve a 3D coordinate measuring uncertainty < 0.1  $\mu$ m. The first prototype of the 3D-microprobe is based on a Si full membrane. Figure 1 shows a membrane with a commercial probing pin of 5 mm length and 300  $\mu$ m probing sphere. On the backside of the membrane the piezoresistive elements for deflection measurement are located [3]. This prototype can be used not only for dimensional measurements but – after calibration - also for force measurements.

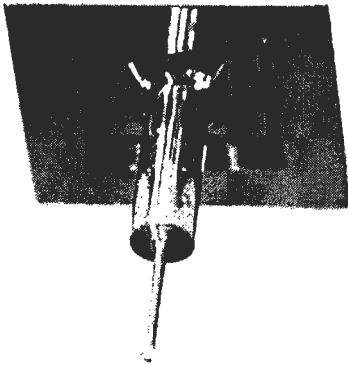


**figure 1:** Prototype of the 3d-micro-probing system based on a Si boss-membrane.

Tactile dimensional measurements at soft materials e.g. PMMA require lower probing forces than the 3d-microprobe based on a full membrane offers. In order to reduce the probing forces a stripe membrane was developed.

When using the first wire bonded prototype for dimensional measurements many failures occurred due to the mechanical sensitive wire bonding contacts. A new design based on spring contact pins for electrically connecting the probing system and with an integrated circuit on the membrane for connecting the piezoresistors to Wheatstone bridges was developed.

## Reduction of probing forces

The reduction of probing forces was achieved by reducing the membrane's flexural stiffness. The full membrane was replaced by membrane

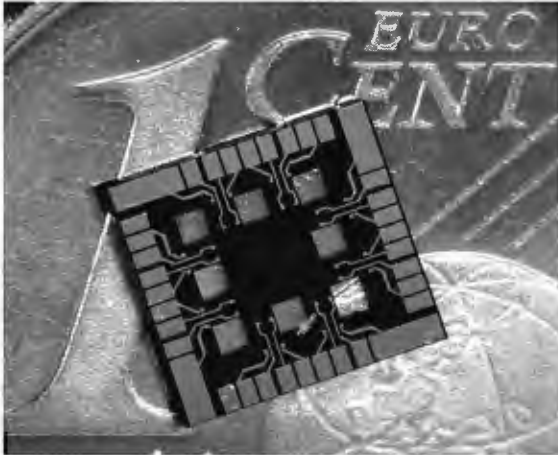


**figure 2:** Boss stripe membrane in comparison to one European Cent

strips, two on each side of the boss [see figure 2]. To find the optimal positions of the piezoresistors in order to detect the maximum three-dimensional deformation vector a FEM simulation has been carried out [5,6]. The maximum mechanical stress is located at the edge of the membrane and in the transition region between the boss and the membrane. The 16 piezoresistors are placed at these positions. The wiring of the resistors to Wheatstone bridges was done externally. Each bridge is detecting one of the three components of the applied force vector.

For calibration of the probing system and for measuring the probing forces and deflections a micro force measuring system [4] consisting of a 1d precision translation stage (moving range 80  $\mu\text{m}$ , resolution 1 nm, repeatability 5 nm) and a commercial compensation balance (resolution 0.2  $\mu\text{N}$ , repeatability 0.5  $\mu\text{N}$ ) [7] were used. The first experimental results of the stripe probe compared with characteristic data of the full membrane probe is shown in table 1.

**Table1:** Comparison of mechanical properties of full and stripe membrane 3D microprobe (probing pin length: 5 mm)

property	membrane type		ratio
	full	stripe	
normal stiffness $k_z$	48 mN/ $\mu\text{m}$	10 mN/ $\mu\text{m}$	1 : 0.2
tangential stiffness $k_x, k_y$	2 mN/ $\mu\text{m}$	0.4 mN/ $\mu\text{m}$	1 : 0.2
ratio $k_z/k_y/x$	24	25	1 : 1
vertical deflection limit	43 $\mu\text{m}$	55 $\mu\text{m}$	1 : 1.28
horizontal deflection limit	120 $\mu\text{m}$	195 $\mu\text{m}$	1 : 1.63
max. vertical probing force	2N	0.45 N	1 : 0.23
max. horizontal probing force	0.5N	85 mN	1 : 0.17

Main properties of the stripe membrane probing system are a reduction of probing forces by a factor of 5 and an increase of deflection range until the membrane is damaged by 28 % in vertical and by 63 % in horizontal probing direction. The maximum probing forces until the membranes break are decreased to 450 mN in vertical and 85 mN in horizontal probing direction. However many probing systems have been damaged, due to bond wires which lost contact. To overcome this

problem a new contacting technique using spring contact pins was developed.

### Membrane with integrated circuit and spring contact pins

A robust design for the 3D-microprobe means to make the assembly more simple and to avoid assembly parts that lead to failures, e.g. wire bonding. A two layer metallisation technology [8] was used to integrate the Wheatstone bridge circuits on the membrane. All other measures of the 3D-microprobe were kept constant. The 3D-microprobe with the integrated circuits has 12 contact pads, six are used for separate input voltages and six pads are used for the three output signals [fig.3].

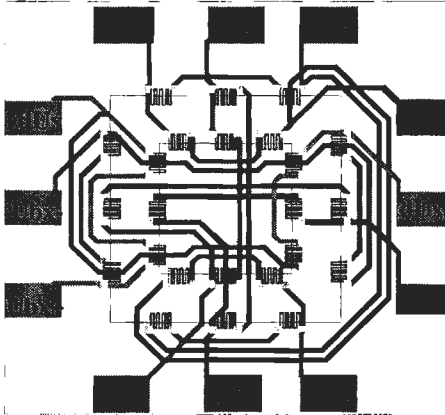


**figure 3:** Prototype of the 3d-micro probe with integrated circuit

This 3D-microprobe has two advantages: on the one hand the wiring of the piezoresistors became very reliable, because the electrical contacts are no longer realised by wire bonding but by pin contacts, and on the other hand the replacement of membrane is simplified.

Calibration of the first prototype shows that the mechanical properties of the probe are comparable with that of the old design: the vertical stiffness amounts to 50 mN/ $\mu\text{m}$  and the horizontal stiffness to 2 mN/ $\mu\text{m}$ . The measured sensitivity is 0.35 [(mV/V)/ $\mu\text{m}$ ]<sub>xy</sub> for probing in x- and y-direction and 1.17 [(mV/V)/ $\mu\text{m}$ ]<sub>z</sub> for probing in z-direction.

However the new design with integrated Wheatstone circuits has one drawback: the yield of the fabrication process is lower due to the more complex fabrication processes.

### Minimised size of the probing system

For the integrated circuit microprobe a new mounting device with reduced size was developed (figure 4). The main advantages are a more simple setup because several adapter plates are no longer needed and simultaneously a more easier exchange of the membrane due to the pin contacts was achieved. Moreover the weight could be decreased compared to the old version.

### Outlook

One of the most important, actual problems in the further development of the 3D-microprobe is the reduction of the probing ball diameter and the improvement of fabrication efficiency of the integrated circuit membranes. In future a 3D-microprobe with a probing sphere diameter of 100  $\mu\text{m}$  is planned. Since such small probing elements are not commercially available new technical and technological methods will have to be developed.

## Conclusions

The results of the 3D-microprobe development and research indicate that there is a good chance to develop a 3d-microprobe which could be used in industry for dimensional measurements on 3d-microstructures.



Another important task is to achieve equal stiffness in all probing directions ( $k_x = k_y = k_z$ ). The solution of this problem requires a new technical and design approach. The most important tasks in the further development of the 3D-microprobe are to test the new probing system in practical use and determine its accuracy and repeatability for three dimensional coordinate measurements. It is also possible to expand the range of applications and functional possibilities of the 3D-microprobe with integrated circuit. The new more reliable 3d-microprobe can for example also be used for micro hardness measurements.

## References

- [1] Brand, U; Kleine-Besten, T; Schwenke, H: *Development of a special CMM for dimensional metrology on microsystem components*, in: Proc. ASPE Conf., Scottsdale, Arizona, 22<sup>nd</sup>-27<sup>th</sup> Oct. 2000, 542-546
- [2] Bütetisch, S.; Büttgenbach, S.; Kleine-Besten, T.; Brand, U.: *Silicon three-axial tactile sensor for micromaterial characterisation*, in: 3<sup>rd</sup> Int. Conf. Micro Materials, 2000, pp. 420-425
- [3] Kleine-Besten, T.; Loheide, U. Brand, S. Bütetisch, S. Büttgenbach: *Development and characterization of new probes for dimensional metrology on microsystem components*, in: Proc. 1<sup>st</sup> euspen Int. Conf., 1999, pp. 387-390
- [4] Hoffmann, W; Loheide, S; Kleine-Besten, T; Brand, U; Schlachetzki, A: *Methods of characterising micro mechanical beams and its calibration for the application in micro force measurement systems*, in: Proc. MicroTec 2000 Conf. in Hannover, 819-823
- [5] Kleine Besten T.; *Messung dreidimensionaler Mikrostrukturen (in german)*. Ph. D. Thesis, Technical University, Braunschweig, Germany, 2000
- [6] Mehner J.; *Mechanische Beanspruchungsanalyse von Siliziumsensoren und -aktoren unter dem Einfluss von elektrostatischen und Temperaturfeldern*, Ph. D. Thesis, Technical University Chemnitz-Zwickau, 1994
- [7] Compensation balance (Type: SAG 245) of the Mettler Toledo AG, Switzerland
- [8] Büttgenbach, S; *Mikromechanik, Einführung in die Technologie und Anwendung*. 2. Ausgabe, Teubner Verlag, Stuttgart, 1994

## **Application of Lateral Effect Position Sensitive Detectors (PSD) to Angles Measuring in a Self-centring Probe.**

J.J. Aguilar, J.A. Yagüe, J.A. Albajez, J. Santolaria

University of Zaragoza, Spain

### **Abstract:**

In this paper the application of Position Sensitive Detectors as angles measuring system for a self-centring probe is explained. Some studies of repeatability and characterisation of the system have been carried out as well as some tests to determine and eliminate the influence in the electronic noise of different factors such as temperature, background light or near electronic devices. The results of these studies are shown in this paper.

### **Objective and application:**

Self-centring probes are part of a project destined to develop a new and faster system to verify Machine Tools [1]. These probes have been designed to measure some balls placed on a reference artefact. One of the designs of these probes is based on three rotating "fingers" that touch the balls and turn around their respective axes a determined angle. From the three angles and the geometric parameters of the probe, the centre of the measured ball is obtained in a single measuring. To know that angle some sensors were studied to be applied to this design. One of them was the LED+PSD system. An adequate study of this system can widely reduce the cost of the probe and increase its efficiency, with the consistent saving of time and money.

### **Explanation of the measuring system:**

Position Sensitive Detectors (PSDs) are opto-electronic devices (silicon photodiodes) that provide an analog output directly proportional to the position of a light spot on its detection area [2, 3, 4]. Theoretically, these devices provide outstanding resolution and position linearity, fast response time and simple operating circuits. A Light Emitting Diode (LED) could be used as a light source in this measuring system. Apparently this could be a very good solution for this application that requires very good repeatability (less than  $0.5\mu\text{m}$ ) and accuracy (less than  $1\mu\text{m}$ ) in every sensor. However, some problems related to electronic noise appear in the transmission of the analog signal from the sensor to the computer that receives the data [3].

For this application the most important objective is obtaining the adequate repeatability and resolution, whereas linearity is not so important because the system is going to be calibrated and the possible problems in that field will be corrected with that process. Therefore, identifying and eliminating the possible causes of electronic noise have been the main goals of the tests in order to take the maximum profit from the sensor.

### **LED and PSD features:**

The PSD used has been the Hamamatsu S3932. It is a ceramic-packaged one-dimensional sensor with an active area of  $1\times 12\text{mm}$ . Its theoretical position resolution is  $0.3\mu\text{m}$  and its rise time is  $3\mu\text{s}$  [5]. A two-dimensional tetra-lateral PSD was initially tested too but its results of repeatability ( $\pm 2\mu\text{m}$ ) were not good enough for this application. Maybe other type of two-dimensional PSD could provide better results,

but one very important objective of the project is obtaining a low-cost sensor and the two-dimensional PSDs with better features are quite more expensive than the one used. The S3932 does what is required of it in relation to cost and metrological results. The LED used have been the Hamamatsu L2791 and the L2791-02, which includes a lens to focus the light spot. Both of them have an adequate wavelength to the PSDs used.

### **Explanation of the tests and results:**

One of the main advantages of the PSDs is that, because of being analog devices, the electronic operation circuits are very simple [4]. Only an adequate voltage source to feed the system and a basic circuit composed by some operational amplifiers to transform the intensities that the PSD provides into voltages and to operate with them are necessary to work with it. However, when eliminating the possible noise sources is wished too, some extra electronic is necessary. A very stable voltage source is necessary to feed the LED and the PSD and a filter is useful too in order to make this voltage even more stable.

### **Influence of the light spot size and form:**

A one-dimensional PSD produces two output currents related to the position of the centroid of a light spot. The intensity of the incident light spot does not affect the calculation of the position but, on the other hand, the more intensity is increased the better the SNR (signal to noise ratio) of the system will be [3, 4]. Although the size and the form of the ray should not be important for the repeatability of the sensor, using a LED with a lens on its edge (the L2791-02) was necessary in order to eliminate some problems that appeared with a LED without lens (L2791). These problems appeared when the distances between the emitter and the receptor changed or when the incidence of the ray happened very near of the edges of the sensor. This is due to the fact that, in those occasions, the part of the ray that fell inside the active area decreased very quickly because of its wide angle of aperture. This caused that the intensity of light decreased too.

### **Influence of the electronic noises in the repeatability results:**

Identifying and eliminating the possible causes of electronic noise were the two main tasks of the work. It is known that working with changes of temperature or with background light introduces errors in the measuring of the PSD [3, 4]. In the challenge of getting the best long-term repeatability possible for this sensor some repeatability tests were carried out changing this conditions. In these tests the LED was placed over the PSD in a fixed position and the measurement provided by the sensor for an hour was visualised and analysed in order to identify the possible error sources. In this way results of long-term (one hour) and short-term tests (one minute) were obtained.

At the beginning some tests were achieved with the previously explained basic electronic necessary to make the system work. They showed very bad results with long and short-term repeatabilities of  $\pm 15\mu\text{m}$ . Although it is possible calculate the position only by analog components, it is well known that analog circuits are more vulnerable to noise than the digitals so, after converting the output currents of the PSD to voltages, they were digitalized via two A/D converters and, finally, sent to a microcontroller to communicate with a computer using a RS232 interface. Moreover, the microcontroller performed a median or average filtering of the data. The reason of using two converters and not only one was avoiding the appearance of some sporadic picks of nearly  $1\mu\text{m}$  probably caused by a phase difference in the reading of

the two signals of the PSD. Simultaneous sampling has shown better performance in the presence of noise. Moreover, the main identified noise frequencies were of 50Hz and 100Hz so, instead of using an analog low pass filter (which could reduce the SNR) using a frequency multiple of the noises and average enough number of samples to get a frequency notch at 50Hz was decided. With this new circuitry the results of long-term repeatability improved from  $\pm 15\mu\text{m}$  to  $\pm 1\mu\text{m}$  (see figure 1) and

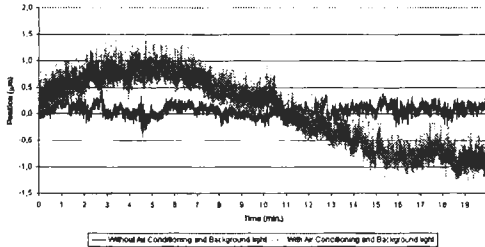


**figure 1:** Repeatability in a single point in different conditions

the short-term ones from  $\pm 15\mu\text{m}$  to  $\pm 0.2\mu\text{m}$ .

After eliminating the errors caused by an inadequate electronic circuit and other electronic devices, the environmental noises could be identified in an easier way. Working with stable temperature ( $20\pm 1^\circ\text{C}$ ) obtained thanks to the air conditioning and without protecting the system from the background light the short-term repeatability results kept being very good

( $\pm 0.2\mu\text{m}$ ), but in the long-term some periodic noises were observed. One of these noises had a cycle of 45 minutes and was caused by the air flowing when the air conditioning turned on, what caused variations in the temperature of the system. To avoid this factor the air conditioning was turned off and those cycles disappeared, obtaining long-term repeatabilities of  $\pm 0.5\mu\text{m}$ . Despite working in the infrared range, visible light produces enough current to introduce an offset in the position. The background light also increases the noise in the signal. In order to eliminate the most of the possible fonts of light the measuring system was covered by a black box to preserve it from any light or residual airflow. The results obtained in these conditions show a very little improve in the general stability of the signal but keeping the values of repeatability inside of  $\pm 0.2\mu\text{m}$  for the short-term tests and  $\pm 0.5\mu\text{m}$  for the long-term ones (see figure 1).

**Characterisation results:**

The good results obtained in the repeatability tests in a single point of the PSD were

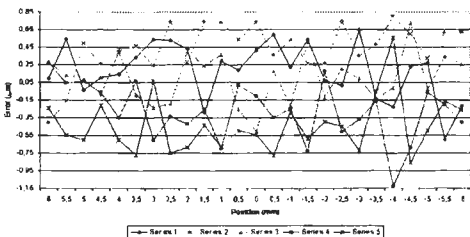


**figure 2:** Repeatability along all the range

only valid if they were so good along all the active area of the sensor. To test this, the system was mounted in a Coordinate Measuring Machine. The PSD was aligned with one of the movement axes of the machine and the LED was mounted in the moving probe. The correct alignment between the LED and the PSD was controlled by monitoring the intensity of the light spot, which is supposed to

remain constant. With this test set-up moving the LED to a desired position over the PSD and comparing the readings of the CMM and the sensor was simple. The repeatability along all the active area showed a value of  $\pm 1\mu\text{m}$ , as figure 2 shows for 5 series of measurements. Varying the distance between LED and PSD apparently



did not affect and tests with separations of 5, 7 and 9mm were carried out obtaining similar results. However, it is probable that its repeatability is even better because the resolution of the CMM where the system was tested is  $0.5\mu\text{m}$ . This can introduce these  $0.5\mu\text{m}$  of error in the measurement because of a non-exact positioning of the machine in the desired point. Testing the real resolution of the sensor is difficult with this test set-up because of the same positioning problem. However, some tests have been done and the sensor showed a resolution better than  $1\mu\text{m}$ . The system showed a good linearity in an 85% of its measuring range. However, this is a factor of little importance while its behaviour is constant because, as have been said before, the system has been calibrated and these deviations from the linearity have been corrected.

### Application to angles measuring:

The good results of the repeatability in the previous tests, where the distance between emitter and receptor is constant, had to be checked in the real measuring situation with the sensor mounted over one of the finger and with the distance between them changing. The figure 3 shows the mounting with a Read-head as extra sensor to compare the results obtained by the PSD. Some tests were carried out that showed a very similar repeatability to the one of the previous characterisation tests in the measuring of the distance that the LED moved along the PSD, that is  $\pm 1\mu\text{m}$ .

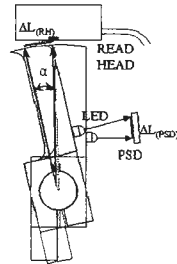


figure 3: Finger

### Conclusions:

The obtained results show that working with the A/D converters and the rest of the explained electronic circuit protects the system from many noises. However, mainly other two factors have to be beard in mind: background light and temperature. The first one is not a problem in the self-centring probe application because the sensor will be placed inside an encapsulated frame. The temperature variations are not supposed to be a problem either because the measuring will be very fast to avoid them during the test and because they will be relative to the first of the reference balls. Therefore the absolute variations of temperature will not affect to the results.

### References:

- [1] E. Trapet, J.J. Aguilar, H. Spaan, J.A. Yagüe, V. Zeleny: "Design, Modelling, Manufacturing and Test of two Alternatives of Self-centering Probes to verify Machine-Tools", Euspen 3<sup>rd</sup> International Conference, 2002.
- [2] R. Pallás: "Sensores y acondicionadores de señal", Ed. Mancorbo, 1998.
- [3] C. Narayanan: "Modelling, signal processing and noise analysis of lateral effect position-sensitive detectors", The University of Texas at Austin, 1994.
- [4] SiTek, UDT Instruments, On-trak: "Position Sensitive Detectors. Theory of Operation". Internet web sites, 2001.
- [5] Hamamatsu: "Products features", 1999.

## Evaluation of Microdefects on SiO<sub>2</sub> Filmed Wafer Surface from the Scattering Light

T. HA<sup>1</sup>, T. MIYOSHI<sup>2</sup>, Y. TAKAYA<sup>3</sup>, S. TAKAHASHI<sup>4</sup>

Osaka University, Osaka, Japan

<sup>1</sup>spartan@optim.mech.eng.osaka-u.ac.jp, <sup>2</sup>miyoshi@mech.eng.osaka-u.ac.jp,

<sup>3</sup>takaya@mech.eng.osaka-u.ac.jp, <sup>4</sup>takahasi@mech.eng.osaka-u.ac.jp

### Abstract

An automated light scattering measurement system for the analysis of spatially scattered light from microdefects has been developed. This system has the capability of automated three dimensional detection for certain given optical conditions such as incident angle, polarization state of the light and so on. The utility of this system is demonstrated by measurements of the light scattering from microscratches and the PSL (polystyrene latex) sphere with the size of 300nm on a SiO<sub>2</sub> filmed wafer. We try to classify and size the defects. Experimental results show that scattering light intensity patterns are characterized by the types and the sizes of defects and optimized arrangement of detectors enable the right evaluation of defects.

### Introduction

The detection and evaluation of defects in silicon wafer process is a critical aspect in the continued improvement of the yield and reliability in semiconductor industry [1]. Especially, the prompt evaluation of yield-limiting process defects (killer defects) is essential and a light scattering method have been one of the powerful methods to meet this need. If a defect exists on surface, the characteristic scattering light appears at certain ranges of solid angle for each defect. It is expected that the types and the sizes of defects can be estimated from the detected intensity values by locating each detector at an optimized position. In addition, incident conditions such as incident angle and polarization of light can emphasize the differences of the characteristic scatter depending on the defect type. Therefore, we have developed an automated light scattering measurement system that is designed to achieve these objectives. Firstly, the system can detect the scattered light in wide range of angle in order to evaluate the characteristic scatter by scanning the detector. Secondly, this system has the ability to change incident conditions. In this paper, light scattering measurements are performed for the PSL sphere and microscratches on a SiO<sub>2</sub> filmed wafer with this system.

## Light Scattering Measurement

### System overview

Figure 1 illustrates the coordinates used to describe the incident and scattering directions. The incident and scattering polar angle,  $\theta_i$  and  $\theta_s$ , are defined in regard to the sample normal corresponding to Z-axis, and the azimuthal scattering angle  $\phi_s$  is defined with respect to the plane of incidence. Figure 2 shows a schematic diagram of the automated light scattering measurement system. This system utilizes Ar<sup>+</sup>(488nm) laser as the incident beam and a highly sensitive PMT (photomultiplier tube) for the scattered light detection. The illuminator is coupled to an optical fiber introducing laser light and the polarization state can be adjusted by setting retardation plates ( $\lambda/2, \lambda/4$ ). There are three automated rotation stages (R1, R2 and R3) and one automated XY stage in this system. The R1 and R2 stage enable to

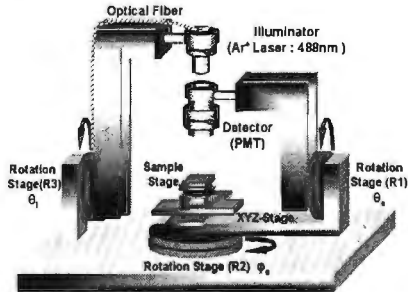
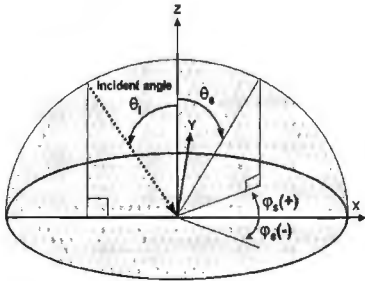


**figure 1** : Coordinate system **figure 2** : Schematic diagram of the system

rotate the detector unit mounting the PMT in both directions of  $\theta_s$  and  $\phi_s$ . The light intensity distribution spatially scattered from a defect can be measured by driving these two rotation stages continuously [2]. R3 stage( $\theta_i$ ) and XY stage facilitate change in incident angle and scanning position, respectively.

**Experimental setup and results**

The standard PSL sphere and the microscratches made by FIB (focused ion beam) process on a SiO<sub>2</sub> film surface (film thickness: 500nm) are used as microdefects. Several experiments are carried out for these microdefects with size variation. The sizes of scratches used in these experiments are listed in Table 1. Each scratch has a length of 200 $\mu$ m. Scratch A, B and C have almost the same defect width but different defect depth. Each microdefect have smooth cross-sectional profile. For example, figure 3 indicates an AFM image of defect B. PSL spheres with the size of 300nm are chosen for evaluation of scattering pattern in comparison to the Scratch C. The incidence angle of 55.6 $^\circ$ , Brewster's angle of SiO<sub>2</sub> film, is selected and the orientation of scratch is set in parallel to Y-axis of which direction is perpendicular to incident plane. The experimental results only for P polarization are presented in this paper, because a remarkable difference between the scattering patterns for P and S polarized incident beam is not found. The scattering patterns for the PSL sphere and scratch C are illustrated in figures 4 and 5. In this case, spatial interference between the illuminator and the detector occurs when detector is located on optical path. These figures are plotted except this interference area and strong specular reflection area. It is shown that the PSL sphere scatters light principally into the front left and front right (Area a) with respect to incident direction. In contrast, the scratch scatters primarily toward the normal (Area b). Considerably strong and characteristic tendencies are shown in the plane of  $\phi_s = -30^\circ$ .

**table 1** : Sizes of microscratches

	Depth (nm)	Width (nm)
A	D 36	W 252
B	D 71	W 287
C	D 114	W 281

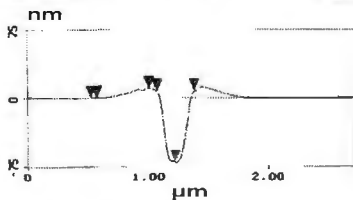


**figure 3**: Cross-sectional profile(defect)

We will discuss about the scattering pattern at this plane hereafter. Figure 6 shows two dimensional scattering intensity distributions for  $-30^\circ$  in azimuth. Vertical and horizontal axis represents scattering light intensity in nW and scattering angle in degrees, respectively.

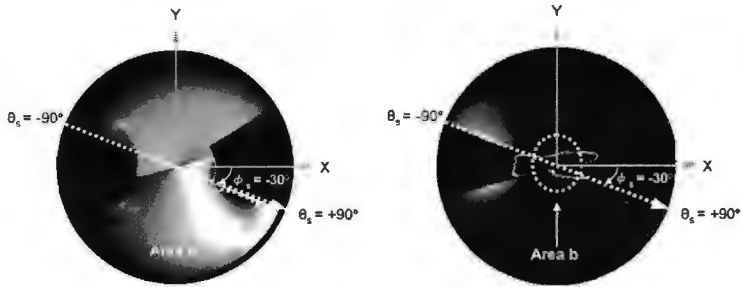


**figure 4:** Scattering pattern of PSL sphere **figure 5:** Scattering pattern of scratch C

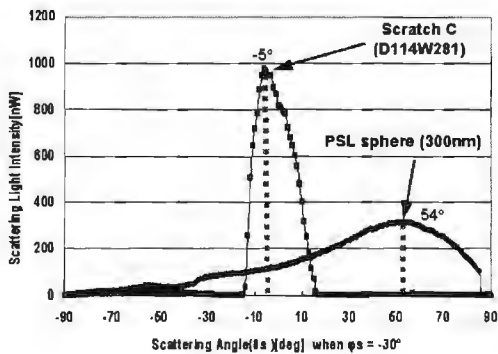


**figure 6 :** Scattering pattern of scratch C and PSL sphere ( $\phi_s = -30^\circ$ )

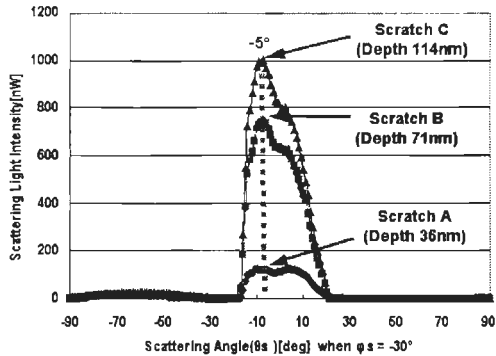


figure 7: Scattering Patterns of Scratch A, B and C ( $\varphi_s = -30^\circ$ )

As the graphs indicate, the characteristic scattering light angle distributions differ according to the type of defect. In the case of the scratch C, most of the scattering light intensity concentrates in the vicinity of  $-5^\circ$  while the PSL sphere scatters around  $54^\circ$  with wide side robe. Therefore, comparing these scattered light intensities make it possible to classify the types of defects. Figure 7 shows two dimensional scattering intensity distributions for the scratch A, B and C which have the different defect size in depth. The characteristic scattering light appears at the same polar angle, near  $\theta_s = -5^\circ$ , for each defect. The deeper the depth becomes, the higher scattering light intensity is detected. It is clearly shown that the depths of defect can be evaluated by detecting the light that scatters toward the normal.

## Conclusions

It is important to find optimal arrangement of detectors for the defect detection and classification on a  $\text{SiO}_2$  filmed wafer surface. Experimental results using the developed measurement system show that the scattering light patterns for the microscratches significantly differ from those of the PSL sphere. In addition, it is known that the scattered light intensities at the characteristic angles are related to defect size. It is expected that not only classification but also sizing of microdefects would be realized by measuring the angular pattern of scattered light intensities

## Reference

- [1] S. Stokowski, M. Vaez-Iravani, "Wafer Inspection Technology Challenges for ULSI Manufacturing", NIST Characterization and Metrology for ULSI Technology, Mar. 1998
- [2] T. HA, T. MIYOSHI, Y. TAKAYA, S. TAKAHASHI, "DEVELOPMENT OF AUTOMATED LIGHT SCATTERING MEASUREMENT SYSTEM FOR Si WAFER MICRODECTS", Proceeding of 4th ISAAT, Nov. 2001 pp.383-386

# Nanotechnology and Microsystem Technology in Electrical Metrology

H.E. van den Brom, C.J. van Mullem

NMi Van Swinden Laboratorium B.V. (NMI-VSL), P.O. Box 654, 2600 AR Delft, The Netherlands

## Abstract:

In electrical metrology the role of nanotechnology and microsystem technology (MST) is becoming more and more indispensable. Various national metrology institutes (NMI) are performing research on relating electrical units to quantum mechanical phenomena that occur in systems on micro and nanoscale. Furthermore, new reference standards based on micro-electromechanical systems (MEMS) are being developed. At NMI-VSL, research based on both technologies is performed in different fields of electrical metrology in order to obtain higher accuracy and stability.

## Introduction

The relation between metrology and nanotechnology and MST is two-fold. In order to compare the results of nanotechnology or MST, measurements should be traceable to the same primary standard: the devices that are fabricated or used should be calibrated. Size reduction of the devices obviously increases the demands on the standards. On the other hand, nanotechnology and MST offer a solution in the need from industry that pushes the national metrology institutes (NMIs) towards their limits in asking for higher and higher accuracy.

During the last decade, electrical metrology has gained much from developments in nanotechnology and MST. There are two distinctive developments going on in this field. The first is research on and development of so-called quantum standards. The idea is to realize electrical quantities by means of laws of nature instead of "artifacts". An example is the primary standard of resistance: the Ohm can be related to the quantum Hall effect instead of a physical high quality resistor. The latter can be drifting in time, which is difficult to verify, or it might change its value when treated not too carefully.

The second development going on in this field is the use of microsystems, such as silicon based sensors, transducers and actuators, for the realization of reference standards. An example of these microsystems can be found in transducers for comparing AC signals to DC signals. NMIs are already applying these microsystems for the most accurate measurements.

In this paper we will focus on research and development activities in this field performed at NMI-VSL. Three topics are taken as an example: 1) a current standard based on single electron tunneling (SET) devices; 2) an AC voltage standard based on Josephson junction arrays; 3) MEMS devices for AC-DC transfer.

## Single electron tunneling devices

Using present day nanotechnology techniques, electronic devices can be fabricated that enable us to manipulate individual electrons. High-speed operation of these nanodevices makes them suitable for use as a high precision instrument for very small electrical currents. The European COUNT project [1,2], coordinated by NMI-VSL, focuses on the development of such nanodevices in order to develop a

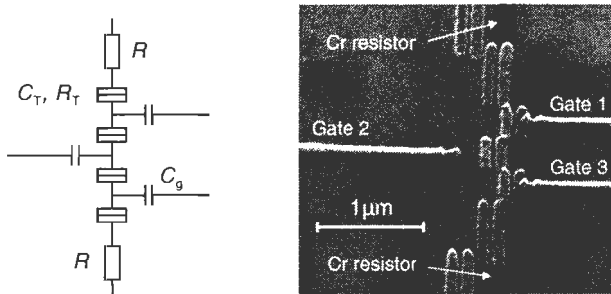


**figure 1:** Equivalent circuit (left) and SEM-image (right) of 4-junction SET pump with Cr resistors in series (taken from the project second annual report; devices are fabricated at PTB).

new primary standard for electrical current.

The instrumentation built in the COUNT project is based on single electron tunneling (SET) nanodevices. These devices consist of controllable islands that are small enough to make the absence or presence of a single extra electron energetically important. The tunnel junctions separating these islands are formed by insulating oxide layers (a few nm thick, typically 20 by 40 nm wide) in between overlaps of two layers of aluminium (30 to 40 nm thick). Changing the parameters in the nanotechnology fabrication process one can control the properties of the devices, such as the total capacitance of the islands and the resistance of the tunnel junctions.

### Single electron pump as a current source

An electron pump is able to actively transport electrons one by one. In this project the nanofabrication of electron pumps with 3, 4 or, if necessary, 5 junctions are investigated. Sufficient accuracy is obtained by depositing on-chip resistive elements [3] (7 nm thick, 80 nm wide, 10  $\mu\text{m}$  long) in series with the pump (see figure 1). Compared to a conventional 7-junction design [4] the reduction of the number of junctions in this so-called R-pump has the major advantage that less complicated electronics is needed. The accuracy of the R-pump will be verified by charging a high stability tuneable cryogenic capacitor [5]. This also provides a link to commercial equipment under investigation.

### Single electron counter as a current meter

Contrary to the case of the electron pump, an electron counter will simply detect electrons one by one. In this project the nanofabrication of a high-speed electron counter is investigated. A small current is applied to an array of typically 50 islands with tunnel junctions in between. One of the islands is capacitively coupled to a single electron transistor (consisting of a single island with two junctions) that senses each individual passing electron (see figure 2). Implementing it into an RF resonant circuit allows for high-speed readout [6].

### Josephson junction arrays

For several years, the Josephson standard is the DC realization of the Volt. This standard is based on the Josephson effect, which occurs in a junction of two superconductors separated by a thin insulating layer. When irradiated with a radio frequency (RF) signal, a DC voltage is developed over the junction that is related to

*Proc. of the 3<sup>rd</sup> euspen International Conference, Eindhoven, The Netherlands, May 26<sup>th</sup> –30<sup>th</sup>, 2002*

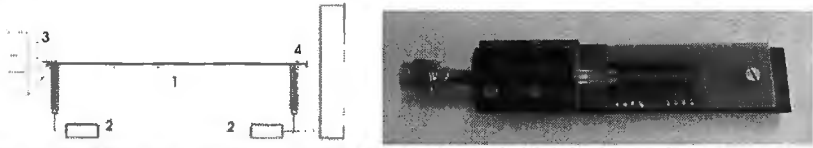


**figure 2:** Schematic overview (left) and photograph (right) of sample holder with coplanar SINIS array of 512 junctions (1), contact pads for reading the desired signal (2), an RF pad (3), and a 50 Ohm termination (4).

the frequency only through constants of nature. The present standard, based on an array of about 30000 junctions, generates a 10 Volt signal with an uncertainty of 0.1  $\mu$ V/V.

Current research on Josephson standards at NMI-VSL focuses on an AC realization of the Volt [7]. Another type of Josephson junctions is necessary, with thin layers of normal (non-superconducting) metal in between. Arrays of this type of junctions are developed and fabricated at PTB (see figure 2). These SINIS (superconductor-insulator-normal metal-insulator-superconductor) junctions typically consist of two 100 nm niobium electrodes with an 8 nm aluminum cover layer, and an 8 nm aluminum normal metal layer in between, separated from the superconducting cover layers by oxide barriers.

The working principle behind this set-up is the drive mechanism [8]. The RF sine wave, which is in fact a continuous series of pulses, is changed into a controlled train of pulses. Each individual pulse then “excites” the Josephson array. When this train of pulses contains a delta-sigma modulated code for an arbitrary wave, after filtering the output of the Josephson array a calculable arbitrary wave will arise. In the European JAWS project [9], also coordinated by NMI-VSL, this set-up will be further developed into an AC voltage standard.

**MEMS devices**

Thermal converters are the most accurate reference devices for the transfer of alternating voltage and current to the equivalent DC quantity (the so-called AC-DC transfer reference standard) [10]. These devices compare values of AC signals to those of the equivalent DC signals by means of their dissipation of heat in a resistive element. Developments in microsystem technology (MST) have resulted in thin-film multi-junction thermal converters (MJTC). National laboratories are already applying thin-film MJTCs for the most accurate measurements.

Micro-electromechanical systems (MEMS) are under study as an alternative for the present-day DC and AC reference standards [11]. Instead of the dissipated heat one

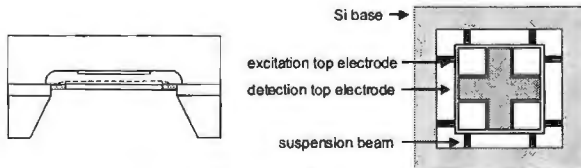


**figure 3:** Operating principle of the bulk-micromachined electrostatic RMS-to-DC converter. The device consists of a silicon wafer with a suspended membrane and a glass wafer with a fixed electrode (taken from Ref. [10]).



can measure the attractive Coulomb force between two conductive plates upon application of AC and DC voltages. The DC voltage, controlled by a capacitance bridge, compensates for the force produced by an AC voltage source. In balance, the root-mean-square (RMS) value of the AC voltage is equal to the DC voltage. This electrostatic RMS-to-DC converter is based on a bulk-micromachined suspended membrane with a fixed counter electrode, with typically 4  $\mu\text{m}$  spacing in between (see figure 3) [12].

Due to capacitive readout and electrostatic control, a MEMS device consumes almost no power. Its input impedance is tunable to any value from near infinite to zero. The output can also be tuned within orders of magnitude by changing the mechanical and electrical parameters. The European EMMA project, in which NMI-VSL participates, focuses on the fabrication, modeling and characterization of these MEMS structures.

## Conclusions

Nanotechnology and MST have offered several new opportunities for different applications in electrical metrology. Research has become possible in order to relate physical measurands to so-called quantum standards. Furthermore, new and more accurate reference standards have been developed. The examples presented in this article show that the technological possibilities are very promising.

## References

1. For more information on the COUNT project see [www.count.nl](http://www.count.nl)
2. H.E. van den Brom et. al., "COUNT – Counting electrons one by one: measurement of very small electrical currents", Proc. 10<sup>th</sup> International Metrology Congress, St. Louis, France, 22-25 October 2001
3. M.W. Keller et al., "Accuracy of electron counting using a 7-junction electron pump", Appl. Phys. Lett., Vol. 69, pp. 1804-1806, 1996
4. S.V. Lotkhov, S.A. Bogoslovsky, A.B. Zorin and J. Niemeyer, "Operation of a 3-junction single electron pump with on-chip resistors", Appl. Phys. Lett., Vol. 78, pp. 946, 2001
5. F. Overney, B. Jeanneret, and M. Furlan, "A tunable vacuum-gap cryogenic coaxial capacitor", IEEE Trans. Instrum. Meas., Vol. 49, pp. 1326-1330, 2000
6. R.J. Schoelkopf, P. Walgren, A.A. Kozhevnikov, P. Delsing and D.E. Prober, "The radio-frequency single-electron transistor (RF-SET): a fast and ultrasensitive electrometer", Science, Vol. 280, pp. 1238-1242, 1998
7. F. Liefink et. al., "Design of a bipolar Josephson array voltage standard for AC synthesis", Proc. BEMC 1999, Brighton, UK, 2-4 November 1999, p. 59
8. S.P. Benz et. al., "Pulse-driven Josephson digital/analog converter", IEEE Trans. Appl. Supercond., Vol. 8, pp. 42-47, 1998
9. For more information on the JAWS project see [www.jaws-project.nl](http://www.jaws-project.nl)
10. M. Klonz, "Current development in accurate AC-DC transfer measurements", IEEE Trans. Instrum. Meas., Vol. 44, pp. 363-366, 1995
11. H. Seppä, J. Kyynäräinen, and A. Oja, "Microelectromechanical Systems in Electrical Metrology", IEEE Trans. Instrum. Meas., Vol. 50, pp. 440-444, 2001
12. G. de Graaf, M. Bartek, Z. Xiao, C.J. van Mullem and R.F. Wolffenbuttel, "Bulk-micromachined electrostatic RMS-to-DC converter", to appear in IEEE Trans. Instr. Meas., 2002

## POSSIBILITIES OF ELABORATION OF MULTI-FUNCTIONAL SENSORS OF PHYSICAL MAGNITUDES.

M.K. Bakhadir Khanov, H.M. Iliev, A. Khamidov, N.F. Zikrillayev,  
M.R. Arzikulova

Tashkent State Technical University, Tashkent, Republic of Uzbekistan

Possibilities of creating new multi-functional sensors of the physical magnitudes on basis of current oscillations with modulation coefficient of 100 p.c. excited in Silicon doped with deep energy level impurities are discussed in the paper.

Oscillations exist in temperature range of 77-350 K. Under determined, constant excitation conditions form and parameters of the oscillations are stable and reproductive. That gives possibility of considering sensors and devices on basis of the oscillations.

Development of science and technology, creation of new, faster computers, solution of ecological problems are difficult to imagine without application of novel semiconductor sensors and devices. The sensors available for the moment and their fabrication technology have come to the limit: both sensitivity and functioning speed can not be improved any more. Thus problems of elaboration of obtaining technology of new materials or improvement of existing devices are need to be solved. Elaboration of reproductive fabrication technology of devices has to increase sensitivity, functioning speed, duration and these devices has to be reliable and easy to use.

Technology of manufacturing semiconductor devices of new class - universal sensors on strongly compensated Silicon is presented. The question is possibility of application of self-sustained oscillation processes for elaboration of new type of functional devices. Self-sustained current oscillations have been investigated in strongly compensated Silicon. Technology of obtaining stable, reproductive self-sustained current oscillations and solid generator with controlled parameters have been elaborated. Being different from already existing sensors the offered ones on the oscillations provide amplitude-frequency modulated output signal. That gives ability of using the sensors without additional circuit technique in devices with distant measuring of the physical magnitudes; translation of information over long distances.

Obtaining technology of strongly compensated Silicon and different structures on it has been elaborated. The technology allows to obtain material with predetermined and reproductive electrical and physical properties. Complex investigation of electrical, physical, photo electrical and optical properties as well as self-sustained current oscillations in strongly compensated Silicon depending on technology, taking into account solubility, diffusion coefficients, concentration of electric active atoms - all these points showed new ways of creating novel types of semiconductor devices.

Table 1 represents basic threshold parameters (electric field  $E$ , frequency  $f$ , amplitude  $I$ ) of the offered temperature sensor on strongly compensated Silicon. The sensor functions in wide temperature interval (77 - 350 K). Threshold  $E$  decreases 10-15 times, while threshold  $f$  and  $I$  change by 6-4 orders respectively.

T, K	E, V/cm	f, Hz	I, A
77	550	$2 \cdot 10^{-3}$	$2,8 \cdot 10^{-1}$
130	350	$5 \cdot 10^{-3}$	$1,5 \cdot 10^{-1}$
160	260	$2 \cdot 10^{-1}$	$7 \cdot 10^{-2}$
180	150	20	$1 \cdot 10^{-2}$
210	100	60	$4 \cdot 10^{-3}$
250	80	600	$1 \cdot 10^{-3}$
270	70	1700	$6 \cdot 10^{-4}$
280	60	2600	$8 \cdot 10^{-5}$
300	50	3250	$1 \cdot 10^{-4}$
320	40	4200	$2 \cdot 10^{-4}$

Ordinary semiconductor magnetic sensors provide low sensitivity. Our investigation of strongly compensated Silicon showed strong dependence of threshold electric field, amplitude and frequency of self-sustained current oscillations on magnetic field. Being different from existing ones the offered sensors on a solid generator are sensitive to both transversal and longitudinal magnetic fields. Amplitude changes 1-20 times in the interval of magnetic field 1-20 kOe, while frequency changes on 180 p.c. independently on direction of magnetic field. Sensitivity of the sensors exceed the one of existing sensors 10 to 15 times. Under stress self-sustained oscillations in samples with crystallographic directions [100] are excited at sufficiently low values of electric field compared with case of absence of the stress. We see stimulation of the oscillations here. Speed of changing of E is  $\alpha = \pm 7 - 8 \cdot 10^{-2}$  V/Pa and that is 4 to 8 times more than that in directions [111] and [110] directions. Relative change of oscillation amplitude depending on the stress shows that in the region of the stress up to

$4 \cdot 10^{-5}$  Pa in samples with directions [100] and [111] increases 15 and 8 times respectively.

Table 2 presents sensitivity of basic parameters and threshold electric field of the generators on Si(Mn) to various external influences.

Fields of Application	Coefficient of sensitivity			
	Threshold Electric field	Threshold frequency	Threshold Oscillation amplitude	Threshold oscillation frequency
Temperature Sensor	$-(2\div 3)$ V/cm·K	$(1\div 2)\cdot 10^2$ Hz/K	$(2\div 3)\cdot 10^{-6}$ A/K	$(1\div 2)\cdot 10^2$ Hz/K
Photo-Sensor	$-(4\div 5)$ V/cm·lx	$(2\div 3)\cdot 10^2$ Hz/lx	$(2\div 3)\cdot 10^{-6}$ A/lx	$-(3\div 4)$ Hz/lx
Pressure Sensor	$-(4\div 6)\cdot 10^{-8}$ V/cm·Pa	$(3\div 4)\cdot 10^{-8}$ Hz/Pa	$(3\div 4)\cdot 10^{-10}$ A/Pa	$-(1\div 2)\cdot 10^{-5}$ Hz/Pa
Sensor of Magnetic Field	$-(3\div 4)\cdot 10^{-3}$ V/cm·Oe	$-(4\div 5)\cdot 10^{-3}$ Hz/Oe	$(6\div 7)\cdot 10^{-11}$ A/Oe	$(4\div 6)\cdot 10^{-2}$ Hz/Oe

It is necessary to underline that coefficient of sensitivity of each physical influence has been determined at constant effect of the others. The universal sensor provides high sensitivity to different external influences and is many functional due to modulated output signal. It is capable of functioning also in remote-control regime.



## Distribution of Surface Contacts on a Simulated Probe Tip

H. A. M. Dowidar, D. G. Chetwynd

The Centre for Nanotechnology & Microengineering, School of Engineering,  
University of Warwick, Coventry CV4 7AL, UK

### Abstract

We report on a simulation study of 3-D stylus contact in surface roughness measurement, which is part a major project to explore tip-surface interactions with the aim of producing guidelines to good practice. A point-for-point comparison algorithm has been set up to investigate the nature of the contact on the stylus as well as the effect of stylus distortion on 3-D surface assessment. The simulation can use styli of arbitrary shape such as conical, pyramid and hemispherical shapes. It uses MATLAB for the simulation code in order to provide good portability. After some of theoretical and practical points about the stylus simulation, discussion concentrates on the statistical distribution of the contact point on the stylus.

### Introduction

Surface micro-topography is measured most commonly by either a fine stylus contact or by one of several optical probing methods. Debate continues on their relative merits and disadvantages, but it is clear that both will be used for a long while to come. There is, therefore, a need for good ways of comparing the output of these methods. There is also need for better guidelines or Standards on applying styli to the fine or delicate surface structures that are increasing demanded by applications across mechanical, electronic, optical and bio-medical engineering.

As part of continuing work towards such ends, we here report on a small study into the geometrical interaction of styli with rough surfaces. A simulation process is used to gain data on the filtering effects of the stylus and on the distribution of contact points. The aim is to inform choices of stylus geometry (e.g. tip radius and cone angles). Longer term, it may help the development of instrument diagnostics for stylus wear and damage.

### Simulation Process

The basic concept of the simulation method has been widely used. It is a simple extension of that used for many years to show how a circular (disc) 'stylus' filters (smoothes) a roughness profile. The method goes back at least to the now-obsolete E-system of establishing reference lines proposed by von Weingraber [1] and Radhakrishnan [2]. The extension from these 2-D methods to 3-D (real) surface modification is obvious, but appears to be hardly reported in the literature. Perhaps computing costs for the perceived benefit have been discouraging. It seems likely that a few investigations into statistical methods of predicting stylus filtering effects may have used it for testing without fully describing the techniques used [e.g. 3].

The simulation is a kinematic process, based on the geometry of ideally rigid materials, etc. A tip is lowered vertically towards a nominally horizontal test surface until a first contact point is encountered. The measured (reported) profile point is then recorded as the height of a reference point on the stylus (e.g. centre of spherical tip or lowest point) positioned at the lateral location of the centre of the tip. We assume that real styli are adequately constrained by their guiding mechanisms to be modelled as single degree of freedom systems. The slightly arcuate motion of many real

profilometers is neglected. This is acceptable on spherical tips and, although less rigorous, for other shapes over small deflections. Effects such as contact friction are also ignored. The algorithm is:

- + represent actual surface on square sampling grid in array  $z(x,y)$ ;
- + represent stylus in smaller array  $s(x,y)$  on same grid;
- + for all points on  $z$  where grids overlap completely;
  - ++ position centre of  $s$  above point of interest  $(X,Y)$ ;
  - ++ add  $s$  from  $z$  over all points in  $s$ ;
  - ++ maximum value identifies the contact point;
  - ++ record value in array  $p$  as measured height at  $(X,Y)$ ;
  - ++ record contact statistics in distribution array;
- + report (plot) output array  $p$  and the contact statistics.

Generally it will be more computationally efficient to store the stylus shape even when that shape is analytically determined. Additionally, the method will cope with any arbitrary stylus shape. The process can readily be refined by adding additional loops to make sampling on the surface and the stylus grids as integer multiples rather than equal, so varying the resolution obtained for the contact geometry.

The special feature of our implementation is the recording of contact conditions, particularly by counting the number of times each point in the stylus array is actually in contact with the test surface.

## Verification

For convenience of testing (since all effects are relative between axes) all results discussed here are set on  $1\ \mu\text{m}$  sampling grids with styli characterised by dimensions of 5 or  $10\ \mu\text{m}$  and surface heights scaled appropriately.

The algorithm is implemented in MATLAB for ease of array handling, etc., at the expense of relatively poor computational speed. A simulation of scanning a  $20\ \mu\text{m}$  tip radius over an area of  $300\ \mu\text{m}$  by  $300\ \mu\text{m}$  takes about two hours to run on a PC workstation of modest performance. Initial testing was by scanning trial styli over flat arrays with delta functions, when an inverted version of the stylus shape is reproduced. Scanning over computed surface structures such as sinusoidal prismatic gratings demonstrated the expected patterns of distortion, with cusping in the valleys. It helped to verify that the software correctly handled cases where, contingently, more than one contact point arises simultaneously. Test surfaces of laterally uncorrelated Gaussian random data were generated by the internal MATLAB function. Scanning these generates accretions of copies of the stylus tip profile and tests the collection of contact statistics since the extreme points dominate the contact conditions.

## Simulation experiments

The output from computed uncorrelated random surfaces is used mainly for verification, but has some practical use. It provides one possible route to a value for the effective cut-off wavelength of a stylus considered as a low-pass filter – a contentious issue since the filtration process is non-linear and not necessarily single-valued. It might also be used to provide limiting values for the mean height of the measured surface above the actual one, which may be significant to the accuracy of measuring small step heights. The spatial distribution of contact points upon the

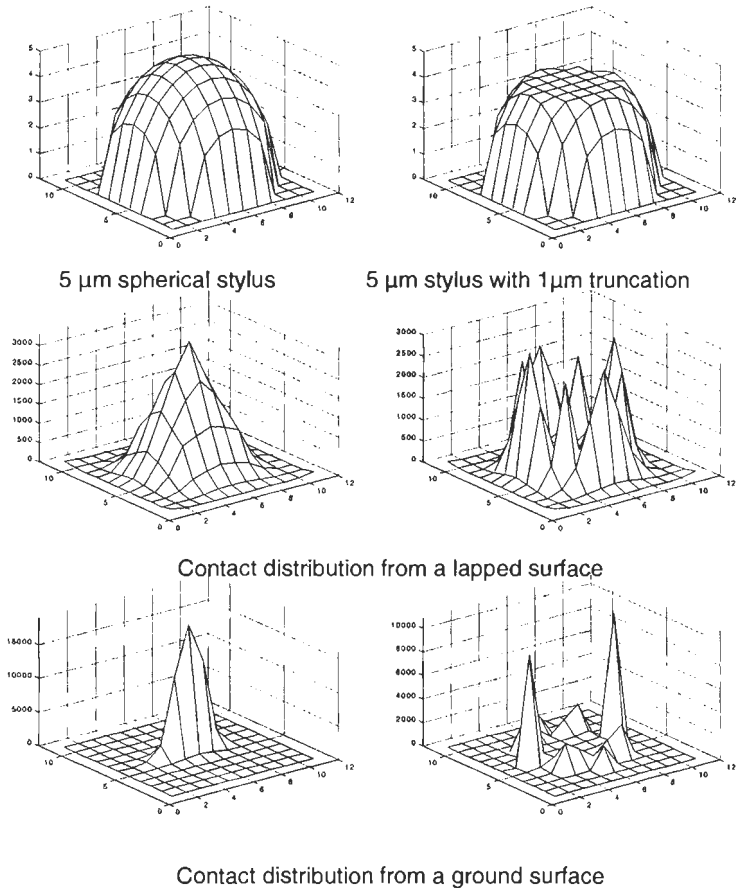


**Fig 1:** Contact points on two styli (top) against different surfaces.

stylus when run against an uncorrelated random 'surface' does not reproduce the stylus shape, as would a true monte-carlo sampling, since only the high points are involved in the contact. The distribution on a spherical tip is symmetrical but more concentrated in the central region.

Statistics about practical contact patterns need to be derived from real surface data. An immediate problem is that collecting such data involves a process of stylus integration, or an optical equivalent. This is one reason for scaling surfaces up a little compared to normal conditions of interest. For the present work surfaces were obtained either from a modified Taylor Hobson Talysurf 5 with an x-y stage and locally-produced control software or from a WYKO NT2000 scanning white light



interferometer. The stylus was nominally 2  $\mu\text{m}$ , so filtering at the order of 1  $\mu\text{m}$ . The lateral resolution of the microscope optics used also introduces a low-pass effect on the order of 1  $\mu\text{m}$ .

Patterns of contact onto styli were broadly similar with both truncated pyramid forms and spherically-tipped cones of appropriate dimensions, so the latter is used as an example. Figure 1 shows examples a 5  $\mu\text{m}$  radius spherical stylus and of the same stylus truncated to model severe wear. The trial surfaces are of fine-ground hard steel that was subsequently randomly lapped and of conventional surface ground steel. The random surface leads to a symmetrical distribution of contact points on the spherical stylus with its mode at the tip centre. The shape is quite similar to that from uncorrelated Gaussian data, but is rather more widely spread out – over 90% of contacts are within 3  $\mu\text{m}$  of the tip centre and only rarely are there contacts with the start of the 90° conical flank region. This result is broadly as might be expected, but the behaviour of the truncated spherical tip on this surface is far from intuitively obvious. There is a multi-mode pattern of contacts spread around the edge of the flat, with very few contacts near its centre. Flanks are contacted a little more often, although it is still a rare occurrence. Plots of the measured surfaces resulting from these styli are not readily distinguished visually. The lapped surface has Ra of 1.7  $\mu\text{m}$  prior to applying a stylus, of 1.54  $\mu\text{m}$  after applying the sphere and 1.50  $\mu\text{m}$  after applying the truncated tip.

Contacts on the spherical and truncated tips (figure 1) when scanned over the ground surface (originally  $\sim 0.4$   $\mu\text{m}$  Ra) show patterns consistent with its overall random nature. The anisotropy is very clear, with contacts highly concentrated along a line normal to the lay in a pattern similar to that of the cross-section of the pattern from the lapped surface. The 'worn' stylus picks up significant numbers of contacts away from the central line, again showing a crown-like distribution with few contacts near the tip centre. The truncation also has greater effect on the measured surface Ra, reducing 0.36  $\mu\text{m}$  of the spherical tip to 0.30  $\mu\text{m}$ .

## Conclusions

A 3-D stylus simulation system has been developed, and verified, to collect statistics on the distribution of contact points on stylus probe tips. It confirms that contact is concentrated towards the centre of a spherical tip, with little influence from the conical flanks. It also suggests that lateral position uncertainties of at least a micrometre will be inevitable with conventional styli and that refining lateral gauging beyond this level may be uneconomic and a source of potentially misleading results.

## References

- [1] H. Von Weingraber, 'Suitability of the envelope line as a reference standard for measuring surface roughness', *Microtecnic*, Vol. 11, pp 6-17, 1957.
- [2] V. Radhakrishnan, 'Effect of stylus radius on the roughness values measured with tracing stylus instruments', *Wear*, Vol. 16, No. 5, Nov, pp 325-35, 1970.
- [3] J.J Wu, 'Spectral analysis for the effect of stylus tip curvature on measuring rough profiles', *Wear*, Vol. 230, No.2, pp 194-200, 1999.

## Characterisation of angle-sensitivity of magnetic field sensors.

G. Kotte, M. Heemskerk, G. Teunisse

NMi Van Swinden Laboratorium, PO Box 654, 2600 AR Delft, The Netherlands

Telephone: ++31 15 2691500; Fax: ++31 15 2692971;

e-mail: gkotte@nmi.nl ; mheemskerk@nmi.nl ; gteunisse@nmi.nl

### Abstract:

Photocopier manufacturer Océ (Venlo, the Netherlands) requested NMi-VSL to develop equipment to determine the position of the magnetic coordinate system of a magnetic field sensor. NMi-VSL has developed an instrument that can be utilised on a magnetic field generator. Using the instrument, angular rotations of a magnetic field sensor in the magnetic field generator can be performed with an uncertainty of  $0,06^\circ$ .

### Problem definition and assumptions.

At NMi-VSL calibrations of magnetic field sensors are performed on a magnetic field generator containing two electro magnets and two poles pointing to each other (see figure 1). Between the pole surfaces the measuring space is situated. The magnetic field is assumed to be homogeneous and perpendicular to the surface of the poles.

The calibration set-up has to meet the following properties:

- Traceable angle measurement towards the direction of the magnetic field of the generator (is perpendicular to the pole surface) in two orthogonal directions. The aim is the determination of the position of the magnetic coordinate system in two perpendicular directions of the sensor regarding a reference plane on the body containing the actual sensor.

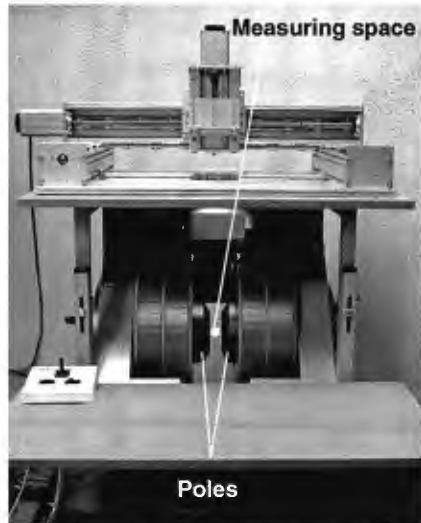


figure 1: The magnetic field generator

- Easy access to the measurement space between the poles of the generator to change sensors, without losing the angle information with respect to the pole surface.
- Small enough, regarding the mutual distance of the poles, to apply the 2-tesla field. Because of the required 2-tesla field the maximum distance between the poles is 25 mm.
- A negligible distortion of the generated magnetic field. One has to watch carefully the choice of materials.

### The measurement set-up.

#### Design considerations.

The starting point for the design is the surface of the poles. To ensure the homogeneity of the magnetic field the surfaces of the poles must be parallel. Three supporting props are normally used between the poles to ensure parallelism. In the design the supporting props are incorporated in the stationary part of the instrument. The plane through the same end of the props is parallel to the pole surface and is used as the reference plane for the angle measurement.

#### The principle of the construction.

The instrument (see figure 2) consists of a fixed-body (1) containing 3 props (2) for positioning the poles of the magnetic field generator. To the fixed-body a movable-body (3) is attached. The movable-body can rotate along the X-axis, the rotation is measured by an angular encoder (4). The movable-body incorporates a shaft (5) with a mounting plane (6) for the magnetic field sensor at the end. The shaft can rotate along the Y-axis, the rotation is measured by an angular encoder (7).

Both axis are perpendicular and in the same plane. This plane is parallel to the plane through the end faces of the props, being the reference plane, and therefore parallel to the end surface of the poles (see figure 3).

A part of the movable-body (8), containing the shaft with the mounting plane, can be removed from the instrument for easy exchange of the magnetic field sensor. To prevent loss of the angular position of the mounting plane with respect to the reference plane a kinematical coupling<sup>1</sup> (9) is applied equipped with a pre-load system.

The main parts of the instrument are made of non-magnetic materials like aluminium and brass. For the kinematical coupling ruby balls are applied. The angular encoder (4) is tailor made to prevent external magnetic fields close to the mounting plane for the sensor.

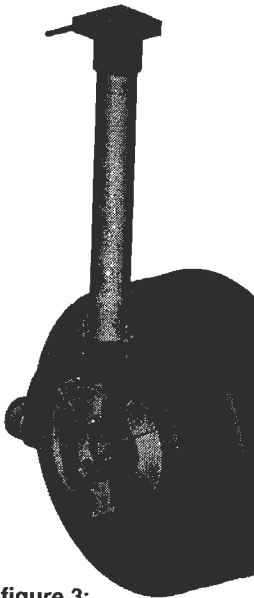


**figure 3:**  
The instrument utilized on the end surface of a pole.

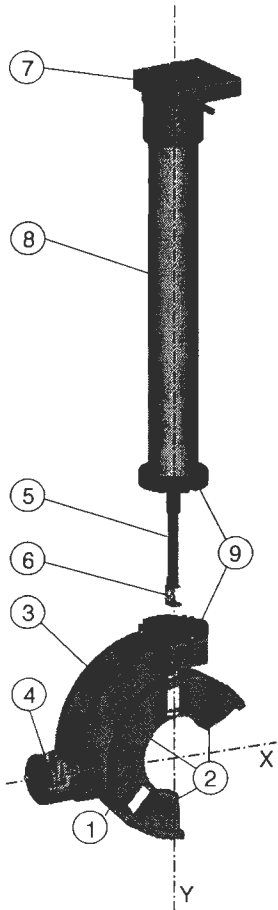


**figure 2:**  
An impression of the realised instrument

## Characterisation.

Before the instrument can be used the indication of the angular position of the mounting plane with respect to the plane through the positioning props must be set. Furthermore the instrument must be characterised to determine the uncertainty in the angle measurement. These activities are executed using an Moller-Wedel 2-axis autocollimator and a set of tailor made mirrors (see figure 4 and 5). The reflecting surface of the mirrors is made parallel to the contact points by which the instrument is contacted.

### Cross talk of both perpendicular axis.

Cross talk of the X-axis and Y-axis is caused by 2 major effects.

- The one-sided bearing of the movable body to the fixed body gives the construction a bigger sensitivity to the quality of the bearing. Actuation of the movable body to produce a rotation in the X-axis, causes a rotation in the Y-axis as well, due to elastic deformation caused by friction in the bearing. Play in the bearing has the same effect.
- Manufacturing accuracy probably causes a squareness deviation between the X-axis and Y-axis. This effect is examined by keeping the elastic deformation constant.

### Hysteresis.

Friction in bearings combined with finite stiffness of the couplings and axis causes hysteresis effects.

### The indication of the angular position of the mounting plane.

Both angular encoders have a reference position to reset the indication after the electronics are switched on. The deviation of the reference position of both encoders to the position where the mounting plane is parallel to the plane through the props is determined in 2 steps.

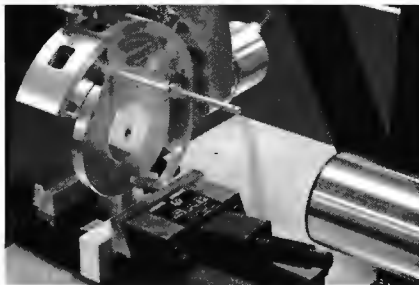
- The measurement axis of the autocollimator are set parallel to the plane through the props using mirror 1 (see figure 7)



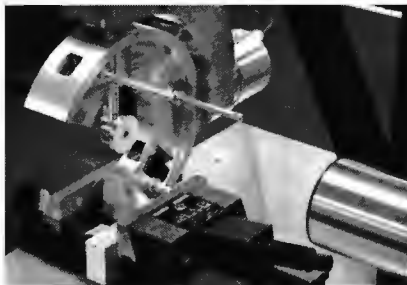
figure 4: The experimental set-up for the characterisation of the instrument



figure 5. The mirror set



**figure 7:** Application of mirror 1 on the 3 props of the fixed body.



**figure 8:** Application of mirror 2 on the mounting plane.

2) Using mirror 2 (see figure 8) the mounting plane is set parallel to the measurement axis of the autocollimator by rotation in the X-axis and Y-axis of the instrument, after the reference positions of the encoders have been passed through. The indication of the angular encoders is the deviation to be determined.

The effect of a remaining deviation in parallelism is determined by rotation of the mirrors and repetition of the measurement.

#### **Reproducibility of the kinematical coupling.**

The kinematical coupling (see figure 6) is tested for its repeatability in the angular positioning.

#### **Results of the characterisation.**

Description	Influence on:	
	X-axis	Y-axis
Cross talk a), (maximum value)	0,001°	0,020°
Cross talk b), (maximum value)	0,005°	0,005°
Hysteresis (maximum value)	0,024°	0,014°
Angular position mounting plane ( $1\sigma$ )	0,019°	0,019°
Kinematical coupling ( $1\sigma$ )	0,0003°	0,0003°



**figure 6.**

Details of the kinematical coupling

#### **Discussion.**

Apart from the calibration of the angular encoders and the contribution of the magnetic field sensors, angle measurements can be performed with an uncertainty of 0,06° based on 95% confidence level. The major contributions to the uncertainty are due to the application of slide bearings applied. Replacement with ceramic ball bearings probably will improve the performance.

#### **References.**

1) M.P. Koster, "Constructieprincipes", Twente University press

## Accurate Displacement Measurement with Inertial Sensors

S.A. Spiewak<sup>1</sup>, D.A. Turcic<sup>2</sup>

<sup>1</sup> Calgary, Canada; <sup>2</sup> Portland, USA

### Abstract:

Small, accurate and robust Microsystems Technology based inertial sensors potentially facilitate displacement measurement with subnanometer resolution and sub-microsecond short term accuracy. The theoretical basis of the measurement is well established. Instantaneous values of the spatial generalized coordinates of a moving body are computed from double integrated accelerations provided by nine sensors located at appropriate locations on it. A combination of accelerometers and gyroscopes can also be used. Despite theoretical simplicity, the practical implementation of this method is difficult and requires eliminating several error sources. The paper describes adaptive filters developed for this purpose. Analytical considerations are illustrated with experimental results obtained in the laboratory and shop-floor conditions.

### Inertial Displacement Sensors

Rapid developments of microelectronics combined with steadily increasing global competition in manufacturing have intensified the efforts to combine the advantages of automation, ultra precision engineering and top-down nanotechnology in the 'next generation' manufacturing processes and equipment. But the demands of high speed, low cost manufacturing strongly contradict, in terms of the desirable process and equipment features, the demands of precision. Achieving a qualitative progress in high volume, state-of-the-art manufacturing processes depends upon the availability of robust, accurate, and minimum-invasive sensors, capable of tracking the actual spatial movements of cutting tools and machined parts.

Microsystems Technology (MST) based inertial displacement sensors, referred to henceforth as IDS, have the potential to alleviate some severe obstacles that have been hampering the advancements of manufacturing processes and equipment. In particular, accelerometers and gyroscopes allow accurate measurement of translational and rotational displacements, relative to the inertial coordinate system of the Earth, without requiring any physical reference bases or fixtures. The upper bound of the measurement error can be estimated from the published data as 0.1  $\mu\text{m}$  for the measurement period of up to 40 seconds, or equivalent 1 nm over the period of 4 seconds [1,2]. It should be remembered, however, that inertial sensors are not suitable for static and quasi-static measurements, so they can rarely be used as the sole measuring systems.

Out of many potential applications of IDS, this paper focuses on rapid evaluation of quasi-static and dynamic performance of manufacturing equipment. At present, such assessment is not only time consuming, but requires considerable expertise and expensive equipment (ball bars, cross-grids or lasers [3-5]). The benefits of using IDS are illustrated by way of example presenting rapid estimation of interface stiffnesses between machine tool components. These stiffnesses are important indicators of the 'health' of spindle bearings, guideways or the tool-spindle joints, and as such are indispensable for the optimization of machining parameters and for the predictive monitoring and diagnosis. The key interface stiffnesses in the investigated spindle-tool unit of a machining center are rapidly evaluated by performing the "tap test" [6] and recording signals from five IDS whose locations are shown in Figure 1.

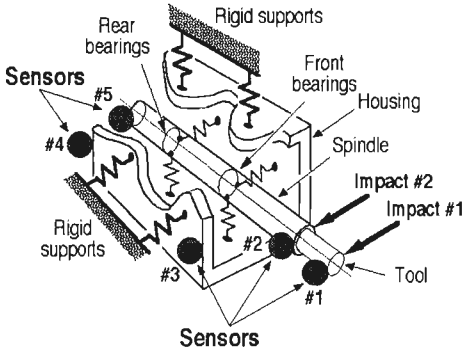


**Figure 1:** Diagrammatic representation of the investigated dynamic system.

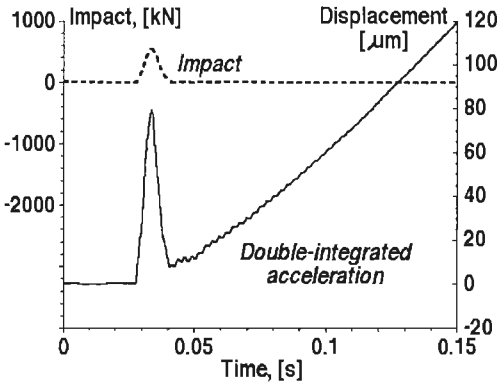


**Figure 2:** The impact and double integrated acceleration of the tool tip.

During the test, CNC system is programmed to hold the unit stationary. The impact is applied first at the end of the long shank milling cutter used (Impact #1). After replacing the cutter with a 'dummy tool' with zero length, the impact is applied again at the spindle nose (Impact #2). The impact is shaped such that the frequencies above one fifth of the first resonance of the system are eliminated. Quasi-static models of spindle shaft and tool deflection are known. The impact force and acceleration responses are recorded at a high sampling rate.

A representative result obtained with *Sensor #1* is shown in Figure 2. The double integrated acceleration suggests that after the impact the tool end moves with a constant speed of 1200  $\mu\text{m/s}$ . This is a gross measurement error since the CNC system would counteract such motion. Further analysis reveals that the ramp response is an artifact of double integration applied to the measured signal distorted by such phenomena as the sensor noise, cross-talk, vibration rectification, limited frequency bandwidth, and uneven gain versus signal frequency.

## Model Based Suppression of Sensor Errors

There are several approaches to improve the accuracy of IDS. They include: (1) the use of multiple sensors and averaging of their output signals, (2) model based attenuation of distortions, (3) isolating sensors from 'harmful' vibrations, and (4) optimal sensor design. This paper is concerned with an off-line method that involves minimization of the "prediction error" between the signals recorded and estimated by a suitable model [7]. The minimized merit function  $v(\Theta, \mathbf{u}_N, \mathbf{e}_N, \mathbf{y}_N)$  is a vector difference between the double integrated measured acceleration  $\mathbf{y}_N$  and a signal  $\hat{\mathbf{y}}_G(\Theta_o, \Theta_s, \Theta_e)$  predicted by an adaptive model of the host object and sensor subjected to the same excitation and disturbances  $\mathbf{u}_N$

$$v(\Theta, \mathbf{u}_N, \mathbf{e}_N, \mathbf{y}_N) = \sum_N \left\{ \left[ \hat{\mathbf{y}}_G(\Theta_o, \Theta_s, \Theta_e) \right]_{\mathbf{u}_N} - \mathbf{y}_N \right\}^2 \quad (3)$$

Sensor imperfections (e.g., nonlinearity and uneven gain) are either accounted for by the model or their combined impact is represented by suitable terms in the minimized merit function. Prediction error computation and subsequent iterative model tuning are schematically illustrated in Figure 3. The set of parameters to be estimated,  $\Theta = \{\Theta_o, \Theta_s, \Theta_e\}$ , comprises parameters of the host object,  $\Theta_o$ , sensor,  $\Theta_s$ , and noise,  $\Theta_e$ .  $N$  is the number of signal samples. The estimates,  $\hat{\Theta}$ , of the needed parameters are found as [7]

$$\hat{\Theta} = \arg \left\{ \min_{\Theta \in D_\Theta} [V(\Theta, \mathbf{u}_N, \mathbf{e}_N, \mathbf{y}_N)] \right\} \quad (4)$$

where  $D_\Theta$  denotes the domain of meaningful parameters.

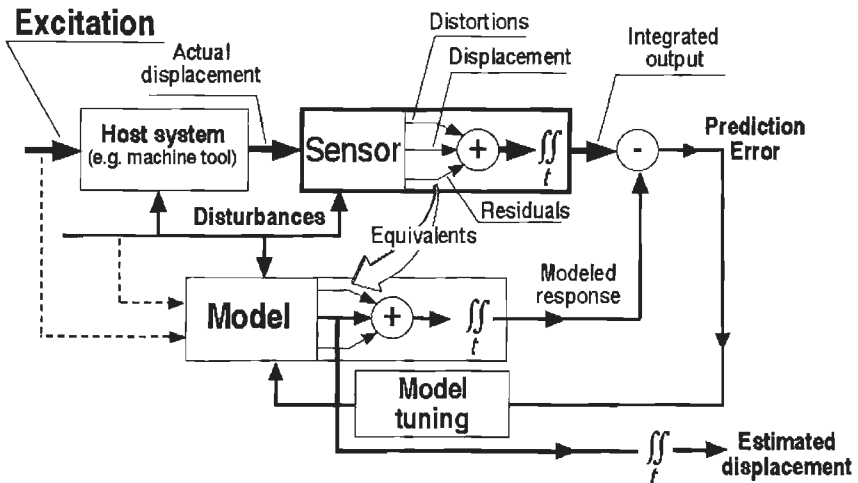


**Figure 3:** A block diagram of the model based, off-line displacement estimation.

The above algorithm applied to the double integrated acceleration signal shown in Figure 2 yields the estimated tool end deflection shown in Figure 4. Its profile is in a good agreement with the analytical prediction. Extensive tests of a representative micromachined accelerometer [8] conducted by the authors allow estimating the total measurement error to be below  $1 \mu\text{m}$ . Similar processing applied to signals from all IDS yields estimated displacements of the tested mechanical structure in response to the applied excitations. As an example, the displacement of spindle nose caused by the force impact at the end of the tool is also plotted in Figure 4. This latter signals is magnified ten times, since it is about the order of magnitude smaller than the tool end deflection. A knowledge of the forces acting on the system, resultant displacements, and deflection models of the spindle housing, shaft and tool facilitates quick and straightforward estimation of the interface stiffnesses of bearings and shaft-tool joint. A systematic validation of the signals used in the presented estimation procedure and the results obtained at various stages of computation is critical to avoiding gross errors. The application of IDS facilitates rapid inspection of the quasi-static force versus displacement plots that reveal nonlinearities of the investigated system and guide in choosing appropriate analysis methods.



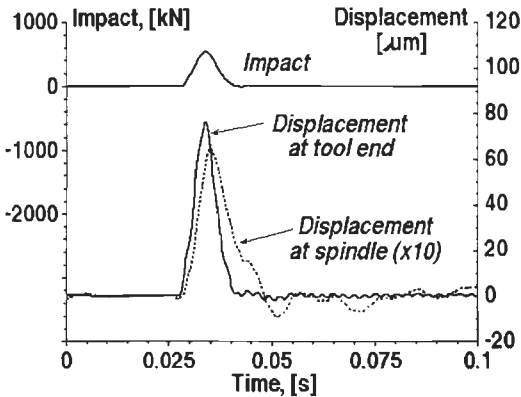


**Figure 4:** Impact force and corrected displacements of the tool tip and the spindle.

This is an important advantage of the proposed method as compared with the traditional modal analysis [6] involving inertial sensors, which is inaccurate and cumbersome when dealing with nonlinear systems.

## Conclusions

Theoretical analysis and experimental results indicate that state-of-the-art micro-machined accelerometers are suitable for Inertial Displacement Sensors that feature nanometer resolution and submicron accuracy. However, achieving such performances necessitates precise attenuation of signal

distortions caused by the employed transducers and disturbances acting on them. While this goal can be achieved in several ways, model based off-line estimation is particularly convenient due to its accuracy, robustness and simplicity of implementation. Since IDS measure displacements with reference to the inertial coordinate system of the Earth and do not require any physical reference base or fixture, they have the potential to eliminate disadvantages of currently used techniques and devices employed for the assessment of spatial dynamic and quasi-static properties of production equipment.

## References

1. Rockstad, H.K., et al., „A Miniature High Resolution Accelerometer Utilizing Electron Tunnelling“, ASME Winter Annual Meeting, DSC-Vol.40, pp.41-52, 1992.
2. Liu, C.H, et al., "Characterization of a High Sensitivity Micromachined Tunnelling Accelerometer with Micro-g Resolution", IEEE Jnl. of Microelectromechanical Systems, 7/2, pp. 235-244, 1998.
3. Huang, P.S., Li, Y., "Laser measurement Instrument for Fast Calibration of Machine Tools", Proc. American Society for Precision Engineering, vol. 14, pp. 644-647, 1996.
4. Knapp, W., Weikert, S., "Testing the Contouring Performance in 6 Degrees of Freedom", Annals of the CIRP, 48/1, pp. 433-436, 1999.
5. Heidenhain Corporation, "Measuring Systems for Machine Tool Inspection and Acceptance Testing", Schaumburg IL., 2001.
6. Ewins, D.J., "Modal Testing: Theory and Practice", New York Research Press, 1984.
7. Ljung, L., "System Identification: Theory for the User", Prentice-Hall, 1987.
8. Kistler Instrument Corp., "Type 8310A(X) K-BEAM Accelerometer", Amherst NY, USA, 2001.

# Dynamic Performance of a Cantilever-Based Topography Probe

D. G. Chetwynd<sup>1</sup>, R. K. Leach<sup>2</sup>

<sup>1</sup>School of Engineering, University of Warwick, Coventry CV4 7AL, UK

<sup>2</sup>Centre for Basic, Thermal & Length Metrology, National Physical Laboratory, Teddington TW11 0LW, UK

## Abstract

A variant of a previously-reported cantilever-based capacitive gauge for surface topography has been constructed as part of an evaluation of probing technologies. Somewhat like a scaled-up atomic force microscope, the probe allows good control of (low) contact forces at a sharp tip. Its relatively low sprung mass may allow use at higher scan speeds than conventional contact probes while maintaining fidelity. After a brief discussion of the design and dynamics of the probe operation, we discuss the results of frequency response tests on oscillating actuators and on sinusoidal surface artefacts. Encouragingly, there is no evidence of speed-related fidelity changes from causes such as surface friction.

## Introduction

Increasing use of high-performance technological surfaces requires improved standards for surface topography measurement and better characterization of calibration artefacts. At present, only stylus-contact methods are subject to standards and even these are rather loosely formulated. There is, therefore, continuous work on upgrading International Standards and calibration facilities. It includes the evaluation of alternative probe technologies, to recommend (or otherwise) their range of application, whether for industry or for specialist laboratories. One particular need is for nanometre-sensitivity probes with very sharp tips and well-defined contact forces in the micronewton to millinewton region. This might be satisfied by cantilever-style micro-displacement probes, rather like scaled-up versions of Atomic Force Microscope (AFM) tips, that have been reported occasionally over the last decade. The concept derives from the original work by Howard and Smith [1].

A variant of the cantilever probe design has recently been built for use on calibration systems. It is intended principally to operate in a 'constant force' mode similar to that of most AFMs. The tip is moved against the test surface until the measured deflection of the cantilever indicates that the contact force (i.e. the force bending the cantilever) is of the desired value. Then, the specimen is moved relative to the tip while the probe is servo-controlled in the z-axis to maintain a constant deflection of the beam. This mode allows high sensitivity in a small, low-mass sensor by relaxing the need for linearity over a significant range. Although calibration usually takes place at slow scanning rates, the low sprung mass also offers potential for measurements at higher speeds than the  $1 \text{ mm s}^{-1}$ , with frequency restricted to a few tens of hertz at micrometre amplitudes, that tend to be the limit of conventional probes. The tip-surface interaction might modify its dynamic performance, and so evaluation must be done under conditions similar to those of the target use. We report here on the first tests of this type.

### Probe design and operation

A schematic of the probe is shown in figure 1, where for clarity it is inverted – normally the diamond tip points vertically downwards. The base is a 'Zerodur' block 30 mm by 10 mm by 5 mm, which has been lapped along one face to leave a 5 mm long, 10 μm high ledge at one end. A 15 mm long glass beam with an evaporated gold coating on its upper surface is bonded to the ledge by a quick-drying silver-loaded paint that provides electrical connection. This results in a glass cantilever, approximately 10 mm long, 3 mm wide and 100 μm thick. Its free end is rather more than 10 μm below a gold electrode on the base when it is hanging freely in its normal orientation. The gold electrodes on the beam and base form a capacitive micrometry sensor of nominally 10 pF. A Berkovich cleaved diamond tip (tip radius less than 100 nm) is glued to the cantilever, nominally in line with the centre of the electrode. The theoretical stiffness of end-deflection of the ideal beam is 52.5 N m<sup>-1</sup>. The probe is hand-built and, with the accumulation of manufacturing errors, actual stiffness and mass are not closely controlled. The free beam and the additional tip are both in the region of 5 – 10 mg. The predicted resonance is at around 350 Hz.

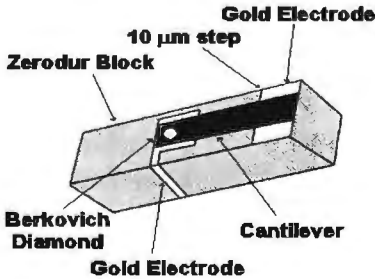


Fig. 1: Schematic of probe head (inverted).

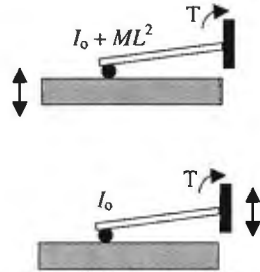
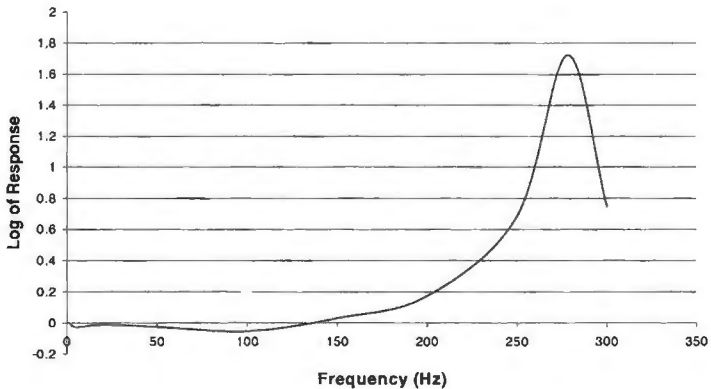


Fig. 2: Simple model of beam and contact

The frequency response of stylus probes is commonly measured by resting on a vibrating surface (a shaker) and comparing actual and reported amplitudes. 'Stylus bounce' occurs when the acceleration of the surface is greater than the acceleration of which the tip is capable. This happens when the reaction force between tip and surface becomes negative and is therefore a function of the static contact force and the amplitude of the oscillation, as well as of frequency. The test may not be fully relevant to the constant force probe. Figure 2 illustrates a simple model in which the cantilever is replaced by a rigid pinned beam and a restoring torque. When the surface moves vertically the reaction force drives the beam about its pin and the total moment of inertia is that of the beam plus the tip mass on its lever length. If the probe body is moved with the surface stationary, the tip does not translate and the moment of inertia about it is simply that of the beam. Here the masses of tip and beam are similar, so the moment of inertia in the second case is perhaps about 25% of that in the first. The resonance might then be different by a factor of about two. In constant force following the actual behaviour will be some intermediate between these two cases. The actual dynamics of follower mode are likely to be dominated by the servo-loop once the probe fundamental is above some hundreds of hertz.

## Experimental evaluation

Despite the above reservations, the probe was evaluated on an electromagnetic vibrating platform, built in-house from a monolithic flexure mechanism to give good stability at small amplitudes [2]. The log-linear response at a drive amplitude of around  $0.5\ \mu\text{m}$  is shown in figure 3. It has a classical form, rather than showing sudden onset of bounce, with a principal resonance at 278 Hz. The pattern is consistent with the design parameters, e.g. it could arise from an effective mass (derived from the total moment of inertia) of 10 mg and a static contact force of around  $100\ \mu\text{N}$ . It suggests that frequencies up to about 150 Hz could be recorded with good fidelity on sub-micrometre amplitude surfaces. 150 Hz corresponds, for example, to a  $50\ \mu\text{m}$  wavelength scanned at  $7.5\ \text{mm s}^{-1}$ . This is a fast speed for high precision topographic measurement. In constant force mode, the probe might be capable of even higher speeds.



**Fig. 3:** Frequency response of the probe on a shaker at  $0.5\ \mu\text{m}$  amplitude

The main sequence of variable speed tests on artefacts also operated the probe in constant height mode, allowing the contact force to vary slightly as the cantilever deflected. This mode avoids frequency effects from a servo-loop, but means that the beam acts in its higher inertia regime. The operation can be compared directly to the shaker tests. Effects caused by lateral sliding are likely to be similar in both modes of operation. The probe was mounted via manual precision height adjuster to a massive support resting on a granite table. It hung above the carriage of a high-precision linear motor driven air-bearing slide (Aerotec Inc.) that also rested on the table. Sinusoidal surfaces of various wavelengths and amplitudes were mounted on the carriage via a manual levelling stage and traversed below the probe in a nominally straight line at a range of speeds. Most surfaces were hard-coated nickel replicas of fly-cut profiles (Rubert Ltd). The probe is intended to be used such that lateral drag forces on the tip put the beam into tension during a measurement. Tests were also performed with the scan in the opposite direction.

The probe was operated with a Queensgate Instruments Nanosensor detector, providing an output of around  $0.6 \text{ V } \mu\text{m}^{-1}$ , with a useful range of about  $4 \mu\text{m}$ . Profiles were logged, at 5 or 1 kHz, by a 16-bit analogue to digital converter in a PC running LABVIEW software. Anti-aliasing filters were set at about 300 Hz, with 50 Hz used for slower tests to suppress any residual interference from electrical mains. There was no discernable difference in behaviour at moderate speeds with a  $100 \mu\text{m}$  sinewave of about  $3 \mu\text{m Rt}$  and a  $50 \mu\text{m}$  one of about  $1.5 \mu\text{m Rt}$ . Neither was there visible difference in the profiles from 'forward' and 'reverse' scans. At  $1 \text{ mm s}^{-1}$  the smaller specimen provides a 20 Hz signal with no visible degradation. Transient behaviour and a little more cycle-to-cycle variation was observed at higher speeds. It is, therefore, difficult to find a consistent, stable analytic (statistical) evaluation method and here simple estimates of amplitude are taken from cycles deemed 'typical' of the trace. Figure 4 shows a 160 Hz signal from the smaller specimen at  $8 \text{ mm s}^{-1}$ . As speed is increased further, the transient becomes more pronounced but the signal still settles. Even at  $14 \text{ mm s}^{-1}$  (close to the 280 Hz resonance), the signal remains similar to the low-speed version after the first 1 mm of scan.

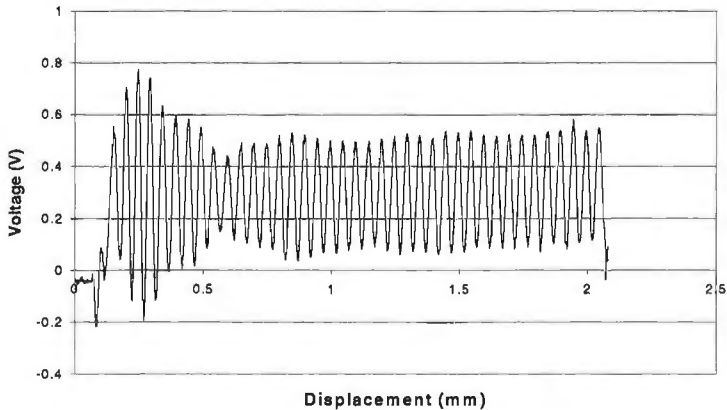


**Fig. 4:** 2 mm trace of  $50 \mu\text{m}$  sinewave at  $8 \text{ mm s}^{-1}$  (160 Hz)

## Conclusions

Although work to obtain more detailed information continues, the tests reported here suggest that glass cantilever probes should in practice operate satisfactorily at higher scan speeds than many of their rivals. They confirm tip-surface interactions do not undermine the response that might be expected from their low inertia. No runs have yet been performed above  $15 \text{ mm s}^{-1}$  in order to minimise risk to the tip, but this is at least an order of magnitude faster than used for most precision profilometry.

## References

- [1] Howard, L. P., Smith, S. T., Long range constant force profiling for measurement of engineering surfaces, *Rev. Sci. Instrum.* **63**, 4289-4295, 1992
- [2] Leach, R. K., Cross, N., Low-cost dynamic calibration of surface texture measuring instruments, *Meas. Sci. Technol.*, **13**, N1-4, 2002

## Accuracy of step height determination by Atomic Force Microscopy - results of an inter-laboratory comparison

M. Senoner<sup>1</sup>, L. Koenders<sup>2</sup>, W. Unger<sup>1</sup>, and G. Wilkening<sup>2</sup>

<sup>1</sup> Bundesanstalt für Materialforschung und -prüfung (BAM), 12200 Berlin  
Laboratorium VIII.23: Mikrobereichs- und Oberflächenanalyse; Rastermikroskopie

<sup>2</sup> Physikalisch-Technische Bundesanstalt, 38116 Braunschweig  
Fachbereich 5.1 Nano- und Mikrometrologie

### Abstract

An inter-laboratory comparison of step height determinations with Atomic Force Microscopy (AFM) was carried out involving 40 participants. Three standards with nominal step heights of 8 nm, 80 nm and 240 nm, respectively, were used as test samples. The trueness and precision of step height determination by the participating laboratories vary in a wide range. For step heights of 80 nm and higher the systematic deviations are predominantly caused by the calibration of the instruments. At smaller step heights the type of instrument used and the mode of contact between probe and surface are the dominating influences on the accuracy of measurements.

### Introduction

The growing importance of nanotechnology in industry leads to higher demands on the accuracy and reproducibility of scanning probe microscopy (SPM). In particular atomic force microscopy (AFM) is becoming a standard method for the analysis of surface topography in the nanometre range. Therefore it is necessary to characterise this method in relation to its accuracy.

An inter-laboratory comparison of step height determinations with AFM involving 40 participants from Germany (37), Switzerland (2) and the Netherlands (1) was carried out between summer 2000 and summer 2001. 19 different types of AFMs made by 10 different manufacturers were used. Participants came from industry (16), universities (10) and research institutes (14) and represent the community of AFM users.

### Samples

The step height standards with nominal step heights of 8 nm, 80 nm and 240 nm, respectively, were fabricated as prototypes by Nanosensors GmbH, Wetzlar, Germany. They are 5 x 7 mm silicon chips with different structures etched into thermal SiO<sub>2</sub> (80 and 240 nm) or direct into Si (8 nm). The AFM measurements were carried out inside an array of 4 µm x 4 µm square holes at the centre of the sample. Reference step heights were determined in 20 µm wide groves surrounding the square holes. They were measured using a Linnik-type Zeiss interference microscope [1].

The 80 nm and the 240 nm step height standards are coated by a metallic (PtIr - Cr) layer of about 70 nm in thickness, whereas the 8 nm standard is not metallised. For the 8 nm standards we found a systematic difference between results of AFM measurements and interferometric measurements, probably due to a different thickness of the native silicon oxide surface layer inside and outside of the etched holes. Therefore we used the median of all AFM measurements as internal reference value for the 8 nm standard.

## Results

In a first step we analysed the results of the participating laboratories in relation to the reference values. Fig. 1 gives a qualitative impression of trueness, i.e., the deviation from the reference value, and the precision, i.e. the straggling of results inside and between the laboratories. For this graphic representation we calculated the median because it is less sensitive to outliers than the arithmetic mean [2].

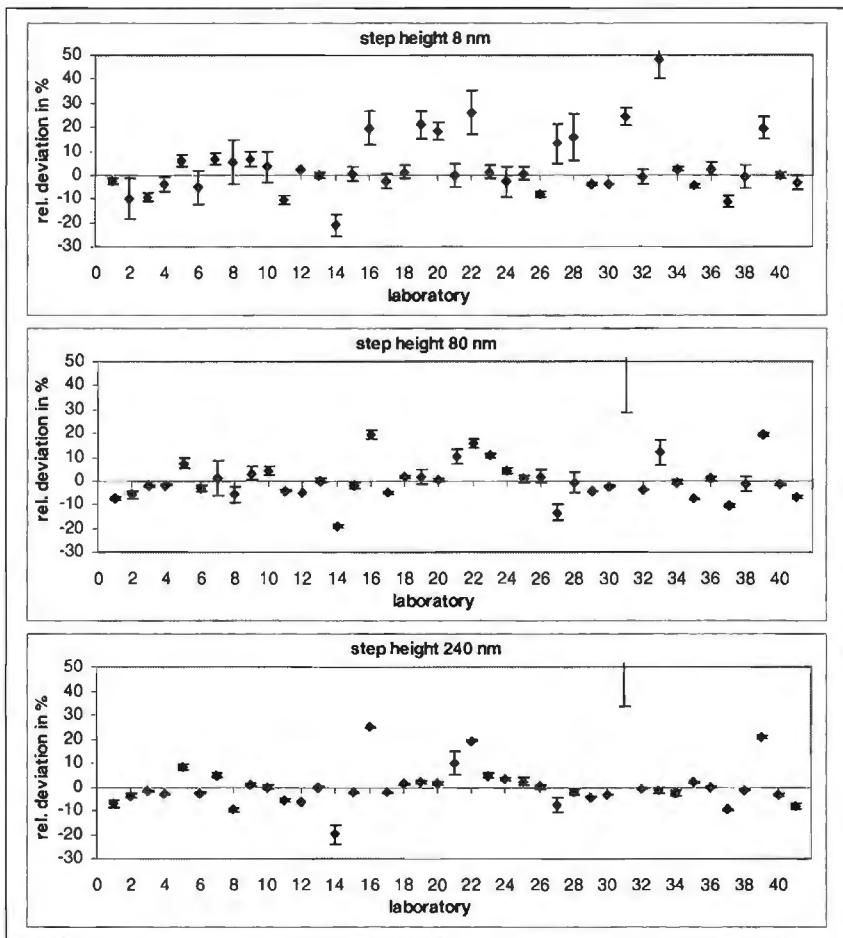


**figure 1:** Relative deviations of the laboratory medians from the reference values for the three step height standards. The bars are standard deviations calculated from the four measurements per laboratory.

For a more quantitative description of trueness and precision of the AFM method we evaluated the statistical parameters defined in ISO 5725 [3]. The bias of the measurement method is a measure of trueness and describes the systematic error of

the method. The repeatability standard deviation describes the straggling of values within

a laboratory, the between-laboratory standard deviation the straggling of values between the laboratories and the reproducibility standard deviation is a combination of both. Additionally we calculated the arithmetic mean of deviations which reflects the mean trueness of the participating laboratories. Table 1 gives the statistical parameters based on ISO 5725 [3], but modified by replacing the arithmetic mean with the median for the sake of robustness [2]. All parameters in table 1 were calculated without the extreme scores of laboratory 31 for 80 nm and 240 nm (see fig. 1).

statistical parameters		step height		
		7,6 nm	81,2 nm	258,1 nm
repeatability standard deviation $s_r$	absolute	0,40 nm	1,9 nm	3,4 nm
	relative	5,3%	2,3%	1,3%
between-laboratory standard deviation $s_L$	absolute	0,96 nm	6,1 nm	19,5 nm
	relative	12,6%	7,5%	7,6%
reproducibility standard deviation $s_R$	absolute	1,04 nm	6,4 nm	19,8 nm
	relative	13,7%	7,9%	7,7%
bias of the measurement method	absolute		-0,6 nm	-2,0 nm
	relative		-0,7%	-0,8%
arithmetic mean of the absolute deviation	absolute	0,65 nm	4,7 nm	13,9 nm
	relative	8,5%	5,7%	5,4%

**table 1:** Parameters characterising the accuracy of atomic force microscopy

The bias of the method is less than 1% and not significant. The absolute standard deviations increase sub linearly with increasing step height from 8 nm to 80 nm and, therefore, the relative standard deviations decrease with step height. Above 80 nm the relative reproducibility standard deviation is nearly constant. That means that the systematic deviations of the individual laboratories increase linearly with step height and point at a dominating influence of the calibration of the instrument. Recent comparisons for stylus instruments [4] and scanning probe microscopes [5] were carried out without the calculation of statistical parameters after ISO 5725 [3] as it has been done in this study.

The deviations of the laboratories (fig. 1) show similar patterns for the 80 nm and 240 nm standards. That points to a common origin of deviation - the calibration. Thus we determined a calibration correction factor for every instrument from a division of the 240 nm reference value by the 240 nm laboratory median. In a second step we multiplied the 8 nm and the 80 nm laboratory medians by this correction factor. Fig. 2 shows the effect of this procedure, which drastically decreases the deviations at 80 nm. The calibration correction reduces the reproducibility standard deviation at 8 nm steps from 1.04 nm to 0.95 nm (reduced by 9%) and at 80 nm steps from 6.4 nm to 3.3nm (reduced by 49%). In addition to reproducibility precision the calibration correction also influences the trueness of the results measured at the 80 nm step height. The fraction of laboratories with systematic deviations below 2% increases from 32% to 61% and the fraction of laboratories with systematic deviations above 4% decreases from 54% to 17%.



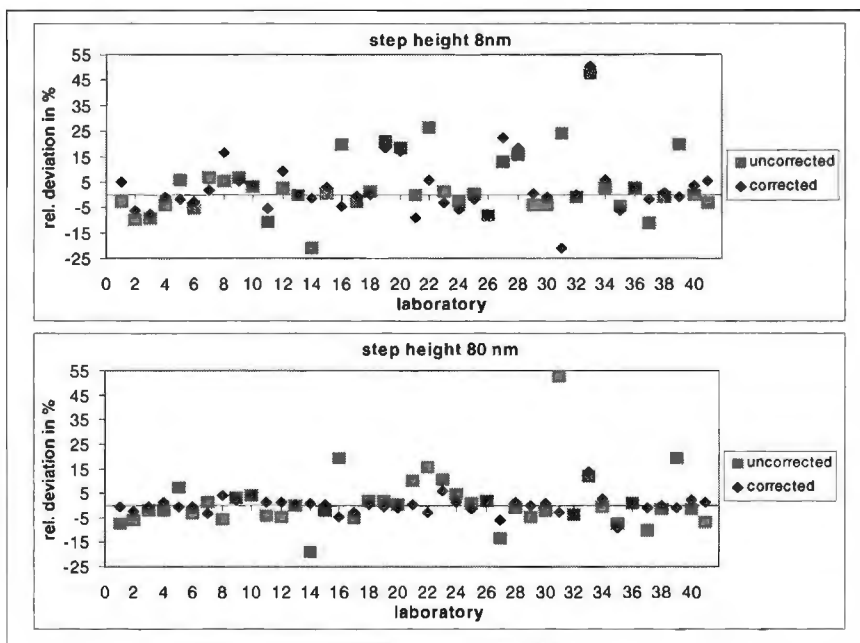


**figure 2:** Influence of a calibration correction on the relative systematic deviation of the laboratory medians for different step height standards

The calibration correction shows on the other hand, that for 8 nm steps other effects than calibration should have a stronger influence on precision and trueness. We found a strong influence of the type of instrument used and the mode of contact between probe and surface. Measurements in the contact mode are less accurate than those in the intermittent-contact mode or the non-contact mode.

## References

- [1] Koenders, L., Krüger-Sehm, R., and Wilkening, G.: Calibration of transfer standards for SPM, Proc. 4<sup>th</sup> Seminar on Quantitative Microscopy, 2000, Semmering, Austria, PTB-Bericht F-39, Braunschweig 2000, 25 - 29
- [2] Senoner, M.: Auswertung von Ringversuchen zur Verfahrensvalidierung, Materialprüfung 43 (2001), 298-303
- [3] ISO 5725 "Accuracy (trueness and precision) of measurement methods and results" part 1 and 2 (1994)
- [4] Haitjema, H.: International comparison of depth-setting standards, Metrologia 34 (1997), 161 - 167
- [5] Rothe, H., Wilkening, G., and Hueser, D.: Recommendations for the metrological calibration of SPMs: a survey on the European SPMet network project, Proc. SPIE Vol. 4449 (2001), 212 -224

## Miscellaneous



# INVESTIGATION OF GROOVED HYBRID AIR BEARING PERFORMANCE

P. Stanev<sup>1</sup>, F. P. Wardle<sup>2</sup>, J. Corbett<sup>1</sup>

<sup>1</sup>Cranfield University, School of Industrial and Manufacturing Science, Cranfield, Bedford, UK

<sup>2</sup>Loadpoint Ltd, Cricklade, Swindon, UK

## Abstract

Herringbone grooves machined into aerodynamic bearings are well known to produce improvements in bearing stiffness and stability at high operating speeds. In this investigation the effect of herringbone grooves on the performance of an externally pressurised air bearing is examined. A mathematical model based on previous research has been developed and used to optimise the design of an air bearing suitable for use in ultra high speed machining spindles. Experimental results show the spindle to run satisfactorily at speeds in excess of  $3.0 \times 10^6$  DN (bearing bore in mm x shaft speed in rpm) being limited only by the maximum speed of its drive motor.

## Introduction

The field of ultra high speed machining embraces applications such as bore grinding, milling, micromachining and printed circuit board drilling where spindle speeds are often well in excess of 100 000 rpm. At such high speeds externally pressurised air bearing spindles are the preferred choice as they offer the principal advantages of improved life and reliability, low friction losses and low motion errors compared to other spindle types. The inherently low load carrying capacity and stiffness of air bearings are a disadvantage in these applications but is minimised by designing for high surface speeds, in excess of  $3.0 \times 10^6$  DN, thus allowing large bearing diameters to be used. Since, at these surface speeds, pressure distributions within aerostatic journal bearings are dominated by aerodynamic effects the bearings are prone to the half speed whirl instability well known on aerodynamic bearings [1]. As for the aerodynamic bearing, half speed whirl on an ultra high speed aerostatic bearing is a destructive instability which ultimately limits bearing speed. Past research [2, 3, 4] has shown that the addition of herringbone grooves to aerodynamic journal bearings can produce large improvements in stability and stiffness at high speeds and grooved bearings are now widely used in light load high speed applications such as optical scanners. With the need for still higher aerostatic bearing speeds as well as improvements in stiffness and in the light of past research on aerodynamic bearings this investigation is primarily concerned with determining the effect of herringbone grooves on the performance of externally pressurised bearings. This type of bearing is referred to as a grooved hybrid bearing (GHB) as it combines aerostatic and aerodynamic design principles.

## Bearing Analysis

The bearing configuration analysed is shown in fig 1. It is supplied with externally pressurised air through one or two rows of orifices placed symmetrically with respect to a radial plane through the bearing centre. The orifices are assumed to feed recesses of known depth and diameter positioned at entry to the bearing gap and the axial positions of orifices and recesses are constrained to be inboard of the grooves. Grooves may be cut into the shaft or the journal and are arranged so that the shearing action produced by shaft rotation pumps air towards the centre of the

bearing, against the aerostatic pressure gradient. In the analysis it is assumed that there are a sufficiently large number of orifices to approximate a line feed and that there are a large number of grooves. The axial length of the grooves, groove angle, depth and width ratio are normal bearing design variables. As in [5] the analysis comprises of two parts: a steady state analysis assuming the shaft to rotate concentrically within the journal and a perturbation analysis assuming the steady state equilibrium is disturbed by a small radial force. The latter assumes linear radial load–deflection characteristics and is accurate for the small deflections encountered in high-speed spindles. Analysis of the airflow within the bearing gap follows that of a grooved aerodynamic bearing [2] with the exception that there is now a net axial mass flow rate of air. For the steady state analysis this mass flow rate is balanced against that through the orifices and recesses to determine the aerostatic pressure in the bearing gap immediately downstream of the recesses.

The analysis was implemented in the form of a computer model for evaluating the effect of important parameters upon bearing performance over a wide range of operating conditions. Parameters included as input data to the model are bearing length, diameter and clearance; position, number and diameter of orifices; recess diameter and depth; groove length, angle, depth and width ratio; air supply pressure and bearing speed. Important output parameters include radial stiffness, stability factors, attitude angle, whirl ratio, pressure in the bearing gap and air mass flow rate. All output parameters are plotted as a function of Compressibility Number defined to be:-

$$\Lambda = 6\mu\omega(R/C)^2/P_a$$

where  $\mu$  is the viscosity of air,  $R$  the bearing radius,  $C$  the bearing clearance over ridges,  $P_a$  is atmospheric pressure and  $\omega$  is the bearing's rotational speed.

### Bearing Optimisation

The computer model was used to perform parametric studies in order to determine the effect of groove parameters on bearing stiffness and stability and hence to define an optimum GHB design. Fig 2 is an example of the effect of groove depth on non dimensional load over a practical range of compressibility numbers. Since the analysis was based on the assumption of linear load-deflection characteristics the non dimensional load parameter is directly proportional to bearing stiffness. Fig 2 shows a number of interesting features. Firstly that at low compressibility numbers the plain aerostatic bearing has a higher stiffness than a GHB, all other parameters remaining the same. Secondly, in contrast to the plain bearing, the GHB continues to increase in stiffness with increasing compressibility number. Thirdly that there is an optimum groove depth, approximately equal to the bearing gap, which gives maximum stiffness at high compressibility numbers. Finally that a GHB with an optimised groove depth will only exhibit a higher stiffness than a plain aerostatic bearing when the compressibility number is relatively high. Fig 3 is an example of the relative effect of groove depth on whirl stability. The stability factor may be regarded as a measure of the maximum mass that the bearing can support without whirling. For all groove depths this mass decreases as compressibility number increases. At low compressibility numbers the stability factor reduces with increasing groove depth whereas at compressibility numbers of more than 20 the converse is true, i.e. stability increases with groove depth. At high compressibility numbers the additional stability due to grooving allows an increase in bearing speed to be achieved before the onset of half speed whirl. This increase is dependent on the bearing-shaft's designed

operating compressibility number and can be substantial for compressibility numbers of more than 30.

The criterion for bearing optimisation was chosen to be maximum stiffness at maximum speed and a stability factor sufficient to prevent whirl throughout the operating speed range. This was applied to the bearings in a machining spindle supporting a 25.4 mm diameter shaft rotating at speeds up to a maximum of 120 000 rpm. Optimised bearing parameters are:-

Bearing diameter (mm)	-	25.4
Bearing length (mm)	-	50.8
Gap over ridge (um)	-	15.0
Axial groove length (mm)	-	12.7
Groove angle (deg)	-	30.0
Groove width ratio	-	0.5
Groove depth (um)	-	16.5
No. of grooves/row	-	16

### Experimental Work

A machining spindle with the optimised bearing design was manufactured for experimental evaluation. The spindle was driven by an integral high frequency motor located midway between the two journal bearings. Axial location was provided by a double acting thrust bearing positioned at the rear of the shaft. The spindle was instrumented to enable bearing pressure, shaft error motion and spindle stiffness to be measured over a range of speeds. To facilitate pressure measurement three transducers were mounted at different axial positions in one of the journal bearings. Shaft error motion was measured in two orthogonal radial planes by capacitance displacement sensors mounted at the spindle nose and stiffness was measured by monitoring displacement whilst applying known radial loads to the end of the shaft via a slave air bearing. Stiffness measurements were limited to speeds of less than 60 000 rpm due to the slave bearing characteristics. At higher spindle speeds the slave bearing was removed.

The spindle was run to a maximum speed of 120 000 rpm, limited by the integral motor and drive. No indication of whirl instability was found within the operating speed range. Fig 4 is an example of experimental measurements taken and shows how the pumping effect of the grooves increases aerostatic pressure within the bearing even when the shaft is rotating concentrically within the journal. These experimental measurements of pressure were taken midway between two orifices in one of the two orifice rows and are compared with a theoretical prediction from the computer model corrected for dispersion of air from discrete feed positions instead of the model's assumed line feed. At rotational speeds in excess of 80 000 rpm pressure increases more rapidly with speed due to centrifugal growth of the shaft reducing bearing clearance and hence increasing compressibility number.

### Concluding Discussion

The addition of herringbone grooves to aerostatic bearings has a significant effect on performance. In the ultra high speed machining spindle application it is the effect of grooves on bearing stiffness and stability which is of primary interest. Parametric studies performed with a computer model show that grooves only have a beneficial effect on these parameters at high compressibility numbers. For bearings designed to operate at compressibility numbers of more than 30 the benefits can be



# Study on an Automatic Geometric Feature Recognition for Sculpture Surface Machining

X. Zhang, J. Wang, K. Yamazaki

IMS Mechatronics Laboratory, Dept. of Mechanical and Aeronautical Engineering,  
University of California, Davis, CA 95616, USA

## Abstract

The paper describes the study results on the systematic methods to automatically recognize the geometric features for sculpture surface machining. The study includes the development of the hierarchical processing sequence for automatic classification of sculpture surface geometry such that the features classified can easily be related to machining methods. The hierarchical structure of the classification consists of four layers, starting from surface subdivision and ending with the particular recognized machining feature. Based on the study results, the computer algorithms have been designed and the feasibility of the proposed methodology has been verified by developing the prototype system.

## Introduction

Higher quality with high productivity in machining of sculpture surfaces is recently primary interested in the high value added manufacturing industries, such as die and mold manufacturing industries, aerospace part manufacturing industries, etc. Normally, manufacturing of sculpture surfaces in the actual factory needs the manual polishing process after the machining process. Since manual polishing is usually a very time consuming process, it becomes a bottleneck to enhance the productivity of sculpture surface machining. One solution to overcome the problem is to enhance the surface quality by machining operation, which may minimize or eliminate the post polishing process. In order to achieve this, very careful tool path generation for CNC finishing operation is required with respect to the specific geometric feature of sculptured surfaces. For this, nowadays the operator has to manually select the local geometry piece by piece to prepare the NC program, which takes a lot of time and becomes a bottleneck to the productivity. Therefore, it is very important to automatically recognize the machining features of the sculptured surfaces from the finish machining technology point of view.

In the past two decades, although the researches on the automatic machining feature recognition were studied and a lot of algorithms were proposed [1,2], most of them focused on the recognition for 2D or 2½D machining features. However, the researches on the recognition of sculptured surface feature have not been yet been well studied.

To meet the requirement and solve the problems mentioned above, the research has been proposed to develop an automatic geometric feature recognition system, which may possibly allow the autonomous operation planning for sculptured surface machining in feature based intelligent CAM system [3]. In this paper, a surface-based evaluation method was presented to recognize the machining features. The basic functionality of the machining feature recognition system was introduced, and the prototype system has also been developed based on the proposed algorithm.



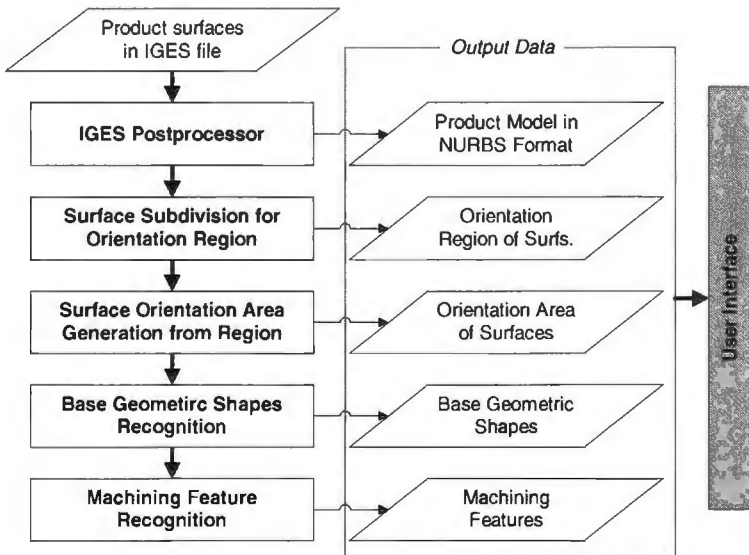


Figure 1: System frame of automatic feature

## Processing sequence of automatic feature recognition system

### System components

Figure 1 shows the structure of the automatic feature recognition system developed in the study, which consists of five steps of processes—IGES postprocessor, surface subdivision into orientation regions, surface orientation area generation from regions, base geometric shape recognition and machining feature recognition.

The first module, IGES postprocessor, translates a CAD data file into a proposed object-oriented data structure, which represents the product surface in the form of trimmed NURBS surfaces shown in Figure 2 (a).

The second module analyzes product surface model to generate the connectivity edge list among surfaces in Figure 2 (b) and subdivides each NURBS surface into orientation regions, which is mainly performed in the 2D parametric domain, as shown in Figure 2 (c). Each surface patch will be subdivided into five different types of regions (horizontal, +x, -x, +y, -y) by checking their surface normal vector over a certain point density grid. And the tiny surfaces will be detected by counting the number of inside rectangles on the grid. Surface coordinates, normal vector and curvature will be calculated on the grid and these will be saved with the surface for the downstream usage.

The third module first generates the connecting edge list among the regions and establishes the links both from 2D edge to 3D edge of the same region and from 2D edge to 2D edge of different regions. Then the orientation areas are generated by collecting all the connecting regions with the same orientation in Figure 2 (d). The

boundary loops of each orientation area will also be generated by searching the connectivity edge list of orientation regions. And outside loop and inside loop can be distinguished by checking the coordinate bounding box of each loop.

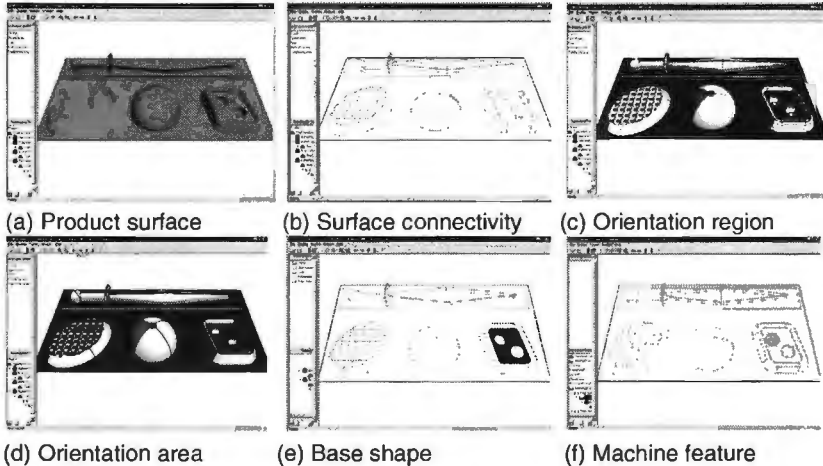


**Figure 2:** Example of Sequential Processing Steps

The fourth module analyzes the connecting orientation areas and recognizes the base geometric shapes in Figure 2 (e). It starts from searching a horizontal area. It is noted that the boundary edges of the horizontal area are 2D curves, which orientations determine whether the side areas connecting to the edge are upside or downside to the horizontal area. By checking each boundary loop of the horizontal area, the type of the sidewall will be decided, and then the type of base shape could be determined.

The last module analyzes the recognized base geometric shape and recognizes machining features by checking their curvature pattern, inclination and position of surfaces, shown in Figure 2 (f). After the determining the type of base shape, we will calculate the bounding box of the base shape in 2D. If the orientation areas are totally outside of the bounding box, they will be discarded from the base shape.

### Base geometric shapes and machining features

The number of possible features that can be recognized is infinite; however, it is possible to classify possible features into a finite number of families. If this can be done, a process planning system can be designed to support each feature family instead of individual features. With this in mind, the system proposed in this paper first recognizes the base shapes, and then recognized the machining features based on the base shapes and related machining strategy.

In the paper, we define one feature as one portion of product surface to be machined. All the features can be categorized into four base shapes: cavity, open cavity, core and face. Within each general feature type there are several regular shape feature types (such as hole, slot, boss etc.) as well as freeform feature types. Since the base shape has been recognized in term of horizontal area, the strategy, from top to down or from bottom to up, has been adopted to find out the base shapes. Therefore, categories of base geometric shapes are shown in Figure 3.

which include top-down core, top-down cavity, bottom-up cavity, open cavity, and bottom-up core. To recognize all possible base shapes on the product surface, it is noted that some of the special features are also included in Figure 3, like peak vertex and horizontal sharp edges. Figure 4 shows all the 2½D-machining features supported by the prototype. Meanwhile, the constant inclination surface could be recognized, which can be machined using one tool if necessary.

### **Implementation of the system**

The prototype has been developed using Pentium III PC computer on the Windows NT operating system. The development platform is Visual C++ V6.0, and the 3D graphics display interface is OpenGL.

Right now, the prototype system can read in product surface model in trimmed NURBS surface format from an IGES text file. It can also display the product model with rotate, zoom and pan capabilities both in shading and wire-frame mode. The object for display can be switched to any level of the five levels of machining model and the recognized base shapes and machining features can be displayed one after another. A product model from company was utilized to test the capability of the prototype. Some analyzed results for each step are shown in Figure 2. Currently this system can only deal with the recognition of 2½D machining feature, constant inclination surfaces and flat horizontal surfaces from the sculpture surface model. More complicated features will be recognized after the machining strategy is determined.

### **Conclusions**

- The definition and classification of geometric features for sculptured surface machining have been studied.
- Algorithm of geometric feature recognition has been proposed and the prototype system has been developed.
- The prototype system has been tested with product models from industry and satisfactory results have been obtained.

### **References**

1. Shah, J.J., "Assessment of feature technology", Computer-Aided Design, Vol.21, 1990, p.331-343.
2. Han, J.H., et al. "Manufacturing feature recognition from solid model: a status report", IEEE Trans. on Robotics and Automation, Vol.16, No.6, 2000, p782-796.
3. Yamazaki, et al., "Autonomous process planning with real-time machining for productive sculptured surface manufacturing based on automatic recognition of geometric features", Annals of the CIRP, Vol.44, No.1, 1995, p439-444.

# Interaction between adjustment philosophy and precision engineering

J.F.F. Klinkhamer<sup>1</sup>

<sup>1</sup> TNO TPD, Delft, The Netherlands

## Abstract:

In the design of opto-mechanical systems, the adjustment approach is of vital importance to the success of the product and should be an integral part of the concept design. This is even truer in developments where cost of goods is of importance.

In this paper a method is presented in which a document holding the adjustment procedures created in an early stage of the design and how it evolves with the (opto)mechanical design. Also the (proposed) procedure steps have to be subjected to a verification process, in which for each step it shall be checked whether an operator is capable of performing the required adjustment.

## Introduction

The introduction of Design for Manufacture (DFM) and Design for Assembly (DFA) methodologies (see e.g. [1] and [2]) has already stressed the importance to take manufacturing and assembly issues into account in the design process. In the design of a complex opto-mechanical system the necessary adjustments can have an impact that easily exceed the time required for manufacturing and assembly. As such it is even more important to include the adjustment approach in the design process.

Opto-mechanical adjustments will require involvement of several disciplines:

- the measurement system will often be based on optical principles
- the mechanics has to provide the adjustable components and the means to mount the measurement system
- electronics and software will be required to translate the optical signals and introduce e.g. image processing
- an operator has to perform the actual adjustment in a production environment

This number of players and the complexity of the actions that is mostly involved requires that the procedures and tools which are defined for the adjustments are laid down in a document. The previously stress importance to include development of adjustments in the design process means that the first version of this document has to be available already in the concept phase of the system design.

## Survey

Figure 1 visualizes the adjustment-related activities that can be performed during the design process. It is also indicated what the contents of the adjustments documents is, and how it evolves during the design process.

The next sections clarify the different steps

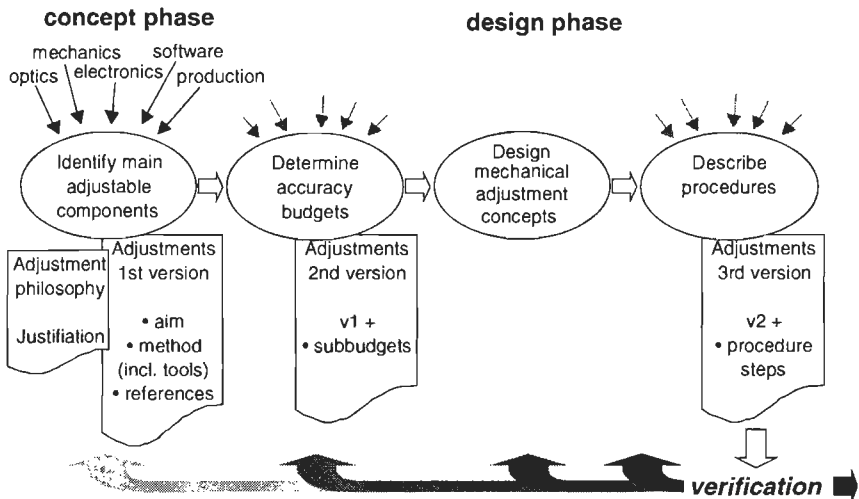


**figure 1:** Development of adjustment approach embedded in product development, with evolution of adjustments document

### Concept phase

First it has to be clear that good adjustment philosophy is an integral part of a good concept. The method presented here does not in any way replace that

In this phase the components to be adjustable and the degrees of freedom in which they should be adjusted are defined. The tendency to 'make everything adjustable' (as mechanical engineers often say of optical designers) has to be traded off against manufacturability and cost. The result of this trade-off can be described in a chapter of the document describing the concept. This 'adjustment philosophy' already creates a degree of clarity for the design team. However, during the definition of the concept thought concerning the aim, requirements and method of the adjustment will inevitably be suggested. In my recent projects I started to the adjustments document with these (sometimes-immature) ideas, in order to give insight in the design work, and to encourage discussion concerning the adjustments.

In the first version of the document each defined adjustment procedure is identified, as given in the example in table 1.

Note that in this phase only the outline of the procedure is described. Details will follow later. Note also that a co-ordinate system is assumed to be known. The definition of co-ordinate systems used in an opto-mechanical design is worth special attention; unclear definitions can cause costly mistakes. My personal experience is that a definition based on the optical system ( $z$  across the optical axis) is a good basis.

**Table 1** : Example of one entry of an adjustment procedure in the concept phase

<b>Rx, Ry adjustment of end mirror in projection optics</b>	
Aim:	Align optical axis of IO to optical axis of PO
Notes	The procedure assumes that when a ray exiting perpendicular to the F-lens face exits the optics frame perpendicular to the interface plane to the IO, that the aim is reached
Tools:	Theodolite Flat mirror to be mounted on interface plane to IO coupling plate Reference block to be mounted on position of F-lens
Precond:	Setup as drawn in figure #
Postcond	End mirror adjusted and locked
Accuracy	Rx: 500 urad (total) Ry: 500 urad (total)
Procedure	Autocollimate on flat mirror adjusting theodolite, remove flat mirror and adjust end mirror until autocollimation is restored.

### Design phase

Knowing only what the total accuracy of an adjustment is may feel natural in the concept phase, but it is not sufficient to start the detailed mechanical design. Therefore one of the first things to do after the adjustment sequence has been described, is to determine what part of the budget is available as accuracy for the mechanical adjustment. (In one project I started defining the mechanical budgets, based on a worst case approach, because the worst-case accuracy was feasible without complex design anyhow.)

After that, it is possible to start with the design of the mechanics holding the optical elements, since it is known which components are to be adjusted and how. Using the basic information of the adjustment procedures, the envelope of the tools can be estimated and included in the design, and when necessary development of tools can start.

It is very possible that the feasibility of the adjustment concept is already attacked in this phase. One of the reasons to introduce the document is to offer the designers a clear target.

In the design phase not only the hardware has to be worked out in greater detail, also the procedures have to be designed. This means that rough outline that was present in the concept phase has to be transformed into a step-by-step procedure. It is similar to making a 3D drawing, only when the subsequent steps are clearly described conflicts will become visible. As an example, table 2 gives the first procedure steps for the adjustment procedure mentioned in table 1.

**Table 2** : Example of procedure steps for an adjustment procedure

	Mount PO in laser tool
	Mount PO Reference Mirror Block in PO
	Mount Flat Mirror tool on PO
	Mount detector of light power meter behind hole of Flat Mirror Tool
	Set laser beam perpendicular to flat mirror tool (see figure #) Criterion: reflected laser spot has to return to the pinhole in front of laser <i>This aligns the laser beam in RxRy with the nominal IO co-ordinate system</i> <i>Accuracy for this step: Rx: 500 urad, Ry: <math>\pm 500</math> urad, which means a concentricity of the laser spot with the pinhole of TBD mm</i>
	Shift xy-position of laser beam until light power meter indicates maximum light power <i>This aligns the laser beam in xy with the nominal IO co-ordinate system</i> <i>Accuracy of this step: x: <math>\pm 0.05</math> mm, y: <math>\pm 0.05</math> mm</i>

### Verification

Making the adjustments document available in the design team may already improve the design process because the whole team has an insight in the adjustments. It will thus be avoided that an adjustment has to be added after all the hardware has been built. But the definition of the adjustments in an early stage of the project also opens the possibility to verify whether the designed procedure is practically feasible.

For this verification several methods are available:

- review with operator that are familiar with similar adjustments
- analysis of the feasibility and accuracies of the adjustment
- test using a (laboratory) testbench
- simulation of the procedure

The simulation can be especially fruitful if the adjustment is based on the human capability to deal with coupled degrees of freedom. In this way the feasibility of an adjustment in six degrees of freedom with internal couplings was shown to be feasible before the actual hardware was built.

A failure in the verification may only mean that the procedure is in need of rewriting. It also may lead to the necessity to redesign a tool, or in the worst case to modify or change the concept. As such the introduction of the adjustments document and associated process does not remove the risk of a serious redesign. It only offers earlier and wider distribution of the adjustments within the system as a whole.

### References

- [1] D.M. Anderson: Design for Manufacturability, CIM Press, Lafayette, CA, 1990.
- [2] K.Crow: Design for Manufacturability / Assembly guidelines, DRM Associates, 1998.
- [3] K. Otto: Robust Product Design Using Manufacturing Adjustments, Design Theory and Methodology Conference, ASME, Minneapolis, MN, pp.1-8, 1994

## Phase reconstruction using spline regression

X. Liu, Y. Gao

Department of Mechanical Engineering, Hong Kong University of Science and Technology, Clear Water Bay, Kowloon, Hong Kong

### Abstract

In shearing interferometry, the current phase reconstruction algorithms have a problem in dealing with shears being greater than the sampling resolution that is determined by the CCD in use. To solve the problem, a new algorithm is proposed to handle the phase reconstructions without compromising on the sampling resolution. The algorithm makes use of the smoothing characteristics of general wavefront phases together with a spline regression. Results of computational studies show that the proposed algorithm is feasible and effective.

### Introduction

Various approaches have been attempted for phase reconstruction problem in shearing interferometry [1-7]. However, most of them are based on the premise that the sampling point distances are equal to the shear quantities, which means lower resolution when the shear quantities are large.

In this case that shear quantities are many times of the sample point distance, say  $sN$  for  $x$  direction and  $tN$  for  $y$  direction, the obtained shearing phase data are not the differences of the test phase on neighbor sampling points, but the differences of the sampling points whose distances are  $sN$  or  $tN$ . As a result, the test phase cannot be recovered from the phase difference data directly by the current algorithm such as integration while keep the lateral resolution as the sampling resolution.

To solve the phase reconstruction problem with high lateral resolution in such case, a novel algorithm is proposed. Firstly the obtained bi-direction phase differences data by shearing interference measurement are distributed into  $sN \times tN$  groups to form  $sN \times tN$  pairs of bi-direction phase difference data, with the distance between the picked points in every difference data equals to shear quantities, so that the current phase recovery operation can be applied to them respectively to obtain  $sN \times tN$  recovered results. These recovered results are obviously from the same test wavefront phase with only tiny translations from the test phase. Making use of the smoothing characteristic of general wavefront phase, a spline smoothing regression algorithm then can be applied to the combined recovered results to obtain the translation values. The values are applied to the  $sN \times tN$  recovered results to form the final test phase.

### New reconstruction algorithm

In shearing interferometry, bi-direction shearing interfering phases are obtained to reconstruct the test wavefront phase. Suppose  $N \times M$  is the area size of the test wavefront phase  $w_{i,j}$  ( $1 \leq i \leq N$ ,  $1 \leq j \leq M$ ) in sampling point,  $sN$  and  $tN$  are the shear quantities by sampling point number along  $x$  and  $y$  direction. When the shear quantities are both only one sampling distance, which means  $sN=1$  and  $tN=1$ , the test phase can be obtained from the shearing phase differences  $\varphi^x_{i,j}$  and  $\varphi^y_{i,j}$  ( $1 \leq i \leq N$ ,  $1 \leq j \leq M$ ) by the current algorithms [1-4]. When  $sN > 1$  and  $tN > 1$ , however, the obtained shearing phase data are not the differences of the test phase on neighbor sampling points, but the differences between the two sampling points whose distances are  $sN$



or  $tN$ . In the case the test phase cannot be recovered from  $\varphi^x_{i,j}$  and  $\varphi^y_{i,j}$  directly by the current algorithms while keep the lateral resolution as the sampling resolution.

In the proposed algorithm for the objective to keep the sampling resolution as the lateral resolution in such case, the phase difference data  $\varphi^x_{i,j}$  and  $\varphi^y_{i,j}$  are firstly separated into  $sN \times tN$  groups, respectively, with that the distance between any two neighbour points in every group equals to the shear quantities,  $sN$  in  $y$  direction and  $tN$  in  $x$  direction, which consist of  $sN \times tN$  pairs phase difference data as follows:

$$\begin{array}{ll}
 \text{Pair } (i-1)sN+j: & \varphi^y_{i,j}, \varphi^y_{i,j+tN}, \dots, \varphi^y_{i,j+m^*tN} \\
 \varphi^x_{i,j}, \varphi^x_{i,j+tN}, \dots, \varphi^x_{i,j+m^*tN} & \varphi^y_{i+sN,j}, \varphi^y_{i+sN,j+tN}, \dots, \varphi^y_{i+sN,j+m^*tN} \\
 \varphi^x_{i+sN,j}, \varphi^x_{i+sN,j+tN}, \dots, \varphi^x_{i+sN,j+m^*tN} & \dots\dots \\
 \dots\dots & \varphi^y_{i+n^*sN,j}, \varphi^y_{i+n^*sN,j+tN}, \dots, \varphi^y_{i+n^*sN,j+m^*tN} \\
 \varphi^x_{i+n^*sN,j}, \varphi^x_{i+n^*sN,j+tN}, \dots, \varphi^x_{i+n^*sN,j+m^*tN} & (1)
 \end{array}$$

where  $n=N/sN, m=M/tN, 1 \leq i \leq sN, 1 \leq j \leq tN$ .

An existing algorithm is applied to every pair of phase difference data to build a phase respectively as:

$$\begin{array}{c}
 \text{Group } (i-1)sN+j: \\
 p_{i,j}, p_{i,j+tN}, \dots, p_{i,j+m^*tN} \\
 p_{i+sN,j}, p_{i+sN,j+tN}, \dots, p_{i+sN,j+m^*tN} \\
 \dots\dots \\
 p_{i+n^*sN,j}, p_{i+n^*sN,j+tN}, \dots, p_{i+n^*sN,j+m^*tN} \\
 1 \leq i \leq sN, 1 \leq j \leq tN \quad (2)
 \end{array}$$

Theoretically, the phases correspond to the test phase in the same points, with only tiny translations from the test phase. Assume the tiny translations are  $a_1, a_2, \dots, a_{(i-1)tN+j}, \dots, a_{sN^*tN}$  ( $1 \leq i \leq sN, 1 \leq j \leq tN$ ) for corresponding built phase, respectively. After translating, the phases should match the test phase on corresponding points as:

$$\begin{array}{c}
 \text{Group } (i-1)sN+j: \\
 p_{i,j+a_{(i-1)sN+j}}, p_{i,j+tN+a_{(i-1)sN+j}}, \dots, p_{i,j+m^*tN+a_{(i-1)sN+j}} \\
 p_{i+sN,j+a_{(i-1)sN+j}}, p_{i+sN,j+tN+a_{(i-1)sN+j}}, \dots, p_{i+sN,j+m^*tN+a_{(i-1)sN+j}} \\
 \dots\dots \\
 p_{i+n^*sN,j+a_{(i-1)sN+j}}, p_{i+n^*sN,j+tN+a_{(i-1)sN+j}}, \dots, p_{i+n^*sN,j+m^*tN+a_{(i-1)sN+j}} \\
 1 \leq i \leq sN, 1 \leq j \leq tN \quad (3)
 \end{array}$$

Then all translated phases can be combined to obtain the result of test phase as:

$$W_{i+(k-1)^*sN, j+(l-1)^*tN} = p_{i+(k-1)^*sN, j+(l-1)^*tN+a_{(i-1)tN+j}} \quad (4)$$

The reconstruction problem becomes one to find the translation relations  $a_1, a_2, \dots, a_{(i-1)sN+j}, \dots, a_{sN^*tN}$ .

**Spline regression**

A natural way of smoothness associated with a function  $f \in W_2^m [0,1]$  is  $\int_0^1 f^{(m)}(t)^2 dt$  while a standard measure of goodness-of-fit to the data is the (average) residual sum-of-squares  $n^{-1} \sum_{i=1}^n (y_i - f(t_i))^2$  [8]. Thus the overall assessment of the quality of a candidate estimator  $f$  is provided by the convex sum as:

$$(1 - q)n^{-1} \sum_{i=1}^n (y_i - f(t_i))^2 + q \int_0^1 f^{(m)}(t)^2 dt \tag{5}$$

for some  $0 < q < 1$ . An optional estimator could then be obtained by minimizing this functional over  $W_2^m [0, 1]$ . The parameter  $q$  in (5) governs the tradeoffs between smoothness and goodness-of-fit and, for that reason, is usually referred to as the smoothing parameter [8].

For our problem, according to the smoothing characteristics of the test wavefront, when  $q$  is set to be 0 in (5) for more emphasises on smoothness, the overall assessment of the smooth quality of the wavefront can be provided by minimized the representation as:

$$\sum = \sum_{i=1}^{N-1} \sum_{j=1}^{M-1} (w_{i-1,j-1} + w_{i-1,j+1} + w_{i+1,j-1} + w_{i+1,j+1} - 4w_{ij})^2 \tag{6}$$

Substitute Eq. (4) into Eq. (6), using regression to minimize the value of  $\sum$ , a linear equation set can be obtained as:

$$A_{sN \times IN, sN \times IN} \mathbf{a} = \mathbf{p} \tag{7}$$

where  $\mathbf{a}$  is the translation vector to be determined,  $\mathbf{p}$  is a vector whose elements are representations of  $p_{i,j}$  in (2). Solve Eq. (7),  $\mathbf{a}$ , and  $a_1 \dots a_{sN \times IN}$ , can be obtained, and so is the test profile (Eq. (4)).

**Computational testing**

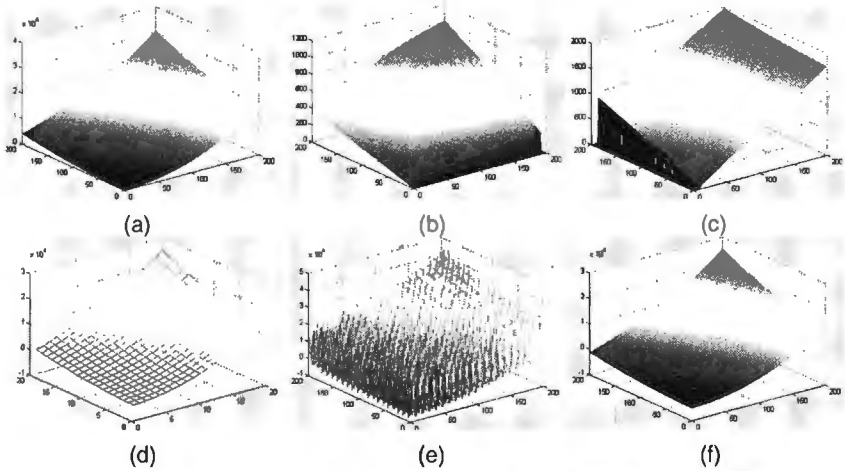
To explore the feasibility of the algorithm, computer simulation is carried out. A phase representation was utilized as:

$$w(x, y) = \frac{2\pi}{0.6328} (1.45x\sqrt{x^2 + y^2} + 7.0y\sqrt{x^2 + y^2} + 0.3\sqrt{x^2 + 3y^2} + \sqrt{x^2 + y^2}) \tag{8}$$

Equation (8) is used to create a phase for reconstruction testing. Figure 1 (a) shows the 200X200 sampling points of the simulated phase with the sampling point distance as 0.08mm. Figure 1 (b) and (c) show the phase differences corresponding to shear quantities  $sN$  and  $tN$  in  $x$  and  $y$  direction.

Both  $sN$  and  $tN$  are set to be 10 sampling distance. Based on the proposed reconstruction algorithm, the two phase differences are firstly divided into 10 pairs for respective phase recovery by our early algorithm [4], one corresponding recovered result is shown as Figure 1 (d). They are combined to be shown as Figure 1 (e).

The spline regression algorithm is applied to it obtain the data  $\mathbf{a}$ , then the reconstructed phase is shown as Figure 1 (f). Figure 1 (g) shows the reconstruction error comparing the original simulated phase. The reconstruction error  $PV=0.008\mu\text{m}$ , the relative error was as low as 0.00002%.



## Conclusions

The limitation of the current test phase reconstruction algorithms in shearing interferometry is examined. A new algorithm is proposed to solve the phase reconstruction problem experienced when the shear is many times of the sampling interval. The algorithm makes use of the smoothing characteristics of general wavefronts and spline regression. The results of the computational studies demonstrated the feasibility of the proposed algorithm.

## References

- [1] B. R. Hunt, Matrix formation of the reconstruction of phase from phase differences, *J. Opt. Soc. Am.*, **69**(3), 1979.
- [2] Okuda S, Nomura T, Kamiya K, Miyashiro H, *et al*, High-precision analysis of a lateral shearing interferogram by using the integration method and polynomials, *App. Opt.*, **39**(28), 2000.
- [3] Xinkang Tian, Masahide Ltoh, and *et al*, Simple algorithm for large-grid phase reconstruction of lateral-shearing interferometry, *App. Opt.*, **34**(31), 1995.
- [4] X. Liu, Y. Gao, and Z. Li, An accurate phase recovery algorithm for lateral shearing interferometry, *Proc 5<sup>th</sup> ISMTII, International Symposium on Measurement Technology and Intelligent Instruments*, Cairo, Egypt, 2001.
- [5] Francois Roddier, and Claude Roddier, Wavefront reconstruction using iterative Fourier transforms, *App. Opt.*, **30**(11), 1991.
- [6] Wei Shen, Ming Wen Chang, and Der-shen Wan, Zernike polynomial fitting of lateral shearing interferometry, *Opt. Eng.*, **36**(3), 1997.
- [7] Elster C, Exact two-dimensional wavefront reconstruction from lateral shearing interferograms with large shears, *App. Opt.*, **33**(2), 2000.
- [8] Randall L. Eubank, *Nonparametric regression and spline smoothing*, 2e, Marcel Dekker, Inc., New York, 1999.

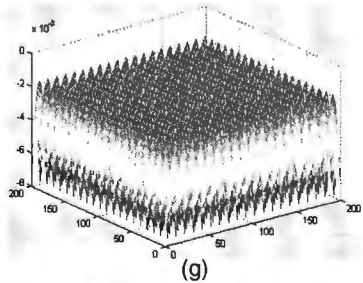


**Figure 1** Testing profiles and the recovered profiles

# Ultraprecision Fabrication of Glass Ceramic Aspherical Mirror by ELID-grinding with Nano-level Positioning Hydrostatic Driving Machine

T.SUZUKI, H.OHMORI, Y.UEHARA, Y.YAMAGATA, W.LIN, Y.DAI, K.EBIZUKA, A.MAKINOUCI AND H.TASHIRO

The Institute of Physical and Chemical Research (RIKEN), 2-1 Hirosawa, Wako, Saitama, 351-0198, Japan

## Abstract

Glass-ceramic aspherical mirrors used as optical elements in space astronomical observatory must be machined with very high profile accuracy and surface smoothness. Precision grinding processes are very effective in fabrication of such profiles. In particular, ELID (Electrolytic In-Process Dressing) grinding method is possible to achieve ultraprecision smooth surface of hard and brittle materials. To obtain ultra smooth surface required by astronomical observatory, final polish process which required long time after conventional grinding process was necessary. ELID grinding method using an ultraprecision grinding machine tool with nano-level hydrostatic guide will be very effective in reducing the time required for final polishing process. In this paper, a new ELID grinding system is introduced and experimental results of fabricating glass-ceramic paraboloidal mirror are discussed. The profile accuracy of the fabricated glass-ceramic mirror was within  $0.54\mu\text{m P-V}$ .

## Introduction

Efficient ultraprecision grinding process is important for research and developments in especially optics like astronomical observatory. It is also important in the field of industry to form ultraprecision dies for aspherical lenses,  $f-\theta$  lenses, prism and so on. Also ultraprecision metrological system combined with machine tool is very important for ultra high precision machining with high repeatability.

In this paper, a 4-axis ultraprecision non-contact hydrostatic driving system to meet the needs of 3-dimensional nano-level fabrication is introduced. A fabrication experiment of the paraboloidal mirror (130mm in diameter) of Zerodur glass-ceramic material using this ELID grinding system was carried out to verify the system performance. The ground profile was measured by an on-machine metrology profile probe, then profile error was calculated to compensate and feedback to NC data during the grinding processing in order to achieve higher profile accuracy.

## ELID grinding Process

The ELID (Electrolytic in-process dressing) grinding method was proposed by Ohmori et al [1]. It consists of a metal bonded diamond abrasive wheel, electrolytic power supply, electrode, and electrolytic coolant. The metal bonded diamond abrasive wheel is connected to the positive terminal of a power supply via electrical contact and a fixed electrode is connected to the negative. A clearance of approximately 0.1mm was kept between the grinding wheel and the electrode.

Figure 1 shows the schematic illustration of the ELID grinding process. Initial electrolytic process removes metal matrix of the grinding wheel to form oxide layers to let the abrasive protrude from the grinding wheel surface. As the protruded abrasives wear during grinding process, the oxide layer also becomes thinner. The

wear of the oxide layer increases the wheel's electric-conductivity, oxidizing the metal bonded diamond wheel again. By this electrolytic process, the thickness of oxide layer is maintained to give stable abrasive protrusion.

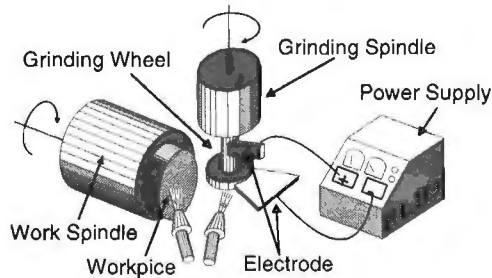


Figure 1 Machine tool and workpiece setup for ELID grinding

### Ultraprecision Non –Contact Hydrostatic Machine Tool

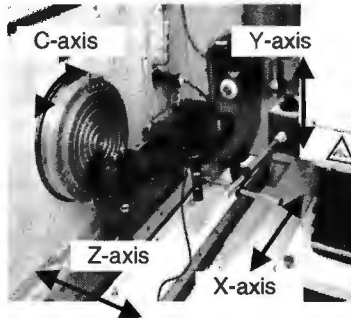
The configuration of the 4-axis ultraprecision non-contact hydrostatic machine tool is shown in Figure 2 and Figure 3. Aspherical and axis-asymmetric curved surfaces can be formed with this machine by single point diamond cutting or grinding process using ELID grinding method. The machine has three linear axes X, Y, Z and one rotational axis C. Those linear axes are controlled by a non-contact hydrostatic screw system and double laser linear scale to reach nanometer precision. The straightness and position repeatability of the linear axis for full stroke were better than 150nm and 20nm respectively. In addition, step response of 2nm was verified. The rotation spindle C is the ultraprecision pneumatic spindle which holds the workpiece. The maximum rotation speed of the ultra high precision grinding spindle mounted on Y-axis is 20,000 rpm. The profile accuracy can be measured by using the on-machine metrology probe mounted on the Y-column without removing the workpiece from the machine tool. Specifications of the ultrahigh precision machine tool are listed in Table 1.

**Table 1** Specifications of 4-axes ultrahigh precision machine tool

Linear axis X, Y, Z	Moving range: X: 350mm,Y: 100 mm, Z: 150 mm Scale resolution: 0.7nm / 8.7nm
C axis	Precision air bearing Max speed: 1,500rpm Rotary encoder resolution: 1/4,096deg
Grinding spindle	Precision air bearing Rotary speed: 6,000~20,000rpm
On-machine metrology probe	Measuring range Axis symmetric: $\Phi$ 200mm Axis-Asymmetric: L250mmxH50mm



(a) Configuration



(b) Construction 4-axis

Figure 3 4-axis ultraprecision machine

### Ultraprecision Grinding of Glass- Ceramic Paraboloidal Mirror

An ultraprecision machine tool system was used to fabricate a concave paraboloidal mirror in this experiment. The material of the mirror used was Zerodur. The grinding wheel used were cast iron fiber bonded diamond grinding wheels with grain size of #400, #1200, #2000 and #4000. The ELID power supply used was ED920. Table 2 shows the ELID grinding conditions, and Figure 4 shows the state of paraboloidal mirror processing. In addition, compensation feedback using on-machine metrology probe was applied during paraboloidal mirror fabrication.

**Table 2** Grinding conditions

	Rough Grinding (#400, #1200, #2000)	Finish Grinding (#4000)
Wheel Diameter	$\Phi$ 75mm	
Tool Feed	20~5 $\mu$ m	10~1 $\mu$ m
Rotation Speed	10000rpm	
Depth of Cut	5 $\rightarrow$ 1 $\mu$ m	1 $\rightarrow$ 0.5 $\mu$ m
ELID Condition	60V, 5A, on:2 $\mu$ s off:2 $\mu$ s Rotation Speed 6,000rpm	

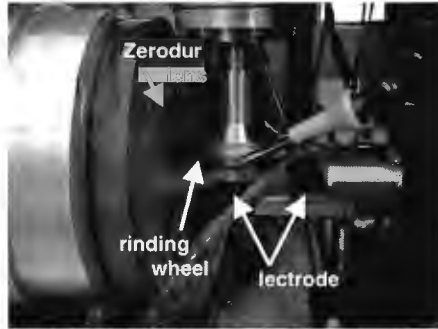


Figure 4 State of paraboloidal lens processing

### Experiment Results

Figure 5 shows a photo of the on-machine metrology probe measuring Zerodur specimen. Figure 6 shows the results of the form measured by the on-machine metrology instrument. The finished surface was completely transparent and mirror like. The profile accuracy of  $0.54\mu\text{m}$  p-v, and surface roughness of  $24\text{nm}$  (average) at the center was obtained. The processing could be completed within about thirty hours in total, which could be considered to be an efficient and stable process as an ultrahigh precision fabrication.

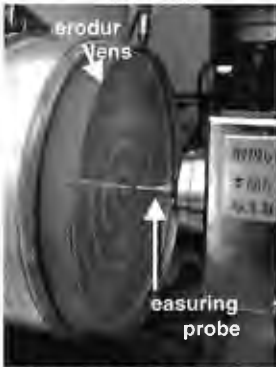


Figure 5 Paraboloidal lens processing

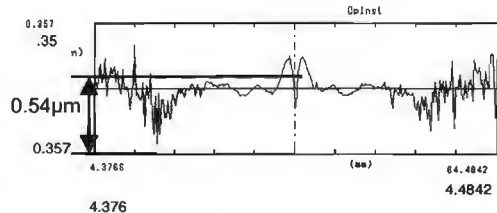


Figure 6 Profile accuracy of #4000

### Conclusion

A new non-contact hydrostatic ultraprecision machine tool system is introduced and a fabrication of paraboloidal glass-ceramic mirror was successfully carried out. The result implies the potential performance of the system, but there is still room to improve machining conditions in

order to obtain more stable value in accuracy and roughness

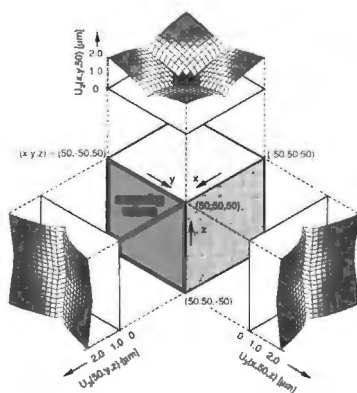
### References

- [1] H. Ohmori et al.: Electrolytic in-process dressing (ELID) grinding technique for ultraprecision mirror surface machining, International journal of the JSPE, 1992, 26(4), p278-278



National Institute for Metrology and Technology

## NMI Setting Standards for Measurements



Measurement with absolute accuracy

Providing traceability to international measurement standards

Creating essential references

Enabling improvement of quality of products and production

Underpinning innovation in production technology

NMI can provide you with:

Calibrations, Uncertainty Analysis, Training and Education, Consultancy,  
Contract Research

NMI is appointed by Dutch Government and responsible for the National  
Measurement Standards and Reference Materials.

More information:

Dr. Ir. R.H. Bergmans, Scientist

phone +31 15 269 1641

Drs. A.H.L. Aalbers, Department Manager

phone +31 15 269 1537

e-mail: [length@nmi.nl](mailto:length@nmi.nl)

Nederlands Meetinstituut

Van Swinden Laboratorium B.V.

P.O. Box 654

2600 AR Delft

The Netherlands





 **Agilent Technologies**  
Introducing the HP Way

**Assemblon**  
ASSEMBLY SOLUTIONS - AMMORAL ENGINEERING

 **ASML**

 **PHILIPS**

 **IBS**  
Precision Engineering Inc.

**TOP**



**LIOP**  
PRECISION

**NEW WAY**

NanoFocus

**Mitutoyo**

**TU/e** Technische Universiteit Eindhoven

Bibliotheek

Postbus 90159  
5600 RM Eindhoven  
Tel: 040 - 247 22 24



200213373



**euspen**